

ABSTRACT

Title of Document: THE SCALING OF PERFORMANCE AND
LOSSES IN MINIATURE INTERNAL
COMBUSTION ENGINES.

Shyam Menon

Directed By: Dr.Christopher Cadou, Associate Professor,
Department of Aerospace Engineering

Miniature glow ignition internal combustion (IC) piston engines are an off-the-shelf technology that could dramatically increase the endurance of miniature electric power supplies and the range and endurance of small unmanned air vehicles provided their overall thermodynamic efficiencies can be increased to 15% or better. This thesis presents the first comprehensive analysis of small (<500 g) piston engine performance. A unique dynamometer system is developed that is capable of making *reliable* measurements of engine performance and losses in these small engines. Methodologies are also developed for measuring volumetric, heat transfer, exhaust, mechanical, and combustion losses. These instruments and techniques are used to investigate the performance of seven single-cylinder, two-stroke, glow fueled engines ranging in size from 15 to 450 g (0.16 to 7.5 cm³ displacement). Scaling rules for power output, overall efficiency, and normalized power are developed from the data. These will be useful to developers of micro-air vehicles and miniature power systems.

Report Documentation Page		Form Approved OMB No. 0704-0188
Public reporting burden for the collection of information is estimated to average 1 hour per response, including the time for reviewing instructions, searching existing data sources, gathering and maintaining the data needed, and completing and reviewing the collection of information. Send comments regarding this burden estimate or any other aspect of this collection of information, including suggestions for reducing this burden, to Washington Headquarters Services, Directorate for Information Operations and Reports, 1215 Jefferson Davis Highway, Suite 1204, Arlington VA 22202-4302. Respondents should be aware that notwithstanding any other provision of law, no person shall be subject to a penalty for failing to comply with a collection of information if it does not display a currently valid OMB control number.		
1. REPORT DATE 2010	2. REPORT TYPE	3. DATES COVERED 00-00-2010 to 00-00-2010
4. TITLE AND SUBTITLE The Scaling of Performance and Losses in Miniature Internal Combustion Engines		5a. CONTRACT NUMBER
		5b. GRANT NUMBER
		5c. PROGRAM ELEMENT NUMBER
6. AUTHOR(S)	5d. PROJECT NUMBER	
	5e. TASK NUMBER	
	5f. WORK UNIT NUMBER	
7. PERFORMING ORGANIZATION NAME(S) AND ADDRESS(ES) University of Maryland, College Park, College Park, MD, 20742		8. PERFORMING ORGANIZATION REPORT NUMBER
9. SPONSORING/MONITORING AGENCY NAME(S) AND ADDRESS(ES)		10. SPONSOR/MONITOR'S ACRONYM(S)
		11. SPONSOR/MONITOR'S REPORT NUMBER(S)
12. DISTRIBUTION/AVAILABILITY STATEMENT Approved for public release; distribution unlimited		
13. SUPPLEMENTARY NOTES		
14. ABSTRACT Miniature glow ignition internal combustion (IC) piston engines are an off-the-shelf technology that could dramatically increase the endurance of miniature electric power supplies and the range and endurance of small unmanned air vehicles provided their overall thermodynamic efficiencies can be increased to 15% or better. This thesis presents the first comprehensive analysis of small (<500 g) piston engine performance. A unique dynamometer system is developed that is capable of making reliable measurements of engine performance and losses in these small engines. Methodologies are also developed for measuring volumetric, heat transfer, exhaust mechanical, and combustion losses. These instruments and techniques are used to investigate the performance of seven single-cylinder, two-stroke, glow fueled engines ranging in size from 15 to 450 g (0.16 to 7.5 cm³ displacement). Scaling rules for power output, overall efficiency, and normalized power are developed from the data. These will be useful to developers of micro-air vehicles and miniature power systems. The data show that the minimum length scale of a thermodynamically viable piston engine based on present technology is approximately 3 mm. Incomplete combustion is the most important challenge as it accounts for 60-70% of total energy losses. Combustion losses are followed in order of importance by heat transfer, sensible enthalpy, and friction. A net heat release analysis based on in-cylinder pressure measurements suggest that a two-stage combustion process occurs at low engine speeds and equivalence ratios close to 1. Different theories based on burning mode and reaction kinetics are proposed to explain the observed results. High speed imaging of the combustion chamber suggests that a turbulent premixed flame with its origin in the vicinity of the glow plug is the primary driver of combustion. Placing miniature IC engines on a turbulent combustion regime diagram shows that they operate in the flamelet in eddy regime whereas conventional scale engines operate mostly in the wrinkled laminar flame sheet regime. Taken together, the results show that the combustion process is the key obstacle to realizing the potential of small IC engines. Overcoming this obstacle will require new diagnostic techniques measurements, combustion models, and high temperature materials.		

15. SUBJECT TERMS					
16. SECURITY CLASSIFICATION OF:			17. LIMITATION OF ABSTRACT Same as Report (SAR)	18. NUMBER OF PAGES 454	19a. NAME OF RESPONSIBLE PERSON
a. REPORT unclassified	b. ABSTRACT unclassified	c. THIS PAGE unclassified			

The data show that the minimum length scale of a thermodynamically viable piston engine *based on present technology* is approximately 3 mm. Incomplete combustion is the most important challenge as it accounts for 60-70% of total energy losses. Combustion losses are followed in order of importance by heat transfer, sensible enthalpy, and friction. A net heat release analysis based on in-cylinder pressure measurements suggest that a two-stage combustion process occurs at low engine speeds and equivalence ratios close to 1. Different theories based on burning mode and reaction kinetics are proposed to explain the observed results. High speed imaging of the combustion chamber suggests that a turbulent premixed flame with its origin in the vicinity of the glow plug is the primary driver of combustion. Placing miniature IC engines on a turbulent combustion regime diagram shows that they operate in the ‘flamelet in eddy’ regime whereas conventional-scale engines operate mostly in the ‘wrinkled laminar flame sheet’ regime. Taken together, the results show that the combustion process is the key obstacle to realizing the potential of small IC engines. Overcoming this obstacle will require new diagnostic techniques, measurements, combustion models, and high temperature materials.

THE SCALING OF PERFORMANCE AND LOSSES IN MINIATURE INTERNAL
COMBUSTION ENGINES

By

Shyam Kumar Menon

Dissertation submitted to the Faculty of the Graduate School of the
University of Maryland, College Park, in partial fulfillment
of the requirements for the degree of
[Doctor of Philosophy]
[2010]

Advisory Committee:

Associate Professor Christopher P Cadou, Chair/Advisor
Associate Professor Kenneth Yu
Professor Gregory Jackson
Professor J. Gordon Leishman
Professor Manoussos Grillakis

© Copyright by
[Shyam Menon]
[2010]

Acknowledgements

I would like to acknowledge several people who have helped me in many different ways in achieving this degree and making graduate school at Maryland one of the best experiences in my life. First and foremost, I would like to acknowledge my advisor in graduate school, Dr. Christopher Cadou who has helped train me into someone capable of conducting scientific research. His knowledge of engineering methods and practices, attention to detail, high standards of work and diligence are just some of the things that I have tried to imbibe and hope to uphold in my future career. I am grateful to him for finding the resources and funds to allow me to complete my degree. I would like to thank other faculty members including the members of my advisory committee who have kept my best interests in mind and helped me in various ways during my stay here. I appreciate greatly the friendship and company of two of my very good friends and office mates, Anand Veeraragavan and Kiran Dellimore who have made my stay here interesting and enjoyable. I would also like to acknowledge several of my co-workers from the Aerospace department including Tim Leach, John Day, Nathan Moulton, Dan Waters, Daanish Maqbool, Jeff St.Claire, Amardip Ghosh, Fernando Raffan, Andrew Voegle and Evandro Valente for their help with various projects and just being great people to work with. I would be amiss if I did not acknowledge the really good undergraduate students who I had an opportunity to work with in the lab and who played a vital role to getting some of my experiments built and operated. For this I am grateful among others to Andrew Churchill , Pete Gackenbach, Jon Geerts, Joshua Park and Ted Bubert.

I would like to acknowledge many of the great friends that I have made here at the University of Maryland who I've had fun living with (Ashok, Abhi, Lavanya, Som, Renga, Adarsh, Shiv, Ed, Wallace, Asif), playing squash with (Rahul, Mike L & Mike S, Ruud, Anand B) and others who I might have missed out here.

My parents, (Mr. P.G. Kumar and Mrs. Nirmala Kumar), I thank you for your presence, love and blessings which has gone a long way in making any of this even possible. My sister, Shalini and brother-in-law, Rutu, I would like to thank both of you for your support and being always available to hear me out in happy and tough times.

Finally, I would like to thank the support of our funding agencies which made this research work possible. I would like to thank Minor Appleman and Vince Castelli at the Naval Air Surface Warfare Center Carderrock for partial support of this work. I would like to thank Dr. Tom Doligalski and the Army Research Office for supporting this research work through the MAV-MURI program.

Table of Contents

Acknowledgements.....	ii
Table of Contents.....	iv
List of Tables.....	ix
List of Figures.....	xi
List of Figures.....	xi
Chapter 1 : Introduction.....	1
1.1 Miniature Power Systems.....	1
1.1.1 Demand for Compact Portable Power.....	1
1.1.2 Representation of Target Region.....	5
1.1.3 Energy Density and Power Density.....	7
1.1.4 Comparison of Energy Storage Materials.....	8
1.1.5 Case Study.....	10
1.1.6 Hobby Engines.....	12
1.1.7 Comparison of Small Scale Power Systems.....	13
1.2 Losses in Miniature IC Engines.....	19
1.2.1 Thermal Loss.....	19
1.2.2 Frictional Loss.....	23
1.2.3 Combustion Loss.....	24
1.2.4 Mass Leakage Loss.....	26
1.2.5 Flow and Scavenging Losses.....	27
1.3 Previous Work.....	28
1.3.1 Performance Measurements in Miniature IC Engines.....	28
1.3.2 Scaling Issues in IC Engines.....	35
1.3.3 Fundamental Investigations of Miniature IC Engines.....	36
1.4 Motivation, Objectives and Approach.....	43
Chapter 2 : Small Engine Dynamometer System.....	47
2.1 Engine Testing Methods.....	47
2.2 Two–Stroke Engine Cycle.....	49
2.3 Engines.....	52
2.4 Engine Construction.....	53
2.5 Fuels.....	59
2.6 Challenges.....	61
2.7 Dynamometer Setup.....	62
2.7.1 Torque Measurement Principle.....	62
2.7.2 Vibration Control.....	65
2.7.3 Hysteresis Brake.....	65
2.7.4 Transmission Setups.....	69
2.7.5 Engine Cooling.....	73
2.8 Sensors and Measurements.....	74
2.8.1 Torque.....	74
2.8.2 Speed.....	77
2.8.3 Air Flow.....	78

2.8.4 Fuel Flow	80
2.8.5 Temperatures.....	81
2.8.6 Fuel Pressure.....	82
2.9 Control System.....	82
2.9.1 Theory	83
2.9.2 Implementation	85
2.10 Data Acquisition	86
2.10.1 Sensor Measurements	86
2.10.2 User Interface.....	88
2.10.3 Data Monitoring and Recording	89
2.11 Computed Quantities	90
2.12 Engine Test Procedure	92
2.12.1 Engine ‘Break-In’	92
2.12.2 Load Cell Calibration.....	93
2.12.3 Engine Start-Up.....	94
2.12.4 Engine Performance Map Measurement Procedure	95
2.12.5 Engine Shut-Down	96
2.13 Uncertainty Analysis.....	96
2.14 Atmospheric Corrections	96
Chapter 3 : Engine Performance Data and Scaling Analyses	98
3.1 Measurement Results	98
3.1.1 Engine Performance – AP Hornet 09.....	100
3.1.2 Engine Performance – Cox 010	107
3.1.3 Engine Performance – Cox 020	110
3.1.4 Engine Performance – Cox 049	114
3.1.5 Engine Performance – AP Wasp 061.....	117
3.1.6 Engine Performance – AP Yellowjacket 15	120
3.1.7 Engine Performance – OS 25 FX.....	123
3.1.8 Engine Performance – OS 40 FX.....	126
3.1.9 Engine Performance – OS 46 FX.....	131
3.2 Scaling analysis.....	134
3.2.1 Literature Survey of Engine Data	134
3.2.2 Scaling of Engine Physical Properties	137
3.2.3 Peak Engine Performance Data	141
3.2.4 Scaling of Peak Engine Torque, Power and Overall Efficiency	142
3.2.5 Scaling of Normalized Power and BMEP	148
3.3 Determination of Minimum Engine Size.....	151
Chapter 4 : Measurement and Scaling of Engine Losses.....	155
4.1 Energy Balance in An Engine.....	155
4.1.1 First Law Analysis	155
4.1.2 Second Law Analysis.....	156
4.2 Energy Balance in A Two Stroke Engine	157
4.2.1 Scavenging Losses	158
4.2.2 Blowby Losses	160
4.2.3 Energy Balance with Control Volume around Complete Engine	161
4.3 Criteria for Comparing Engine Loss Mechanisms.....	165

4.3.1 Constant Engine Speed and Equivalence Ratio	166
4.3.2 Constant Mean Piston Speed and Equivalence Ratio	166
4.4 Intake Losses	167
4.4.1 Measurement Technique	167
4.4.2 Scaling of Intake Losses	168
4.5 Heat Transfer Losses	172
4.5.1 Measurement Technique	172
4.5.2 Measurement Results	182
4.5.3 Estimation of Mixture Transport Properties	188
4.5.4 Scaling of Thermal Losses	194
4.6 Frictional Losses	197
4.6.1 Measurement Technique	197
4.6.2 Measurement Results	201
4.6.3 Scaling of Frictional Losses	205
4.7 Exhaust Gas Enthalpy	208
4.7.1 Measurement Technique	208
4.7.2 Scaling of Exhaust Gas Enthalpy	208
4.8 Incomplete Combustion Losses	211
4.8.1 Measurement Technique	211
4.8.2 Scaling of Combustion Losses	211
4.9 Scaling of Engine Loss Mechanisms	213
4.9.1 Constant Engine Speed and Fuel Air Mixture Ratio	213
4.9.2 Constant Engine Speed of 12000 rpm and Fuel Air Mixture Ratio	216
4.9.3 Constant Mean Piston Speed and Fuel Air Mixture Ratio	219
4.10 Summary of Engine Losses	222
Chapter 5 : In-Cylinder Pressure Measurements	225
5.1 In-Cylinder Pressure Measurements	225
5.2 Experimental Setup	226
5.2.1 Fiber Optic Pressure Sensor	226
5.2.2 Engines	230
5.2.3 Sensor Installation	231
5.2.5 Data Acquisition	239
5.2.6 Dynamometer Setup	240
5.2.7 Test Procedure	242
5.3 Analysis of results	242
5.3.1 Peak Cylinder Pressure and Corresponding Crank Location	242
5.3.2 Cycle-To-Cycle Variation	242
5.3.3 Burn Rate Analysis	243
5.3.4 Estimation of Weibe Profiles	247
5.3.5 Heat Release Rate	248
5.3.6 Heat Release Fraction	252
5.3.7 Ignition Timing	252
5.3.8 Burn Duration	253
5.3.9 Indicated Power Output	254
5.3.10 Power Loss	255
5.4 Measurement Results	255

5.4.1 Cylinder Pressure Trace	257
5.4.2 Peak Cylinder Pressure and Location	263
5.4.3 Cycle to Cycle Variation	266
5.4.4 Net Heat Release Rate	268
5.4.5 Ignition Timing And Burn Duration	277
5.4.6 Mass Burned Fraction	280
5.4.7 Heat Release Rate	282
5.4.8 Scaling Analysis	284
Chapter 6 : Combustion Visualization and Analysis	289
6.1 Combustion Analysis in Miniature IC Engines	289
6.2 Setup for In-Cylinder Optical Visualization	291
6.2.1 Experimental Setup	291
6.2.2 Experimental Procedure	300
6.2.3 Effect of Mixture Ratio	302
6.2.4 Effect of Engine Speed	311
6.3 Combustion Regimes in Miniature Engines	315
6.3.1 Turbulence Length Scales and Combustion Regimes	317
6.3.2 Damköhler Number and Reynolds Number	318
6.3.3 Regime Diagrams	320
6.3.4 Procedure for Placing Engines on the Regime Diagram	322
6.3.5 Combustion Regimes in Miniature IC Engines	327
Chapter 7 : Investigation of Engine-Generator Setup	334
7.1 Generators	334
7.2 Apparatus	336
7.3 Procedure	340
7.4 Data Processing	340
7.5 Results	341
7.6 Power and Energy Density	354
Chapter 8 : Conclusions and Future Work	357
8.1 Summary and Conclusions	357
8.2 Key Findings and Contributions	362
8.3 Future Work	364
Appendix A	368
A.1 Energy Balance With Control Volume Around Each Engine Component	368
Appendix B	374
Appendix C	379
C.1 Elements Considered in Reaction Mechanism for Hydrocarbon And Nitrogen	379
C.2 Species Considered in Reaction Mechanism for Hydrocarbon And Nitrogen	379
Appendix D	381
D.1 Transport Properties File for the Nitromethane/Methanol Reaction Mechanism	381
Appendix E	385
E.1 Cylinder Pressure Measurements For The OS 40 FX Engine	385
E.2 Cylinder pressure measurements for the OS 46 FX Engine	395
Appendix F	404

F.1 Estimation of mass burning fraction from gross heat release rate.....	404
Appendix G.....	406
G.1 Measurement Error	406
G.2 Uncertainty of a computed result.....	407
G.3 Uncertainty analysis for a least squares fit.....	408
Appendix H.....	411
H.1 Estimation of Pressure Drop in Engine Intake Tubing	411
Bibliography	413

List of Tables

Table 1–1: Classification of UAV’s based on altitude, range and endurance capabilities.	2
Table 1–2: Survey of several applications requiring compact portable power.	5
Table 1–3: Operating parameters for electrical and combustion based power systems used on a miniature unmanned air vehicle.	11
Table 2–1: Specifications of miniature IC engines tested in the study.	52
Table 2–2: Properties of glow fuel constituents and overall properties of the mixture.	60
Table 2–3: Hysteresis brake ratings and engines used with corresponding brakes. ...	66
Table 2–4: Specifications for the load cells used on in this research work.	75
Table 2–5: Specifications for the air flow meters used in this research work.	80
Table 2–6: Specifications of the weighing scales used in fuel flow rate measurement.	81
Table 2–7: Values for the PID control variables used in this study.	85
Table 3–1: Summary of engine performance data for the AP Hornet engine.	102
Table 3–2: Summary of engine performance data for the Cox 010 engine.	109
Table 3–3: Summary of engine performance data for the Cox 020 engine.	112
Table 3–4: Summary of engine performance data for the Cox 049 engine.	116
Table 3–5: Summary of engine performance data for the AP Wasp engine.	119
Table 3–6: Summary of engine performance data for the AP Yellowjacket engine.	122
Table 3–7: Summary of engine performance data for the OS 25 FX engine.	125
Table 3–8: Summary of engine performance data for the OS 40 FX engine.	129
Table 3–9: Summary of engine performance data for the OS 46 FX engine.	133
Table 3–10: Peak values for engine performance parameters.	141
Table 3–11: Comparison of BMEP values for different classes of engines.	150
Table 3–12: Results for thermodynamic break even analysis using normalized power and power output.	154
Table 4–1: Engine operating speeds corresponding to a constant mean piston speed of 4.77 ms^{-1} for all the engines tested in this work.	167
Table 4–2: Peak value of delivery ratio and corresponding engine operating speed for the engines tested in this work.	172
Table 4–3: Peak value of delivery ratio and corresponding engine operating speed for the engines tested in this work.	187
Table 4–4: Specifications for the motors used in the frictional power loss measurements.	199
Table 4–5: Linear fitting relationships developed for the frictional power loss for different engines.	203
Table 5–1: Specifications for the fiber optic pressure sensor made by Optrand Inc. used in this work.	228
Table 5–2: Specifications of miniature IC engines tested in the study.	231
Table 5–3: Specifications of the two different shaft encoders utilized in this work.	236
Table 5–4: Port opening and closing timing for the three engines tested in this work.	256

Table 5–5: Comparison between polytropic exponent estimated using cylinder pressure measurements and those used in an analytical model for a 4 cylinder SI engine.	260
Table 6–1: Limiting values for the various operating settings on the high speed Phantom camera and the values selected in this particular research.	297
Table 6–2: Propeller sizes used with the OS 46 FX engine along with the corresponding engine speeds and fuel–air mixtures explored in this study.....	301
Table 6–3: Operating conditions for different engines investigated in the work of Abraham et al. Engines 1–5 were operated on propane and 6–7 were operated on octane.	327
Table 6–4: Variable parameters explored in the analysis of combustion regimes for methanol fueled two–stroke miniature IC engines.	327
Table 7–1: Manufacturer’s specifications for the AC generator tested here.	336
Table 7–2: Positions of switches, corresponding resistors connected and net resistance for the different settings on the load bank.	339
Table 7–3: Throttle setting, fuel/air mixture ratio and equivalence ratio for the engine operating conditions reported in this section.	341
Table 7–4: Performance of the engine–generator system consisting of the OS 46 engine with the Sullivan S675–300 generator at operating conditions corresponding to peak power output.....	355
Table H–1: Pressure drop calculation in engine air flow setup for the OS 46 engine operating at a speed of 17000 rpm. Engine air flow rate at this operating point is 0.75 gs ⁻¹ (36.7 lpm). Total pressure drop equals 0.003 bar.....	412

List of Figures

Figure 1–1: Altitude and endurance capabilities for a wide range of unmanned air vehicles.	3
Figure 1–2: Altitude and endurance capabilities for close range unmanned air vehicles.	4
Figure 1–3: Power requirement and mass for miniature unmanned air vehicles.....	4
Figure 1–4: Power consumption and stored energy capacity for miniature applications with contours of constant endurance. Marked quadrilateral represents area of interest in this work.	7
Figure 1–5: Energy density by mass and energy density by volume for a wide range of energy storage materials sources.	9
Figure 1–6: Photograph of an AP Yellowjacket engine [18]......	13
Figure 1–7: Photograph of a PAW 049 engine [19].	13
Figure 1–8: Ragone plot of power and energy density with contours of constant endurance with data plotted for an aircraft internal combustion engine.....	16
Figure 1–9: Ragone plot of power and energy density with contours of constant endurance comparing different power systems.....	17
Figure 1–10: Surface to volume ratio for different types of piston engines as a function of displacement volume.....	20
Figure 1–11: Simple scaling analysis for a combustor device.....	21
Figure 1–12: Heat transfer coefficient as a function of initial pressure of fuel–air mixture in a micro–combustor with varying chamber height [41].	22
Figure 1–13: Residence time as a function of displacement volume for a large number of IC engines.	25
Figure 1–14: Photograph of the dynamometer setup used by Gierke to estimate performance characteristics of model airplane engines [65].	29
Figure 1–15: Schematic of the dynamometer developed by Gierke showing sensors used for measurements [65].	30
Figure 1–16: Torque measurement principle used by Raine in the dynamometer used to characterize model airplane engines [69].	31
Figure 1–17: Performance data obtained for an engine with displacement 9.95 cc (0.607 cu.in.) with a cylinder head temperature of 477 K (400 °F) and fuel with 67% methanol, 25% oil and 8% nitromethane[70].	33
Figure 1–18: Photograph of a setup used to estimate performance from an Enya model airplane engine [71].	34
Figure 1–19: Photograph of a setup used to estimate performance from a Cox 0.16 cc (0.01 cu.in.) displacement model airplane engine [72]......	35
Figure 1–20: Photograph of a setup used to estimate performance from a 4.9 cc (0.3 cu.in.) displacement, OS engines model airplane engine [77]......	37
Figure 1–21: Photograph of the cylinder head of the OS 30 FS engine showing the location of the pressure sensor and the glow plug [77].	38
Figure 1–22: Schematic of the measurement setup for in–cylinder pressure and crank angle location from a two–stroke glow fuel engine [78].	40
Figure 1–23: Photograph of a setup used to obtain in–cylinder pressure measurement and chemiluminescence images from a model airplane engine [79].	41

Figure 1–24: Close up photograph of the cylinder head showing the locations of the glow plug, the optical window and the pressure sensor [79].	41
Figure 1–25: Chemiluminescence images obtained inside the cylinder of a model airplane engine operating at 9600 rpm during one engine cycle [79].	43
Figure 2–1: Steps involved in a two–stroke engine cycle.	50
Figure 2–2: Pressure volume diagram for the two–stroke engine cycle.	50
Figure 2–3: Photographs of the model airplane engines evaluated in this study.	53
Figure 2–4: A complete view of the OS 40 FX engine. Figure reproduced from OS 40 FX manual with permission from OS engines.	54
Figure 2–5: An exploded view of the OS 40 FX engine. Figure reproduced from OS 40 FX manual with permission from OS engines [85].	55
Figure 2–6: Photograph of a #8 glow plug manufactured by OS Engines.	57
Figure 2–7: Photograph of a Cox 010 cylinder head incorporating the glow plug.	58
Figure 2–8: Exhaust muffler for the OS 40 FX engine. Figure reproduced from OS 40 FX manual with permission from OS engines [85].	58
Figure 2–9: Schematic layout of the dynamometer cradle assembly and brake with a geared transmission system.	64
Figure 2–10: Structural layout of the dynamometer cradle assembly and brake.	64
Figure 2–11: Structural layout of the engine cradle assembly.	65
Figure 2–12: HB–450 hysteresis brake connected to brake support plate with attached nose cone.	66
Figure 2–13: Cross sectional view of the Magtrol hysteresis brake [94].	67
Figure 2–14: HB–140 hysteresis brake attached to brake support plate.	68
Figure 2–15: HB–8 hysteresis brake attached to brake support plate.	69
Figure 2–16: Photograph of the small engine dynamometer system at the University of Maryland with geared transmission.	70
Figure 2–17: Photograph of the small engine dynamometer system at the University of Maryland with a belt transmission.	71
Figure 2–18: Schematic layout of the dynamometer for a direct drive type transmission system.	72
Figure 2–19: Photograph of the dynamometer with a direct drive type transmission system.	73
Figure 2–20 Photograph of the dynamometer with a direct drive type transmission system.	73
Figure 2–21: Photograph of the LSP–2 beam load cell.	74
Figure 2–22: Photograph of the Sensotec Model 311AT load cell.	75
Figure 2–23: Vector diagram showing the forces acting on the torque–measuring cradle and the mechanical constraints imposed on the cradle/load cell system.	76
Figure 2–24: Photograph of the ElectroSensors speed measurement system with the pulser disc, Hall effect sensor and the SA420 signal conditioner.	77
Figure 2–25: Photograph of the Monarch optical speed sensor.	78
Figure 2–26: Photographs of the TSI air flow meters used in this research.	80
Figure 2–27: Photographs of the Acculab weighing scales used for fuel flow rate measurement.	81
Figure 2–28: Photograph of the Omega PX139 pressure sensor.	82
Figure 2–29: Stable and unstable operating regimes of a model engine.	84

Figure 2–30: PID Control loop on dynamometer.	85
Figure 2–31: Schematic layout of the components of the data acquisition system also showing the measurement sensors and control signals associated with different DAQ modules.	86
Figure 2–32: Schematic layout of the data acquisition system for measuring fuel flow rate.....	88
Figure 2–33: NI– LABVIEW™ interface for measurement and engine control.....	89
Figure 2–34: Typical calibration data for the load cell.....	93
Figure 3–1: Performance map for the AP Hornet engine. Data sets represent different engine speeds.	100
Figure 3–2: Peak performance of the AP Hornet engine as a function of engine speed.	101
Figure 3–3: Efficiency as a function of $1/\phi$ for rich mixture ratios at different engine speeds for the AP Hornet 09 engine.	104
Figure 3–4: Efficiency as a function of ϕ for lean mixture ratios at different engine speeds for the Cox 049 engine.	105
Figure 3–5: Performance map for the Cox 010 engine. Data sets represent different engine speeds.	107
Figure 3–6: Peak performance of the Cox 010 engine as a function of engine speed.	108
Figure 3–7: Performance map for the Cox 020 engine. Data sets represent different engine speeds.	110
Figure 3–8: Peak performance of the Cox 020 engine as a function of engine speed.	111
Figure 3–9: Performance map for the Cox 049 engine. Data sets represent different engine speeds.	114
Figure 3–10: Peak performance of the Cox 049 engine as a function of engine speed.	115
Figure 3–11: Performance map for the AP Wasp engine. Data sets represent different engine speeds.	117
Figure 3–12: Peak performance of the AP Wasp engine as a function of engine speed.	118
Figure 3–13: Performance map for the AP Yellowjacket engine. Data sets represent different engine speeds.	120
Figure 3–14: Peak performance of the AP Yellowjacket engine as a function of engine speed.....	121
Figure 3–15: Performance map for the OS 25 FX engine. Data sets represent different engine speeds.	123
Figure 3–16: Peak performance of the OS 25 FX engine as a function of engine speed.	124
Figure 3–17: Performance map for the OS 40 FX engine at low engine speeds. Data sets represent different engine speeds.....	126
Figure 3–18: Performance map for the OS 40 FX engine at high engine speeds. Data sets represent different engine speeds.....	127
Figure 3–19: Peak performance of the OS 40 FX engine as a function of engine speed.	128

Figure 3–20: Performance map for the OS 46 FX engine. Data sets represent different engine speeds.	131
Figure 3–21: Peak performance of the OS 46 FX engine as a function of engine speed.	132
Figure 3–22: Scaling of overall engine mass with engine displacement.	138
Figure 3–23: Scaling of bore to stroke ratio with engine displacement.	138
Figure 3–24: Scaling of piston area with engine displacement.	139
Figure 3–25: Scaling of compression ratio with engine displacement.	140
Figure 3–26: Scaling of peak engine torque with engine displacement.	142
Figure 3–27: Scaling of peak engine power output with engine displacement.	143
Figure 3–28: Scaling of overall efficiency at peak power with engine displacement.	145
Figure 3–29: Scaling of specific fuel consumption (SFC) at peak power with engine displacement.	145
Figure 3–30: Delivery ratio as a function of displacement volume for the engines tested in this work at the operating points as presented in Fig. 3–28.	147
Figure 3–31: Scaling of peak normalized power with piston area.	149
Figure 3–32: Scaling of peak engine BMEP with engine displacement.	150
Figure 3–33: Determination of break–even point based on normalized power and piston area.	151
Figure 3–34: Determination of break–even point based on peak power output and engine displacement.	152
Figure 3–35: Determination of break–even point based on overall efficiency for engines without mufflers and engine displacement.	153
Figure 4–1: Schematic showing the scavenging process in a two stroke crankcase scavenged engine.	159
Figure 4–2: Energy balance in a two stroke engine with control volume drawn around the entire engine.	161
Figure 4–3: Delivery ratio at different fuel air mixture ratios and a constant engine speed of 10000 rpm for all engines.	168
Figure 4–4: Delivery ratio as a function of engine displacement for constant engine speeds of 10000 rpm, 12000 rpm and a constant mean piston speed of 4.77 ms^{-1} . All data sets correspond to an equivalence ratio of ~ 1	169
Figure 4–5: Heat transfer path from cylinder gases to the environment (Adapted from Heywood).	173
Figure 4–6: Experimental data for convective heat transfer correlation from Taylor and Toong [167].	178
Figure 4–7: Layout of dynamometer setup used to establish mean gas temperature data.	181
Figure 4–8: Photograph of the dynamometer setup for the measurement of mean gas temperature for the OS 40 FX engine.	182
Figure 4–9: Measurements of cylinder head temperature and fuel air mixture ratio as a function of coolant inlet temperature for a constant engine speed of 7000 rpm and a fuel–air mixture setting of 0.45 for the OS 25 FX engine.	183
Figure 4–10: Data sets for different fuel air mixture ratios and engine speeds for the OS 25 FX engine used to establish values for mean gas temperature.	184

Figure 4–11: Data sets for different fuel air mixture ratios and engine speeds for the OS 40 FX engine used to establish values for mean gas temperature.	185
Figure 4–12: Estimated mean gas temperature as a function of fuel air mixture ratio. Also presented are data points first estimated by Pinkel [170], later reported and inferred here from Taylor [167].	186
Figure 4–13: Calculations of mixture viscosity for three different equivalence ratios in the burnt and unburnt state as a function of mixture temperature.	190
Figure 4–14: Estimate for mixture averaged viscosity as a function of temperature.	190
Figure 4–15: Calculations of mixture thermal conductivity for three different equivalence ratios in the burnt and unburnt state as a function of mixture temperature.	191
Figure 4–16: Estimate for mixture averaged thermal conductivity as a function of temperature.	192
Figure 4–17: Calculations of mixture specific heat at constant pressure for three different equivalence ratios in the burnt and unburnt state as a function of mixture temperature.	193
Figure 4–18: Estimates of mixture averaged specific heat at constant pressure as a function of temperature.	194
Figure 4–19: Heat transfer losses from all engines as function of fuel air mixture ratio for a constant engine speed of 10000 rpm. Error bars are plotted for a single point in each data set and represent average uncertainty for the entire dataset.	195
Figure 4–20: Scaling of convective heat transfer losses and ratio of energy loss to engine power output as a function of displacement for two different constant engine speeds of 10000 and 12000 rpm and a constant mean piston speed of 4.77 ms^{-1} . All data sets correspond to an equivalence ratio of ~ 1	196
Figure 4–21: Schematic showing the layout of the motoring setup on the dynamometer.	198
Figure 4–22: Photograph of the engine motoring setup showing the DC motor and speed controller.	199
Figure 4–23: Photograph of the engine motoring setup showing the plastic spur gearing and the engine being motored.	200
Figure 4–24: Frictional power loss measured from all the engines as a function of engine speed.	202
Figure 4–25: Slopes for the frictional power loss correlation developed for the data presented in figure 4–24 as a function of engine displacement.	202
Figure 4–26: Product of displacement volume and engine speed at conditions of peak power output plotted as a function of engine displacement. Also presented is the ratio of frictional power loss to engine power output at the same conditions.	205
Figure 4–27: Frictional power loss from all engines as function of fuel air mixture ratio for a constant engine speed of 10000 rpm. Error bars are plotted for a single point in each data set and represent average uncertainty for the entire dataset.	206
Figure 4–28: Scaling of mechanical losses and the ratio of mechanical losses to engine power output as a function of engine displacement for two different constant engine speeds of 10000 and 12000 rpm and a constant mean piston speed of 4.77 ms^{-1} . All data sets correspond to an equivalence ratio of ~ 1	207

Figure 4–29: Enthalpy released in exhaust for all engines as a function of fuel air mixture ratio at a constant engine speed of 10000 rpm. Error bars are plotted for a single point in each data set and represent average uncertainty for the entire dataset.	209
Figure 4–30: Scaling of exhaust enthalpy loss and the ratio of exhaust loss to engine power output as function of engine displacement for two different constant engine speeds of 10000 and 12000 rpm and a constant mean piston speed of 4.77 ms^{-1} . All data sets correspond to an equivalence ratio of ~ 1 .	210
Figure 4–31: Energy lost in incomplete combustion for all engines as a function of fuel air mixture ratio at a constant engine speed of 10000 rpm. Error bars are plotted for a single point in each data set and represent average uncertainty for the entire dataset.	212
Figure 4–32: Scaling of incomplete combustion losses and the ratio of combustion loss to engine power output as a function of engine displacement for two different constant engine speeds of 10000 and 12000 rpm and a constant mean piston speed of 4.77 ms^{-1} . All data sets correspond to an equivalence ratio of ~ 1 .	213
Figure 4–33: Scaling of component enthalpy losses for all engines as a function of engine displacement at a constant engine speed of 10000 rpm and a constant equivalence ratio of ~ 1 .	214
Figure 4–34: Scaling of the ratio of component energy loss to power output for all engines as a function of engine displacement at a constant engine speed of 10000 rpm and an equivalence ratio of ~ 1 .	215
Figure 4–35: Scaling of component efficiencies for all engines as a function of engine displacement at a constant engine speed of 10000 rpm and an equivalence ratio of ~ 1 .	216
Figure 4–36: Scaling of component enthalpy losses for all engines as a function of engine displacement at a constant engine speed of 12000 rpm and an equivalence ratio of ~ 1 .	217
Figure 4–37: Scaling of the ratio of component energy loss to power output for all engines as a function of engine displacement at a constant engine speed of 12000 rpm and an equivalence ratio of ~ 1 .	218
Figure 4–38: Scaling of component efficiencies for all engines as a function of engine displacement at a constant engine speed of 12000 rpm and an equivalence ratio of ~ 1 .	219
Figure 4–39: Scaling of component enthalpy losses for all engines as a function of engine displacement at a constant mean piston speed of 4.77 ms^{-1} and an equivalence ratio of ~ 1 .	220
Figure 4–40: Scaling of the ratio of component energy loss to power output for all engines as a function of engine displacement at a constant mean piston speed of 4.77 ms^{-1} and an equivalence ratio of ~ 1 .	221
Figure 4–41: Scaling of component efficiencies for all engines as a function of engine displacement at a constant mean piston speed of 4.77 ms^{-1} and an equivalence ratio of ~ 1 .	222
Figure 4–42: Composition of energy losses for different engines. a)Cox 010 engine at 10000 rpm and equivalence ratio ~ 1 ; b) OS 46 engine at 10000 rpm and equivalence ratio ~ 1 ; c) Data for automotive spark ignition engine at maximum power as	

compiled by Heywood; d) Data for automotive Diesel engine at maximum power as compiled by Heywood.	224
Figure 5–1: Photographs of the Optrand fiber optic pressure sensor – model M3.5x0.6mm.....	227
Figure 5–2: Block diagram of the Optrand fiber optic pressure sensor [188].	229
Figure 5–3: Block diagram of the sensor head of the Optrand fiber optic pressure sensor [188].....	229
Figure 5–4: Dimensions of the Optrand fiber optic pressure sensor.	230
Figure 5–5: Optrand fiber optic pressure sensor mounted on the stock cylinder head of the OS 46/OS 40 FX engine.	232
Figure 5–6: Voltage output from the optical speed sensor plotted as a function of time. The straight lines highlighted in red represent the location of piston top dead center (TDC).	234
Figure 5–7: Photograph of the Model 121 bearingless auto aligning shaft encoder manufactured by Encoder Products.	235
Figure 5–8: Photograph of the Model 260 shaft encoder manufactured by Encoder Products.....	235
Figure 5–9: Schematic showing the construction of the glass disk and location of light emitters and phototransistors on an incremental shaft encoder [193].....	237
Figure 5–10: Schematic of the waveform outputs from different tracks on the incremental shaft encoder as well as the index pulse [193]. Index pulse is gated to channel B.	238
Figure 5–11: National Instruments USB–6221 BNC data acquisition module used to sample voltage signals from the cylinder pressure sensor.	240
Figure 5–12: Dynamometer setup for the cylinder pressure measurements on the OS 40 FX engine.....	241
Figure 5–13: Energy transfer processes occurring in the cylinder treated as a closed control volume with the ports closed.	249
Figure 5–14: Measured power output for the OS 25 FX engine with and without a cylinder pressure sensor at different operating speeds and fuel–air mixture ratios. .	257
Figure 5–15: Cylinder pressure averaged over 50 cycles plotted as a function of crank angle degrees from bottom dead center (BDC) for the OS 25 FX engine operating at a speed of 10000 rpm and an equivalence ratio of 1.05.	259
Figure 5–16: Cylinder pressure plotted as a function of cylinder volume for a fired engine cycle for the OS 25 FX engine operating at a speed of 10000 rpm and an equivalence ratio of 1.05.....	260
Figure 5–17: Cylinder pressure averaged over 50 cycles plotted as a function of crank angle for the OS 25 FX engine operating at a speed of 10000 rpm and different equivalence ratios.....	261
Figure 5–18: Cylinder pressure averaged over 50 cycles plotted as a function of crank angle for the OS 25 FX engine operating at an equivalence ratio of ~ 0.98 and different engine speeds.	263
Figure 5–19: Peak cylinder pressure averaged over 50 cycles plotted as a function of equivalence ratio for the OS 25 FX engine operating at different engine speeds.....	264
Figure 5–20: Peak cylinder pressure over 50 cycles plotted as a function of equivalence ratio for the OS 25 FX engine operating at different engine speeds.....	265

Figure 5–21: Average location of peak cylinder pressure averaged over 50 cycles plotted as a function of equivalence ratio for the OS 25 FX engine operating at different engine speeds.	266
Figure 5–22: Coefficient of variation calculated for maximum cylinder pressure plotted as a function of equivalence ratio for the OS 25 FX engine operating at different engine speeds.	267
Figure 5–23: Coefficient of variation calculated for maximum cylinder pressure plotted as a function of equivalence ratio for the OS 25 FX engine operating at different engine speeds.	268
Figure 5–24: Net heat release rate and a moving average estimated for the same over 5 data points plotted a function of crank angle for the OS 25 FX engine operating 10000 rpm and an equivalence ratio of 1.05.	270
Figure 5–25: Five point moving average of the net heat release rate estimated for the OS 25 FX engine plotted as a function of crank angle for the engine operating at 10000 rpm and different equivalence ratios.	271
Figure 5–26: Five point moving point average of the net heat release rate estimated for the OS 25 FX engine plotted as a function of crank angle for the engine operating at different speeds and an equivalence ratio of ~ 0.95.	272
Figure 5–27: Five point moving point average of the net heat release rate estimated for the OS 25 FX engine plotted as a function of crank angle for the engine operating at different speeds and an equivalence ratio of ~ 0.95.	273
Figure 5–28: Results of work done by Asad and Zheng [216] showing experimentally measured heat release rates for a number of fueling strategies and alternate modes of combustion in light duty diesel engines.	274
Figure 5–29: Five point moving point average of the net heat release rate estimated for the OS 25 FX engine plotted as a function of crank angle for the engine operating at 5000 rpm and different equivalence ratios.	277
Figure 5–30: Ignition location averaged over 50 cycles as a function of equivalence ratio for the OS 25 FX engine operating at different speeds.	278
Figure 5–31: Burn duration in crank angle degrees averaged over 50 cycles and plotted as a function of equivalence ratio for the OS 25 FX engine operating at different engine speeds.	279
Figure 5–32: Mass burned fraction profiles averaged over 50 engine cycles plotted as a function of crank angle for the OS 25 FX engine operating at 10000 rpm and different equivalence ratios.	281
Figure 5–33: Mass burned fraction profiles averaged over 50 engine cycles plotted as a function of crank angle for the OS 25 FX engine operating at different speeds and an equivalence ratio of ~ 0.95.	282
Figure 5–34: Heat release fraction averaged over 50 engine cycles plotted as a function of crank angle for the OS 25 FX engine operating at 10000 rpm and different equivalence ratios.	283
Figure 5–35: Heat release fraction averaged over 50 engine cycles plotted as a function of crank angle for the OS 25 FX engine operating at different speeds and an equivalence ratio of ~ 0.95.	284
Figure 5–36: Cylinder pressure traces for the three different engines tested in this work at constant engine speed and equivalence ratio.	285

Figure 5–37: Various estimated quantities for the three different engines tested in this work at 3 engine speed/equivalence ratio combinations as a function of engine displacement.	286
Figure 5–38: Mass burned fraction profiles for the three different engines tested in this work at four speed/equivalence ratio combinations.	287
Figure 5–39: Net heat release rates for the three different engines tested in this work at conditions of different constant engine speeds and equivalence ratios plotted as a function of crank angle degrees.	288
Figure 6–1: Photographs showing the top and bottom of a stock cylinder head for the OS 46 FX engine.	291
Figure 6–2: Two views of the CAD design in PRO/e for the clamping ring and the quartz bowl to replace the stock cylinder head for the OS 46 FX engine.	292
Figure 6–3: Photographs showing the top and bottom sides of the aluminum clamping ring with glow plug attached.	293
Figure 6–4: Photographs showing the top and bottom sides of the quartz bowl.	293
Figure 6–5: Photograph of the OS 46 FX engine with the quartz window assembly.	294
Figure 6–6: Photograph of the quartz bowl showing accumulation of soot particles after extended use.	295
Figure 6–7: Photograph of the quartz window showing miniature cracks after use on the OS 46 FX engine.	296
Figure 6–8: High speed Phantom camera (model v12.1) made by Vision Research Inc. used to acquire combustion images through the quartz window.	297
Figure 6–9: Photograph of the engine test setup on a stand with nose cone and propeller for engine loading.	299
Figure 6–10: High speed false color images of a single engine cycle during the combustion phase in the OS 46 FX engine at 8000 rpm and a fuel air mixture ratio of 0.21. Uncertainty in crank angle location is about 40 degrees CAD.	303
Figure 6–11: High speed false color images of the cycle immediately following the cycle shown in Fig. 6–9. The OS 46 FX engine is operating at 8000 rpm and a fuel air mixture ratio of 0.21. Uncertainty in crank angle location is about 40 degrees CAD.	304
Figure 6–12: High speed images of the combustion process in an optically accessible single cylinder research engine operating at a speed of 700 rpm and an equivalence ratio of 0.52 in a purely HCCI combustion mode on gasoline fuel at the University of Michigan[223]. The images are taken 1.4 crank angle degrees apart.	305
Figure 6–13: Consecutive images of flame propagation in a spark ignition engine where t represents the time after the spark in milliseconds [226].	306
Figure 6–14: High-speed images showing combustion processes in an engine operated in a spark ignition mode as well as in HCCCI mode [227].	307
Figure 6–15: High speed false color images of a single engine cycle during the combustion phase in the OS 46 FX engine at 8000 rpm and a fuel air mixture ratio of 0.21 showing the formation of soot as well as evidence of a thin films of fuel burning on the walls of the quartz window. Uncertainty in crank angle location is about 40 degrees CAD.	308

Figure 6–16: Plot showing total image intensity for images taken during the course of the engine cycle for an OS 46 FX engine at a speed of 8000 rpm and a fuel–air mixture ratio of 0.21. The red circles denote points where the propeller crosses the field of view of the camera and which provide a positive time reference for the images.	310
Figure 6–17: Normalized maximum cycle intensity plotted for all the engine cycles captured by the high speed camera for different operating conditions of fuel–air mixture ratio at a constant engine speed of 8000 rpm for the OS 46 FX engine. The stoichiometric value for fuel–air mixture ratio based on fuel chemistry is about 0.227.	311
Figure 6–18: High speed false color images acquired during the combustion phase of a single cycle of the OS 46 FX engine operating at a speed of 14000 rpm and a fuel–air mixture ratio of 0.25. Uncertainty in crank angle location is about 20 degrees CAD.	312
Figure 6–19: High speed false color images acquired during the combustion phase of a consecutive cycle of the OS 46 FX engine operating at a speed of 14000 rpm and a fuel–air mixture ratio of 0.25. Uncertainty in crank angle location is about 20 degrees CAD.	313
Figure 6–20: Normalized maximum cycle intensity for the OS 46 FX engine operating at a speed of 14000 rpm and a fuel–air mixture ratio of 0.25.	314
Figure 6–21: Coefficient of variation of maximum image intensity as a function of fuel–air mixture ratio for the OS 46 FX engine operating at speeds of 7000, 8000, 9000, 10000 and 14000 rpm.	315
Figure 6–22: Operating points for internal combustion engines listed in Table 6–3 on the combustion regime diagram.	321
Figure 6–23: Operating points for methanol fueled two–stroke miniature internal combustion engines showing the effect of variation in engine size and equivalence ratio.	329
Figure 6–24: Operating points for methanol fueled two–stroke miniature internal combustion engines showing the effect of variation in engine size and engine speed.	330
Figure 6–25: Operating points for methanol fueled two–stroke miniature internal combustion engines showing the effect of variations in engine size and ignition timing.	331
Figure 6–26: Operating points for methanol fueled two–stroke miniature internal combustion engines showing the effect of variation in engine size and charge dilution.	333
Figure 7–1: Front side photograph of the Sullivan Products S675–300 AC generator evaluated in this study.	335
Figure 7–2: Rear side photograph of the S675–300.	336
Figure 7–3: Photograph of the OS 46 FX engine in combination with the Sullivan generator.	337
Figure 7–4: Photograph of the engine–generator setup on the dynamometer.	337
Figure 7–5: Schematic layout of the load bank setup for engine–generator tests. ...	338
Figure 7–6: Photograph of the resistor load bank used to apply electrical load to the engine–generator setup.	339

Figure 7–7: Applied load and associated engine/generator speed for different engine operating conditions.....	342
Figure 7–8: Generator current and speed at different engine operating conditions..	343
Figure 7–9: Measured RMS values for AC voltage and speed for different engine operating conditions.....	343
Figure 7–10: Measured RMS values for AC voltage and speed for different engine operating conditions.....	344
Figure 7–11: Engine torque and speed at different engine operating conditions.	345
Figure 7–12: Measured engine and generator power output and operating speeds at different engine operating conditions. Also presented are estimates for generator power loss.	346
Figure 7–13: Generator power output and required mechanical power input for different load currents and speeds.....	347
Figure 7–14: Power required by generator to produce different load currents at different operating speeds. Power output from the OS 46 FX engine at different constant engine speeds and fuel–air mixture settings are also presented.	348
Figure 7–15: Engine, generator and system efficiencies and speed at different engine operating conditions.....	349
Figure 7–16: Generator efficiency as a function of output current.....	350
Figure 7–17: Schematic of the optimization procedure to determine best operating point for an engine/generator combination for maximum system efficiency.	351
Figure 7–18: AC and mechanical frequencies at different engine operating conditions.....	354
Figure 7–19: Power density and energy density of different systems along with a data set corresponding to the OS 46 engine alone and in an engine–generator system consisting of the OS 46 engine with the Sullivan S675–300 model generator operating at conditions of peak power output.....	356
Figure A–1: Energy balance in a two stroke engine with control volumes drawn around individual engine components.	368
Figure B–1: Delivery ratio at different fuel air mixture ratios and a constant engine speed of 12000 rpm for all engines.....	374
Figure B–2: Delivery ratio at different fuel air mixture ratios and a constant mean piston speed of 4.77 ms^{-1} for all engines.....	374
Figure B–3: Heat transfer loss at different fuel air mixture ratios and a constant engine speed of 12000 rpm for all engines.	375
Figure B–4: Heat transfer loss at different fuel air mixture ratios and a constant mean piston speed of 4.77 ms^{-1} for all engines.....	375
Figure B–5: Frictional loss at different fuel air mixture ratios and a constant engine speed of 12000 rpm for all engines.....	376
Figure B–6: Frictional loss at different fuel air mixture ratios and a constant mean piston speed of 4.77 ms^{-1} for all engines.....	376
Figure B–7: Enthalpy released in exhaust at different fuel air mixture ratios and a constant engine speed of 12000 rpm for all engines.....	377
Figure B–8: Enthalpy released in the exhaust at different fuel air mixture ratios and a constant mean piston speed of 4.77 ms^{-1} for all engines.....	377

Figure B-9: Incomplete combustion losses at different fuel air mixture ratios and a constant engine speed of 12000 rpm for all engines.....	378
Figure B-10: Incomplete combustion losses at different fuel air mixture ratios and a constant mean piston speed of 4.77 ms^{-1} for all engines.....	378
Figure E-1: Cylinder pressure plotted as a function of crank angle for a fired engine cycle for the OS 40 FX engine operating at a speed of 10000 rpm and an equivalence ratio of 0.95.....	385
Figure E-2: Cylinder pressure plotted as a function of cylinder volume for a fired engine cycle for the OS 40 FX engine operating at a speed of 10000 rpm and an equivalence ratio of 0.95.....	385
Figure E-3: Cylinder pressure averaged over 50 cycles plotted as a function of crank angle for the OS 40 FX engine operating at a speed of 10000 rpm and different equivalence ratios.....	386
Figure E-4: Cylinder pressure averaged over 50 cycles plotted as a function of crank angle for the OS 40 FX engine operating at an equivalence ratio of ~ 0.95 and different engine speeds.	386
Figure E-5: Peak cylinder pressure averaged over 50 cycles plotted as a function of equivalence ratio for the OS 40 FX engine operating at different engine speeds.....	387
Figure E-6: Peak cylinder pressure over 50 cycles plotted as a function of equivalence ratio for the OS 40 FX engine operating at different engine speeds.....	387
Figure E-7: Location of peak cylinder pressure averaged over 50 cycles plotted as a function of equivalence ratio for the OS 40 FX engine operating at different engine speeds.....	388
Figure E-8: Coefficient of variation for peak cylinder pressure plotted as a function of equivalence ratio for the OS 40 FX engine operating at different engine speeds.	388
Figure E-9: Coefficient of variation for location of peak cylinder pressure plotted as a function of equivalence ratio for the OS 40 FX engine operating at different engine speeds.....	389
Figure E-10: Net heat release rate and a moving average estimated for the same over 5 data points plotted a function of crank angle for the OS 40 FX engine operating 10000 rpm and an equivalence ratio of 1.48.....	389
Figure E-11: Five point moving point average of the net heat release rate estimated for the OS 40 FX engine plotted as a function of crank angle for the engine operating at 10000 rpm and different equivalence ratios.....	390
Figure E-12: Five point moving point average of the net heat release rate estimated for the OS 40 FX engine plotted as a function of crank angle for the engine operating at different speeds and an equivalence ratio of ~ 0.95	390
Figure E-13: Ignition timing location averaged over 50 cycles plotted as a function of equivalence ratio for the OS 40 FX engine operating at different engine speeds.....	391
Figure E-14: Burn duration in crank angle degrees averaged over 50 cycles and plotted as a function of equivalence ratio for the OS 40 FX engine operating at different engine speeds.	391
Figure E-15: Mass burnt fraction profiles averaged over 50 engine cycles plotted as a function of crank angle for the OS 40 FX engine operating at 10000 rpm and different equivalence ratios.....	392

Figure E-16: Mass burnt fraction profiles averaged over 50 engine cycles plotted as a function of crank angle for the OS 40 FX engine operating at different speeds and an equivalence ratio of ~ 0.95	392
Figure E-17: Heat release fraction averaged over 50 engine cycles plotted as a function of crank angle for the OS 40 FX engine operating at 10000 rpm and different equivalence ratios.....	393
Figure E-18: Heat release fraction averaged over 50 engine cycles plotted as a function of crank angle for the OS 40 FX engine operating at different speeds and an equivalence ratio of ~ 0.95	393
Figure E-19: Indicated and brake power output plotted as a function of equivalence ratio for the OS 40 FX engine operating at different speeds.	394
Figure E-20: Power loss plotted as a function of equivalence ratio for the OS 40 FX engine operating at different speeds.	394
Figure E-21: Cylinder pressure plotted as a function of crank angle for a fired engine cycle for the OS 46 FX engine operating at a speed of 10000 rpm and an equivalence ratio of 1.03.....	395
Figure E-22: Cylinder pressure plotted as a function of cylinder volume for a fired engine cycle for the OS 46 FX engine operating at a speed of 10000 rpm and an equivalence ratio of 1.03.....	395
Figure E-23: Cylinder pressure averaged over 50 cycles plotted as a function of crank angle for the OS 46 FX engine operating at a speed of 10000 rpm and different equivalence ratios.....	396
Figure E-24: Cylinder pressure averaged over 50 cycles plotted as a function of crank angle for the OS 46 FX engine operating at an equivalence ratio of ~ 1.2 and different engine speeds.	396
Figure E-25: Peak cylinder pressure averaged over 50 cycles plotted as a function of equivalence ratio for the OS 46 FX engine operating at different engine speeds.....	397
Figure E-26: Peak cylinder pressure over 50 cycles plotted as a function of equivalence ratio for the OS 46 FX engine operating at different engine speeds.....	397
Figure E-27: Location of peak cylinder pressure averaged over 50 cycles plotted as a function of equivalence ratio for the OS 46 FX engine operating at different engine speeds.....	398
Figure E-28: Coefficient of variation of peak cylinder pressure plotted as a function of equivalence ratio for the OS 46 FX engine operating at different engine speeds.	398
Figure E-29: Coefficient of variation of location of peak cylinder pressure plotted as a function of equivalence ratio for the OS 46 FX engine operating at different engine speeds.....	399
Figure E-30: Net heat release rate and a moving average estimated for the same over 5 data points plotted a function of crank angle for the OS 46 FX engine operating 10000 rpm and an equivalence ratio of 1.04.....	399
Figure E-31: Five point moving point average of the net heat release rate estimated for the OS 46 FX engine plotted as a function of crank angle for the engine operating at 10000 rpm and different equivalence ratios.....	400
Figure E-32: Five point moving point average of the net heat release rate estimated for the OS 46 FX engine plotted as a function of crank angle for the engine operating at different speeds and an equivalence ratio of ~ 1.2	400

Figure E-33: Ignition timing location averaged over 50 cycles plotted as a function of equivalence ratio for the OS 46 FX engine operating at different engine speeds.....	401
Figure E-34: Burn duration in crank angle degrees averaged over 50 cycles and plotted as a function of equivalence ratio for the OS 46 FX engine operating at different engine speeds.	401
Figure E-35: Mass burnt fraction profiles averaged over 50 engine cycles plotted as a function of crank angle for the OS 46 FX engine operating at 10000 rpm and different equivalence ratios.....	402
Figure E-36: Mass burnt fraction profiles averaged over 50 engine cycles plotted as a function of crank angle for the OS 46 FX engine operating at different speeds and an equivalence ratio of ~ 1.2	402
Figure E-37: Heat release fraction averaged over 50 engine cycles plotted as a function of crank angle for the OS 46 FX engine operating at 10000 rpm and different equivalence ratios.....	403
Figure E-38: Heat release fraction averaged over 50 engine cycles plotted as a function of crank angle for the OS 46 FX engine operating at different speeds and an equivalence ratio of ~ 1.2	403

Chapter 1 : Introduction

1.1 Miniature Power Systems

1.1.1 Demand for Compact Portable Power

Recent years have seen a rising demand for miniature power systems that offer portability, long life, and ease of use. This demand has been accelerated by the rapid miniaturization of electro-mechanical systems in different areas of technology, resulting in a wide range of devices requiring compact portable power. As the overall size of the device shrinks and mass/size limitations of the power system become increasingly stringent, there is a growing shift towards using electrochemical batteries to power miniature applications. Investigating the performance of miniature reciprocating internal combustion (IC) engines that can provide an energy source based on hydrocarbon fuel combustion to replace electrochemical batteries forms the major motivation for this research work. The two main applications targeted here are propulsion systems for miniature unmanned air vehicles (MAV's) and energy sources for compact man-portable devices (radios, GPS, sensors, etc.).

1.1.1.1 Propulsion Systems for Unmanned Air Vehicles

Unmanned air vehicles (UAV) represent a rapidly growing segment of the aerospace industry with myriad applications including high-altitude imagery, border patrol, maritime surveillance, environmental sensing, media reporting and law enforcement. Consequently, these vehicles are set to become significant components of military, civil and commercial aviation. These vehicles are often classified based

on mission requirements. Table 1–1 illustrates a sub–division of UAV’s based on altitude, range and endurance capabilities.

Category	Name	Range	Operational Altitude	Endurance
HALE	High Altitude Long Endurance	> 1000 km	> 12,000 m	24 – 48 h
MALE	Medium Altitude Long Endurance	> 500 km	< 12,000 m	24 – 48 h
LALE	Low Altitude Long Endurance	>1000 km	<7,000 m	24 – 48 h
SUAV	Short Range UAV	< 500 km	<7,000 m	1 – 12 h
UAV–CR	Close Range UAV	< 200 km	<3,000 m	1 – 5 h
MAV	Miniature air vehicle	< 10 km	up to 300 m	1 – 2 h

Table 1–1: Classification of UAV’s based on altitude, range and endurance capabilities.

Figure 1–1 shows the results of a survey of a wide variety of UAV’s from different manufacturers with colored regions marking the categories listed in Table 1–1. Different symbols are used to represent vehicles that use electrical propulsion systems as opposed to combustion based power systems. As seen in Fig.1–1, combustion based power systems are used in the vast majority of the vehicles with electrical power systems being more common in the case of close range UAV’s.

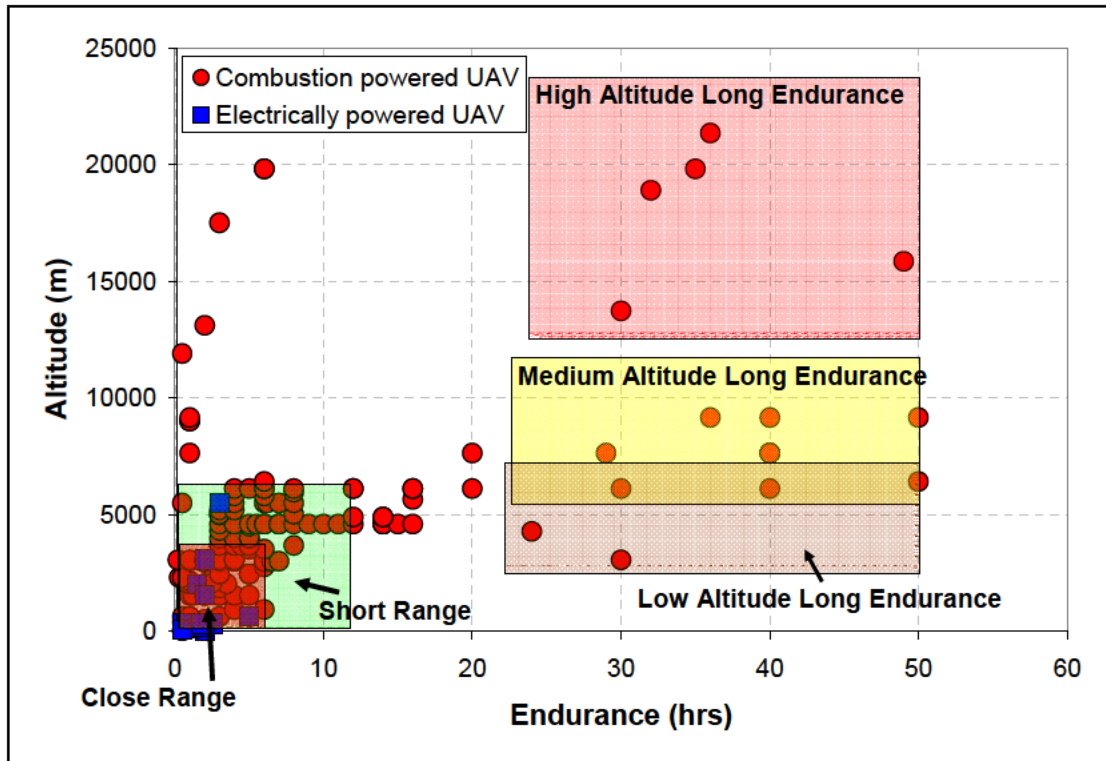


Figure 1–1: Altitude and endurance capabilities for a wide range of unmanned air vehicles.¹

Figure 1–2 presents a magnified picture of the region occupied by close range UAV's. Miniature air vehicles operating at an altitude of less than 300 m with an operating range of about 10 km and endurance of about 1–2 hours are seen to be primarily powered by electrical power systems. The system typically comprises an electric motor driven by regular/rechargeable batteries. Figure 1–3 shows the power requirements of miniature air vehicles surveyed here with vehicle mass on the x-axis and power required on the y-axis. The power requirement for these vehicles is seen to be of the order of less than a kilowatt and scales approximately linearly with vehicle mass. The major application for miniature unmanned air vehicles is in providing real-time information, surveillance and reconnaissance (ISR) in civilian and military applications.²

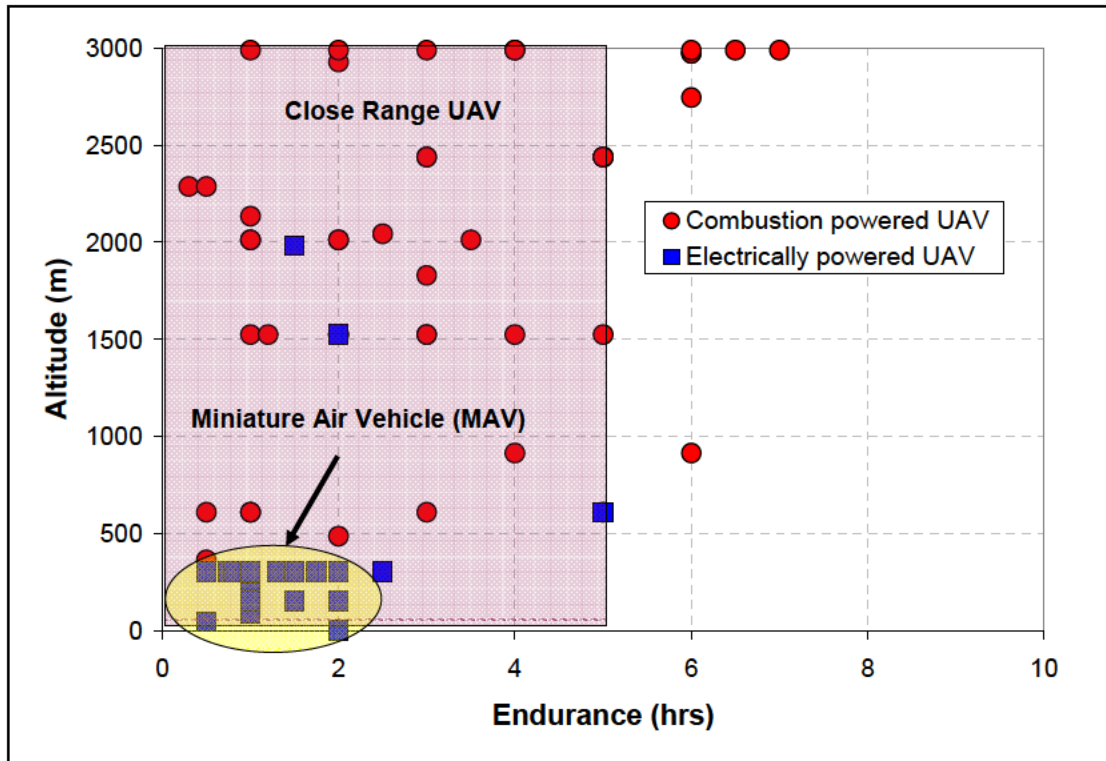


Figure 1-2: Altitude and endurance capabilities for close range unmanned air vehicles.

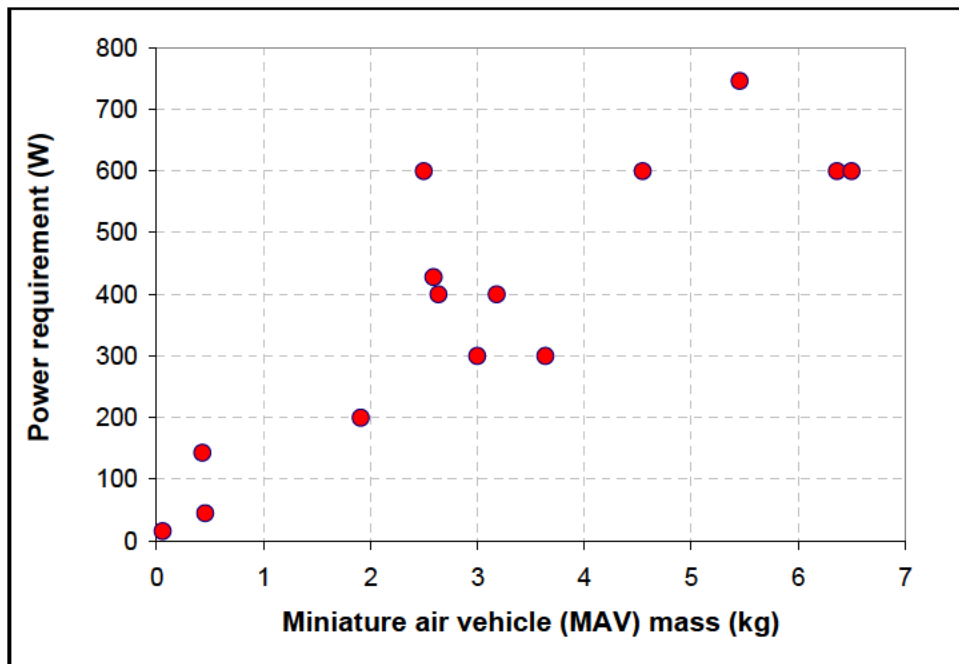


Figure 1-3: Power requirement and mass for miniature unmanned air vehicles.

1.1.1.2 Power Source for Portable Applications

As mentioned previously, rapid miniaturization of electromechanical systems has resulted in the development of several human portable applications requiring compact power supply.³ These include portable electronics, power tools, microclimate and refrigerators. Portable electronics include cell phones, smart phones, personal digital assistants, and netbooks. Military applications for compact power include portable power packs that are used as energy sources for soldier-specific devices such as portable computer, radio, GPS and weapon systems. Table 1–2 presents a survey of the power and energy requirements for some of these devices.

Number	Device Name	Power (W)	Endurance (hr)	Energy capacity (W–hr)
1	Smartphone ⁴	0.9	5	4.5
2	Netbook ⁵	6.63	9.5	63
3	Soldier portable power pack ⁶	20	72	1440
4	Portable TV ⁷	100	2	200
5	Microclimate ⁸	120	4	480
6	Energy efficient refrigerator ⁹	130	10	1300
7	Power tools ¹⁰	500	2	1000

Table 1–2: Survey of several applications requiring compact portable power.

1.1.2 Representation of Target Region

A simple way to visualize the performance requirements of a variety of applications is to place each device in power and energy space as shown in Figure 1–4. The stored energy requirement is computed using the following relation,

$$Q_{\text{device}} = P * t \quad (1-1)$$

where Q_{device} is the energy capacity of the device in W-hr, P is the power required to operate the device and t is the endurance (run-time) required from the device.

Superimposed on the plot are contours of constant endurance (which equals energy capacity divided by power consumption). The chart shows that increasing endurance requires increasing energy storage and decreasing power consumption. In the context of a vehicle or man-portable device where total system mass and/or volume are constrained, this means that one maximizes endurance by using high energy density propellants and maximizing overall system efficiency. Based on the power and energy requirements of the applications discussed above, it is possible to identify a region that encapsulates devices currently powered by batteries and display potential for the use of a combustion based power system. This region – illustrated by the rhomboid boundary in Fig. 1–4, is defined by a power requirement of between 10–1000 W and an endurance time of between 1–100 hours. The variety of applications included within the boundary results in a range of different masses for individual devices and their power plants. In this research, the weight of the power plant is limited to be less than a kilogram and this forms the size constraint of the systems studied here.

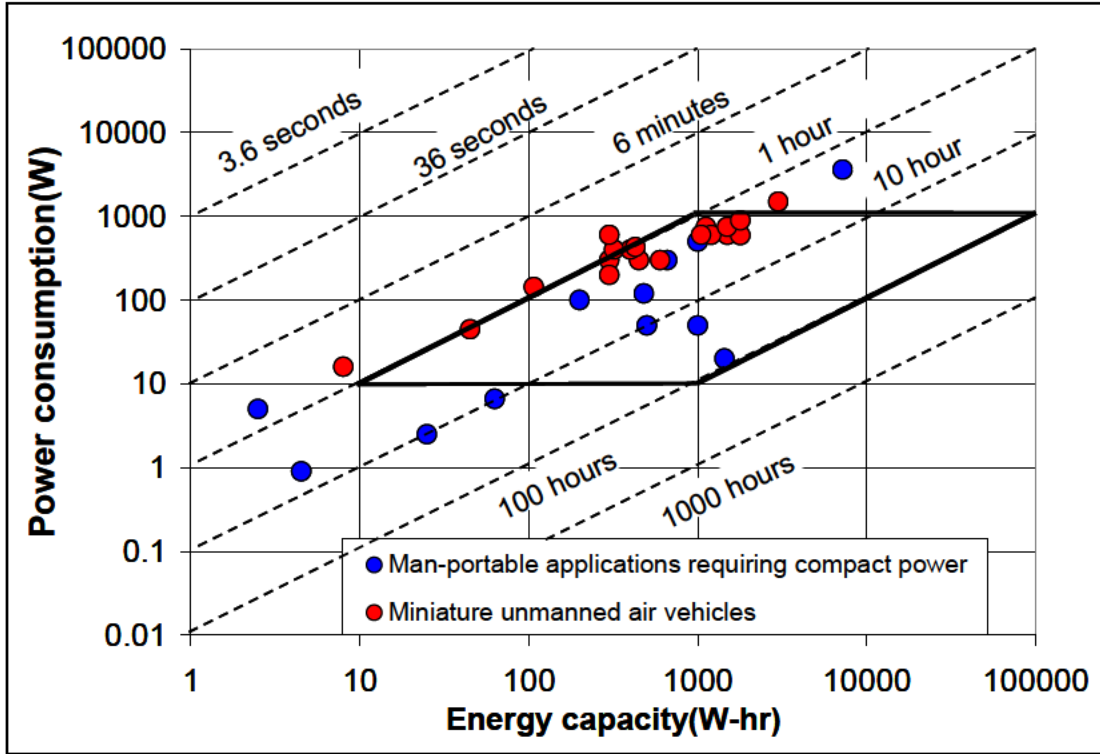


Figure 1-4: Power consumption and stored energy capacity for miniature applications with contours of constant endurance. Marked quadrilateral represents area of interest in this work.

1.1.3 Energy Density and Power Density

In addition to satisfying the power/stored energy/endurance requirements from the device/application standpoint, the power plant has to also satisfy a size and weight requirement. This is especially important in portable applications where system mass is critical to mission requirements. Therefore, power and energy density are also important. They are defined as,

$$\text{Power density} = \frac{\text{Power output}}{\text{Power plant weight}} \quad (1-2)$$

$$\text{Energy density} = \frac{\text{Available energy}}{\text{Power plant weight}} \quad (1-3)$$

The available energy term in Eqn. 1–3 represents actual available energy which is defined in Eqn. 1–4 as follows,

$$\text{Available energy} = \text{Stored energy in fuel} * \text{Device conversion efficiency} \quad (1-4)$$

The energy stored in the fuel can be expressed in terms of the heating value of the fuel (Q_R) and mass flow rate of fuel through the device (\dot{m}_{fuel}) as follows,

$$\text{Stored energy in fuel} = Q_R * \dot{m}_{fuel} \quad (1-5)$$

Therefore, maximizing available energy (which translates directly to range and/or endurance) means maximizing the energy density of the fuel and the conversion efficiency. The energy densities of various fuels and a case study comparing the performance of an electrochemical and a combustion based system are presented in the following sections. The results of these analyses illustrate the major motivation for replacing batteries by combustion based power systems for the devices surveyed and presented in Fig. 1–4.

1.1.4 Comparison of Energy Storage Materials

Figure 1–5 compares energy density by mass and by volume for several energy storage materials. Liquid hydrocarbon fuels such as gasoline, diesel, jet–A and propane have a significant advantage over lithium–ion and lead acid electrochemical materials in terms of energy density by mass and by volume. Hydrogen in its gaseous form has the largest energy content by mass. However, its low density results in low energy content per unit volume that necessitates large storage volume. This can be improved either by utilizing high pressure tanks (at a considerable weight penalty), liquid hydrogen (also at a considerable weight penalty¹¹), or by storing it chemically such as aqueous NaBH_4 . In the latter case, however, the maximum H_2 weight fraction

is only 10%, so the net energy density is still quite low. “Glow fuel” which has been included in the analysis here, is the common term used to refer to mixtures of methanol, nitromethane and castor oil that are used to power miniature hobby engines intended for radio control applications. A typical blend is 70% Methanol, 20% oil and 10% nitromethane, which has an energy density of about 20 MJ/kg. While this is lower than other liquid hydrocarbons, it is still much greater than the best batteries.

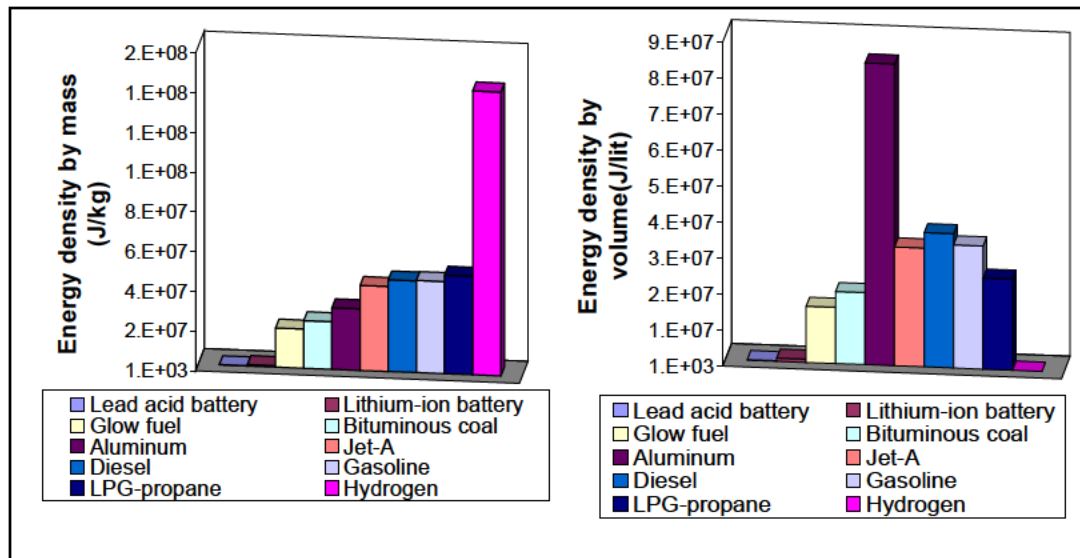


Figure 1-5: Energy density by mass and energy density by volume for a wide range of energy storage materials sources.^{12 13 14 15}

The high energy density of liquid hydrocarbon fuels is what gives today’s automobiles and aircraft practical levels of range and endurance. Replacing batteries with fuel tanks and miniature energy conversion devices having conversion efficiencies on par with those of conventional scale engines could increase the endurance by a factor of 10 or more. Realistic improvements in endurance based on currently achievable levels of conversion efficiency are demonstrated in the case study presented in the following section.

1.1.5 Case Study

Consider a simple example using the specifications of a ‘typical’ mini UAV patterned after the Aeroenvironment FQM–151 Pointer used by the U.S army and Marine Corps.¹⁶ The Pointer is launched by hand and is equipped with a color or night–vision camera. The air vehicle and the ground control unit are compact enough to be carried in backpacks. The gross weight of the vehicle is 4.3 kg and the operating power requirement is about 300 W.

The performance of this UAV was analyzed by comparing the range and endurance capabilities of the vehicle while operating with batteries and a miniature combustion based system. A 300 W brushless DC motor powered by lithium polymer batteries was chosen to represent the electrical power system. The combustion based system chosen for comparison here is a miniature IC engine that is commercially available off the shelf. The performance characteristics of the engine were obtained from previously published work.¹⁷ The engine produces about 150 W of power with a peak overall efficiency of about 9%. Two engines are considered to satisfy the power requirement for the UAV. The mass of the power system including the fuel was assumed to be 75% of the mass of the UAV.

The Breguet range equation (Eqn. 1–6) is used to determine the influence of power system performance on the overall performance of the vehicle. This equation is for a fixed–wing aircraft and shows that the critical aspects of the power system that govern the range and/or endurance are its overall thermal efficiency (η_{th}) and the energy per unit mass (or energy storage efficiency) of the fuel (Q_r). The other terms in this expression describe aspects of the vehicle that are independent of the

propulsion system. These include the efficiency of the propeller or other propulsive device (η_p), the acceleration of gravity (g), the airframe's lift-to-drag ratio (L/D), and the ratio of the fuel weight to the empty weight of the vehicle (χ). Here, the propeller efficiency is assumed to be 0.7 and L/D is assumed to be 8.

$$R = \eta_p \eta_{th} \frac{Q_r}{g} \frac{L}{D} \ln(1 + \chi) \quad (1-6)$$

Table 1–3 shows that a miniature IC engine operating on glow fuel can provide a 36% improvement in range and endurance. This is in spite of the fact that the overall efficiency of the combustion based power system is lower than that of the electrical based power system by almost a factor of 10. The miniature internal combustion engine considered in this case study belongs to a family of engines commonly referred to as ‘model airplane engines’ or ‘hobby engines’. A brief discussion of these engines is presented in the next section.

	Electrical power system	Combustion based power system	
Engine/Motor weight	0.18	0.3	kg
Battery/Fuel weight	2.83	2.71	kg
Total power plant weight	3.01	3.01	kg
Overall system efficiency	93	9	%
Energy density	1500	20,000	kJ/kg
Range	855	1162	km

Table 1–3: Operating parameters for electrical and combustion based power systems used on a miniature unmanned air vehicle.

1.1.6 Hobby Engines

Development of engines for radio control applications began in the 1930's and was based on designs of two-stroke motorcycle engines. Since then, a large number of 'hobby engines' have been constructed for use in radio controlled airplanes, helicopters, cars and boats. The majority are piston type reciprocating engines but, Wankels and miniature turbine engines have also been developed.

Reciprocating-type hobby engines can be subdivided into glow fuel engines and model diesel engines based on the fuel utilized in each device. 'Glow fuel' is a blend of methanol, nitromethane and castor oil in varying proportions. Ignition in glow engines is achieved by using a platinum coated coil (or glow plug) located at the top of the combustion chamber to facilitate ignition during the compression process. So, they are augmented compression ignition (CI) engines. 'Model diesel' consists of a mixture of kerosene, ether and castor oil. Although engines using this fuel are referred to as 'diesels', they actually appear to operate in compression ignition (CI) or homogenous charge compression ignition (HCCI) modes. Timing is controlled using a contra piston located on the cylinder head to adjust the compression ratio. Figures 1-6 and 1-7, respectively, show photographs of an AP Yellowjacket glow fuel engine and a PAW 049 diesel engine.^{18 19} Aftermarket cylinder heads for converting a glow fuel engine to diesel operation have also been developed.²⁰ While the engines in Figures 1-6 and 1-7 are similar, the diesel version is significantly more robust because it must support a larger compression ratio.



Figure 1–6: Photograph of an AP Yellowjacket engine [18].

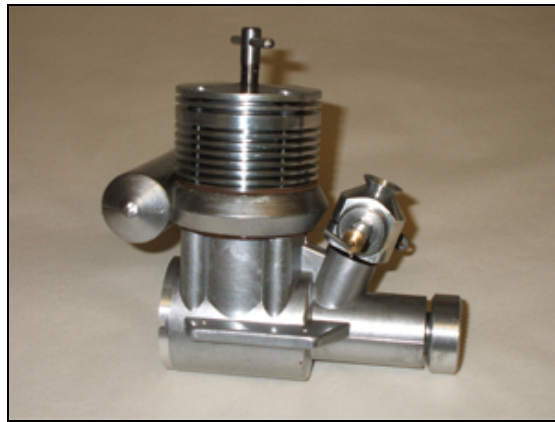


Figure 1–7: Photograph of a PAW 049 engine [19].

1.1.7 Comparison of Small Scale Power Systems

Apart from hobby engines considered in the case study presented earlier, development of miniature power systems is underway at several universities and research laboratories. These systems include novel micro–machines utilizing hydrocarbon combustion as well as different types of fuel cells. The common goal is to exploit the high energy density of hydrocarbon fuels to develop battery replacements. This section compares some of these devices. In making this comparison, care is taken to ensure that the devices are of a size suitable to be used in the miniature applications intended here (power plant size less than a kilogram). As

mentioned earlier, this is important as efficiency of power systems decreases considerably with size.

The power systems are compared by plotting them in specific energy (x-axis) and specific power (y-axis) space. This is called a ‘Ragone plot’.²¹ To understand how power systems are represented in specific energy /power space, it is useful to think of a power system as consisting of two components: the energy storage material (fuel) and the energy conversion device (engine or fuel cell). In batteries, the energy conversion devices (electrodes) are not separable from the energy storage material so they are represented as single points on a Ragone plot. However, in fuel-based systems, the size of the fuel tank is independent of the size of the engine. Mass fraction is defined as,

$$\zeta = \frac{m_f}{m_e} \quad (1-7)$$

where m_f is the fuel mass and m_e is the mass of the energy conversion device (ie. engine or fuel cell). The total mass (M) of the power system is given by,

$$M = m_f + m_e \quad (1-8)$$

The power density of the system is given by,

$$\frac{P}{M} = \frac{1}{(1 + \zeta)} \frac{P}{m_e} \quad (1-9)$$

The energy density is given by,

$$\frac{E}{M} = \frac{\zeta}{(1 + \zeta)} \eta Q_R \quad (1-10)$$

where Q_R is the energy density of the fuel and η is the overall efficiency of the energy conversion device.

Figure 1–8 shows the relationship between energy and power density in Ragone space for a non–battery based power system. The power plant represented here is a six–cylinder Lycoming O–435 spark ignition (SI) gasoline engine commonly used in fixed wing aircraft and helicopters.²² The data points on the curve denote different values of fuel mass and correspondingly in the mass fraction ζ . The figure shows that the curve approaches one of two asymptotes depending on whether the fuel mass fraction is large or small. Increasing the fuel mass fraction drives the energy density of the system toward the maximum possible energy density (which is the product of the overall thermodynamic efficiency of the power system with the energy content of the fuel (ηQ_R)) but comes at the price of reduced power density. Conversely, decreasing the fuel mass fraction drives the power density of the system toward its maximum (which is set by the power/weight ratio of the energy conversion device) but comes at the price of energy density or range/endurance. This tradeoff between power and energy density (or capability vs. range/endurance) means that most ‘practical’ systems occupy the ‘knee’ region where $0.1 < \zeta < 10$.

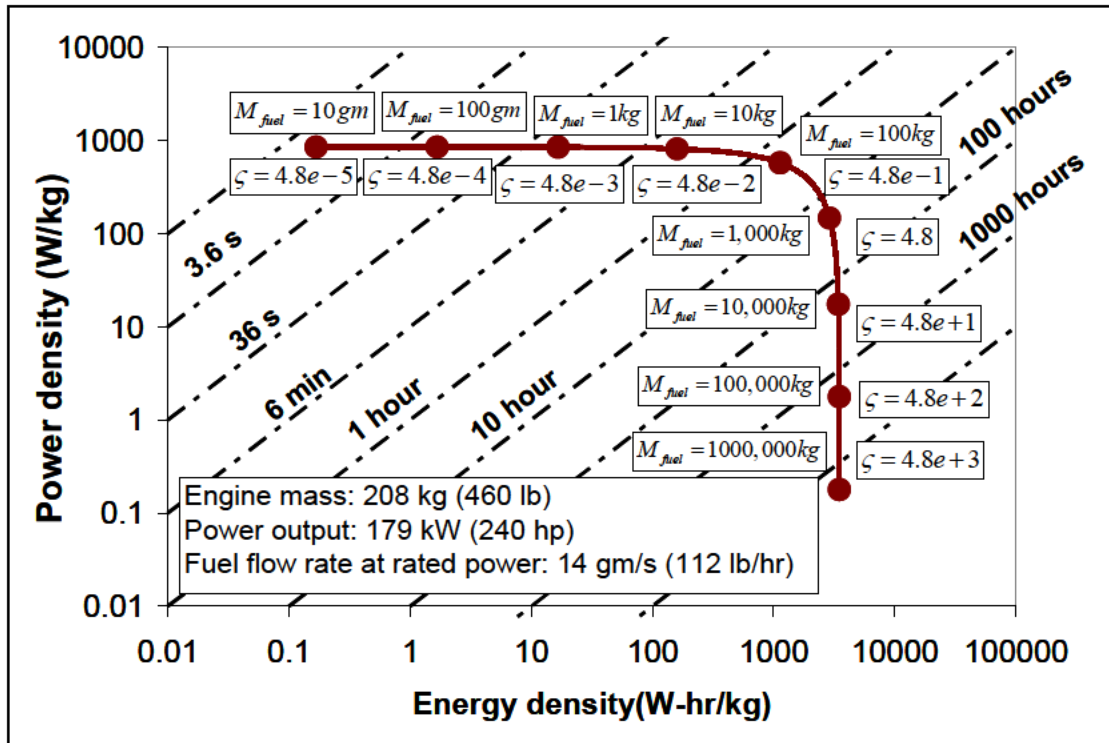


Figure 1–8: Ragone plot of power and energy density with contours of constant endurance with data plotted for an aircraft internal combustion engine.

Figure 1–9 is a Ragone plot comparing several types of sub-kilogram power systems to the DOD target power/energy density goals identified earlier.^{23 24} The black rhombus marks the DOD region of interest, the symbols show various types of batteries, the curves show the performance of various fuel-based power systems (where the data points marked correspond to $\zeta=1$), and the diagonal lines show contours of constant range or endurance.

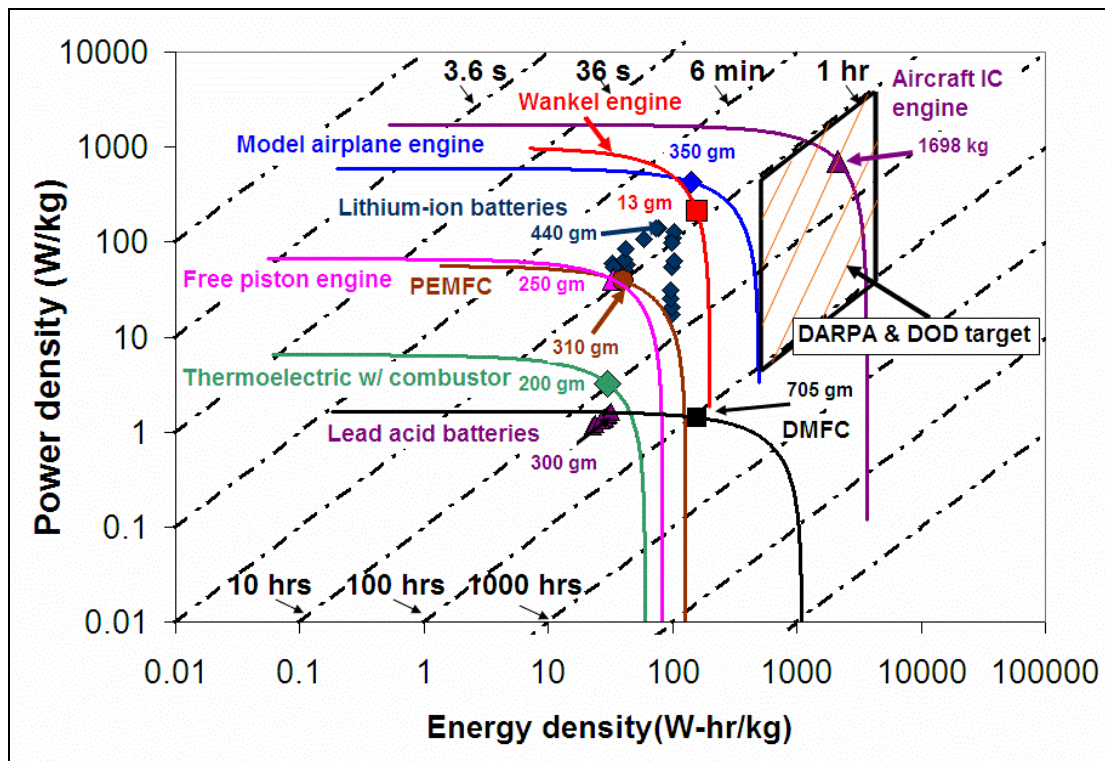


Figure 1–9: Ragone plot of power and energy density with contours of constant endurance comparing different power systems.

None of the existing technologies for power plants (engine and fuel) weighing less than a kilogram meet the DOD specifications at present, but some are much closer than others. Lead acid batteries have the lowest energy density among the power systems compared here.²⁵ Lithium ion batteries are somewhat better with peak energy densities of about 130 W–hr/kg.²⁶ Proton exchange membrane (PEM) fuel cells have a higher peak power density than direct methanol fuel cells (DMFC’s) because of the higher energy content of hydrogen.^{27 28} However, they have lower peak energy density because of increased storage weight of hydrogen fuel. A thermoelectric device developed for use with a combustor offers only a minor improvement on lead acid batteries with a peak power density of 6.5 W/kg and peak energy density of 63 W–hr/kg.²⁹ The HCCI based free piston engine shows improved

power and energy density as compared to the thermoelectric device.³⁰ The rotary Berkeley Wankel engine has been operated on gaseous hydrogen with a peak power density of about 1000 W/kg and a peak energy density of 200 W-hr/kg.³¹ However, the weight of the fuel is not taken into account here and the final power and energy densities of the system would be considerably reduced because of inefficiencies associated with hydrogen storage. A micro gas-turbine engine being developed at the Massachusetts Institute of Technology (MIT) has stated goals of achieving power and energy densities of about 1000 W/kg and 3500 W-hr/kg.³² It is to be noted that the novel engines mentioned here such as the free piston, rotary and micro gas-turbine engines are a long way from realization in the sense that they are hampered by various engineering problems complicating the development of a self-sustaining working prototype even in laboratory settings.

The best performer on this chart is a miniature hobby engine weighing about 150 g that can produce up to 150 W of mechanical power with a peak overall efficiency of about 8%.³³ This output can be used directly to provide propulsive power for micro-air vehicles or coupled with a commercially available generator³⁴ to provide electrical power with a relatively small additional efficiency penalty. Several appropriate-size generators are available commercially.³⁵

Figure 1-9 includes a dataset for a conventional aircraft IC engine which is a 12-cylinder turbocharged, four-stroke spark ignition engine run on gasoline weighing close to 700 kg.³⁶ This data illustrates the fact that the DARPA/DOD requirements for power and energy density are routinely achieved in conventional scale engines. The

key issue is to accomplish the same at the scales considered here (power plant mass less than a kilogram).

1.2 Losses in Miniature IC Engines

1.2.1 Thermal Loss

Heat transfer losses from combustion gases to the coolant in a conventional size IC engine accounts for 25–35% of the energy released during the combustion of the fuel–air mixture.³⁷ The majority of heat is transferred by forced convection from hot gas to the cylinder walls, conduction through the metal wall and forced convection from the engine to the coolant. Heat is also lost by radiation from the flame to the combustion chamber and through the exhaust manifold.³⁸

Heat transfer effects are expected to become more important at reduced length scales because miniaturization increases surface to volume ratio, temperature gradients and view factors³⁹, leading to higher heat transfer by convection, conduction, and radiation, respectively. Figure 1–10 presents data from a variety of piston engines that show how surface/volume ratio increases as engines get smaller.

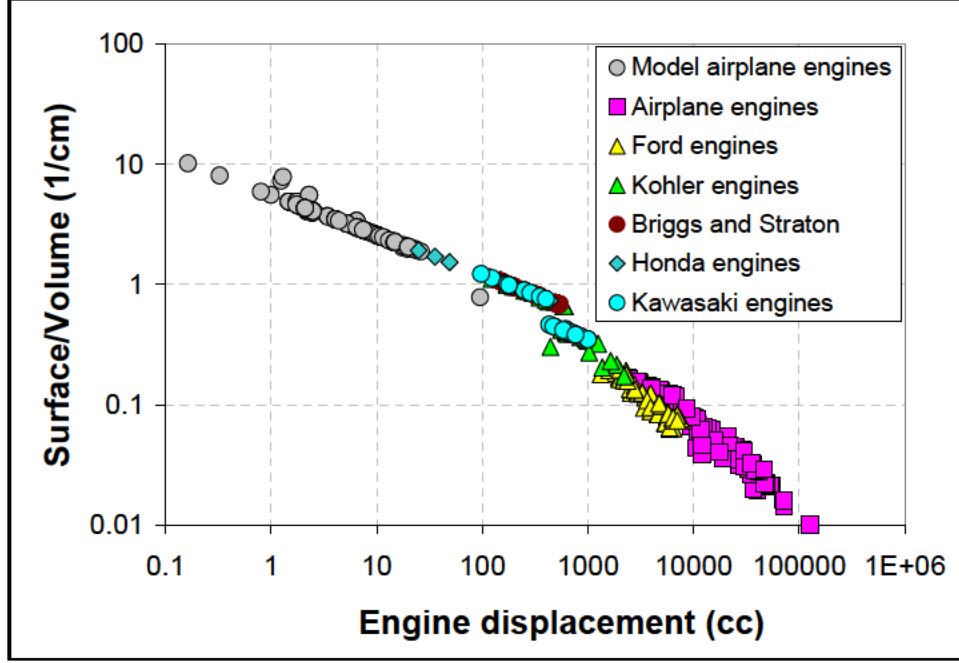


Figure 1–10: Surface to volume ratio for different types of piston engines as a function of displacement volume.

Figure 1–11 shows how thermal losses limit the degree to which a heat engine can be miniaturized. It is based on a simple analysis of a cylindrical combustor of diameter and length l . The rate of chemical energy release is given by,

$$\dot{Q}_m \sim \dot{m}_{air} S_L l^2 Q_R \quad (1-11)$$

where Q_{fuel} is the energy density of the fuel, S_L is the laminar flame speed, and f is the fuel/air ratio. The rate of heat loss to the environment is given by,

$$\dot{Q}_{loss} \approx Nu k l (T_{gas} - T_{wall}) \quad (1-12)$$

where Nu is the Nusselt number for heat loss to the environment ($Nu \sim 3.2$ for free convection⁴⁰), k is the thermal conductivity of the environment, and l is the length scale. The net energy available for useful work is the difference between the input power and heat loss and is given by,

$$\dot{Q}_{net} = \dot{Q}_{in} - \dot{Q}_{loss} \quad (1-13)$$

As the size of the combustor is reduced, the input power drops as the square of the combustor diameter (l^2), while the heat loss decreases as l . This suggests that eventually the heat loss will outstrip the heat production as scale is reduced.

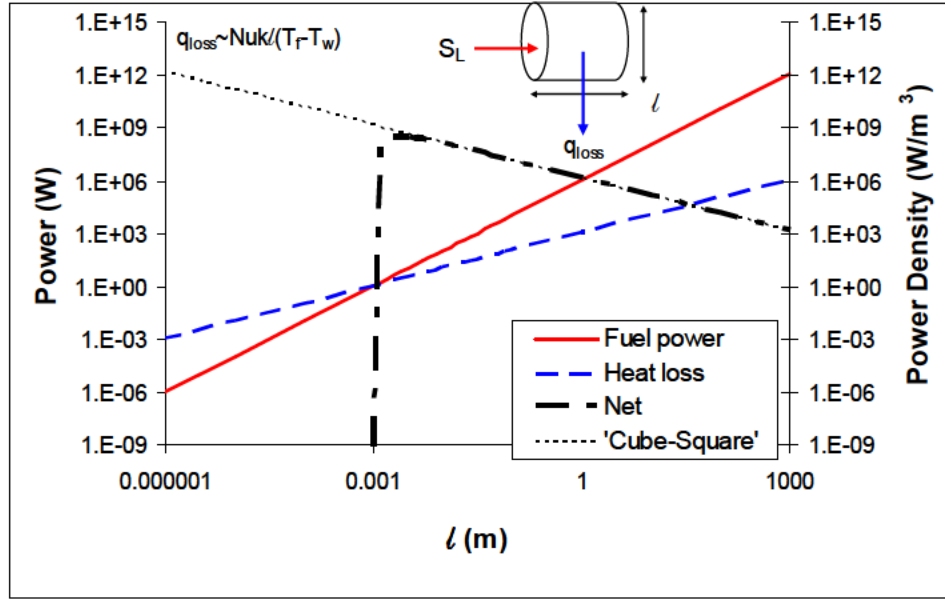


Figure 1–11: Simple scaling analysis for a combustor device.

A more detailed numerical investigation of heat transfer in micro-combustors by Lee et al.⁴¹ produced similar results. Figure 1–12 shows normalized heat transfer coefficient as a function of chamber height and pressure at the engine intake. The results show that the heat loss experienced by a unit mass of combustible gas mixture increases as the size of the engine decreases.

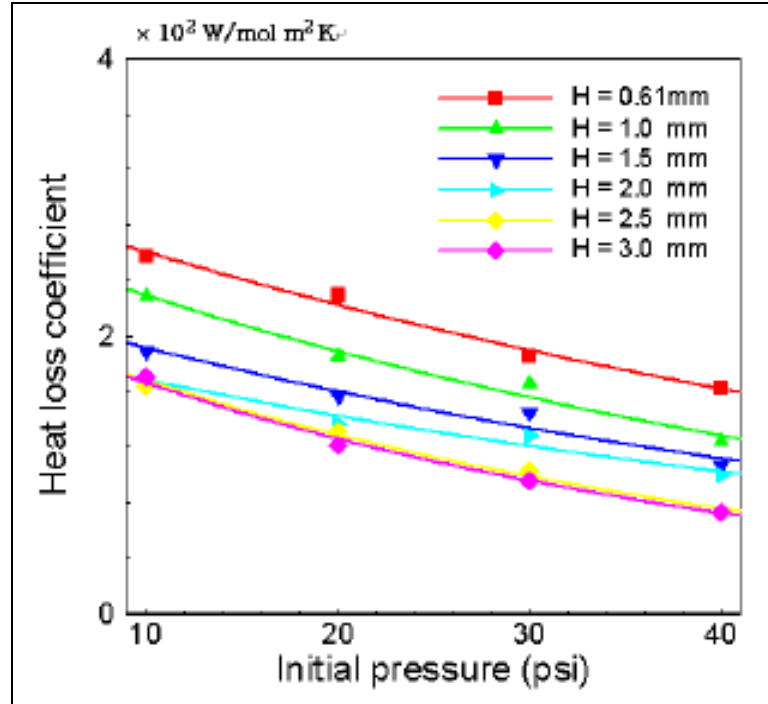


Figure 1-12: Heat transfer coefficient as a function of initial pressure of fuel-air mixture in a micro-combustor with varying chamber height [41].

The results presented in Fig. 1-11 and Fig. 1-12 have three important implications:

1. The so called ‘cube squared law’, which states that the power per unit volume of a device scales inversely with the length scale of the device⁴² and is often used to explain why miniaturization is advantageous, breaks down at small scales.
2. There is a minimum size below which a heat engine becomes impractical or impossible.
3. The minimum possible engine size is set by the rate at which the overall thermodynamic efficiency of the system decreases with size.

Other consequences of increased thermal loss at small scales are reduced reaction rate and pre-heating of reactants entering the combustion chamber. The former effect is potentially disadvantageous because it could lead to incomplete

combustion and reduced chemical conversion efficiency. The latter effect could be beneficial as previous work has shown that pre-heating increases reaction rates/flame speeds⁴³ or it could be detrimental as it could reduce the density of the incoming fuel–air mixture resulting in lower power output from the engine.⁴⁴ These effects will be discussed in later sections.

1.2.2 Frictional Loss

Frictional losses arise from rubbing at the piston–cylinder liner interface and in the engine’s bearings. Flow friction losses arise from fluid friction along the internal flow path of the engine. Frictional losses account for about 24% of energy released from the combustible mixture for a conventional–scale IC engine.⁴⁵ Because these losses, like thermal losses, scale with surface to volume ratio, they are also expected to become more important as engine size is reduced.

Equation 1–14 is an empirical correlation traditionally used to estimate friction power loss in conventional scale spark ignition and diesel engines.⁴⁶

$$P_{friction} = \left(a + b \left(\frac{N}{1000} \right) + c \left(\frac{N}{1000} \right)^2 \right) * V_{disp} * N \quad (1-14)$$

The coefficients a, b and c are determined empirically and depend on the type of engine cycle (spark ignition or diesel). Each term in Eqn. 1–14 can be attributed to different component losses in the engine. The first is associated with the contact friction between two surfaces in motion, the second is associated with hydrodynamic shearing in the lubricant film between the moving surfaces, and the third is associated with flow losses in engine accessories like water and oil pumps where turbulent dissipation increases with the square of engine operating speed. Since engine

operating speed tends to increase with decreasing engine size, Eqn. 1–14 suggests that frictional power losses could be proportionally larger in small IC engines.

1.2.3 Combustion Loss

Combustion losses in miniature engines arise from incomplete combustion resulting in the release of unburned fuel in the exhaust. This is commonly attributed to insufficient reaction time and thermal/radical quenching.⁴⁷ Each of these processes will be analyzed separately.

1.2.3.1 Insufficient Burning Time

Miniature IC engines operate at relatively high speeds that routinely range between 2000–20,000 rpm. This means that the residence time (which is defined as the physical time available for combustion of the fuel–air mixture) is shorter than in conventional–scale engines that operate at lower speeds. Figure 1–13 shows how residence time decreases with engine size and approaches 1 ms in the smallest hobby engine currently available.

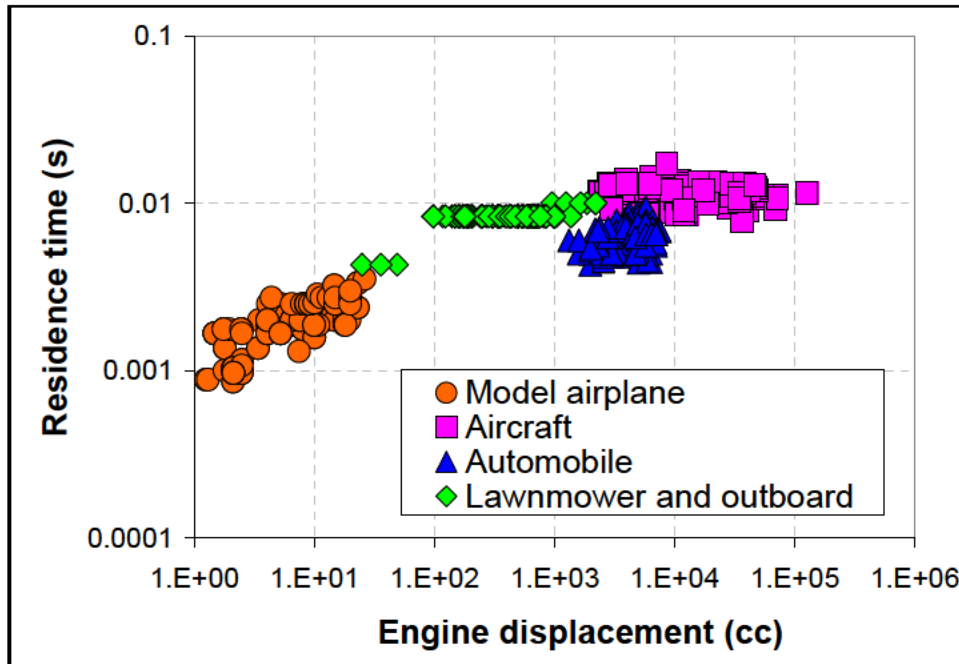


Figure 1–13: Residence time as a function of displacement volume for a large number of IC engines.

1.2.3.2 Thermal/Radical Quenching

Quenching or flame extinction typically occurs at combustion chamber walls.⁴⁸ In micro scale engines, quenching has been postulated to occur via one of two mechanisms: thermal and/or radical quenching.⁴⁹ Thermal quenching occurs when heat losses to the walls of the chamber are too high to sustain combustion. Radical quenching occurs when the radical species involved in the chain branching and propagating reactions adsorb on the chamber walls instead. Both of these effects become important as the length scale of the device becomes comparable to the flame thickness. This effect can also be attributed to the increased surface to volume ratio in miniature engines.⁵⁰

A considerable amount of work has investigated flammability/thermal quenching, flame speed, flame stability, and the effect of wall temperature in

millimeter and sub-millimeter scale tubes with rectangular and circular cross sections.⁵¹ The first investigations of quenching⁵² focused on the ability of a pre-mixed flame to propagate through a series of tubes with progressively smaller internal diameters. The tube ID where the flame can no longer propagate upstream was called the ‘quenching diameter’ and was tabulated as a function of fuel/air ratio for a variety of fuels. The fact that this minimum diameter is apparatus specific – i.e., it depends on the tube material, wall thickness, length, and thermal boundary condition at its support point – was not commonly appreciated and many researchers came to think of the quenching diameter as a property of the fuel mixture and that combustion below the quenching limit was not possible. Recent work has corrected this misperception by reporting sub-quenching distance combustion in a variety of geometries.^{53 54}

Some work suggests that the combustion process in hobby engines occurs in a mixed HCCI and flame propagation regime.⁵⁵ If true, this could reduce the importance of heat loss to the walls as HCCI combustion results in the development of multiple ignition points. Other work, however suggests that combustion in hobby engines occurs in a thin, continuously vaporizing fuel film attached to the cylinder wall. Vaporization is driven by heat transfer from the gas and wall and the resulting diffusion flame leads to fuel-rich combustion spots close to the cylinder walls.⁵⁶ This mode of combustion would be much more susceptible to wall heat transfer.

1.2.4 Mass Leakage Loss

A significant difference in the design of miniature IC engines compared to conventional engines is the lack of piston rings. Piston rings are designed to prevent high pressure gas in the combustion volume from driving unburned charge through

the gap in the piston–cylinder arrangement into the crankcase in the case of two–stroke cycle engines.⁵⁷ The reason for the lack of piston rings in miniature IC engines is because of the high amount of frictional losses it would add to the system.⁵⁸ The absence of piston rings is made up for by a cylinder design incorporating a tapered sleeve reducing the gap area during the parts of the engine cycle when maximum pressure is developed in the engine cylinder. This is supplanted by an oil film developed in the gap area from the oil contained in the fuel. In spite of these strategies, mass lost by blowby has been determined to be one of the major challenges in the miniaturization of engines.⁵⁹

1.2.5 Flow and Scavenging Losses

The effect of internal air flow resistance on the ability of the engine to ingest fresh charge for each stroke is described by a parameter known as the delivery ratio. It is the ratio of the actual mass of air present in the cylinder at bottom dead center to the mass of air that would be present if the cylinder (at bottom dead center) were completely filled with air at atmospheric pressure. The major factors that cause delivery ratio to decrease are charge heating, choking of the intake passages, and fluid friction through the engine flow path.⁶⁰ These effects could be significantly higher at the small length scales and high operating speeds prevalent in miniature IC engines. Therefore, one would expect that smaller engines would have smaller delivery ratios and, therefore, be able to burn less fuel and make less power per unit cylinder volume than conventional–scale engines.

Scavenging is the process of transferring fresh charge in a two stroke engine from the crankcase into the working cylinder volume. The fresh charge, which is

under pressure because of the piston motion, is introduced in a manner designed to expel the burnt mass from the previous cycle through the exhaust port. Charge short-circuiting, which is the process where fresh charge is lost through the exhaust port during the scavenging process has been identified to be a major loss mechanism for two-stroke cycle engines and can decrease efficiency by up to 35%.⁶¹ Short circuiting gets worse with increasing operating speed⁶² which suggests that loss of scavenging efficiency could be another challenge associated with engine miniaturization.

1.3 Previous Work

1.3.1 Performance Measurements in Miniature IC Engines

Scientific investigations of performance of miniature hobby engines are very scarce. Hobby magazines have published some reviews of small engine performance over the years but the data they provide is incomplete. Usually, the evaluation of an engine simply consists of measuring peak rpm with different propellers installed. At most, power output and torque as a function of engine rpm at wide open throttle are reported.^{63 64}

The most extensive investigations of small engine performance have been reported by David Gierke in articles that have appeared in various hobby magazines over the past 30 years. Gierke developed a simple dynamometer in 1973 and used it to test a variety of small aircraft engines. Most of his efforts focused on measuring the engine's power curve although specific fuel consumption was reported in a few instances. The present state of the dynamometer is not clear, but his articles document a number of improvements that were made over the years to assemble a more complete picture of engine performance. The engine was mounted on a reaction arm

which was held in place using a spring scale. This apparatus provided the torque measurement.

Engine speed was measured using a tachometer. Fuel flow rate was measured using a graduated cylinder and a stopwatch. Power output was corrected to standard atmospheric conditions. The engine was loaded using different propellers. Torque and power curves were generated for a number of engines using this dynamometer.^{65 66 67} A good overview of 2-stroke glow engines is also included in his publication.⁶⁸ Figure 1–14 shows a picture of the dynamometer and Fig. 1–15 shows a schematic of the same.

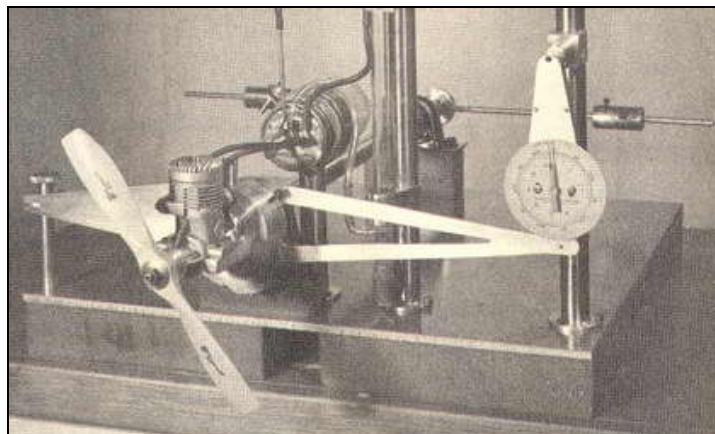


Figure 1–14: Photograph of the dynamometer setup used by Gierke to estimate performance characteristics of model airplane engines [65].

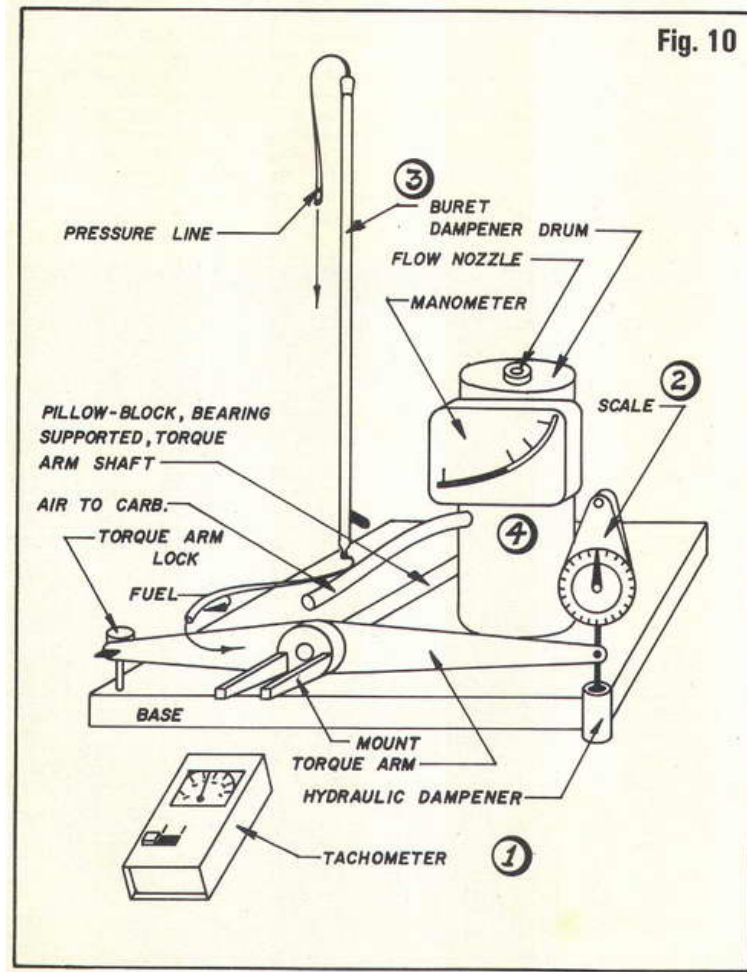


Figure 1–15: Schematic of the dynamometer developed by Gierke showing sensors used for measurements [65].

More recently, Raine et al.⁶⁹ developed a dynamometer system capable of making performance measurements in miniature IC engines. A unique pendulum arrangement was used to measure the deflection of a load because of the torque applied by the engine. The engine is mounted on gimbaled bearings so that it is free to rotate. The rotation of the engine support in response to the load applied by the rotating propeller causes the pendulum to deflect. The angle of deflection is measured using a protractor and used to calculate engine torque. This arrangement is shown in Fig. 1–16.

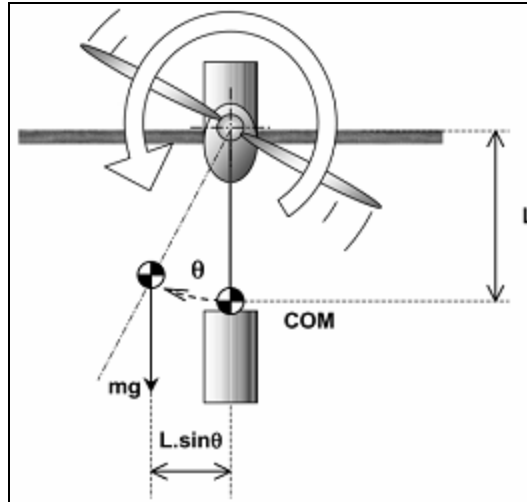


Figure 1–16: Torque measurement principle used by Raine in the dynamometer used to characterize model airplane engines [69].

The engine load was adjusted by changing the propeller size. A 7.54 cc (0.46 cu.in.) displacement engine was tested with 10% nitromethane in the fuel. Exhaust gas analysis was used with measurements of fuel flow rate to determine overall efficiency for different throttle settings. The maximum efficiency obtained was about 20% at a rated power of 650 W.

A study conducted at Wright Patterson AFB by Roberts et al. examined 15 different engines as part of an investigation into engine–generator systems for compact power supply.⁷⁰ The engines ranged in size from 4.75 cc (0.29 cu.in.) to 16.4 cc (1 cu.in.) displacement. A Westinghouse universal motor was used to apply engine load by functioning as a generator as well as to motor the engine to establish mechanical efficiency. The study found several interesting results:

- Mechanical efficiency was found to be surprisingly high with a value of close to 60% for most of the engines.

- None of the engines produced the power levels quoted by the manufacturer leading to the conclusion that manufacturers tend to overrate engine power output.
- Engine performance was found to be erratic and measurements were not repeatable even when the test conditions were carefully controlled.
- Volumetric efficiency measured using a rotameter was found to give inaccurate results (often $> 100\%$) because of the pulsating nature of the flow into the engine carburetor.
- Part of the reason for poor fuel economy was attributed to poor scavenging resulting in loss of fresh charge in the exhaust.

Figure 1–17 shows the performance data obtained from one of the engines tested in the Wright Patterson study.

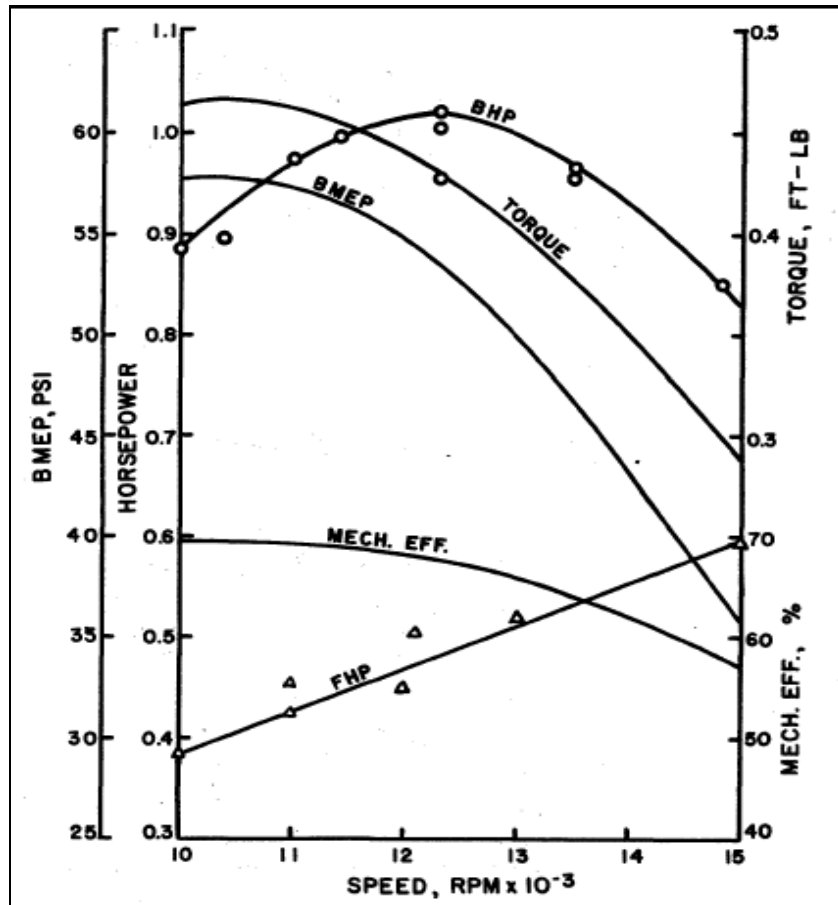


Figure 1-17: Performance data obtained for an engine with displacement 9.95 cc (0.607 cu.in.) with a cylinder head temperature of 477 K (400 °F) and fuel with 67% methanol, 25% oil and 8% nitromethane[70].

Shin et al.⁷¹ developed a small engine dynamometer to measure the performance of an Enya model airplane engine converted to operate on gasoline fuel. The measurements were primarily made to tune a simulation program that would enable engine power output at higher altitudes to be predicted. Motoring tests were also conducted to determine engine frictional and pumping losses. Figure 1-18 shows a photograph of the setup.

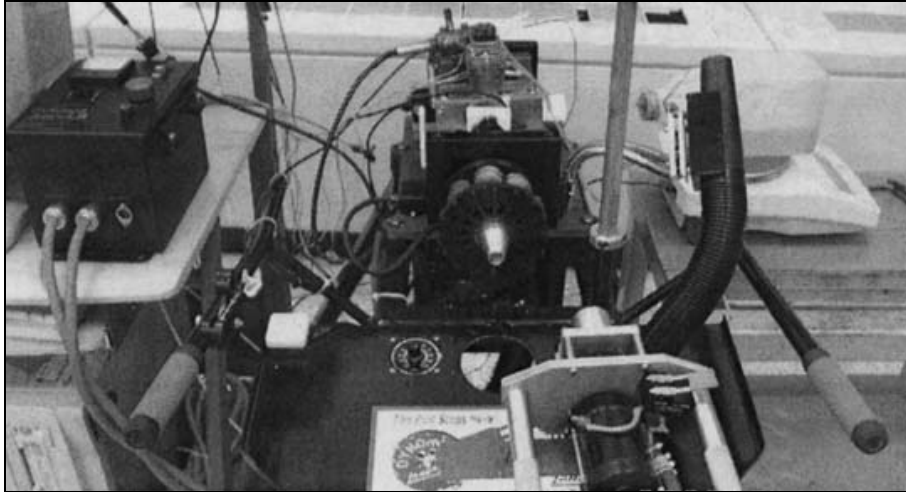


Figure 1–18: Photograph of a setup used to estimate performance from an Enya model airplane engine [71].

The motoring results indicated that below an engine speed of 8500 rpm, the engine operated in a hydrodynamic lubrication regime while above 8500 rpm, frictional losses grew substantially indicating that the engine was operating in a mixed lubrication regime. Engine power was also found to decrease drastically at higher altitudes.

Sookdeo⁷² made some preliminary measurements of the performance of the smallest commercially available glow fuel engine (Cox Tee Dee 0.16 cc (0.01 cu.in.) displacement volume). The engine was found to produce a peak power output of 10.2 W with an overall efficiency of 6.2%. A throttled version of the engine produced 9.85 W with an overall efficiency of 3.4%. Figure 1–19 shows a photograph of the experimental setup. The investigation was limited in scope because it was not possible to control the engine speed.



Figure 1–19: Photograph of a setup used to estimate performance from a Cox 0.16 cc (0.01 cu.in.) displacement model airplane engine [72].

1.3.2 Scaling Issues in IC Engines

Heywood et al.⁷³ investigated the scaling of engine performance, configuration, size and geometry by comparing data for spark ignition engines from various sources. Additionally, historical trends were analyzed to understand changes in engine performance brought about by improvements in technology like electronic fuel injection, variable valve timing and supercharging. They found that peak engine torque correlated very well with engine size and normalized power – the ratio of power output to mean piston speed – correlated very well with piston area.

A scaling study carried out by Peterson⁷⁴ was the first to identify size limits for a heat engines that are set by thermal losses to the environment. The model considered a Carnot heat engine with a combustor operating at the temperature corresponding to maximum thermodynamic efficiency. A heat exchanger recovering energy from the exhaust gas is coupled to the engine model. The length of the system

was varied from mesoscale to microscale dimensions while calculating system efficiency for each scale. This showed millimeter scale systems to be viable while sub-millimeter scale systems were found to be infeasible because of excessive thermal losses.

Sher et al.^{75 76} have published several numerical investigations of engine performance scaling where processes in the engine are represented using simple algebraic expressions. The first of these studies identified heat loss from the engine as the limiting factor affecting the miniaturization of IC engines and the minimum size was estimated to be 0.007 cc for methane and 0.033 cc for propane. Charge leakage through the piston–cylinder gap was also identified as a limiting factor – especially at high operating speeds. The second of these studies utilized a phenomenological model of the processes taking place in an HCCI engine during the combustion phase of the cycle. Mechanical friction was assumed to be solely because of the fluid friction in the piston–cylinder gap and was found to be negligible. They found that increasing the compression ratio was actually detrimental as it increased blowby losses. The minimum size of an engine operating on a liquid hydrocarbon fuel in HCCI mode was found to be between 0.3 and 0.4 cc while operating with a compression ratio of about 1.2 at 48000 rpm. In this second study, mass leakage by blowby was found to be the main limiting factor in engine miniaturization.

1.3.3 Fundamental Investigations of Miniature IC Engines

Studies have been carried out to gain a more fundamental understanding of physical processes occurring in miniature glow fuel engines. Attempts have been made to understand fuel–air mixing, combustion and ignition phenomena.

Dunn–Rankin et al.⁷⁷ investigated the performance of a 4.9 cc (0.3 cu.in.) displacement engine using a DC motor connected to a resistor pack to apply a load. The engine was tested on fuels with different compositions. Cylinder pressure measurements were made during fired and motored runs using a fiber optic pressure sensor. Figure 1–20 shows a photograph of the setup used in the experiments and Fig. 1–21 shows the location of the pressure transducer in the cylinder head of the engine.

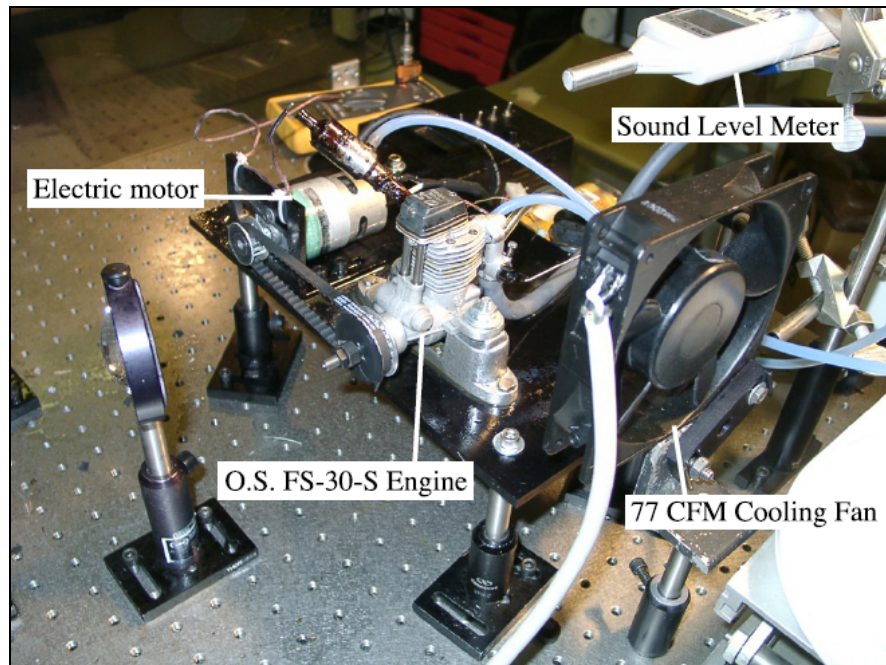


Figure 1–20: Photograph of a setup used to estimate performance from a 4.9 cc (0.3 cu.in.) displacement, OS engines model airplane engine [77].

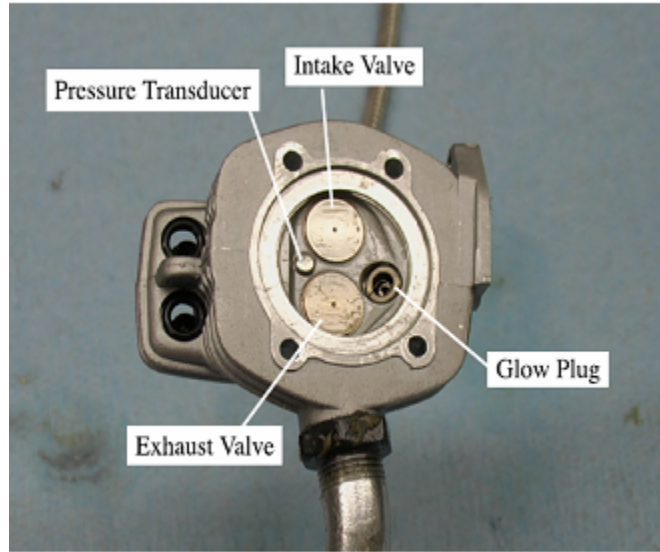


Figure 1–21: Photograph of the cylinder head of the OS 30 FS engine showing the location of the pressure sensor and the glow plug [77].

The following were some of the key findings:

- The measured power output was 80 W which was less than the maximum reported by the manufacturer.
- The efficiency at maximum measured power output (80 W) was approximately 9%.
- A thermodynamic analysis estimated the Damköhler number and the turbulent Reynolds number and showed that the combustion mode in miniature glow engines is similar to that in large scale IC engines, i.e., in the laminar wrinkled flame regime. Residence time appeared to be sufficient for complete combustion of the fuel air charge in each cycle.
- The combustion mode appeared to be a combination of a diesel and partially–premixed modes where fuel vapors from the wall formed fuel–rich zones next to it leading to a diffusion driven combustion process.

- Flame quenching in crevices formed in the piston–cylinder gap and the gaps between the glow plug threads are quoted to be a significant contributor to unburnt fuel in the exhaust and energy loss.

Raine et al.⁷⁸ used a cylinder pressure sensor to measure heat release and mass burning rates in small two–stroke engines operating using different fuels and different types of glow plugs. Figure 1–22 shows the instrumentation setup used in this study. Some of the key findings of this study are:

- Increasing the nitromethane content in the fuel made the fuel mixture leaner because of increased oxygen content, reduced the lower heating value (LHV) of the mixture as the enthalpy of nitromethane is less than that of methanol, and leads to an increased fuel flow rate for the same mixture setting.
- Combustion duration was similar to that observed in other (larger) research engines in spite of the significant differences in engine design and operating conditions.
- Several cases showed large cycle–to–cycle variations in cylinder pressure where a partially burning cycle is followed by a cycle with higher than average indicated mean effective pressure (IMEP). This was attributed to the presence of trapped residuals from the previous cycle.
- Although the fuel–air mixture ratio was not measured, estimated values showed the mixture to be consistently richer than stoichiometric.
- Using a ‘hot’ glow plug extended the rich flammability limit of the mixture possibly because heat from the glow plug enhanced fuel vaporization.

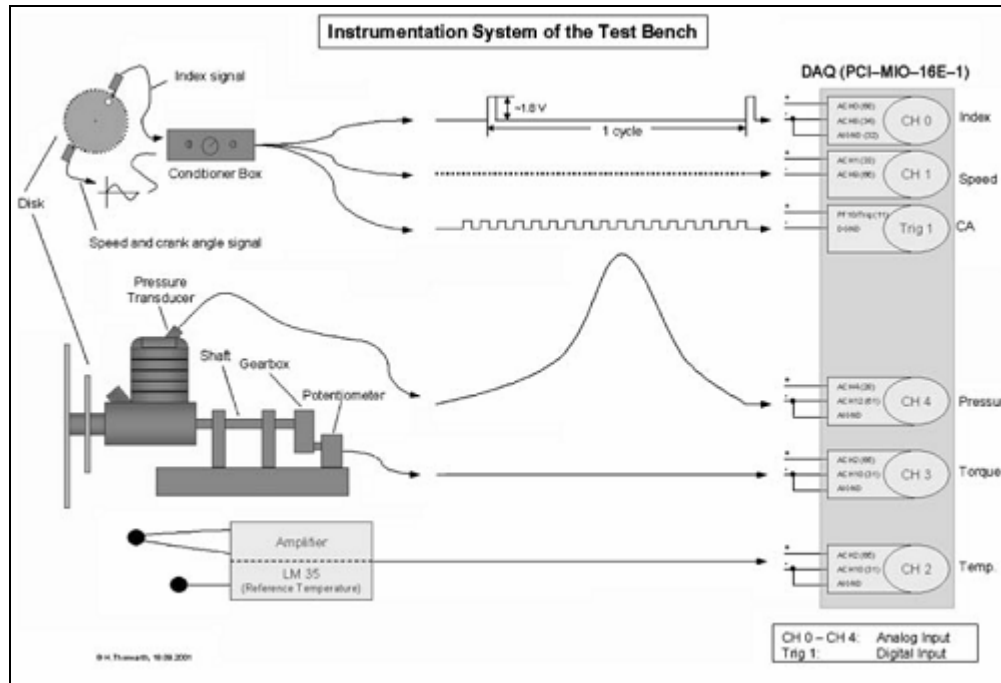


Figure 1–22: Schematic of the measurement setup for in-cylinder pressure and crank angle location from a two–stroke glow fuel engine [78].

Manente⁷⁹ has performed the only optical investigation into the nature of glow fuel ignition and combustion processes to be found in literature. In-cylinder pressure was measured using a Kistler piezo electric pressure transducer while crankcase and exhaust pressures were monitored using piezo–resistive pressure sensors. The exhaust gas was analyzed using an emission gas tester as well as NDIR.

Optical access to the cylinder was provided by a quartz window and enabled him to obtain high speed photographs of in-cylinder combustion processes as well as chemiluminescence measurements of hydroxyl, formaldehyde and C2 radical species. The engine load was varied by using different sized propellers. Figure 1–23 is a photograph of the experimental setup. Figure 1–24 is a close-up of the engine showing modified cylinder head and the locations of the cylinder pressure sensor and glow plug.

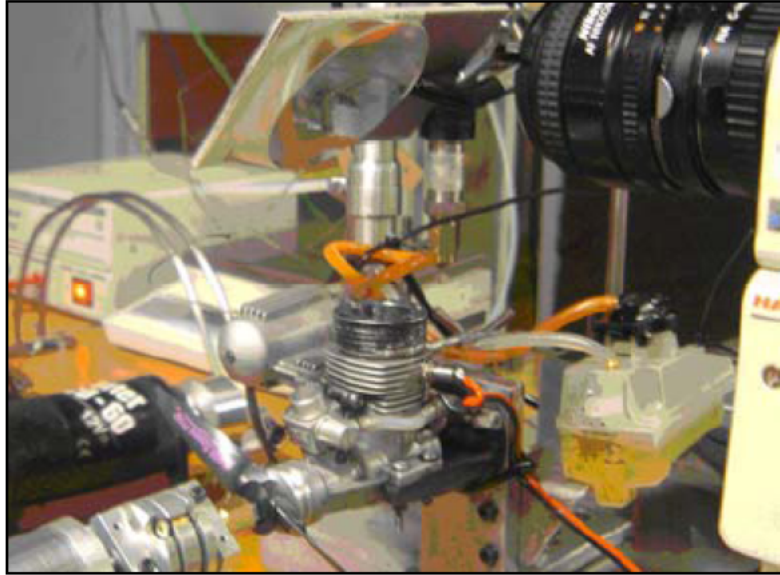


Figure 1–23: Photograph of a setup used to obtain in-cylinder pressure measurement and chemiluminescence images from a model airplane engine [79].

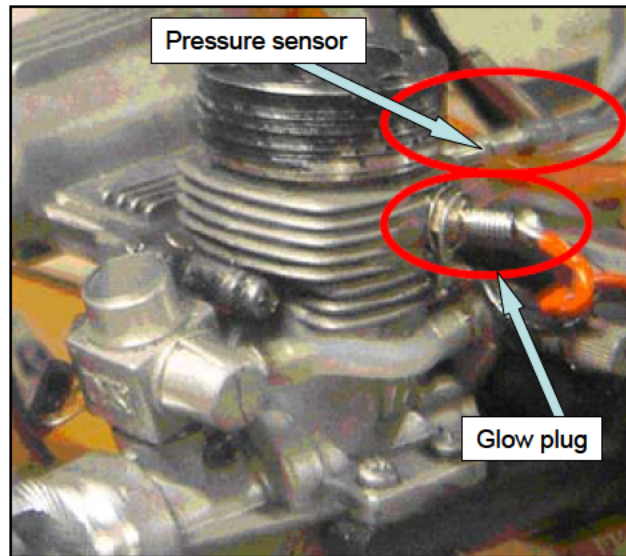


Figure 1–24: Close up photograph of the cylinder head showing the locations of the glow plug, the optical window and the pressure sensor [79].

The following were some of the key findings:

- Pre-heating of the air at the engine inlet reduced performance by decreasing the density of the inlet air. Throttling the exhaust also reduced engine

performance by increasing pumping losses and possibly unfavorably affecting combustion phasing.

- The peak efficiency obtained for the 4.1 cc (0.25 cu.in.) displacement engine was found to be about 9%. Peak indicated mean effective pressure was measured to be 300 kPa (3 bar) at 16500 rpm corresponding to a peak power output of 337 W. The manufacturer rated power output for this engine is 1014 W at 16000 rpm. The study investigated a variety of fuel blends.
- Cylinder pressure rise rate is found to be small (relative to conventional gasoline/diesel engine combustion) and very gradual. This was similar to phenomena observed in previous studies where a large amount of exhaust gas was retained in the engine to aid autoignition⁸⁰.
- Chemiluminescence images revealed a two-fold ignition process: an HCCI-like homogeneous auto ignition of part of the mixture in the warm/hot part of the combustion volume and a heterogeneous ignition on the glow plug orifice. This combined ignition mode was called “glow plug assisted compression ignition” (GACI). Figure 1–25 is a series of chemiluminescence images showing the combustion process when the engine is running at 9600 rpm.
- At higher engine speeds, the glow plug assisted ignition mode appeared to dominate and the better conversion efficiency was attributed to improved turbulent mixing at high speeds which produced a more uniform chemical and thermal distribution. The average propagation speed of a combustion wave in the cylinder was computed to be about 86 ms^{-1} and the thickness of the reaction region (3–4 mm) showed evidence that the combustion process was

far from being in the typical flame propagation regime seen in conventional scale spark ignition engines.

- The engine was converted to run in a pure HCCI mode and similar experiments were conducted for that setup as well. The maximum efficiency in this case was found to be about 5% with a maximum power of 280 W. The rate of combustion pressure rise was found to increase in this case. The drop in overall efficiency was reasoned to occur because of an increase in the thickness of a boundary layer developed near the cylinder walls where low temperature conditions precluded complete oxidation of the fuel–air mixture.

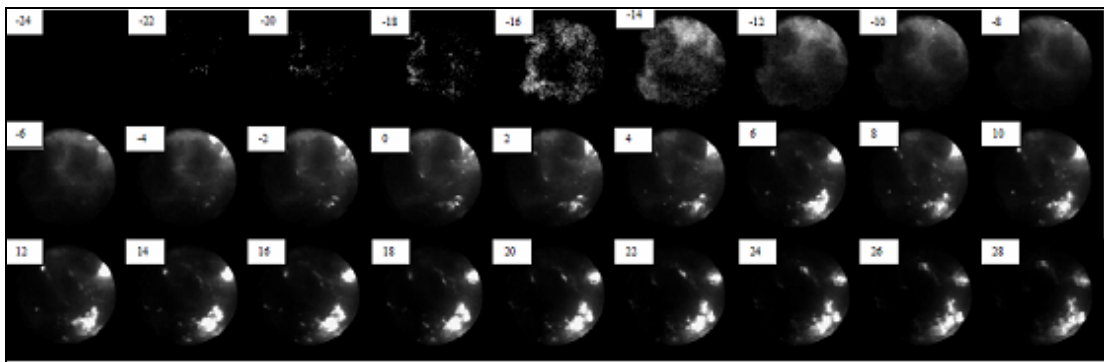


Figure 1–25: Chemiluminescence images obtained inside the cylinder of a model airplane engine operating at 9600 rpm during one engine cycle [79].

1.4 Motivation, Objectives and Approach

The discussion in Section 1.1 highlighted the need for a high energy density power plant to extend the range and endurance capabilities of a variety of devices requiring compact portable power. The comparison of existing and proposed miniature power plants in Fig. 1–8 shows the promise of miniature IC engines in meeting targets set by DARPA/DOD for the next generation of portable power devices. First, they are closer than any other technologies to meeting the DOD

specifications. Second, these engines are commercially available today. Third, these engines have been optimized for the hobby industry where cost and ease of operation drive the design. They have not been optimized for efficiency so there should be substantial room for improvement. Fourth, a lot is known about IC engines already so it should be relatively easy to achieve these efficiency improvements by adapting tools and techniques for use at small scale that have been already been proven at larger scales.

The main obstacle to the use of hobby engines as a compact power source and battery replacement is the lack of a *quantitative* understanding of their performance. Manufacturers of hobby engines usually supply information on one operating point – if they supply any information at all – and the few experiments that have been done indicate that this information is often unreliable.^{81 82} An important obstacle to realizing the potential of hobby engines is a lack of basic understanding of the performance that is available today and the physical processes (loss mechanisms) that establish and limit this performance. Therefore, the objectives of this thesis are as follows;

1. Quantify the level of performance available from a series of small engines ranging in size from 15 to 500 g.
2. Identify and quantify the physical processes that limit engine performance in different size engines.
3. Develop scaling relationships for losses and overall performance with engine size.

4. Use these relationships to identify the minimum ‘practical’ size of a heat engine.
5. Develop strategies for improving the efficiency of miniature heat engines by identifying and quantifying the different energy loss mechanisms in the engine.
6. Understand whether or not the combustion process in these small engines is the same or different (via a turbulent premixed flame or in an HCCI mode) as in conventional-scale premixed charge engines.

The overall objective of this project is to gain a thorough understanding of the performance of miniature glow fuel IC engines and to understand the effect of scaling of size on engine performance and loss mechanisms. The approach taken here consists of the following steps:

- A detailed investigation of engine performance will be made for a set of miniature glow fuel IC engines that have the potential to develop portable power applications as discussed in previous sections. This will be done using a dynamometer which has been specially constructed to handle challenges posed by measurements in miniature IC engines.
- The measurements obtained will be used to investigate parameters that could best correlate performance with engine size. These parameters will be used to identify a minimum possible size for an IC engine, based purely on overall performance.
- The major sources of energy loss mechanisms in miniature engines will be identified and their effects individually quantified using different techniques.

- The scaling of engine loss components will be investigated to determine the relative importance of each with decreasing engine size and to identify the critical loss mechanisms limiting engine miniaturization.
- A more fundamental study of the engine cycle will be undertaken utilizing in-cylinder pressure sensors to estimate heat release rate, mass burning fraction, peak cylinder pressure, cycle-to-cycle variation and ignition timing. These parameters will be investigated across different engines where such measurements are possible and the effect of scaling of size on them will be analyzed.
- An engine with optical access will be investigated using high speed photography to understand the mode of combustion in these engines.
- A combined study of an engine-generator setup used to generate electrical power for a compact portable power system will be presented.

Chapter 2 : Small Engine Dynamometer System

This chapter describes the small engine dynamometer system utilized for performance characterization of miniature glow ignited two stroke engines studied in this work. A brief description of the working cycle and construction of engines tested in this work is followed by a detailed description of the dynamometer hardware, sensors and data acquisition systems. Finally, engine test procedure and methods of uncertainty analysis and correction of measurements to standard atmospheric conditions are reviewed.

2.1 Engine Testing Methods

The performance of reciprocating internal combustion (IC) engines is usually measured using a dynamometer. A dynamometer is a device used to measure the torque and speed of a rotating machine operating in a controlled environment. It consists of a speed sensor, torque (force) sensor, and a controllable absorber and/or motor. Adding a feedback control loop enables machinery to be operated at constant speed or constant torque. Dynamometers are classified as absorption, motoring or universal depending upon the specific application. An absorption dynamometer absorbs the power produced by the prime mover and is used to measure engine performance like torque, speed, and power. A motoring dynamometer provides the motoring force for turning the prime mover and is used to estimate frictional and pumping losses in IC engines. A universal dynamometer can operate in absorption or motoring modes allowing both operations to be carried out on the same setup.

Absorption dynamometers are classified according to the manner in which the absorbed energy is dissipated.

- Friction dynamometers: The energy absorbed from the prime mover is converted into heat. Frictional elements like mechanical brakes are used to dissipate the absorbed energy.
- Hydraulic and air dynamometers: The motion of a working fluid such as air or water provides the frictional force and allows the absorbed energy to be converted to heat which is transmitted to the fluid.
- Magnetic and eddy current dynamometers: An applied magnetic field provides resistance to the motion of the prime mover and the energy absorbed is dissipated via joule heating.

Dynamometer systems used in applications involving IC engines are classified into ‘chassis’ type or ‘engine’ dynamometers. Engine dynamometers are used to measure the performance of the engine itself. Chassis dynamometers measure power at the wheels and hence estimate the actual ‘road load’ power of the vehicle including the losses in the transmission. The dynamometer is a complete system which, apart from being able to measure torque and speed, has capabilities to control engine operation by regulating engine load. The dynamometer used in this work is an absorption type dynamometer with a magnetic hysteresis brake for energy absorption/load control.

2.2 Two-Stroke Engine Cycle

The engines tested in this research operate on the two stroke cycle. The characteristics of two stroke cycle engines that make them advantageous for use in compact portable applications are:

- **Simplicity:** Two-stroke engines employ piston motion to cover and uncover port openings which allow the transport of fuel and air from the intake manifold into the engine cylinder. This arrangement reduces complexity and weight considerably by eliminating the camshafts, pushrods, rocker arms, and springs associated with other types of valving.
- **Power-to-weight ratio:** Two stroke engines have higher power to weight ratios because they produce a power stroke once every two piston strokes as opposed to once every four strokes in a four-stroke engine. This makes two stroke engines more attractive in miniature applications requiring high power density.

A brief discussion of the two stroke engine cycle is provided to highlight the important processes occurring during the course of a single cycle. Figure 2-1 shows the steps involved in the version of the two-stroke engine cycle that is commonly used in model aircraft engines. Figure 2-2 marks the corresponding steps on a pressure-volume diagram of an engine cycle.

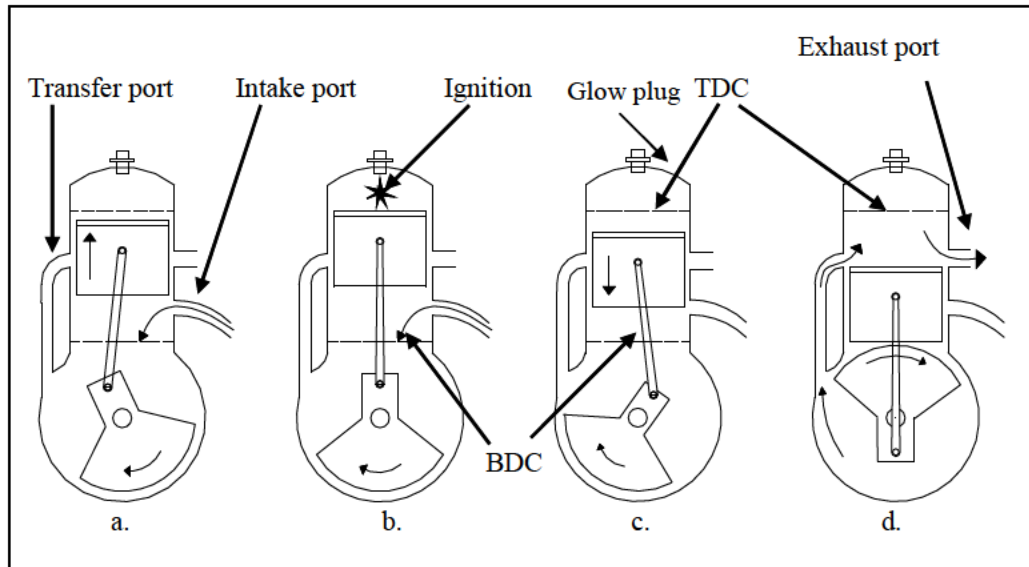


Figure 2-1: Steps involved in a two-stroke engine cycle.⁸³

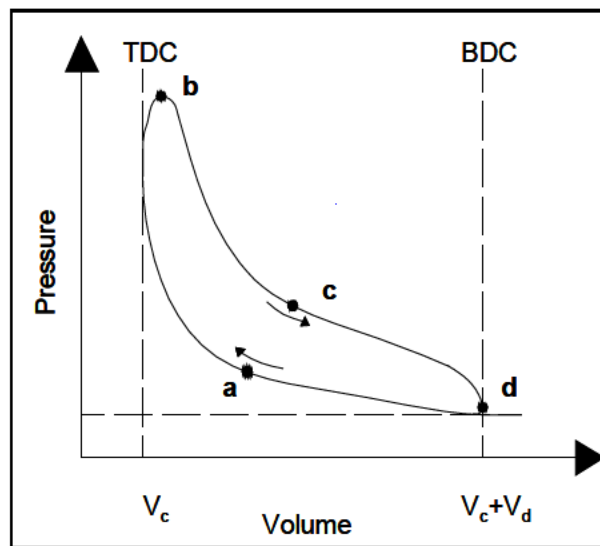


Figure 2-2: Pressure volume diagram for the two-stroke engine cycle.⁸⁴

- **Intake and compression strokes (parts a & b):**

Starting from bottom dead center (BDC) in Fig. 2-1, the fresh charge in the cylinder is compressed by the upward motion of the piston. This causes the pressure and temperature of the cylinder contents to increase and at some point near the top dead center (TDC), the charge ignites. Ignition is aided by the catalytic glow plug

which provides a hot spot for ignition. The igniting charge releases energy rapidly raising the pressure and temperature in the cylinder volume.

Meanwhile, the increase in crankcase volume associated with the upward motion of the piston causes a pressure drop in the crankcase. The port of a rotary valve in the hollow crankshaft is situated so that it begins to sweep by the base of the carburetor as the piston approaches TDC. This allows fresh fuel–air mixture to be drawn into the crankcase through the valve port and hollow crankshaft by the difference in pressure between the environment and crankcase.

Power and exhaust strokes (parts c & d):

The hot, high pressure gases in the cylinder volume drive the piston downwards and perform work on the piston. At this point, the intake valve is closed and the down stroke of the piston results in compression of the fresh charge in the crankcase volume. At some point during its downward motion, the piston uncovers the exhaust port releasing burned gases out of the engine.

Meanwhile on the other side of the piston, its downward motion compresses the fresh mixture which is trapped in the crankcase because the rotary valve has closed. As the piston continues downward, it eventually uncovers the transfer ports which allow the fresh (and now compressed) charge from the crankcase to be blown into the engine cylinder. The motion of the fresh incoming charge forces exhaust gases from the cylinder and out of the exhaust port by a process known as scavenging.

2.3 Engines

Table 2–1 summarizes the engines investigated in this study. All are single cylinder, naturally aspirated, 2–stroke, carbureted engines, designed to operate on mixtures of methanol, nitromethane and oil.

	Engine Model	Displacement		Mass	Engine speed range	Bore	Stroke
A	OS 46 FX	0.46	7.54	488	2.5–17	22	19.6
B	OS 40 FX	0.4	6.55	386	2–17	20.5	19.6
C	OS 25 FX	0.25	4.1	248	2.5–19	18	16
D	AP Yellowjacket	0.15	2.46	150	3.5–18	15.5	12
E	AP Hornet	0.09	1.47	128	4–18	12.5	12
F	AP Wasp	0.061	1.0	54	3–25	11.25	10
G	Cox 049	0.049	0.8	42	10–20+	10.24	9.6
H	Cox 020	0.02	0.33	25	10–20+	7.45	7.5
I	Cox 010	0.01	0.16	15	10–25+	6.02	5.74
		cu. in.	cc	gm	krpm	mm	mm

Table 2–1: Specifications of miniature IC engines tested in the study.

Figure 2–3 shows pictures of the engines whose details are listed in Table 2–1.

		
A. OS 46 FX	B. OS 40 FX	C. OS 25 FX
		
D. AP Yellowjacket	E. AP Hornet	F. AP Wasp
		
G. Cox 049	H. Cox 020	I. Cox 010

Figure 2–3: Photographs of the model airplane engines evaluated in this study.

2.4 Engine Construction

Figure 2–4 shows a complete view and Fig. 2–5 shows an exploded view of the OS 40 FX engine. The construction of this engine is representative of engines A–F in Fig. 2–3. The major variation with engines G–I is the absence of a muffler as will be discussed below. All engines use a carburetor with throttle to mix fuel and air. The throttle valve is controlled by a throttle lever. A stop screw limits the travel of the

throttle valve in airplane applications. Fuel flow and the resulting fuel to air ratio is controlled using a needle valve. The flow through the carburetor into the crankcase is controlled by a rotary valve which consists of a port machined in the side of the hollow steel crankshaft.

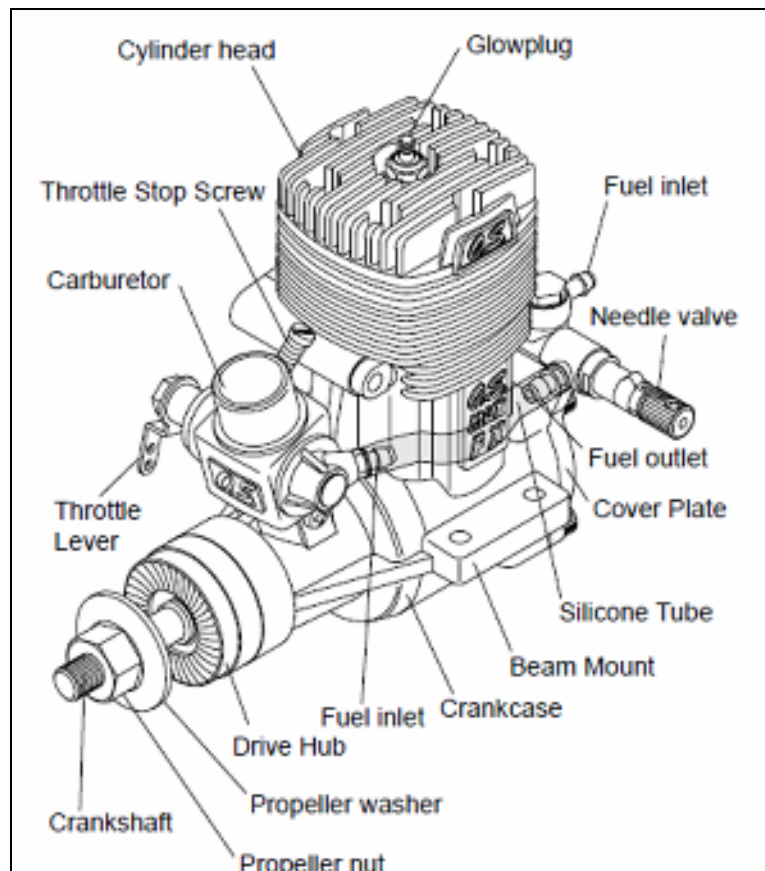


Figure 2–4: A complete view of the OS 40 FX engine. Figure reproduced from OS 40 FX manual with permission from OS engines.⁸⁵

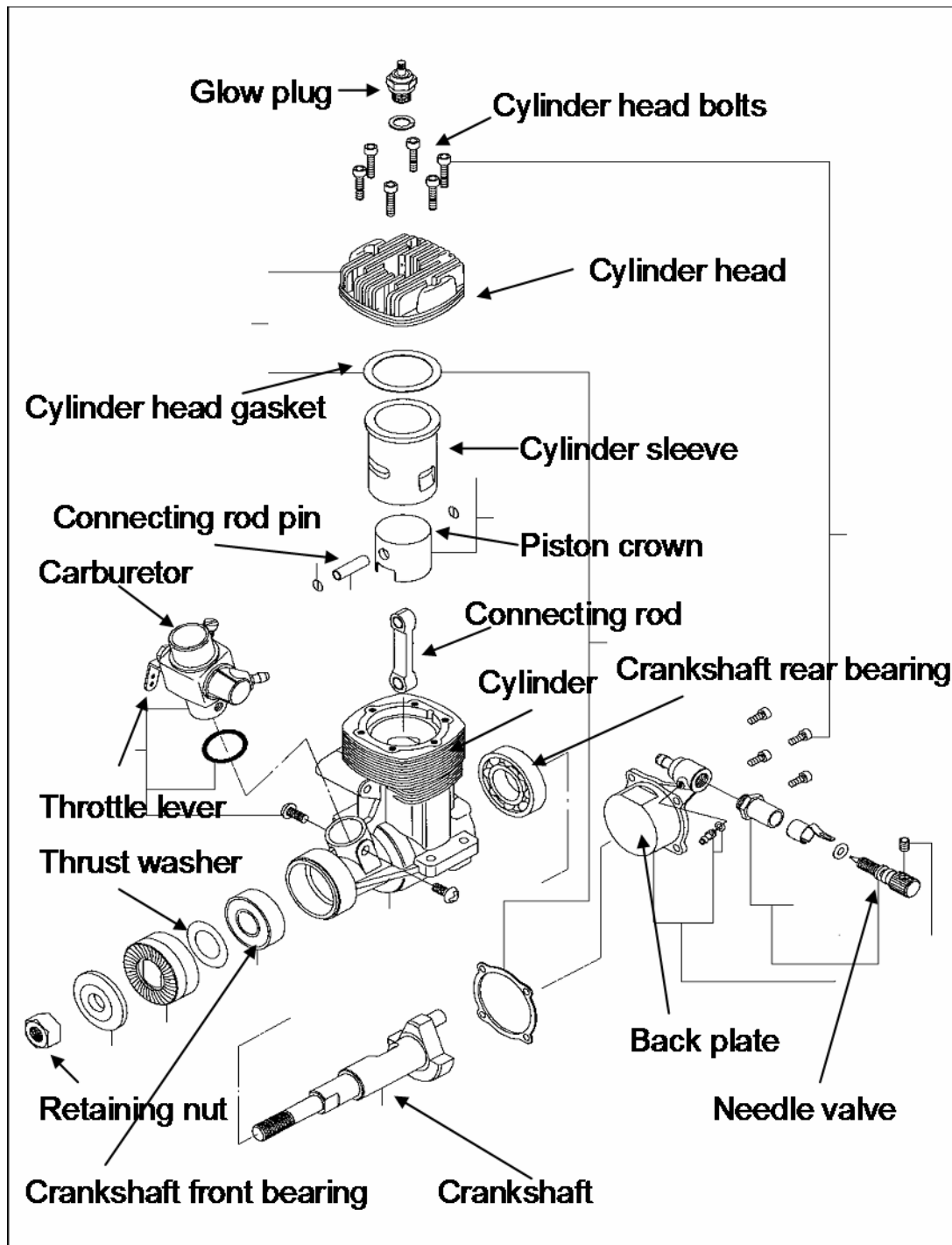


Figure 2-5: An exploded view of the OS 40 FX engine. Figure reproduced from OS 40 FX manual with permission from OS engines [85].

The crankshaft is supported by front and rear ball bearings. A thrust washer mounted ahead of the front ball bearing allows axial load from the propeller to be

transferred to the bearing. A retaining nut holds the propeller in place on the threaded engine shaft. A metal back plate attached using screws and a copper gasket seals the rear of the engine. The crankshaft is connected to the piston via the connecting rod and the connecting rod pin. The connecting rod pin is held in place by a pair of snap rings. The engine cylinder and carburetor are typically cast out of aluminum. The piston is typically made of cast aluminum.

The cylinder sleeve is usually some kind of bimetallic material and brass coated with chrome or nickel is common. The transfer ports are machined into the cylinder sleeve as is a small plenum that connects to the crankcase. The engines tested in this work primarily use Schnurle porting to achieve an effective scavenging process. Two of the transfer ports or Schnurle ports are set at 90 degrees from the exhaust port on either side of it. A third port referred to as ‘boost’ port is set at 180 degrees from the exhaust port. The ports are machines so as to allow the Schnurle ports to open first during the downward motion of the piston followed by the boost port. The fresh mixture transferred into the cylinder from the Schnurle ports force the burnt gas to the top of the cylinder from where they are purged by the motion of inflow through the boost port. Additionally, it has been suggested that the mass flow through the Schnurle ports prevents the mass inflow through the boost port from quenching the glow plug.⁸⁶

In the case of engines A–E as shown in Fig. 2–3, the cylinder head bolts on to the engine casing using cylinder head bolts. In the case of engines F–I in Fig. 2–3, the cylinder head simply screws on to the engine casing. The top of the cylinder liner for all engines is slightly lower than the top of the engine casing. A part of the cylinder

head that contacts the outside of the engine casing and the top of the cylinder liner provides gas sealing. Sealing is also achieved by the copper gaskets used in all engines between the cylinder head and the liner. Fins on the cylinder and cylinder head provide increased surface area for convective cooling. Ignition of the charge is facilitated by a glow plug. The glow plug consists of a platinum coated wire mounted in a threaded housing that screws into the cylinder head. One end of the wire is connected to the housing and the other end to an insulated electrode that protrudes from the top enabling the wire to be heated electrically by passing a current through it. A copper washer provides pressure sealing. Figure 2–6 is a photograph of an OS#8 glow plug commonly used in the OS engines. In the Cox 020 and 010 engines, the plug is incorporated into the cylinder head as a single component. Figure 2–7 is a photograph of the cylinder head of the Cox 010 engine with the integrated glow plug. During engine startup the glow plug is heated up by passing a current through it. After startup, some have speculated that the plug remains hot because of catalytic reactions of methanol vapors on the surface of the platinum catalyst as well as because of heat transfer from the hot gases.⁸⁷ Note that the glow plug operates in steady–state and is not used to control ignition timing.



Figure 2–6: Photograph of a #8 glow plug manufactured by OS Engines.



Figure 2–7: Photograph of a Cox 010 cylinder head incorporating the glow plug.

Engine exhaust is ported through a muffler in the case of engines A–F in Fig. 2–3. However, no mufflers are used in the three smallest engines, G–I shown in Fig. 2–3. The muffler is equipped with a baffle which creates a high pressure region inside the muffler which is used to pressurize the fuel tank. Figure 2–8 is an exploded view of the muffler assembly on the OS 40 FX engine. The exhaust pressure acts like a fuel pump as it drives fuel from the tank into the carburetor. However, this causes the fuel–air mixture ratio to depend on engine load/speed in addition to the carburetor and throttle valve settings.

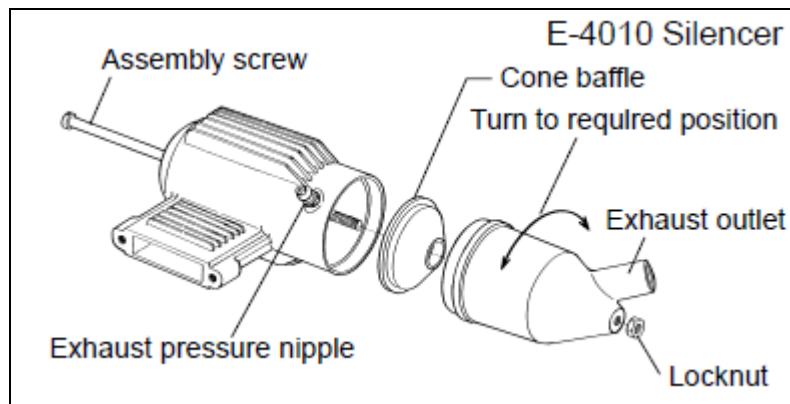


Figure 2–8: Exhaust muffler for the OS 40 FX engine. Figure reproduced from OS 40 FX manual with permission from OS engines [85].

The smallest three (Cox) engines do not have mufflers. While aftermarket muffler kits are commercially available for these engines, they were not used here.

2.5 Fuels

The engines used in this work are designed to operate on ‘glow fuel’ which is a mixture of methanol (CH_3OH), nitromethane (CH_3NO_2), and castor oil ($\text{C}_{18}\text{H}_{34}\text{O}_3$). Different fuel mixtures are commercially available. Mixtures with larger amounts of nitromethane and lesser amounts of castor oil generally produce more power but at the expense of engine operating life. This work uses a relatively conservative 70% methanol, 10% nitromethane, 20% castor oil mixture made by Byron fuels.

The heating value of the mixture was measured by a commercial fuel testing laboratory using standard procedures⁸⁸ and found to be 19.07 MJ/lit (21.82 MJ/kg). Table 2–2 gives the composition and density of the fuel mixture as well as an estimate of the overall heating value of the mixture based on the heating values of the individual constituents. The density of the fuel mixture is given by,

$$\rho_{mix} = \rho_m \chi_m + \rho_{nm} \chi_{nm} + \rho_o \chi_o \quad (2-1)$$

where χ_m , χ_{nm} , and χ_o , are the volume fractions of methanol, nitromethane and castor oil in the fuel. Similarly ρ_m , ρ_{nm} , and ρ_o are the densities of the various components. The heating value of the mixture is given by,

$$Q_{r,mix} = \rho_m Q_{r,m} \chi_m + \rho_{nm} Q_{r,nm} \chi_{nm} + \rho_o Q_{r,o} \chi_o \quad (2-2)$$

where $Q_{r,m}$, $Q_{r,nm}$ and $Q_{r,o}$ represent energy per unit volume for methanol, nitromethane and castor oil.

The stoichiometric fuel/air ratio for the fuel mixture used in the experiments was found to be 0.152 (or 0.227 on a mass-basis) when the castor oil is assumed to be inert. The stoichiometric fuel/air ratio was estimated assuming the fuel with its composition as mentioned in Table 2–2 is completely oxidized leaving behind only CO₂, H₂O and N₂. If only the methanol and nitromethane components remain, then the effective heating value should be 13.3 MJ/lit (15.2 MJ/kg). However, the measured heating value of the fuel mixture is 19.07 MJ/lit (21.82 MJ/kg) indicating that the castor oil can burn – at least in the calorimeter. This data indicates that the heating value of the oil is 42.24 MJ/lit (44 MJ/kg).

Component	χ	ρ	Q_r
CH ₃ OH	0.7	0.81	21.12
CH ₃ NO ₂	0.1	1.13	11.6
Castor Oil	0.2	0.96	44.0
Mixture	1.0	0.875	21.8
		g/cm ³	MJ/kg

Table 2–2: Properties of glow fuel constituents and overall properties of the mixture.⁸⁹

As seen in Table 2–2, the energy density of nitromethane is approximately half that of methanol. However, previous work has shown the power output of an engine increases by about 20% when nitromethane is added to the fuel.⁹⁰ The addition of nitromethane allows for the combustion of a richer mixture since it incorporates two oxygen atoms into its chemical structure. Fewer moles of air are required to burn the mixture and this more than compensates for the reduction in the energy density of the fuel.⁹¹ The addition of nitromethane also influences ignition timing since nitromethane has a lower ignition temperature compared to methanol. However, an

excessive amount of nitromethane can lead to premature ignition, increased engine temperatures, and reduced engine life.

These engines are lubricated by oil mixed in with the fuel. As a result, it is expected that some amount of oil also burns in the cylinder. Castor and synthetic oils are widely used as the lubricant component in model airplane engine fuels. The primary engine cooling mechanism is convective heat transfer from the finned cylinder head to the surrounding air flow. A secondary mode of cooling is via the evaporation of the methanol fuel itself (methanol has a relatively high latent heat of evaporation) as it flows through the engine passages.

2.6 Challenges

Table 2–1 presented the common operating parameters of the engines being tested in this work. There are several factors that complicate performance measurements in these small engines. First, operating speeds are considerably higher than the operating speed limits for commercially available absorbers. Table 2–3 lists the maximum speed of some of the absorbers used in this work. The speed limitations of the absorber require the use of high speed transmissions to transmit engine power to the absorber. Second, fuel flow rates are small ($0.003\text{--}0.29\text{ gs}^{-1}$ ($0.25\text{--}20\text{ cc/min}$) depending on engine size) and not in a range that is accessible by most off-the-shelf liquid flow meters. The fuel flow measurement is complicated further by the fact that the pressure losses through any flow metering instrument must be very small so as not to affect the operation of the carburetor and/or starve the engine of fuel. Third, engine torque levels are low but ambient noise (vibration) levels are high because of the single cylinder engine design. As a result, care must be taken to damp strong 1/rev

(for 2-cycle engines) disturbances and to avoid exciting resonant modes of the measurement system. Since the torque signals are small, failure to control vibration degrades the accuracy of the torque measurement by raising background noise. Excessive vibration also can damage the force sensor. Fourth, air flow into the engine is highly unsteady involving some amount of reverse flow in each engine cycle. This causes difficulties in measuring engine air flow rate and consequently estimating the fuel-air mixture ratio. Fifth, the cycle to cycle variation inherent in these engines causes engine speed to fluctuate at a fixed setting of throttle and fuel-air mixture ratio. This necessitates the use of a control system to establish constant operating speed. Finally, the measurement system needs to be mechanically flexible so as to accommodate a wide range of engines with minimal mechanical modifications. The current setup is able to support both gear and belt drives required for engines of different sizes. Additionally, the setup allows the distance of the moment arm to be changed so as to maximize the signal strength from the load cell for each engine.

2.7 Dynamometer Setup

2.7.1 Torque Measurement Principle

The working principle of a dynamometer system involves applying a load to an operating engine and measuring the engine torque. In most dynamometer systems, the engine is mounted to a fixed support and the torque required to hold the brake stationary, is measured.⁹² Engine torque is typically measured using a load cell mounted on a moment arm from the absorber unit. While this approach adequately serves the measurement purposes for larger engines, it was found to be infeasible in the case of smaller engines like the ones being considered here.

The engines of interest here operate at considerably higher speeds compared to conventional scale engines and standard commercially available absorbers. This speed mismatch makes it necessary to use a transmission system to reduce shaft speed going from the engine to the absorber. If the dynamometer is configured in the conventional arrangement with engine torque measured at the brake, it becomes necessary to account for power losses in the transmission setup. These losses are difficult to account for without embarking on a separate program to measure them directly and can be significant ($> 5\%$) compared to the power output of the small engines of interest here. Therefore, losses in the transmission can be a significant source of error. The solution implemented here is to develop a new dynamometer where the absorber is fixed and torque is measured at the engine supports by mounting it on a rotating cradle held in place with a load cell attached at a known radius from the cradle's axis of rotation.

Figure 2–9 shows a schematic and Fig. 2–10 shows the structural layout of the dynamometer. The engine is still connected to the absorber using a transmission, but losses in the transmission are no longer able to influence the engine torque measurement. Power output is computed using engine torque and measured engine speed. The operational details of the dynamometer have been documented elsewhere.⁹³

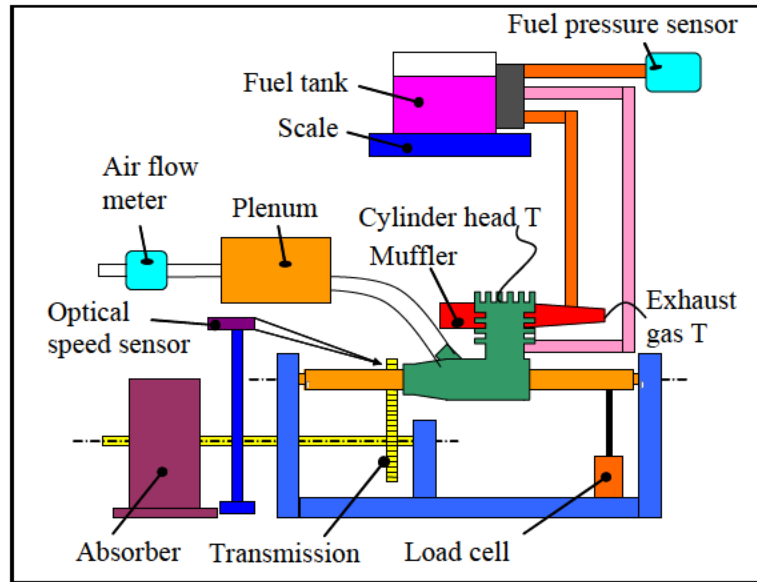


Figure 2–9: Schematic layout of the dynamometer cradle assembly and brake with a geared transmission system.

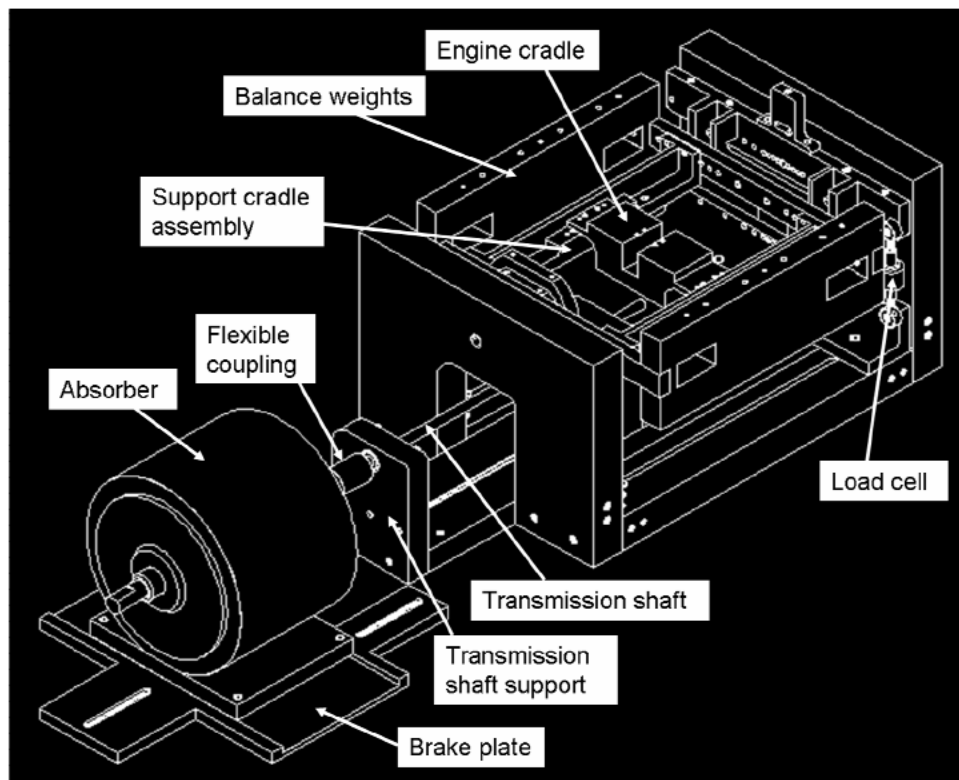


Figure 2–10: Structural layout of the dynamometer cradle assembly and brake.

2.7.2 Vibration Control

Figure 2–11 is a drawing of the cradle support assembly. A pair of weights attached to either side of the cradle assembly balances the cradle and increase the moment of inertia of the system. The latter lowers the resonant frequency of the spring–mass system (the load cell is the ‘spring’ and the cradle moment of inertia is the ‘mass’) making it more difficult for the 1/rev disturbances of the engine to excite less well–damped lower order modes of the system. The idea is to add enough weight to push the first harmonic below the lowest possible operating frequency of the engine. This, combined with clamping the cradle during startup, prevents load cell destroying resonances.

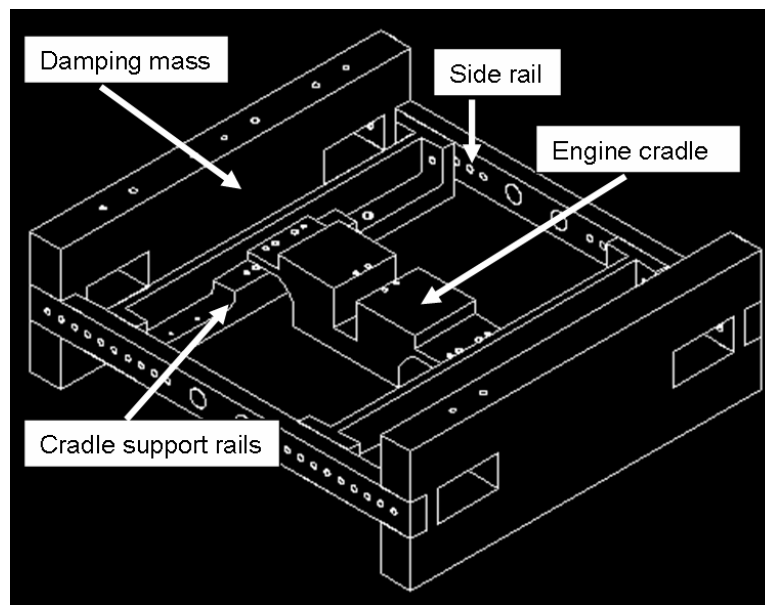


Figure 2–11: Structural layout of the engine cradle assembly.

2.7.3 Hysteresis Brake

Magtrol HB series hysteresis brakes were used to load the engines. Table 2–3 lists the engines tested and their corresponding brakes.

Model	Minimum torque at rated current		Maximum speed	Engines used with each brake	Type of transmission used
HB-450	3.17	450	8000	OS 46, OS 40	Gear/Belt
HB-140	0.98	140	12000	OS 25, AP 15, AP 09	Gear/Belt
HB-8	0.06	8	20000	AP 061, Cox 049	Direct drive
HB-2.5	0.017	2.5	20000	Cox 020, Cox 010	Direct drive
	N-m	oz-in	rpm		

Table 2-3: Hysteresis brake ratings and engines used with corresponding brakes.

Figure 2-12 is a photograph of a Magtrol HB series 450 brake and Fig. 2-13 is a cross-sectional drawing of the brake illustrating the important components.⁹⁴ The brake consists of a reticulated pole structure and a rotor/shaft assembly with high magnetic permeability. The two parts are separated by an air gap. In the absence of a current in the field coil, no force is exerted on the rotor/shaft assembly and it is free to spin. When a current is applied to the windings, a magnetic field is created across the air gap and through the rotor. The motion of the rotor in the magnetic field produces an eddy current in the rotor and a braking torque associated with the resistance to current flow in the rotor.

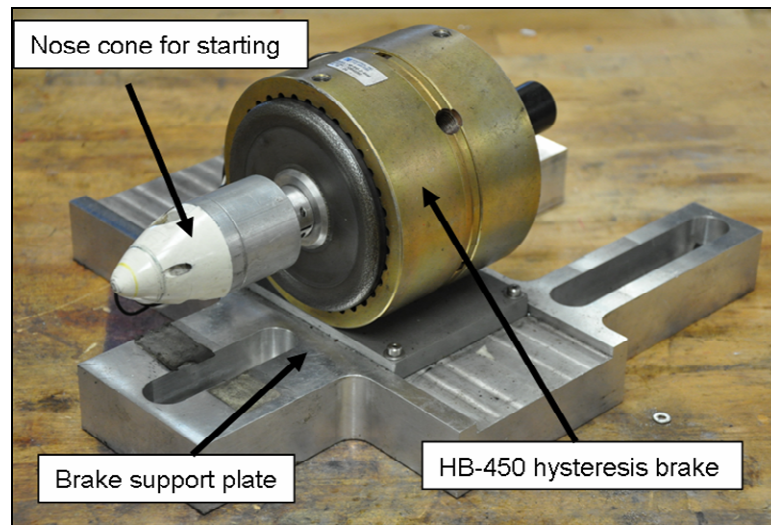


Figure 2-12: HB-450 hysteresis brake connected to brake support plate with attached nose cone.

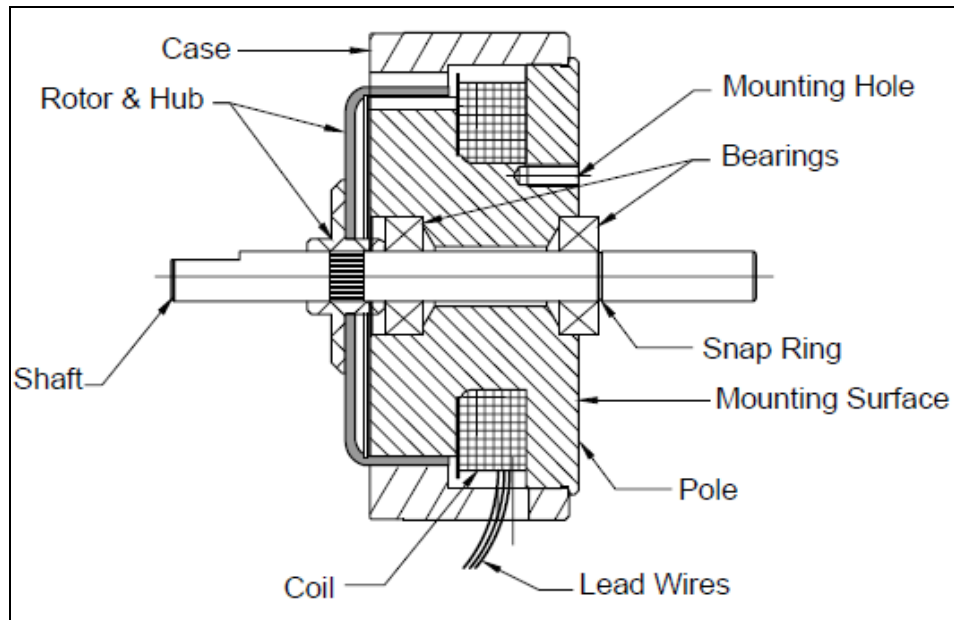


Figure 2–13: Cross sectional view of the Magtrol hysteresis brake [94].

The hysteresis brake has the following advantages over types of devices which use shearing or frictional forces to achieve the braking load:

- Infinitely variable loads – Torque is adjusted by varying current flow through the coil. The minimum torque is equal to the bearing frictional drag while the maximum torque is produced at the rated current.
- Smooth and quiet operation.
- Low wear – The only components of the brake exposed to wear are the shaft bearings. Other devices contain components like pulleys, ropes and other rotating machinery, all of which are subjected to wear.
- The applied torque is solely a function of the current passing through the coils and is hence independent of operating speed. This greatly facilitates engine control.

The use of different brakes was found to be necessary to achieve controlled operation of engines of different power ratings. The rotors in the hysteresis brakes are

capable of exerting a considerable amount of inertial loading because of their heavy mass and high rotating speeds. During initial attempts to use large brakes (HB-450) with smaller engines (displacement < 6 cc), it was found that the engine would fire but be unable to sustain any operation upon disengagement of the starter motor. This was because of the inability of the engine to accelerate the rotor from starting to a stable operating speed. Accordingly, smaller hysteresis brakes with smaller inertial loads were acquired to test engines with smaller displacement. Figures 2-14 and 2-15 show photographs of the smaller brakes (HB-140 and HB-2.5) used in this work along with their mounting supports.

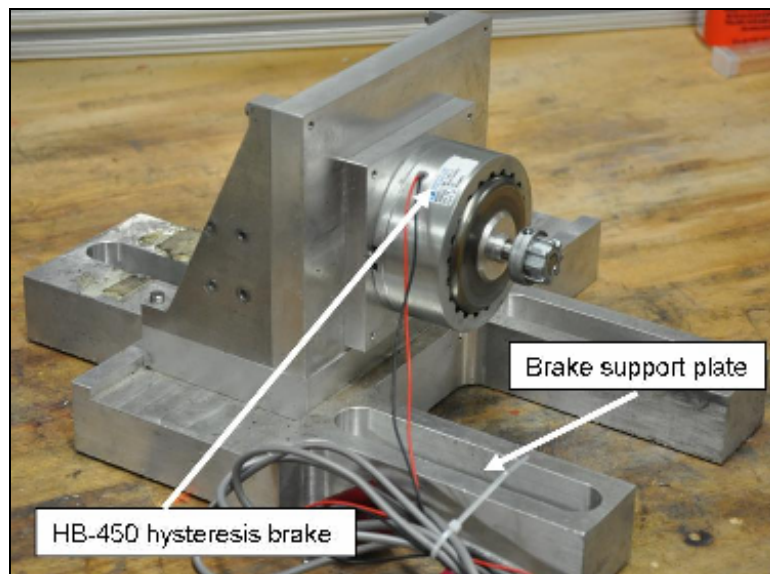


Figure 2-14: HB-140 hysteresis brake attached to brake support plate.

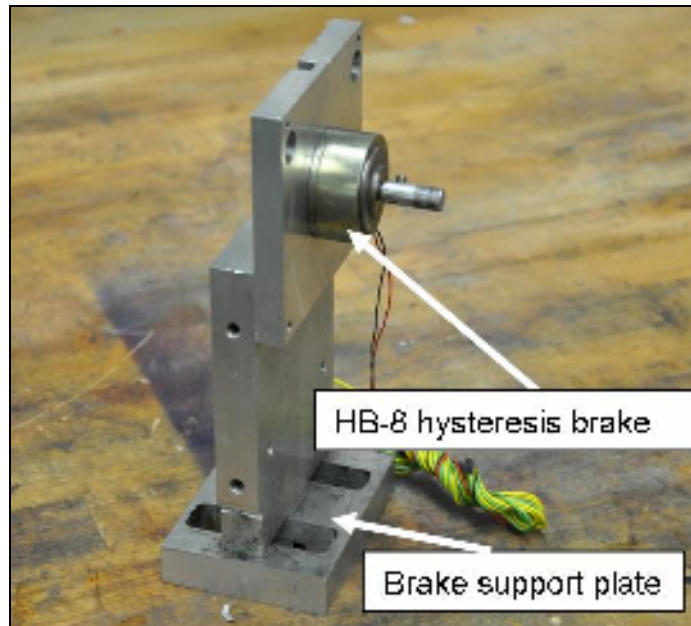


Figure 2–15: HB–8 hysteresis brake attached to brake support plate.

The hysteresis brakes can be operated in two modes. In an internal control mode the 0–5 Volt signal to the brake is manipulated by the use of a 10 turn potentiometer. In the external control mode, the voltage output from the data acquisition system is output to the hysteresis brake. A switch on the power supply box allows the control to switch from one mode to another.

2.7.4 Transmission Setups

Table 2–3 shows the maximum rated speed of the hysteresis brakes HB–450 and HB–140 to be limited to 8000 and 12000 rpm because of mechanical constraints. However, the operating speed range of the engines tested is considerably higher. As mentioned previously, this required the use of a transmission system for the engines A–F from Fig. 2–3 to allow for use of the hysteresis brakes without exceeding the specifications for maximum speed. In the case of the three smallest engines made by Cox engines, the absorber (HB–8 & HB–2.5) speed limit was high enough to enable

the engine to be directly coupled to it. The details of these transmission setups are discussed below.

Figure 2–16 shows a photograph of the geared transmission setup. Steel spur gears were used in this transmission setup. The driver gear is connected to the engine shaft via aluminum adaptors and held on by a retaining nut. The driven gear is connected to the transmission shaft and held on by the use of an expanding shaft adaptor. The transmission shaft is connected to the hysteresis brake using a flexible adaptor with rubber bushings.

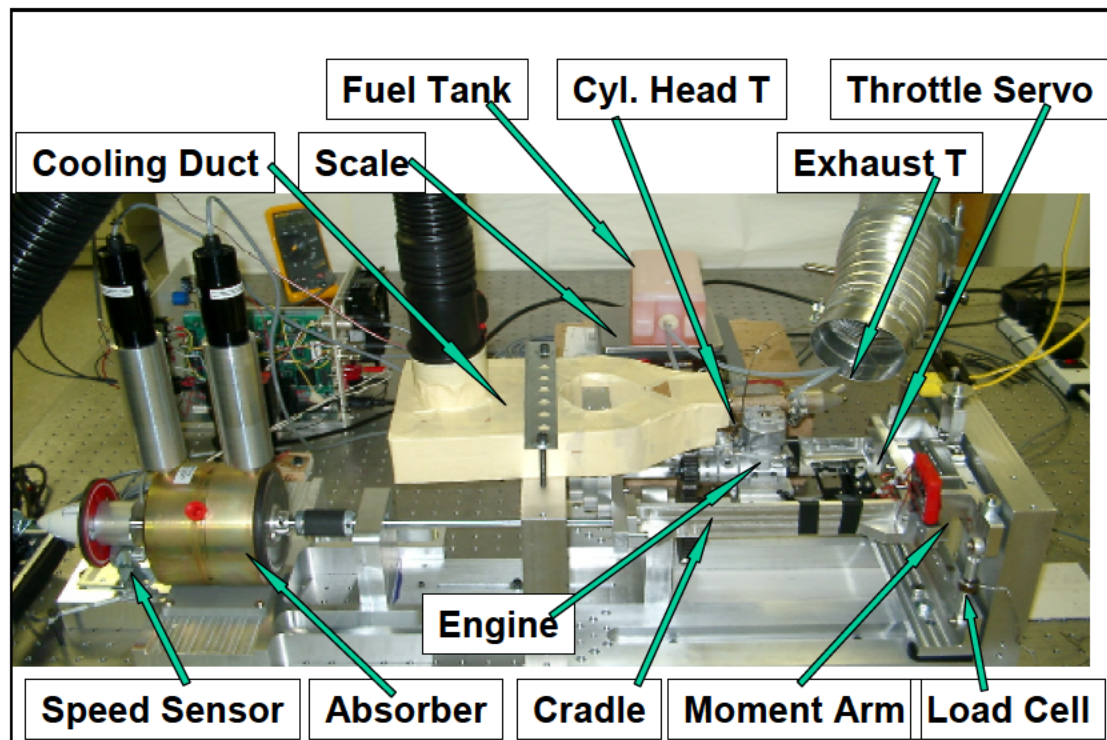


Figure 2–16: Photograph of the small engine dynamometer system at the University of Maryland with geared transmission.

Figure 2–17 is a photograph of the belt driven transmission setup. In this case, a special shaft is utilized that threads on to the outside of the engine shaft. The other end of the shaft is supported by a roller bearing mounted in a pillow block as shown

in the figure. The driver pulley itself is supported on the specialized shaft. The driven pulley is supported by a pillow block mounted on the support base. V-belts are used to connect the driver and driven pulleys. Belt tensioning is provided by an idler pulley that is supported on a separate attachment. The idler pulley provides a compression side force to the part of the belt in compression during engine operation.

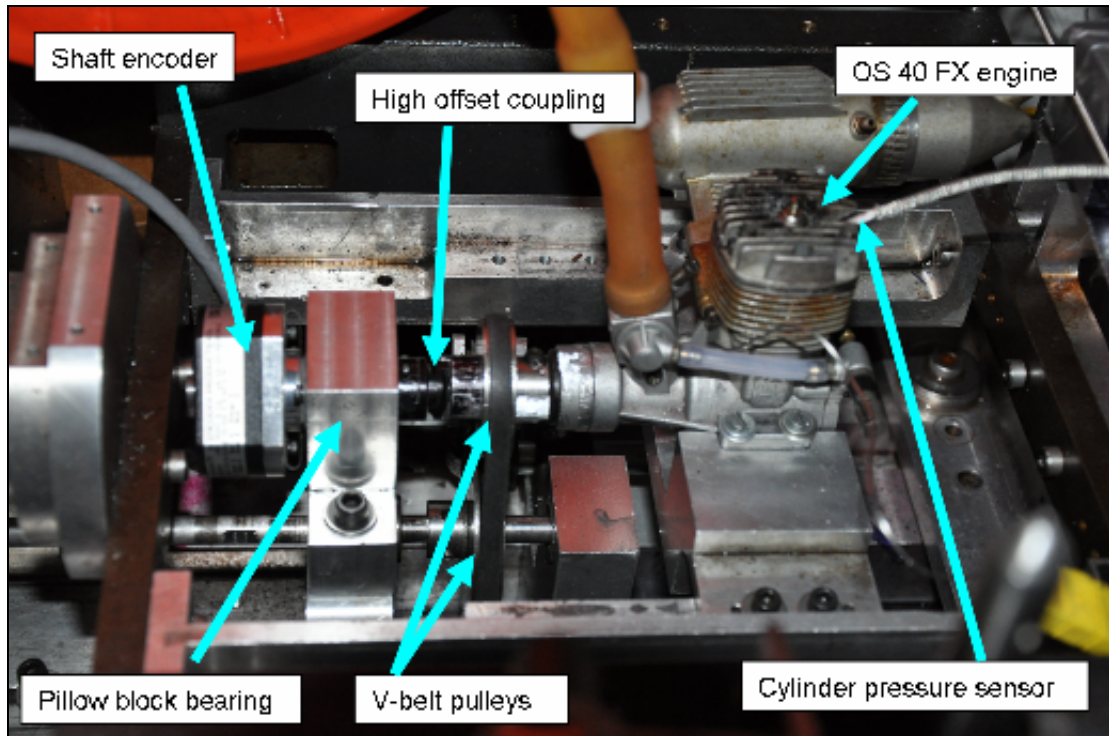


Figure 2–17: Photograph of the small engine dynamometer system at the University of Maryland with a belt transmission.

Figure 2–18 shows the layout and figures 2–19 and 2–20 show photographs of the direct drive setup. This setup is used in the performance measurement of the three smallest Cox engines. In this case, the hysteresis brakes used to load the engine can sustain sufficiently high operating speed to allow the engine shaft to be directly coupled to the brake. The coupling is achieved via flexible shaft couplers which allow for axial and radial misalignment of the mating shafts. A separate arrangement is

developed to allow for engine starting in the case of the direct drive setup. A spur gear is attached to one end of the hysteresis brake. During startup, the starter motor is applied to the nose cone mounted on the transmission shaft. A spur gear mounted on the transmission shaft is engaged with the gear mounted on the hysteresis brake. Once the engine starts up, the transmission shaft is pulled back and the starter gear is disengaged.

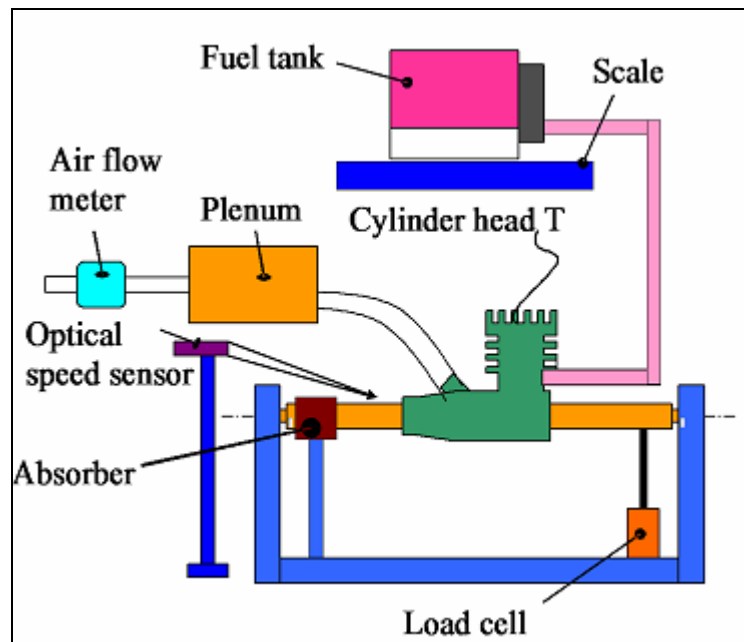


Figure 2–18: Schematic layout of the dynamometer for a direct drive type transmission system.

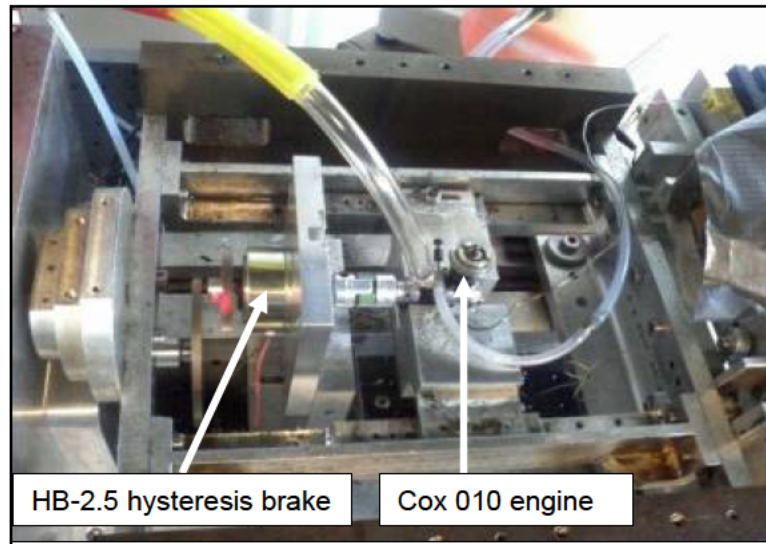


Figure 2–19: Photograph of the dynamometer with a direct drive type transmission system.

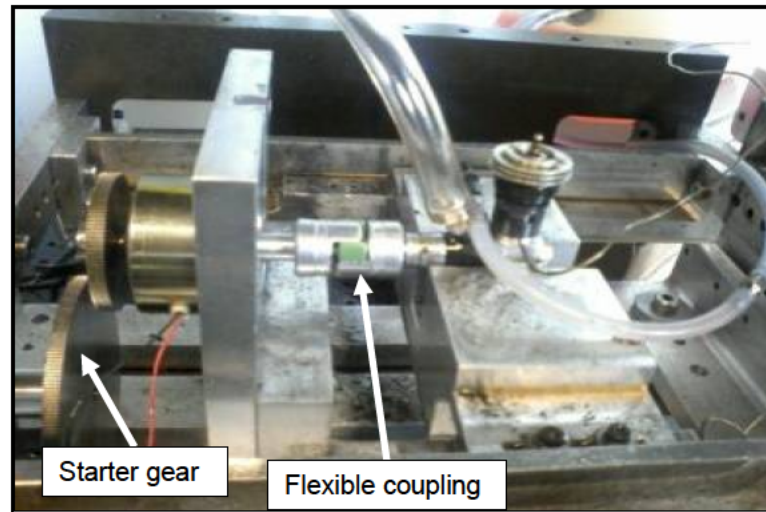


Figure 2–20 Photograph of the dynamometer with a direct drive type transmission system.

2.7.5 Engine Cooling

The engines are convectively cooled with fins machined into the cylinder head and the engine barrel surfaces. A blower operating at constant speed replaces the propeller wash that normally cools these engines. The blower is a model 51591 electric blower made by TORO Inc. with a maximum air speed of 100 ms^{-1} (225 mph) and maximum flow rate of $0.13 \text{ m}^3/\text{s}$ (70 cubic feet per minute). The blower has two

power settings and it was operated at the lower speed setting for all the tests conducted here. The output from the blower is connected to a flexible hose which is further connected to a cooling duct as seen in the photograph in Fig. 2–16.

2.8 Sensors and Measurements

2.8.1 Torque

Engine torque is determined by measuring the reaction force applied to the engine cradle in response to an applied load. The reaction force is measured by a load cell mounted on a moment arm. Three different kinds of load cells were used in this work and Table 2–4 lists the specifications of each. Figures 2–21 and 2–22 show photographs of each load cell. Two of the load cells are made by Sensotec while the third is manufactured by Transducer Techniques. All three load cells use bonded foil type strain gauges connected into a Wheatstone bridge circuit. An amplifier made by Sensotec (model UV) is used to convert the milli-volt signal output from the sensors to a (0–5 VDC) voltage for the data acquisition system.

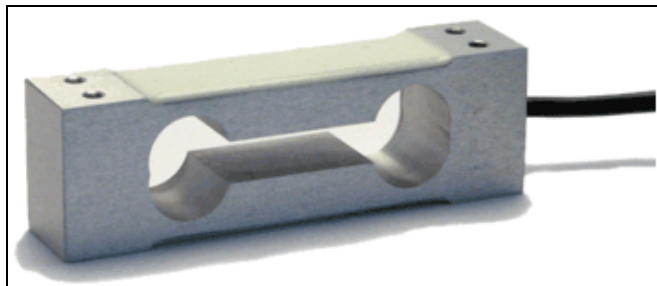


Figure 2–21: Photograph of the LSP–2 beam load cell.



Figure 2–22: Photograph of the Sensotec Model 311AT load cell.

Model	AL–311 AT	AL–311 AT	LSP–2	
Manufacturer	Sensotec	Sensotec	Transducer techniques	
Range	2.26	1	2.26	kg
Linearity	+/- 0.15	+/- 0.15	+/- 0.02	% of full scale
Non–repeatability	+/- 0.1	+/- 0.1	+/- 0.02	% of full scale
Hysteresis	+/- 0.15	+/- 0.15	+/- 0.02	% of full scale
Safe overload	150	150	150	% of rated output
Excitation voltage	5	5	10	V

Table 2–4: Specifications for the load cells used on in this research work.

The 1 kg Sensotec load cell was used to measure torque in engines F–I in Fig. 2–3. The larger 2.2 kg Sensotec load cell was used for all the other engines. The LSP–2 load cell was used in for the OS 46 FX experiments involving in–cylinder pressure measurement. This was primarily because the LSP series load cells were found to be much more robust and less failure–prone than the Sensotec load cells.

The load cells were placed at different locations on the cradle’s moment in order to maximize maximum signal strength. Figure 2–23 illustrates the torque

measurement principle. The x and y axes intersect at the center of rotation of the cradle and the z axis extends along the cradle's axis of rotation.

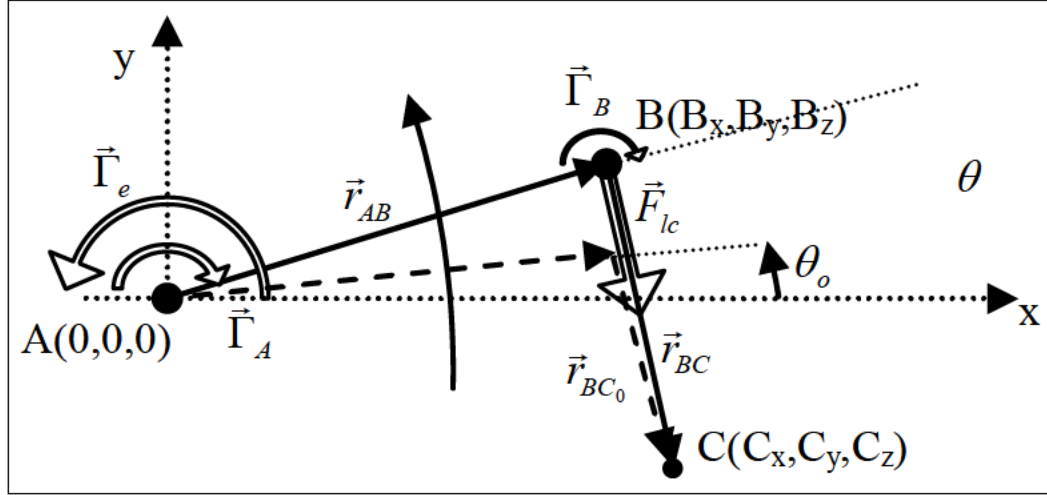


Figure 2–23: Vector diagram showing the forces acting on the torque-measuring cradle and the mechanical constraints imposed on the cradle/load cell system.

The torque $\vec{\Gamma}_e$ exerted by the engine on the cradle is balanced by three torques,

$$\vec{\Gamma}_e = \vec{\Gamma}_A + \vec{\Gamma}_B - \vec{r}_{AB} \times \vec{F}_{lc} \quad (2-3)$$

The main contributor is the force on the load cell (\vec{F}_{lc} , third term in Eqn. 2–3). The moment arm (\vec{r}_{AB}) extends from the cradle's center of rotation (A) to the load cell attachment point (B). $\vec{\Gamma}_A$ and $\vec{\Gamma}_B$ account for the parasitic torques associated with the cradle bearing and the load cell attachment points. These are approximately 1.4e-3 N-m for the apparatus used in this study. Measurements of $|\vec{F}_{lc}|$ made by the load cell are used to determine the torque produced by the engine. One of the drawbacks of this method is that the load cell deforms under the influence of the load while allowing

the cradle to deflect through an angle $\theta - \theta_o$. However, previous analyses showed this effect is negligible and does not need to be accounted for here.⁹⁵

2.8.2 Speed

Two methods of acquiring engine speed were pursued in this work. The first utilized a magnetic ‘pulser’ disc with a Hall effect sensor developed by ElectroSensors while the second approach used an optical speed sensor developed by Monarch Instruments.

The system manufactured by ElectroSensors consists of a magnetic ‘pulser’ disc containing sixteen alternating poles that is attached to the hysteresis brake shaft. A Hall effect sensor detects the passage of these poles and a model SA420 signal conditioner outputs an analog voltage proportional to rotational frequency. The accuracy of this system is $\pm 0.1\%$ of the reading. Figure 2–24 shows a photograph of the components of this system.



Figure 2–24: Photograph of the ElectroSensors speed measurement system with the pulser disc, Hall effect sensor and the SA420 signal conditioner.⁹⁶

In case of the optical speed sensor, engine speed is obtained by measuring the frequency of a square wave signal (TTL level of 3.6 V) produced by the sensor (Model ROS-W) from Monarch Instruments that detects the passage of a piece of reflective tape attached to the engine shaft. Figure 2–25 is a photograph of the sensor. The sensor contains an infrared light source and detector and the frequency of the square wave is measured using a National Instruments data acquisition system which will be described later. The sensor is capable of measuring rotational speeds up to 250,000 rpm.



Figure 2–25: Photograph of the Monarch optical speed sensor.

The ElectroSensors speed measurement system requires the ‘pulser’ disc to be attached to the brake shaft and the proximity switch to be placed at a small gap distance away from the disc. The installation of the optical speed sensor is much simpler and this sensor was used in all the dynamometer measurements except that for one engine (AP Yellowjacket – 2.45 cc (0.15 cu.in.) displacement).

2.8.3 Air Flow

The air flow into the engine intake is unsteady because of pressure fluctuations within the engine caused by the piston motion and the opening and

closing of intake and transfer ports. In addition to these natural pressure fluctuations, reverse flow (ie. backward air flow through the carburetor) also occurs at low engine speeds as the intake valve is designed to stay open during some part of the downward motion of the piston. This is done to allow for sufficient air flow at high engine speeds when the inertia of the moving air is enough to draw air into the carburetor even during the downward motion of the piston.⁹⁷ However at lower engine speeds this design results in back flow of air through the intake valve. The unsteady fluctuations in air flow and the reverse flow phenomena make it difficult to make good air flow measurements.

The mass flow meters used in this work were made by TSI Inc. Their specifications are listed in Table 2–5 and Fig. 2–26 is a photograph of the air flow meters. Preliminary measurements with the air flow meter directly connected to the engine intake resulted in erroneously large engine volumetric efficiencies. Therefore, an air plenum was placed between the flow meter and the engine intake to damp out unsteady fluctuations seen by the flow meter. The plenum is sized to be about 3000 times the displacement volume of the largest engine tested here. The pressure drop across the plenum and associated tubing could degrade engine performance by lowering the effective atmospheric pressure experienced by the engine. However, these losses have been quantified and found to have a negligible effect on engine performance. Appendix H shows details regarding the method of estimation of pressure drop in the engine intake tubing.

Model	41211	40211	
Range	20	300	Standard L/min
	0.0003	0.005	m ³ /s
Accuracy	0.005	0.05	Standard L/min
	8.3e-8	8.3e-7	m ³ /s
Response	4	4	ms
Inlet diameter	6.4	22	mm

Table 2-5: Specifications for the air flow meters used in this research work.

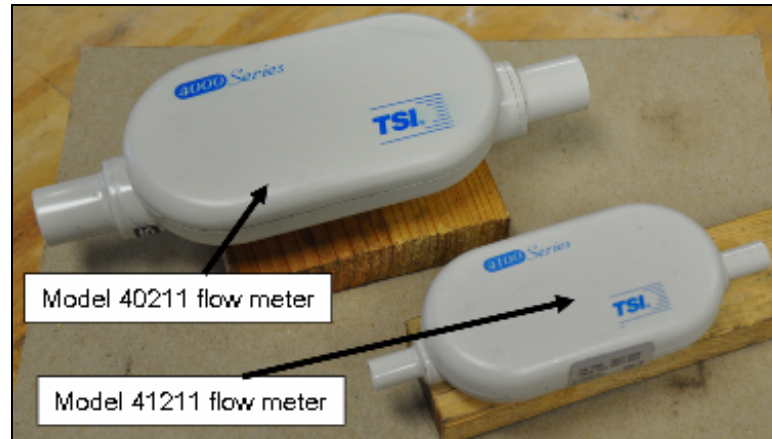


Figure 2-26: Photographs of the TSI air flow meters used in this research.

2.8.4 Fuel Flow

Fuel flow rate is determined gravimetrically by making a series of measurements of the mass of the fuel in the fuel tank at regular intervals over a specified period of time. The time period varies depending on the size of the engine being tested. For the largest engine tested here (engine-A in Fig. 2-3), the fuel mass was sampled for about 45 seconds. For the smallest engine tested, engine-I, the fuel mass was sampled for about 3 minutes. The mass is recorded using a scale with an electronic readout (Acculab VI-4800, Acculab ALC 810.2), that is continually read into the data acquisition system using an RS-232 port connection. A least squares fit is then performed on the readings to get the time rate of change of the weight of the fuel in the tank. This gives the fuel weight flow rate which is easily converted to mass

flow rate. Figure 2–27 shows a photograph and Table 2–6 gives the specifications of the scales.

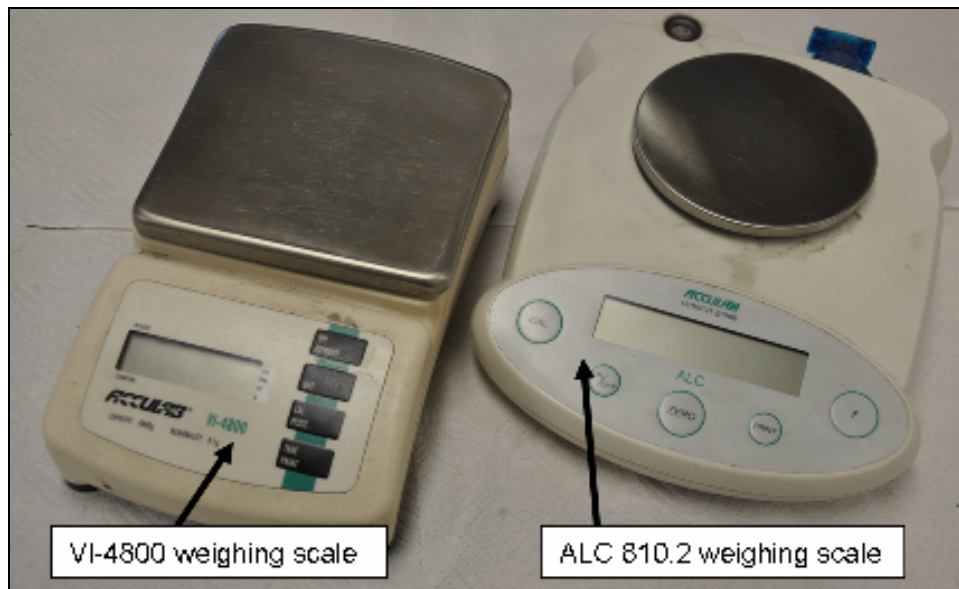


Figure 2–27: Photographs of the Acculab weighing scales used for fuel flow rate measurement.

Model	Acculab VI–4800	Acculab ALC 810	
Range	4800	810.2	g
Readability	0.1	0.01	g
Repeatability	+/-0.1	+/-0.01	g
Linearity	+/-0.1	+/-0.02	g
Stabilization time	3	2	seconds

Table 2–6: Specifications of the weighing scales used in fuel flow rate measurement.

2.8.5 Temperatures

Cylinder head temperature is measured using a stainless steel sheathed K type thermocouple held in contact with the cylinder head. A similar thermocouple inserted into the muffler exit measures exhaust gas temperature. Care is taken to ensure that the bead remains in the gas flow without touching the walls of the muffler. This is accomplished by using flexible thermocouples which can be bent so as to prevent the

bead from touching the muffler surface. Air temperature is measured using a K-type thermocouple.

2.8.6 Fuel Pressure

The pressure in the fuel tank is monitored using an Omega PX-139 series differential pressure transducer with a range of ± 103.4 kPa (15 psi) that is connected to a port on the fuel tank by some flexible tubing. Figure 2-28 is a photograph of the sensor.

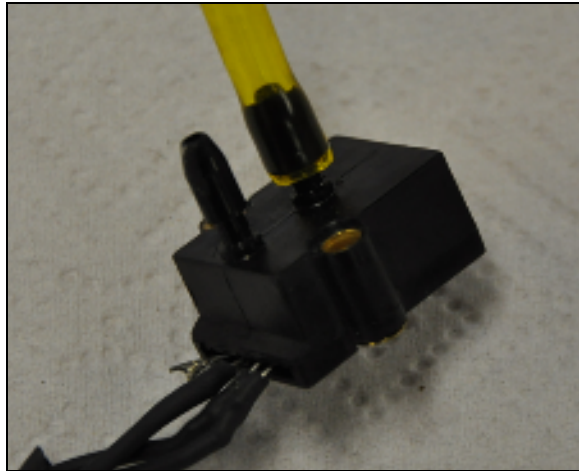


Figure 2-28: Photograph of the Omega PX139 pressure sensor.

2.9 Control System

Typically, engine performance curves are obtained either by keeping the torque constant while varying the engine speed or by keeping the speed constant while varying the engine torque. The tests performed here take the latter approach; the control system holds speed constant while fuel-air ratio is varied. The throttle is kept wide open for all of the measurements reported here.

2.9.1 Theory

An operating point of the engine–dynamometer system corresponds to a situation where the power produced by the engine exactly equals the power consumed by the absorber. One way to visualize this is as the intersection of the characteristic power–speed curve of the engine with that of the absorber as illustrated in Fig. 2–29. Whether or not the operating point is stable depends upon the respective shapes of the engine and absorber power curves. The power curve of the hysteresis brake is a straight line with slope proportional to the field current (other absorbers like propellers and water brakes have non–linear power–speed characteristics). The power curve of the engine – which we would like to determine – has the general shape of an inverted parabola. Point *a* is stable operating point because small disturbances in speed create forces that tend to push the system back to its original speed. An increase in speed causes the engine to decelerate because the brake is consuming more power than the engine is producing while decrease in speed causes the engine to accelerate because the engine is producing more power than the brake is consuming. In contrast, point *c* is not stable because a small increase in speed would cause the engine to accelerate away from point *c*, and a small decrease in speed would cause the engine to decelerate away from point *c*.

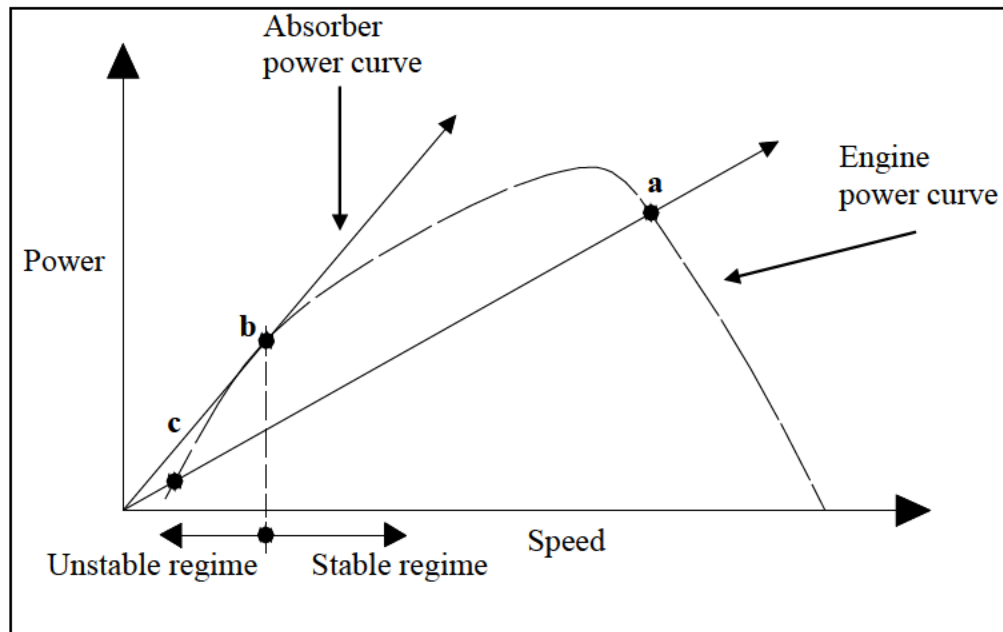


Figure 2–29: Stable and unstable operating regimes of a model engine.

Therefore, a control system which varies engine load at a rate fast enough to overcome fluctuations in engine speed and maintain a constant operating point is necessary to explore the full operating range of the engine. Even when operating in the stable regime, a control system damps fluctuations in engine operating speed and helps maintain a steady operating point for the engine. This improves the accuracy of the performance measurements.

The first experiments performed on the dynamometer utilized a ‘manually operated’ controlled mode of engine operation where engine load was adjusted manually by changing the voltage output to the hysteresis brake using a control knob. There were several problems with this method in addition to the inability to explore the full operating space of the engine that eventually caused it to be abandoned. First, it was very tedious and greatly increased the time required to take measurements. This had the added disadvantage of allowing more time for things to break. Second, it introduced new errors because it wasn’t possible to control the speed exactly as one

varied the mixture ratio. Third, it was extremely difficult and time consuming to get to work for very rich or very lean mixtures where there is a considerable amount of cycle-to-cycle variation. This method was replaced with an automated PID control scheme implemented in LABVIEW™ and described below.

2.9.2 Implementation

Figure 2–30 shows the control loop setup and Table 2–7 shows the values for PID variables used in the setup. Engine operating speed is compared with the desired set speed in real time to determine the braking load to the engine.

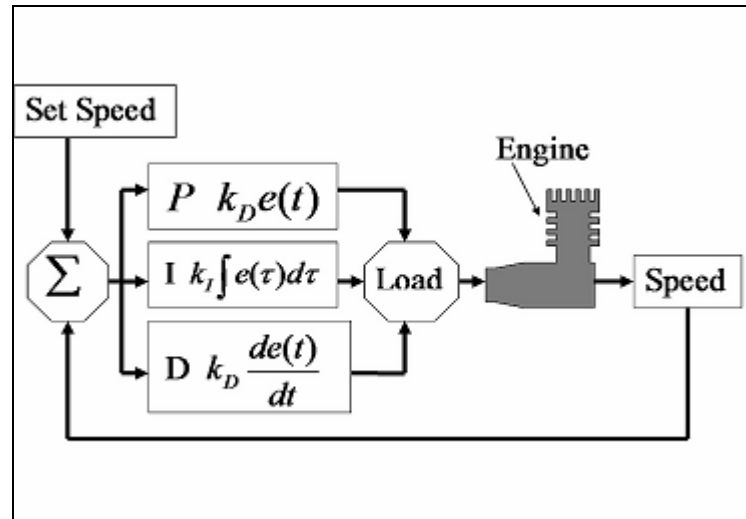


Figure 2–30: PID Control loop on dynamometer.

PID control variables	Values
P	–0.0015
I	–0.0005
D	0

Table 2–7: Values for the PID control variables used in this study.

2.10 Data Acquisition

2.10.1 Sensor Measurements

A LABVIEW™ data acquisition system is used to condition and log signals from all of the sensors. Figure 2–31 shows a schematic layout of the hardware components of the data acquisition system. The signals from various sensors as well as output voltages from the control system are wired into modules inserted into slots in two SCXI-1000 chassis. Each chassis is connected to a PCI E-series card that performs the analog to digital conversion. The cards are resident in a computer that has LABVIEW™ and DAQ drivers installed on it.

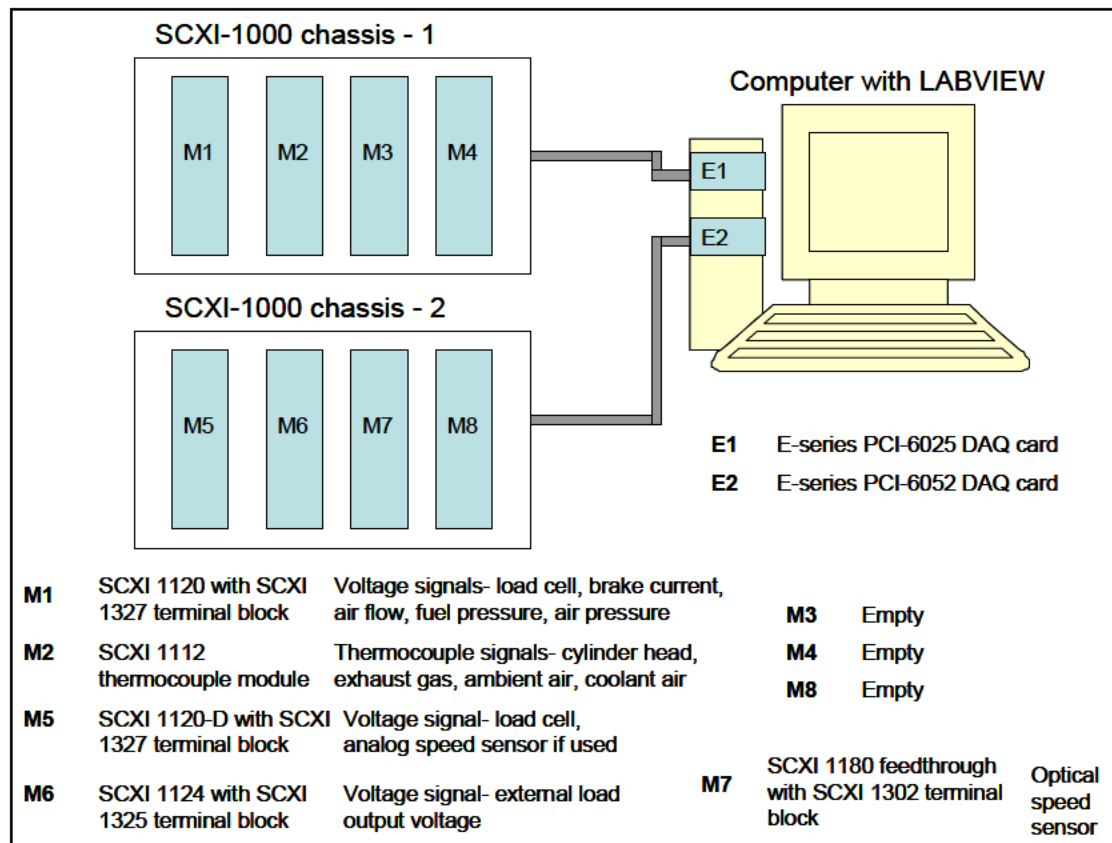


Figure 2–31: Schematic layout of the components of the data acquisition system also showing the measurement sensors and control signals associated with different DAQ modules.

Analog signals acquired from the load cell, air flow meter, fuel and ambient air pressure sensors and the brake are amplified and low-pass filtered using a National Instruments SCXI 1120 instrumentation amplifier. An SCXI 1327 screw terminal module provides connectivity and voltage attenuation if required to the SCXI 1120 module. Thermocouple signals from the cylinder head, exhaust port, coolant inlet and ambient air are amplified using a National Instruments SCXI 1112 thermocouple amplifier. The signals from both modules mounted on an SCXI 1000 chassis are routed to an eight channel, 16 bit card (E-series PCI-6025E) resident in a PC which performs analog to digital conversions. Dynamometer control is implemented on a secondary SCXI-1000 chassis which is connected to a PCI 6052 E-series DAQ card. The output from the optical speed sensor is wired to the pins on an SCXI-1302 terminal block which provides connectivity to the counter pins on the DAQ card through an SCXI-1180 feed through panel. The counter pins on the DAQ card are used to estimate the frequency of the square wave signal giving engine speed. A LABVIEWTM code compares operating engine speed to the desired speed and outputs a 0–5 V signal to the brake which is relayed through an SCXI-1124 module. The RS-232 port on a separate PC is used to acquire data from the scale in order to establish the fuel mass flow rate. Figure 2–32 shows a schematic of the setup for fuel flow rate measurements.

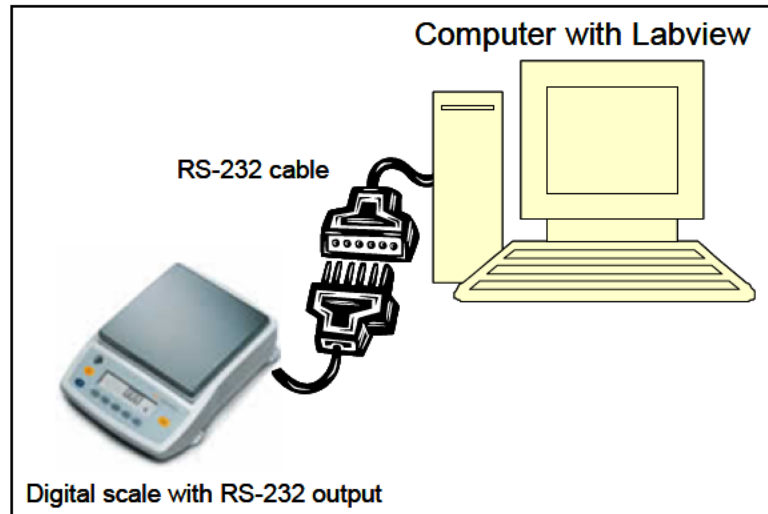


Figure 2–32: Schematic layout of the data acquisition system for measuring fuel flow rate.

2.10.2 User Interface

Figure 2–33 shows a picture of the LABVIEW™ user interface used to set user inputs and record engine data. The user interface allows the user to observe real-time estimates of various measurements including load cell output, engine speed, fuel and air pressures, various temperatures and air flow rate. In addition it allows the user to configure data acquisition parameters including the number of measurement readings to be acquired and the rate at which they are obtained. The inputs for dynamometer control allow the user to specify desired engine speed and the P, I and D parameters that the control program uses to maintain set speed. Engine torque and power output can be monitored in real time if the load cell calibration parameters are input on the user interface screen. The user interface also displays the output voltage set by the control loop and the engine speed in real time. It has buttons that allow the user to start the data acquisition as well as indicators to show the status of data acquisition.

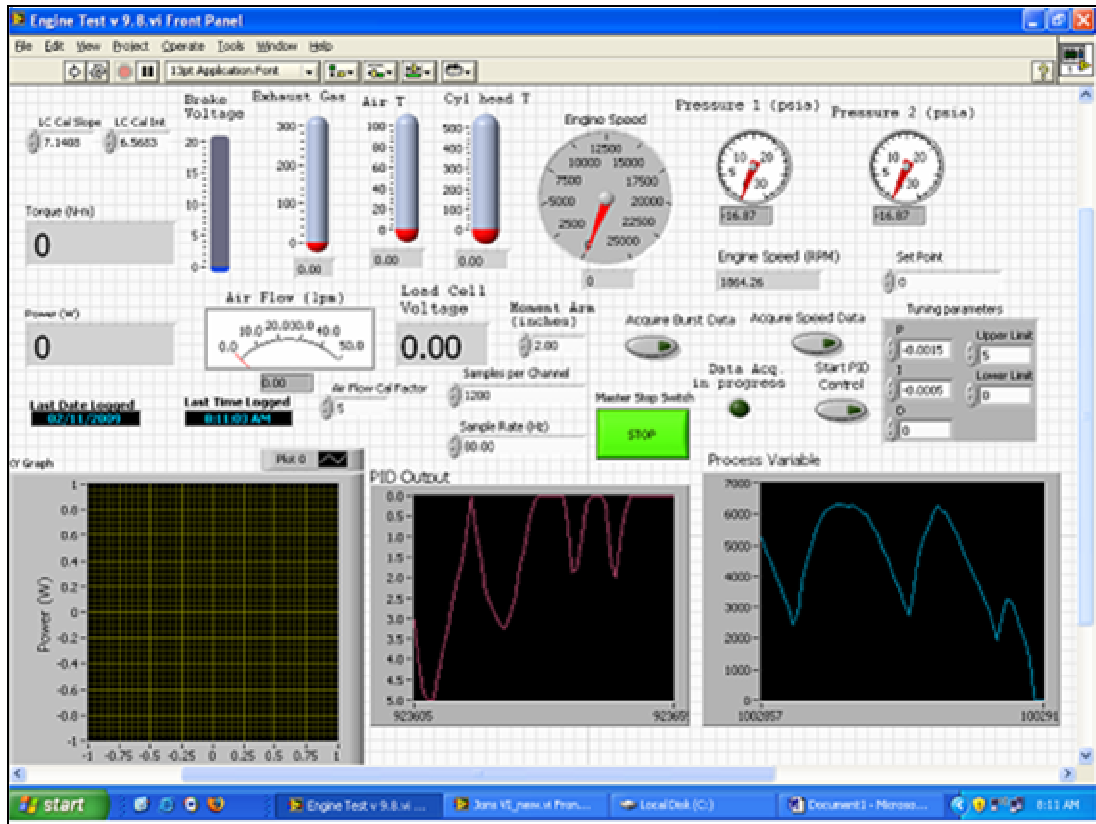


Figure 2–33: NI– LABVIEW™ interface for measurement and engine control.

2.10.3 Data Monitoring and Recording

Data from the dynamometer is recorded in one of two modes. In the default strip chart mode, the channels are scanned once per second and the data are written to a file which provides a record of everything that happened in the course of an experiment. This record is useful for documenting the actual test points as well as for debugging. These data are also written to virtual indicators and strip charts displayed on the software panel to provide real–time graphical indications of the state of the experiment.

To acquire performance data points it is desired to acquire a large number of data points from all the sensors which can be averaged during post–processing to

estimate all the relevant quantities. This is achieved by the use of a button provided on the user interface panel that causes the software to enter a ‘burst’ mode of operation in which a fixed number of samples are acquired using a hardware trigger. The data thus obtained is stored in a buffer in the DAQ card and is then transferred to the computer. The number of data points to be obtained in this manner and the rate at which they are acquired are user configurable. The large data set allows the calculation of uncertainties associated with each signal. The data acquired in the stripchart and ‘burst’ modes are written to the hard drive at a fixed location and used for post-processing.

2.11 Computed Quantities

The principal measurements provided by the system are load cell force F_{LC} , engine speed N , fuel mass flow rate \dot{m}_f and air mass flow rate \dot{m}_a . Engine torque is computed using the product of the load cell compression force and the length of the moment arm using,

$$\Gamma = F_{LC} * r_{MA} \quad (2-4)$$

The power output of the engine is given by,

$$P = \Gamma \omega \quad (2-5)$$

where ω is the angular speed in radians/second.

The overall efficiency of the engine is given by,

$$\eta_o = \frac{P}{\dot{m}_f Q_r} \quad (2-6)$$

where Q_r is the heating value of the fuel. The efficiency of the engine is also reported in terms of the brake specific fuel consumption (BSFC) which is given by,⁹⁸

$$BSFC = \frac{\dot{m}_f}{P} \quad (2-7)$$

BSFC is usually reported in kg/kW–hr (or lb/hp–hr).

Fuel–air mixture ratio is computed from the air and fuel flow rate measurements as,

$$F / A = \frac{\dot{m}_f}{\dot{m}_a} \quad (2-8)$$

Equivalence ratio is computed using the actual fuel–air mixture ratio and the stoichiometric value estimated for glow fuel.

$$\phi = \frac{(F / A)_{actual}}{(F / A)_{stoichiometric}} \quad (2-9)$$

Brake mean effective pressure is another parameter used commonly to gauge engine performance and to compare performance between engines of different classes. It is defined as the equivalent pressure which when applied to the piston over the duration of the engine cycle yields the same work output as produced by the engine.⁹⁹ It has the units of pressure and for a two–stroke engine is computed using,

$$BMEP = \frac{P}{V_{disp} N} \quad (2-10)$$

where V_{disp} is the displacement volume for the engine.

A quantity known as normalized power has been found to be useful in understanding the scaling of engine performance. It is computed using the following expression,¹⁰⁰

$$P_{norm} = \frac{P}{S_{mean}} \quad (2-11)$$

The quantity S_{mean} is the mean piston speed given by the expression,

$$S_{mean} = 2L\omega = 2L(2\pi N / 60) \quad (2-12)$$

where L is the stroke length.

2.12 Engine Test Procedure

2.12.1 Engine ‘Break-In’

Each new engine has to be broken in according to the procedures recommended by the engine manufacturer. The main purpose is to smooth out the working surfaces of the engine parts and to align them to ensure efficient and safe operation of the engine.¹⁰¹ The process involves running the engine on a test stand with the appropriate sized propeller. The engine is started on a very rich fuel–air mixture ratio and typically allowed to run for about 5 minutes. Manufacturers of OS engines typically recommend about 2 turns of needle valve rotation for engine break–in. The manufacturers of other engines tested in this work also recommend the same. After the engine has been run for about 2 minutes on the rich setting, the mixture is leaned somewhat and the engine is again allowed to run for the same duration. The engines are generally always operated at a rich mixture ratio. Therefore, in a relative sense, a leaner mixture is still rich of stoichiometric for the fuel considered. This cycle is repeated a few times for a total duration of about 30 minutes. An engine broken in correctly displays a smooth and rapid response to changes in throttle position and is able to idle at very low engine rpm’s at a very low throttle setting.

2.12.2 Load Cell Calibration

During engine operation on the dynamometer, a number of flexible wires and tubes are attached to the cradle carrying the engine to be tested. These include tubes carrying fuel from the fuel tank to the engine and to relay exhaust gas pressure from the muffler to the fuel tank. The wires include thermocouple wires connected to the cylinder head and the exhaust muffler. Because of the variability in the position of these wires and tubes from one test run to another, the load cell is required to be calibrated for every test run to establish the relationship between output voltage from the sensor and applied force. This calibration is done by running the data acquisition program and attaching a series of known weights to the moment arm at a known location. A data ‘burst’ is acquired for each new application of weights so that random fluctuations can be averaged out. Typical results from a calibration experiment are presented in Fig. 2–34.

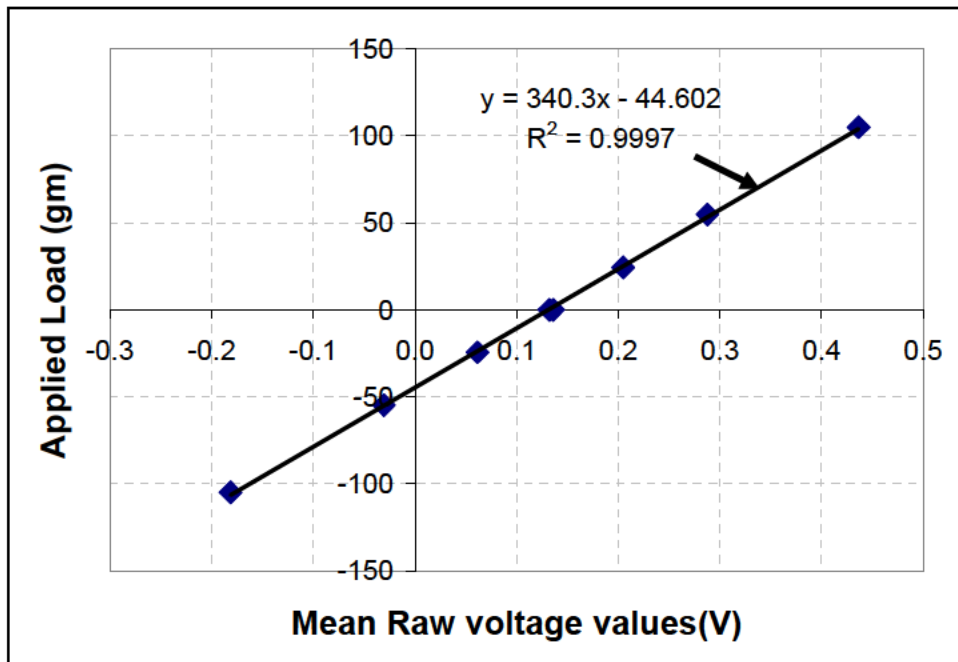


Figure 2–34: Typical calibration data for the load cell.

During dynamometer tests it was observed that in a majority of runs, some adjustments of the wires or tubes were required after initial engine startup. In addition in a number of engine runs, the failure of a part such as a flexible coupling or the flooding of the engine cylinder with excess fuel required readjustment of the dynamometer setup. The most efficient method of establishing load cell calibration was found to be when it was done at the end of the engine run with diligent care being taken to ensure that none of the flexible tubes or wires shifted in position once engine measurements were begun.

2.12.3 Engine Start-Up

The operation and control of all the engines tested on the dynamometer follow very similar patterns. The engine is started on the dynamometer by adjusting the mixture to a rich setting (typically 2–3 counter-clockwise turns of the needle valve), attaching the glow plug charger and turning the engine using an electric starter motor. This is usually done via the transmission shaft and a nose cone mounted to the free end of the absorber shaft. Since the propeller is no longer mounted on the engine, cooling air is provided by a blower. The speed and power output of the engine are controlled using a needle valve that changes the fuel–air mixture ratio and a throttle valve (on most engines) that controls the quantity of air entering the engine. As indicated in an earlier section, the cradle is locked using a retaining screw prior to starting the engine in order to protect the load cell while the engine passes through the fundamental frequency of the cradle–cell system. The retaining screw is removed once the engine has passed through the fundamental resonant frequency to a normal ‘idling’ speed (usually >5000 rpm).

2.12.4 Engine Performance Map Measurement Procedure

The dynamometer system enables the operator to control the load, throttle position, mixture, and speed during an experiment. All tests have been conducted at a fully open throttle position.

The hysteresis brake is set to internal control mode and the load potentiometer is set to zero. The engine is started, the desired engine speed is input into the LABVIEWTM program and the PID control loop is switched on. The hysteresis brake is switched to the external mode that allows computer control and the PID controller maintains a constant engine speed by adjusting the load. Now, the operator incrementally varies the mixture valve setting from the richest starting setting to the leanest setting that allows the set speed to be maintained. If the mixture is made too rich, the engine is unable to maintain the set speed and begins to slow down. If the mixture is made too lean, it could result in stalling the engine. So the idea is to get measurements at as lean a mixture as possible without stalling the engine. Burst measurements are made at each mixture increment. When the mixture sweep is complete, the mixture is made rich once again, the operating speed is set to a new value and the process described above is repeated until the complete operating map of the engine is obtained. All engines were tested in the same manner.

Engines were compared based on the peak power and peak efficiency observed in the full operating map. It is necessary to measure the entire operating map because there is no way to identify these peak performance points ahead of time. Knowledge of the complete operating map is also necessary for selecting optimum engine–propeller, engine–generator, or engine–gearbox configurations.

2.12.5 Engine Shut-Down

The cradle is re-locked to the cradle support before the fuel is exhausted or the engine is shut down. This prevents possible damage to the load cell as the engine decelerates through the fundamental resonant frequency of the cradle-load cell system. The throttle valve is closed in order to shut down the engine. After the engine stops, the cradle is unlocked and a second calibration of the torque measuring system is performed.

2.13 Uncertainty Analysis

A thorough analysis of measurement uncertainty is critical to establishing the accuracy of engine performance estimates and the scaling laws derived from them. The analysis requires defining the types of errors and developing a clear method for estimating them. These are discussed appendix G following the guidelines proposed in ASME standard PTC19.1.¹⁰² The details of this uncertainty analysis pertaining to the measurements performed on the dynamometer have been previously documented elsewhere.¹⁰³

2.14 Atmospheric Corrections

Engine performance varies with the number of oxygen molecules per unit volume in the atmosphere. Since this varies daily depending upon the local pressure, temperature, and humidity, engine performance is usually corrected to standard atmospheric conditions so that measurements made on different days may be compared. The methods for accomplishing this are well known¹⁰⁴ and are summarized here:

A correction factor α_c times the measured power P gives the power P_r corrected to standard reference conditions,

$$P_r = \alpha_c P \quad (2-24)$$

The correction factor for a naturally aspirated compression ignition engine depends on the atmospheric factor f_a and the engine factor f_m ,

$$\alpha_c = (f_a)^{f_m} \quad (2-25)$$

The atmospheric factor accounts for the effects of atmospheric pressure p , temperature T and humidity ϕ and is computed as follows,

$$f_a = \left(\frac{p_r - \phi_r p_{sr}}{p - \phi p_s} \right) \left(\frac{T}{T_r} \right)^{0.7} \quad (2-26)$$

The subscripted terms correspond to the reference conditions and the non-subscripted terms correspond to test conditions.

The engine factor for a 2-stroke engine is,

$$f_m = 0.036q_c - 1.14 \quad (2-27)$$

$$q_c = q/r_r \quad (2-28)$$

where q is the fuel mass per cycle per liter of air (set by the fuel/air ratio) and r_r equals 1 for the loop-scavenged engines considered here.

Chapter 3 : Engine Performance Data and Scaling Analyses

The first part of this chapter summarizes the results of the dynamometer testing of the nine miniature engines listed in Fig. 2–3. In the second part, these performance measurements are used to develop scaling laws for small engine performance. The objectives of this chapter are to quantify the performance of miniature IC engines that are available today, to demonstrate how this performance scales with engine size and to identify a minimum possible length scale to build an engine using current technology.

3.1 Measurement Results

As discussed earlier, the three independent parameters in the dynamometer experiments are throttle position, fuel–air mixture ratio, and engine speed. In the experiments reported in this chapter, the throttle position is always fully open. This is because we are interested in quantifying the maximum performance of each engine and not necessarily in generating full operating maps for each engine. However, the influence of fuel–air mixture setting and engine speed are not so clear-cut. Therefore, it was necessary to vary both through their full operational range. Experience showed that the most reliable way to achieve this was to incrementally vary the mixture setting (from rich to lean) while using the dynamometer controller to maintain a particular engine speed. This process was repeated for different engine speeds until the entire mixture ratio and operating speed range of the engine was spanned.

Two figures and a table are used to summarize the performance of each engine. The first figure shows torque, power, fuel/air ratio (equivalence ratio) and efficiency

(BSFC) as a function of fuel flow rate at various engine speeds. The fuel flow rate is proportional to the mixture setting. At a constant engine speed, peak power output is achieved at the point corresponding to peak torque. The second figure for each engine shows the peak or ‘best’ values for torque and power. It also shows the corresponding values for overall efficiency (BSFC), delivery ratio and fuel–air mixture ratio.

There are common trends which can be observed in the performance maps of all engines tested in this work with respect to torque, power, delivery ratio and overall efficiency as a function of engine speed and fuel consumption. However, the location of the peak values with respect to engine speed change from one engine to another. Additionally, there are seen to be interesting behavior in some cases which deviate from torque and power curves typically observed in conventional scale engines.

A detailed discussion of the results obtained from one representative engine – the Hornet 09 engine (engine D in Fig. 2–3) is presented first. Figures summarizing the performance of other engines along with comments regarding location of peak torque, power and efficiency with respect to engine speed and any observed interesting behavior are presented alongside.

3.1.1 Engine Performance – AP Hornet 09

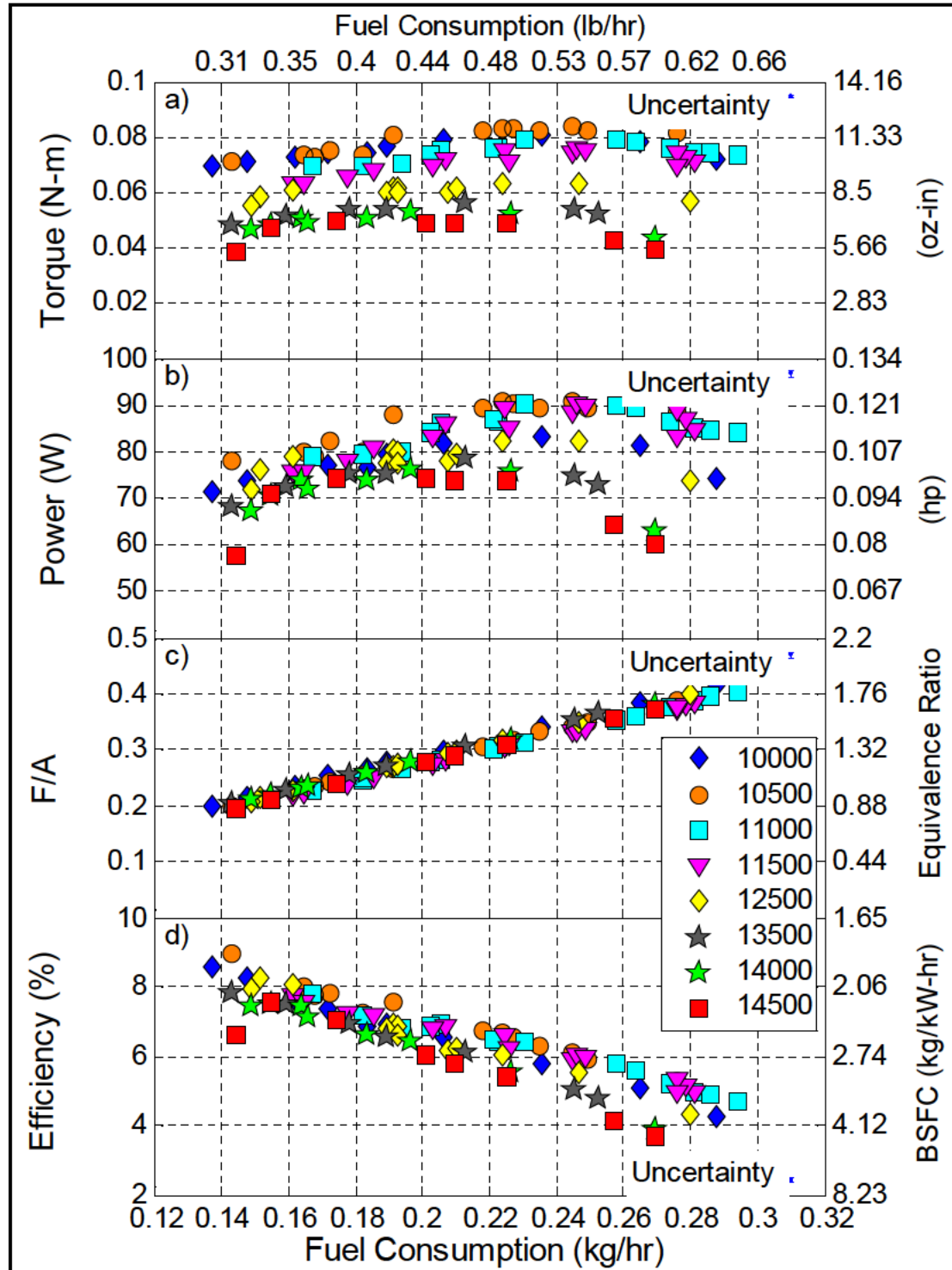


Figure 3-1: Performance map for the AP Hornet engine. Data sets represent different engine speeds.

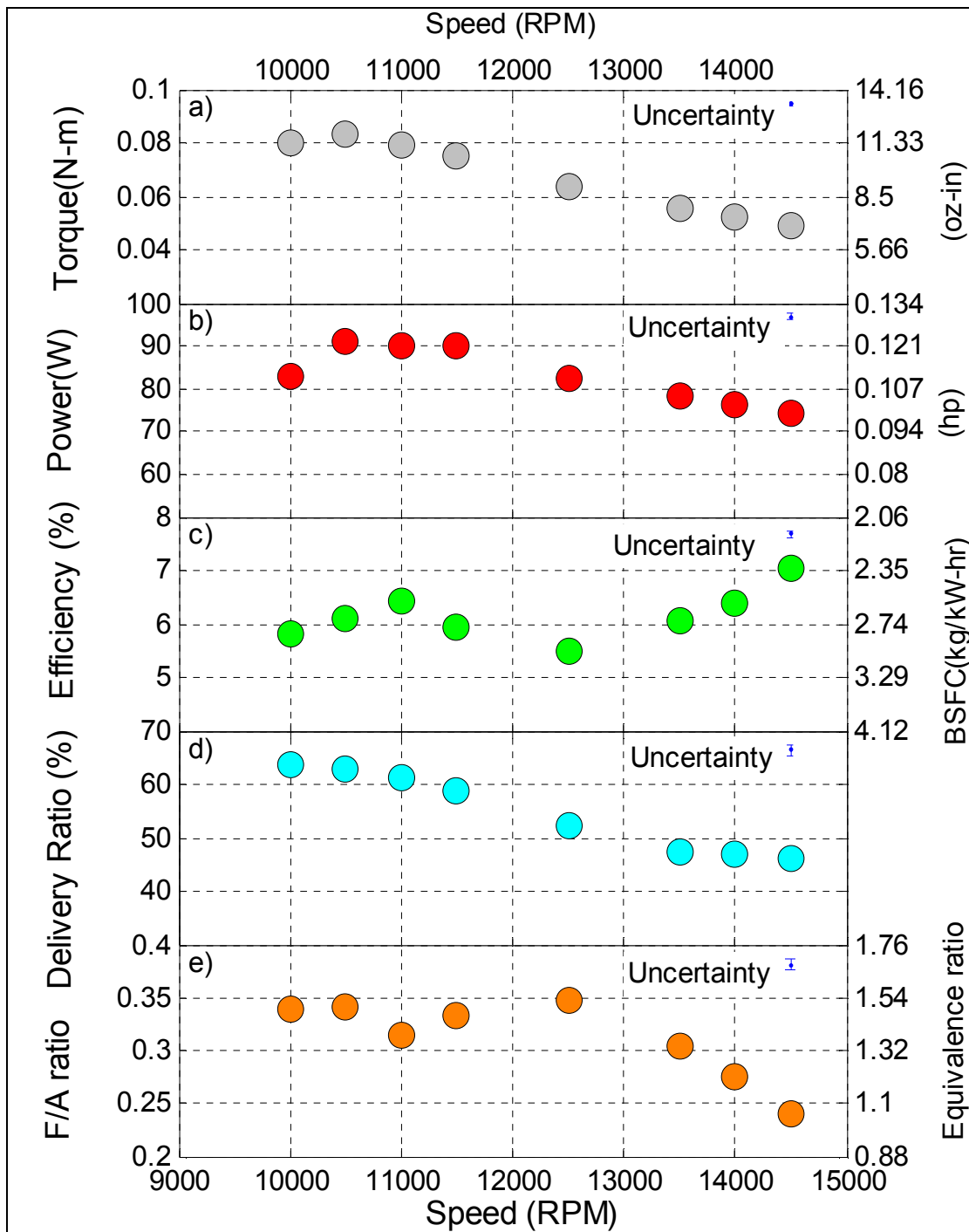


Figure 3–2: Peak performance of the AP Hornet engine as a function of engine speed.

Engine model			AP HORNET		
Engine manufacturer			AP Engines		
Displacement	1.47 cc		0.09 cu.in.		
Bore	12.5 mm		0.49 in.		
Stroke	12 mm		0.47 in.		
Mass	128 g		4.52 oz.		
Geometric compression ratio	13.3				
	Value	Units	@ rpm	@ F/A ratio	Uncertainty
Peak torque	0.083	N–m	10500	0.34	1e–3
	11.75	oz–in	10500	0.34	0.14
Peak power output	90.83	W	10500	0.34	1.12
	0.12	hp	10500	0.34	0.002
Overall efficiency @ peak power	5.14	%	10500	0.34	0.15
BSFC @ peak power	2.69	kg/kW–hr	10500	0.34	0.05
Peak delivery ratio	63.84	%	10000	0.34	2.65
Peak normalized power	21.63	W	10500	0.34	0.27
Peak BMEP	351.96	kPa	10500	0.34	4.33
	51.05	psi	10500	0.34	0.63

Table 3–1: Summary of engine performance data for the AP Hornet engine.

Measurements are made between 10000 to 15000 rpm for the Hornet 09 engine. Figure 3–1 shows torque, power, fuel–air mixture ratio and overall efficiency of the Hornet 09 engine as functions of fuel consumption. Each data set corresponds to one particular operating speed of the engine. The data show that while there is an ‘optimum’ mixture ratio at which engine torque and power are maximum while fuel consumption is minimum, this optimum is not well–defined. Fuel–air mixture ratio decreases linearly as the mixture is leaned by reducing the fuel flow rate. Equivalence ratio is calculated assuming that the stoichiometric fuel–air ratio is 0.227 (see Section

2.5).¹⁰⁵ The data show that engine power output peaks rich of stoichiometric. Heywood has observed engine power output to peak slightly rich of stoichiometric at equivalence ratios between 1 and 1.1. Figure 3–1 shows engine power output to peak at an equivalence ratio of about 1.3 for different engine speeds. Heywood's explanation for observations of peak power output at rich mixture ratios is as follows: High combustion temperatures lead to dissociation causing an increase in the concentration of molecular oxygen in the burnt gases. This allows some additional fuel to be partially burned thereby increasing the peak pressure and power output from the engine.¹⁰⁶

Figure 3–1 shows overall engine efficiency at each engine speed increases with lower F/A, but peaks at an equivalence ratio of less than 1. As mentioned by Heywood, the analysis of fuel–air cycles shows two different behaviors for fuel conversion efficiency depending on equivalence ratio represented by ϕ .¹⁰⁷ For rich mixtures ($\phi > 1$), fuel conversion efficiency is seen to decrease as $1/\phi$. For lean mixtures ($\phi < 1$), fuel conversion efficiency is seen to linearly increase with decrease in ϕ . This can be observed in figures 3–3 and 3–4 which show overall efficiency for rich mixtures plotted as a function of $1/\phi$ and for lean mixtures as a function of ϕ . Figure 3–3 is plotted for the Hornet 09 engine while Fig. 3–4 is plotted using results from the Cox 049 engine since very few data points were obtained at lean mixture settings from the Hornet engine. In case of lean mixtures, the lower combustion temperature is found to reduce dissociation of tri-atomic molecules like CO_2 and H_2O . This results in a greater fraction of fuel energy being transferred to the

expanding gases performing work on the piston resulting in an increase in fuel conversion efficiency.

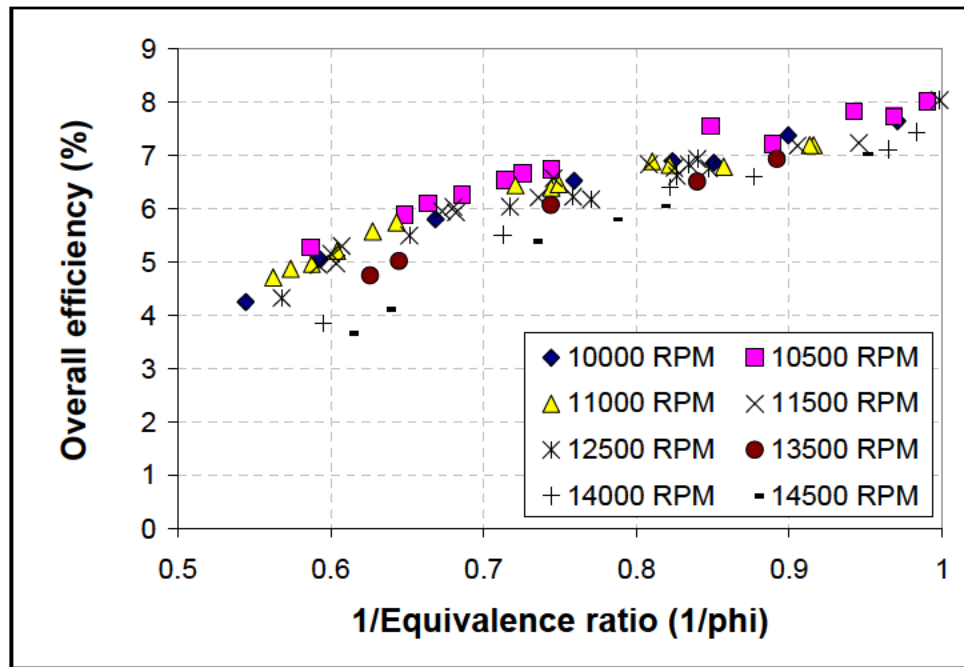


Figure 3–3: Efficiency as a function of 1/phi for rich mixture ratios at different engine speeds for the AP Hornet 09 engine.

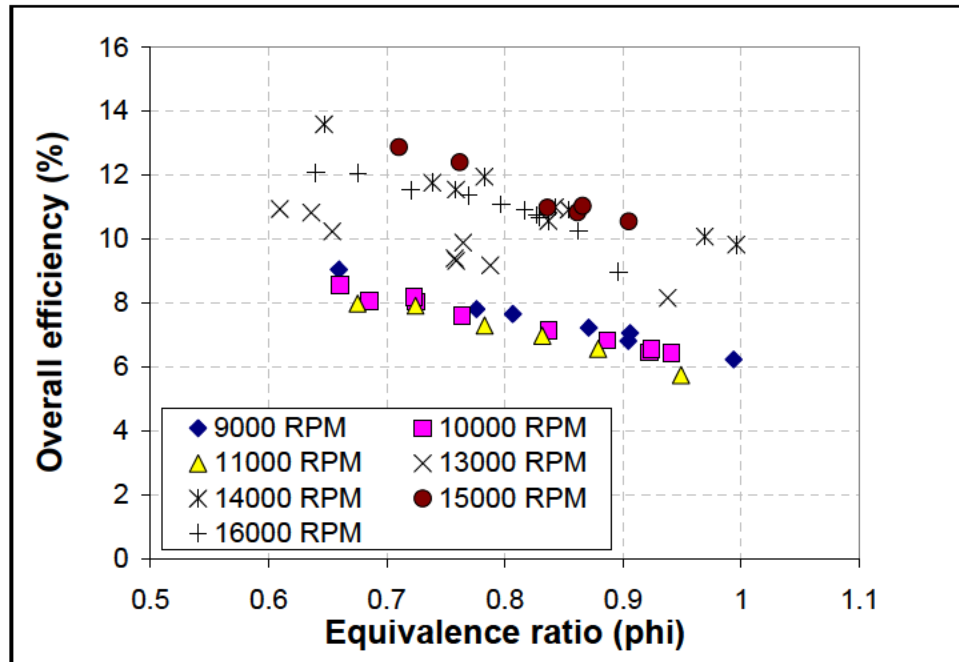


Figure 3–4: Efficiency as a function of ϕ for lean mixture ratios at different engine speeds for the Cox 049 engine.

Figure 3–2 shows the peak values for torque and power and corresponding values for overall efficiency, delivery ratio and fuel–air mixture ratio at each engine speed. The peak torque produced by this engine is 0.0833 N–m at 10500 rpm. Torque produced by the engine decreases rapidly beyond 10500 rpm. Peak power produced by the engine is 92 W at 10500 rpm. While torque decreases with increasing speed after the peak, engine power remains high because the speed increase is able to offset the torque decrease until 11500 rpm beyond which power decreases rapidly.

Efficiency corresponding to peak power shows an initial peak of 6.5% at 11000 rpm when maximum power output is achieved. Efficiency increases again at higher engine speeds achieving an overall peak value of 7% at 14500 rpm. This overall efficiency translates to a brake specific fuel consumption of 2.35 kg/kW–hr.

The trends in efficiency observed in the Hornet 09 and other engines are a result of engine power output and operating fuel–air mixture ratio. Fuel–air mixture ratio is affected not only by the needle valve setting but also by engine speed. Engine speed affects fuel air mixture ratio by influencing air mass flow rate as well as exhaust gas pressure applied to the fuel tank through the muffler port.

For the Hornet 09 engine, better efficiency is attained at higher engine speeds primarily because of operation of the engine at relatively leaner fuel–air mixture ratios as observed in Fig. 3–2. The peak volumetric efficiency for the engine is about 64% at 10000 rpm. This decreases sharply with increased speed as flow friction and choking effects become more important.

A summary of the peak operating characteristics of the engine is provided in Table 3–1. Peak values for normalized power and BMEP are found to be 21.6 W and 352 kPa for this engine. The maximum normalized power and BMEP occur at peak engine torque for all of the engines tested. Figures 3–5 to 3–21 present analogous data for all of the other engines illustrated in Fig. 2–3. Tables 3–2 to 3–9 summarize the peak operating conditions for each engine.

3.1.2 Engine Performance – Cox 010

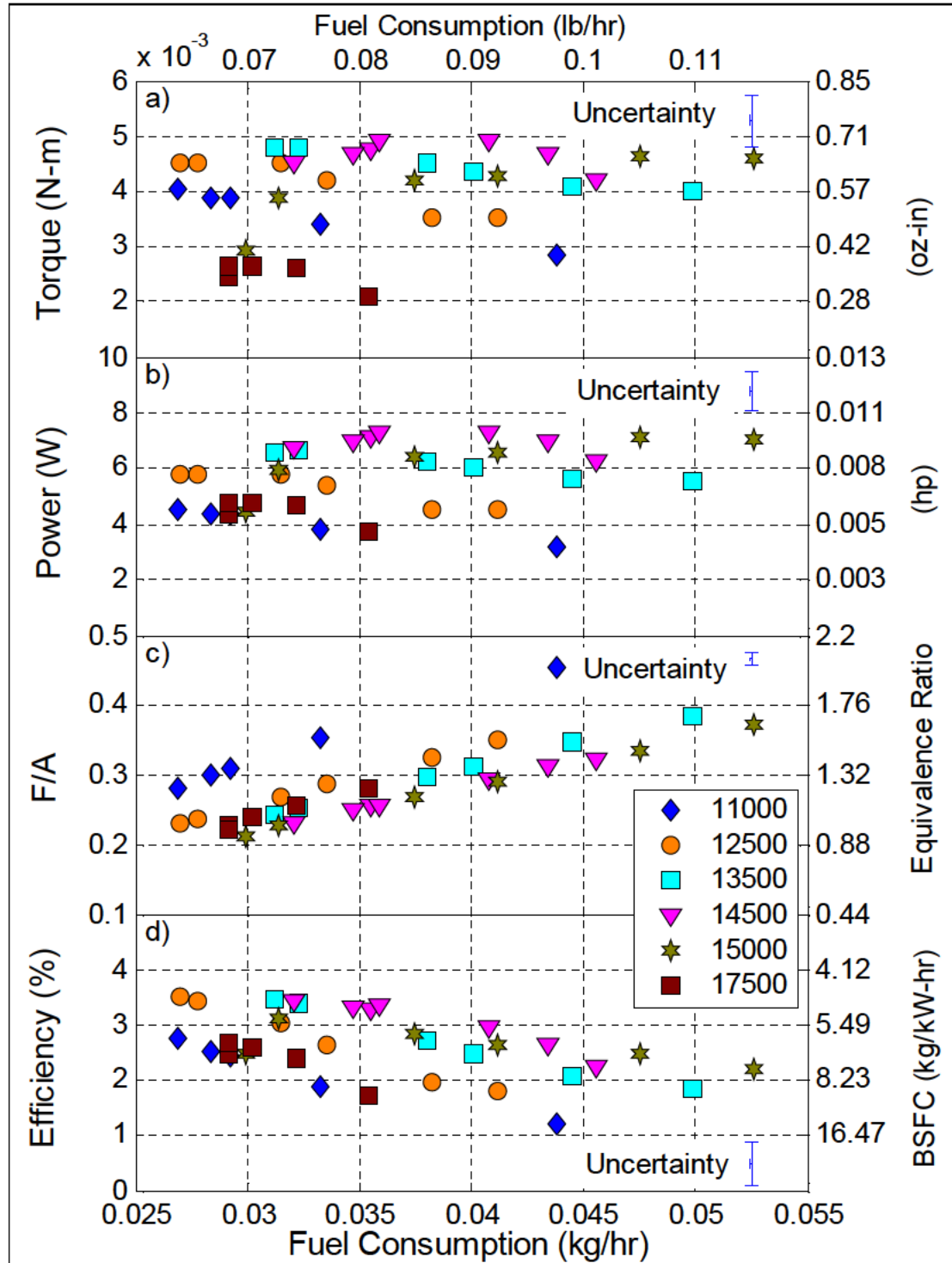


Figure 3-5: Performance map for the Cox 010 engine. Data sets represent different engine speeds.

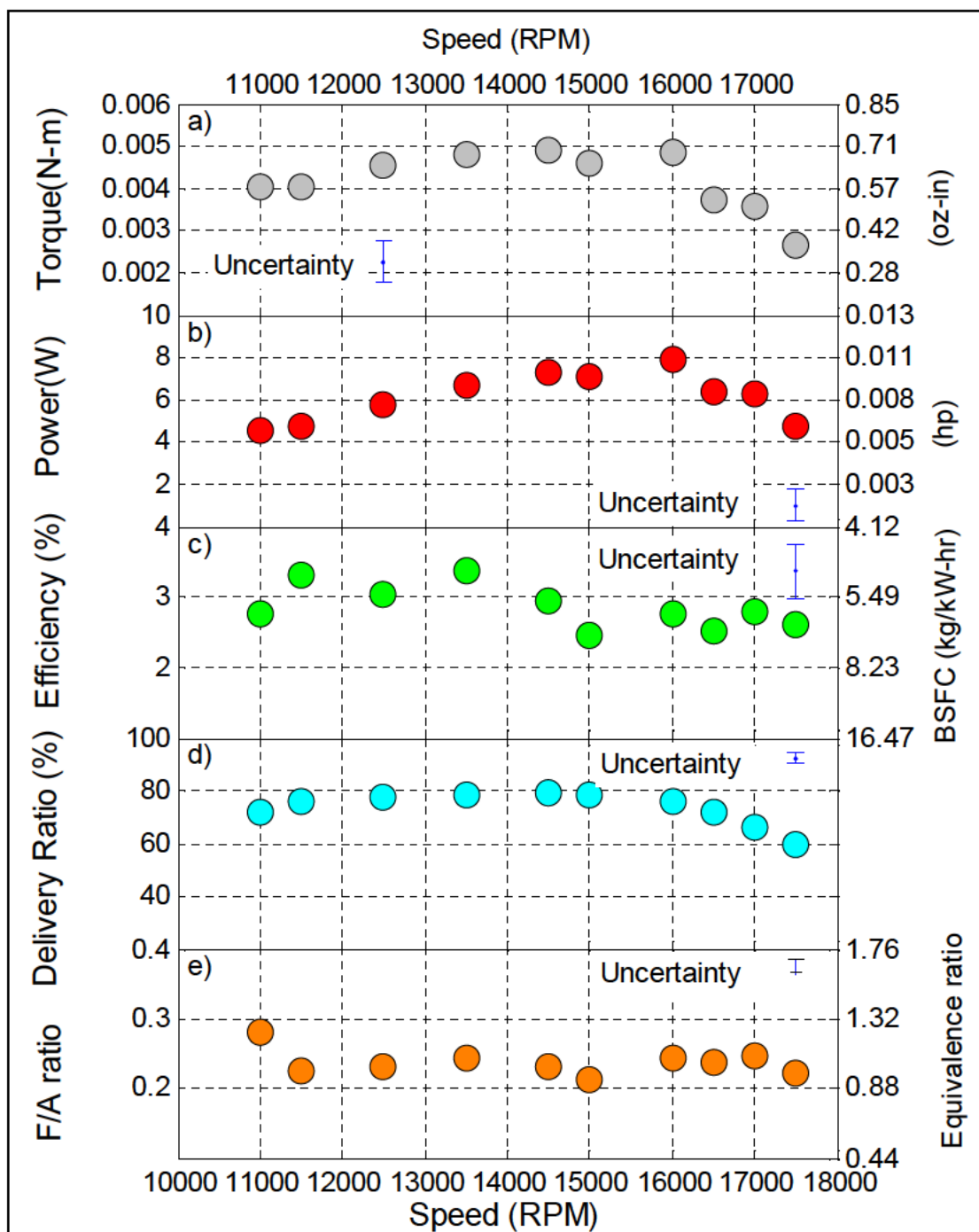


Figure 3-6: Peak performance of the Cox 010 engine as a function of engine speed.

Engine model			Cox 010 Tee Dee		
Engine manufacturer			Cox Engines		
Displacement	0.164 cc		0.010 cu.in.		
Bore	6.04 mm		0.24 in.		
Stroke	5.72 mm		0.23 in.		
Mass	15 g		0.53 oz.		
Geometric compression ratio	5				
	Value	Units	@ rpm	@ F/A ratio	Uncertainty
Peak torque	0.005	N–m	14500	0.29	9e–4
	0.71	oz–in	14500	0.29	0.13
Peak power output	7.96	W	16000	0.32	1.62
	0.01	hp	16000	0.32	0.002
Overall efficiency @ peak power	2.76	%	16000	0.32	0.56
BSFC @ peak power	5.96	kg/kW–hr	16000	0.32	1.26
Peak delivery ratio	80.43	%	14500	0.32	4.2
Peak normalized power	2.65	W	14500	0.29	0.53
Peak BMEP	184.63	kPa	14500	0.29	36.9
	26.78	psi	14500	0.29	5.35

Table 3–2: Summary of engine performance data for the Cox 010 engine.

Figure 3–6 shows efficiency corresponding to peak power to be almost constant at different engine speeds. The slight drop in efficiency from 13500 rpm to 15000 rpm is observed to occur because of a leaner fuel–air mixture ratio.

3.1.3 Engine Performance – Cox 020

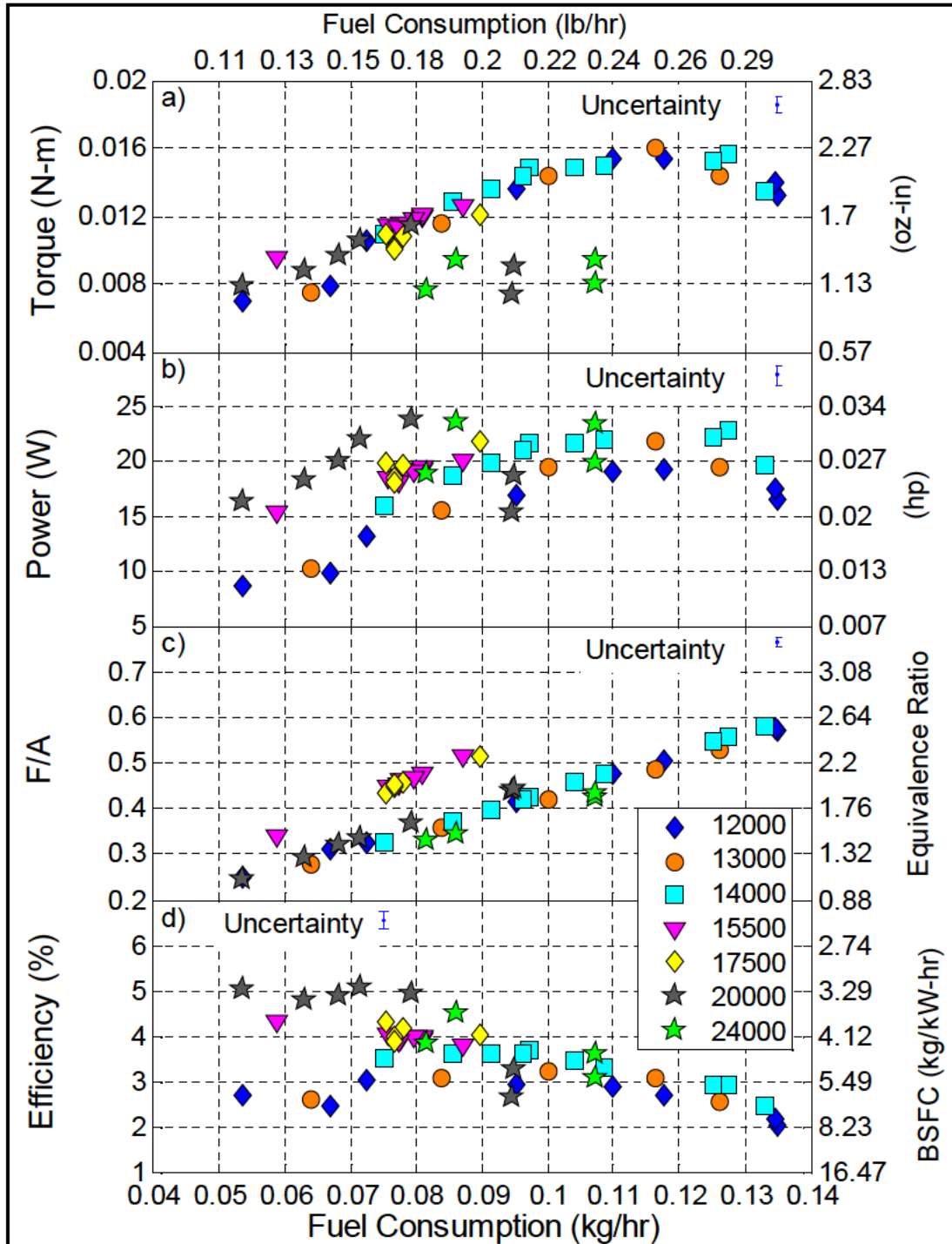


Figure 3-7: Performance map for the Cox 020 engine. Data sets represent different engine speeds.

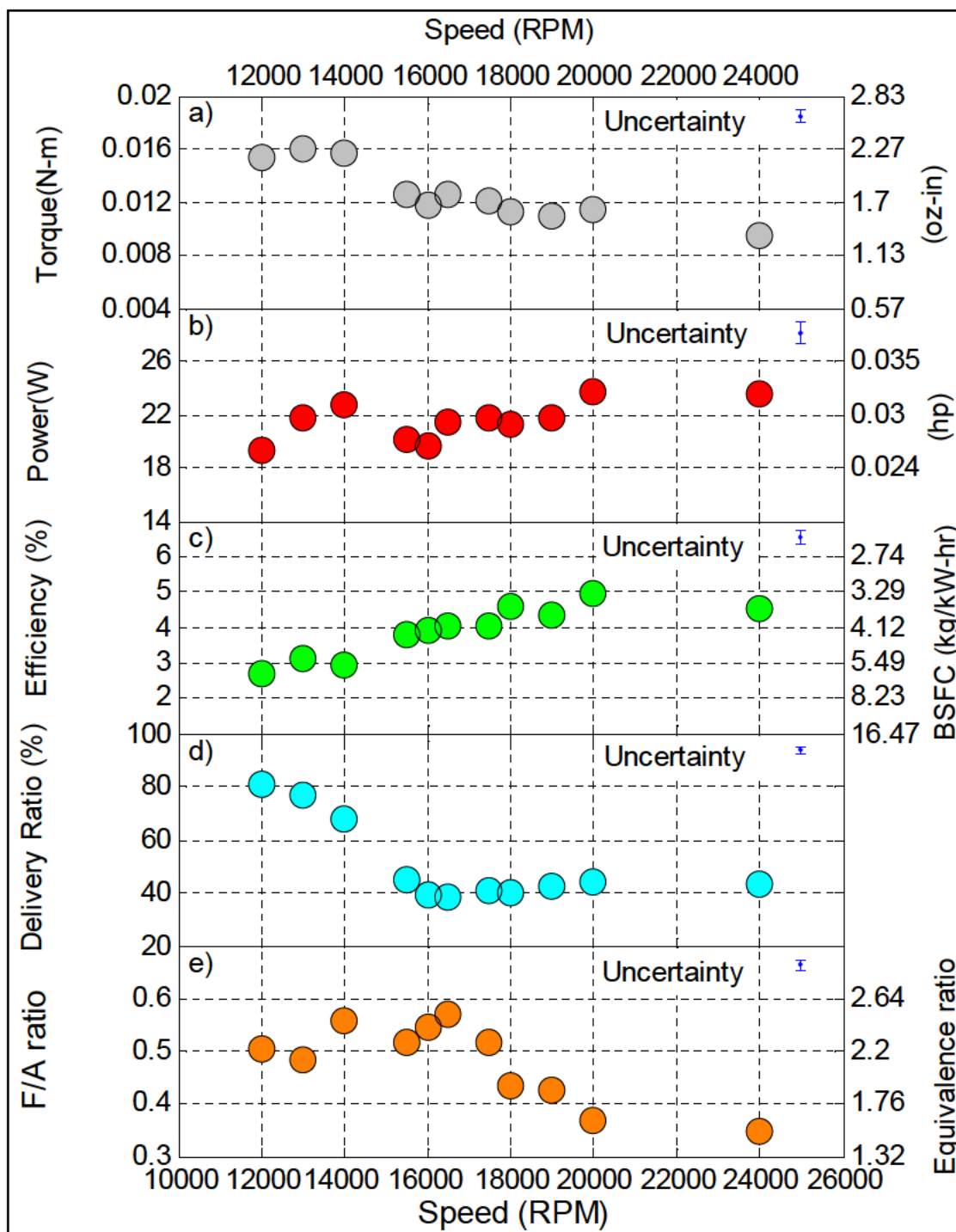


Figure 3-8: Peak performance of the Cox 020 engine as a function of engine speed.

Engine model			Cox 020 Pee Wee		
Engine manufacturer			Cox Engines		
Displacement	0.327 cc		0.020 cu.in.		
Bore	7.45 mm		0.293 in.		
Stroke	7.5 mm		0.295 in.		
Mass	25 g		0.88 oz.		
Geometric compression ratio	6.45				
	Value	Units	@ rpm	@ F/A ratio	Uncertainty
Peak torque	0.016	N–m	13000	0.48	9.7e–4
	2.27	oz–in	13000	0.48	0.14
Peak power output	23.75	W	20000	0.37	2
	0.03	hp	20000	0.37	0.003
Overall efficiency @ peak power	4.93	%	20000	0.37	0.42
BSFC @ peak power	3.34	kg/kW–hr	20000	0.37	0.30
Peak delivery ratio	81.61	%	12000	0.51	3.77
Peak normalized power	6.7	W	13000	0.48	0.41
Peak BMEP	306.62	kPa	13000	0.48	18.62
	44.47	psi	13000	0.48	2.7

Table 3–3: Summary of engine performance data for the Cox 020 engine.

Figure 3–8 shows a trend in delivery ratio which is observed in several engines. There is an initial peak in delivery ratio followed by a drop and an increase in delivery ratio at higher engine speeds. This results in the delivery ratio having two peaks. This behavior has been previously observed for crankcase scavenged two–stroke engines.^{108 109} For the Cox 020 engine the peak occurs once at 12000 rpm and again at 22000 rpm. This is reflected in torque and power outputs which are also seen to have two peaks. Maximum torque is achieved at 12000 rpm. However, maximum power is achieved at 20000 rpm because of the product of a relatively large torque

with a high engine speed. Peak efficiency is also attained at the higher engine speed because of the large power output coupled with operation at lean mixture ratios as can be seen in Fig. 3-8.

3.1.4 Engine Performance – Cox 049

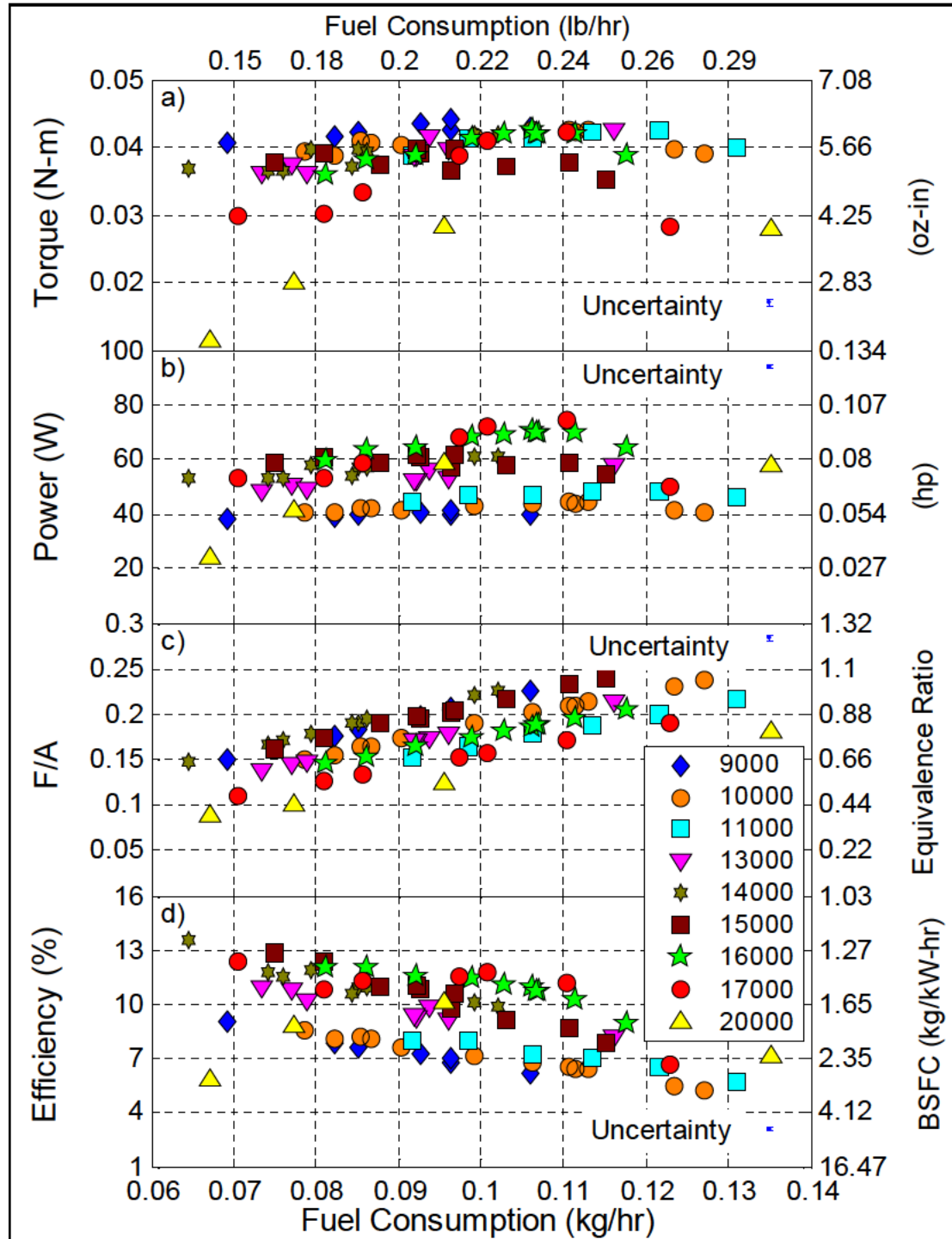


Figure 3-9: Performance map for the Cox 049 engine. Data sets represent different engine speeds.

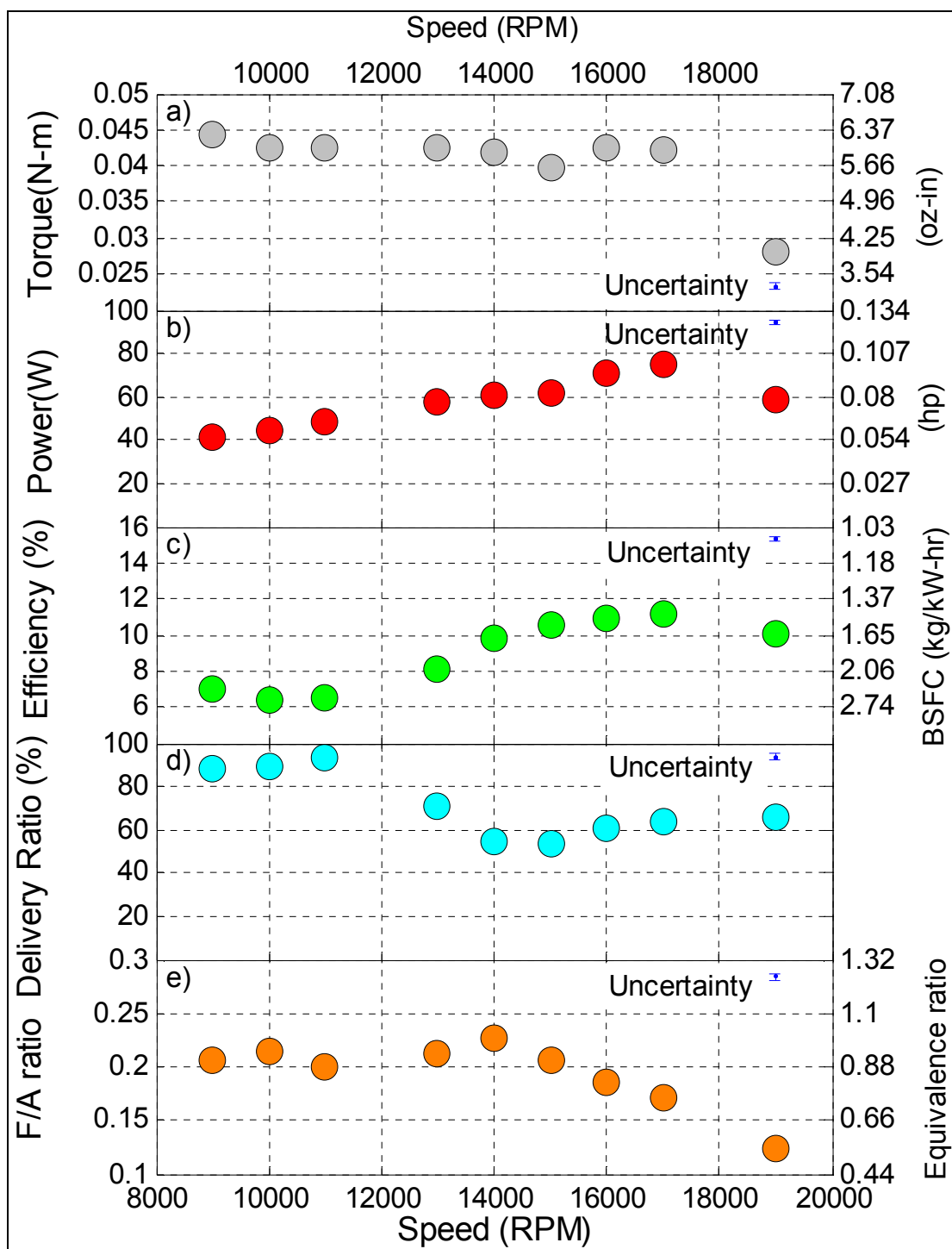


Figure 3–10: Peak performance of the Cox 049 engine as a function of engine speed.

Engine model			Cox 049 Babe Bee		
Engine manufacturer			Cox Engines		
Displacement	0.803 cc		0.049 cu.in.		
Bore	10.24 mm		0.403 in.		
Stroke	9.6 mm		0.378 in.		
Mass	42 g		1.48 oz.		
Geometric compression ratio	7.59				
	Value	Units	@ rpm	@ F/A ratio	Uncertainty
Peak torque	0.044	N–m	9000	0.21	9.8e–4
	6.23	oz–in	9000	0.21	0.14
Peak power output	74.63	W	17000	0.17	1.75
	0.1	hp	17000	0.17	0.002
Overall efficiency @ peak power	11.12	%	17000	0.15	0.26
BSFC @ peak power	1.48	kg/kW–hr	17000	0.15	0.05
Peak delivery ratio	93.61	%	11000	0.19	3.90
Peak normalized power	14.35	W	9000	0.21	0.32
Peak BMEP	343.34	kPa	9000	0.21	7.67
	49.8	psi	9000	0.21	1.11

Table 3–4: Summary of engine performance data for the Cox 049engine.

Figure 3–10 also shows delivery ratio to have two peaks, one at 11000 rpm and another close to 18000 rpm. Peak torque does not change much between 9000 to 17000 rpm but drops rapidly thereafter. Peak power is achieved at 17000 rpm as is engine efficiency. Delivery ratio falls between 11000 and 14000 rpm but efficiency continues to increase as power output increases.

3.1.5 Engine Performance – AP Wasp 061

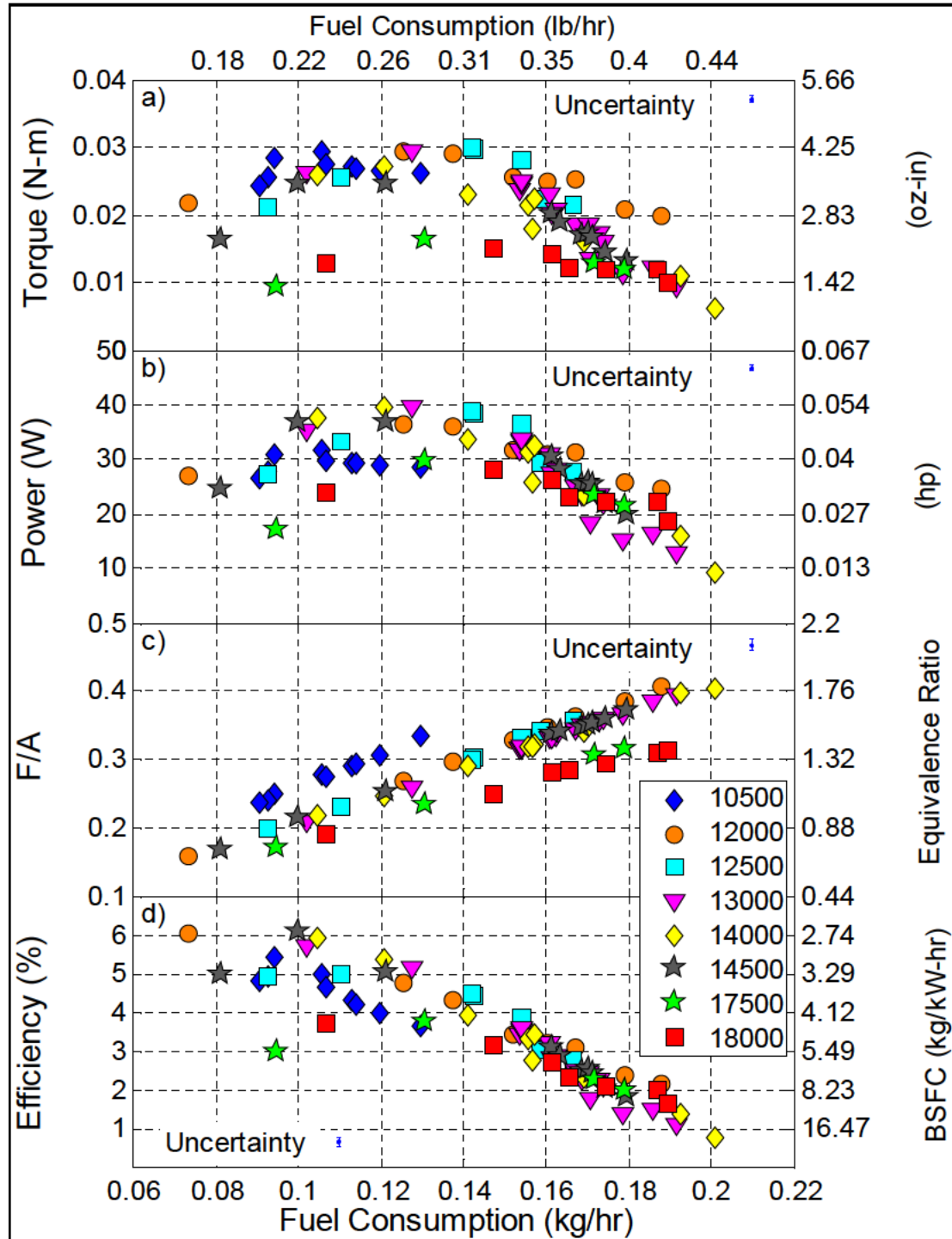


Figure 3-11: Performance map for the AP Wasp engine. Data sets represent different engine speeds.

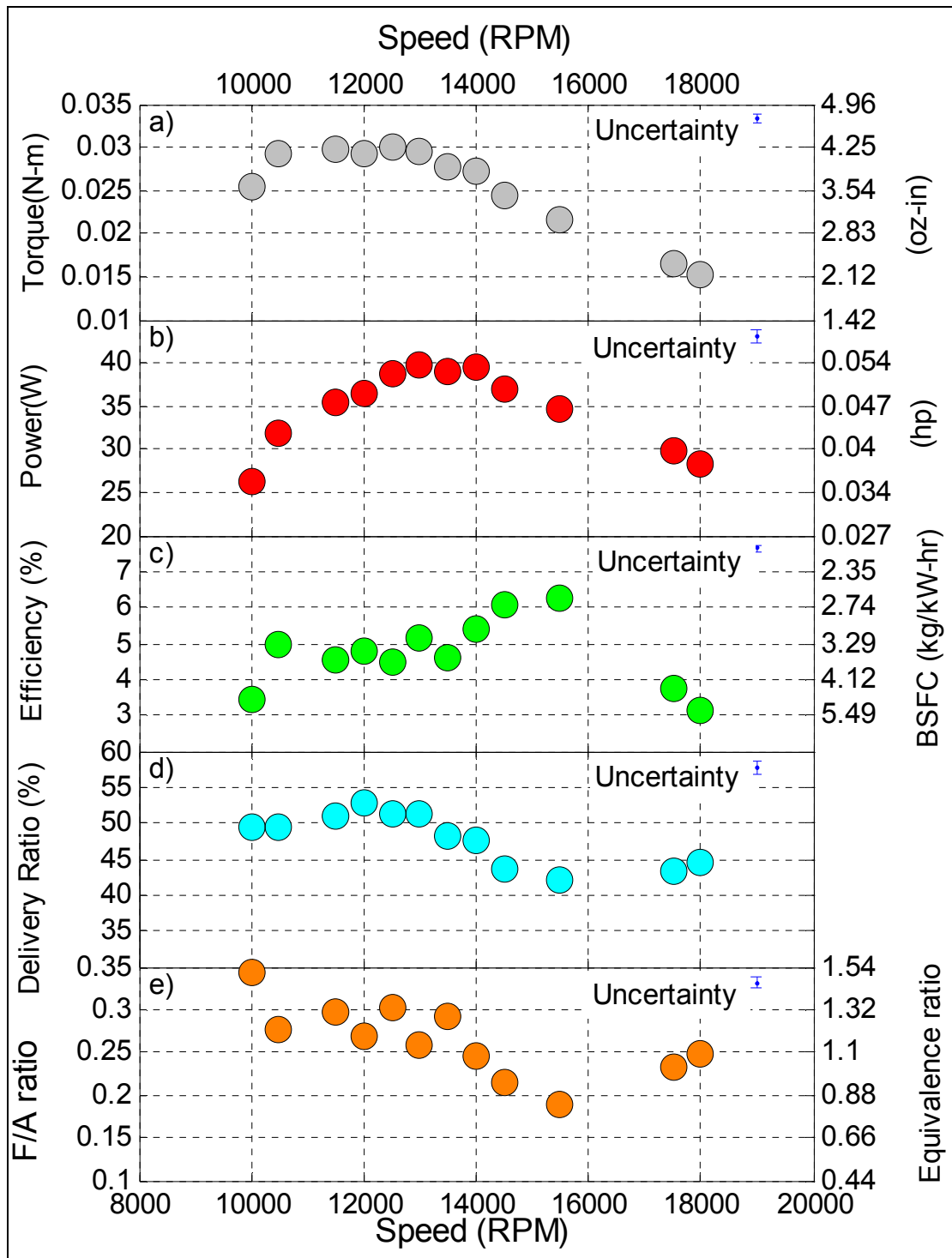


Figure 3-12: Peak performance of the AP Wasp engine as a function of engine speed.

Engine model			AP WASP		
Engine manufacturer			AP Engines		
Displacement	0.999 cc		0.061 cu.in.		
Bore	11.25 mm		0.442 in.		
Stroke	10 mm		0.394 in.		
Mass	54 g		1.905 oz.		
Geometric compression ratio	9.28				
	Value	Units	@ rpm	@ F/A ratio	Uncertainty
Peak torque	0.0299	N–m	12500	0.30	9.75e–4
	4.23	oz–in	12500	0.30	0.14
Peak power output	39.73	W	13000	0.26	1.33
	0.05	hp	13000	0.26	0.002
Overall efficiency @ peak power	5.14	%	13000	0.26	0.17
BSFC @ peak power	3.2	kg/kW–hr	13000	0.26	0.13
Peak delivery ratio	52.67	%	12000	0.27	2.23
Peak normalized power	9.33	W	12500	0.30	0.32
Peak BMEP	186.6	kPa	12500	0.30	6.13
	27.06	psi	12500	0.30	0.89

Table 3–5: Summary of engine performance data for the AP Wasp engine.

Figure 3–12 only shows a minor improvement in delivery ratio at higher engine speeds. Torque and power however only show a single peak and both continue to drop beyond an engine speed of 15000 rpm. Efficiency however shows a marked improvement from 13000 rpm to 16000 rpm in spite of decreasing delivery ratio in this interval. This is because of engine operation at increasingly leaner mixture ratios in this range of speed.

3.1.6 Engine Performance – AP Yellowjacket 15

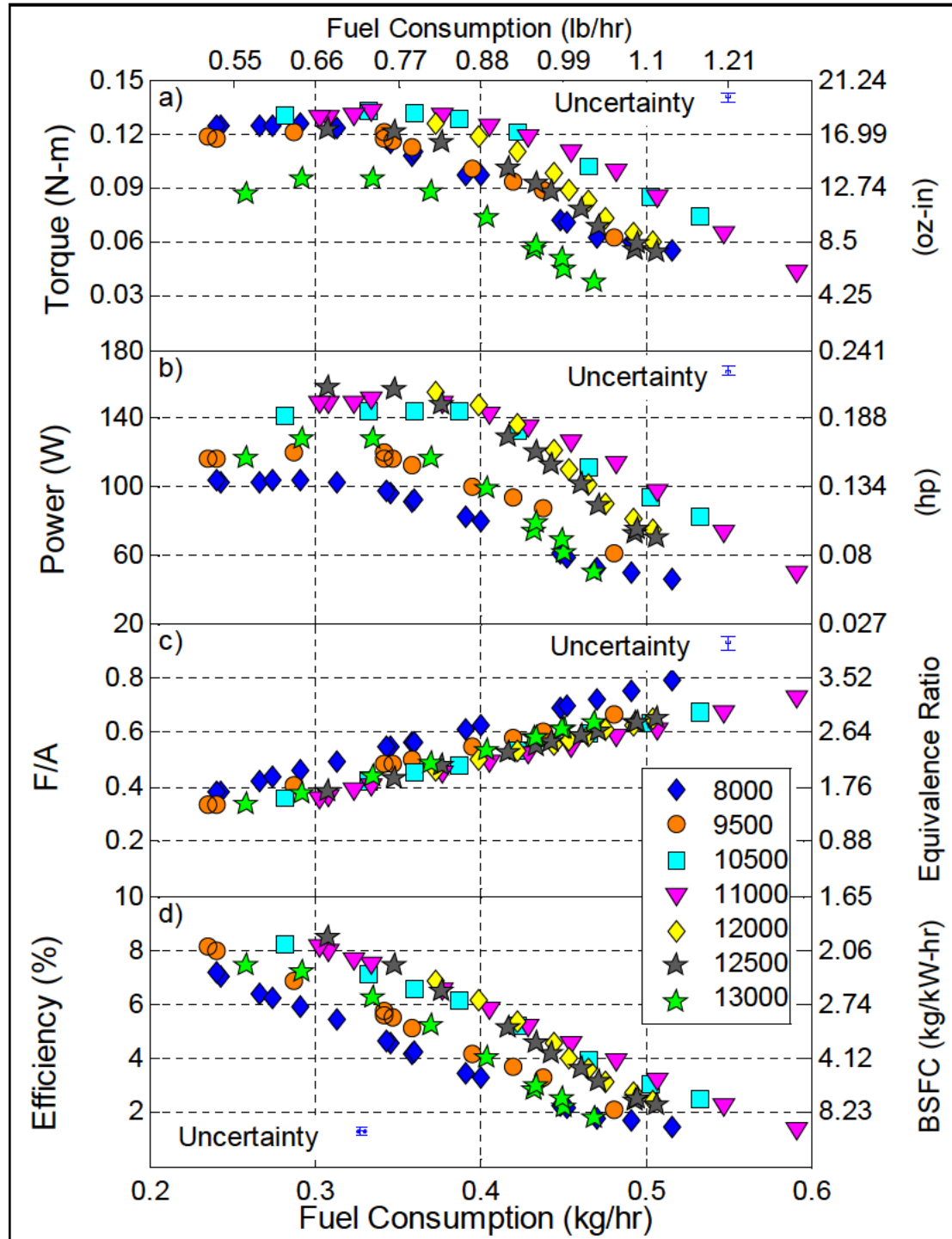


Figure 3–13: Performance map for the AP Yellowjacket engine. Data sets represent different engine speeds.

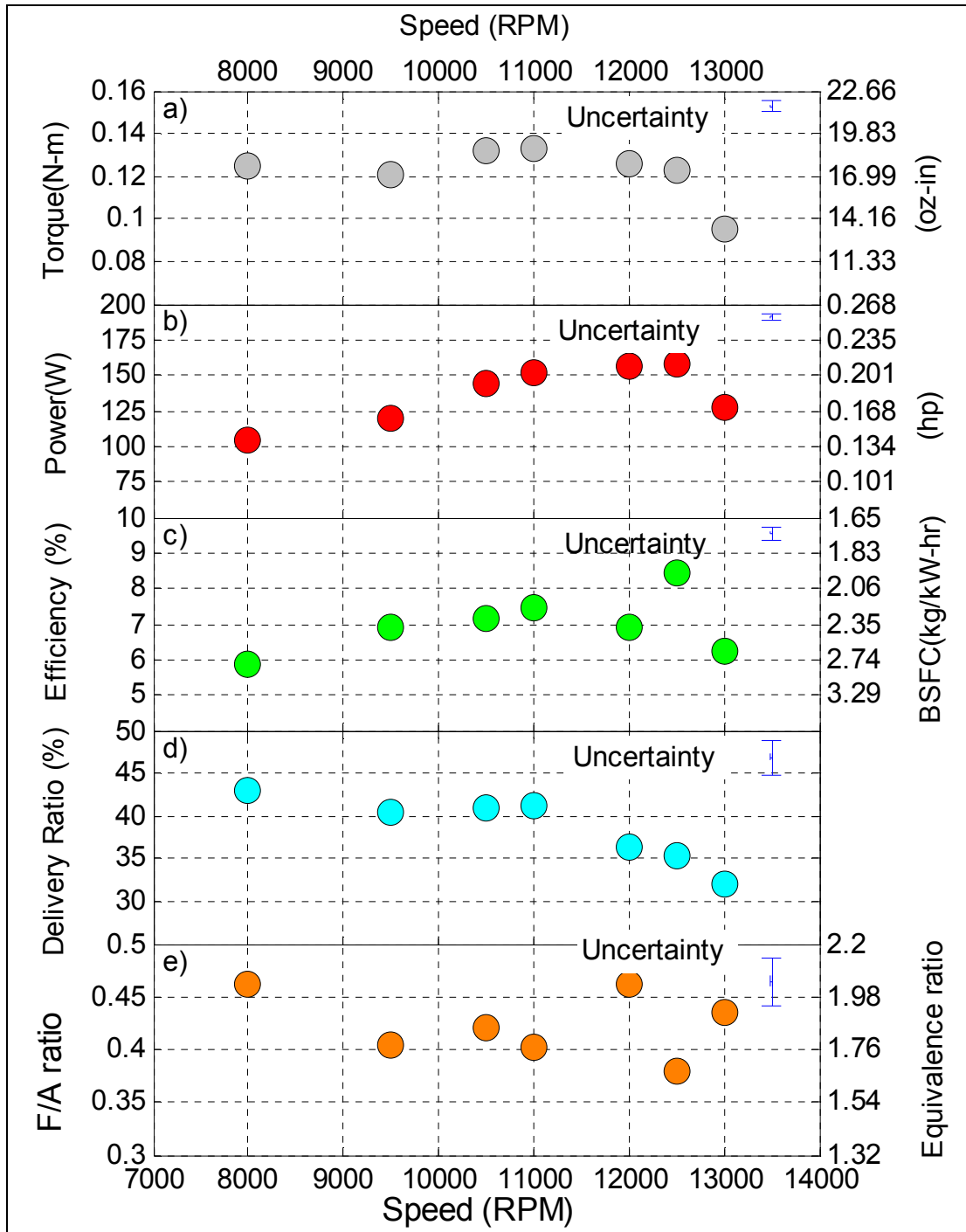


Figure 3–14: Peak performance of the AP Yellowjacket engine as a function of engine speed.

Engine model			AP YELLOWJACKET		
Engine manufacturer			AP Engines		
Displacement	2.46 cc		0.15 cu.in.		
Bore	15.5 mm		0.61 in.		
Stroke	12 mm		0.47 in.		
Mass	150 g		5.29 oz.		
Geometric compression ratio	10.43				
	Value	Units	@ rpm	@ F/A ratio	Uncertainty
Peak torque	0.133	N-m	11000	0.40	4.8e-3
	18.83	oz-in	11000	0.40	0.68
Peak power output	157.76	W	12500	0.38	2.41
	0.21	hp	12500	0.38	0.003
Overall efficiency @ peak power	8.45	%	12500	0.38	0.24
BSFC @ peak power	1.95	kg/kW-hr	12500	0.38	0.03
Peak delivery ratio	68.68	%	10000	0.34	4.48
Peak normalized power	34.69	W	11000	0.40	1.25
Peak BMEP	338.75	kPa	11000	0.40	12.22
	49.13	psi	11000	0.40	1.77

Table 3–6: Summary of engine performance data for the AP Yellowjacket engine.

Figure 3–14 shows efficiency dropping from 11000 to 12000 rpm followed by a peak at 12500 rpm. This is because of the engine operating at a rich mixture ratio at 12000 rpm. No evidence of improvement in delivery ratio at higher engine speeds is seen for this particular engine.

3.1.7 Engine Performance – OS 25 FX

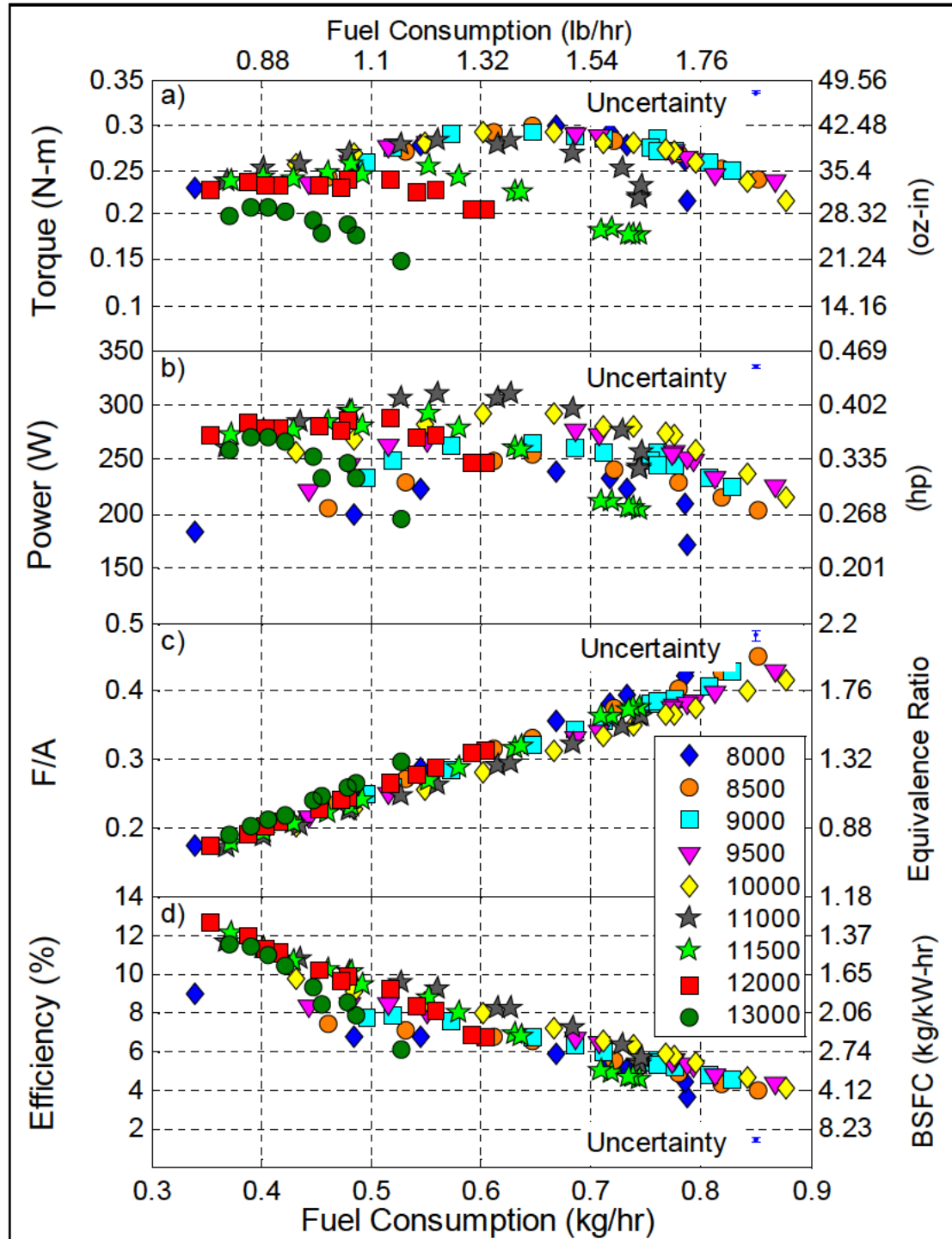


Figure 3–15: Performance map for the OS 25 FX engine. Data sets represent different engine speeds.

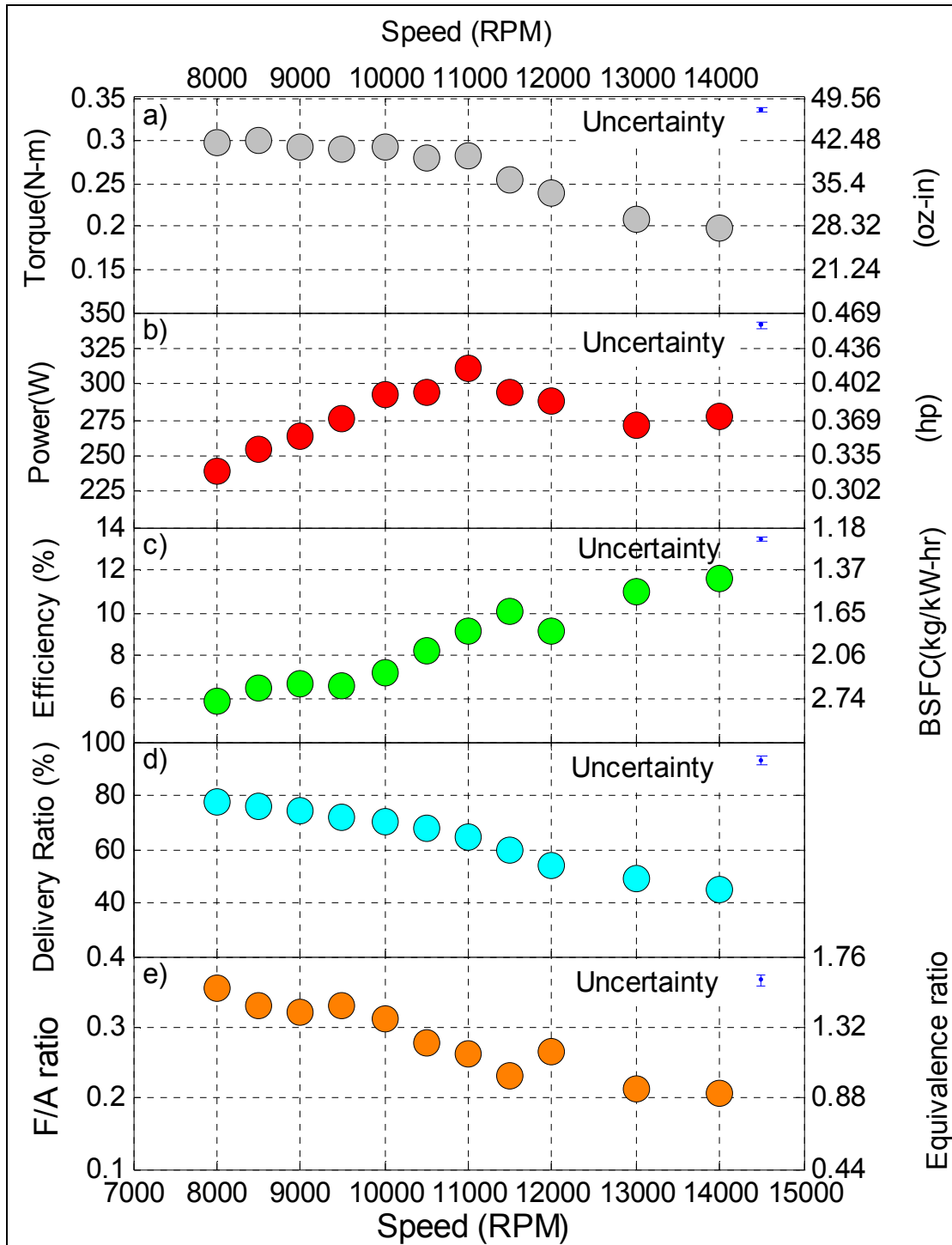


Figure 3-16: Peak performance of the OS 25 FX engine as a function of engine speed.

Engine model		OS 25 FX			
Engine manufacturer		OS Engines			
Displacement	4.097 cc	0.25 cu.in.			
Bore	18 mm	0.71 in.			
Stroke	16 mm	0.63 in.			
Mass	248 g	8.75 oz.			
Geometric compression ratio	17.96				
	Value	Units	@ rpm	@ F/A ratio	Uncertainty
Peak torque	0.299	N-m	8500	0.33	4.1e-3
	42.34	oz-in	8500	0.33	0.58
Peak power output	310.52	W	11000	0.36	4.72
	0.42	hp	11000	0.36	0.006
Overall efficiency @ peak power	9.12	%	11000	0.36	0.14
BSFC @ peak power	1.81	kg/kW-hr	11000	0.36	0.03
Peak delivery ratio	80.61	%	8000	0.17	4.27
Peak normalized power	56.19	W	8500	0.33	0.81
Peak BMEP	438.92	kPa	8500	0.33	6.33
	63.66	psi	8500	0.33	0.92

Table 3-7: Summary of engine performance data for the OS 25 FX engine.

Figure 3-16 shows efficiency increasing from 10000 rpm to 13000 rpm in spite of a decrease in delivery ratio during the same interval. This is observed to occur because of a corresponding decrease in equivalence ratio in the same speed interval. Again, no evidence of improvement in delivery ratio at higher engine speeds is seen for this particular engine.

3.1.8 Engine Performance – OS 40 FX

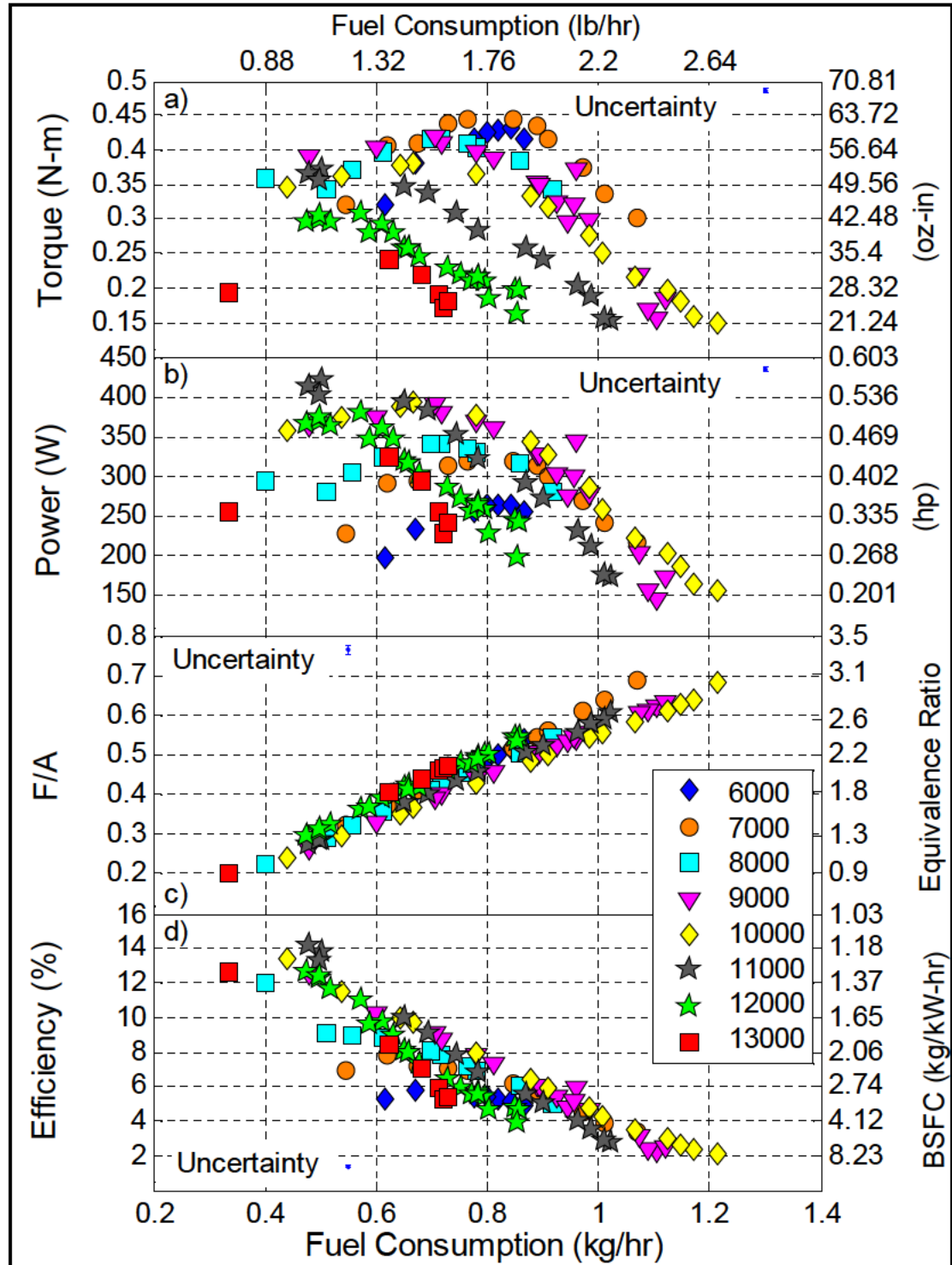


Figure 3–17: Performance map for the OS 40 FX engine at low engine speeds. Data sets represent different engine speeds.

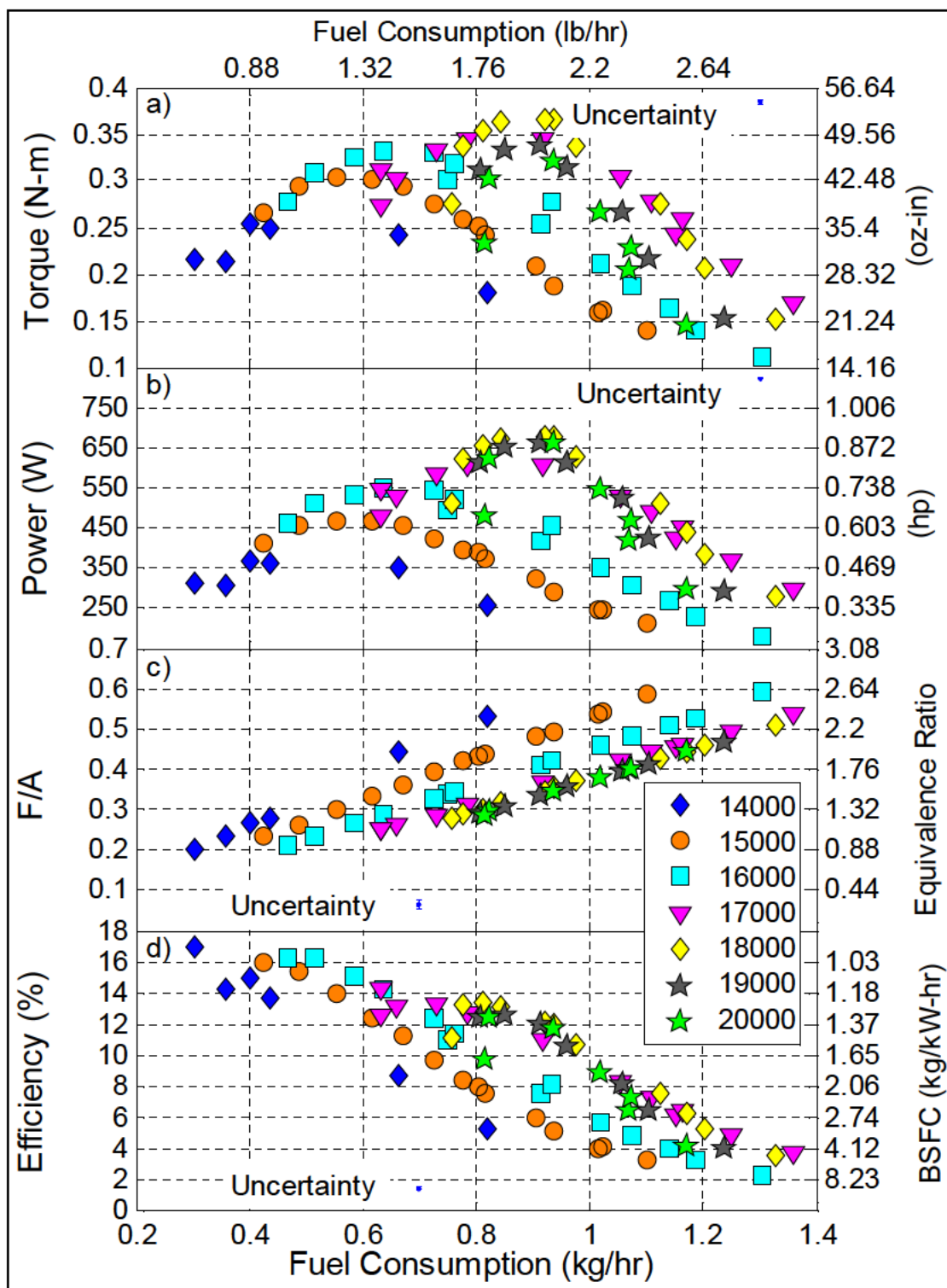


Figure 3–18: Performance map for the OS 40 FX engine at high engine speeds. Data sets represent different engine speeds.

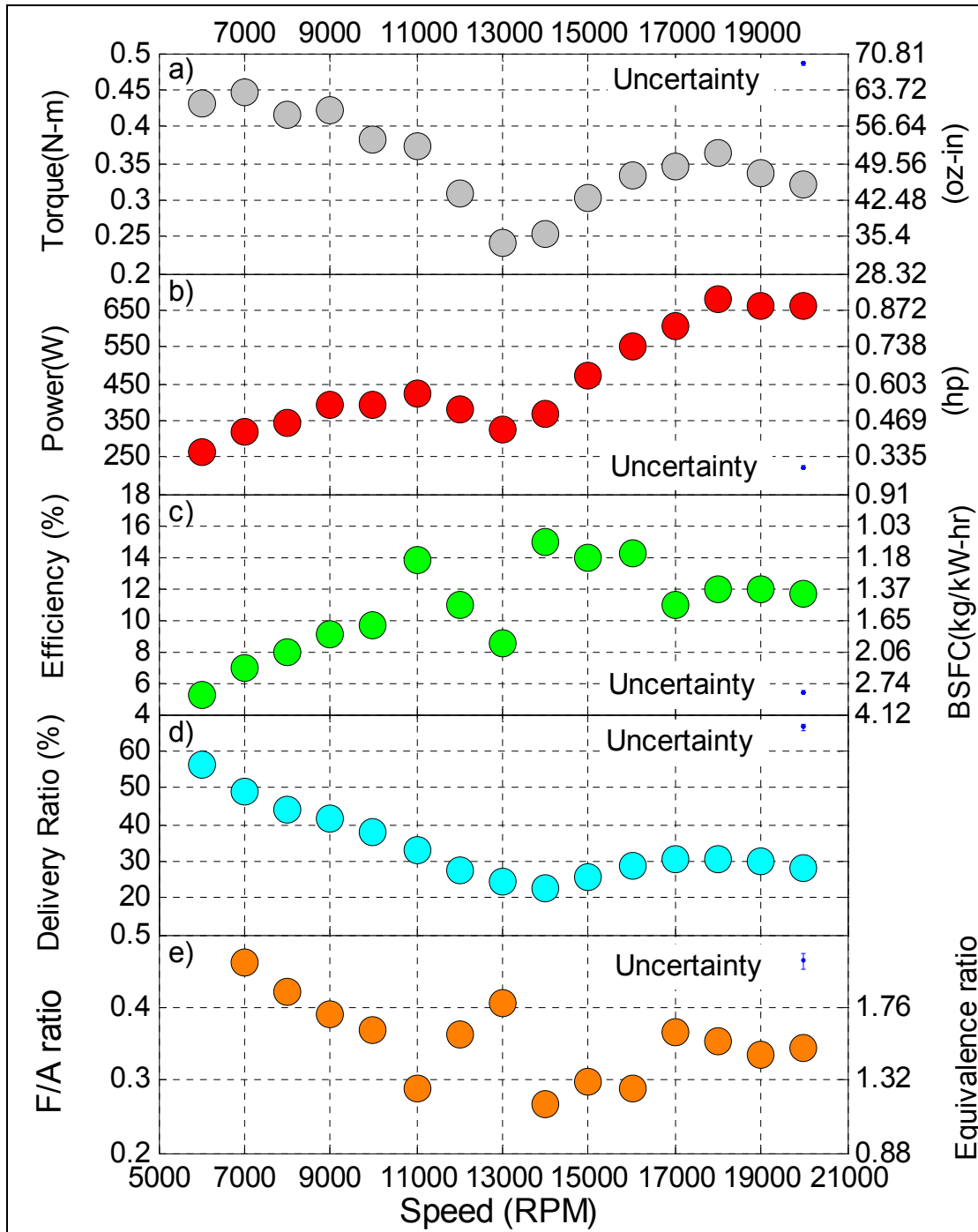


Figure 3–19: Peak performance of the OS 40 FX engine as a function of engine speed.

Engine model			OS 40 FX		
Engine manufacturer			OS Engines		
Displacement	6.55 cc		0.40 cu.in.		
Bore	20.5 mm		0.81 in.		
Stroke	19.6 mm		0.77 in.		
Mass	386 g		13.62 oz.		
Geometric compression ratio	14.5				
	Value	Units	@ rpm	@ F/A ratio	Uncertainty
Peak torque	0.446	N-m	7000	0.46	4.6e-3
	63.16	oz-in	7000	0.46	0.65
Peak power output	676.83	W	18000	0.35	8.71
	0.91	hp	18000	0.35	0.012
Overall efficiency @ peak power	11.87	%	18000	0.35	0.15
BSFC @ peak power	1.39	kg/kW-hr	18000	0.35	0.02
Peak delivery ratio	57.27	%	6000	0.4	3.23
Peak normalized power	70.03	W	7000	0.46	0.74
Peak BMEP	418.83	kPa	7000	0.46	4.45
	60.75	psi	7000	0.46	0.65

Table 3–8: Summary of engine performance data for the OS 40 FX engine.

Figure 3–19 shows a marked difference in the nature of torque and power curves on either side of 13000 rpm. This is primarily driven by a double peak observed in delivery ratio, once at 6000 rpm and again at 17000 rpm. Improvement in delivery ratio at speeds higher than 13000 rpm results in a marked improvement in engine torque and power, more so than previously observed in other engines. Efficiency is seen to continuously increase with a peak at 14000 rpm except for a

region between 11000 rpm and 13000 rpm where there is seen to be a sharp drop in efficiency. This can be attributed to a corresponding increase in operating equivalence ratio in this speed range.

3.1.9 Engine Performance – OS 46 FX

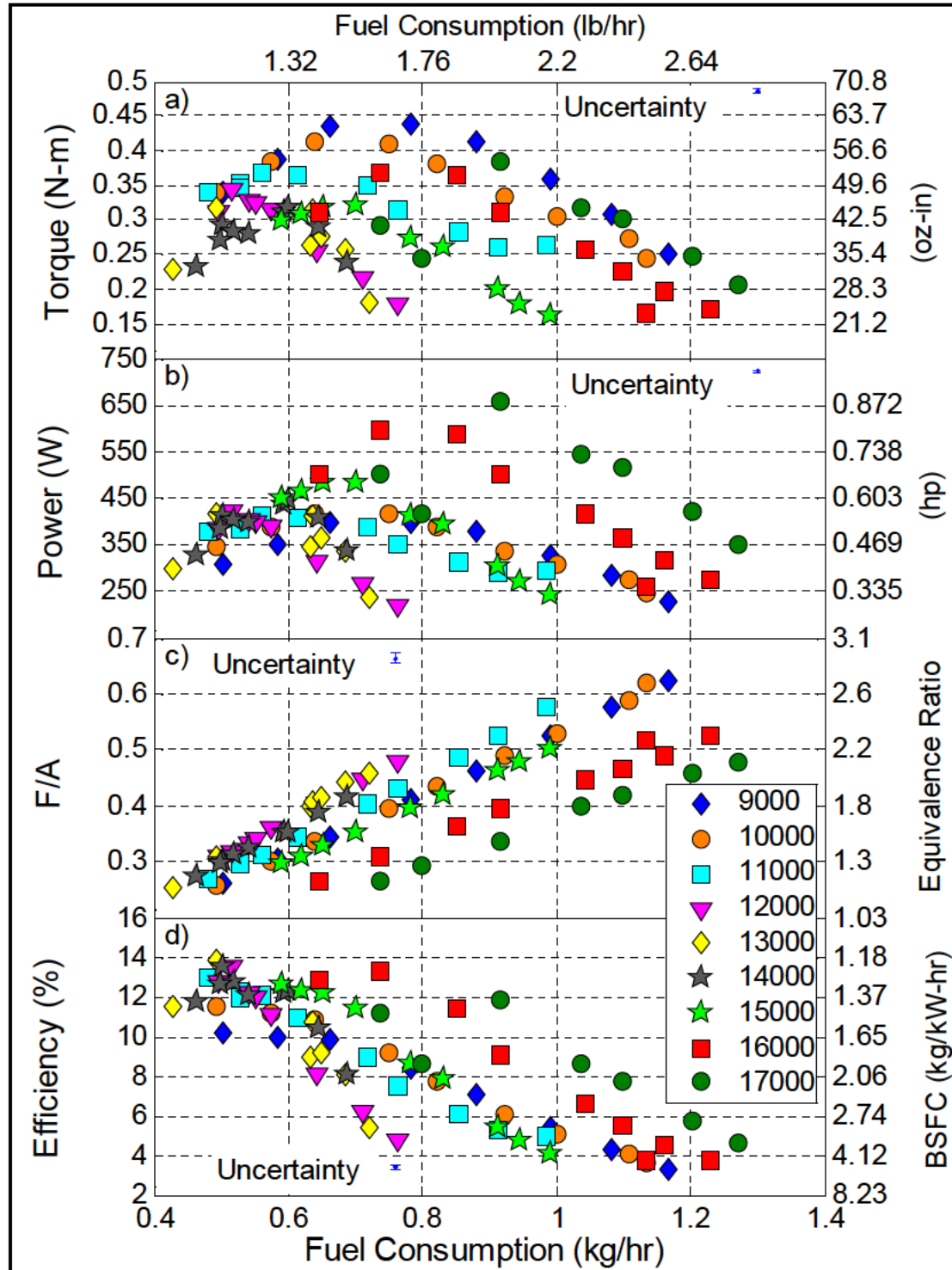


Figure 3–20: Performance map for the OS 46 FX engine. Data sets represent different engine speeds.

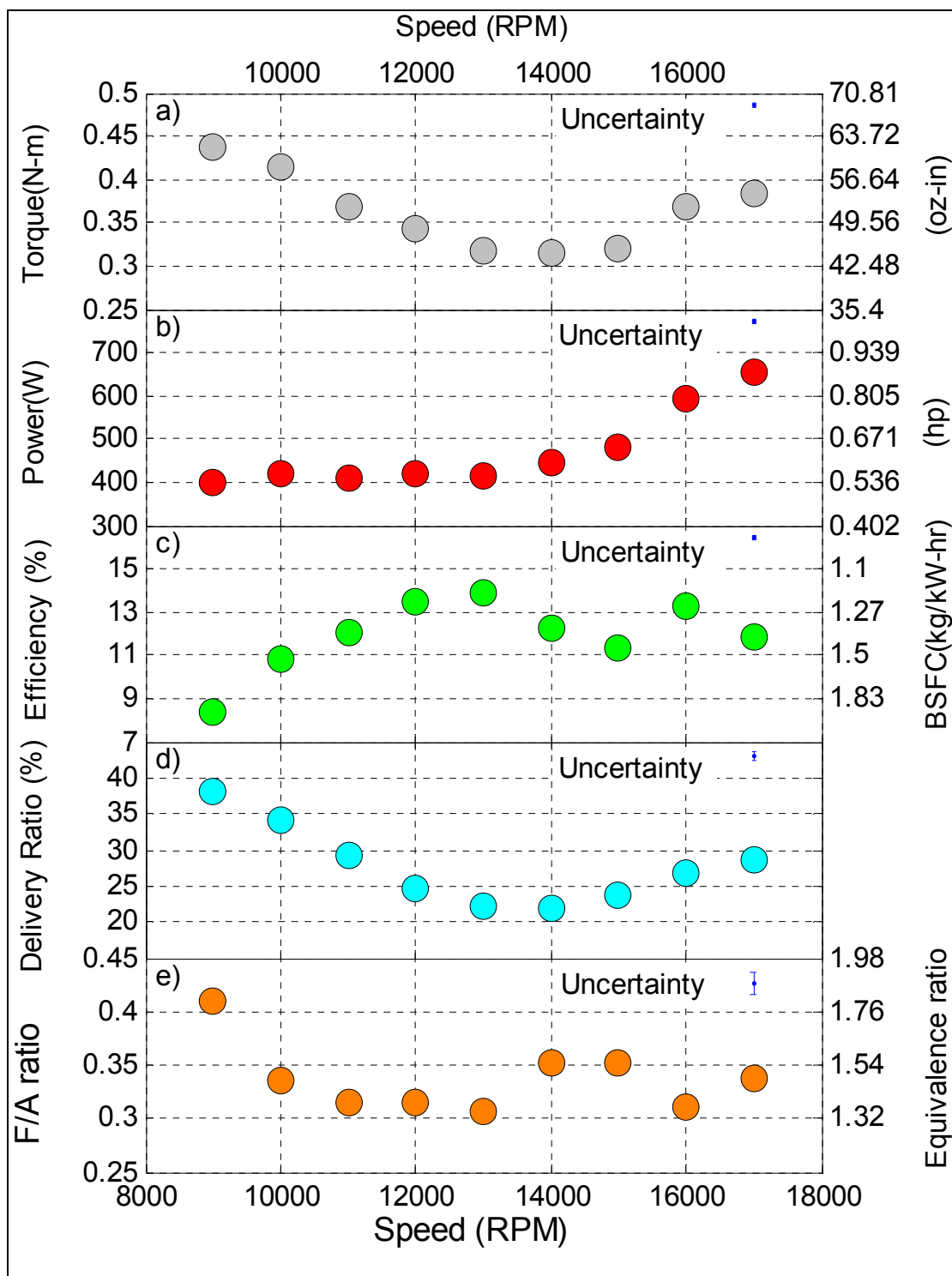


Figure 3-21: Peak performance of the OS 46 FX engine as a function of engine speed.

Engine model			OS 46 FX		
Engine manufacturer			OS Engines		
Displacement	7.54 cc		0.46 cu.in.		
Bore	22 mm		0.87 in.		
Stroke	19.6 mm		0.77 in.		
Mass	488 g		17.21 oz.		
Geometric compression ratio	16.5				
	Value	Units	@ rpm	@ F/A ratio	Uncertainty
Peak torque	0.437	N-m	9000	0.41	4.7e-3
	61.88	oz-in	9000	0.41	0.66
Peak power output	681.09	W	17000	0.34	8.3
	0.913	hp	17000	0.34	0.011
Overall efficiency @ peak power	11.79	%	17000	0.34	0.15
BSFC @ peak power	1.39	kg/kW-hr	17000	0.34	0.02
Peak delivery ratio	38.42	%	9000	0.26	2.05
Peak normalized power	67.9	W	9000	0.41	0.75
Peak BMEP	353.13	kPa	9000	0.41	3.89
	51.22	psi	9000	0.41	0.56

Table 3-9: Summary of engine performance data for the OS 46 FX engine.

Figure 3-21 also shows two peaks for delivery ratio, once at 9000 rpm and again at 17000 rpm. A corresponding behavior is observed in engine torque. Engine power output is however seen to be almost constant between 9000 to 14000 rpm and increase in magnitude beyond 14000 rpm.

3.2 Scaling analysis

3.2.1 Literature Survey of Engine Data

A literature survey of reciprocating engine performance was carried out in order to develop a general understanding of how engine performance scales with size. The survey follows a similar approach as McMahon and Bonner¹¹⁰ who plotted peak power output as a function of mass for a large number of internal combustion engines. Unlike McMahon and Bonner, however, engine data was grouped into one of four categories of reciprocating engines: aircraft engines, automotive engines, other small engines like those used in outboard motors, lawnmowers, tractors, and other outdoor power equipment, and model aircraft engines. Finally, a large set of engine data obtained from manufacturers of model airplane engines was included to extend the scaling analysis to the smallest scales. The data for model airplane engines was first collected and summarized by Troy¹¹¹ and further used in the analysis performed here.

The aircraft engines surveyed here are four stroke multiple cylinder engines with the number of cylinders varying from 4 to 36. A majority of them are supercharged for improved performance at altitude. The data was obtained from a publication series compiled and published by Wilkinson¹¹² that includes basic engine properties and performance including brake specific fuel consumption (BSFC). The BSFC data is used to infer overall efficiency based on the heating value of 80/87 grade aviation gasoline fuel. Peak engine torque is estimated from the speed at peak power.

The automobile engines surveyed here are also four stroke engines with the number of cylinders varying between 4 and 12. The majority of these are naturally

aspirated and use electronic fuel injection as is typical of modern automobile engines. Performance data for these engines was obtained from an internet database.^{113 i} While the data is fairly comprehensive, no specific fuel consumption data are reported and engine efficiency must be estimated from maximum power and torque operating points in the manner described below:

The volumetric efficiency of the engine at peak power is assumed to be 100% enabling engine air flow to be estimated from engine speed and displacement. Actual values for volumetric efficiency in conventional scale reciprocating engines depends on a whole host of factors including engine speed, port timing, valve area and lift, exhaust pressure etc. While the simple assumption made here is probably not true for most engines, it allows a best case scenario to be calculated for overall efficiency to allow us to focus on the scaling analysis.

Similarly, the fuel–air ratio is assumed to be stoichiometric (gasoline) so that the fuel flow rate may be estimated from the air flow rate. The heating value of gasoline is used to estimate the energy input into the engine. Efficiency can then be estimated using the engine power output and energy input into the engine.

The data set for small outdoor power applications was assembled from information from four different manufacturers.^{114 115 116 117} These are primarily 4–stroke gasoline engines but also include a few 4–stroke diesel engines. The number of cylinders varies between 1 and 4 and most are naturally aspirated and use a carburetor for fuel–air mixing. The data, while reasonably comprehensive, also lacks information on specific fuel consumption or overall efficiency. Therefore, it was

ⁱ The data obtained from this source was checked with other internet resources to ensure validity.

necessary to estimate engine efficiency using the same procedure outlined above for automobile engines.

The data set for model airplane engines consists exclusively of single cylinder two stroke (and a few four stroke) engines which are naturally aspirated and use carburetors for fuel–air mixing. The fuel is ‘glow fuel’ which, as described previously, consists of a mixture of methanol, nitromethane and oil. While data provided by manufacturers is fairly reliable when it comes to physical properties like bore, stroke, displacement and weight, if any performance data is provided at all, it is usually limited to maximum power output and the corresponding engine speed. In addition, investigations by several researchers have shown that this data is not reliable and often over–predicts engine performance.^{118 119} Regardless of the veracity of the manufacturer supplied data, it is included in the survey in order to obtain an approximate idea of the scaling of engine performance. Of the nine engines investigated here, only four had performance data supplied by the manufacturer. In the cases where performance data is not available; an approach similar to that used for automotive engines is followed. However, the results have a higher probability of error because the volumetric efficiencies of miniature engines are probably much smaller than 100%. The scaling of the engines’ physical properties with size is examined first. Then scaling of engine performance parameters is investigated.

3.2.2 Scaling of Engine Physical Properties

Figure 3–22 shows engine mass plotted as a function of displacement volume. Two different power laws can be established that describe the scaling of engine mass with displacement. Engines used in ground applications appear to follow a different scaling law with higher associated engine mass as compared to those used in aircraft applications. This is presumably because of lighter materials used in engines intended for aerial use in order to deliver a higher power to weight ratio. Data regarding engine mass was unavailable for the automotive engines surveyed in this work. Figure 3–23 shows the scaling of bore to stroke ratio with engine size while Fig. 3–24 shows a similar relationship between piston area and engine displacement. As seen in Fig. 3–24, two different scaling relationships can be observed. For engines having a displacement less than 1000 cc, engines tend to mostly have a ‘square’ design where the bore to stroke ratio is close to 1. As engines get larger, this changes to a slightly ‘under square’ design. However, for engines having a displacement greater than 1000 cc, a ‘square’ design appears to become more common.

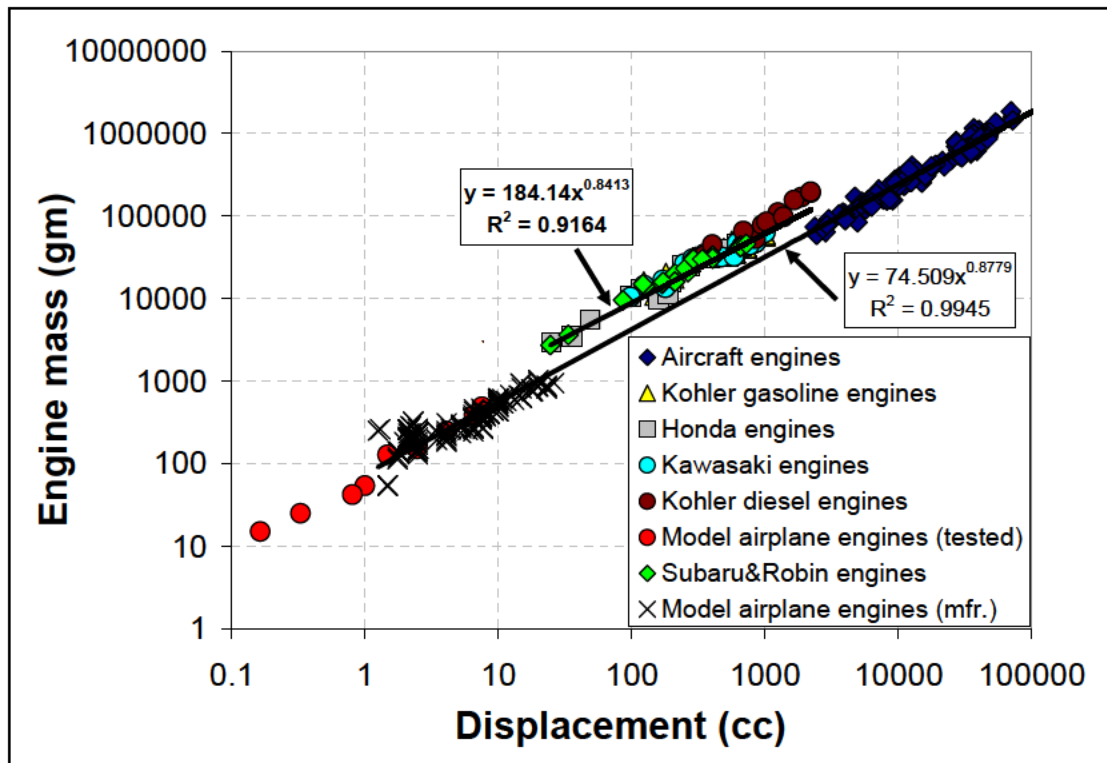


Figure 3–22: Scaling of overall engine mass with engine displacement.

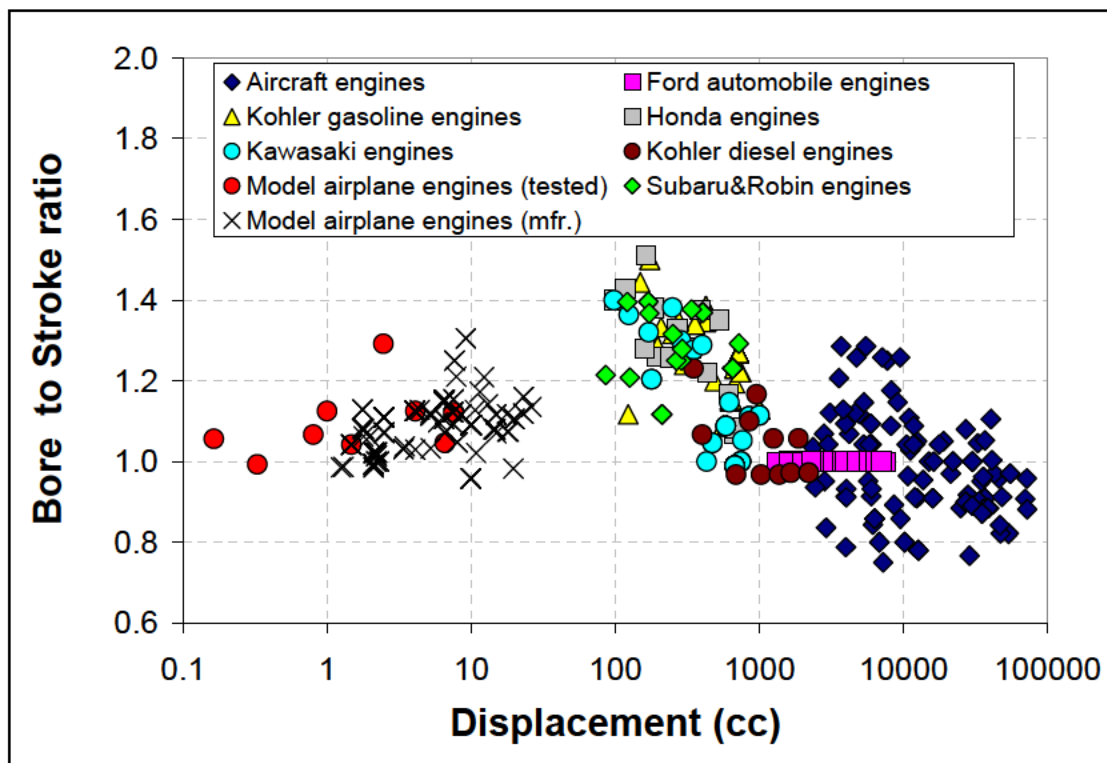


Figure 3–23: Scaling of bore to stroke ratio with engine displacement.

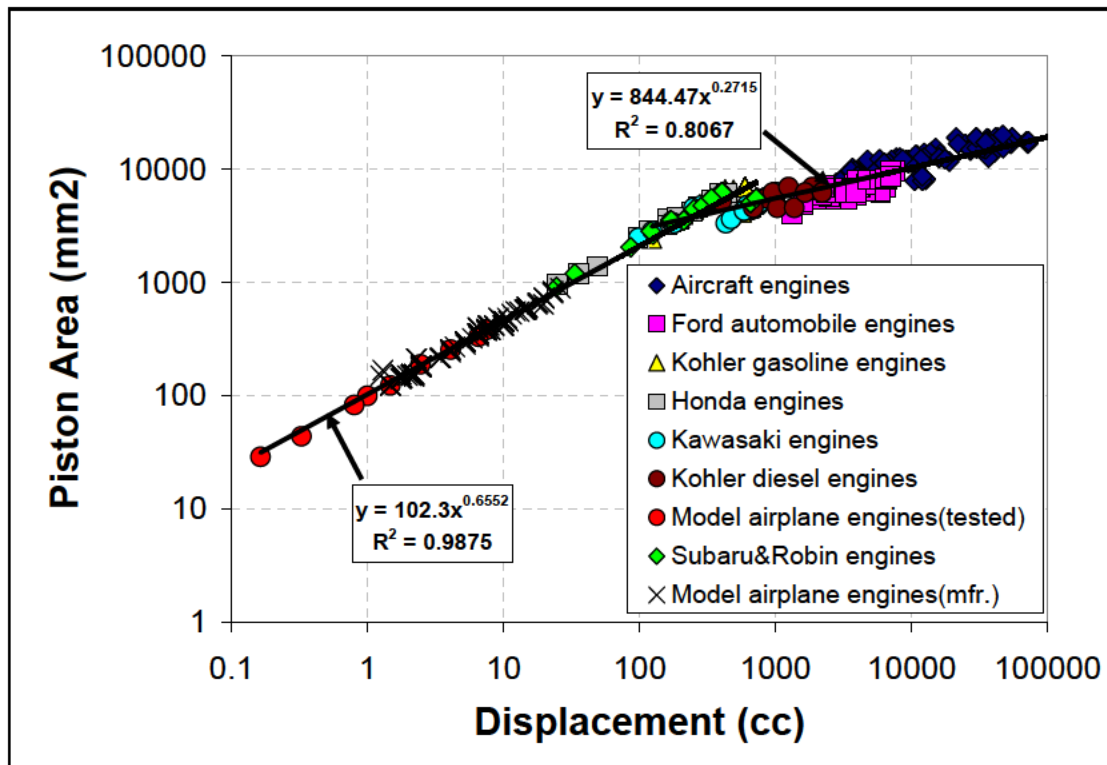


Figure 3–24: Scaling of piston area with engine displacement.

Geometric compression ratio is plotted as a function of engine displacement in Fig. 3–25. It shows that compression ratios fall within a relatively narrow band of values for most of the conventional scale engines. Gasoline engines have compression ratios between 5 and 12 and diesel engines have compression ratios between 16 and 22. Higher compression ratios for SI engines afford higher efficiency but the value is ultimately limited by fuel auto-ignition (detonation) limits.¹²⁰ Aircraft engines have somewhat lower compression ratios – possibly to reduce weight and increase reliability. Compression ratio data is unavailable from manufacturers of model airplane engines. Unlike the other classes of engines, the compression ratio in model aircraft engines seems to depend strongly on scale as it decreases from about 16.5 for the largest engine tested here to about 5 for the smallest engine. The high

compression ratio measured in the largest engine is possibly because of the high octane quality of methanol fuel allowing engines to operate with higher compression ratios without risk of detonation.¹²¹ As engines decrease in size, higher compression ratio could possibly lead to increased blowby past the piston resulting in loss of engine performance. In the absence of piston rings, the only way to prevent blowby would be to reduce piston–cylinder gap which would result in a large frictional loss penalty. The net result pertaining to engine design could be to reduce compression ratio in smaller engines at the expense of thermal efficiency without considerably increasing blowby and frictional losses.

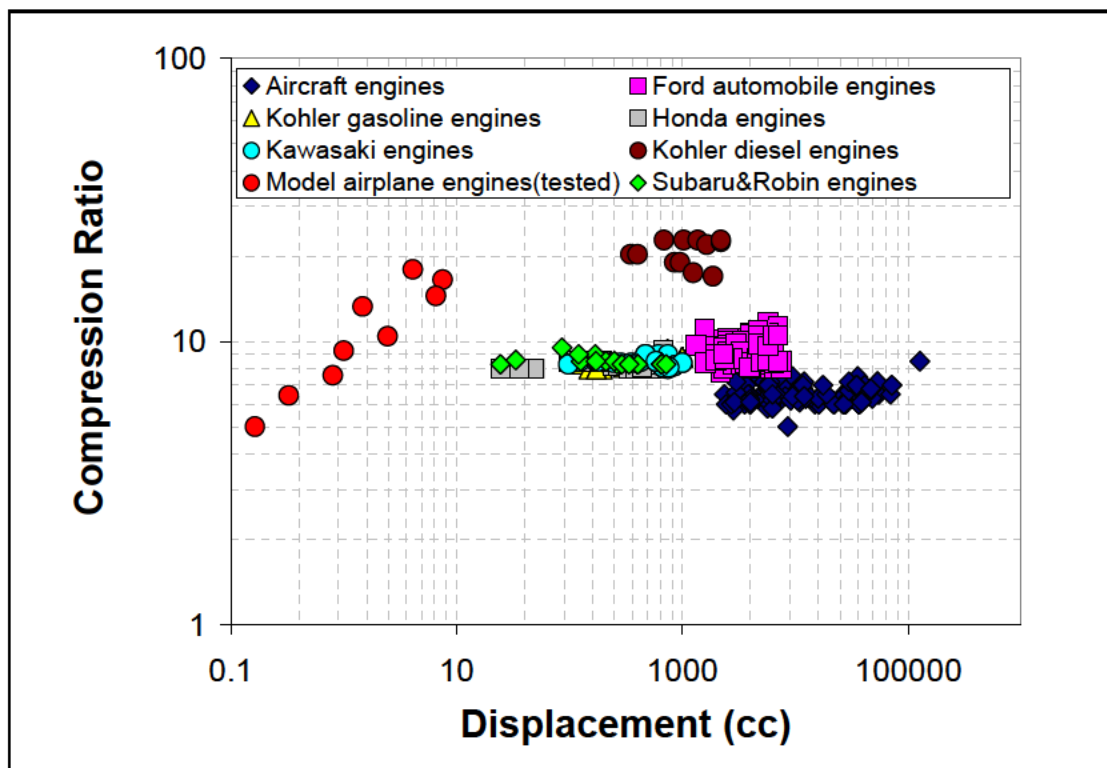


Figure 3–25: Scaling of compression ratio with engine displacement.

3.2.3 Peak Engine Performance Data

Table 3–10 summarizes the engine performance measurements used in the scaling analysis. A key step in understanding how engine performance scales with size is identifying appropriate parameters to investigate. Torque, power, and overall efficiency are obvious choices as all are considerably influenced by the operating conditions of the engine viz., operating speed and fuel–air mixture ratio. Therefore, the first step in the scaling analysis here is to compare the maximum values obtained for power, torque and overall efficiency from each engine (summarized in Table 3–10) as a function of engine size.

Engine	Disp.	Mass	Peak torque	Peak power		Overall efficiency @ peak power	Peak volumetric efficiency
				Measured	Mfr.		
Cox 010	0.16	15	0.0049	7.96	N/A	2.76	80.4
Cox 020	0.33	25	0.016	23.75	N/A	4.93	81.6
Cox 049	0.8	42	0.0442	74.64	N/A	11.12	93.6
Wasp 061	1	54	0.029	39.73	N/A	5.14	52.6
Hornet 09	1.47	128	0.083	90.83	N/A	5.14	63.8
Yellow jacket 15	2.46	150	0.133	157.76	186.4	8.45	68.7
OS 25 FX	4.1	248	0.299	310.52	626.4	9.12	80.6
OS 40 FX	6.55	386	0.445	676.83	1014	11.88	57.3
OS 46 FX	7.54	488	0.437	655.93	1208	11.8	38.4
	cc	gm	N–m	W		%	%

Table 3–10: Peak values for engine performance parameters.

3.2.4 Scaling of Peak Engine Torque, Power and Overall Efficiency

Figure 3–26 shows peak torque as a function of engine displacement. It includes data points from the literature survey as well as measured values on the dynamometer. Two power laws are fit to the data: one for the small engines measured in this study and another for engines identified in the literature survey. The similarity of both power laws and the high degree of correlation ($R^2 > 0.98$) suggests that, generally speaking, a single power law describes the scaling of torque with displacement independent of the engine size or type. This is consistent with previous work.¹²² Note that the correlation derived from the survey data does not include data points provided by manufacturers of model airplane engines which the measurements show are too large.

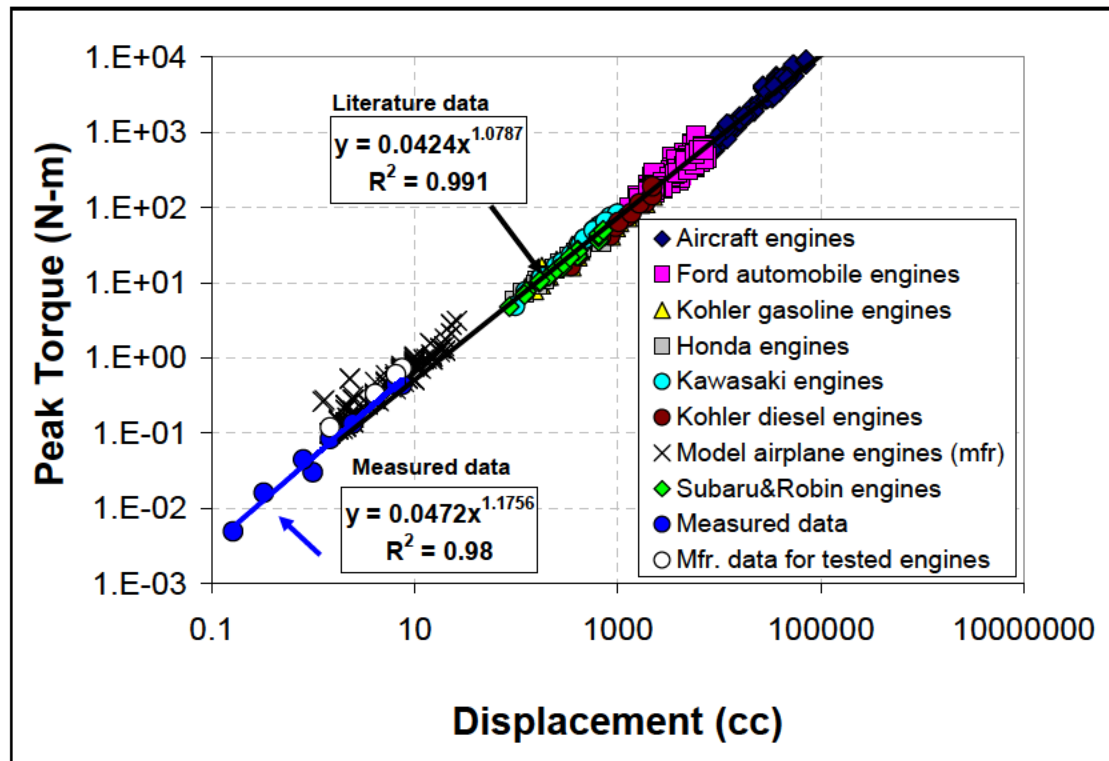


Figure 3–26: Scaling of peak engine torque with engine displacement.

The story is somewhat different when it comes to peak power and efficiency. Figure 3–27 shows the scaling of peak power as a function of engine displacement. An additional data set obtained from different sources relating to power output from 2–stroke engines has been added to this figure. This data set was found necessary to distinguish between two scaling laws depending on whether the engine has a two or four–stroke design. This is not surprising as it is well known that two–stroke designs generally produce more power per unit displacement than four–strokes. The miniature engine measurements are consistent with this trend and seem to follow the same power–law scaling as their larger two–stroke cousins. The measurements also show that manufacturers of miniature model aircraft engines tend to over predict performance by 35–40% so these data were not used in developing the power law.

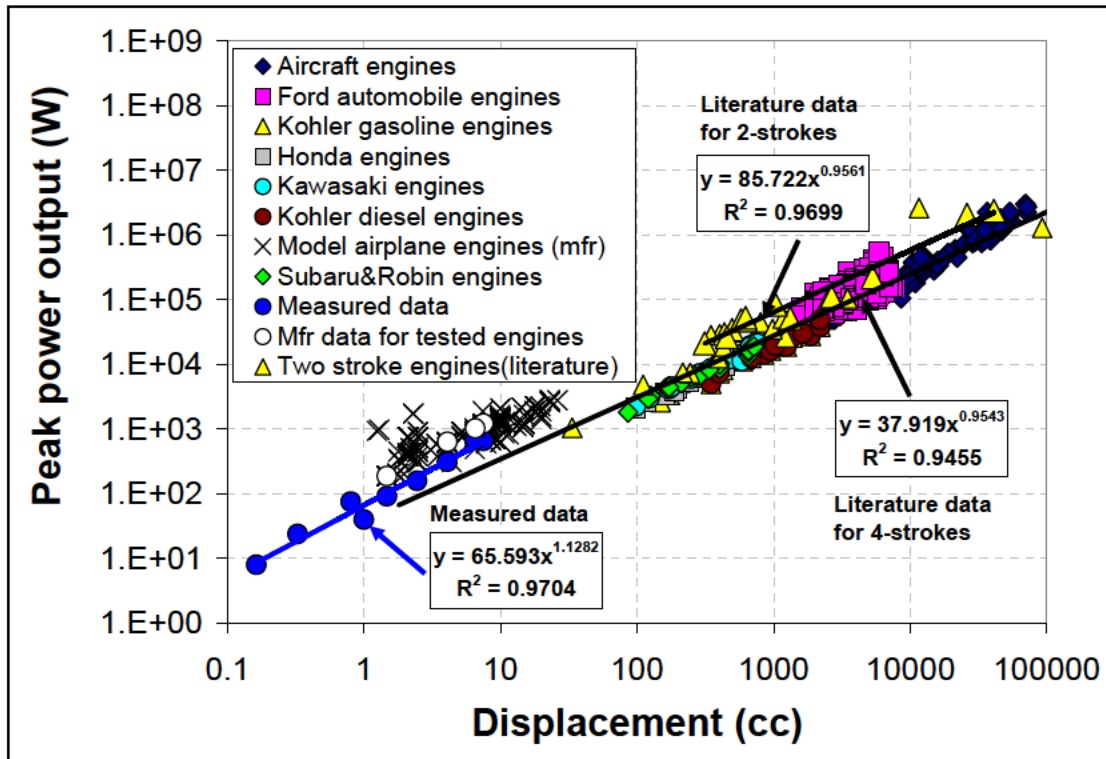


Figure 3–27: Scaling of peak engine power output with engine displacement.

While the scaling of overall efficiency with size presented in Fig. 3–28 follows the general trend predicted by the simple ‘back of the envelope’ analysis presented in Chapter 1, the mechanisms behind this general decrease in efficiency with scale are considerably more complex and uncertainⁱⁱ. The diamond symbols of gray color seen in Fig. 3–28 represent efficiency estimated for conventional scale engines on the basis of manufacturer supplied data and the procedure outlined previously in Section 3.2.1. However, this data was found to have a large amount of scatter in it. Another set of data representing measured overall efficiency was compiled using information presented in different IC engine textbooks. This data along with efficiency estimates for piston aircraft engines whose specific fuel consumption is reported in the operating manual is represented in Fig. 3–28 by yellow circles. SFC is converted to overall efficiency using the heating value of AVGas (44.65 MJ/kg).¹²³ The yellow circles and the blue circles which correspond to small engine measurements made in our laboratory thus represent ‘reliable’ efficiency data.

Although efficiency generally decreases with engine size, the scatter in the survey data based on estimated and measured data is large and the power law correlation is poor ($R^2 \sim 0.3$). This is because of the variation in engine configuration with respect to 2/4 stroke operation, spark/compression ignition design, naturally aspirated/turbo/super charged operation resulting in considerable variation in efficiency for engines of the same displacement.

ⁱⁱ Figure 3-29 shows the scaling of specific fuel consumption in g/kW-hr as a function of displacement for the data points shown in figure 3-28.

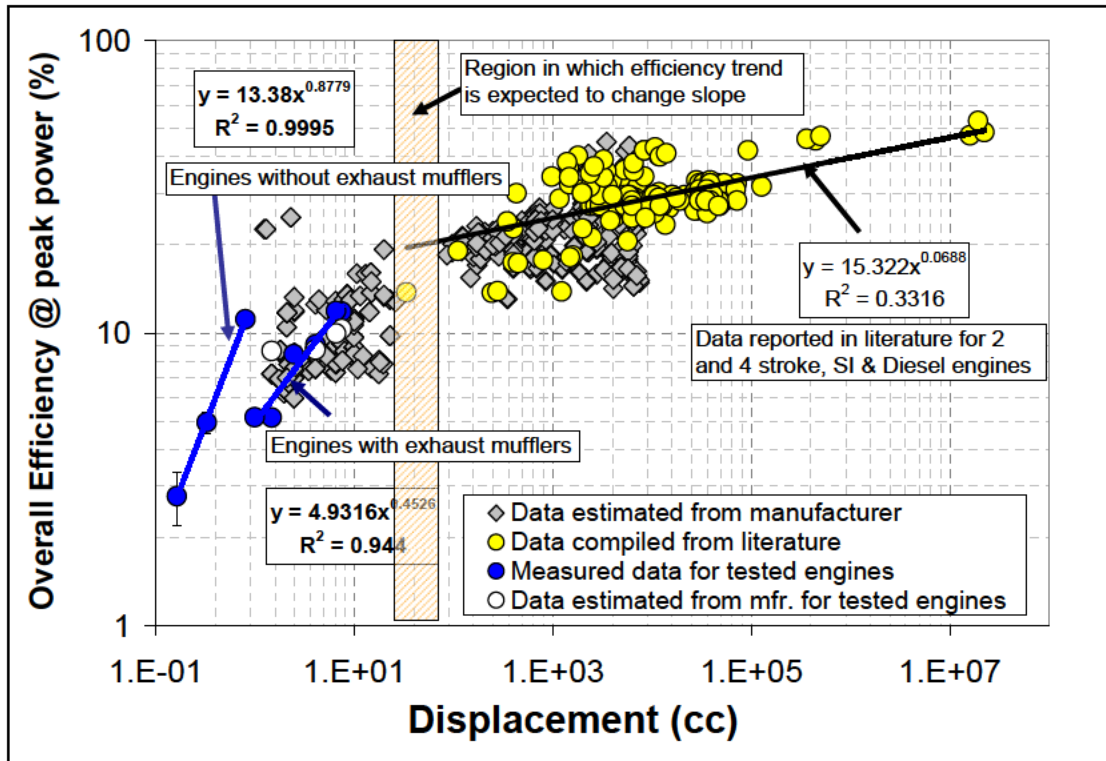


Figure 3–28: Scaling of overall efficiency at peak power with engine displacement.

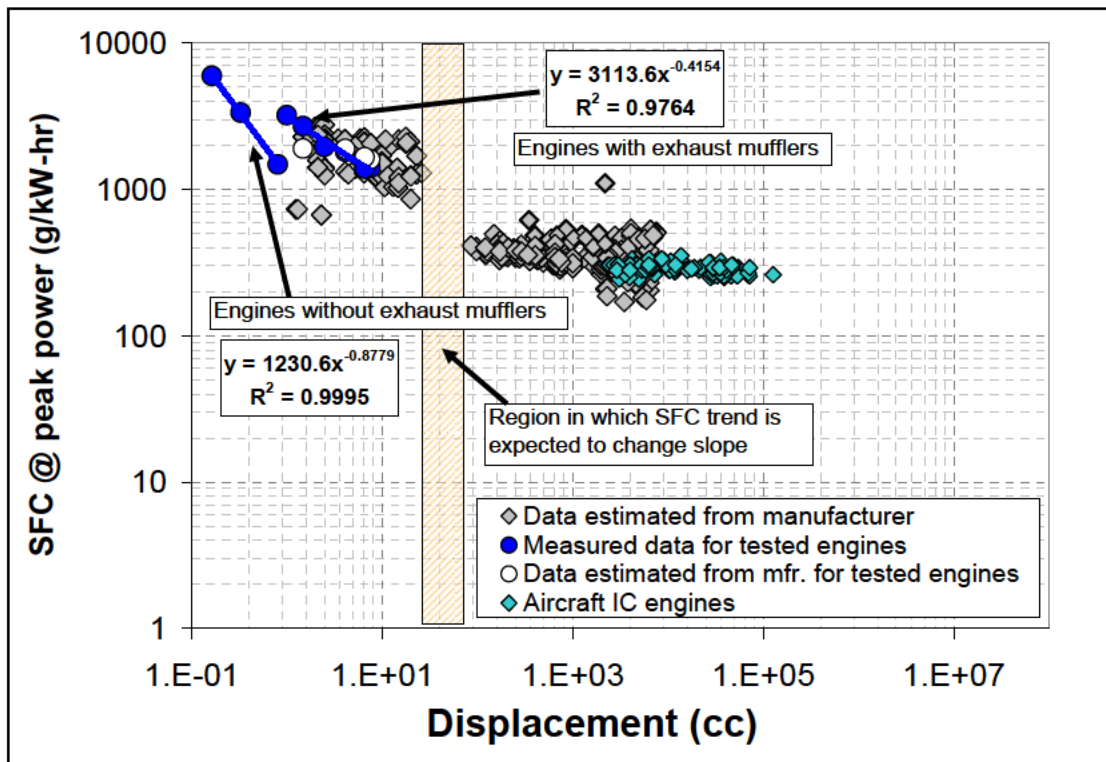


Figure 3–29: Scaling of specific fuel consumption (SFC) at peak power with engine displacement.

In contrast, the measured efficiencies of model airplane engines show a much stronger correlation with size. However the nature of the correlation depends strongly on whether or not the engine has a muffler: the engines without mufflers (G–I in Fig. 2–3) seem able to maintain reasonable levels of efficiency at smaller scales better than those with mufflers (A–F in Fig. 2–3). This suggests that flow losses through the engine may drive performance at the smallest scales. To understand this process better, the delivery ratio at each peak efficiency point is plotted in Fig. 3–30. Delivery ratio is defined as the ratio of the actual mass of air present in the cylinder at bottom dead center to the mass of air that would be present if the cylinder (at bottom dead center) were completely filled with air at atmospheric pressure. It can be expressed as,

$$DR = \frac{\text{mass of air delivered to the engine}}{\text{reference mass of air}} \quad (3-1)$$

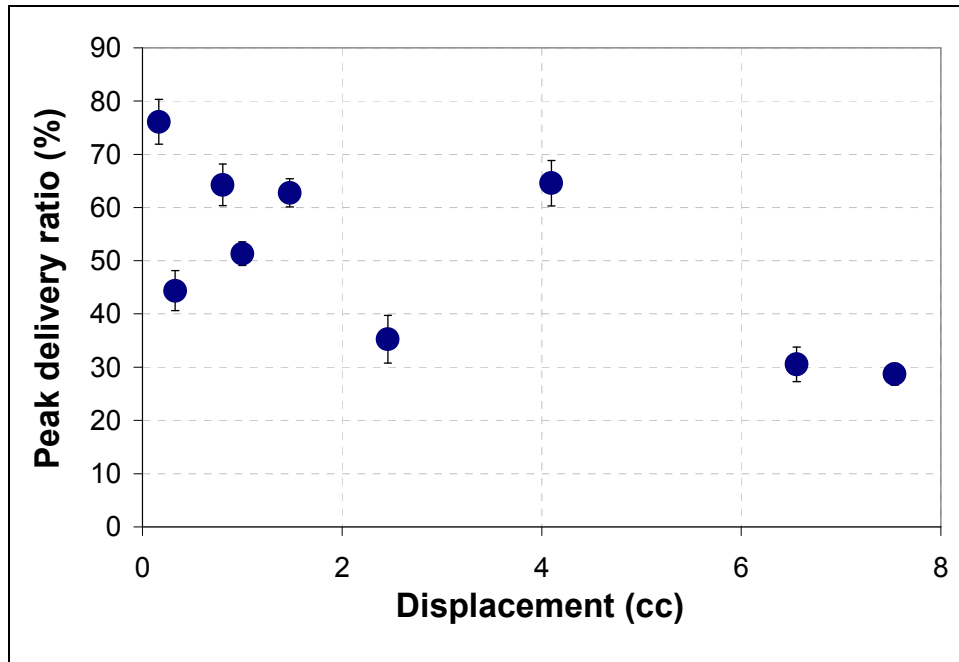


Figure 3–30: Delivery ratio as a function of displacement volume for the engines tested in this work at the operating points as presented in Fig. 3–28.

It shows that the delivery ratio of the three smallest engines without mufflers is on average greater than the larger engines with mufflers. Therefore, the relatively higher delivery ratio for the smaller engines allows them to maintain a higher overall efficiency through improved gas flow. However, the effects of decreasing engine size ultimately result in a drastic drop in overall efficiency in both groups of engines (as seen in Fig. 3–28) so what this really says is that reducing flow resistance can delay the onset of catastrophic degradation of efficiency with thereby making it possible to get closer to the minimum thermodynamic size without incurring unacceptable efficiency losses.

Given the trends shown in Fig. 3–28 and Fig. 3–29, it can be observed that the rate at which overall efficiency drops in miniature engines with size is higher than the rate at which it drops in conventional scale automobile/aircraft/lawnmower etc.

engines. Based on the results of the analysis done here, the overall efficiency trend for engines is expected to change slope at a displacement volume of between 15-20 cc. This could be attributed to the relative increase in engine losses associated with miniaturization.

3.2.5 Scaling of Normalized Power and BMEP

Previous work has shown that the performance of a wide range of engines can also be well represented by plotting peak normalized power (Eqn. 2-11) as a function of piston area.¹²⁴ Figure 3-31 is such a plot for the small engines measured in this thesis as well as the larger engines considered in the engine survey. Two different scaling laws seem to exist for the larger engines considered in the survey. Aircraft IC engines and automobile IC engines appear to follow one scaling law for normalized power with a correlation of 0.7. The smaller set of engines from the survey which represent power sources for applications like lawnmowers, portable generators, chainsaws etc. appear to follow a different scaling law with a lower correlation coefficient of 0.5. The scaling law established for data from model airplane engines appears to show a similar trend as the one established for engines used in lawnmower and similar applications. The normalized power correlation seems to work much better for the smaller engines than the larger ones.

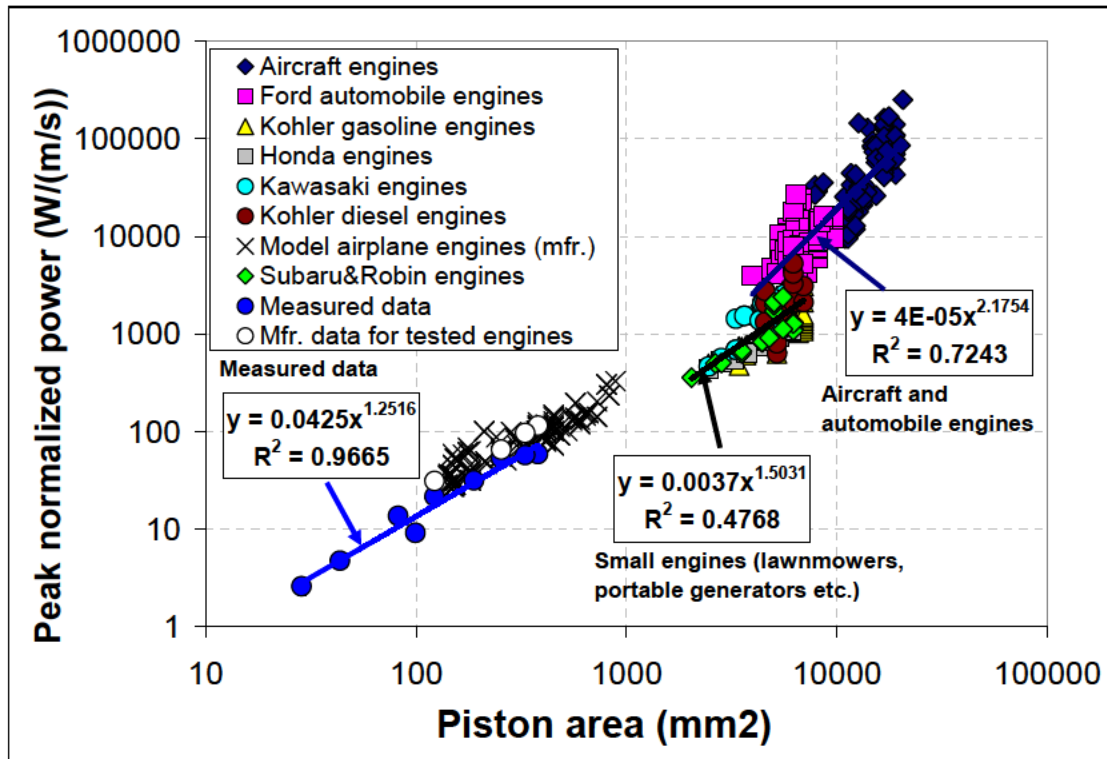


Figure 3–31: Scaling of peak normalized power with piston area.

Another approach to understanding engine performance scaling is plotting peak brake mean effective pressure (BMEP, Eqn. 2–10) as a function of displacement.¹²⁵ Figure 3–32 shows that this approach doesn't work very well either for the measurements made in this thesis ($R^2 \sim 0.5$) or the engines from the literature survey ($R^2 \sim 0.4$). However, BMEP is useful as an 'accepted' indicator of the overall quality of an engine's design.¹²⁶ Table 3–11 below compares BMEP of various classes of engines to those of the engines measured in this study. The results show that maximum BMEP of miniature glow ignited engines are at least a factor of two lower than those of the other engine classes. The major reason for this can be attributed to the much lower level of 'technology' involved in the construction of miniature glow ignited engines. Since power to weight ratio and simplicity of engine

operation are key for marketability of these engines, performance levels are considerably lower than that of conventional scale piston engines.

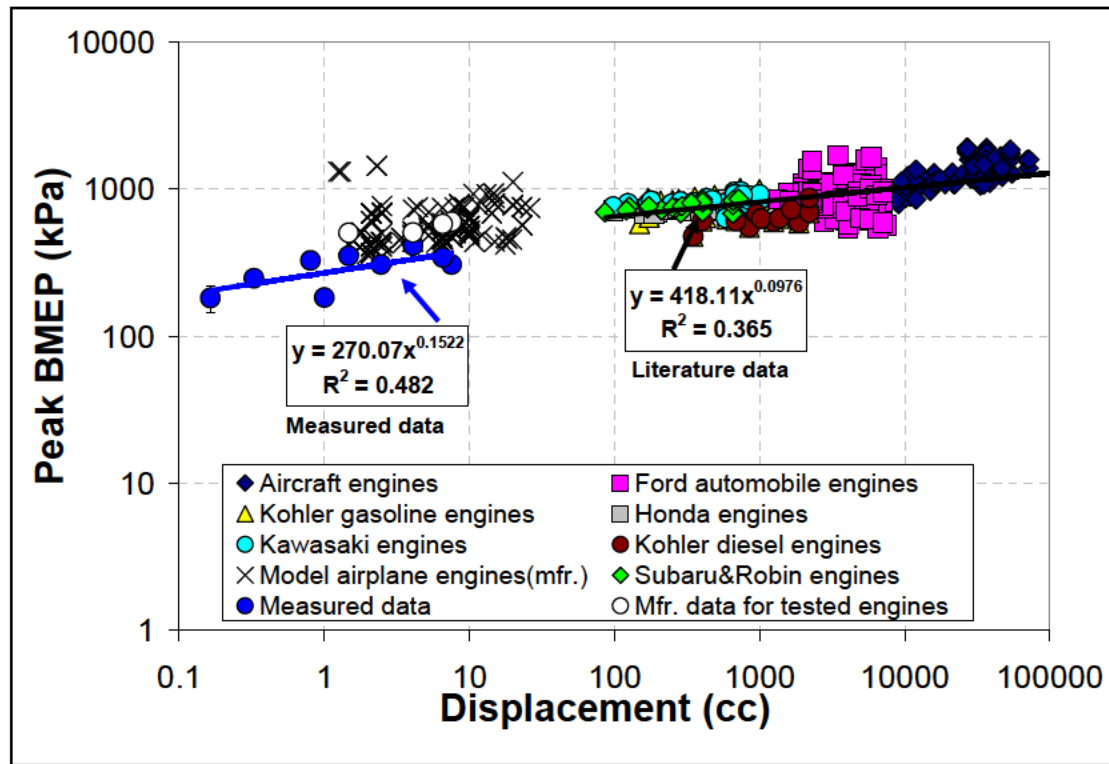


Figure 3–32: Scaling of peak engine BMEP with engine displacement.

Type of engine	Maximum BMEP (kPa)
Naturally aspirated glow ignited two stroke	200–400
Naturally aspirated diesel	700–900
Naturally aspirated SI	850–1050
Turbocharged SI	1250–1700
Turbocharged diesel	1000–1200
Turbocharged after cooled diesel	1400
Large, low speed two stroke	1600

Table 3–11: Comparison of BMEP values for different classes of engines.

3.3 Determination of Minimum Engine Size

One of the main objectives of the engine scaling analysis is to establish the minimum size of a practical (ie. acceptably efficient) IC engine. Net power output and overall efficiency measured using the dynamometer tests and normalized power estimated using the measured data are used to estimate this minimum engine size.

Figure 3–33 shows normalized peak power output versus piston area for the small engines tested in this work. The linear trend in data is interpolated to obtain the x–intercept where normalized engine power output would drop to zero. This is the thermodynamic break–even point which represents the minimum possible IC engine size predicted by our measurements. It is obtained at a piston area of about 12.3 mm² which corresponds to a cylinder bore of 3.9 mm.

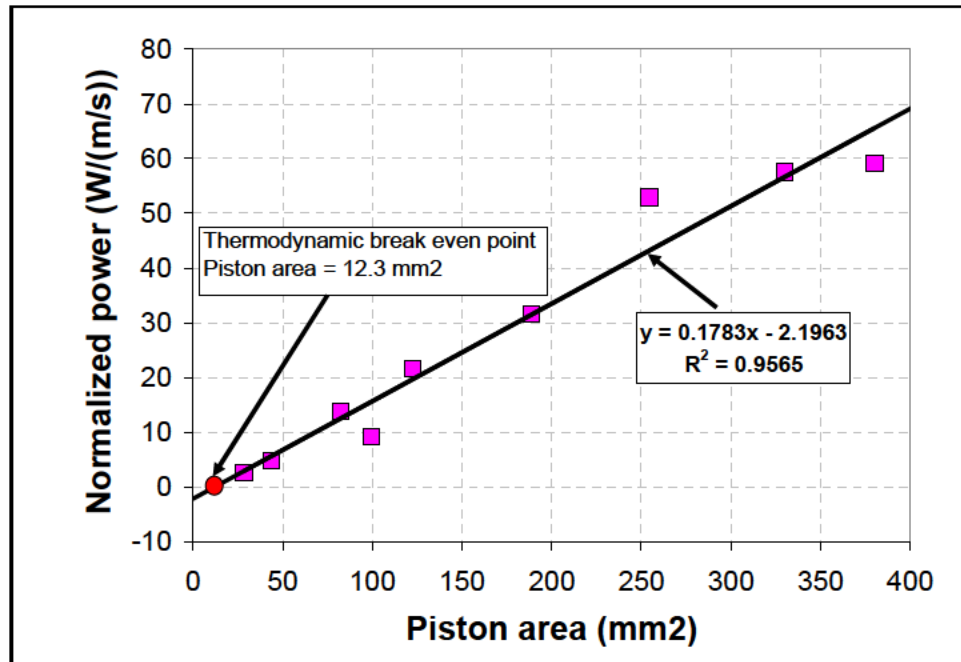


Figure 3–33: Determination of break–even point based on normalized power and piston area.

Figure 3–34 shows peak power output plotted as a function of engine displacement. In the same manner as before, the linear trend in data is interpolated to

find the zero intercept with the x-axis. This is obtained for an engine displacement of 0.34 cc. This corresponds to a bore diameter of about 7.8 mm which is found to be slightly larger than the bore of the smallest engine tested in this work. The thermodynamic break even point is thus seen to be more conservative when estimated using normalized power as compared to that obtained using peak power output.

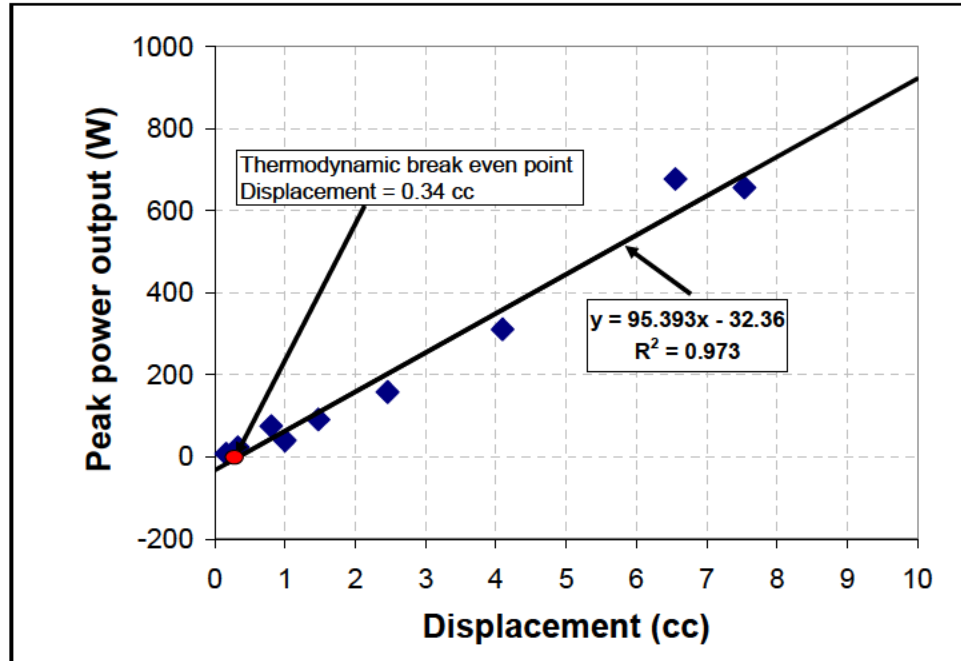


Figure 3–34: Determination of break–even point based on peak power output and engine displacement.

An attempt is also made to estimate a break even point based on measured overall efficiency. The scaling law for efficiency based on measurements acquired from engines without a muffler is used for this purpose. It is assumed that at miniature scales, to conserve weight and size, engines will be operated without a muffler. Thermodynamic break even is assumed to occur in this case when overall efficiency falls to a value of 1%. This is found to correspond to an engine displacement of 0.012 cc and a piston diameter of 2.56 mm as shown in Fig. 3–35.

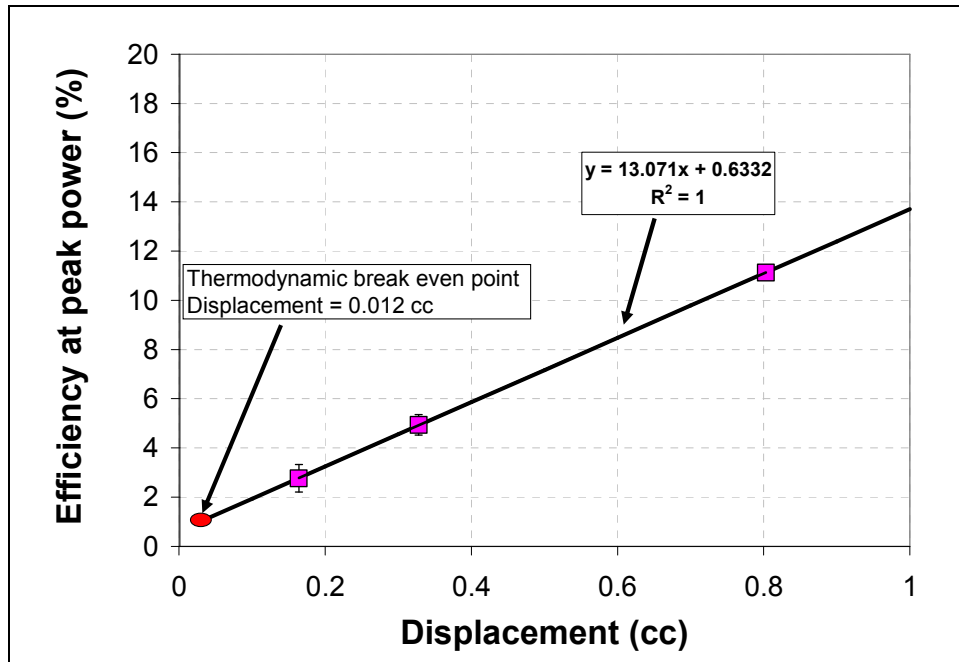


Figure 3–35: Determination of break–even point based on overall efficiency for engines without mufflers and engine displacement.

Previous work by Peterson and Sher has attempted to estimate miniaturization limits of IC engines based on numerical modeling. Leach has provided a theoretical prediction of a critical length scale $\sim 1\text{mm}$ for the idealized problem of a pre-mixed flame propagating in a channel.¹²⁷ The results of these scaling analyses along with the predictions of minimum engine size based on performance measurements of miniature glow ignited engines are summarized in Table 3–12.

Scaling criterion	Bore diameter	Stroke length	Piston area	Displacement	
Normalized power	3.96	3.6	12.3	44.35	0.044
Power output	7.8	7.1	47.8	339.22	0.34
Efficiency @1% w/o muffler	2.56	2.32	5.14	11.94	0.012
Peterson ¹²⁸ , Leach ¹²⁹ , Scaling analysis	1	0.91	0.79	0.714	7e-4
Sher (2009) ¹³⁰	7.49	6.81	44.06	300	0.3
Sher (2005) – Methane ¹³¹	2.14	1.95	3.59	7	0.007
Sher (2005) – Propane	3.59	3.26	10.12	33	0.033
	mm	mm	mm ²	mm ³	cc

Table 3–12: Results for thermodynamic break even analysis using normalized power and power output.

Chapter 4 : Measurement and Scaling of Engine Losses

4.1 Energy Balance in An Engine

The process of understanding how engine performance changes with size involves identifying the loss mechanisms, defining efficiency parameters for each mechanism, and devising methods to measure each loss. Energy loss mechanisms are best identified by performing an energy balance on the engine using either a first or second law analysis. These are discussed in the following sections.

4.1.1 First Law Analysis

A first law analysis of the energy balance in a device typically involves application of energy conservation to a control volume. In the case of an internal combustion engine, this can be pursued in different ways depending on where the control volume is located. In one approach, the control volume is drawn around the contents of the working cylinder inside the engine and energy conservation is applied over the course of a complete engine cycle involving intake, compression, combustion, expansion and exhaust. During each of these processes, phenomenological models are used to describe the geometry of the cylinder, valves and ports, thermodynamic properties of the burnt and unburnt mixtures, transfer of mass and energy across the system boundaries as well as the nature of the combustion process.¹³² A similar approach can be followed for other components of the engine such as the intake manifold, the exhaust manifold, the crankcase etc. to track the energy losses in each individual component.

In another approach, a control volume is drawn around the complete engine. While energy interactions of the engine with the environment are completely represented, some internal interactions are removed from consideration. In either case, energy in the form of thermal, mechanical or chemical energy is conserved during the course of an engine cycle and is simply converted from one form to another. First law analysis of the engine cycle has been used widely for complete analysis of engine performance and its sensitivity to change in operating conditions.^{133 134}

4.1.2 Second Law Analysis

The second law analysis of an engine cycle is also referred to as an ‘availability analysis’. The availability of a system in a given state can be defined as the maximum useful work which can be realized from the system interacting with the surroundings as it reaches a state of thermal, mechanical and chemical equilibrium.¹³⁵ Thermal equilibrium is defined as the state when there is no temperature difference between the system and its surroundings. Similarly, mechanical equilibrium is defined as the state when there is no pressure difference between the system and its surroundings. Chemical equilibrium is said to be attained when the only components that exist in the system are those which cannot chemically react with the environment. In the case of an engine, this means that all of the reactive species in the fuel have to be oxidized or reduced so that the final components of the system are the same as that of the atmosphere, viz. O₂, CO₂, H₂O and N₂. Unlike energy, availability is not a conserved quantity because of irreversible processes that occur within the engine. The energy that is lost or becomes unavailable because of irreversible processes during the

course of the interaction of the system with the environment is also defined as exergy. In the case of reciprocating engines, these irreversible processes occur throughout the engine cycle. Combustion of the fuel–air mixture, mechanical friction between the rubbing surfaces in an engine, mixing of fuel and air, throttling of intake air are some of the engine processes that contribute to the destruction of availability and result in exergy. Exergy is quantified by performing a second–law analysis and has been widely applied to internal combustion engines.^{136 137} A second law analysis of an internal combustion engine requires careful estimation of several irreversible processes that are difficult experimentally. One example is throttling losses at the intake and exhaust ports.

A first law analysis of an engine is presented in Section 4.2. It identifies the major energy loss mechanisms in the engine and describes the experimental techniques used to quantify each. Efficiency parameters are derived for each loss mechanism that can be computed using measurements obtained on the engine dynamometer.

4.2 Energy Balance in A Two Stroke Engine

Section 4.1.1 described two approaches for drawing control volumes. One separates the engine into component parts where control volumes are drawn around each individual component. The other draws the control volume around the entire engine and analyzes the mass and energy exchange processes between the engine and the environment. Which method is chosen depends to a large extent on how well exchanges of mass, momentum, and energy between components are known and can be represented mathematically.

Two processes make component-based control volumes difficult to use in crankcase scavenged two-stroke engines. One involves the inefficient transfer of fresh charge from the crankcase to the cylinder volume. The other involves mass loss from the combustion chamber via the piston-cylinder liner gap. Measuring these losses is difficult in conventional scale engines and even more so in the miniature engines investigated here.

4.2.1 Scavenging Losses

Figure 4-1 is a schematic illustrating the scavenging process in a two stroke crankcase scavenged engine. Transfer ports whose opening is controlled by piston motion are uncovered towards the end of the exhaust blowdown process. This causes fresh crankcase charge compressed by piston motion to be forced into the cylinder volume. A majority of fresh mixture aids in pushing out burnt gases and is retained within the engine. However, a small amount of fresh charge is lost by short-circuiting through the exhaust port and represents scavenging loss.

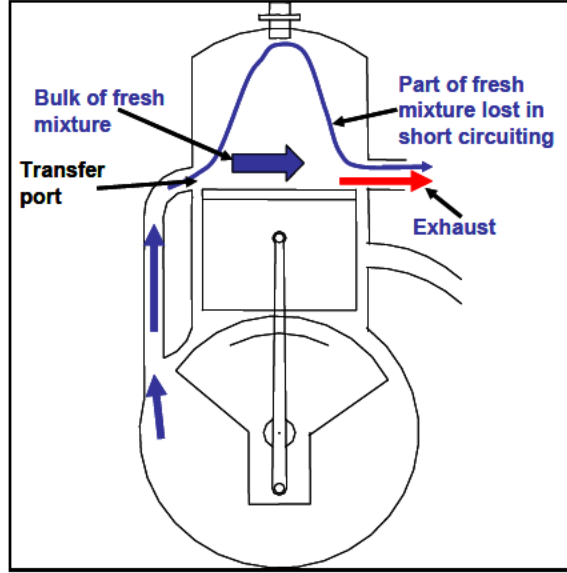


Figure 4–1: Schematic showing the scavenging process in a two stroke crankcase scavenged engine.

Scavenging losses are quantified using the trapping efficiency defined as,

$$\eta_{trapping} = \frac{(\dot{m}_{total})_{CYL}}{(\dot{m}_{total})_{CC}} \quad (4-1)$$

where $(\dot{m}_{total})_{CC}$ is the total mass of fresh charge in the crankcase and $(\dot{m}_{total})_{CYL}$ is the mass of charge transferred into the cylinder volume. A variety of experimental methods for determining trapping efficiency have been developed for conventional scale two–stroke engines. One technique involves sampling the contents of the cylinder after the closing of the transfer port using an impact tube embedded in the cylinder.¹³⁸

A second technique samples the engine exhaust to estimate the quantity of a tracer substance injected into the engine intake.¹³⁹ The tracer gas is assumed to burn completely during the combustion process so the amount of tracer gas present in the

exhaust would be proportional to the degree of short-circuiting through the exhaust port and can then be used to estimate trapping efficiency.

A third method uses analytical models to estimate trapping efficiency based on the knowledge of delivery ratio (see Section 4.2.3). However, they rely on one of two idealized representations of the scavenging process.¹⁴⁰ The ‘perfect displacement’ model assumes that the fresh gas displaces the burnt gas from the cylinder without any mixing. The ‘complete mixing’ model assumes that fresh charge mixes completely and instantaneously with the burnt charge and that a fraction of this mixture is lost through the exhaust port. The actual process occurring in the engine lies somewhere between these extreme cases.

4.2.2 Blowby Losses

There are few experimental methods for measuring blowby losses.¹⁴¹ Blowby losses have been measured using hot wire type air mass flow sensors and positive displacement meters in conventional scale engines.¹⁴² This technique is however limited to engines which do not use crankcase scavenging. In case of crankcase scavenged engines, analytical methods have been pursued¹⁴³, but they are in considerable doubt as they require accurate prediction of the oil film in the piston–cylinder gap that resists the pressure–driven flow from combustion–chamber to crankcase. Absent this information, the accuracy of the predictions is suspect.

Computational approaches could be taken to estimate scavenging and blowby losses but would require a rigorous treatment of the processes within the cylinder and crankcase volume along with an accurate description of the geometry of the moving parts. Since simple and accurate methods of estimating scavenging and blowby losses

are not available, the energy balance performed here will involve drawing the control volume around the entire engine. The details are presented in the next section. For completeness, the alternate approach involving the separation of the engine into different components is presented in appendix A.

4.2.3 Energy Balance with Control Volume around Complete Engine

Figure 4–2 shows the control volume used to perform the energy balance along with the mass and energy interactions of the engine with the environment.

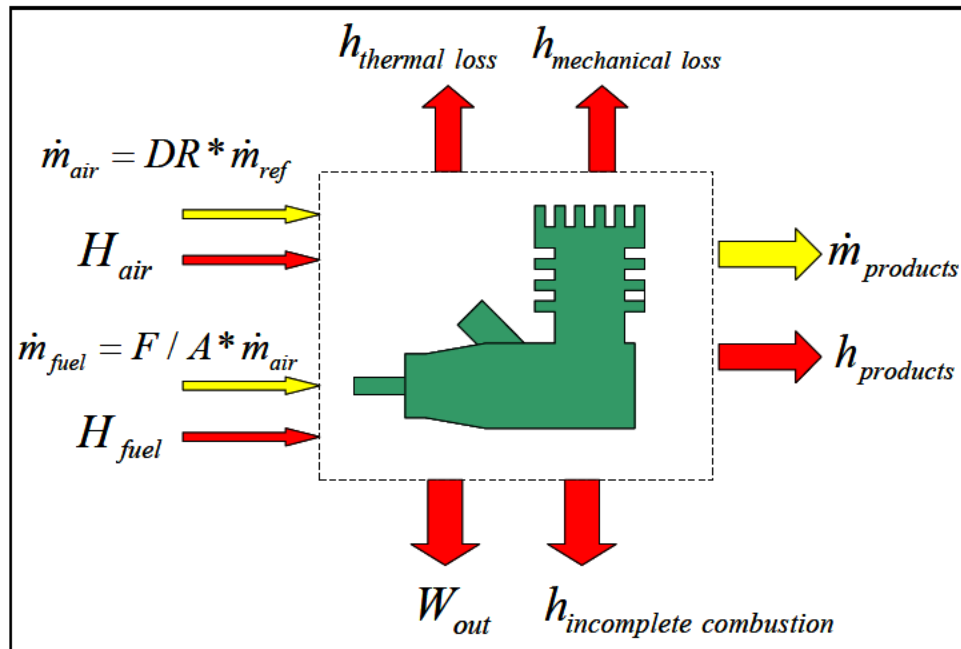


Figure 4–2: Energy balance in a two stroke engine with control volume drawn around the entire engine.

Air enters the engine through the carburetor intake and mixes with the fuel entering through the injector port. The flow of air entering the engine is less than the ideal airflow which is the product of the displacement volume and the engine speed. The delivery ratio is defined as,

$$DR = \frac{\dot{m}_{air}}{\dot{m}_{air,ideal}} \quad (4-2)$$

where the numerator is the actual air flow and the denominator is the ideal air flow which is given by,

$$\dot{m}_{air,ideal} = V_{disp} * N / 60 * \rho_{air} \quad (4-3)$$

The mass of air entering the engine at any operating speed is then given by,

$$\dot{m}_{air} = DR * \dot{m}_{ref} = DR * V_{disp} * N / 60 * \rho_{air} \quad (4-4)$$

The engine utilizes a carburetor for fuel–air mixing so it is assumed that the fuel flow rate is proportional to the air flow rate. The fuel/air ratio is defined as the mass flow rate of the fuel divided by the mass flow rate of air,

$$F / A = \frac{\dot{m}_{fuel}}{\dot{m}_{air}} \quad (4-5)$$

Combining equations 4–4 and 4–5 gives,

$$\dot{m}_{fuel} = DR * V_{disp} * N / 60 * \rho_{air} * F / A \quad (4-6)$$

The total enthalpy of the fuel–air mixture entering the engine is given by,

$$h_{IN} = \dot{m}_{air} * (h_f^0)_{air} + \dot{m}_{fuel} * (h_f^0)_{fuel} \quad (4-7)$$

Assuming that the enthalpy of the air is negligible compared to and the heat released by the fuel, the enthalpy of the mixture can be expressed as,

$$h_{IN} = \dot{m}_{fuel} * (h_f^0)_{fuel} \quad (4-8)$$

Combining equations 4–7 and 4–8 gives,

$$h_{IN} = DR * V_{disp} * N / 60 * \rho_{air} * F / A * (h_f^0)_{fuel} \quad (4-9)$$

Equation 4-9 gives the total energy release inside the control volume and so is not represented in Fig. 4-2. Part of this energy is converted into useful work at the engine shaft. Part is lost to the environment via convective heat transfer to the engine walls, conduction through the cylinder walls, and forced convection to the environment. Part is lost in to mechanical and fluid friction inside the engine. The remainder of this energy is discharged to the environment in the exhaust gas. The energy in the exhaust gas is partly thermal and partly chemical in the form of unburned fuel.

Therefore, the overall energy balance on the control volume is given by,

$$h_{IN} = W_{out} + h_{loss} \quad (4-10)$$

where h_{loss} represents the sum of the component losses,

$$h_{loss} = h_{thermal\ loss} + h_{mechanical\ loss} + h_{incomplete\ combustion} \quad (4-11)$$

The enthalpy term corresponding to thermal loss contains contributions from convective heat transfer to the engine walls as well as sensible enthalpy lost in the exhaust.

$$h_{thermal\ loss} = h_{convective\ loss} + h_{exhaust} \quad (4-12)$$

Overall conversion efficiency from fuel enthalpy to effective energy output can be written as,

$$\eta_{overall} = \frac{W_{out}}{h_{IN}} = \frac{h_{IN} - h_{loss}}{h_{IN}} \quad (4-13)$$

Work output can be alternately be expressed as,

$$W_{out} = \eta_{overall} * h_{IN} \quad (4-14)$$

Using equations 4-9 and 4-14, we have,

$$W_{out} = \eta_{overall} * DR * V_{disp} * N / 60 * \rho_{air} * F / A * (h_f^0)_{fuel} \quad (4-15)$$

The overall conversion efficiency defined earlier can be expressed as the product of the component efficiencies which correspond to the different loss mechanisms,

$$\eta_{overall} = \eta_{thermal} * \eta_{mechanical} * \eta_{combustion} \quad (4-16)$$

This gives,

$$h_{eff,out} = \eta_{thermal} * \eta_{mechanical} * \eta_{combustion} * DR * V_{disp} * N / 60 * \rho_{air} * F / A * (h_f^0)_{fuel} \quad (4-17)$$

where the component efficiencies are defined as,

$$\eta_{thermal} = \frac{h_{IN} - h_{thermal\ loss}}{h_{IN}} \quad (4-18)$$

$$\eta_{mechanical} = \frac{h_{IN} - h_{thermal\ loss} - h_{mechanical\ loss}}{h_{IN} - h_{thermal\ loss}} \quad (4-19)$$

$$\eta_{combustion} = \frac{h_{IN} - h_{thermal\ loss} - h_{mechanical\ loss} - h_{incomplete\ combustion}}{h_{IN} - h_{thermal\ loss} - h_{mechanical\ loss}} \quad (4-20)$$

Therefore, the major energy loss mechanisms along with their corresponding efficiency parameters are:

- Air intake losses – Delivery Ratio
- Energy loss via heat transfer and sensible enthalpy loss in the exhaust – Thermal efficiency

- Energy loss because of incomplete combustion – Combustion efficiency
- Energy loss because of fluid and mechanical friction – Mechanical efficiency

Since scavenging and mass blowby losses occur internal to the control volume, they do not explicitly enter into the calculation steps shown above and all the parameters required to estimate the efficiencies described in this approach can be obtained from separate experiments conducted on the dynamometer. The details of the techniques used to estimate the efficiencies defined by equations 4–2, 4–18, 4–19 and 4–20 will be presented in sections 4.4 to 4.8. Prior to this, the criteria for comparing energy losses from different engines are described.

4.3 Criteria for Comparing Engine Loss Mechanisms

The main objective in identifying and quantifying these loss mechanisms is to compare them for different engines so as to understand the effect of size on engine losses. The scaling analysis of engine performance in Chapter 3 shows that overall engine efficiency decreases considerably with engine size. While one should expect component efficiencies to follow a similar trend, one should also expect some processes to be more important than others. The goal here is to identify the most important loss mechanisms in order to develop the roadmap for improving small engine efficiency. This is accomplished by making measurements over a large number of operating conditions for each engine and establishing standard conditions at which losses are compared across different engines. This is explained in the following sections.

4.3.1 Constant Engine Speed and Equivalence Ratio

Estimates of frictional losses in the engine intake, moving parts, and other fluid friction were observed to have a strong dependence on operating speed and engine size. Meanwhile, losses because of heat transfer were found to depend strongly on the operating equivalence ratio and engine size. Therefore, comparing engine losses at constant speed and equivalence ratio allows engine size to be the sole parameter influencing the magnitude of component engine losses. The results presented in this section compare engines at two speeds – 10000 rpm and 12000 rpm and at an equivalence ratio of 1.

4.3.2 Constant Mean Piston Speed and Equivalence Ratio

Mean piston speed is a measure of the average linear speed of the piston moving within the cylinder and is computed using the following expression,

$$S_{mean} = 2L\omega = 2L(2\pi N / 60) \quad (4-21)$$

Mean piston speed is a characteristic speed that influences several processes within the engine. The delivery ratio of engines of different sizes is similar when operated at the same mean piston speed.^{144 145} Mean piston speed is also regarded as a measure of the turbulence intensity within the combustion chamber.¹⁴⁶ Measurements of in-cylinder turbulence have shown turbulence intensities to be linearly related to mean piston speed.¹⁴⁷ Combustion and heat release processes within the engine as well as convective heat transfer processes are also affected by turbulence originating in the intake port.¹⁴⁸ Therefore, comparing energy losses at constant speed and equivalence ratio could potentially hold cylinder turbulence constant, further isolating the effect of engine size on engine performance. This statement is speculative and the

aim of the investigation here is to identify trends in scaling of loss mechanisms at constant mean piston speed that could possibly validate this assumption.

In this work, a constant piston speed of 4.77 ms^{-1} was selected as the point to compare engine performance because it was achievable by all engines. Table 4–1 lists the corresponding operating speed from each engine that yield the constant piston speed of 4.77 ms^{-1} .

Engine	Displacement	Stroke	Mean piston speed	Engine speed
OS 46 FX	7.54	19.6	4.77	7301
OS 40 FX	6.55	19.6	4.77	7301
OS 25 FX	4.1	16	4.77	8944
AP 15	2.46	12	4.77	11925
AP 09	1.47	12	4.77	11925
AP 061	0.99	10	4.77	14310
Cox 049	0.8	9.6	4.77	14906
Cox 020	0.33	7.5	4.77	19080
Cox 010	0.16	5.72	4.77	25022
	cc	mm	ms^{-1}	rpm

Table 4–1: Engine operating speeds corresponding to a constant mean piston speed of 4.77 ms^{-1} for all the engines tested in this work.

4.4 Intake Losses

4.4.1 Measurement Technique

Intake losses are essentially the losses in an engine which reduce the actual air flow through the engine from the ideal air flow. As mentioned previously, intake losses are characterized using the delivery ratio (Eqn. 4–2). Delivery ratio is computed directly from the air flow measurement at each operating condition.

4.4.2 Scaling of Intake Losses

Figures 4–3 shows that delivery ratio is mostly independent of fuel air ratio for all engines tested in this work at a constant operating speed of 10000 rpm. Results of an analysis similar to that presented in Fig. 4–3 for an operating speed of 12000 rpm and for a mean piston speed of 4.77 ms^{-1} are presented in figures B–1 and B–2 in appendix B.

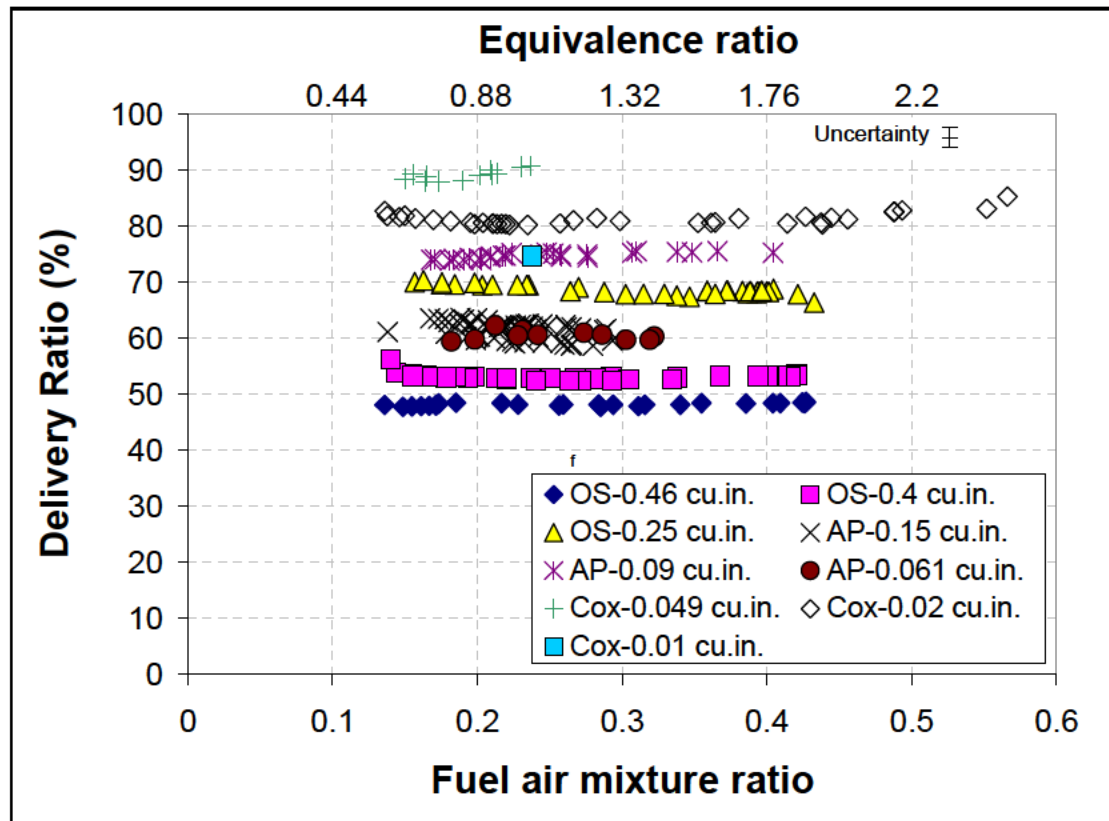


Figure 4–3: Delivery ratio at different fuel air mixture ratios and a constant engine speed of 10000 rpm for all engines.

Figure 4–4 shows how delivery ratio scales with engine size (displacement) for two fixed values of engine speed (10000 and 12000 rpm) and a fixed mean piston speed of 4.77 ms^{-1} . The equivalence ratio is about 1 for each case. The figure shows that overall the delivery ratio tends to decrease with engine displacement at 10000

rpm and 12000 rpm but this trend disappears when the engines are compared at the same mean piston speed.

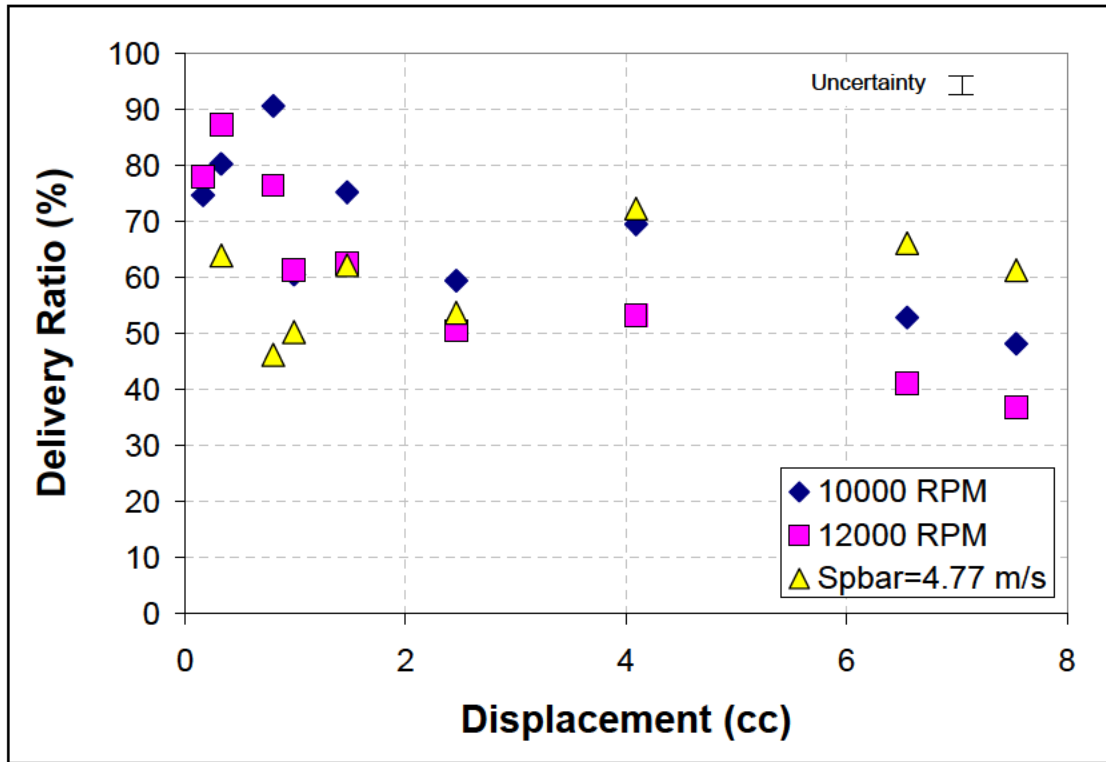


Figure 4-4: Delivery ratio as a function of engine displacement for constant engine speeds of 10000 rpm, 12000 rpm and a constant mean piston speed of 4.77 ms^{-1} . All data sets correspond to an equivalence ratio of ~ 1 .

In the case of majority of engines, delivery ratio at 10000 rpm is seen to be higher than that obtained at 12000 rpm. The Cox 010 (0.16 cc), Cox 020 (0.33 cc) and the AP 061 (1 cc) engines are seen to be exceptions where the delivery ratio at 12000 rpm is slightly higher than that obtained at 10000 rpm. The higher value of delivery ratio at lower speeds is consistent with phenomena observed in conventional scale spark ignition and diesel engines where effects of flow friction and choking in the intake pipe result in a drop in delivery ratio at higher engine speeds.¹⁴⁹ However, this does not imply that delivery ratio drops with size continuously for engine speeds

higher than 10000 rpm. As seen in the performance data presented in Chapter 3, double peaks in delivery ratio have been observed in some engines.

In the four largest engines (OS-46, OS-40, OS-25 and AP-15), the delivery ratio actually increases with decreasing size until the AP-15 engine. Delivery ratio at both constant speeds increases slightly for the AP-09 engine and drops again for the AP-061 engine. Finally, the delivery ratios of the smallest three Cox engines (Cox 010, Cox 020 and Cox 049) are higher on average than those of the other engines, but this time the delivery ratio decreases with decreasing engine size. .

Since a consistent trend is not apparent, delivery ratio appears to be influenced by factors other than engine size. However, it is clear that the intake characteristics of the three smallest engines are different from those of the six larger engines. Since the major difference between the three smallest engines and the others is the absence of a muffler, it may be gas dynamic effects due to the muffler influence the results seen in delivery ratio.

Finally, the disappearance of any trend in delivery ratio with engine size in Figure 4-4 when engines are compared at constant mean piston speed are consistent with earlier work by Taylor¹⁵⁰ who studied three similar engines where the engine design and structural materials were kept constant while the scale of the engines was varied. The engines were single cylinder four-stroke engines having bore diameters of 63.5 mm (2.5 inch), 101.6 mm (4 inch) and 152.4 mm (6 inch) respectively. He found that the volumetric efficiency was effectively constant (~1% variation) for engines running at a constant mean piston speed, inlet and exhaust pressures, inlet and coolant temperatures, and fuel-air mixture ratios. This finding seems to be

confirmed by Fig. 4–4. While the engine–to–engine variability is much larger than the 1% difference found in the MIT study, there is no clear trend with scaleⁱⁱⁱ.

The reasons for this difference are not entirely clear but could be due in part to the more complex gas dynamics of crankcase scavenged two stroke engines relative to four stroke engines. One of the reasons for this difference could be that the two–stroke design depends much more on wave action than four–stroke engines with valves to achieve the maximum possible engine intake. As a result, they are more sensitive to engine design, port dimensions, scavenging scheme, operating speed, and power. Of these parameters, engine speed would have the most important influence on delivery ratio since the impedance (or admittance) of the intake manifold is directly proportional to the frequency of pulses entering it.¹⁵¹ Therefore, one would expect the optimum delivery ratio to occur at a particular engine speed in a two–stroke engine. Table 4–2 below shows the engine speed associated with peak delivery ratio for the engines tested in this work.

ⁱⁱⁱ It is to be noted that no data could be obtained for the Cox 010 engine at a constant mean piston speed of 4.77 m/s as it was found to be inoperable at the corresponding engine speed of 25022 rpm.

Engine	Displacement	Peak delivery ratio	Engine speed @ peak delivery ratio
Cox 010	0.16	80.4	14500
Cox 020	0.32	81.6	12000
Cox 049	0.8	93.61	11000
AP Wasp	1	52.67	12000
AP Hornet	1.47	63.83	10000
AP Yellowjacket	2.46	68.68	10000
OS 25 FX	4.09	80.61	8000
OS 40 FX	6.55	57.27	6000
OS 46 FX	7.54	38.42	9000
	cc	%	rpm

Table 4–2: Peak value of delivery ratio and corresponding engine operating speed for the engines tested in this work.

4.5 Heat Transfer Losses

4.5.1 Measurement Technique

4.5.1.1 Engine heat transfer analysis

Figure 4–5 shows the overall heat transfer process occurring from the in-cylinder gases to the environment through the cylinder walls. The symbols in the figure represent the following: T_g – gas temperature, $T_{s,g}$ – temperature of inner hot surface of the cylinder wall, $T_{s,c}$ – temperature of the outer cold surface of the cylinder wall, T_c – temperature of the coolant, \bar{T}_g – mean temperature of the hot gas, \bar{T}_c – mean temperature of the coolant, h_g – heat transfer coefficient on the gas side, k_w – thermal conductivity of the cylinder wall, t_w – thickness of the cylinder wall and h_c – heat transfer coefficient on the coolant side. The heat flux is assumed to be one dimensional.

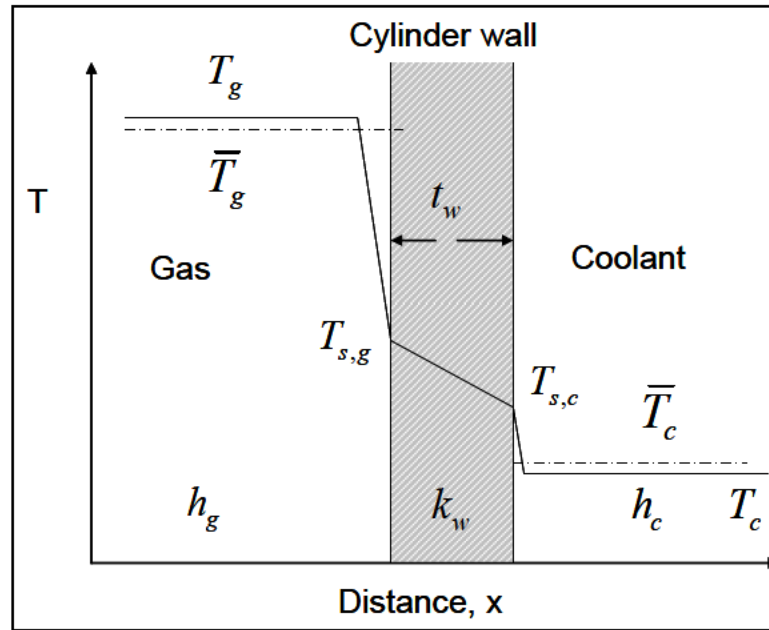


Figure 4-5: Heat transfer path from cylinder gases to the environment (Adapted from Heywood¹⁵³).

Heat transfer from the cylinder wall to the outer wall in contact with the coolant occurs via conduction. Heat transfer from the outer wall to the environment (or coolant) occurs primarily via convection (forced).^{iv}

Heat transfer from the hot gas to the inside walls of the cylinder occurs via convection, conduction, and radiation. While conduction is negligible, convection and radiation both play significant roles. Convective heat transfer within the engine cylinder is a time and space variant problem because of the wide variation of in-cylinder temperature during the course of a single cycle and at different locations in the cylinder itself at any instant of time.¹⁵³ Heat transferred by radiation from the hot gases to the wall is seen to be less than 5% of the peak convective heat transfer for

^{iv} Estimates of heat transfer via radiation from the outer wall of the cylinder (at a temperature of 140 °C) to ambient conditions are about 3 Watts for the largest engine tested in this work. This value is much smaller than the energy transferred via convective cooling. Heat transferred via conduction is also minor since temperatures at the mounting surfaces of the engine in contact with the dynamometer are seen to be only slightly higher than ambient conditions. Estimates of radiative heat loss were done by Jon Geerts.

conventional scale SI engines.¹⁵⁴ Heat transferred by radiation from the flame to the cylinder walls is however found to be significant especially in the case of diesel engines operating at lean equivalence ratios.¹⁵⁵ This is seen to be because of high temperature of diesel engine flames approaching the adiabatic flame temperature. No information regarding heat transfer to cylinder walls from hot gases or the flame structure via radiation could be found for glow ignition engines. Conductive heat transfer in the gas is assumed to be much less important than convection and radiation and therefore is not usually considered.

Typical modeling approaches involve developing correlations for heat transfer from the cylinder gases to the cylinder walls.¹⁵⁶ Various correlations for time averaged¹⁵⁷, instantaneous spatially averaged¹⁵⁸, and instantaneous local¹⁵⁹ heat transfer coefficients have been developed with each providing an increasingly detailed and complex representation of engine heat transfer. The problem is that developing the complex heat transfer models requires detailed in-situ measurements that are extremely difficult to implement in these small engines. Therefore, the approach followed here is to estimate the time and space averaged temperature over one cycle of the hot gases within the cylinder associated with an ‘apparent’ convection process¹⁶⁰ that lumps conductive, convective, and radiative processes together. The advantage of this approach is that it can be implemented directly on the dynamometer without the need for detailed in-situ measurements of the gas-wall interaction.

4.5.1.2 The ‘apparent’ heat transfer model

The one dimensional heat flux through the gas, cylinder walls and the coolant shown in Fig. 4–5 is represented using the equations below.

Heat transfer from the gas to the cylinder wall is given by,

$$\dot{Q} = A_g * h_g * (T_g - T_{s,g}) \quad (4-22)$$

where A_g is a representative area on the hot side. Heat transfer from the inside (hot)

of the cylinder wall to the outside (cold) is given by,

$$\dot{Q} = A_g * \frac{k_w}{t} * (T_{s,g} - T_{s,c}) \quad (4-23)$$

Heat transfer from the outside surface to the environment is given by,

$$\dot{Q} = A_c * h_c * (T_{s,c} - T_c) \quad (4-24)$$

where A_c is a representative area on the cold side. Combining equations 4–22, 4–23

and 4–24 leads to the following expression for the net heat transfer,

$$\dot{Q} = h_e * A_R * (\bar{T}_g - T_c) \quad (4-25)$$

where h_e is an effective overall heat transfer coefficient given by,

$$h_e = \frac{1}{1/h_g + t/k_w + A_g/(h_c A_c)} \quad (4-26)$$

where A_R is a representative area chosen for the 1–dimensional heat transfer process and T_g is the mean gas temperature. The choice of reference area will be explained next and the determination of T_g will be explained in the next section.

The reference area is taken to be the area of the piston face as in previous investigations of larger engines.¹⁶¹ This is justified because the highest temperatures occur near TDC where the area of the piston face and cylinder head is much greater than the area of the exposed wall and most of the cylinder wall is exposed to the gas

much later in the expansion process after it has cooled considerably. Measurements of heat flux across the cylinder wall in piston engines confirm this showing that the wall heat flux is very spatially inhomogeneous and approximately an order of magnitude smaller than the heat flux to the cylinder head.¹⁶² There is no reason to believe that the situation would be any different in miniature engines.¹⁶³

Heat flux to the piston could still be significant as is seen to be the case in small high speed diesel engines with swirl and bowl in piston combustion chambers.¹⁶⁴ The pistons in the engines tested in this work do not have a bowl configuration. Additionally, the cylinder head being actively cooled provides a path of lower resistance to heat flux. The majority of heat flux is thus assumed to occur from hot gas to the engine cylinder head surface.

The effective heat transfer coefficient defined in Eq. 4-26 can be written non-dimensionally as a Nusselt number,

$$Nu = \frac{h_e b}{k_g} \quad (4-27)$$

Detailed heat transfer measurements in conventional-scale engines have developed correlations for the Nusselt number as a function of the Reynolds and Prandtl numbers¹⁶⁵ that are similar in form to those obtained for turbulent flow in pipes or flow over flat plates¹⁶⁶ and usually take the form,

$$Nu = a Re^m Pr^n \quad (4-28)$$

One such correlation for the time averaged heat flux has been developed by Taylor and Toong based on heat transfer measurements in 19 different engines,¹⁶⁷

$$Nu = \frac{h_e b}{k_g} = \phi \left(\frac{Gb}{\mu} \right)_g^m = \phi Re_g^m \quad (4-29)$$

In this expression, b is the piston bore, k_g is the thermal conductivity of the gas, μ is the dynamic viscosity of the gas and ϕ and m are constant values. G is defined as the mass flow through the engine per unit piston area and is expressed as,

$$G = \frac{\dot{m}_g}{A_p} \quad (4-30)$$

The 19 engines were a very diverse group that included two and four-stroke engines, gasoline and diesel engines, and air and liquid cooled engines. Cylinder bore sizes ranged from 63.5 mm (2.5 inch) to 711.2 mm (28 inch). Finally, data were acquired over a wide range of piston speeds, mixture ratios and inlet air density. The heat transfer coefficient in Taylor and Toong's work is based on the hot gas side Reynolds number and a 'mean' hot gas temperature that represents the average temperature within the cylinder volume over the course of an engine cycle as formulated earlier in Eq 4-25.

Taylor and Toong's results are presented in Fig. 4-6 and indicate that,

$$Nu = 10.4 \left(\frac{Gb}{\mu} \right)_g^{0.75} \quad (4-31)$$

appears to be somewhat 'universal' as it correlates measurements made in many different types and sizes of engines. Therefore, it appears to be reasonable to use the same correlation to estimate cylinder-to-wall heat transfer in miniature engines.

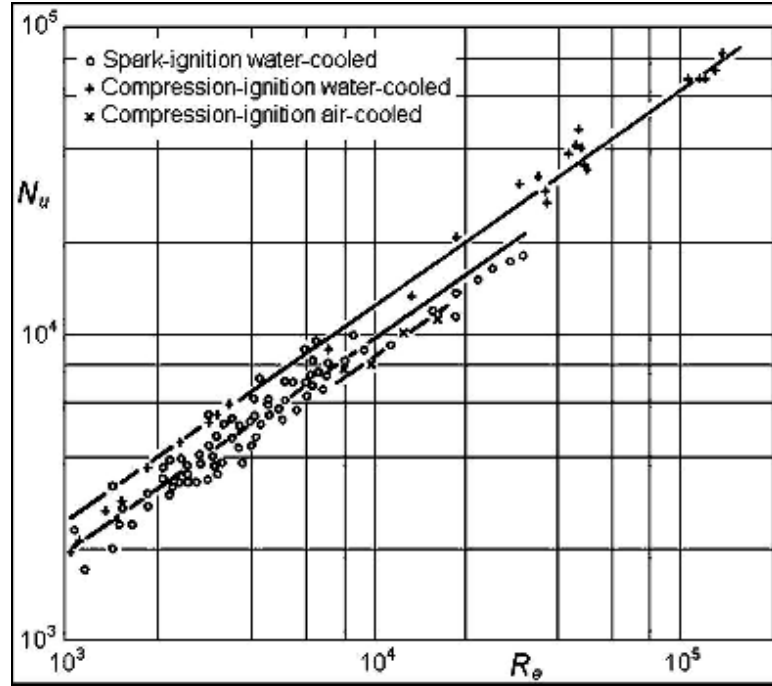


Figure 4–6: Experimental data for convective heat transfer correlation from Taylor and Toong [167].

Substituting 4–31 into 4–27 and then 4–25 leads to the following expression for the cylinder-to-wall heat transfer,

$$\dot{Q} = 10.4 * \frac{k_g}{b} * \left(\frac{Gb}{\mu} \right)_g^{0.75} * A_p * (\bar{T}_g - T_c) \quad (4-32)$$

where \bar{T}_g is the mean gas temperature. The key unknown in Eqn. 4–32 required to estimate the engine heat flux is the mean gas temperature. Estimation of transport properties for the gas including thermal conductivity and dynamic viscosity also require knowledge of mean gas temperature apart from the species composition. The definition and determination of the mean gas temperature are discussed next.

4.5.1.3 Estimation of mean gas temperature

The mean gas temperature \bar{T}_g is defined as the equilibrium temperature that the cylinder wall would attain in the absence of any heat removal from the outside.¹⁶⁸

It is defined as follows,

$$\int A(\theta)h_c(\theta)(T(\theta) - T_{g,a})d\theta = 0 \quad (4-33)$$

where the integral is evaluated over one engine cycle.

A technique for measuring the mean gas temperature has been used by Pinkel¹⁶⁹ and others in air cooled internal combustion engines like a single cylinder Wright R-1820-G aircraft engine. It involves measuring heat transfer as a function of cylinder head temperature, plotting the results, and extrapolating on the plot to find the effective adiabatic temperature. Pinkel and others demonstrated in several studies published in NACA technical reports^{170 171} that mean gas temperature was solely a function of fuel air mixture ratio and was independent of engine size, operating speed and brake mean effective pressure. They also showed that mean gas temperature is independent of spark timing (unless timing was extremely advanced or retarded) and is only slightly affected by the inlet air temperature.^v Therefore, it appears reasonable to assume that the mean gas temperature would also be a pure function of fuel-to-air ratio (F/A) in miniature engines,

$$\bar{T}_g = f(F / A) \quad (4-34)$$

The experimental method used to measure mean gas temperature in the miniature engines of interest in this work is adapted from Pinkel and goes as follows:

^v A change in inlet air conditions of 10 °C produces a change of 4 °C in the mean gas temperature (Taylor). However, the inlet air is drawn from the laboratory room and since room air temperature is controlled, there is not much of a change in engine inlet air temperature across measurements.

- The engine is operated at fixed throttle and mixture–ratio settings while the dynamometer controls engine load to maintain a constant speed.
- Thermocouples measure cylinder head surface and coolant (air) temperatures. The temperature of the coolant is varied using electrical heater elements installed in the cooling air supply ducts as illustrated in Fig. 4–7.
- Measurements of coolant and cylinder head temperature are repeated for different heater settings.
- The adiabatic condition corresponds to the situation where the coolant and cylinder head temperatures are equal. Therefore, the effective mean gas temperature is determined by plotting $(T_{cyl}-T_{inf})$ vs. T_{cyl} and drawing a straight line through the points. The temperature where the line intersects the x–axis ($T_{cyl}-T_{inf}=0$) is the mean gas temperature.
- Similar measurements are made at different speeds and fuel–air mixture ratios and in engines of different sizes in order to establish that the mean gas temperature is purely a function of F/A.
- The estimated mean gas temperature from all data sets is plotted as a function of fuel–air mixture ratio to obtain a correlation for mean gas temperature with mixture ratio.

Figure 4–7 shows the dynamometer setup and thermocouple locations used in estimating the mean gas temperature experiments. The only difference between this setup and previous ones is the addition of an array of 4 ceramic resistance heaters used to change the temperature of the cooling air provided to the engine. The

120VAC heaters are operated singly and then in increasingly large groups to raise the coolant air temperature in well-defined steps.

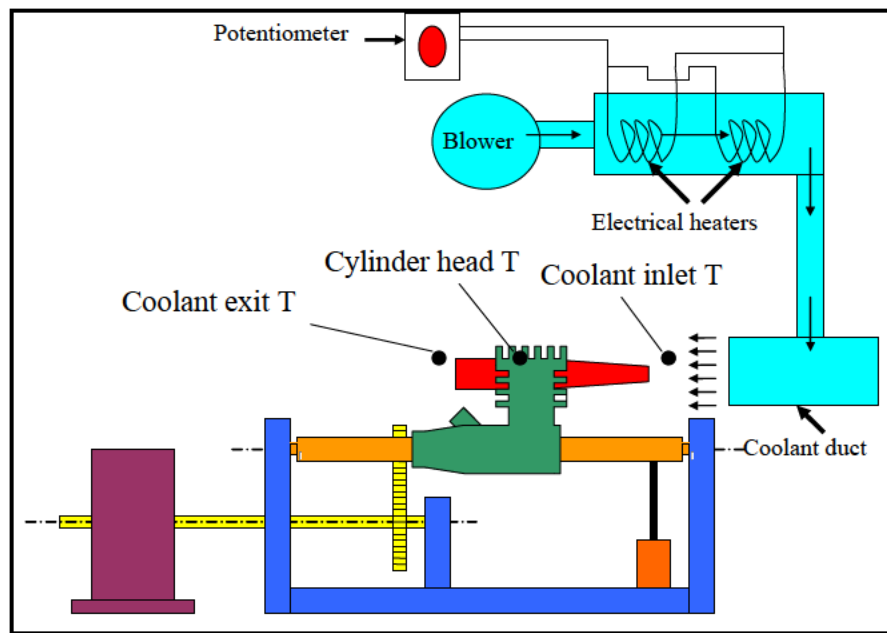


Figure 4-7: Layout of dynamometer setup used to establish mean gas temperature data.

The major challenge is maintaining a constant fuel-air mixture ratio while the coolant air temperature is varied. The reason is that the needle valve that controls the fuel flow rate is located behind the cylinder in most cases and sometimes on the carburetor itself. In either case, the fuel intake assembly comes in contact with the cooling air provided to the engine. Changing the cooling air temperature changes the density and viscosity of the fuel which, in turn, changes the fuel flow rate and the F/A ratio. Hence, special care had to be taken to insulate the fuel from the heating effects of the coolant air flow. This was achieved by covering the fuel intake assembly with insulation so as to prevent heat transfer to the fuel entering the engine. Figure 4-8 is a photograph showing how this was accomplished. Measurements were obtained at two different speeds and multiple F/A ratios for two different engines, the OS 25 FX and the OS 40 FX.

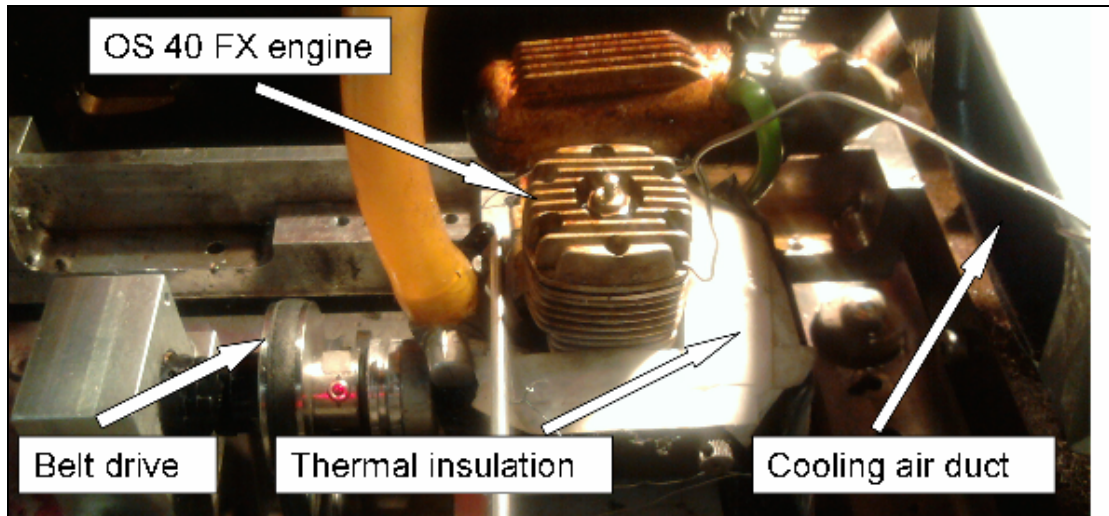


Figure 4–8: Photograph of the dynamometer setup for the measurement of mean gas temperature for the OS 40 FX engine.

One of the assumptions implicit in this technique is that the temperature measured at one location on the cylinder head represents the average temperature of the cylinder head surface. Therefore, some effort was made to check this. It was found that thermocouple measurements made at various locations on the cylinder head varied by less than 10 °C. The effect of this variation is relatively minor as it leads to an uncertainty of about ± 15 °C in the mean gas temperature and is accounted for when estimating the uncertainty.

4.5.2 Measurement Results

Figure 4–9 shows the variation of cylinder head temperature and fuel–air mixture ratio as a function of coolant inlet temperature in the OS 25 FX engine operating at a constant speed of 7000 rpm and a fuel–air mixture ratio of 0.45 (equivalence ratio of about 2). The figure shows that cylinder head temperature increases linearly with increasing coolant air temperature and that fuel–air mixture ratio stays fairly constant throughout the experiment.

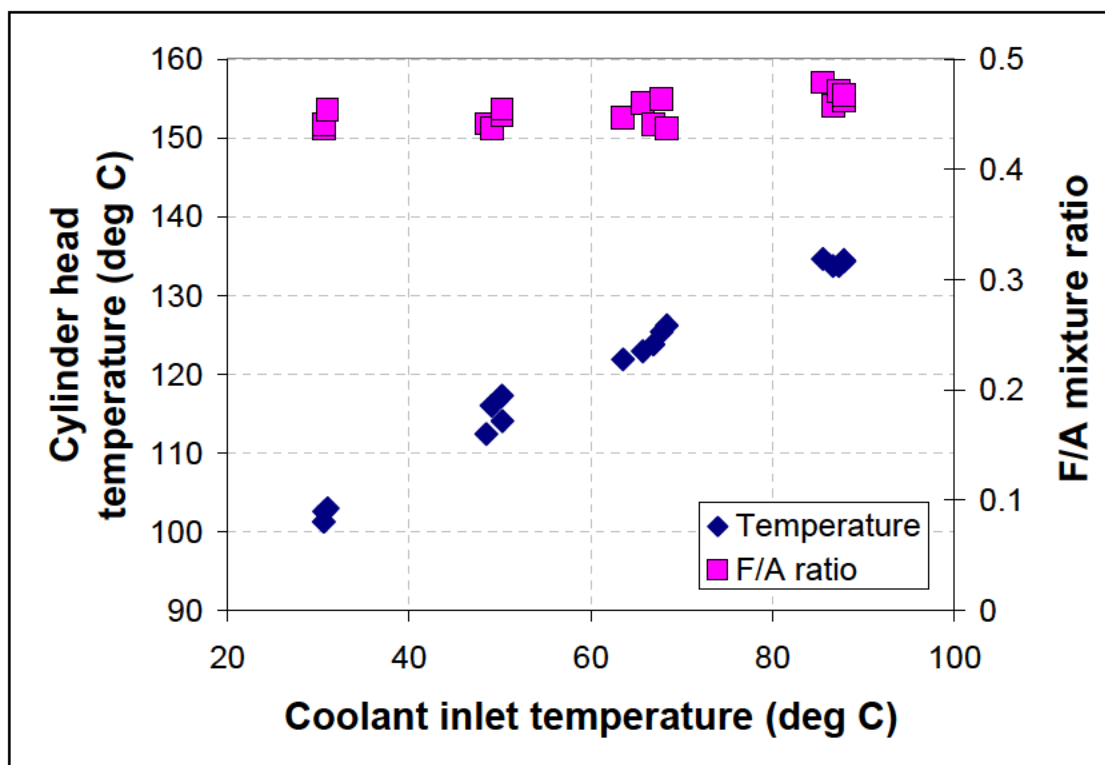


Figure 4-9: Measurements of cylinder head temperature and fuel air mixture ratio as a function of coolant inlet temperature for a constant engine speed of 7000 rpm and a fuel-air mixture setting of 0.45 for the OS 25 FX engine.

Figure 4-10 summarizes the results of the mean gas temperature experiments in the OS 25 FX engine. Data is presented for two different engine speeds, 7000 and 9000 rpm. Three data sets are presented for 7000 rpm and five for 9000 rpm. In each case, the coolant temperature is varied through three or four different heater power settings resulting in an average change in coolant air temperature of about 50 °C. The difference between cylinder head surface temperature and coolant temperature is plotted on the y-axis against the surface temperature on the x-axis. An estimate for mean gas temperature for each case is obtained by extrapolating a linear fit to each data set to find the zero-intercept on the x-axis.

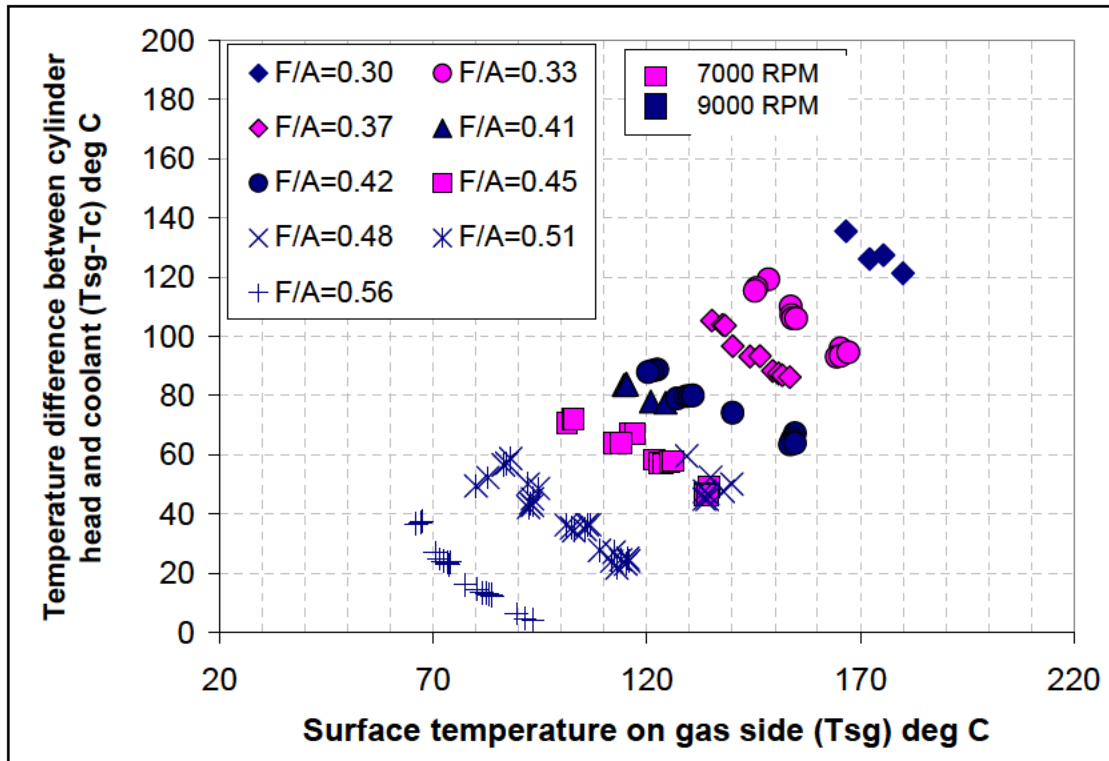


Figure 4–10: Data sets for different fuel air mixture ratios and engine speeds for the OS 25 FX engine used to establish values for mean gas temperature.

Figure 4–11 summarizes the mean gas temperature results for the OS 40 FX engine. In this case results are obtained for engine speeds of 8000 and 9000 rpm. Six data sets are presented for 8000 rpm and seven for the case of 9000 rpm. As before, the mean gas temperature is estimated by finding the zero-intercept for the linear fit to each data set.

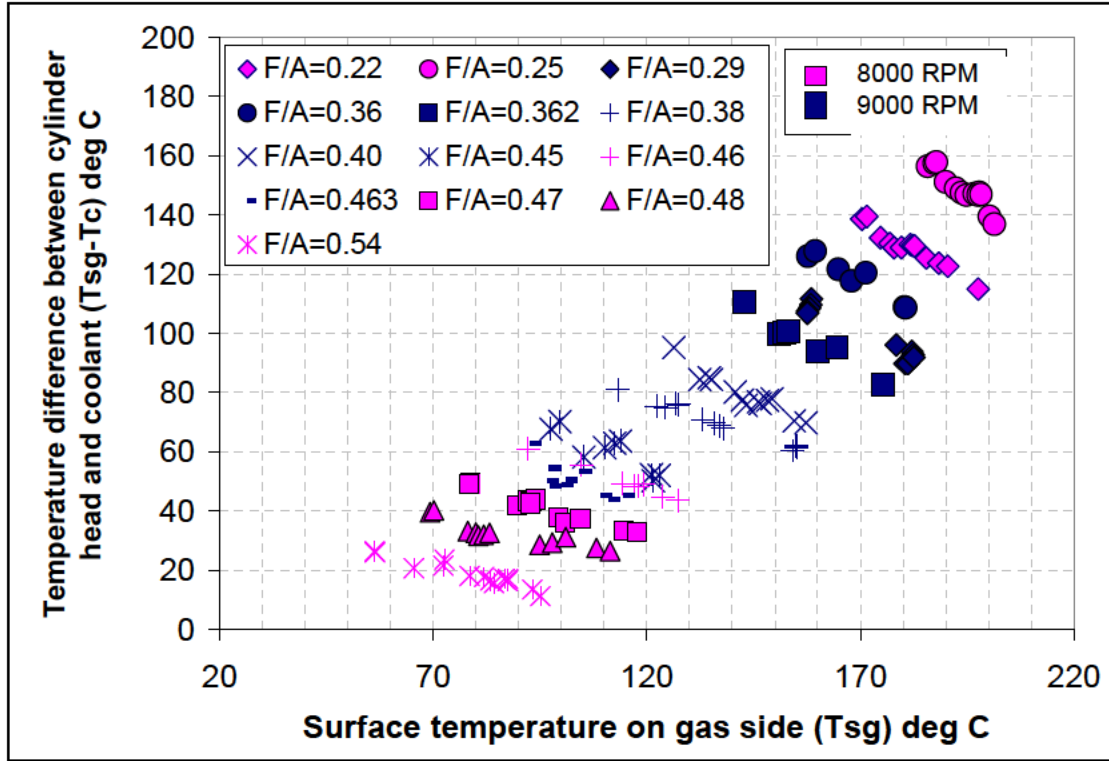


Figure 4–11: Data sets for different fuel air mixture ratios and engine speeds for the OS 40 FX engine used to establish values for mean gas temperature.

Figure 4–12 shows estimated mean gas temperature for all experiments as a function of fuel–air mixture ratio. Table 4–3 summarizes the data obtained from the OS 25 FX and OS 40 FX engines with regard to mean gas temperature. A second order polynomial fit to the data points yields a correlation of 0.9. The equation of the polynomial is given by,

$$y = -1312.4x^2 + 364.94x + 313.5 \quad (4-35)$$

where y is the mean gas temperature in degrees Celsius and x is the fuel–air mixture ratio. This is qualitatively similar to findings in larger engines by Taylor¹⁷² where the mean gas temperature decreases with fuel–air mixture ratios. The data presented by Taylor for mean gas temperature as a function of equivalence ratio obtained from the work by Pinkel is also presented in Fig. 4–12. Mean gas temperature values reported

by Pinkel are about twice as much as those estimated here. While fuel energy content would have a large influence on mean gas temperature, engine characteristics such as combustion efficiency and heat transfer are also estimated to play a key role resulting in the lower mean gas temperature for the engines investigated in this work. The data obtained by Pinkel used gasoline fuel, having an energy content ($Q_R = 44 \text{ MJ/kg}$) almost twice as much as that of the glow fuel ($Q_R = 21.2 \text{ MJ/kg}$) used in this work.

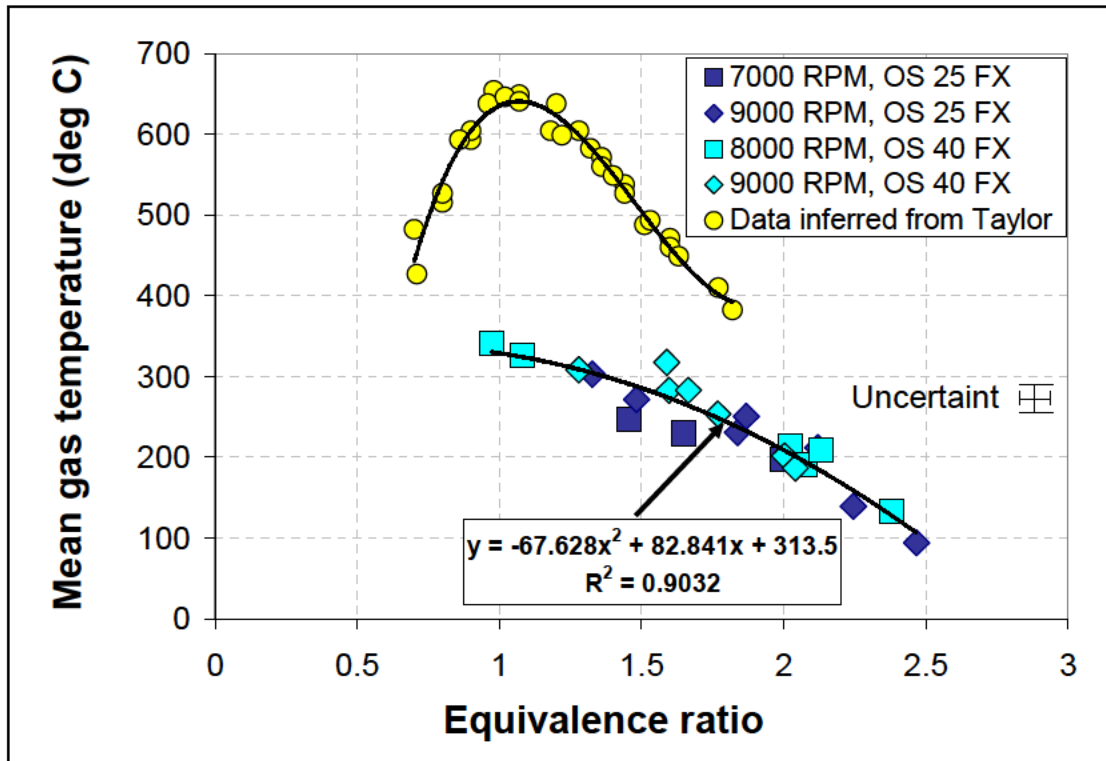


Figure 4–12: Estimated mean gas temperature as a function of fuel air mixture ratio. Also presented are data points first estimated by Pinkel [170], later reported and inferred here from Taylor [167].

Engine	Speed	Fuel–air mixture ratio	Equivalence ratio	Mean gas temperature
OS 25 FX	7000	0.33	1.47	247.38
OS 25 FX	7000	0.37	1.67	229.26
OS 25 FX	7000	0.45	2.02	197.35
OS 25 FX	9000	0.3	1.34	302.86
OS 25 FX	9000	0.34	1.5	271.42
OS 25 FX	9000	0.42	1.86	230.33
OS 25 FX	9000	0.42	1.89	250.63
OS 25 FX	9000	0.48	2.15	211.68
OS 25 FX	9000	0.51	2.27	139.18
OS 25 FX	9000	0.56	2.49	93.91
OS 40 FX	8000	0.22	0.98	341.74
OS 40 FX	8000	0.25	1.09	325.71
OS 40 FX	8000	0.46	2.05	213.50
OS 40 FX	8000	0.47	2.1	190.02
OS 40 FX	8000	0.48	2.16	209.38
OS 40 FX	8000	0.54	2.41	133.29
OS 40 FX	9000	0.29	1.29	308.28
OS 40 FX	9000	0.36	1.61	317.43
OS 40 FX	9000	0.36	1.62	282.79
OS 40 FX	9000	0.37	1.69	282.86
OS 40 FX	9000	0.40	1.79	253.51
OS 40 FX	9000	0.45	2.03	201.64
OS 40 FX	9000	0.46	2.07	186.46
	rpm			°C

Table 4–3: Peak value of delivery ratio and corresponding engine operating speed for the engines tested in this work

For any engine operating condition, measured mass flow rate is used to compute the mass flow rate per unit piston area (G) is estimated. Mean gas temperature is estimated at the operating equivalence ratio using Eqn. 4–35. Air transport properties like thermal conductivity and dynamic viscosity are based on the mean gas temperature. The heat transfer losses can then be estimated using Eqn. 4–32.

4.5.3 Estimation of Mixture Transport Properties

The fuel–air mixture within the engine cylinder undergoes considerable changes in composition and temperature over the course of the engine cycle. Depending on the temporal location in the engine cycle or spatial location in the cylinder volume, the mixture could be composed entirely of unburnt species, completely burnt species, or a mixture of burnt and unburnt species. The composition of the mixture also depends on the operating fuel air mixture ratio and the mean gas temperature. Therefore, it is difficult to establish appropriate values for transport properties for use in equations like 4–32. As a result, it is necessary to investigate the influence of property variations with temperature, fuel–air mixture ratio and degree of reaction. This was accomplished studied using a chemical reaction mechanism involving the major reacting species in the fuel – methanol and nitromethane.

A detailed chemical reaction mechanism consisting of 77 species and 484 reactions has been developed by Bendtsen, Glarborg and Dam–Johansen¹⁷³ for reactions occurring in hydrocarbon and nitrogen mixtures. This mechanism, which provides pathways for the oxidation of methanol and nitromethane, is used to determine transport properties for various fuel–air mixtures and chemical compositions as a function of temperature. The change in transport properties due to reaction of the fuel was also considered. Two extreme cases of completely burnt and completely unburnt mixture were examined. The computations were implemented in CANTERA¹⁷⁴ and the species considered in the reaction mechanism is listed in Appendix B. Transport properties for some of the species had to be obtained from external sources since they were not included in the original file.¹⁷⁵ These are

provided in Appendix C. Thermodynamic data for all species is obtained from the gas research institute's GRI-MECH.¹⁷⁶

Three different compositions are considered in this analysis corresponding to equivalence ratios of 1, 2 and 3. This spans the full range of equivalence ratios observed in the engines considered in this work. All of these engines usually operate rich of stoichiometric. Transport properties were evaluated at temperatures ranging from 300 to 800 K. This spans the observed 373 K to 623 K range of mean gas temperatures. Fuel composition was held constant in each case at 70% methanol, 10% nitromethane and 20% oil by volume. Oil was treated as a non-reacting species in the calculations.

Figure 4–13 shows the effect of mixture composition, state of reaction, and temperature on the dynamic viscosity of the gas mixture in the cylinder. The effect of change in temperature on viscosity is far greater than that of changing mixture ratio or gas composition. Based on this, a mixture averaged dynamic viscosity can be defined as a function of temperature as shown in Fig. 4–14. A third order polynomial fit is used to fit the data obtained by averaging the values for dynamic viscosity at a fixed temperature for the different cases presented in Fig. 4–13.

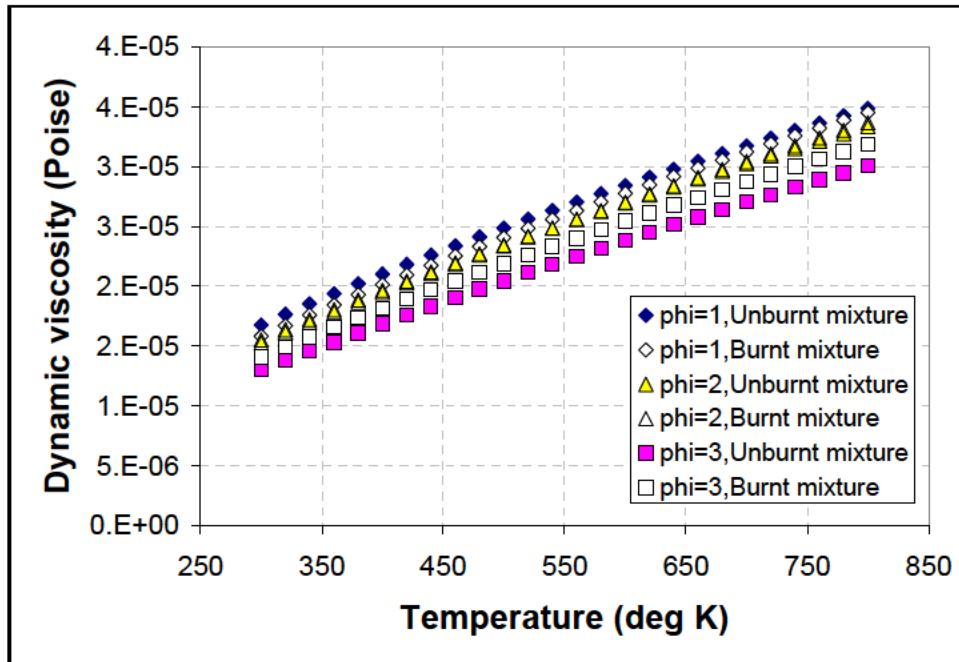


Figure 4–13: Calculations of mixture viscosity for three different equivalence ratios in the burnt and unburnt state as a function of mixture temperature.

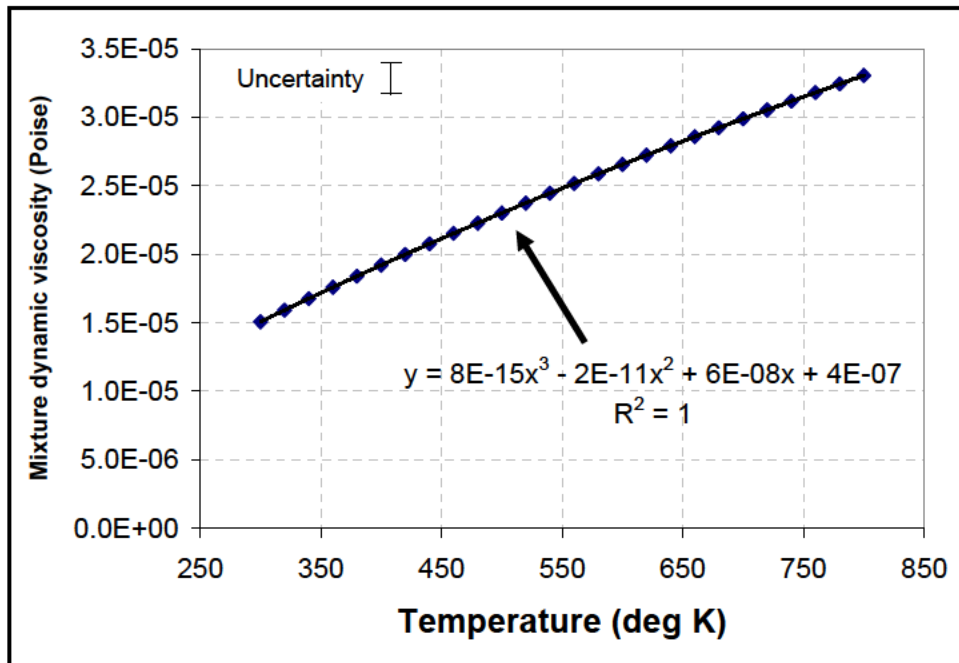


Figure 4–14: Estimate for mixture averaged viscosity as a function of temperature.

Figure 4–15 shows the effects of equivalence ratio, state of reaction and temperature on the thermal conductivity of the fuel–air mixture. Thermal conductivity

increases slightly with equivalence ratio for unburnt mixtures and to a larger extent for burnt mixtures at constant temperature. In all cases, thermal conductivity increases with increasing temperature. An effective average value for thermal conductivity is defined for each particular temperature and the values obtained in this manner are plotted in Fig. 4–16 as a function of mixture temperature. A linear fit is developed to approximate the thermal conductivity as a function of mixture temperature.

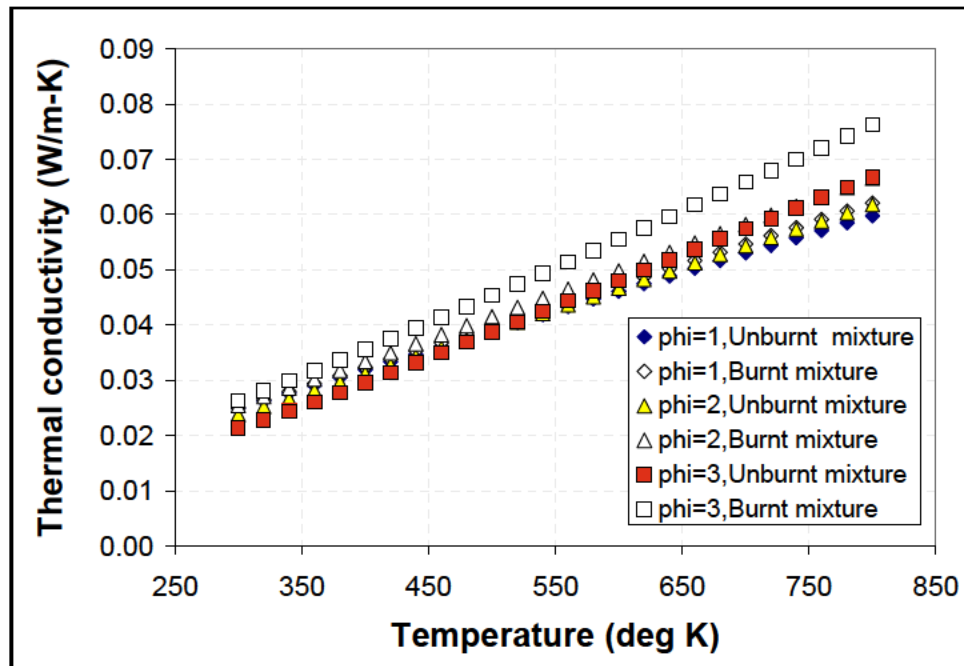


Figure 4–15: Calculations of mixture thermal conductivity for three different equivalence ratios in the burnt and unburnt state as a function of mixture temperature.

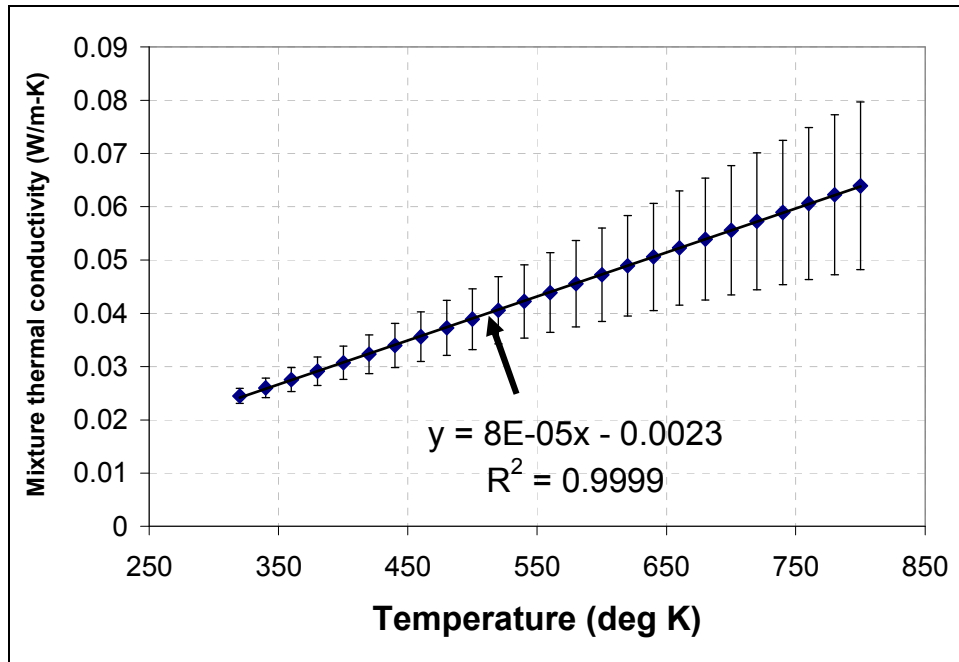


Figure 4–16: Estimate for mixture averaged thermal conductivity as a function of temperature.

Figure 4–17 shows specific heat at constant pressure for fuel–air mixtures of three different compositions in the completely unburnt and completely burnt state as a function of mixture temperature. Specific heat of the mixture at constant pressure is not required to estimate the heat transfer losses. However, it is needed to estimate sensible enthalpy loss in the exhaust as will be discussed in Section 4.7. The figure shows that at a constant temperature, specific heat at constant pressure increases with increasing equivalence ratio. It also increases to a lesser extent in going from an unburnt to a burnt mixture. The specific heat at any composition and state of reaction is seen to increase further with an increase in mixture temperature. At higher temperatures, the specific heats of the unburnt and burnt mixtures are approximately the same and vary only with equivalence ratio.

The variation in specific heat with temperature, composition and state of reaction are captured using linear fits for each equivalence ratio as shown in Fig. 4–

18. Each fit represents an average between the burnt and unburnt mixtures. The value of the specific heat of the mixture at a particular engine operating condition is obtained by using the linear fit corresponding to the equivalence ratio closest to that measured during engine operation.

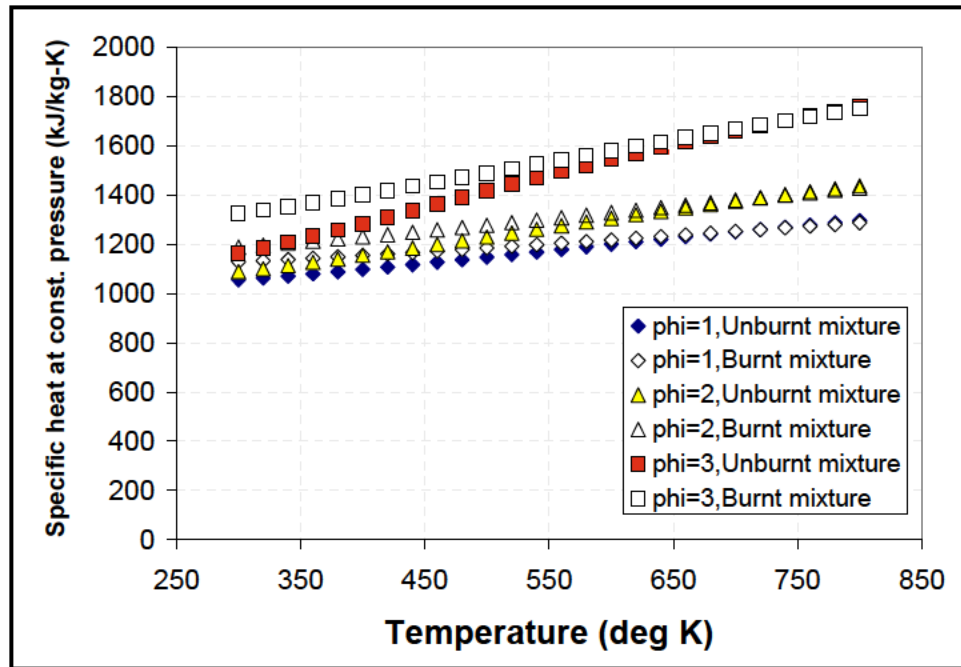


Figure 4–17: Calculations of mixture specific heat at constant pressure for three different equivalence ratios in the burnt and unburnt state as a function of mixture temperature.

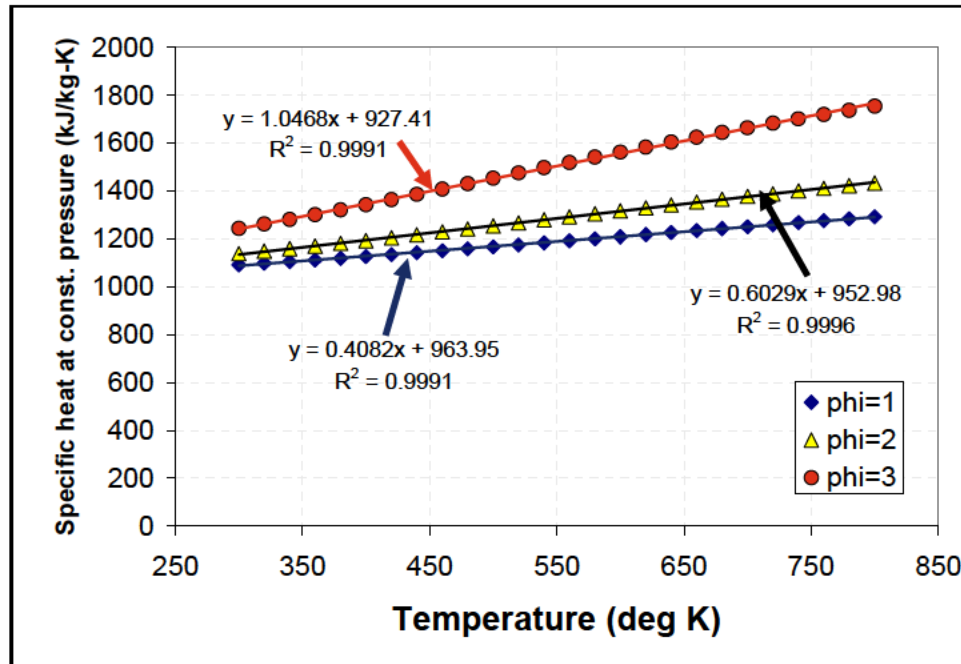


Figure 4–18: Estimates of mixture averaged specific heat at constant pressure as a function of temperature.

4.5.4 Scaling of Thermal Losses

Figure 4–19 compares estimated thermal losses in each of the 9 engines investigated when operating at 10000 rpm for a range of fuel–air mixture ratios. Enthalpy loss via heat transfer is directly proportional to the mass flow rate of the gas mixture through the engines and the piston area as seen in Eqn. 4–32. Since the engines are all operating at the same speed, the net heat transfer generally decreases with decreasing engine size. The mean gas temperature is directly related to the fuel–air mixture ratio as expressed in Eqn. 4–35 and illustrated in Fig. 4–12. Increasing the fuel–air mixture ratio decreases the mean gas temperature thereby decreasing thermal losses. Similar results are obtained when the engines are operated at 12000 rpm as well at a constant mean piston speed of 4.77 ms^{-1} . These results are presented in figures B–3 and B–4 in appendix B.

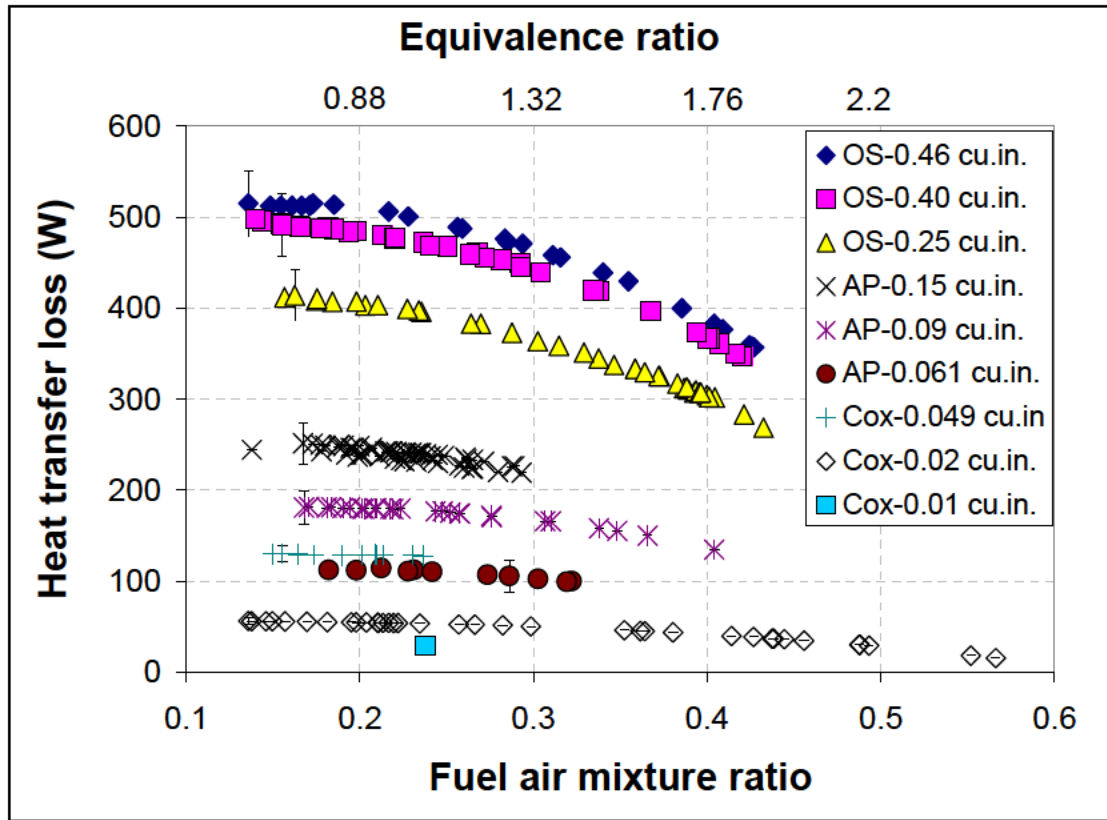


Figure 4–19: Heat transfer losses from all engines as function of fuel air mixture ratio for a constant engine speed of 10000 rpm. Error bars are plotted for a single point in each data set and represent average uncertainty for the entire dataset.

Figure 4–20 shows heat transfer loss as a function of engine displacement for three different cases: two at constant engine speeds of 10000 and 12000 rpm respectively, and one at a constant mean piston speed of 4.77 ms^{-1} . The equivalence ratio is approximately 1 for all three cases. The ratio of heat transfer loss to engine power output at the corresponding operating condition is presented on the right hand side y-axis. The filled symbols represent the magnitude of thermal loss and are plotted on the left hand y-axis while the empty symbols represent the ratio of heat transfer loss to engine power output and are plotted on the right hand y-axis. The figure shows that the magnitude of thermal loss increases with increasing engine size

for all cases and varies little between the three different cases. The effect of increasing surface area to volume ratio in miniature engines is apparent from the increasing trend observed in the ratio of heat transfer loss to engine power output with decreasing engine size. The values obtained for the two cases of 10000 and 12000 rpm are found to track each other. For the case of 10000 rpm, the ratio of heat transfer loss to engine power output is seen to grow from about 1.8 to 9 going from the largest to the smallest engine. The similar range obtained for 12000 rpm lies between 1.8 and 7.5. Heywood has summarized ranges for component energy losses observed in conventional scale SI and Diesel engines.¹⁷⁷ Based on these estimates, the ratio of heat transfer loss to engine power output is about 0.8 for an automotive scale spark ignition (SI) engine and about 0.7 for a Diesel engine.

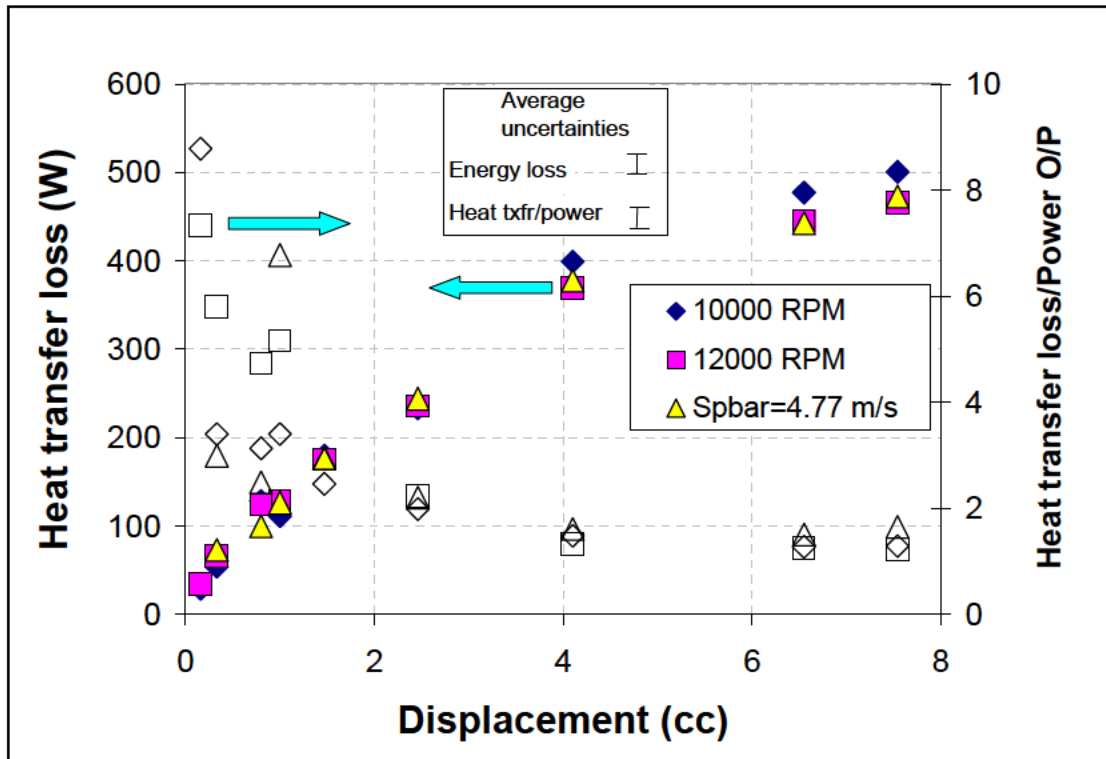


Figure 4–20: Scaling of convective heat transfer losses and ratio of energy loss to engine power output as a function of displacement for two different constant engine speeds of 10000 and 12000

rpm and a constant mean piston speed of 4.77 ms^{-1} . All data sets correspond to an equivalence ratio of ~ 1 .

4.6 Frictional Losses

4.6.1 Measurement Technique

Figure 4–21 is a schematic illustration of the motoring experiment used to measure frictional losses and hence engine mechanical efficiency. The motoring experiment shares most of its components with the dynamometer. Engine torque, power, air flow and engine temperatures are measured as before. The key difference is the use of an electric motor to drive (or ‘motor’) the engine at different speeds. It should be noted that the frictional losses measured in this manner include those due to both mechanical rubbing friction and fluid friction as the fuel–air mixture moves through internal engine passages. However, fluid friction losses are small compared to those due to rubbing friction. Motoring experiments in two–stroke engines are typically carried out with cylinder heads in place¹⁷⁸ whereas cylinder heads and valves are often removed when motoring four–stroke engines since pumping losses tend to be much higher.

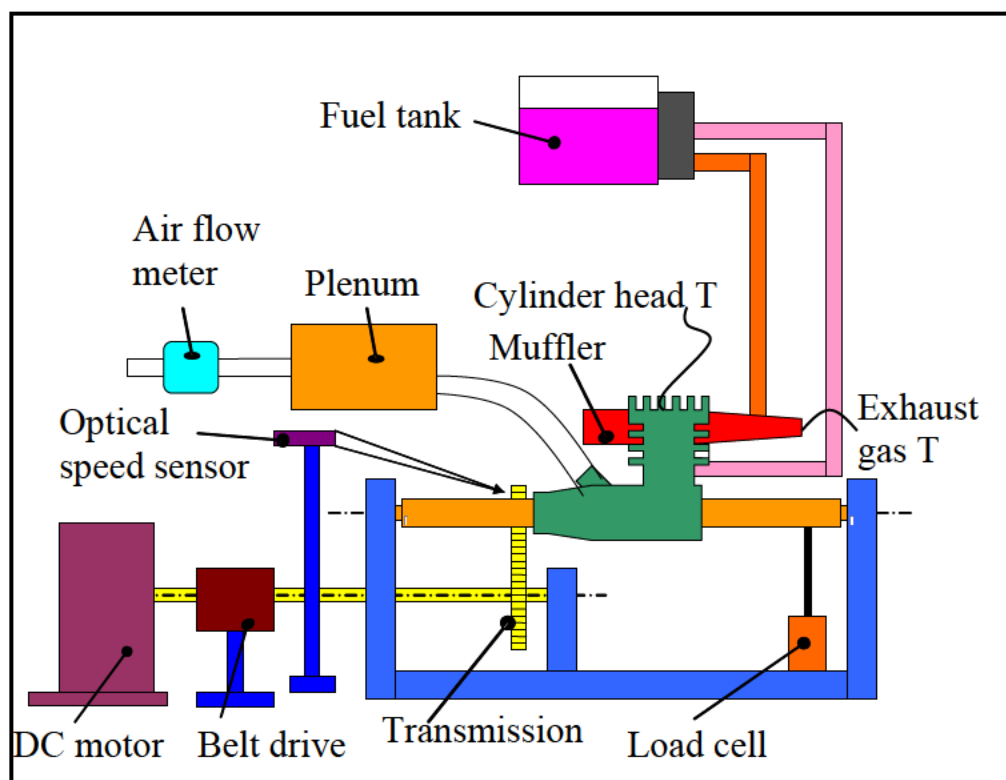


Figure 4–21: Schematic showing the layout of the motoring setup on the dynamometer.

Figures 4–22 and 4–23 are photographs of the experimental setup. The engine to be tested is mounted on the dynamometer’s cradle and is connected to an electric motor using a combination of gear and belt drives that depends on the particular engine. Specifications of the two drive motors used in this work are given in Table 4–4. The 372 W (0.5 hp) DC motor was used to make frictional power loss measurements in engines B–I in Fig. 2–3. The OS–46 engine required the 1491 W (2 hp) AC motor to drive it to its normal operating speed. The DC motor is controlled using a DC motor speed controller made by Leeson. The AC motor is controlled by a variable frequency drive made by Dayton Inc. Since the operating speeds of most engines tested here are greater than 10000 rpm and much higher than the maximum speed of either motor listed in Table 4–4, a transmission is necessary to get the engine up to its regular operating speed. The first stage is a V–belt drive whose ratio can be

adjusted by changing the sizes of the attached pulleys. The second stage is a set of nylon gears. Plastic gears are advantageous as they reduce the inertial load on the motor allowing it to achieve higher operating speeds.

	Motor 1	Motor 2	
Type	DC	AC	
Manufacturer	Leeson	Dayton	
Rated power	0.5	2	W
Rated speed	1750	3450	rpm
Voltage	90	230	V
Frequency	N/A	60	Hz
Rated current	5	6.2	A
Torque	2.02	4.12	N-m
Phase	N/A	3	
Speed control	Leeson DC motor speed controller, Model – 174308	Dayton variable frequency drive, Model – KBP8	

Table 4–4: Specifications for the motors used in the frictional power loss measurements.

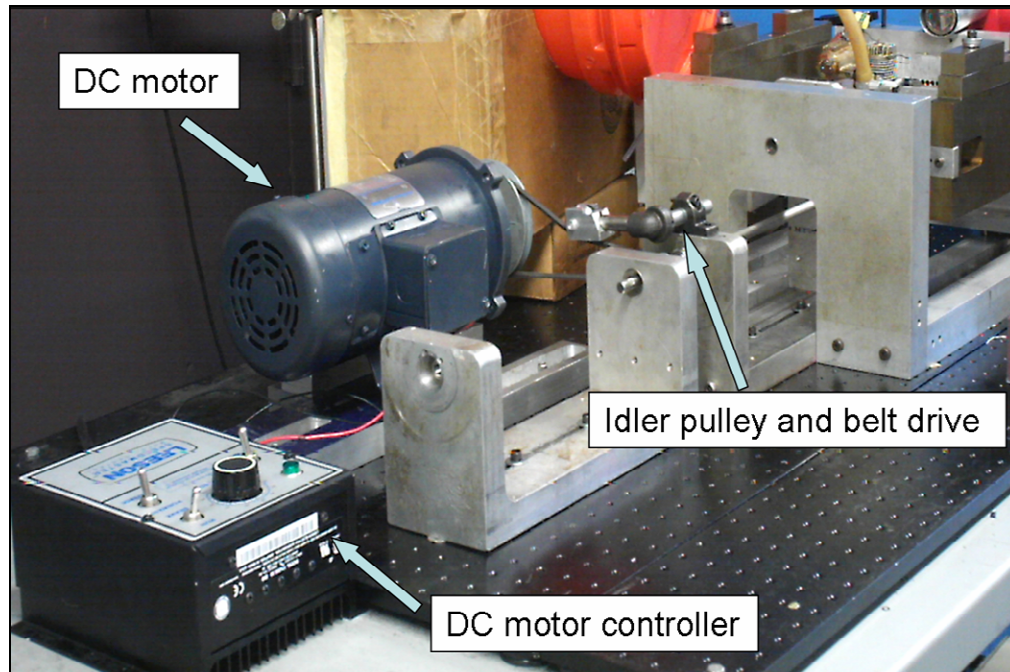


Figure 4–22: Photograph of the engine motoring setup showing the DC motor and speed controller.

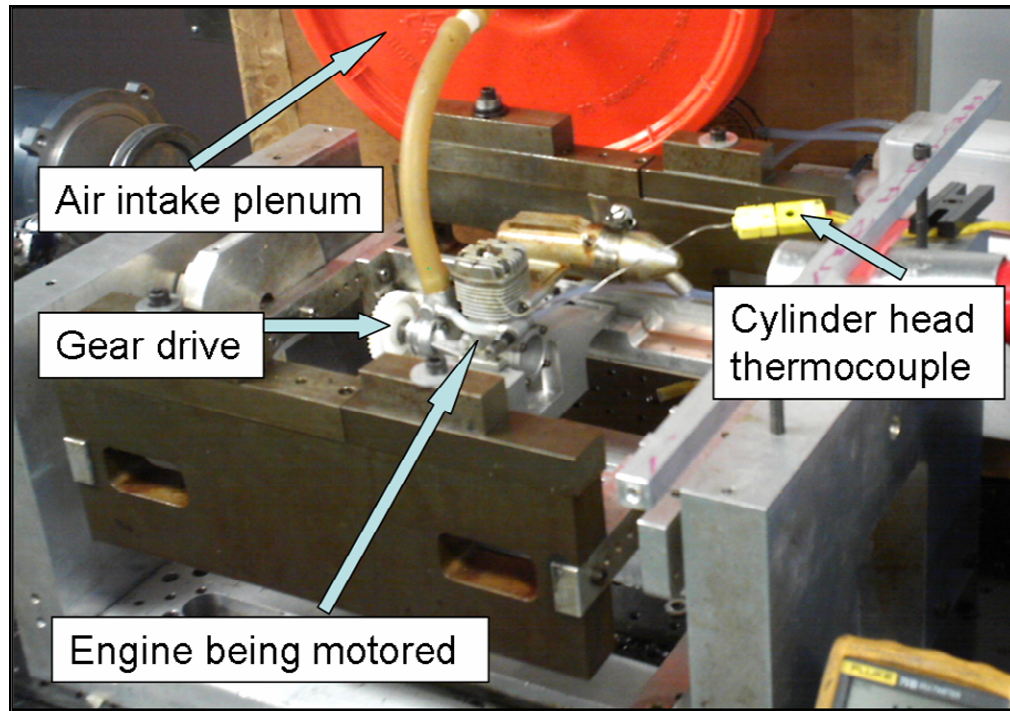


Figure 4–23: Photograph of the engine motoring setup showing the plastic spur gearing and the engine being motored.

The fuel flow system is retained in order to keep the engine lubricated. The unburnt fuel and oil are exit through the exhaust port as in fired operation. In case of engines with mufflers (A–F in Fig. 2–3), it was necessary to point the discharge downward so as to prevent accumulation of unburnt fuel within it.

While the motoring speed could be varied quickly using the speed controller, the temperature of the engine reached equilibrium more slowly. Therefore, it was necessary to wait 3 to 5 minutes between operating points in order to allow the system to stabilize. This was accomplished by measuring cylinder head temperature through the transient phase until it reached a steady state. Cylinder head temperature tends to increase during the transient phase until it reaches an equilibrium value. The increase in engine temperature results in a decrease in the viscosity of the oil which in turn results in a decrease in frictional losses. The measured value of frictional loss at

equilibrium is hence less than that in the transient operating condition. Measurements are made at regular intervals of engine speed between the minimum and maximum achievable speeds for each specific engine/motor/ transmission system. The measurements of frictional power loss obtained at equilibrium for each engine speed are used to develop the chart shown in Fig. 4–24.

4.6.2 Measurement Results

Figure 4–24 shows frictional power as a function of rotational speed for all 9 engines tested in this study. It shows that for any engine, frictional power loss increases linearly with increasing engine speed. Further at a constant speed, frictional losses increase with increasing engine size. Figure 4–25 shows the slopes developed for the linear correlation of frictional power loss plotted as a function of displacement volume.

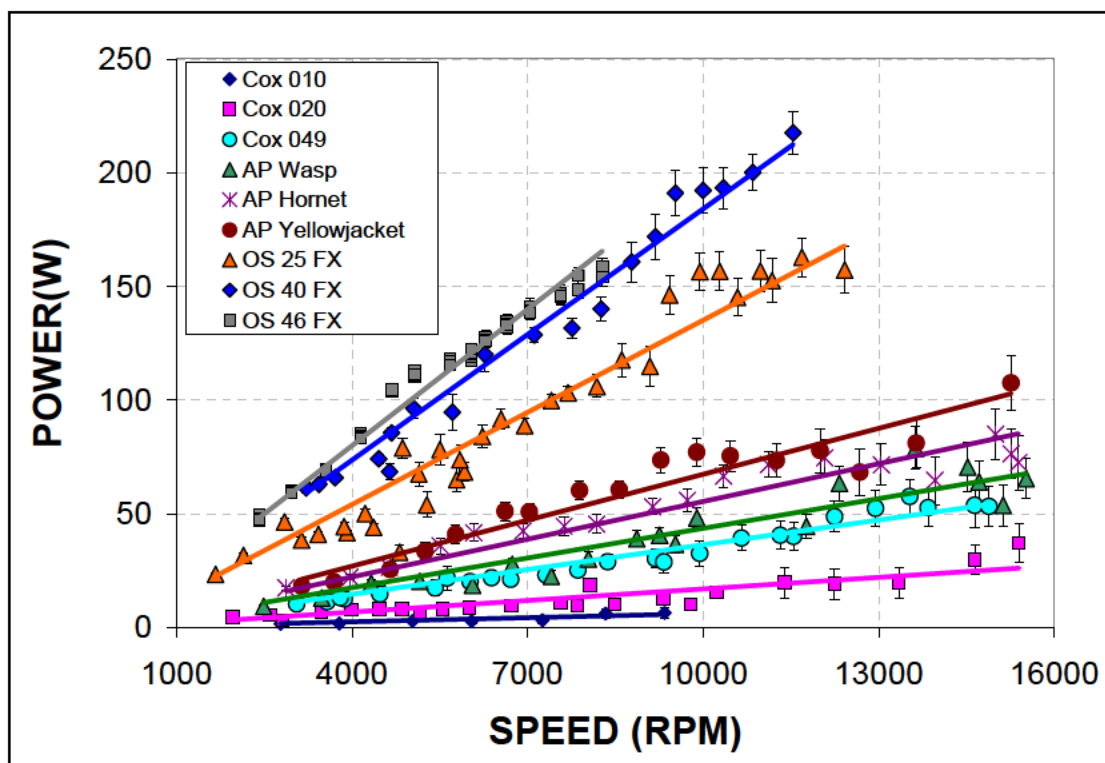


Figure 4-24: Frictional power loss measured from all the engines as a function of engine speed.

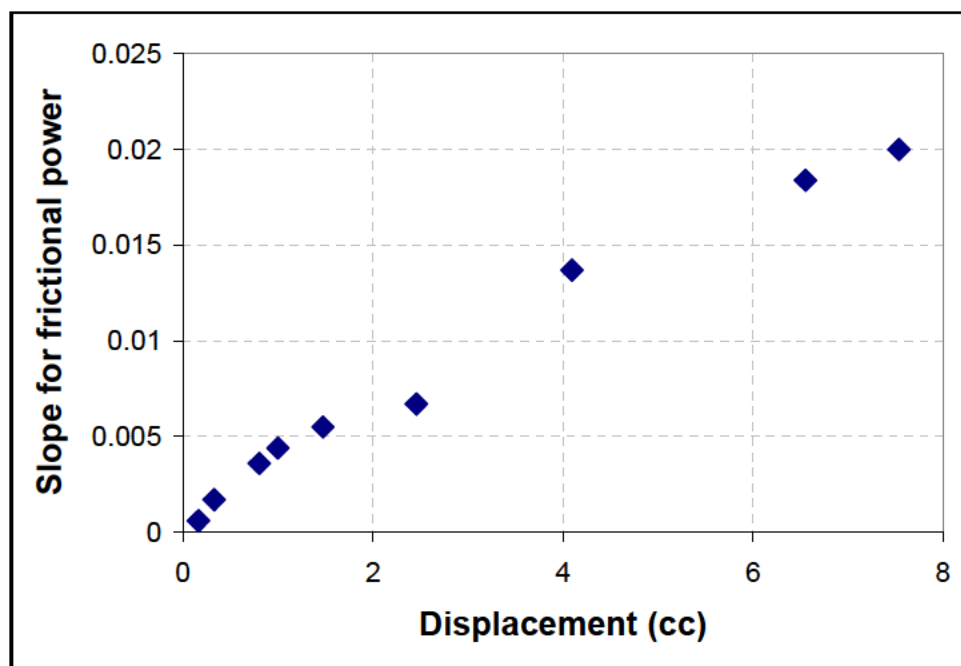


Figure 4-25: Slopes for the frictional power loss correlation developed for the data presented in figure 4-24 as a function of engine displacement.

The value of R^2 for each fit is presented in Table 4–5 along with the slope. Notice that R^2 ranges from 0.8 to 0.9 indicating that the linear fit is not the best representation of the data. The deviation from linearity is most likely due to a lack of thermal equilibrium at the time of measurement.

Engine	Displacement	Slope for linear fit (y)	Coefficient of correlation (R^2)
Cox 010	0.16	0.0006	0.81
Cox 020	0.33	0.0017	0.8
Cox 049	0.8	0.0036	0.96
Wasp 061	0.99	0.0044	0.88
Hornet 09	1.47	0.0055	0.89
Yellowjacket 15	2.46	0.0067	0.91
OS 25 FX	4.09	0.0137	0.94
OS 40 FX	6.55	0.0184	0.98
OS 46 FX	7.54	0.02	0.98
	cc		

Table 4–5: Linear fitting relationships developed for the frictional power loss for different engines.

Equation 4–36 is an empirical correlation usually used to estimate friction power loss in conventional scale engines.¹⁷⁹

$$P_{friction} = \left(a + b \left(\frac{N}{1000} \right) + c \left(\frac{N}{1000} \right)^2 \right) * V_{disp} * N \quad (4-36)$$

In the equation, a, b and c are empirically determined coefficients which depend on the type of engine cycle (spark ignition or diesel). Boundary lubrication is said to occur when two moving surfaces are in direct physical contact with each other. Hydrodynamic lubrication is said to occur when the surfaces are completely separated by the lubricant. Frictional losses are considerably lower in hydrodynamic lubrication as compared to boundary lubrication. The third regime, mixed lubrication occurs

when the effective lubrication regime is somewhere between boundary and hydrodynamic lubrication regimes.

Heywood and Sher¹⁸⁰ attribute each term in Eq. 4–36 to a different regime of lubrication: The term that varies directly with N is attributed to boundary lubrication which occurs when the lubricant film is considerably reduced in thickness and is unable to prevent direct metal to metal contact. The second term that varies as the square of N is attributed to hydrodynamic lubrication where frictional losses occur due to the viscous effects of the lubricant film. The third term that varies as the cube of N arises primarily from turbulent dissipation in fluids that are pumped through engine passages. These fluids include cooling water, lubricating oil, and air pumped through the radiator and over the exterior of the engine. Since the engines tested here have no such accessory pumps, c in Eq. 4–36 should be zero. Since experiments show that power losses are linearly proportional to speed, b in Eqn. 4–36 should also be zero. This leads to the simplified expression for friction power loss in miniature IC engines,

$$P_{friction} = a * V_{disp} * N \quad (4-37)$$

The fact that the friction power varies linearly with engine speed suggests that the majority of the frictional loss in miniature IC engines is due to rubbing friction between the moving surfaces associated with surface to surface contact due to break down of the lubrication film. Eq. 4–37 also suggests that friction power scales with the product of engine displacement and speed. The former increases with increasing engine size (obviously) but the latter decreases with engine size. Figure 4–26 shows a plot of the product VN on the left y-axis and the ratio of frictional power loss to

engine power output on the right y-axis as a function of engine displacement. The data points correspond to the operating conditions of peak engine power output. The product VN is seen to increase with engine size leading to higher frictional loss. The ratio of frictional power loss to engine power output however increases as the engines are made smaller.

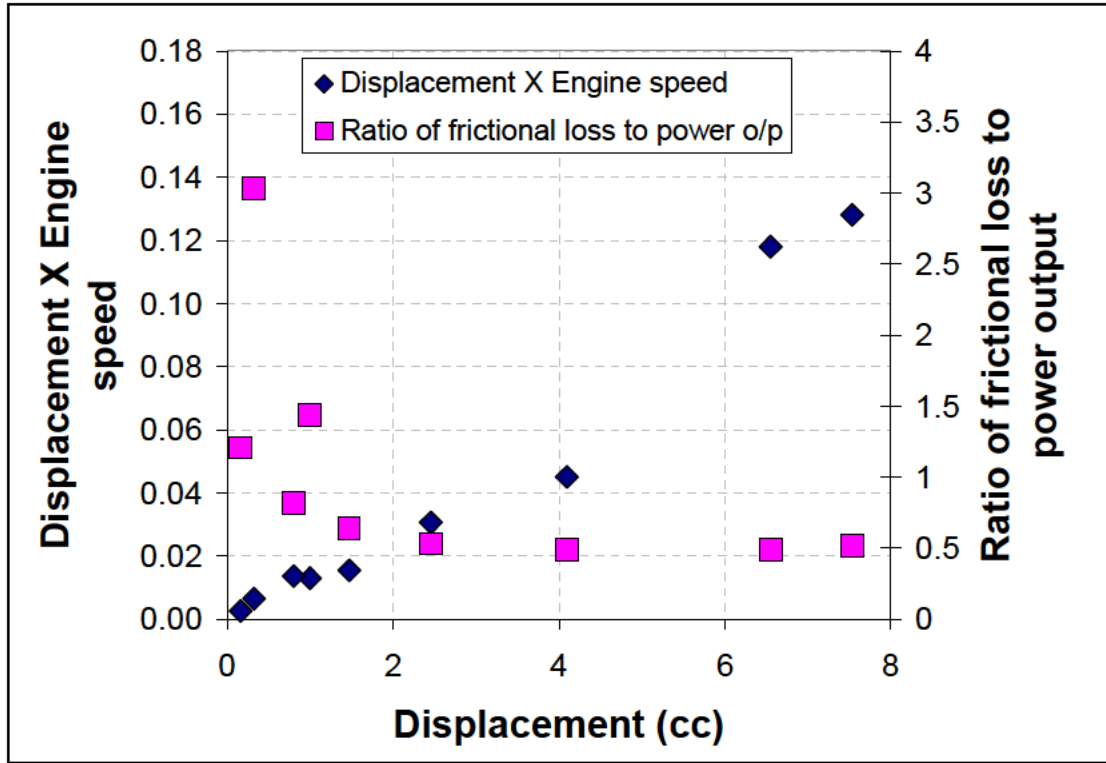


Figure 4–26: Product of displacement volume and engine speed at conditions of peak power output plotted as a function of engine displacement. Also presented is the ratio of frictional power loss to engine power output at the same conditions.

4.6.3 Scaling of Frictional Losses

Figure 4–27 shows frictional power loss as a function of fuel–air mixture ratio for different engines at a constant engine speed of 10000 rpm. The magnitude of losses increases from the smallest engine (Cox 010) to the largest engine (OS 46 FX) regardless of operating fuel–air mixture ratio. The figure also suggests that changing

F/A does not change the lubrication regime. Similar results are obtained for an operating speed of 12000 rpm and for a mean piston speed of 4.77 ms^{-1} . These are presented in figures B–5 and B–6 in appendix B.

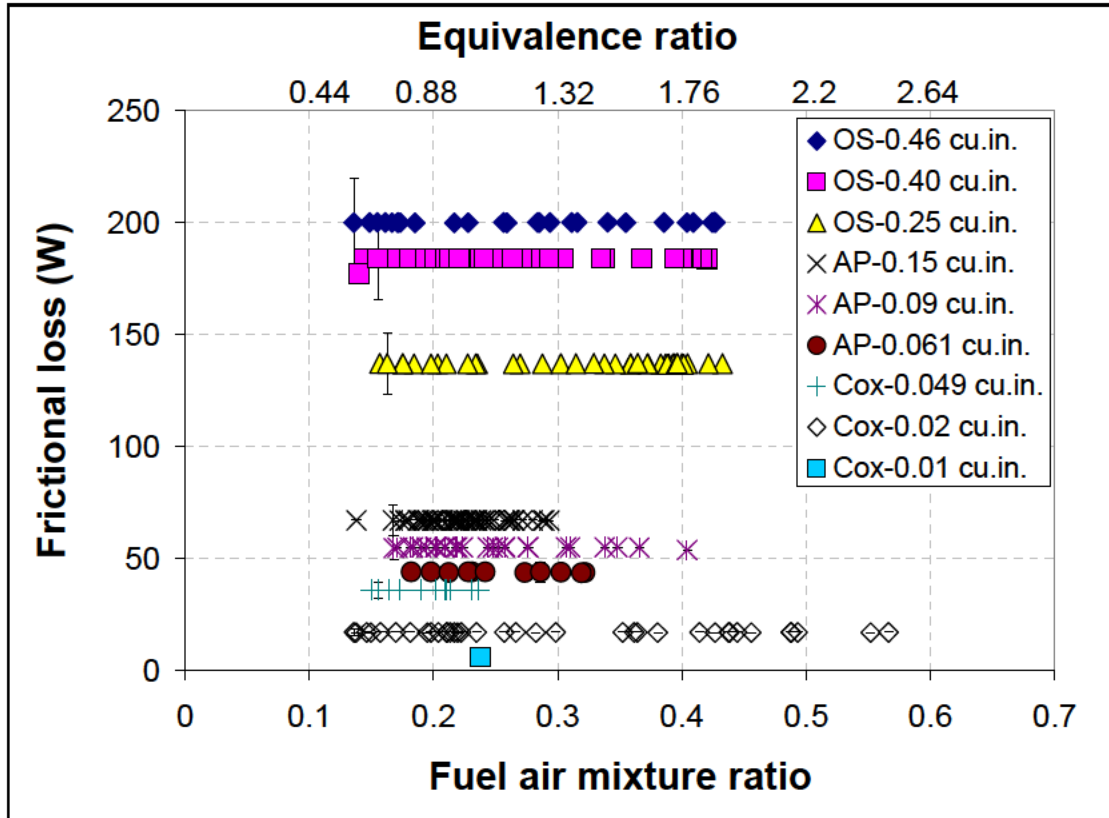


Figure 4–27: Frictional power loss from all engines as function of fuel air mixture ratio for a constant engine speed of 10000 rpm. Error bars are plotted for a single point in each data set and represent average uncertainty for the entire dataset.

Figure 4–28 shows how frictional power loss and the ratio of mechanical loss to engine power output scale with engine displacement and engine speed. The filled symbols plotted on the left hand y-axis show mechanical power loss in Watts while the empty symbols plotted on the right hand y-axis show the ratio of mechanical losses to engine power output. As expected, mechanical losses increase with increasing engine size at constant engine speed. Mechanical losses also increase with

increasing engine speed for a constant engine displacement. The ratio of mechanical loss to engine power output increases with decreasing engine size but not as rapidly as seen for thermal losses. For engine speeds of 10000 and 12000 rpm, the ratio of mechanical power loss to engine power output varies from 0.5 to 1.8 and from 0.5 to 2.1. This compares to value of 0.25 seen in automobile scale SI engines and a value of 0.11 for automobile scale Diesel engines.

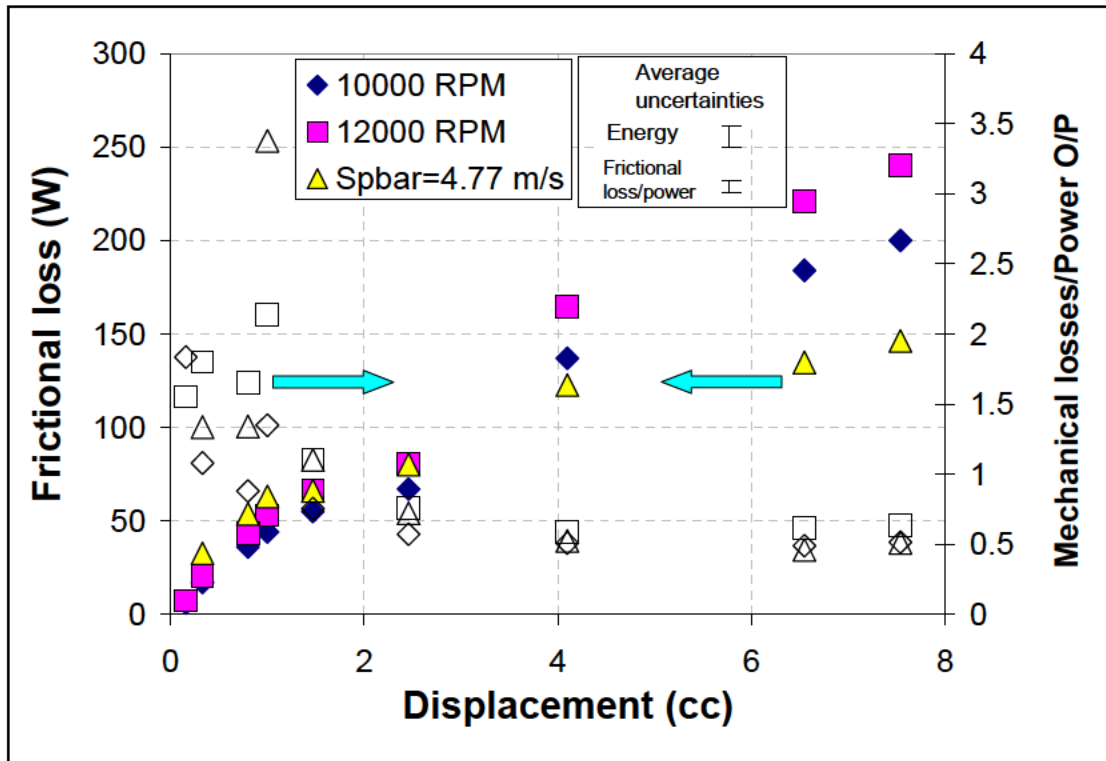


Figure 4–28: Scaling of mechanical losses and the ratio of mechanical losses to engine power output as a function of engine displacement for two different constant engine speeds of 10000 and 12000 rpm and a constant mean piston speed of 4.77 ms^{-1} . All data sets correspond to an equivalence ratio of ~ 1 .

The engine speed required to maintain a constant mean piston speed decreases with engine size as seen in Table 4–1. This results in a different behavior for mechanical losses at a constant mean piston speed. The magnitude of losses still

increases with engine size but not at the same rate as that observed for constant engine speed.

4.7 Exhaust Gas Enthalpy

4.7.1 Measurement Technique

The sensible energy remaining in the exhaust is given by,

$$h_{exhaust} = \dot{m}_{gas} * C_{p_{gas}} * T_{exhaust} \quad (4-38)$$

where \dot{m}_{gas} is the mass flow rate exiting the muffler and C_p and T are respectively the specific heat and temperature of the gases exiting the muffler. The mass flow rate of gas out the exhaust is the sum of the fuel and air mass flow rates at any operating condition. The temperature of the exhaust gas along with the fuel and air mass flow rates are measured during the dynamometer tests. The specific heat of the gas is calculated at the temperature corresponding to that of the exhaust gas using the relationships established in Fig. 4-18.

4.7.2 Scaling of Exhaust Gas Enthalpy

Figure 4-29 shows sensible energy released in the exhaust as a function of fuel-air mixture ratio for the 9 engines tested in this work at a constant operating speed of 10000 rpm. Enthalpy released in the exhaust increases with increasing engine size at a constant fuel-air mixture ratio because the mass flow rate increases with increasing engine size. Exhaust gas enthalpy also increases slightly with increasing fuel-air mixture ratio in the 3 largest engines tested here but is not sensitive to mixture ratio in the smaller engines. This is possibly because for engines at the smallest scales, energy release is combustion limited. Only a certain amount of

fuel is able to burn regardless of the mixture ratio of the charge going into the engine. The enthalpy released in the exhaust gas for engines operating at a constant speed of 12000 rpm and a mean piston speed of 4.77 ms^{-1} are presented in figures B–7 and B–8 in appendix B.

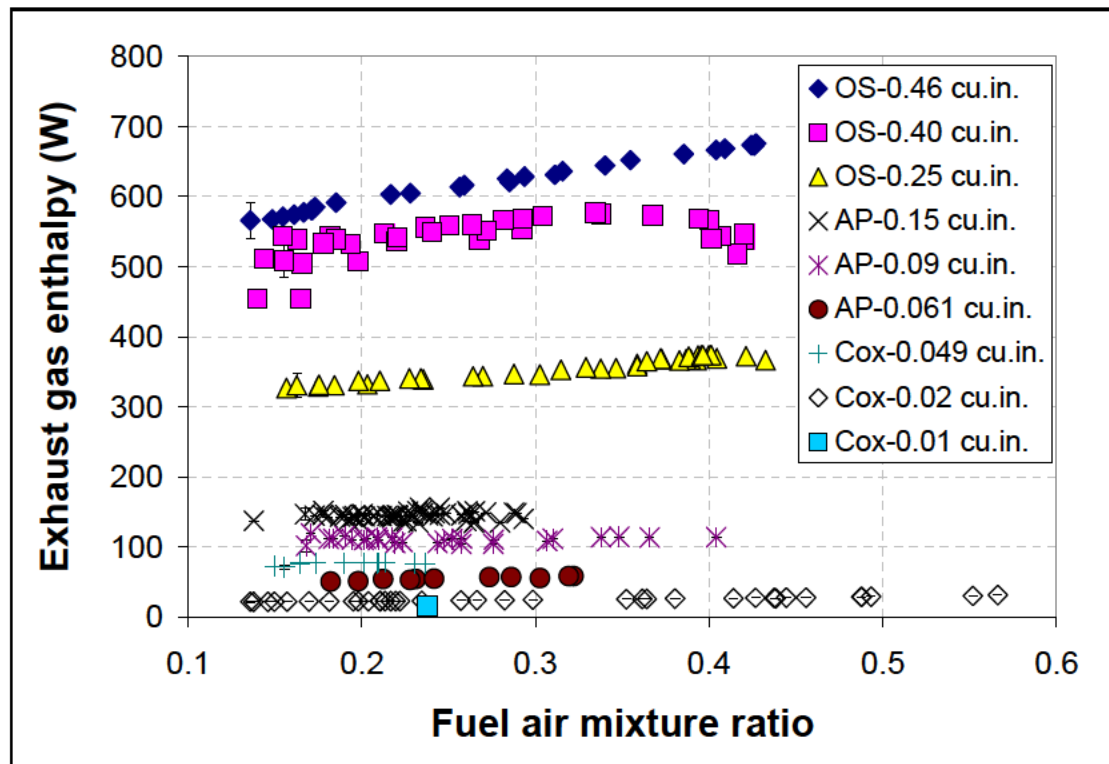


Figure 4–29: Enthalpy released in exhaust for all engines as a function of fuel air mixture ratio at a constant engine speed of 10000 rpm. Error bars are plotted for a single point in each data set and represent average uncertainty for the entire dataset.

Figure 4–30 shows exhaust gas enthalpy plotted in filled symbols as a function of engine displacement for two constant engine speeds – 10000 and 12000 rpm and a constant mean piston speed of 4.77 ms^{-1} . The equivalence ratio is also approximately 1 for all cases presented here. The figure shows that exhaust gas enthalpy increases with increasing engine size when the speed and fuel–air mixture ratio are held constant. It also increases with increasing engine size for constant mean

piston speed and fuel–air mixture ratio. The open symbols in the figure show the ratio of exhaust gas enthalpy to engine power output. This is seen to increase with decreasing engine size going from 1.6 to 5 for the case of 10000 rpm and from 1.8 to 3.6 for the case of 12000 rpm. This compares to a value of 1.3 in automobile scale SI engines and 0.8 for automobile scale Diesel engines.

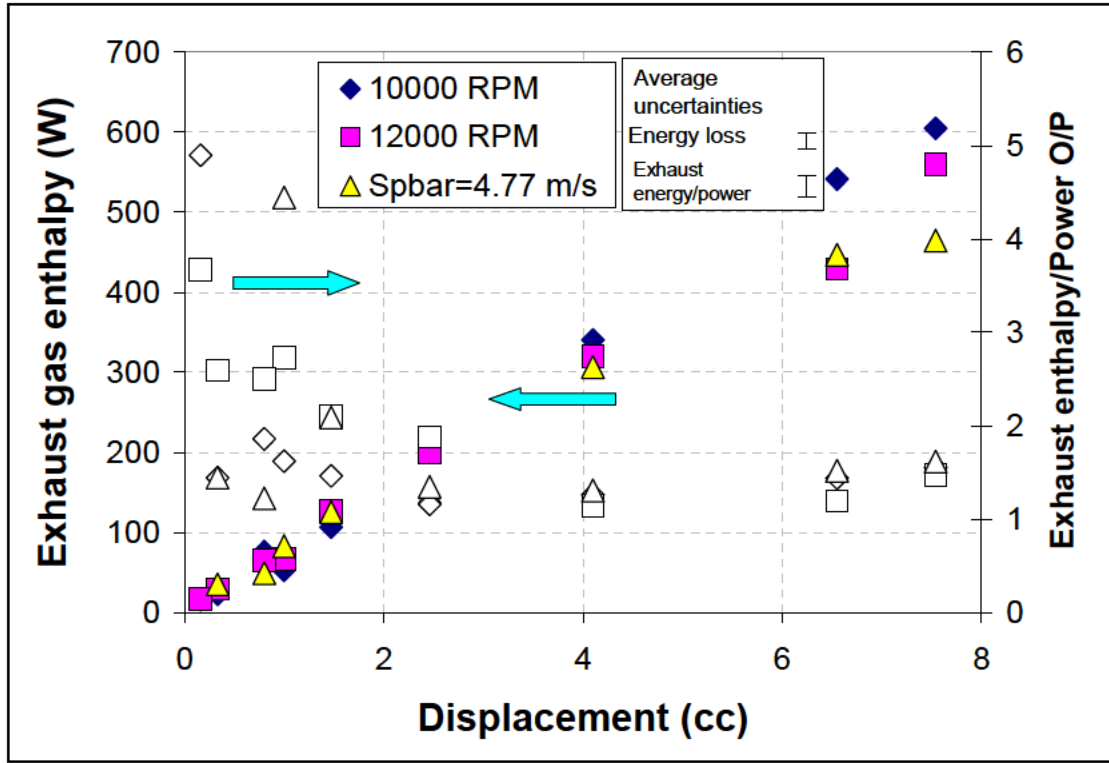


Figure 4–30: Scaling of exhaust enthalpy loss and the ratio of exhaust loss to engine power output as function of engine displacement for two different constant engine speeds of 10000 and 12000 rpm and a constant mean piston speed of 4.77 ms^{-1} . All data sets correspond to an equivalence ratio of ~ 1 .

4.8 Incomplete Combustion Losses

4.8.1 Measurement Technique

Incomplete combustion losses refer to the energy carried by unburnt fuel in the exhaust. Unlike all of the other loss processes that are measured directly, the loss due to incomplete combustion is inferred from the dynamometer measurements of total engine power (on the left hand side of Eqn. 4–17) and independent measurements of thermal and mechanical efficiency, F/A ratio, etc. The value of the combustion efficiency is selected in order to satisfy Eq. 4–17.

4.8.2 Scaling of Combustion Losses

Figure 4–31 shows incomplete combustion losses as a function of F/A for the 9 engines considered in this study. The operating speed is 10000 rpm for all engines and the incomplete combustion energy loss is computed by substituting the combustion efficiency that satisfies Eq. 4–17 into Eq. 4–20. The figure shows that the incomplete combustion loss increases with engine size at constant mixture ratio and is considerably higher than any of other component loss. It also increases with increasing fuel air mixture ratio since the engines operate rich. The energy lost due to incomplete combustion for engines operating at a constant speed of 12000 rpm and a mean piston speed of 4.77 ms^{-1} are presented in figures B–9 and B–10 in appendix B.

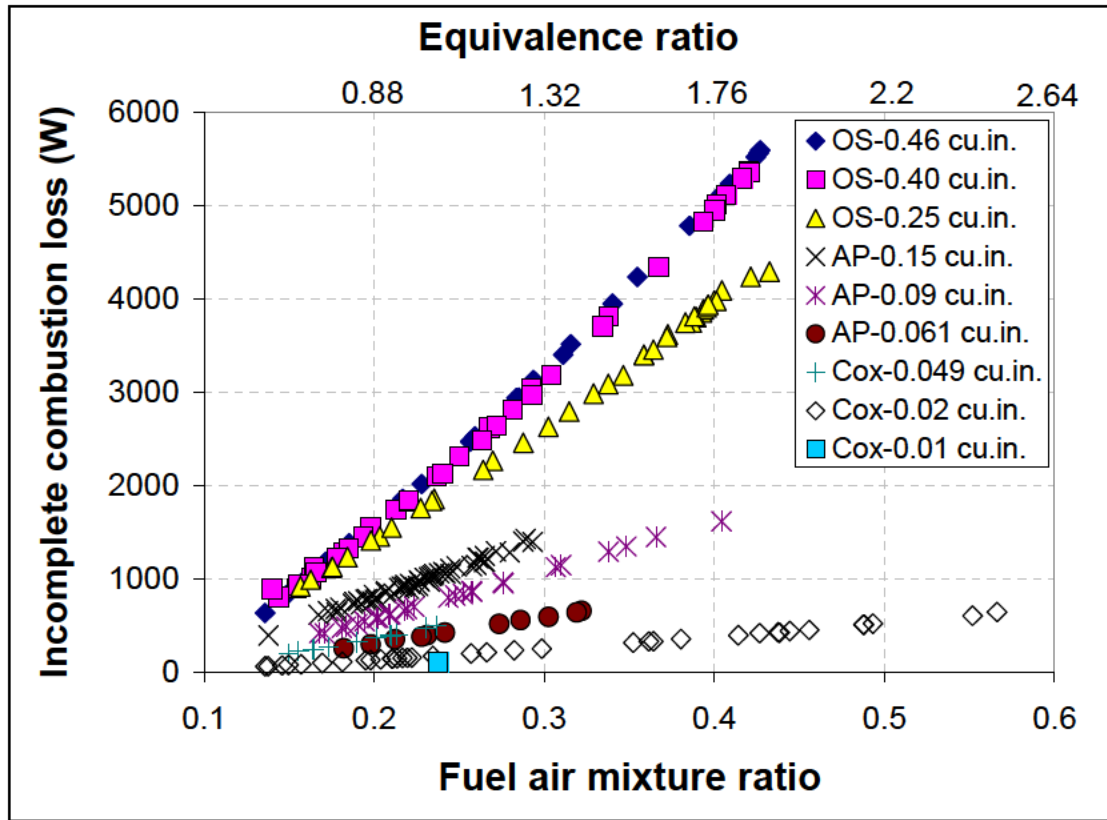


Figure 4–31: Energy lost in incomplete combustion for all engines as a function of fuel air mixture ratio at a constant engine speed of 10000 rpm. Error bars are plotted for a single point in each data set and represent average uncertainty for the entire dataset.

Figure 4–32 shows energy loss due to incomplete combustion and the ratio of combustion loss to engine power output as a function of engine displacement for two constant engine speeds (10000 and 12000 rpm) and one mean piston speed (4.77 ms^{-1}). The equivalence ratio in each data set is about 1. The filled symbols show enthalpy loss while the empty symbols show the ratio of combustion to engine power output. Incomplete combustion losses increase with increasing engine size and vary little between the two constant engine speeds considered here. However, the variation is larger in the constant mean piston speed data. In this case, ratio of combustion loss to engine power output is seen to increase with decreasing engine size going from 5 to

31 or 5 to 26 for the two cases of 10000 and 12000 rpm. This compares to an estimate of 0.13 for a automobile scale SI engine and 0.04 for a automobile scale Diesel engine.

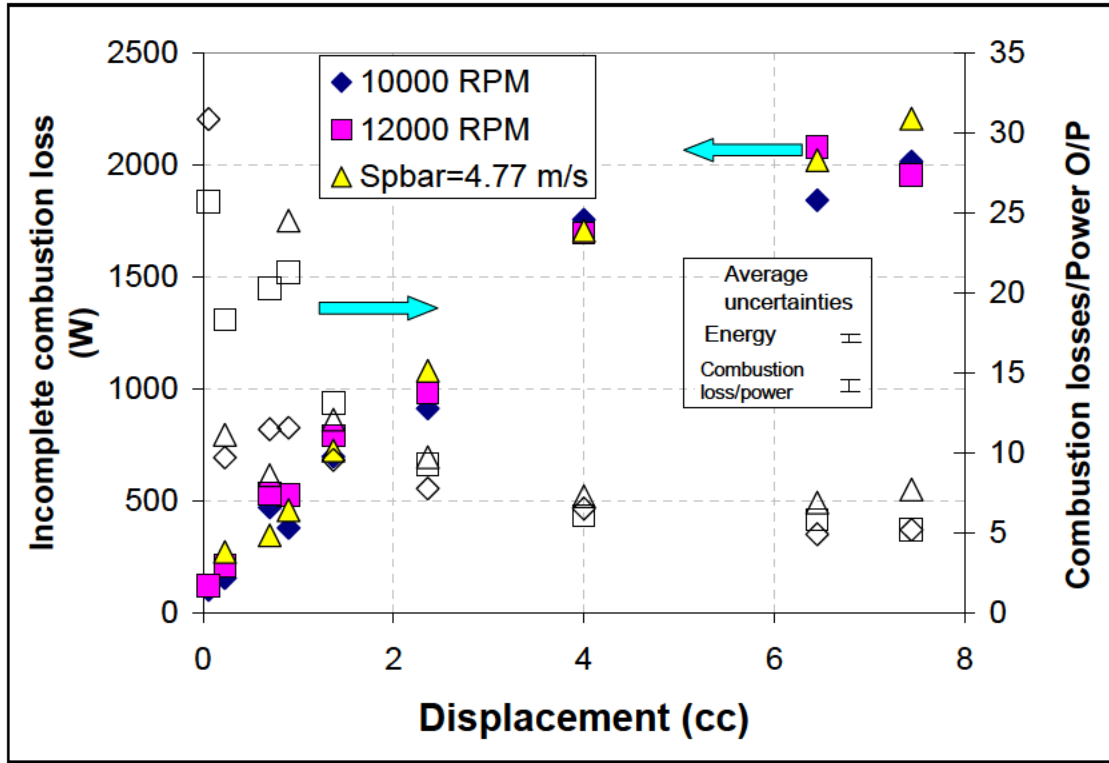


Figure 4–32: Scaling of incomplete combustion losses and the ratio of combustion loss to engine power output as a function of engine displacement for two different constant engine speeds of 10000 and 12000 rpm and a constant mean piston speed of 4.77 ms^{-1} . All data sets correspond to an equivalence ratio of ~ 1 .

4.9 Scaling of Engine Loss Mechanisms

4.9.1 Constant Engine Speed and Fuel Air Mixture Ratio

Figure 4–33 shows the scaling of engine energy losses with engine size. Data is presented for engines operating at a constant speed of 10000 rpm and an equivalence ratio of about 1. Energy lost due to incomplete combustion is plotted on

the y-axis to the right of the figure because it is much larger than the other component energy losses. Mechanical losses are the lowest component losses in all of the engines. Figure 4–34 shows the scaling of the ratio of component energy loss to power output for the same operating conditions as in Fig. 4–34. Data for incomplete combustion loss correspond to the right hand y-axis and the others correspond to the left hand y-axis. All the component losses increase in magnitude relative to engine power output with decreasing engine size. The effect of incomplete combustion is seen to be the largest followed by thermal loss, exhaust enthalpy loss and frictional loss.

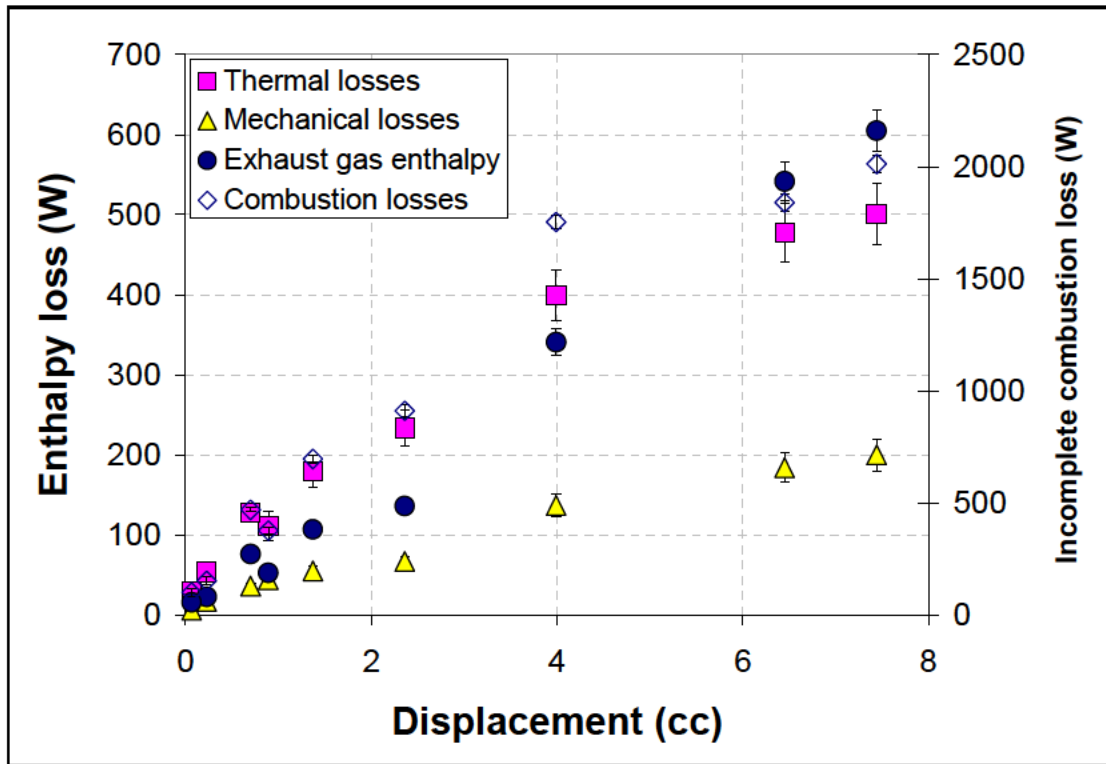


Figure 4–33: Scaling of component enthalpy losses for all engines as a function of engine displacement at a constant engine speed of 10000 rpm and a constant equivalence ratio of ~ 1 .

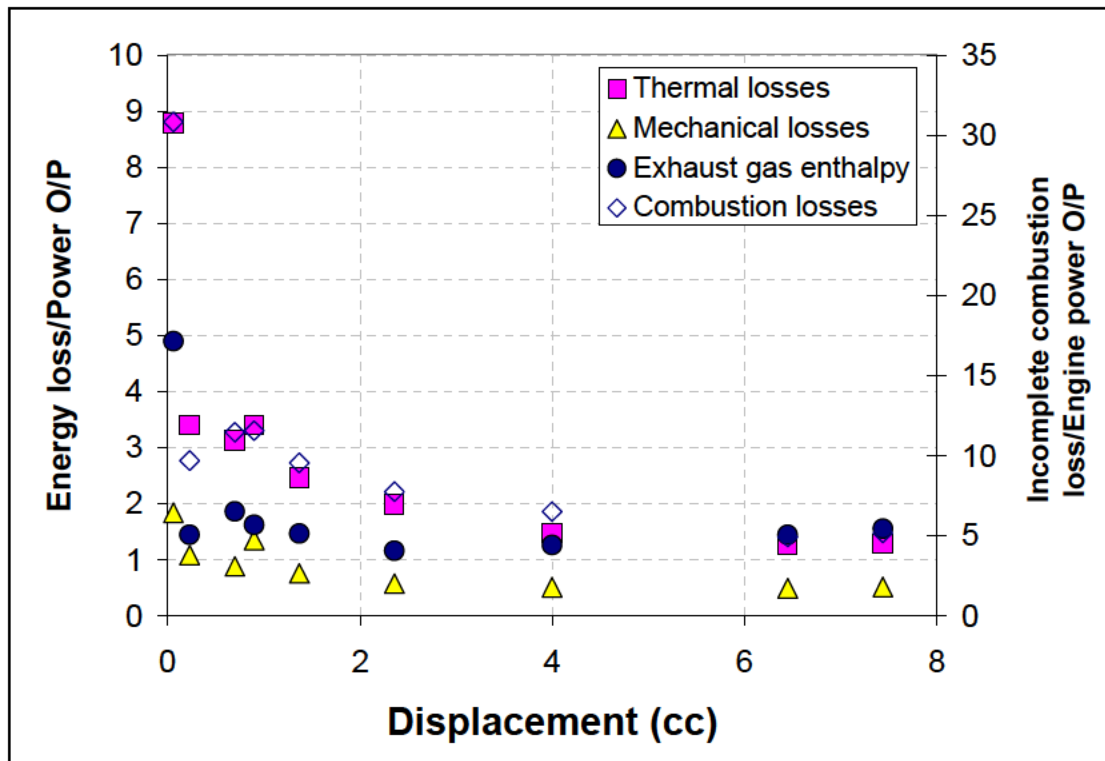


Figure 4–34: Scaling of the ratio of component energy loss to power output for all engines as a function of engine displacement at a constant engine speed of 10000 rpm and an equivalence ratio of ~ 1 .

Figure 4–35 shows the scaling of component efficiency parameters with engine size. Data is presented for all engines operating at a speed of 10000 rpm and a constant equivalence ratio of about 1. The largest contributor to overall cycle inefficiency is the combustion process which is between 4% and 16% efficient. Mechanical losses are the smallest contributor to overall cycle inefficiency. Thermal efficiency which encapsulates the effect of energy loss via convective heat transfer and sensible enthalpy lost in the exhaust is about 70% and varies only slightly with engine size. Combustion and thermal efficiencies improve with increase in engine size as does mechanical efficiency but to a smaller extent. Delivery ratio generally decreases with increasing engine size and, as mentioned previously, is probably

driven by losses due to the muffler. This would explain why the three smallest engines that do not have mufflers have the highest volumetric efficiency.

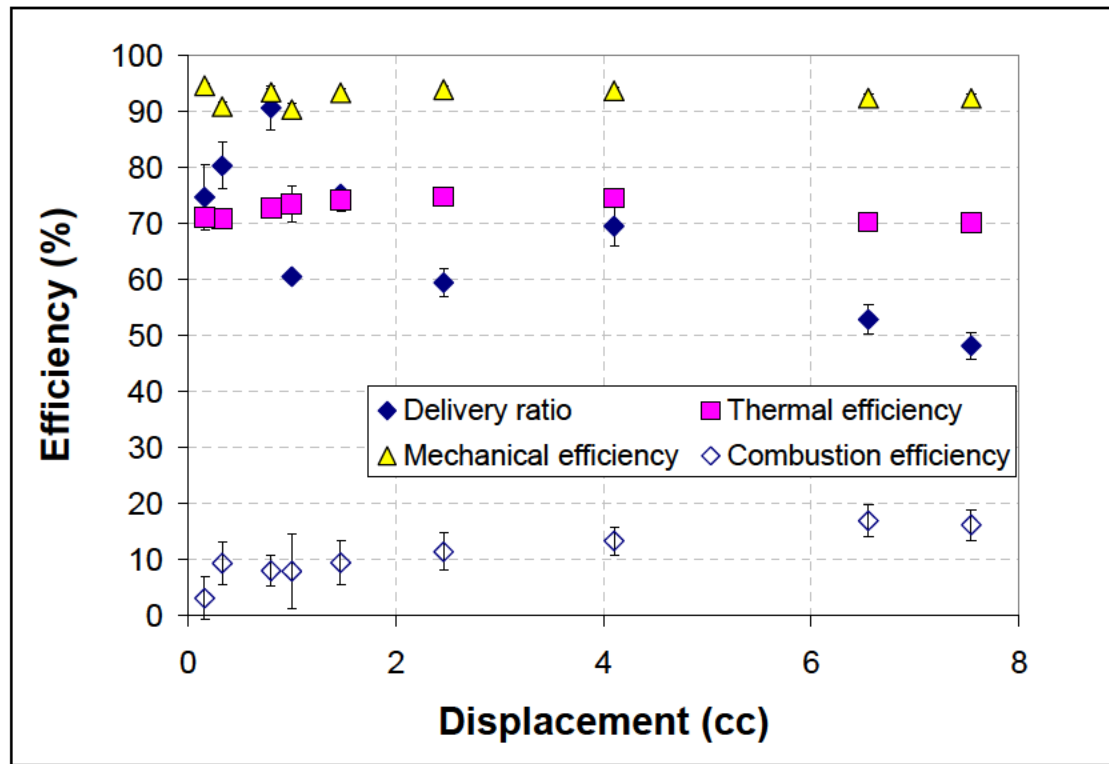


Figure 4–35: Scaling of component efficiencies for all engines as a function of engine displacement at a constant engine speed of 10000 rpm and an equivalence ratio of ~ 1.

4.9.2 Constant Engine Speed of 12000 rpm and Fuel Air Mixture Ratio

Figure 4–36 shows the scaling of component losses and energy released in the exhaust with engine size for a constant operating speed of 12000 rpm and a constant equivalence ratio of about 1. Figure 4–37 shows the scaling of the ratio of component energy loss to power output for the same operating conditions and Fig. 4–38 shows the scaling of component efficiencies with engine size. The results are similar to those observed at 10000 rpm. However, in this case, energy released in the exhaust is seen to be greater than thermal losses for engines having a displacement greater than about 6cc.

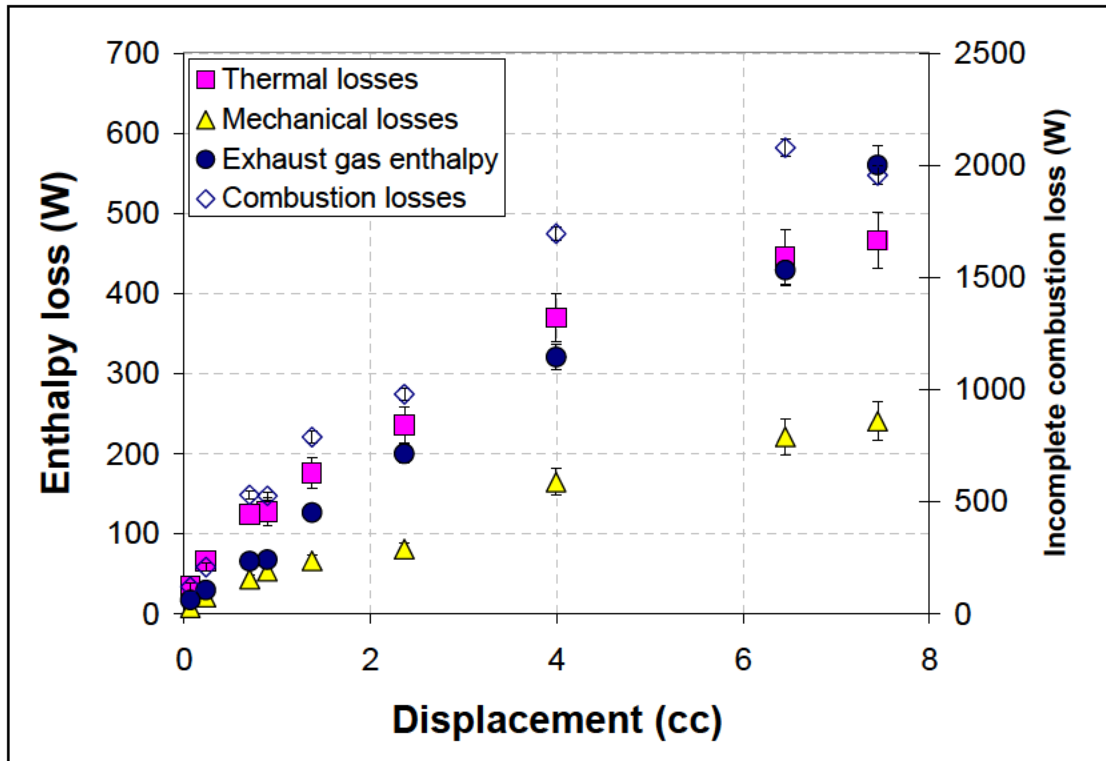


Figure 4–36: Scaling of component enthalpy losses for all engines as a function of engine displacement at a constant engine speed of 12000 rpm and an equivalence ratio of ~ 1 .

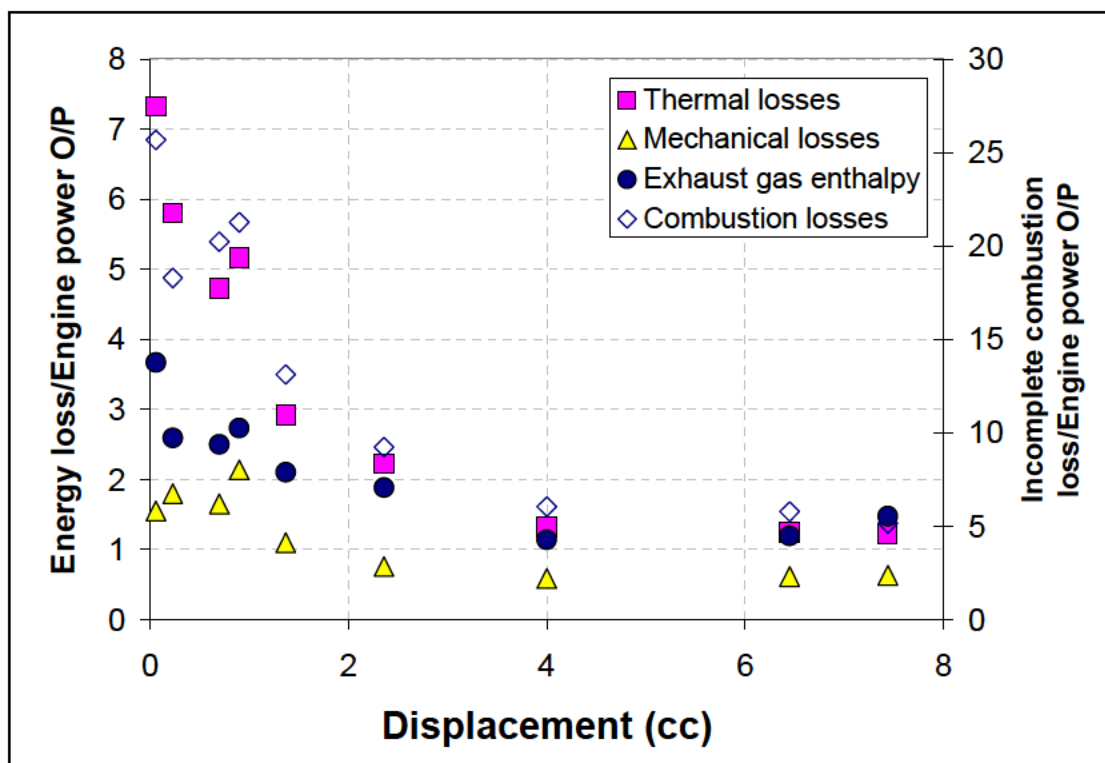


Figure 4–37: Scaling of the ratio of component energy loss to power output for all engines as a function of engine displacement at a constant engine speed of 12000 rpm and an equivalence ratio of ~ 1 .

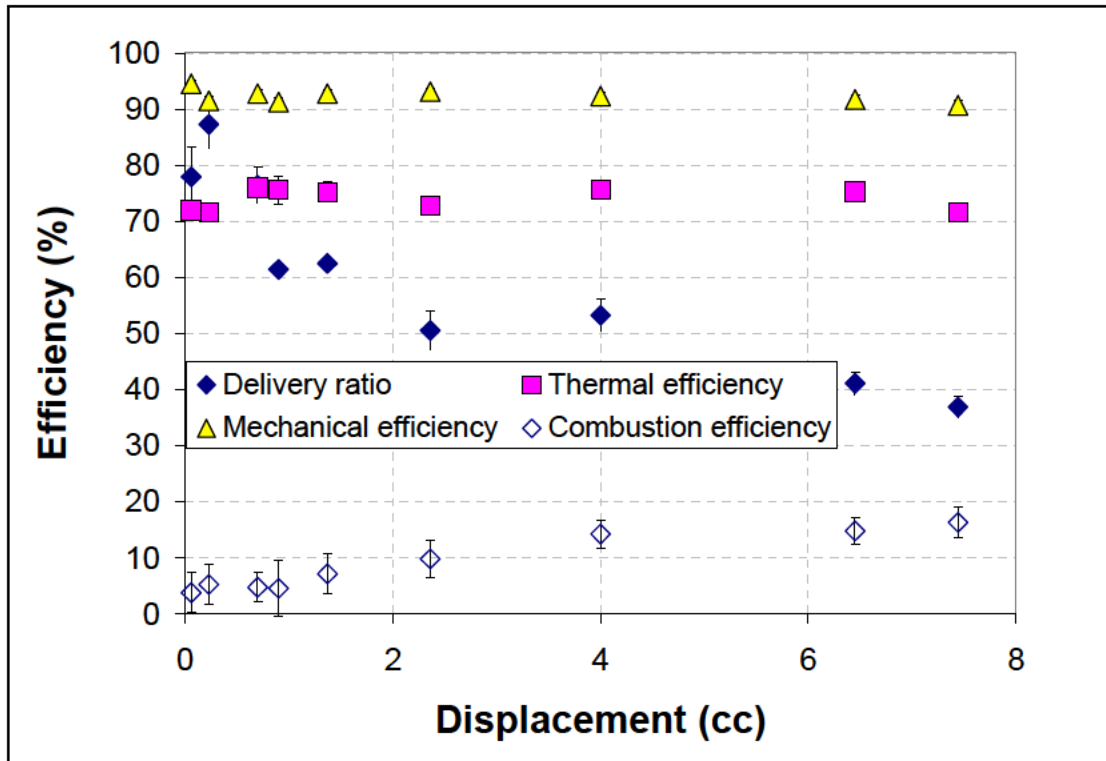


Figure 4–38: Scaling of component efficiencies for all engines as a function of engine displacement at a constant engine speed of 12000 rpm and an equivalence ratio of ~ 1 .

4.9.3 Constant Mean Piston Speed and Fuel Air Mixture Ratio

Figure 4–39 shows the scaling of component losses and energy released in the exhaust with engine size for a constant mean piston speed of 4.77 ms^{-1} and a constant equivalence ratio of about 1. Figure 4–40 shows the scaling of ratio of component energy loss to power output for the same operating conditions while Fig. 4–41 shows the scaling of component efficiencies with engine size. The results for scaling of combustion and mechanical losses are similar to those observed previously at 10000 and 12000 rpm.

Delivery ratios are uniformly higher than in the 10000 and 12000 rpm cases because the operating speeds associated with maintaining constant mean piston speed between engines are generally lower.

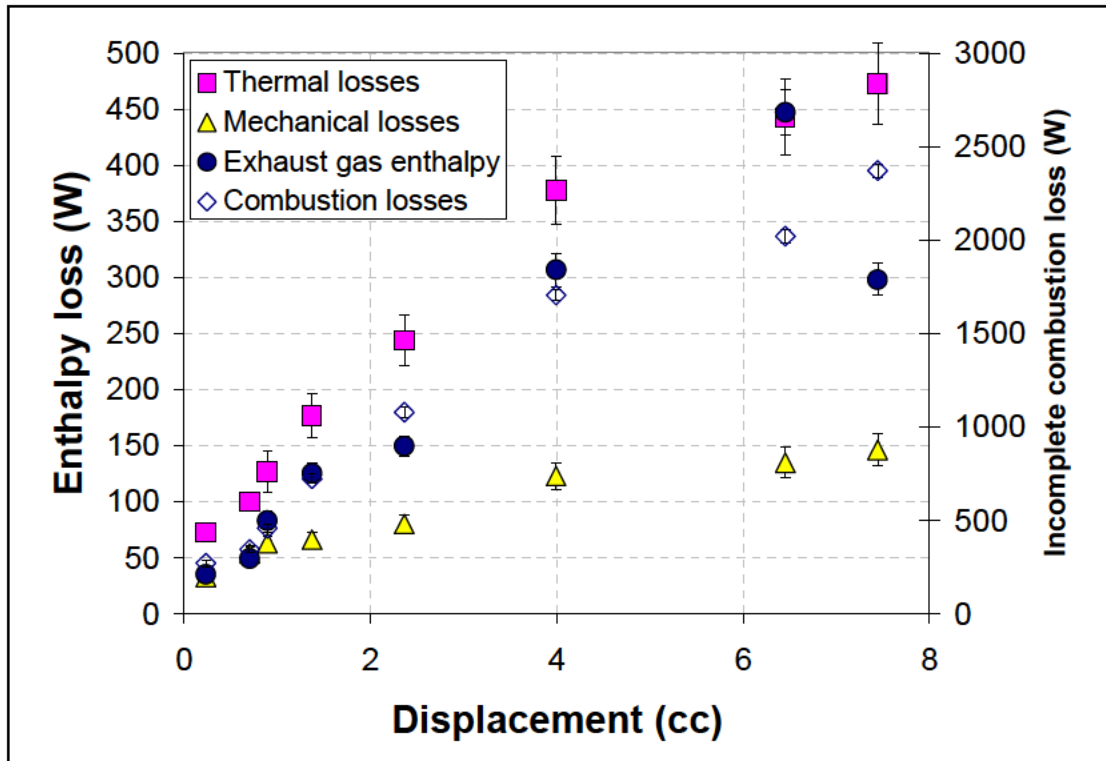


Figure 4–39: Scaling of component enthalpy losses for all engines as a function of engine displacement at a constant mean piston speed of 4.77 ms^{-1} and an equivalence ratio of ~ 1 .

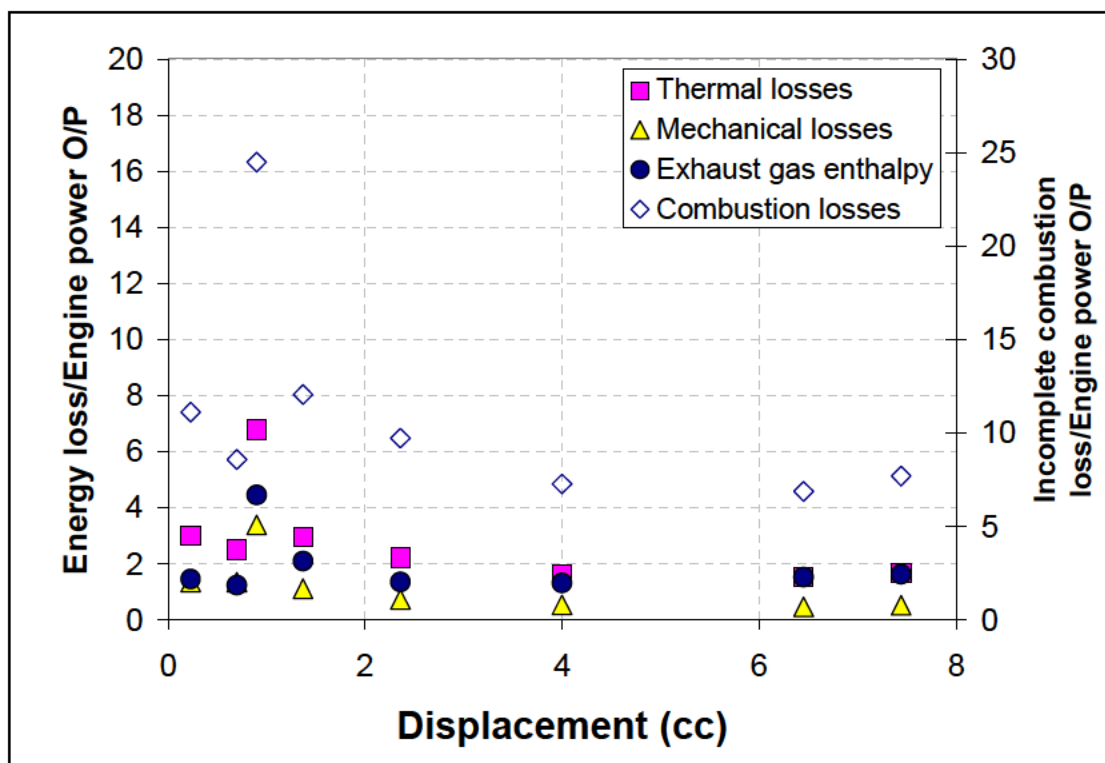


Figure 4–40: Scaling of the ratio of component energy loss to power output for all engines as a function of engine displacement at a constant mean piston speed of 4.77 ms^{-1} and an equivalence ratio of ~ 1 .

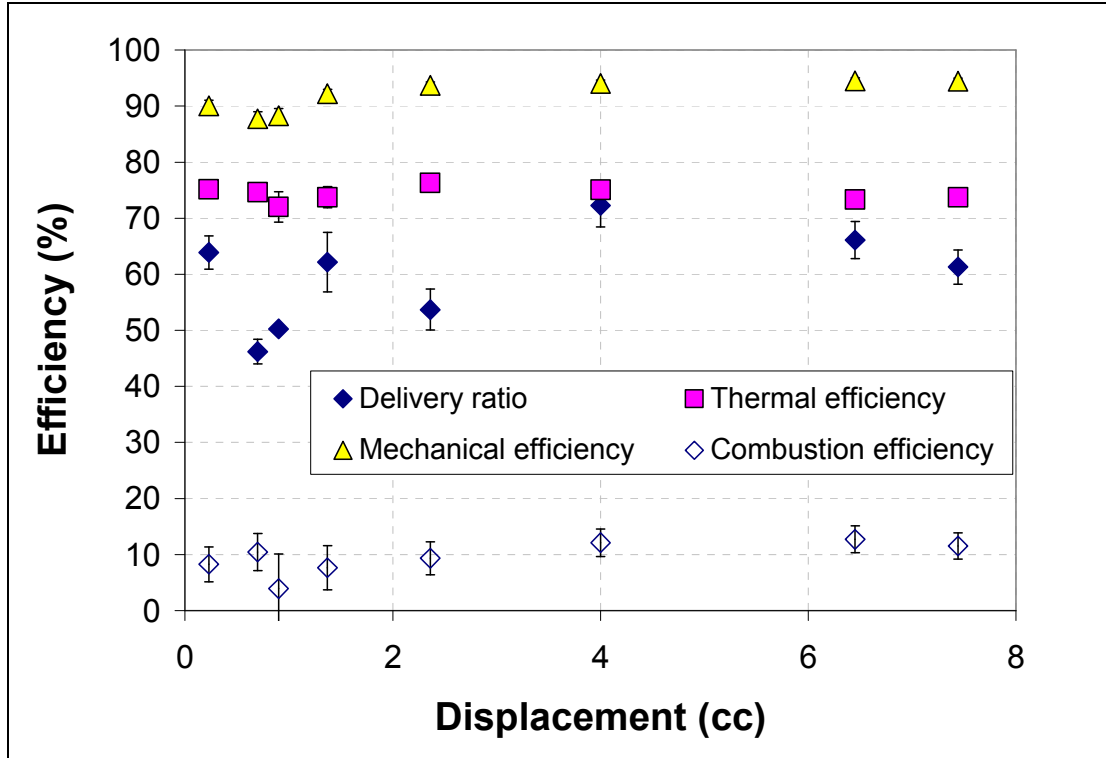


Figure 4–41: Scaling of component efficiencies for all engines as a function of engine displacement at a constant mean piston speed of 4.77 ms^{-1} and an equivalence ratio of ~ 1 .

4.10 Summary of Engine Losses

The investigation of energy loss mechanisms in engine as identified by the control volume analysis presented in Section 4.2 revealed several key findings as summarized below,

- Delivery ratio which characterizes intake losses was found to be chiefly dependent on engine operating speed and flow path configuration (presence/absence of an exhaust muffler). Delivery ratio for smaller engines without mufflers was found to be better than that for larger engines with mufflers at similar operating speeds.

- Mean gas temperature for this class of engines running on glow fuel was estimated as a function of fuel–air mixture ratio and this data was utilized to estimate convective heat transfer losses.
- Mechanical friction and pumping losses were measured and correlations established for friction loss as a linear function of engine speed. Surface to surface contact due to breakdown of the lubrication film was identified to be the major contributor to frictional loss in miniature glow ignited IC engines.
- Sensible enthalpy loss in the exhaust was estimated and found to be independent of mixture ratio at constant speed suggesting that miniature engines are combustion limited.
- Incomplete combustion loss was inferred from the other terms in the energy balance and shown to be by far the greatest contributor to total energy loss.
- A scaling analysis of efficiency components with engine size at similar operating conditions (10000/12000 RPM and $\phi \sim 1$) was performed, which showed the following – mechanical efficiency varied between 90 to 92%, delivery ratio varied from 50–60% for larger engines with mufflers and from 70–90% for smaller engines without mufflers. Thermal efficiency which includes losses due to convective heat transfer and sensible energy in the exhaust varied from 70–75%. Combustion efficiency is found to increase from 3 to 18% with engine size.
- The order of importance of energy loss components was found to be different in miniature IC engines as compared to conventional scale IC engines. Figure 4-42 shows pie charts depicting the contributions of different energy loss

components in percentage form for miniature and automobile scale SI and Diesel engines. The order of importance of engine loss components is seen to be different in miniature engines as compared to automobile scale engines. In case of miniature engines the energy loss components arranged by order of importance are – incomplete combustion, heat transfer, exhaust and friction. For automobile scale engines, the energy loss components arranged by order of importance are – exhaust, heat transfer, friction and incomplete combustion.

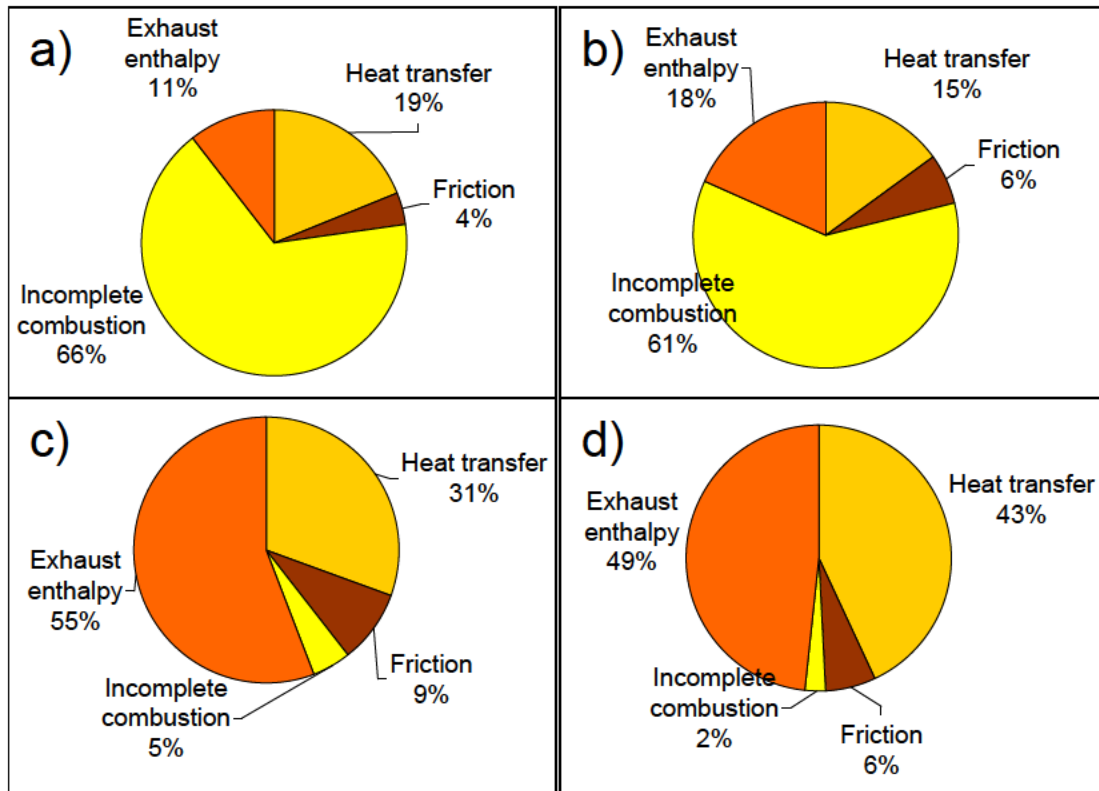


Figure 4–42: Composition of energy losses for different engines. a)Cox 010 engine at 10000 rpm and equivalence ratio ~ 1; b) OS 46 engine at 10000 rpm and equivalence ratio ~ 1; c) Data for automotive spark ignition engine at maximum power as compiled by Heywood¹⁸¹; d) Data for automotive Diesel engine at maximum power as compiled by Heywood.¹⁸²

Chapter 5 : In–Cylinder Pressure Measurements

5.1 In–Cylinder Pressure Measurements

In–cylinder pressure is a fundamental measurement that describes the instantaneous state of the gas mixture in the cylinder volume during an internal combustion engine cycle. Cylinder pressure has been measured in different ways in the past and the data has been used to study various engine phenomena such as ignition¹⁸³, combustion, knock¹⁸⁴ and cycle to cycle variation in the combustion process.¹⁸⁵ Cylinder pressure measurements are also used to estimate heat release rates and mass burning rates that can be input into engine cycle simulations.¹⁸⁶ This greatly simplifies engine simulations by avoiding the need to solve the chemically reacting flow problem. Typically, the measured cylinder pressure can be combined with knowledge of the corresponding crank angle and cylinder volume to provide a simple estimate of the mass burning rate. Heat release rate can be determined by performing an energy balance on the engine cylinder over the course of the engine cycle. A conversion efficiency relating the actual amount of fuel burned to the total amount of fuel carried by the charge mixture can be determined by estimating the gross heat release rate. This requires additional modeling of the heat and mass transfer processes within the engine cylinder. The equations involving these analyses will be described in detail in the sections that follow.

One and two–zone models have been used to describe the combustion process occurring during engine operation. The single zone model assigns identical properties to the burned and unburned regions within the cylinder volume while the two zone model treats the burned and unburned zones as separate entities operating at the same

pressure. The major difference in the analysis as applied to a diesel engine is the fuel injection and vaporization processes which also have to be modeled in order to establish heat release rate.¹⁸⁷ Plotting cylinder pressure as a function of cylinder volume yields a pressure–volume curve that can be integrated to give the net work output of the cycle and the indicated mean effective pressure (IMEP). The power of the engine measured at the output shaft can be used to estimate the brake mean effective pressure (BMEP). The difference between IMEP and BMEP represents the energy loss associated with the conversion from chemical to mechanical power.

The key requirements measuring pressure as a function of cylinder volume are an in–cylinder pressure measurement and a crank angle measurement. Crank angle along with the geometry of the engine parts can be used to estimate instantaneous cylinder volume. In the present work, cylinder pressure is measured using a fiber optic pressure sensor while the crank angle is obtained in one of two ways described in the following sections.

5.2 Experimental Setup

5.2.1 Fiber Optic Pressure Sensor

The traditional instrument for measuring in–cylinder pressure is the piezoelectric pressure transducer. The piezoelectric transducer contains a quartz crystal which, when compressed by the cylinder pressure, generates an electric charge that is proportional to the applied pressure. A charge amplifier converts this charge to a voltage proportional to the cylinder pressure.

Fiber optic pressure sensors are relatively new in the field of engine pressure measurements. They work by measuring the intensity of light reflected from one or

more optical fibers placed in front of a flexing metal diaphragm.¹⁸⁸ The pressure sensor used in this work is produced by Optrand Inc. Figure 5–1 shows photographs of the sensor. Table 5–1 lists the important parameters pertaining to the sensor used in this work.

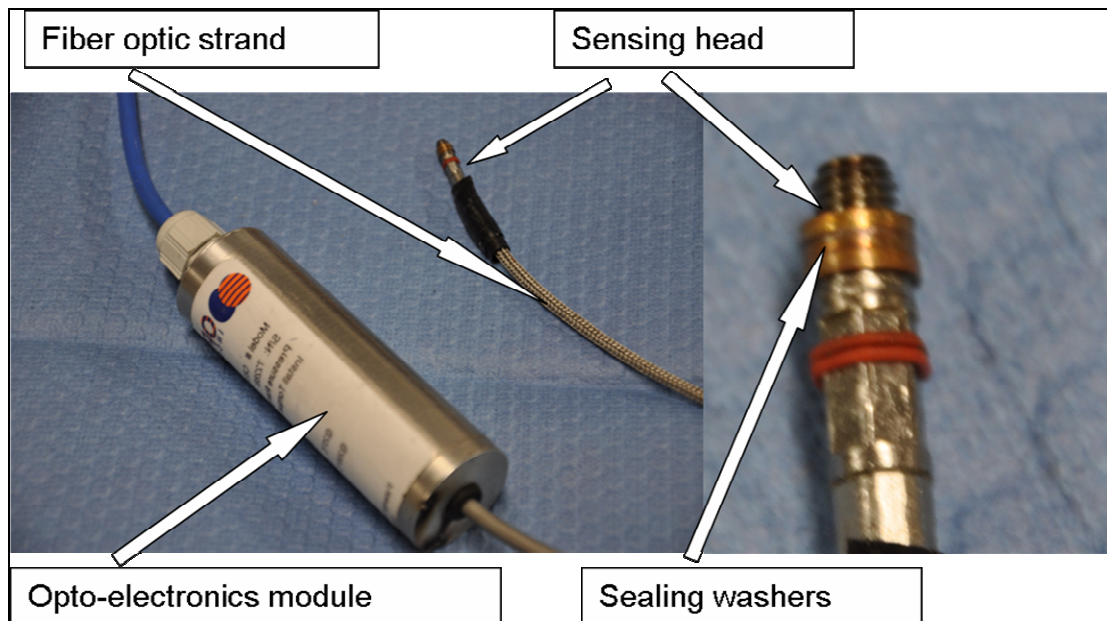


Figure 5–1: Photographs of the Optrand fiber optic pressure sensor – model M3.5x0.6mm.

Sensor type	Fiber optic gauge pressure sensor
Model number	M3.5x0.6
Sensor range	0–3000 psi (0–20864 kPa)
Over pressure	6000 psi (41368 kPa)
Non–linearity and hysteresis	+/- 1–3% of full scale at combustion conditions
Diaphragm resonant frequency	120 kHz
Frequency range	1 Hz – 25 kHz
Sensor housing temperature range	–40 °C to 350 °C
Sensor type	Sealed gauge
Pressure output signal	0.5 – 5 V
Diagnostic output signal	0.5 – 3.6 V
Power supply voltage	9–18 VDC
Current	50 mA
Pressure media	Gaseous or liquid
Vibration	100 G

Table 5–1: Specifications for the fiber optic pressure sensor made by Optrand Inc. used in this work.

Figure 5–2 shows a schematic block diagram of the system which consists of an opto–electronics module, a fiber optic strand and a sensing head that is exposed to cylinder pressure. The opto–electronics module contains all the optical and electronic components of the sensor including a photodiode, an LED, and an application specific integrated circuit (ASIC). The integrated circuit amplifies, filters the photodiode signal, controls the light intensity and provides auto referencing to regulate LED light intensity in response to any undesirable environmental conditions. The LED current level can be monitored to inspect the health of the sensor. The four pin–outs from the sensor include two for power (9–18 VDC), one for sensor output voltage, and one for sensor monitoring.

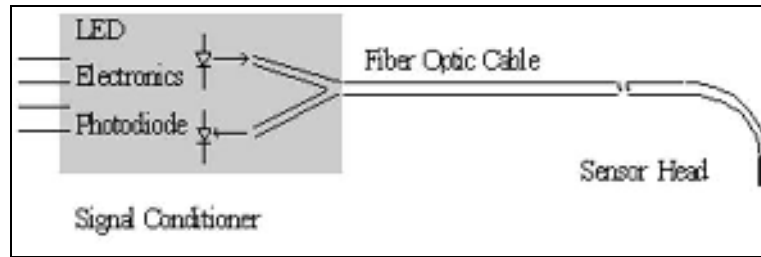


Figure 5–2: Block diagram of the Optrand fiber optic pressure sensor [188].

Figure 5–3 shows a block diagram of the sensor head and Fig. 5–4 shows a dimensioned picture of the M3.5 sensor head used in this work. The sensing metal diaphragm for the sensor used in this application has a diameter of 2.8 mm. The diaphragm has an Optrand patented hat-shaped construction with varying thickness across its diameter.¹⁸⁹ This design allows for large deflection in response to applied pressure while keeping the stresses to a minimum. It is constructed using Inconel, which is a high strength alloy. The diaphragm is welded to the sensor housing. The sensor housing also has a ferrule holding two fibers which are bonded to each other. The head of the sensor has M3.5x0.6 threads which allow the sensor to be screwed into the engine cylinder head. A 5/32” hex head allows the use of a special wrench to tighten the sensor into the mating threads.

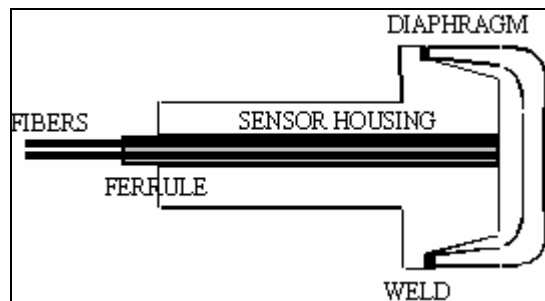


Figure 5–3: Block diagram of the sensor head of the Optrand fiber optic pressure sensor [188].

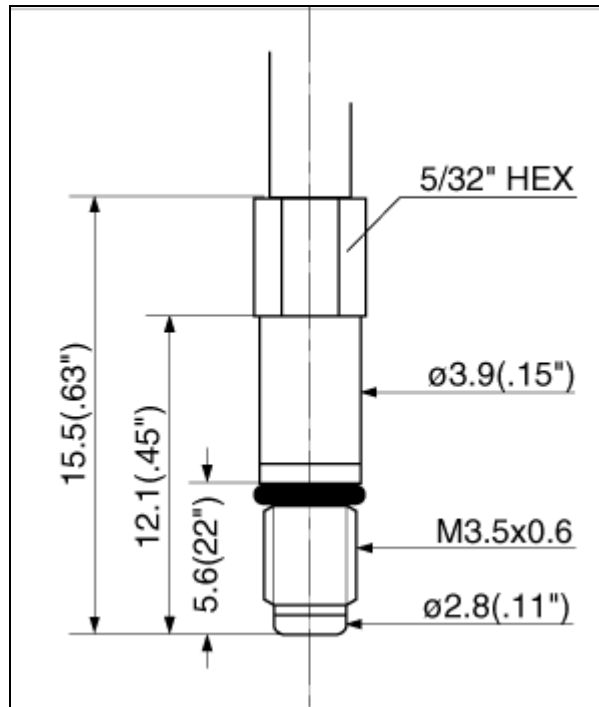


Figure 5–4: Dimensions of the Optrand fiber optic pressure sensor.¹⁹⁰

5.2.2 Engines

Cylinder pressure measurements have been made in three engines: the OS 25 FX, OS 40 FX and the OS 46 FX engines (a–c in Fig. 2–3). The specifications of the engines and the operating speeds at which cylinder pressure measurements are made are summarized in Table 5–2.

Engine Model		Displacement		Mass	Operating speed for cylinder pressure measurements	Geometric compression ratio	Bore	Stroke
A	OS 46 FX	0.46	7.5	488	5,6,7,8,9,10,11	16.52	22	19.6
B	OS 40 FX	0.4	6.5	386	5,6,7,8,9,10,11,12	14.49	20.5	19.6
C	OS 25 FX	0.25	4.1	248	6,8,9,10	17.96	18	16
		cu. in.	cc	g	krpm		mm	mm

Table 5–2: Specifications of miniature IC engines tested in the study.

5.2.3 Sensor Installation

Figure 5–5 shows the installation of the sensor in the cylinder head of an OS–46 FX engine. The small size of the engine cylinder head makes it difficult to install the pressure sensor without leaking and changing the dead volume appreciably. This is accomplished by using a milling machine to drill a hole corresponding to the tap size for the threads on the pressure sensor with the cylinder head mounted upside down on the mill. The cylinder head is then turned over and an end mill is used to produce a flat boss that provides a sealing surface for the pressure sensor’s sealing washers. The smaller hole drilled previously using the drill bit is then tapped using an M3.5x0.6 mm metric tap. A portion of the fins on the cylinder head have to be machined off in order to allow access for the hex wrench to tighten the pressure sensor. Different numbers of sealing washers are used with different engines so as to minimize changes in dead volume over the unmodified engine. The sensor is screwed in just far enough so that it forms very nearly a continuous surface on the bowl within the cylinder head.

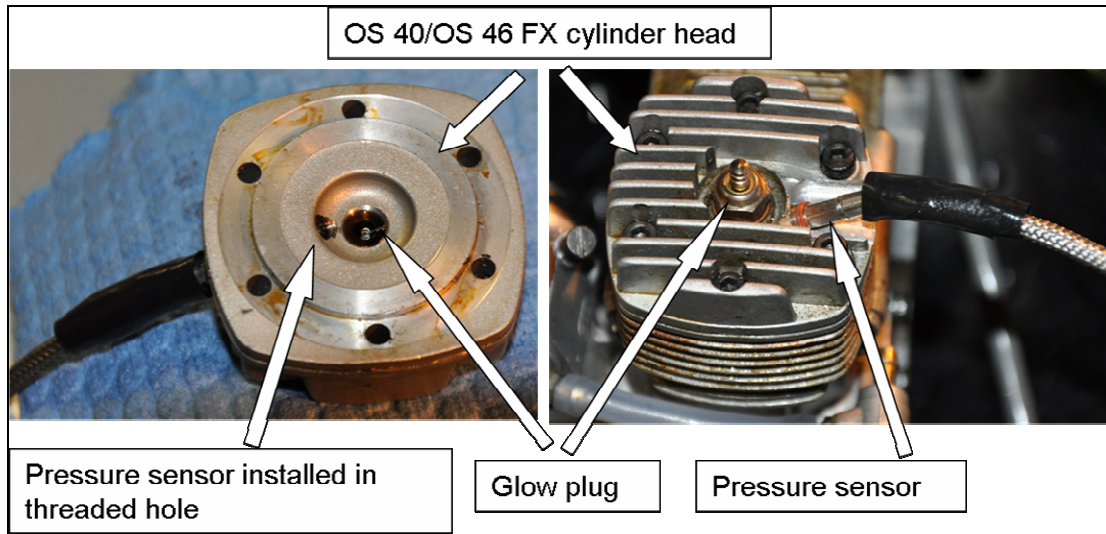


Figure 5–5: Optrand fiber optic pressure sensor mounted on the stock cylinder head of the OS 46/OS 40 FX engine.

5.2.4 Crank angle measurement

Two different methods were used to measure crank angle. The first approach uses the optical speed sensor described in Chapter 2 while the second approach uses the output from a rotary shaft encoder to determine crank angle location. Each technique is described in the following sections.

5.2.4.1 Measurement Using Optical Speed Sensor

The optical speed sensor developed by Monarch instruments is designed to produce a single square pulse in response to the passing of a reflecting tape attached to the engine shaft. The change in signal output occurs at the edges of the tape. Figure 5–6 shows sensor voltage as a function of time as the tape sweeps across the field of view of the sensor. As the leading edge of the tape goes past the sensor, the presence of the reflecting tape across the face of the sensor causes the output voltage to drop from 3.5 V to about 0 V. The voltage output stays close to 0 V until the trailing edge goes past the sensor and the voltage rises back to about 3.5 V. The rise time of the

signal is approximately 0.17 microseconds. During the experiments, the tape glued on to the engine shaft is placed in a manner such that its leading edge aligns with top dead center (TDC) location of the piston. A LABVIEWTM data acquisition program records the output of the speed sensor and pressure sensor at frequency of 60 kHz. This gives between 450 to 260 pressure readings per revolution for engine speeds ranging from 8000–14000 rpm. The voltage output from both sensors is written to a file along with the system time in microseconds. The crank angle location corresponding to each pressure reading is determined by linearly interpolating between each TDC pulse. The time between TDC pulses gives the engine speed. This method of crank angle measurement requires less hardware as compared to the shaft encoder approach discussed in the next section. The speed sensor is the same as that used on the dynamometer for engine speed measurement and control. As will be discussed in the following section, mechanical shock and vibration on the dynamometer setup during engine runs increases chances of damage to the shaft encoder. The measurement resolution (number of pressure measurements per engine cycle) is only limited by the frequency response of the cylinder pressure sensor which is of the order of 120 kHz. Also, the maximum speed at which this measurement can be obtained is only limited by the capabilities of the speed sensor which is of the order of 250 krpm. The chief disadvantage of this method is that the crank angle location is extrapolated using timing between successive voltage signals from the speed sensor. Any variation in speed during the course of engine operation would introduce inaccuracy in the measurement results.

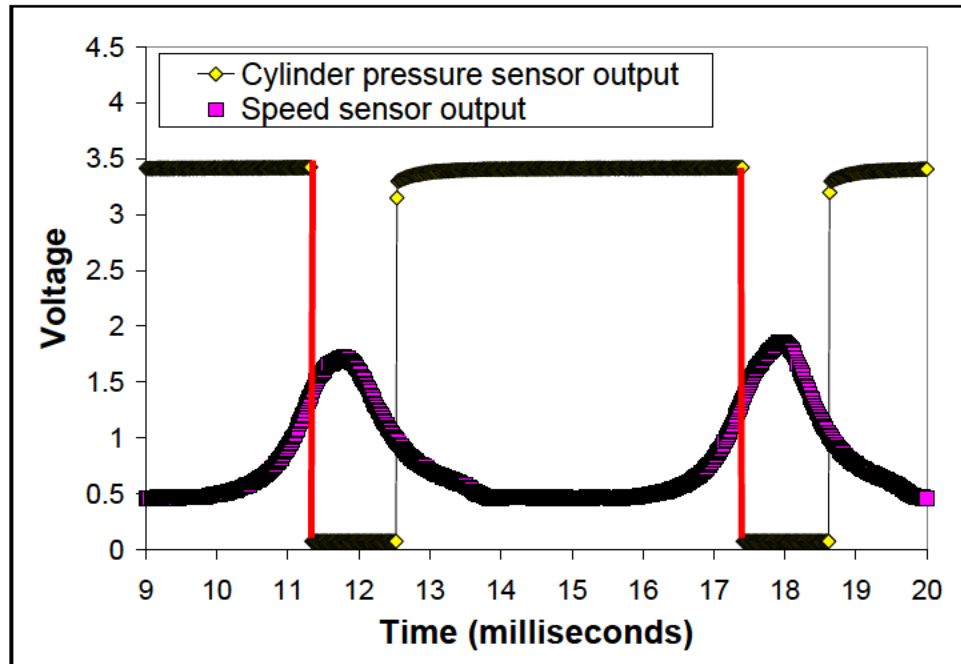


Figure 5–6: Voltage output from the optical speed sensor plotted as a function of time. The straight lines highlighted in red represent the location of piston top dead center (TDC).

5.2.4.2 Measurement Using Shaft Encoder

The second approach to determining the crank angle locations corresponding to individual cylinder pressure measurements used rotary shaft encoders. Two different types manufactured by Encoder Products Inc. were used in this work. The encoders are incremental type quadrature encoders whose output consists of two separate pulse trains as well as an index pulse which can be aligned with any position of the crank shaft. While an absolute encoder produces a unique output for any distinct position of the shaft, the incremental encoder requires an index pulse and a counter to establish the location of the shaft. The index pulse is provided by the encoder and the counting is done using the data acquisition hardware.

Preliminary investigations were conducted using the model 121 auto-aligning shaft encoder illustrated in Fig. 5–7. It features a bearing-less design that allows it to

operate at rotational speeds up to 12000 rpm. Table 5–3 compares the model 121 encoder to the model 260 encoder (Fig. 5–8) which was also used in this work. The model 260 incorporates a bearing that makes it more robust. While the auto-aligning feature of the model 121 made it easier to install on the dynamometer, it was not robust enough and repeated failures led to its eventual replacement by the model 260 which has higher resistance to shock and vibration.



Figure 5–7: Photograph of the Model 121 bearingless auto aligning shaft encoder manufactured by Encoder Products.¹⁹¹



Figure 5–8: Photograph of the Model 260 shaft encoder manufactured by Encoder Products.¹⁹²

Model	121	260
Encoder type	Auto aligning modular thro–bore	Ultra versatile commutated thro–bore
Commutation	None	
Bore size	9.525 mm (0.375 inch)	
Operating temperature	0–100 °C	
Counts per revolution	360	
Number of channels	Quadrature A & B with index	
Output type	Open collector	
Maximum frequency	200 kHz	
Input voltage	5 VDC	
Input current	100 mA	
Output format	Incremental – Two square waves with quadrature and channel A leading channel B for clockwise shaft rotation as viewed from the mounting face	
Index	Once per revolution gated to channel A	
Accuracy	0.1 degree	
Maximum shaft speed	Determined by frequency response	14000 rpm
Maximum acceleration	$1 \times 10^5 \text{ rad/sec}^2$	

Table 5–3: Specifications of the two different shaft encoders utilized in this work.

The basic construction of the encoder of either type (model 121 or model 260) is illustrated in Fig. 5–9.¹⁹³ The encoder consists of a glass disk with radial patterns photographically deposited in the form of tracks. The glass disk is coupled to the shaft whose angular position is to be determined. For the incremental encoders used here, the disk is coated with two tracks. Light from an infrared emitter is interrupted by the radial lines on each track and this interruption is detected by phototransistors placed on the opposite side of the track. The sensor used with each track on the incremental encoder produces a periodic signal while the phase relationship between the two signals determines the direction of rotation.

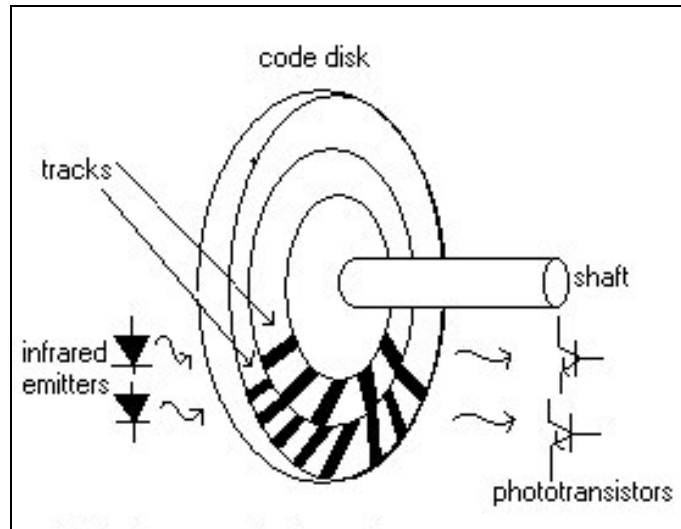


Figure 5–9: Schematic showing the construction of the glass disk and location of light emitters and phototransistors on an incremental shaft encoder [193].

Figure 5–10 shows a schematic illustration of the waveform outputs from the different lines corresponding to shaft rotation and passage of the tracks across the field of view of the phototransistor. The phase relationship between the waveform outputs is used to determine the direction of rotation. In this work, channel A leads channel B. The index pulse which is gated to channel A provides a single reference point which can be aligned with any point of the shaft. A set screw on the shaft encoder allows the rotating part to be locked on to the engine shaft at any location. However, it proved difficult to lock the shaft encoder to the engine shaft with the index pulse exactly aligned with TDC. Therefore, it was necessary to determine the offset angle of the index pulse from TDC before each engine run.

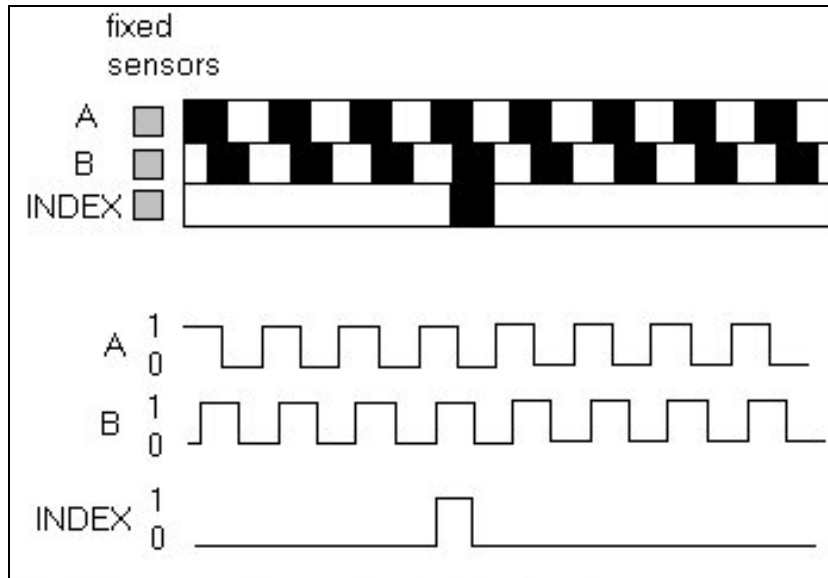


Figure 5–10: Schematic of the waveform outputs from different tracks on the incremental shaft encoder as well as the index pulse [193]. Index pulse is gated to channel B.

An example code available in LABVIEW™ (Measure Angular Position.vi) is used to establish the offset angle of TDC from the index pulse. The procedure is to remove the glow plug from the cylinder head and place a shoulder screw on the piston face. The linear motion of the screw is observed as the engine shaft is manually cranked, while the corresponding crank angle is observed on the LABVIEW™ output screen. Since the piston has a small amount of dwell at TDC, the crank angles corresponding to the piston reaching its topmost position and leaving the topmost position are recorded multiple times. TDC is taken to be the average location between these two events. This average angle is the offset used during post processing to map encoder position to crankshaft position. The offset angle is measured before and after engine runs to ensure that the encoder remained rigidly attached to the crankshaft for the entire run. Both the model 121 and 260 shaft encoders produce 360 pulses per revolution so one pulse corresponds to one degree of crankshaft rotation.

5.2.5 Data Acquisition

An additional National Instruments data acquisition module (NI USB-6221 BNC) shown in Fig. 5-11 is used to measure signals from the cylinder pressure sensor and the A and B and index channel outputs of the quadrature encoder. A different LABVIEWTM program (compared to that described in Chapter 2) simultaneously records data from the cylinder pressure sensor and the shaft encoder. During engine operation, the index pulse from the shaft encoder (channel A) is used to trigger the acquisition of cylinder pressure data for each engine cycle. Since the encoder produces 360 pulses per revolution, pressure data is acquired for every degree of crank angle rotation. Additionally, since the acquisition of data from each engine cycle is triggered by the index pulse, any pulse missed by the shaft encoder in one engine cycle does not lead to a measurement error in the next engine cycle. The code also displays an error message if any single pulse on the encoder is missed and the data obtained in that case is disregarded and the measurement is repeated. This was found to occur a few times at the highest engine speeds. The software is configured to record cylinder pressure measurements for 50 cycles (corresponding to 18000 data points) for each engine operating condition.



Figure 5–11: National Instruments USB–6221 BNC data acquisition module used to sample voltage signals from the cylinder pressure sensor.

5.2.6 Dynamometer Setup

The dynamometer is set up using a belt drive as described in Chapter 2 for the three engines (engines a–c in Fig. 2–3) investigated in this study. Table 5–2 lists the operating speeds at which measurements were made in each engine. At each operating speed, measurements were obtained for multiple fuel–air mixture ratios. The major additions to the previous dynamometer setup are the cylinder pressure sensor mounted on the engine cylinder head and the shaft encoder coupled to the engine shaft. Figure 5–12 shows a photograph of the dynamometer setup for cylinder pressure measurement of the OS 40 FX engine. One end of a steel shaft is mounted and locked on to the through–bore encoder. The shaft is supported by two high speed bearings mounted in the aluminum pillow block. The other end of the shaft is coupled

to a high–offset slotted disc shaft coupling. An acetal disc connects the coupling to a mating one mounted on the end of a steel shaft screwed on to the engine shaft. The steel shaft coupled to the engine shaft also supports the driver pulley which is connected to the driven pulley using a V–belt. Tensioning is provided by an idler pulley arrangement. Among the different approaches discussed previously for determining crank angle, the shaft encoder measurements using the model 260 encoder were found to be most reliable and repeatable. Therefore, this was the encoder used to make cylinder pressure measurements in all three engines investigated here.

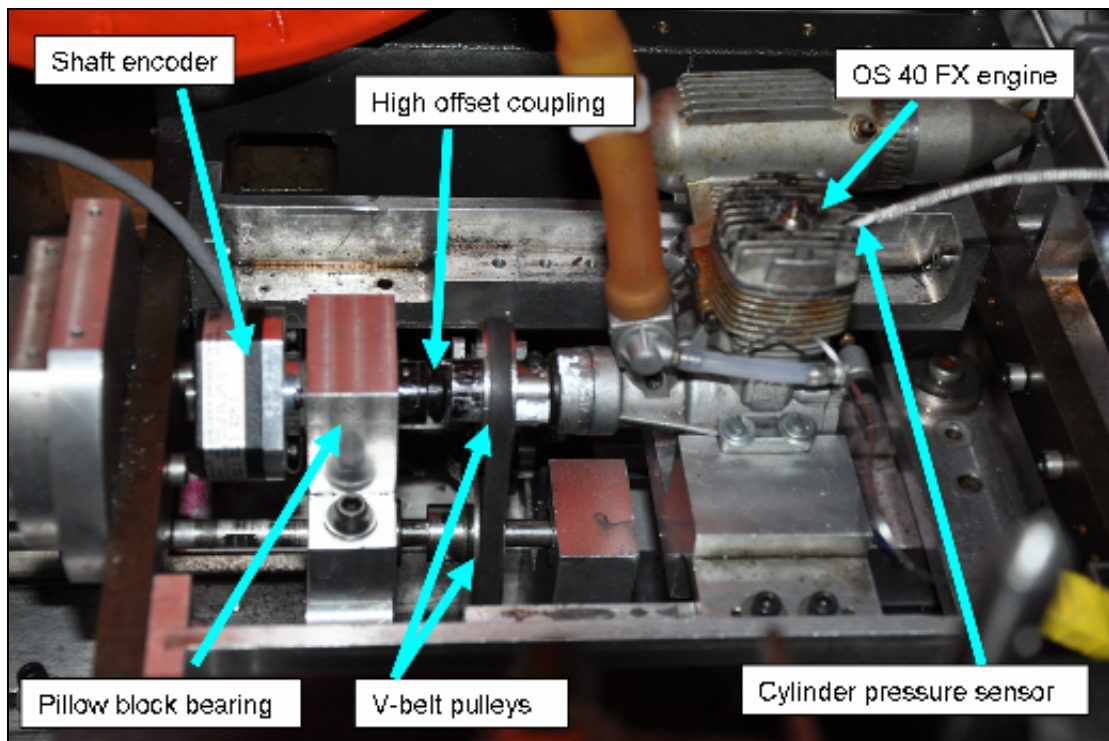


Figure 5–12: Dynamometer setup for the cylinder pressure measurements on the OS 40 FX engine.

5.2.7 Test Procedure

The engine is started on the dynamometer in the usual manner using a starter motor and by applying current to the glow plug. All measurements are performed at wide open throttle (WOT). The control system is switched on and the desired engine speed and mixture needle valve settings are established. Measurements are obtained from all the sensors on the dynamometer including the cylinder pressure sensor and the shaft encoder using the LABVIEWTM codes described earlier. The mixture valve is adjusted to a new mixture setting and the measurements are repeated. The same procedure is then repeated for different engine speeds and finally for different engines.

5.3 Analysis of results

5.3.1 Peak Cylinder Pressure and Corresponding Crank Location

Peak cylinder pressure in each cycle is established directly from the cylinder pressure traces. Since measurements are obtained over 50 cycles at each operating condition, average peak cylinder pressure can be computed. The average crank angle corresponding to peak pressure can also be computed. The peak cylinder pressure over 50 cycles and the corresponding crank angle location is also determined.

5.3.2 Cycle-To-Cycle Variation

The cycle-to-cycle pressure variation is the coefficient of variation of the peak pressures measured in each cycle. The coefficient of variation (COV) gives a normalized measure of the dispersion of the data and is defined as follows,¹⁹⁴

$$COV = \frac{\text{Standard deviation}}{\text{Mean}} = \frac{\sigma}{\mu} \quad (5-1)$$

where μ is the mean and σ is the standard deviation of N samples,

$$\mu = \frac{1}{N} \sum_{i=1}^N x_i \quad (5-2)$$

$$\sigma = \sqrt{\frac{1}{N} \sum_{i=1}^N (x_i - \mu)^2} \quad (5-3)$$

5.3.3 Burn Rate Analysis

Burn rate analysis is commonly used to estimate the fraction of fuel in the cylinder that is burned as a function of crank angle.¹⁹⁵ The mass fraction burned (MFB) is a normalized quantity varying from 0 to 1 that describes rate at which fuel mass is consumed. MFB is useful because it enables one to understand how engine speed, fuel–air mixture ratio, and engine size influence the combustion process. Different approaches have been followed in previous work to estimate the mass fraction burnt (MFB) and two of these are discussed in the sections below.

5.3.3.1 Rassweiler and Withrow Approach¹⁹⁶

The compression and expansion of the charge is modeled as a polytropic process where the pressure–volume relationship is given by,

$$pV^n = \text{constant} \quad (5-4)$$

The polytropic exponent n is assumed to be 1.3.¹⁹⁷ The instantaneous change in cylinder pressure is attributed to a change in pressure due to volume change $(dP_V)_i$

and a pressure rise due to combustion $(dp_C)_i$. Therefore, the net change in pressure at any crank angle interval i can be expressed as,

$$\left(\frac{dp}{d\theta}\right)_i = \left(\frac{dp_C}{d\theta}\right)_i + \left(\frac{dp_V}{d\theta}\right)_i \quad (5-5)$$

The change in pressure due to volume change at the i^{th} interval can be obtained using polytropic relations as,

$$\left(\frac{dp_V}{d\theta}\right)_i = p_{i+1} - p_i = p_i \left[\left(\frac{V_i}{V_{i+1}} \right)^n - 1 \right] \quad (5-6)$$

Substituting Eq. 5-5 into 5-6 and rearranging gives the pressure rise due to combustion in the i^{th} interval,

$$\left(\frac{dp_C}{d\theta}\right)_i = \left(\frac{dp}{d\theta}\right)_i - p_i \left[\left(\frac{V_i}{V_{i+1}} \right)^n - 1 \right] \quad (5-7)$$

where the total pressure rise, $(dp)_i$ is obtained from the cylinder pressure measurements while the pressure rise due to volume change, $(dp_V)_i$ is obtained using cylinder pressure and volume estimated using crank angle position. The mass fraction burned is then estimated as,

$$MFB = x_b = \frac{m_b(i)}{m_b(total)} = \frac{\int_{\theta_{start}}^{\theta} \frac{dp_C}{d\theta}}{\int_{\theta_{start}}^{\theta_{end}} \frac{dp_C}{d\theta}} = \frac{\sum_{\theta_{start}}^{\theta} \Delta p_C}{\sum_{\theta_{start}}^{\theta_{end}} \Delta p_C} \quad (5-8)$$

The value of the polytropic exponent (n) is assumed to be constant in this analysis. Equation 5-8 shows that crank angles corresponding to the beginning and end of the combustion process also need to be estimated. The techniques used to

estimate the start of combustion and combustion duration are detailed in sections 5.3.7 and 5.3.8 below.

5.3.3.2 Mccuiston, Lavoie and Kauffman (MLK) Model^{198 199}

As in the previous method by Rassweiler and Withrow, the compression and expansion processes are approximated using a polytropic process,

$$pV^n = \text{constant} \quad (5-9)$$

At any point during the combustion process when the cylinder pressure is p , the cylinder volume is broken into burned (V_u) and unburned (V_b) components as follows,

$$V = V_u + V_b \quad (5-10)$$

The subscript 0 denotes the beginning of the combustion event and the subscript f denotes the end of the combustion event. Scaling back the unburned gas volume to the point of ignition using Eqn. 5-9 gives,

$$V_{u,0} = V_u \left(\frac{p}{p_0} \right)^{1/n} \quad (5-11)$$

The corresponding burnt gas fraction at the beginning of combustion is given by,

$$x_b = 1 - \frac{V_{u,0}}{V_0} \quad (5-12)$$

Scaling forward to the end of combustion, the burned gas volume is given by,

$$V_{b,f} = V_b \left(\frac{p}{p_f} \right)^{1/n} \quad (5-13)$$

At the end of combustion, the burnt mass fraction is given by,

$$x_b = \frac{V_{b,f}}{V_f} \quad (5-14)$$

Using equations 5-11 and 5-12 we have,

$$x_b = 1 - \frac{V_{u,0}}{V_0} = 1 - \frac{V_u \left(\frac{p}{p_0} \right)^{1/n}}{V_0} \quad (5-15)$$

Substituting equation 5-10 into 5-15 we have,

$$x_b = 1 - \frac{(V - V_b) \left(\frac{p}{p_0} \right)^{1/n}}{V_0} \quad (5-16)$$

Substituting equation 5-13 into 5-16 we have,

$$x_b = 1 - \frac{\left(V - \frac{V_{b,f}}{\left(\frac{p}{p_f} \right)^{1/n}} \right) \left(\frac{p}{p_0} \right)^{1/n}}{V_0} \quad (5-17)$$

Substituting equation 5-14 into 5-17 we have,

$$x_b = 1 - \frac{\left(V - \frac{x_b V_f}{\left(\frac{p}{p_f} \right)^{1/n}} \right) \left(\frac{p}{p_0} \right)^{1/n}}{V_0} \quad (5-18)$$

Further simplification of Eqn. 5-18 gives the following relation for burnt mass fraction,

$$x_b = \frac{P^{1/n}V - P_0^{1/n}V_0}{P_f^{1/n}V_f - P_0^{1/n}V_0} \quad (5-19)$$

The main difference between the MLK model and that of Rassweiler and Withrow is that the MLK model is volume based while Rassweiler's method is mass based. The MLK model, as in the method of Rassweiler and Withrow, requires knowledge of the start of combustion, the duration of burning, and the polytropic exponent (n) to estimate the mass fraction burned.

5.3.4 Estimation of Weibe Profiles

A common mathematical expression used to represent heat release in IC engine simulations is the Weibe profile,²⁰⁰

$$x_b = 1 - \exp \left\{ -a \left[\frac{(\theta - \theta_{ign})}{\Delta\theta_b} \right]^{m+1} \right\} \quad (5-20)$$

In this expression, the constant m defines the shape of the integrated heat release curve, the constant a represents a conversion efficiency parameter related to the amount of fuel present in the charge at the end of the combustion process, θ_{ign} is the crank angle at which ignition begins and $\Delta\theta_b$ is the duration (in degrees) of the combustion event. These constants are determined from measurements of the mass burned fraction. Once the constants are determined, Eqn. 5-20 can be used in an engine simulation to estimate mass burned fraction at any crank angle.

While the mass burned as a function of crank angle is a very useful input for engine cycle simulations, the two methods presented above for determining the mass fraction burned do not provide a way to represent the heat release of combustion. The

next section describes a method for obtaining heat release rate using an in-cylinder thermodynamic model.

5.3.5 Heat Release Rate

Heat release rate as a function of crank angle is a useful relationship that can be established using cylinder pressure measurements. Estimated heat release rate can be used in place of an in-cylinder thermodynamic model that requires detailed treatments of complex in-cylinder processes like fuel evaporation, ignition, flame propagation etc.²⁰¹ Replacing these models with empirical data reduces an engine simulation's complexity and computational time without compromising accuracy. A gross or net heat release rate can be established depending on the formulation of the equations.

A single zone model treats the cylinder contents as a single zone in a single average thermodynamic state and no distinction is made between the burned and unburned gases. A two-zone model represents the cylinder contents using separate zones for burned and unburned mixture. The burned and unburned mixture regions are separated by the flame zone. The thermodynamic properties of the unburned mixture are computed assuming a frozen composition²⁰² in chemical equilibrium. The two-zone approach is more accurate but also more complicated than the single zone approach as it requires knowledge of the location of the flame zone during the combustion process.

Since it is not clear exactly how combustion occurs in these engines and preliminary visualization data are just starting to appear in the literature (see Chapter 6), a single zone model is used to estimate gross and net heat release rates during the

combustion process. The procedure used here to estimate heat release rate is outlined in Heywood.²⁰³

Figure 5–13 shows a control volume drawn around the contents of a two–stroke engine cylinder. The intake, transfer and exhaust ports are closed.

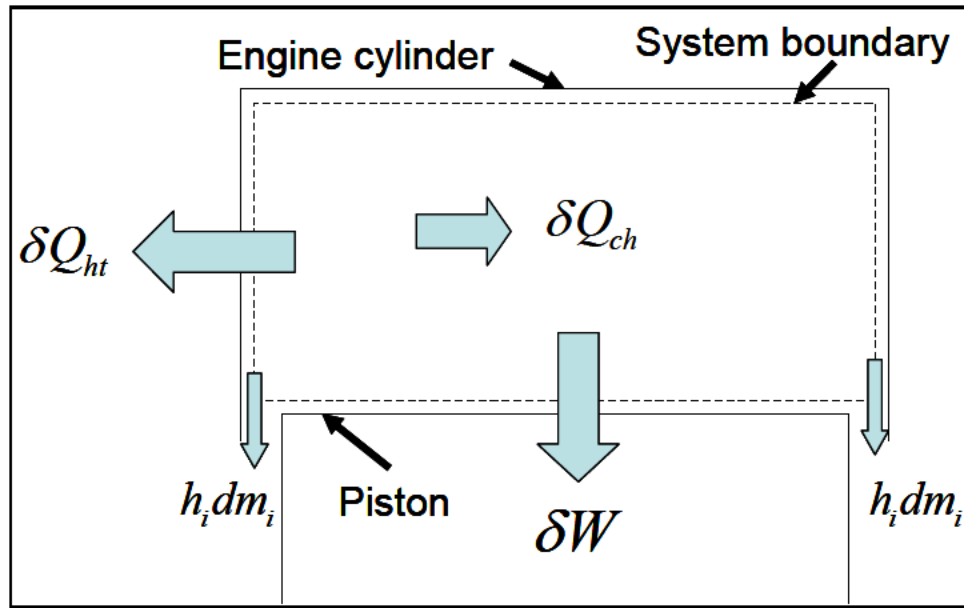


Figure 5–13: Energy transfer processes occurring in the cylinder treated as a closed control volume with the ports closed.

The first law of thermodynamics applied to the energy interactions in the control volume is,

$$\frac{dQ_{ch}}{d\theta} = \frac{dU}{d\theta} + \frac{dQ_{ht}}{d\theta} + \frac{dW}{d\theta} + \sum h_i \frac{dm_i}{d\theta} \quad (5-21)$$

where dQ_{ch} represents the chemical energy released by the combustion of the fuel, dU is the change in internal energy of the fuel–air mixture, dQ_{ht} is the heat transfer from the gas to the cylinder walls, dW is the work output and $\sum h_i dm_i$ is the energy change due to mass transfer in or out of the system. In the small two–stroke engines investigated here, the fuel–air charge is premixed and there is no fuel injection into

the cylinder. Therefore, the only contribution to the mass flux term is blowby losses from the cylinder into the crankcase through the piston–cylinder liner gap and $dm_i = dm_{bb} = dm$. The internal energy of the fuel–air mixture is given by,

$$\frac{dU}{d\theta} = mC_v(T) \frac{dT}{d\theta} + u(T) \frac{dm}{d\theta} \quad (5-22)$$

where T is the mean charge temperature, m is the mass within the boundaries of the control volume, and $C_v(T)$ is the specific heat at constant volume expressed as a function of gas temperature. The mean temperature is assumed to be close to the mass averaged in-cylinder temperature during the combustion process. Combining equations 5–21 and 5–22 gives,

$$\frac{dQ_{ch}}{d\theta} = mC_v(T) \frac{dT}{d\theta} + (h' - u) \frac{dm_{bb}}{d\theta} + \frac{dQ_{ht}}{d\theta} + \frac{dW}{d\theta} \quad (5-23)$$

where h' is the average enthalpy of the blowby gases.

For an ideal gas,

$$pV = mRT \quad (5-24)$$

$$\frac{dT}{d\theta} = \frac{1}{mR} \frac{d(pV)}{d\theta} - \frac{T}{m} \frac{dm}{d\theta} \quad (5-25)$$

Substituting the expression for specific heat at constant volume in Eqn. 5–25 gives,

$$mC_v \frac{dT}{d\theta} = \frac{C_v}{R} \frac{d(pV)}{d\theta} - C_v T \frac{dm}{d\theta} \quad (5-26)$$

From equations 5–23 and 5–26 and replacing the work term δW by $p dV$ we have,

$$\frac{dQ_{ch}}{d\theta} = \frac{C_v}{R} \frac{d(pV)}{d\theta} - C_v T \frac{dm_{bb}}{d\theta} + (h' - u) \frac{dm_{bb}}{d\theta} + \frac{dQ_{ht}}{d\theta} + p \frac{dV}{d\theta} \quad (5-27)$$

This gives,

$$\frac{dQ_{ch}}{d\theta} = \frac{C_v}{R} p \frac{dV}{d\theta} + p \frac{dV}{d\theta} + \frac{C_v}{R} V \frac{dp}{d\theta} - C_v T \frac{dm_{bb}}{d\theta} + (h' - u) \frac{dm_{bb}}{d\theta} + \frac{dQ_{ht}}{d\theta} \quad (5-28)$$

Collecting terms in Eqn. 5-28 gives,

$$\frac{dQ_{ch}}{d\theta} = \left(\frac{C_v}{R} + 1 \right) p \frac{dV}{d\theta} + \frac{C_v}{R} V \frac{dp}{d\theta} - (C_v T + u - h') \frac{dm_{bb}}{d\theta} + \frac{dQ_{ht}}{d\theta} \quad (5-29)$$

The term on the left hand side of Eqn. 5-29 represents the gross heat release rate. The first two terms on the RHS of Eqn. 5-23 are re-written below,

$$\frac{dQ_{net}}{d\theta} = \left(\frac{C_v}{R} + 1 \right) p \frac{dV}{d\theta} + \frac{C_v}{R} V \frac{dp}{d\theta} \quad (5-30)$$

They give the ‘net’ heat release rate: ie. the total heat release rate due to combustion minus the heat lost via blowby and heat transfer to the environment. This is the energy that is left to do useful shaft work. This expression is convenient because it is only a function of pressure and therefore can be computed from cylinder pressure measurements.

Considering the case of the closed system, if methods for estimation of mass blowby rates and instantaneous engine heat transfer are known, the gross heat release as calculated by Eqn. 5-29 can be estimated and further used to calculate the mass burned fraction. Mass burned fraction estimated in this manner can be used to estimate combustion efficiency. The methods of pursuing these are detailed in appendix F. In the investigation performed here, there is insufficient information to accurately model the convective heat transfer from the gas to the wall as well as the blowby losses from the engine cylinder. Hence, Eqn. 5-30 is used to estimate the net heat release.

5.3.6 Heat Release Fraction

A heat release fraction (q_f) that varies from 0 at the beginning of combustion to 1 at the end²⁰⁴ can be calculated using an approach similar to that developed for the mass fraction burned in Section 5.3.3.1,²⁰⁵

$$q_f = \frac{q_f(i)}{q_f(total)} = \frac{\sum_{\theta_{start}}^{\theta} \Delta q_f}{\sum_{\theta_{start}}^{\theta_{end}} \Delta q_f} \quad (5-31)$$

The next two sections describe how the beginning and end of the combustion process is determined.

5.3.7 Ignition Timing

The start of combustion is easier to determine in SI engines because the spark timing is known. In diesel engines, combustion is typically assumed to begin at the start of fuel injection plus some ignition delay. Various correlations have been developed for ignition delay in conventional-scale engines that incorporate the effects of injection timing, fuel drop size, intake air temperature and pressure, engine speed, swirl rate etc.²⁰⁶ However, a different approach is needed for glow engines that have neither spark plugs nor fuel injectors.

Our approach is to consider the net heat release occurring in a closed volume represented by Eqn. 5-30. Prior to ignition, there is no chemical energy release so the net heat release rate must be negative to balance the blowby and thermal losses in 5-29. The only way the net energy release can be positive is if there is chemical energy release from the fuel. Hence, the technique used here to estimate the start of ignition is to use the cylinder pressure measurements and Eqn. 5-30 to generate a plot of net

heat release as a function of crank angle. The crank angle when the slope of this curve becomes positive is taken to be the start of ignition.

5.3.8 Burn Duration

With the onset of combustion already identified, the problem of determining burn duration is really that of determining the point at which combustion ends. This is difficult since the combustion process approaches completion in an asymptotic manner. Two of these methods for estimating end of reaction from cylinder pressure traces are discussed below.

A technique used by Mendera²⁰⁷ is based on the first law of thermodynamics applied to a closed system representing the cylinder volume with intake, exhaust and transfer ports closed. Under these conditions, the first law can be expressed as,

$$\frac{dQ_{ch}}{d\theta} = \frac{dU}{d\theta} + \frac{dQ_{ht}}{d\theta} + \frac{dW}{d\theta} \quad (5-32)$$

where $\frac{dQ_{ch}}{d\theta}$ is the sensible energy released by conversion of fuel chemical energy,

$\frac{dU}{d\theta}$ is the change in internal energy, $\frac{dQ_{ht}}{d\theta}$ is the energy lost by heat transfer and

$\frac{dW}{d\theta}$ is the work output to the piston. Energy loss due to piston blowby is not

accounted for. Mendera posits that the end of combustion occurs where Eqn. 5-32 is minimum. Since the work and heat transfer terms are not directly related to the heat release, Eqn. 5-32 should be minimized when $dU/d\theta$ is minimized or the change in sensible internal energy reaches a minimum. Assuming there is no mass transfer from the cylinder volume during the combustion period,

$$\left(\frac{dU}{d\theta}\right)_{\min} = mC_v \left(\frac{dT}{d\theta}\right)_{\min} \quad (5-33)$$

or

$$\left(\frac{dT}{d\theta}\right)_{\min} = \frac{1}{mR} \left(\frac{d(pV)}{d\theta}\right)_{\min} \quad (5-34)$$

The RHS of Eqn. 5-34 can be determined using the pressure and crank angle traces from the fired cycle along with the corresponding cylinder volume information.

A second technique proposed by Brown²⁰⁸ posits that the end of combustion coincides with the crank angle at which x in Eqn. 5-35 is maximum,

$$x = PV^{1.15} \quad (5-35)$$

This can also be computed using experimentally determined pressure and crank angle traces.

Both techniques were used to estimate the end of combustion but the first one consistently returned crank angles that were beyond the exhaust and transfer port opening angles. Since these angles are inconsistent with the original assumption of a closed system, they were not considered to be reliable. The values returned by the second technique seem to be more realistic and they appear to be qualitatively consistent with the combustion images presented in Chapter 6. Therefore, only results based on the second method of estimating reaction completion are reported.

5.3.9 Indicated Power Output

The cylinder pressure trace over an engine cycle can be plotted as a function of instantaneous cylinder volume to yield a closed pressure–volume curve. The area enclosed by the curve is the indicated work and can be determined using a numerical

integration method. This work uses the MATLABTM function trapz.m to estimate this area. The product of indicated work and engine speed gives the indicated power output.

5.3.10 Power Loss

The difference between indicated power output and power output measured on the dynamometer represents the losses associated with friction, crankcase compression, the engine charging processes, and anything else.

5.4 Measurement Results

Cylinder pressure measurements under fired conditions were obtained for three different engines: the OS 25 FX, OS 40 FX and the OS 46 FX (engines a–c in Fig. 2–3). Each engine was tested at different constant speeds and various equivalence ratios. The operating conditions and basic specifications of the engines are summarized in Table 5–2. Table 5–4 presents the port timings for each of the engines. The intake port referred to in Table 5–4 represents the rotary valve on the crankcase. The intake, transfer and exhaust ports referred to here are explained in further detail elsewhere.²⁰⁹

All results presented and discussed below are for the OS 25 FX engine. Similar results obtained for the OS 40 FX and OS 46 FX engines are presented in Appendix E. While the cylinder pressure sensor reads gage pressure, all pressures reported below are absolute (i.e., sensor output plus ambient pressure).

A number of plots presented in the figures below report measurements at estimated values of equivalence ratio. Equivalence ratio reported here is computed

using a fuel–air mixture ratio based on air and fuel flow rates into the engine along with a stoichiometric value based on fuel chemistry. The possibility of oil mixed into the fuel burning within the engine volume and releasing energy results in uncertainty in the stoichiometric fuel–air mixture ratio. Additionally, the presence of residual gas and loss of fresh mixture due to inefficient scavenging leads to uncertainty in the estimated fuel–air mixture ratio. These effects are difficult to quantify presently. An uncertainty analysis has been performed for the equivalence ratio and results are indicated on the graphs below. Trends are obtained for a number of parameters including peak cylinder pressure, ignition location, burn duration, mass burned fraction, heat release rate etc. which allow an improved understanding of the ignition and combustion processes in miniature glow ignited engines.

Engine	OS 25 FX	OS 40 FX	OS 46 FX
Intake port opening (IPO)	43	34	34
Intake port closing (IPC)	236	231	231
Transfer port opening (TPO)	308	314	314
Transfer port closing (TPC)	52	46	46
Exhaust port opening (EPO)	287	291	291
Exhaust port closing (EPC)	73	69	69
Crank angle degrees after BDC			

Table 5–4: Port opening and closing timing for the three engines tested in this work.

Figure 5–14 shows a plot of measured power output from the OS 25 FX engine at different operating speeds and fuel–air mixture ratios. Two cases are presented. One set of results in filled symbols corresponds to engine operation without the cylinder pressure sensor. The second data set represented by empty symbols corresponds to engine operation with the cylinder pressure sensor. The measured power output in both cases are obtained using dynamometer measurements involving load cell measurements as described previously in Chapter 2. As seen in the

figure, similar levels of power are obtained from the engine in the two cases. This ensures that installation of the sensor produced a minimal change in dead volume and engine compression ratio.

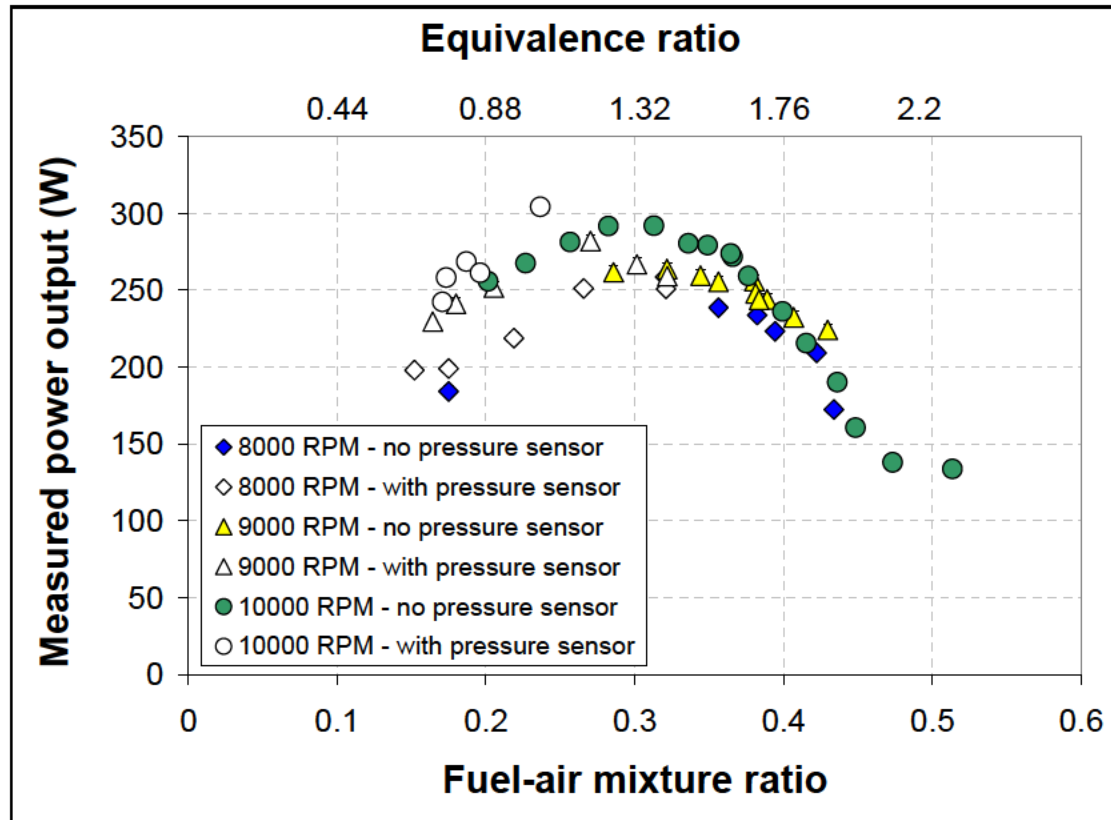


Figure 5–14: Measured power output for the OS 25 FX engine with and without a cylinder pressure sensor at different operating speeds and fuel–air mixture ratios.

5.4.1 Cylinder Pressure Trace

Figure 5–15 is a plot of average cylinder pressure in the OS 25FX as a function of crank angle over 50 cycles. The engine is operating at a speed of 10000 rpm and an equivalence ratio of 1.05. The various port opening and closing events are also marked on the graph. As seen in the figure, cylinder pressure rises smoothly beyond the point of exhaust port closing (EPC) up to and beyond top dead center (TDC). Ignition is estimated to occur at 176 degrees after BDC and there is a slight

change in the slope of the pressure trace immediately afterward. Cylinder pressure continues to rise well beyond TDC and peaks at a crank angle of 199 degrees after BDC. Beyond this point, cylinder pressure begins to drop as the hot gases expand and perform work on the downward moving piston. The pressure continues to fall beyond the point where the rotary valve controlling the intake port closes (IPC). The slope of the pressure trace becomes less negative after IPC indicating that fresh charge is being compressed in the crankcase. At 287 degrees after BDC (107 degrees ATDC), the exhaust port begins to open and the cylinder pressure begins to drop rapidly during the blowdown stage of the cycle. Cylinder pressure goes slightly negative towards the end of the blowdown process and right around the time that the transfer ports open (TPO) at 308 degrees after BDC (128 degrees ATDC). Beyond this point, cylinder pressure rises slightly until it reaches atmospheric conditions. Figures E-1 and E-21 in appendix E show similar results in the OS 40 FX and the OS 46 FX engines.

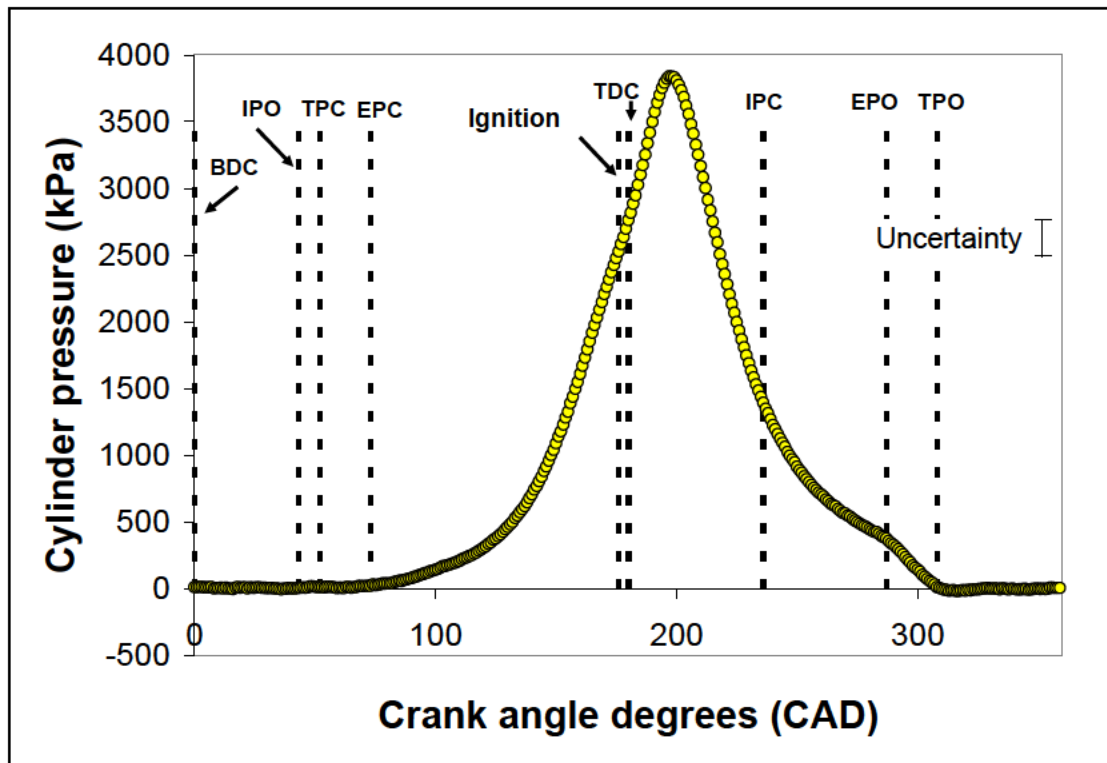


Figure 5–15: Cylinder pressure averaged over 50 cycles plotted as a function of crank angle degrees from bottom dead center (BDC) for the OS 25 FX engine operating at a speed of 10000 rpm and an equivalence ratio of 1.05.

Figure 5–16 is a plot of average cylinder pressure as a function of cylinder volume. The port openings are marked on the graph. The shape of the pressure trace is similar to that observed in conventional-scale two-stroke engines. The compression and expansion parts of the cycle resemble the general form of isentropic curves for the same. The compression and expansion processes can be fit to a power law giving the polytropic exponents. Table 5–5 compares the values obtained for this case with those from a conventional scale engine. In addition, the energy release portion of the cycle appears to occur at mostly constant volume as in the idealized Otto cycle. Figures E–2 and E–22 in appendix E show similar results in the OS 40 FX and the OS 46 FX engines.

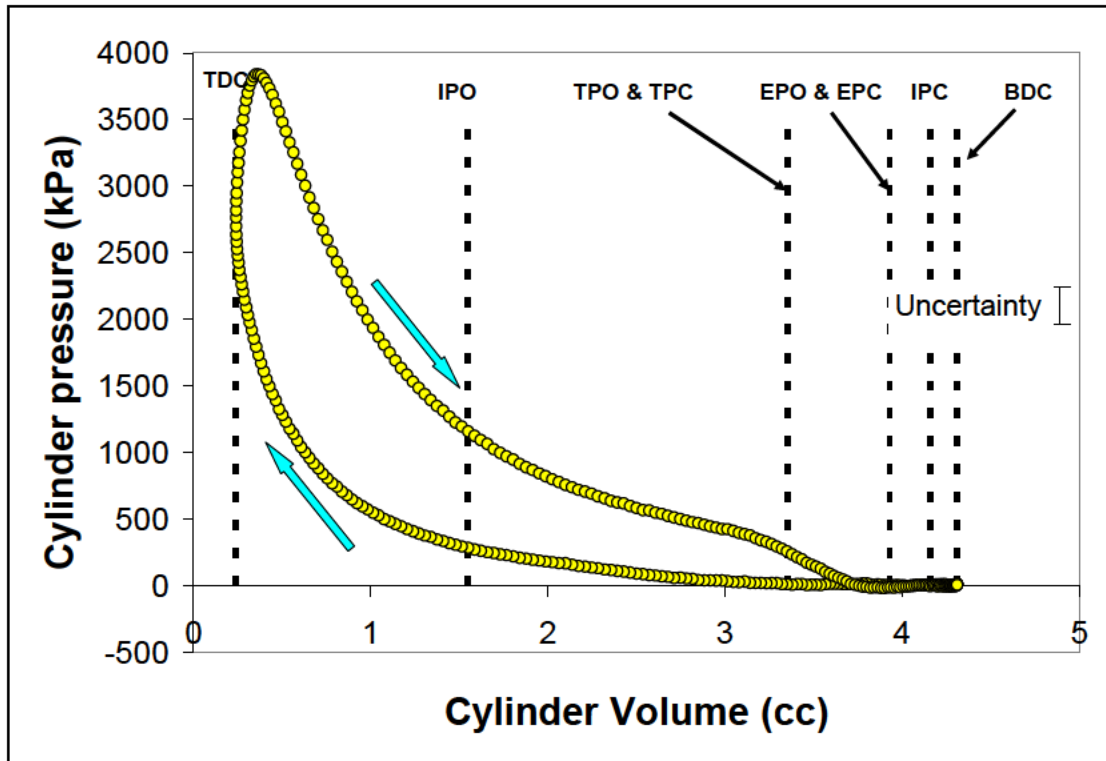


Figure 5-16: Cylinder pressure plotted as a function of cylinder volume for a fired engine cycle for the OS 25 FX engine operating at a speed of 10000 rpm and an equivalence ratio of 1.05.

	Compression	Expansion
OS 25 FX @ 10000 rpm, $\phi = 1.05$	1.53	1.22
Values used in an analytical cylinder pressure model for an SI engine	1.25	1.3

Table 5-5: Comparison between polytropic exponent estimated using cylinder pressure measurements and those used in an analytical model for a 4 cylinder SI engine.²¹⁰

Figure 5-17 is a plot of average in-cylinder pressure as a function of crank angle for seven equivalence ratios ranging from rich (1.49) to lean (0.76) at a constant operating speed of 10000 rpm. It is clear that equivalence ratio has a strong influence on engine performance. The peak cylinder pressure rises as the mixture is leaned and reaches a maximum at an equivalence ratio of 0.83. In conventional scale engines, peak value for IMEP has been observed to occur at mixture ratios slightly rich of

stoichiometric.^{211 212} However, the occurrence of peak cylinder pressure at lean mixture ratios has also been observed.²¹³ Since there is an additional element of uncertainty in the equivalence ratio calculation due to lack of knowledge of fuel chemistry (due to burning of oil), no definitive conclusion can be made as regards equivalence ratio at peak cylinder pressure. However, a trend similar to that in conventional scale engines is observed where peak cylinder pressure decreases as the mixture ratio is made richer or leaner of stoichiometric.

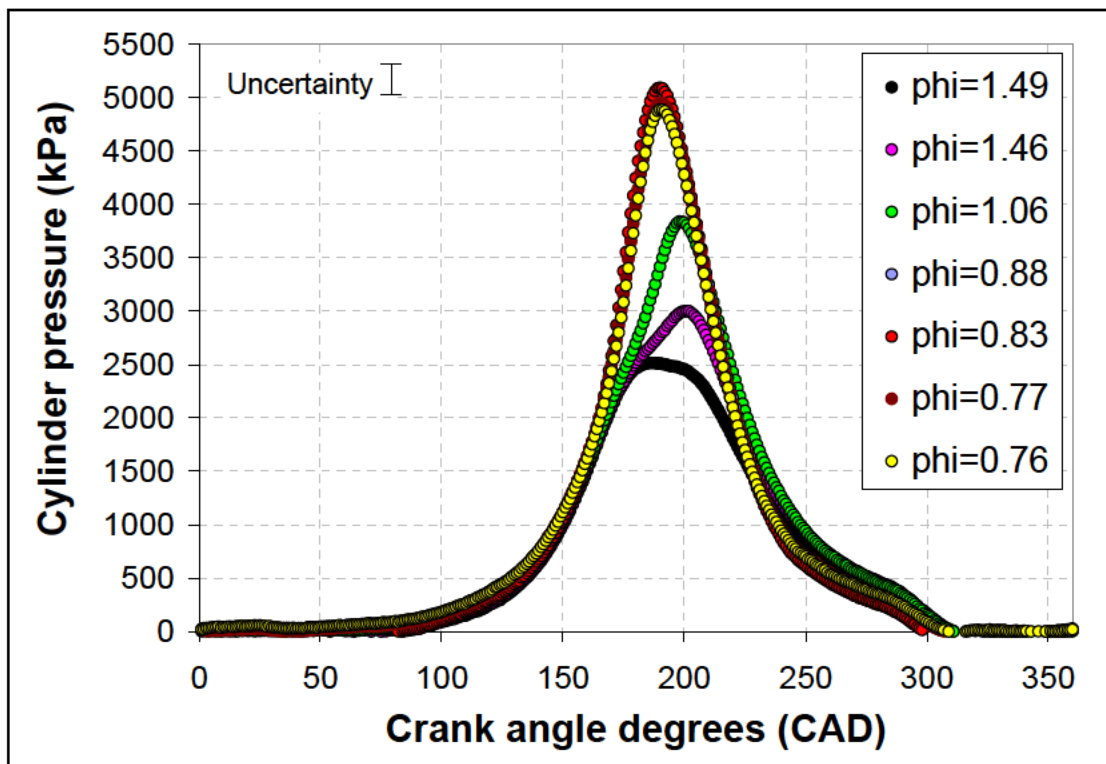


Figure 5–17: Cylinder pressure averaged over 50 cycles plotted as a function of crank angle for the OS 25 FX engine operating at a speed of 10000 rpm and different equivalence ratios.

The shape of the pressure traces also change becoming steeper as the mixture is leaned. The pressure trace for much of the remainder of the cycle stays the same for the different mixture settings. Figure 5–17 also shows that peak cylinder pressure occurs earlier (ie. at smaller crank angles) as the mixture is leaned. These effects are

further investigated in Section 5.4.4. Increased peak cylinder pressure corresponds to increased cycle work and engine work. Figures E-3 and E-23 in appendix E show similar results in the OS 40 FX and the OS 46 FX engines.

Figure 5-18 shows average cylinder pressure as a function of crank angle for 7 different engine speeds and a nearly constant equivalence ratio of about 0.98. The equivalence ratio is not exactly the same across the different cases because it was not explicitly controlled during the dynamometer measurements. Instead, the dynamometer holds speed constant while measurements are made at various mixture valve settings. Figure 5-18 is assembled from a subset of this larger data set where the equivalence ratio was approximately the same. The results show that speed significantly influences the cylinder pressure trace. In general, increasing the speed decreases the peak cylinder pressure. The only exception is the 10000 rpm case where the pressure is lower than the 11000 rpm case and is probably due to the fact that the mixture is leaner (equivalence ratio of 0.88) compared to the other cases. Figure 5-18 also shows that the peak cylinder pressure occurs earlier in the cycle as engine speed decreases. Figures E-4 and E-24 in appendix E show similar results in the OS 40 FX and the OS 46 FX engines.

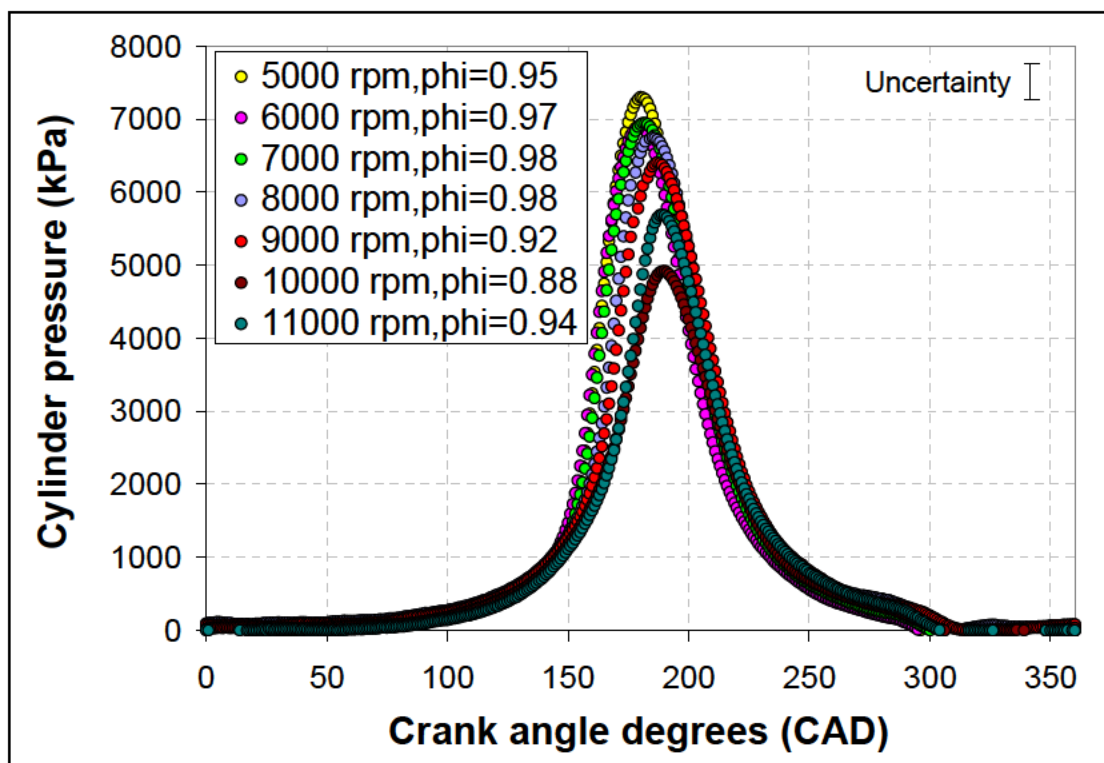


Figure 5–18: Cylinder pressure averaged over 50 cycles plotted as a function of crank angle for the OS 25 FX engine operating at an equivalence ratio of ~ 0.98 and different engine speeds.

5.4.2 Peak Cylinder Pressure and Location

Figure 5–19 shows peak cylinder pressure as a function of equivalence ratio for 7 different engine speeds. The peak pressures here represent the average peak over 50 cycles for each engine operating condition. The figure shows that peak cylinder pressure decreases with increasing engine speed independent of the equivalence ratio. At the lowest four engine speeds (5000, 6000, 7000 and 8000 rpm) peak cylinder pressure is achieved close to stoichiometric and decreases on either side. However, at higher engine speeds (9000, 10000 and 11000 rpm) peak cylinder pressure occurs at mixture ratios leaner than stoichiometric. Figure E–5 and E–25 in appendix E show peak pressures measured in the OS 40 FX and the OS 46 FX engines.

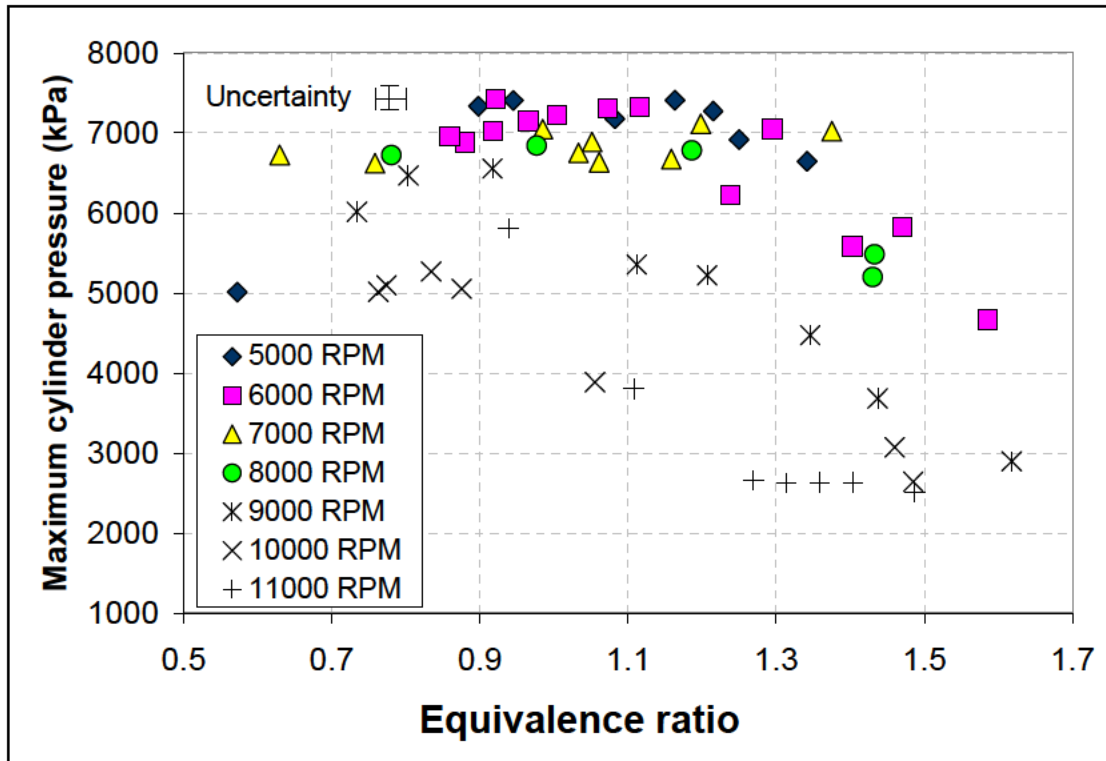


Figure 5–19: Peak cylinder pressure averaged over 50 cycles plotted as a function of equivalence ratio for the OS 25 FX engine operating at different engine speeds.

Figure 5–20 shows peak cylinder pressure as a function of equivalence ratio for 7 different engine speeds for the OS 25 FX engine. This figure differs from Fig. 5–19 in that it reports the maximum pressure achieved over 50 cycles instead of the average of the maximum pressure over 50 cycles. As seen in Fig. 5–19, peak cylinder pressure across different equivalence ratios decreases with increasing engine speed from 5000 rpm to 11000 rpm. The behavior of peak cylinder pressure with equivalence ratio is also similar to that observed earlier. Figures E–6 and E–26 in appendix E show similar results for the OS 40 FX and the OS 46 FX engines.

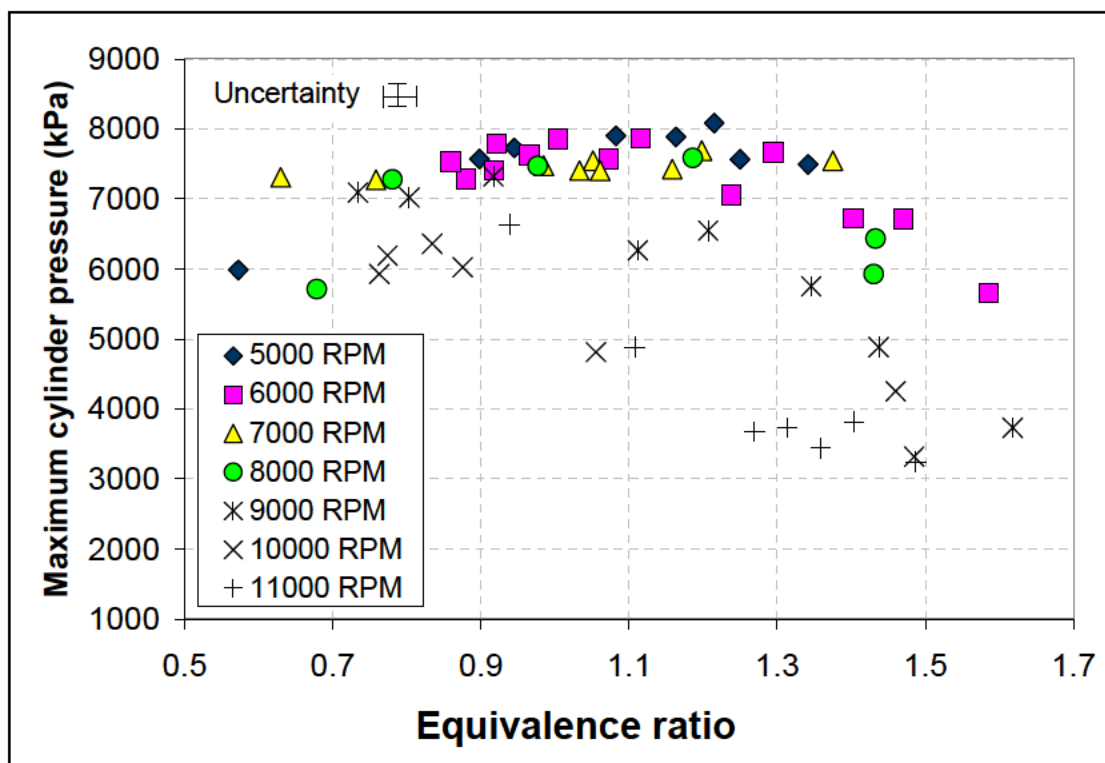


Figure 5–20: Peak cylinder pressure over 50 cycles plotted as a function of equivalence ratio for the OS 25 FX engine operating at different engine speeds.

Figure 5–21 shows the average location of peak in-cylinder pressure as a function of equivalence ratio for 7 different engine speeds. The location (in CAD after BDC) is obtained by averaging the location of peak cylinder pressure over 50 cycles. A clear trend is visible at low speeds (5000–9000 rpm) where the location of peak cylinder pressure shifts to a point earlier in the engine cycle as the mixture ratio decreases to about 0.9. At leaner mixtures to the left of 0.9, the trend reverses and the peak cylinder pressure is shifts to a later point in the cycle. At higher engine speeds (10000 and 11000 rpm) the scatter in data is higher due to greater cycle-to-cycle variations as will be discussed in the following section and a clear trend cannot be observed. Figures E–7 and E–27 show the corresponding results in the OS 40 FX and OS 46 FX engines.

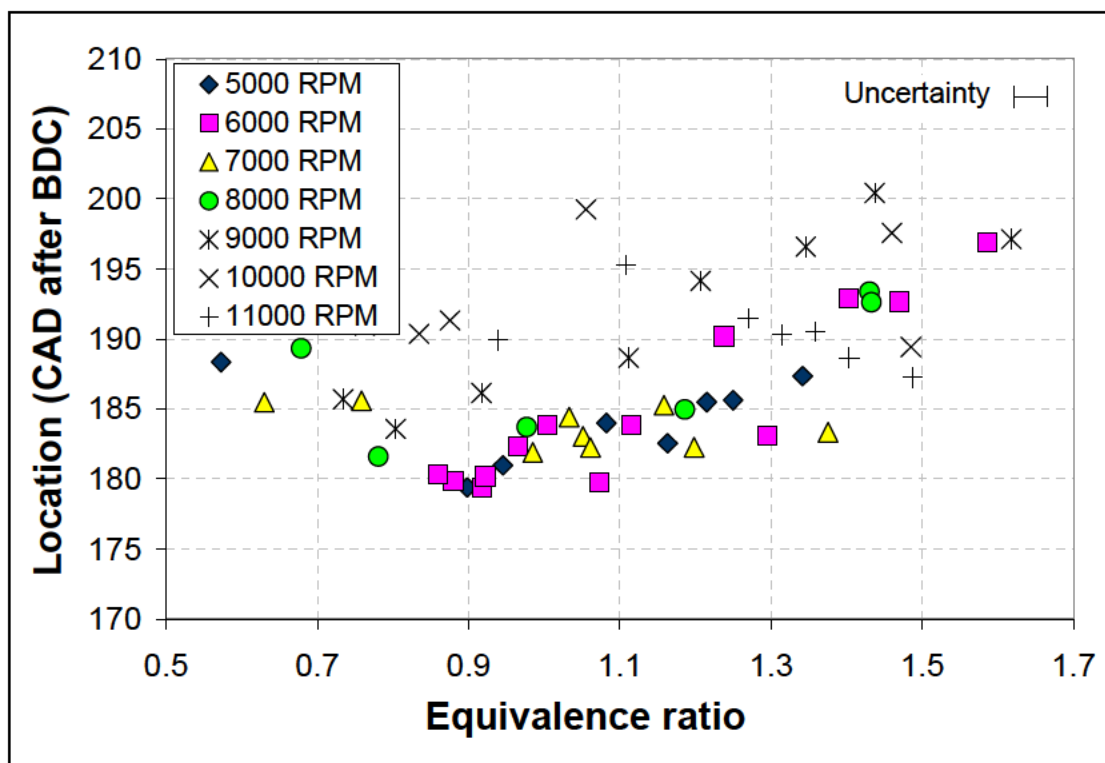


Figure 5–21: Average location of peak cylinder pressure averaged over 50 cycles plotted as a function of equivalence ratio for the OS 25 FX engine operating at different engine speeds.

5.4.3 Cycle to Cycle Variation

Figure 5–22 shows the coefficient of variation (COV) of maximum cylinder pressure computed as described in Section 5.3.2. COV is plotted as a function of equivalence ratio at 7 different engine speeds for the OS 25 FX engine. At a constant equivalence ratio, the coefficient of variation increases with increasing engine speed. At lower speeds (5000, 6000 and 8000 rpm), the COV increases as the mixture ratio is made rich or lean of an equivalence ratio of 0.9. The coefficient of variation is larger at the higher speeds of 9000, 10000 and 11000 rpm and a clear trend with equivalence ratio is not apparent. The corresponding plots for the OS 40 and OS 46 FX engines are presented in figures E–8 and E–28 in appendix E.

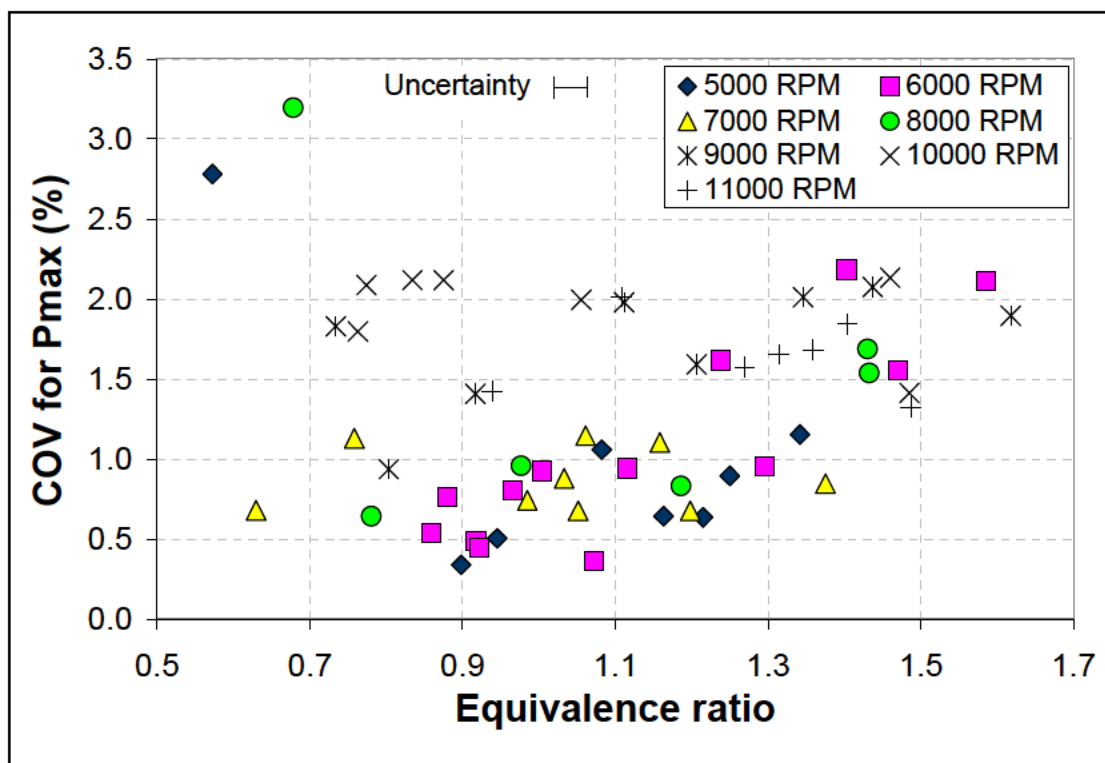


Figure 5-22: Coefficient of variation calculated for maximum cylinder pressure plotted as a function of equivalence ratio for the OS 25 FX engine operating at different engine speeds.

Figure 5-23 shows the coefficient of variation of the location of maximum cylinder pressure plotted as a function of equivalence ratio at 7 different engine speeds for the OS 25 FX engine. The cyclic variation observed in peak cylinder pressure indicates that heat release rate also possibly shifts around on a cycle-to-cycle basis. Similar trends are observed in figures E-9 and E-29 in appendix E for the OS 40 and OS 46 FX engines.

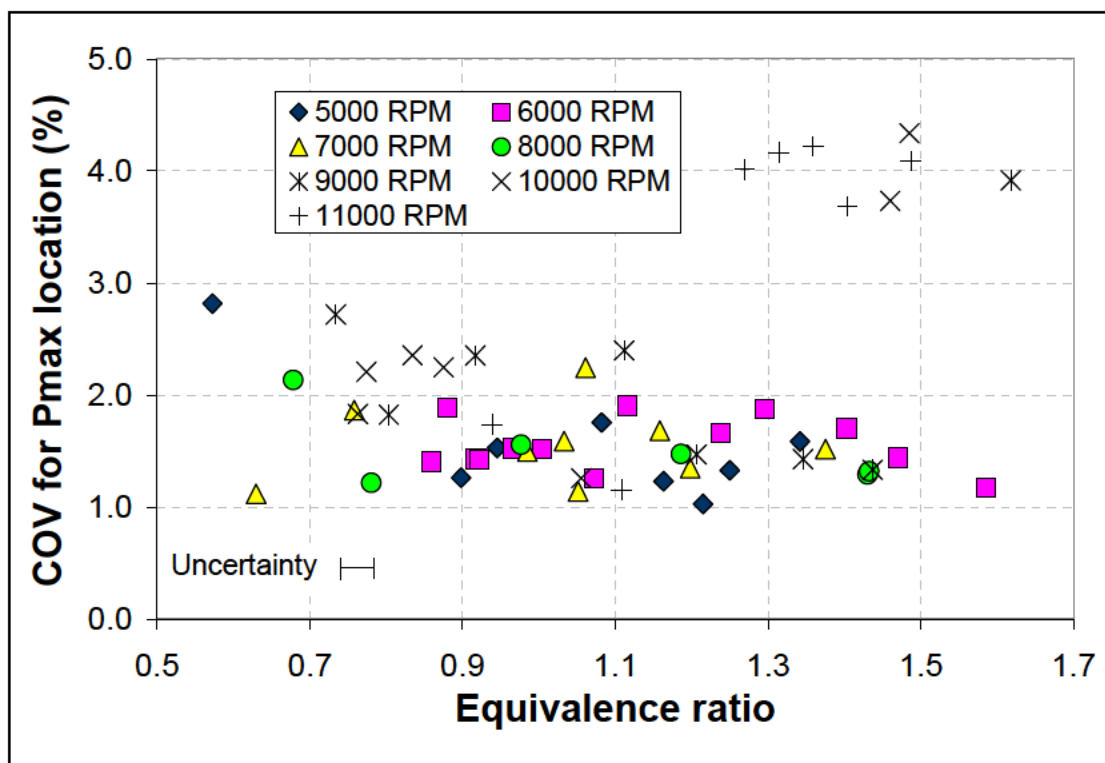


Figure 5–23: Coefficient of variation calculated for maximum cylinder pressure plotted as a function of equivalence ratio for the OS 25 FX engine operating at different engine speeds.

5.4.4 Net Heat Release Rate

Figure 5–24 shows the net heat release rate computed for the OS 25 FX engine operating at a speed of 10000 rpm and an equivalence ratio of 1.05 using the methodology explained in Section 5.3.5. Heat release rate is computed based on the cylinder pressure trace averaged over 50 cycles. The locations of exhaust port opening and closing are also marked in the plot. Some amount of scatter is observed in the estimated net heat release rate – particularly before ignition and at about 240 degrees after BDC in the case shown here. The 5 point moving average shown by the orange diamond markers removes some of the scatter and gives a better picture of engine heat transfer processes.²¹⁴ Net heat release rate begins a slow decrease about 100 degrees after BDC and continues to drop until about 160 degrees after BDC. This

is presumably due to a combined effect of heat transfer from the gases undergoing compression to the cylinder walls as well as possible blowby from the cylinder to the crankcase. Notice that the heat release rate goes positive near TDC. The point at which net heat release rate goes positive is determined to be the location of start of combustion. Similar plots made for the OS 40 FX and OS 46 FX engines presented in figures E-10 and E-30 also show the net heat release rate going positive close to TDC. Heat release rate peaks at about 200 degrees after BDC which is the same location at which average cylinder pressure peaks in Fig. 5-15 which is at the same operating condition. Beyond this point, the heat release rate remains positive but begins to decrease and eventually becomes negative at about 270 degrees after BDC. The exhaust port opens at 287 degrees after BDC. Results similar to those observed in the OS 25 FX engine are obtained for the OS 40 FX and the OS 46 FX engines as shown in figures E-10 and E-30 in appendix E.

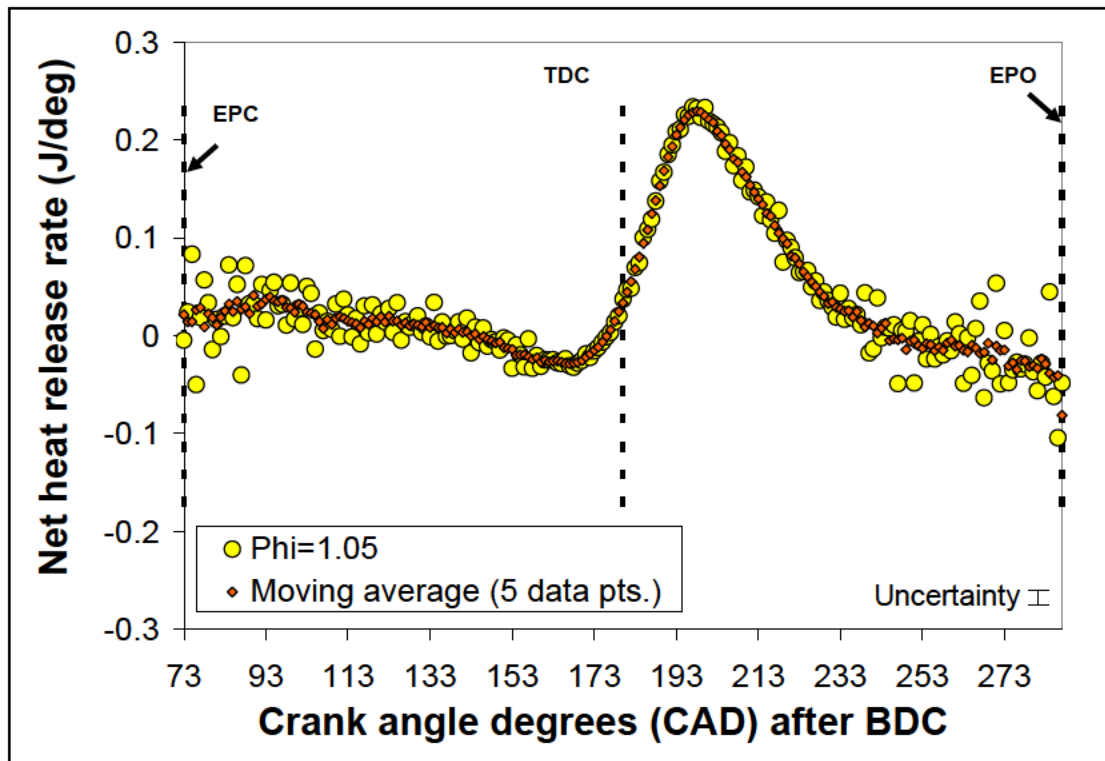


Figure 5–24: Net heat release rate and a moving average estimated for the same over 5 data points plotted a function of crank angle for the OS 25 FX engine operating 10000 rpm and an equivalence ratio of 1.05.

Figure 5–25 compares the net 5 point moving averaged heat release rates estimated at 10000 rpm in the OS 25 FX engine for 7 different equivalence ratios. As seen in the figure, the primary effects of changes in equivalence ratio are reflected in the heat release rate during the combustion portion of the engine cycle. Figure 5–25 shows that the peak heat release rate occurs slightly rich of stoichiometric. Cylinder pressure for the same data set was observed to peak at a lean equivalence ratio of 0.83. This can be explained on the basis of the timing of heat release with respect to piston motion. As seen in Fig. 5–24, the location of peak heat release is progressively retarded as the mixture is moved from a lean setting to a rich setting. For the lean mixtures, early ignition leads to more heat release prior to TDC. This results in a

greater pressure rise which is reflected in the results presented in Fig. 5–17. For richer mixtures where ignition is delayed, the magnitude of heat release is higher but since most of it occurs past TDC, the peak cylinder pressure obtained is lower than that for leaner settings. Results similar to those observed for the OS 25 FX engine are obtained for the OS 40 FX and the OS 46 FX engines as shown in figures E–11 and E–31 in appendix E.

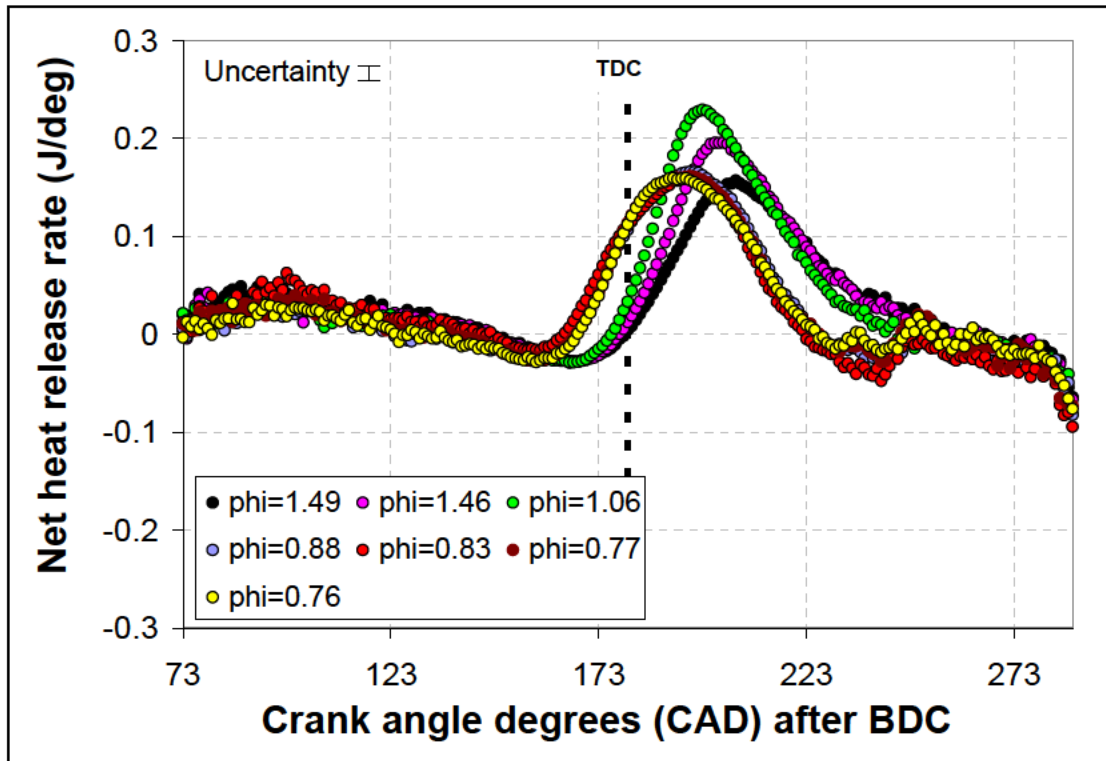


Figure 5–25: Five point moving average of the net heat release rate estimated for the OS 25 FX engine plotted as a function of crank angle for the engine operating at 10000 rpm and different equivalence ratios.

Figure 5–26 compares net 5 point moving average heat release rates in the OS 25 FX engine at 7 different speeds and a constant equivalence ratio of about 0.98. The variation in engine speed has a very interesting effect on the net heat release rate. At high engine speeds (10000 and 11000 rpm) the net heat release rate has a single peak

similar to those observed in Fig. 5–25. However, at 9000 rpm and below, the net heat release rate develops a second peak that occurs well before TDC and increases in strength as engine speed decreases. This can be seen more clearly in Fig. 5–27.

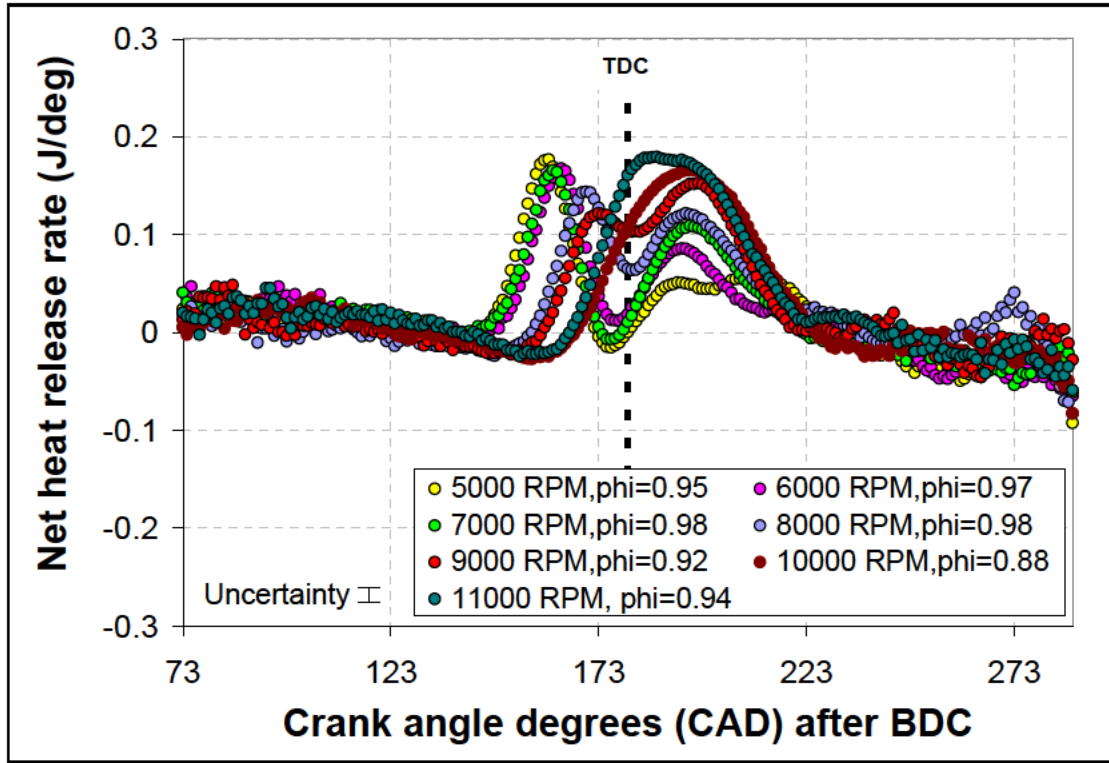


Figure 5–26: Five point moving point average of the net heat release rate estimated for the OS 25 FX engine plotted as a function of crank angle for the engine operating at different speeds and an equivalence ratio of ~ 0.95 .

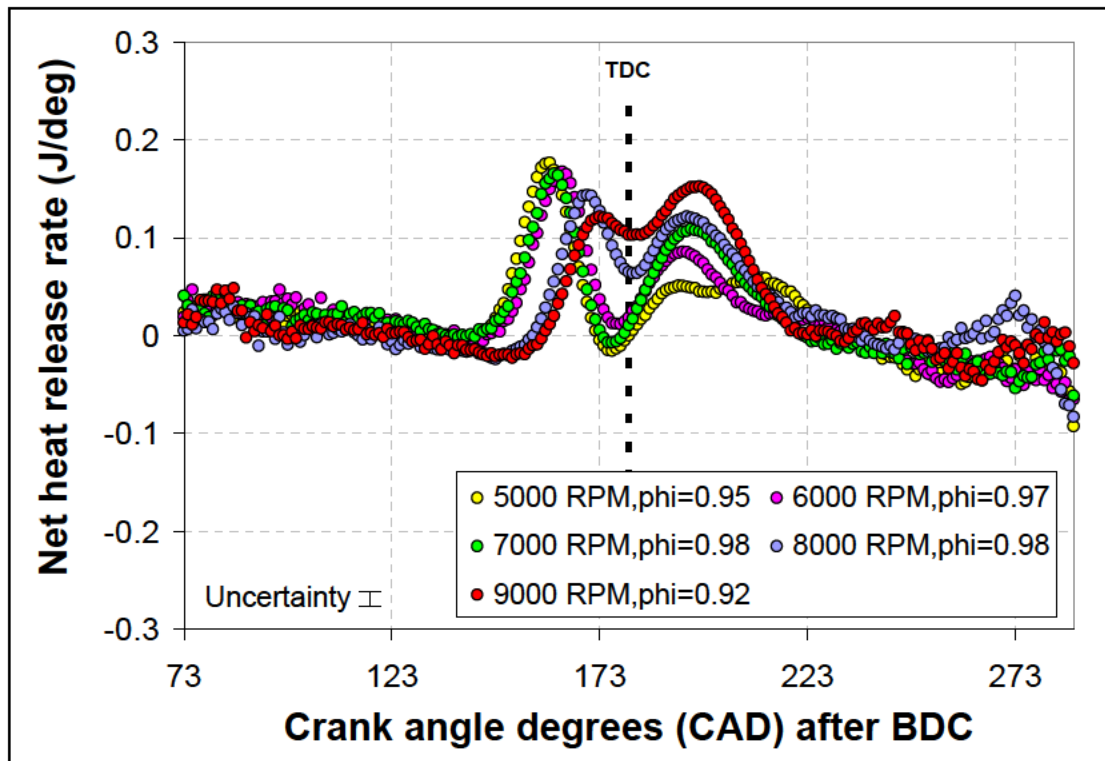


Figure 5–27: Five point moving point average of the net heat release rate estimated for the OS 25 FX engine plotted as a function of crank angle for the engine operating at different speeds and an equivalence ratio of ~ 0.95 .

The heat release rate in these cases decreases sharply between 6 and 19 degrees BTDC after an initial increase and reach a minimum value at around 176 to 185 degrees after BDC. The heat release rate then gradually increases until it reaches a second peak around 191–199 degrees after BDC and starts to drop in a manner similar to that seen earlier in Fig. 5–25 until the exhaust port opens. This suggests that some kind of two–stage combustion process is occurring. A two–stage combustion process and an associated double peak in net heat release rate is a common characteristic of direct injected diesel engines.²¹⁵ This phenomenon is due to an initial premixed combustion phase where energy is released due to burning of a portion of fuel which has mixed with air and vaporized during the ignition delay phase. The

second peak in heat release is due to the mixing controlled combustion which depends on the duration of fuel injection. Fig. 5–28 shows the results of work by Asad and Zheng²¹⁶ for experimentally measured heat release rates for a number of fueling strategies and alternate combustion modes in light duty diesel engines.

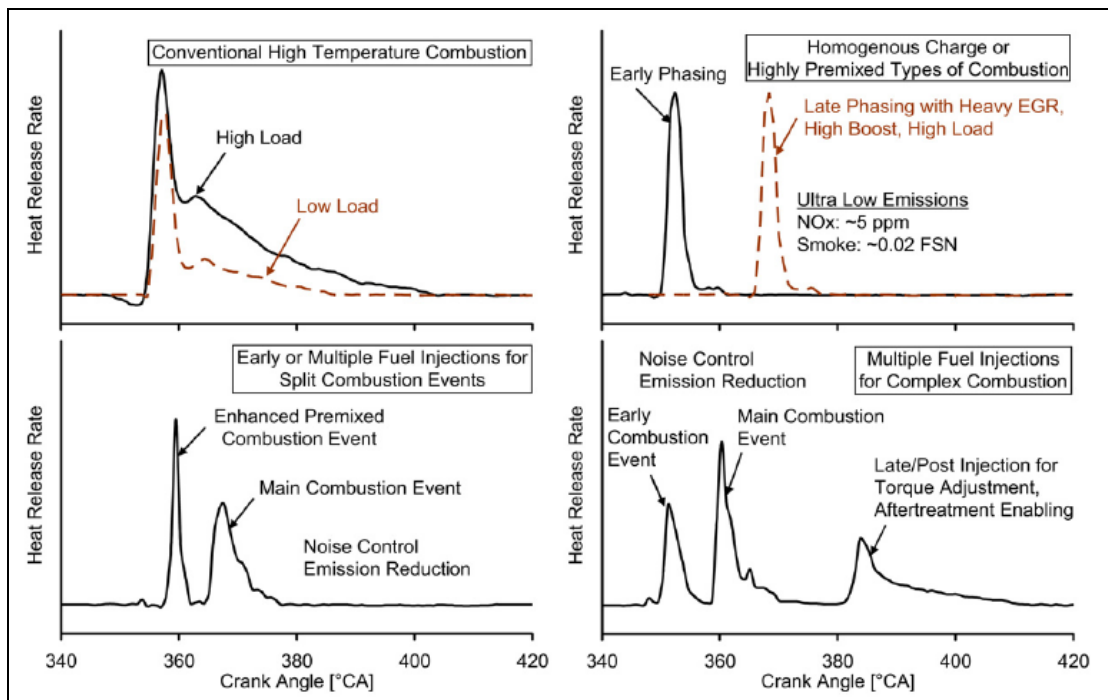


Figure 5–28: Results of work done by Asad and Zheng [216] showing experimentally measured heat release rates for a number of fueling strategies and alternate modes of combustion in light duty diesel engines.

However, no such fuel injection driven phenomena occurs in miniature glow engines. A similar occurrence in spark ignited engines which are premixed similar to miniature glow engines could not be found in published literature. Hence, only speculative explanations for the double peak phenomena observed with heat release rate can be offered at this point.

One possible explanation is based on a two stage combustion process with the primary ignition and combustion of a premixed charge via turbulent flame

propagation followed by diffusion controlled burning of fuel droplets deposited on the cylinder walls. As will be seen in Chapter 6 of this thesis, where high speed combustion images are obtained for a larger glow engine (OS 46 FX), the primary phenomenon driving fuel air combustion appears to be the propagation of a turbulent premixed flame having its origins in the vicinity of the glow plug. However, at lower engine speeds (about 8000 rpm), a secondary burning phenomenon appears to occur near the walls. This observation in conjunction with the observations above suggest that the following possible mechanism for the combustion process: The heat release associated with an initial premixed burning process occurring in the center of the chamber away from the walls vaporizes a liquid fuel film or droplets deposited on the cylinder walls. This fuel diffuses away from the wall into the hot products of the premixed combustion event and eventually ignite. A delay associated with the mixing and ignition time of the secondary process produces the two distinct heat release peaks. Increasing the speed reduces the time available to complete the secondary combustion process resulting in the eventual disappearance of the secondary peak. It also raises the in-cylinder turbulence level which could increase the size of the premixed charge and decrease the size and number of droplets near the walls.

A second explanation for the double peaks observed in heat release rate is based on reaction kinetics. Because ignition starts well before TDC, chain branching reactions are initiated but get suppressed as the piston moves up and the pressure rises. The reactions do not get going again until the pressure starts to fall again after TDC. At low speeds, the reaction can proceed quite far before getting suppressed by the rise in pressure and so the first peak is much larger. As the speed increases, there

is less time for the chain branching reactions to get going before they are cut off and the primary peak gets smaller while the secondary peak gets larger. At very high speeds, there isn't time for the chain branching reactions to get going at all and everything occurs after TDC.

A better understanding of the combustion phenomena can be obtained only through high speed combustion imaging at low speeds in the OS 25 FX engine as well as examination of chemical kinetic calculations at the pressure and temperature conditions in the engine cylinder.

Figure 5–29 shows the net heat release rate as a function of CAD after BDC at 5000 rpm for different equivalence ratios in the OS 25 FX engine. The figure shows that the double peaks become more apparent when the mixture is close to stoichiometric and are increasingly suppressed as one moves away from stoichiometric conditions. One possible explanation is that the larger heat release per unit charge mass expected at stoichiometric conditions and the larger resulting temperature rise increases the droplet vaporization rate leading to a stronger secondary combustion event. Additionally, the larger heat release could also change the pressure sensitivity of the mixture, making the pressure-sensitive chain branching reactions occur quicker.

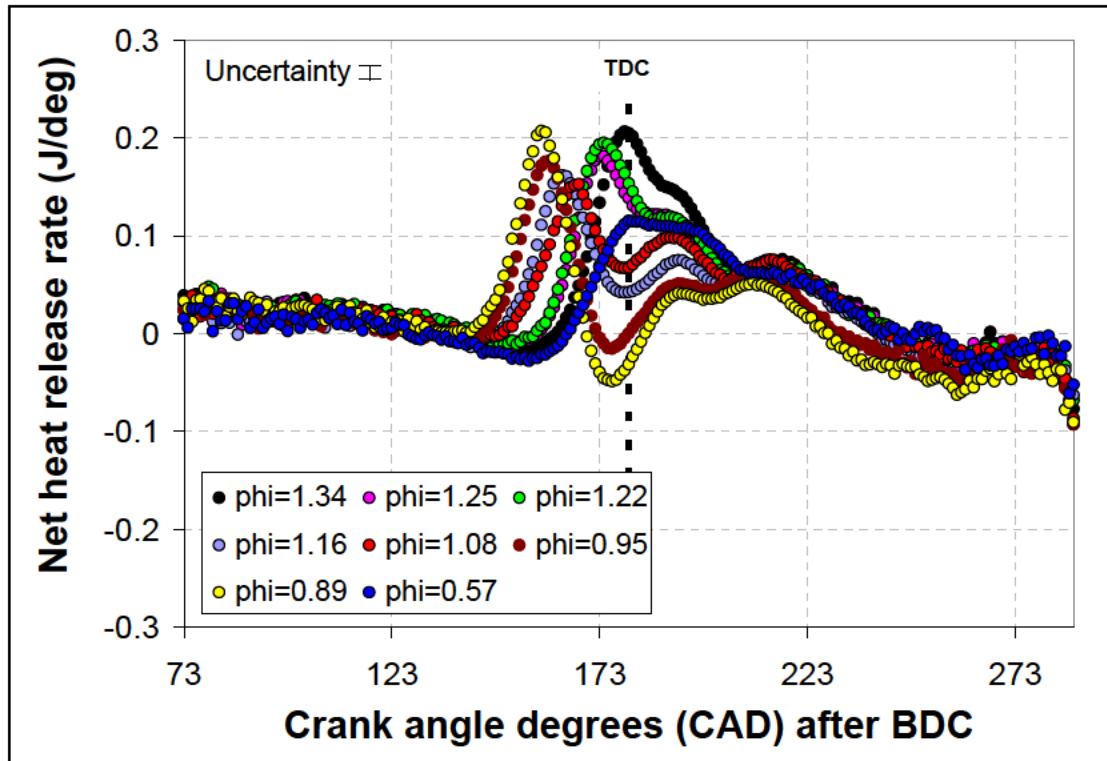


Figure 5–29: Five point moving point average of the net heat release rate estimated for the OS 25 FX engine plotted as a function of crank angle for the engine operating at 5000 rpm and different equivalence ratios.

Similar double peak behavior was observed in the OS 40 FX and the OS 46 FX engines as shown in figures E–12 and E–32 in appendix E. However the phenomenon is not as pronounced and appears to get weaker as engine size increases. This suggests that the occurrence of double peaks in net heat release rate is possibly also a scale dependent phenomenon.

5.4.5 Ignition Timing And Burn Duration

Figure 5–30 shows crank angle after BDC associated with the onset of ignition (estimated using the method outlined in Section 5.3.7) as a function of equivalence ratio for 7 different operating speeds. Clear trends are visible in the 5000, 8000, 9000, 10000 and 11000 rpm data: Ignition occurs progressively earlier at lower

engine speeds and is retarded at higher engine speeds. Ignition also occurs earlier in the cycle as the mixture ratio approaches the stoichiometric value and occurs later in the cycle as the mixture ratio is made rich or lean of stoichiometric. The data for 6000 rpm also seems to follow this trend but is more scattered than the other cases. No clear trends are visible at 7000 rpm. Results similar to those observed for the OS 25 FX engine are obtained for the OS 40 FX and the OS 46 FX engines as shown in figures E-13 and E-33 in appendix E.

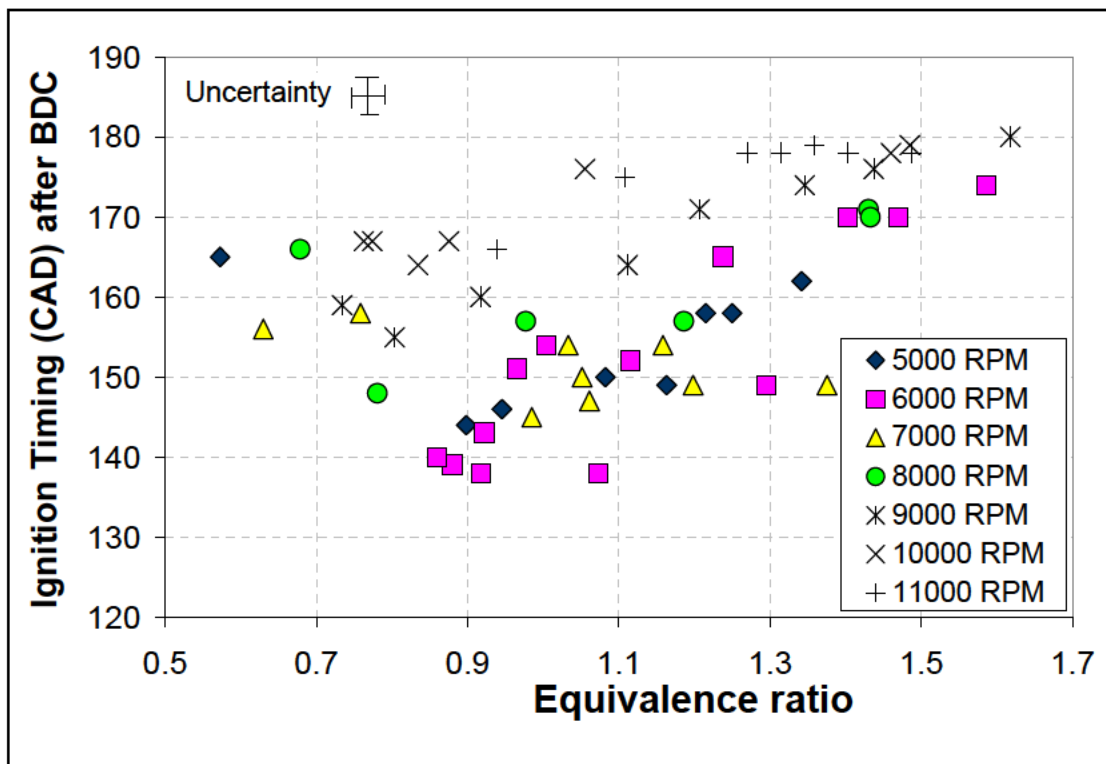


Figure 5-30: Ignition location averaged over 50 cycles as a function of equivalence ratio for the OS 25 FX engine operating at different speeds.

Figure 5-31 shows estimated burn duration in CAD as a function of equivalence ratio for 7 different engine speed. The burn duration generally decreases with increasing engine speed. However, it has different trends with equivalence ratio at different engine speeds. At the lower engine speeds (5000–8000 rpm) burn

duration generally increases as the mixture is brought closer to stoichiometric. At higher engine speeds (9000–11000 rpm) burn duration appears to decrease as the mixture approaches stoichiometric from an initially rich setting and remains almost constant for leaner mixtures. The higher burn duration at lower engine speeds could be due to the secondary burning phenomenon discussed earlier which lengthens the heat release process. The suppression of the secondary ignition process at higher speeds possibly decreases the burn duration. For the larger engines like the OS 46 FX where the secondary burning process is much weaker or does not occur at all (see Fig. E–34 in appendix E) burn duration profiles resemble those observed in conventional scale engines²¹⁷ where burn duration increases with increasing engine speed and decreases as the mixture is brought closer to stoichiometric at constant speed.

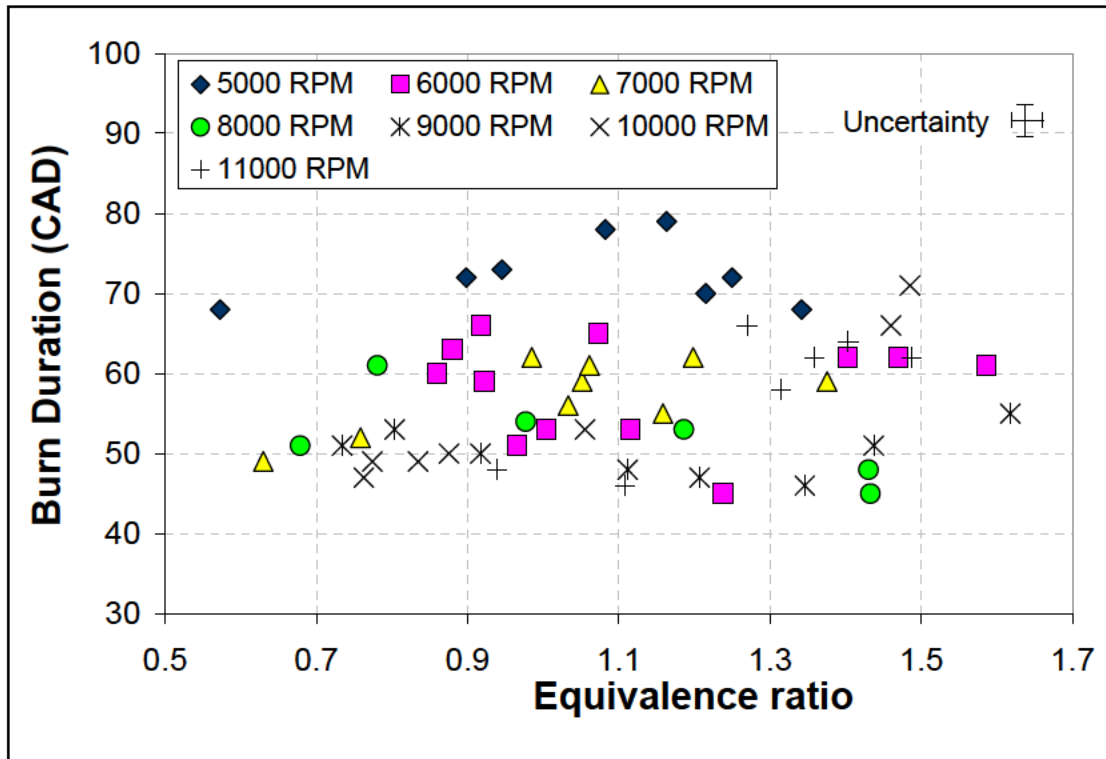


Figure 5–31: Burn duration in crank angle degrees averaged over 50 cycles and plotted as a function of equivalence ratio for the OS 25 FX engine operating at different engine speeds.

5.4.6 Mass Burned Fraction

Figure 5–32 compares the mass burned fraction profiles estimated using the method of Section 5.3.3 (Rassweiler and Withrow²¹⁸) at 10000 rpm for 7 different equivalence ratios. In each case the mass burned fraction goes from 0 to 1. The main objective is to study the effect of engine operating conditions on the rate at which fuel mass is burned. Fig. 5–32 shows that reducing the mixture ratio advances ignition timing as also observed in Fig. 5–30 and reduces the burn duration as observed in Fig. 5–31. The combined effect is that lowering the equivalence ratio shifts the mass fraction burned profile to the left and makes the gradient of the curve steeper at lower equivalence ratios. This is observed in Fig. 5–32 and similar results are obtained for the OS 40 FX and the OS 46 FX engines as seen in figures E–15 and E–35 in appendix E.

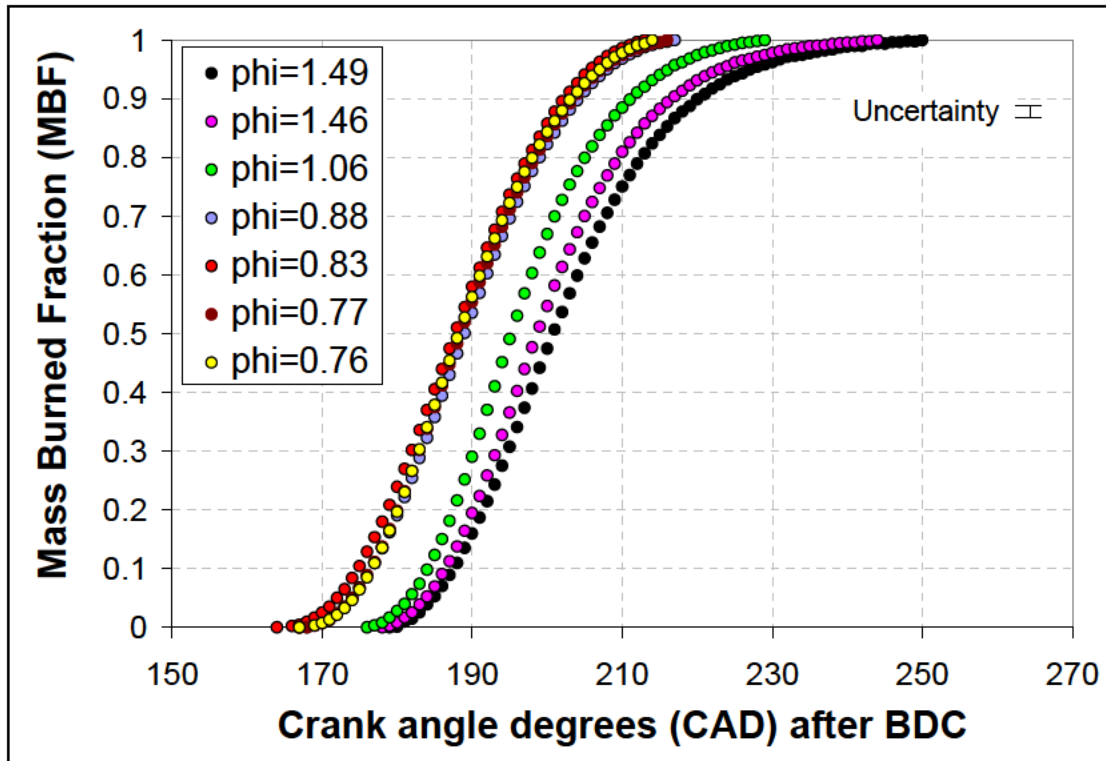


Figure 5–32: Mass burned fraction profiles averaged over 50 engine cycles plotted as a function of crank angle for the OS 25 FX engine operating at 10000 rpm and different equivalence ratios.

Figure 5–33 shows estimated mass burned fraction profiles for 7 different engine speeds and a constant equivalence ratio of about 0.98. The figure shows that engine speed has a considerable influence on the mass burning rate at a constant mixture ratio. In general, the mixture appears to ignite earlier in the cycle as the engine speed is decreased. Similar results are obtained for the OS 40 FX and the OS 46 FX engines as can be seen in figures E–16 and E–36 in appendix E.

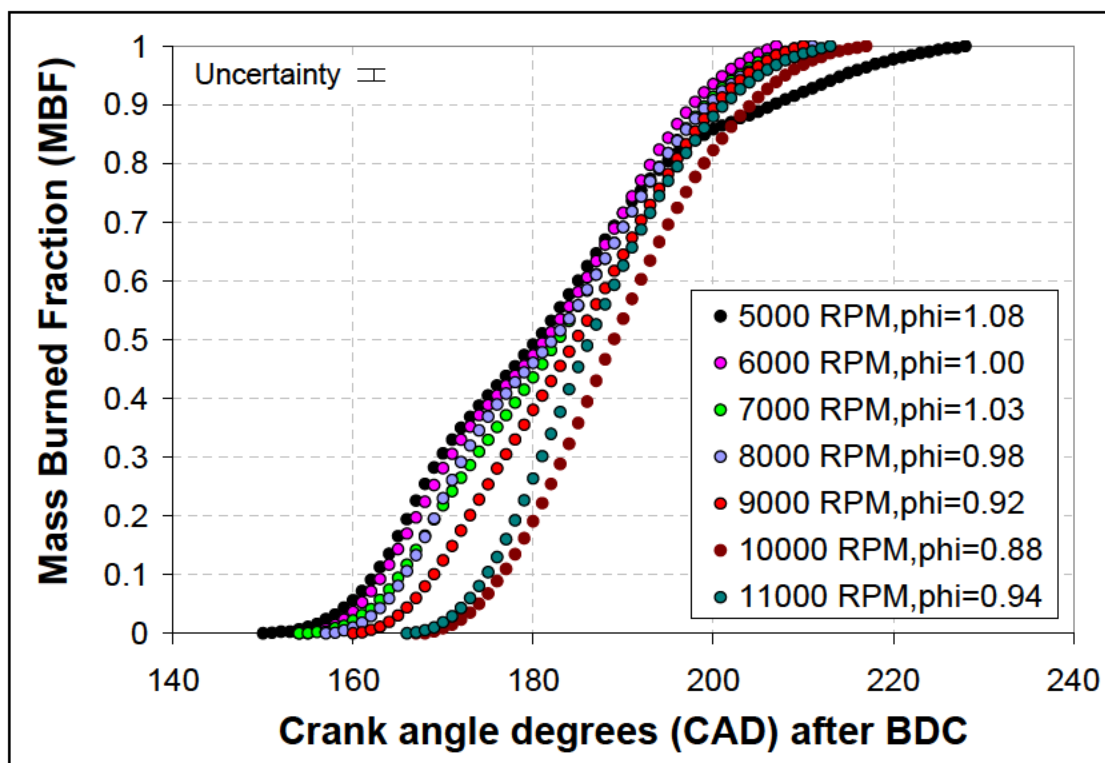


Figure 5–33: Mass burned fraction profiles averaged over 50 engine cycles plotted as a function of crank angle for the OS 25 FX engine operating at different speeds and an equivalence ratio of ~ 0.95 .

5.4.7 Heat Release Rate

Figure 5–34 shows the estimated heat release fraction profile at a constant speed of 10000 rpm and 7 different equivalence ratios. The heat release fraction ranges from 0 to 1 and is computed using the technique explained in Section 5.3.6. The figure shows that moving the mixture closer to stoichiometric advances ignition and reduces burn duration. Similar results are obtained for the OS 40 FX and the OS 46 FX engines as seen in figures E–17 and E–37 in appendix E.

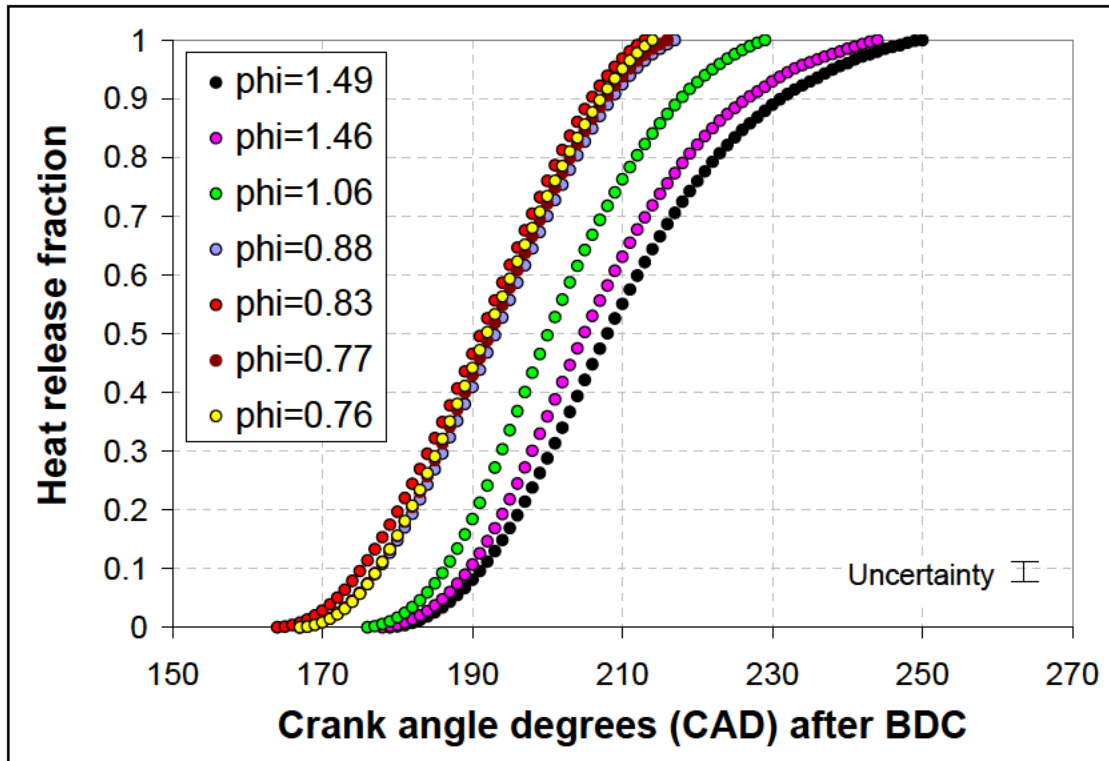


Figure 5–34: Heat release fraction averaged over 50 engine cycles plotted as a function of crank angle for the OS 25 FX engine operating at 10000 rpm and different equivalence ratios.

Figure 5–35 shows mass burned fraction profiles at 7 different engine speeds and a constant equivalence ratio of about 0.98. The results are similar to those presented in 5–33. Results obtained for the OS 40 FX and OS 46 FX engines are presented in figures E–18 and E–38 in appendix E.

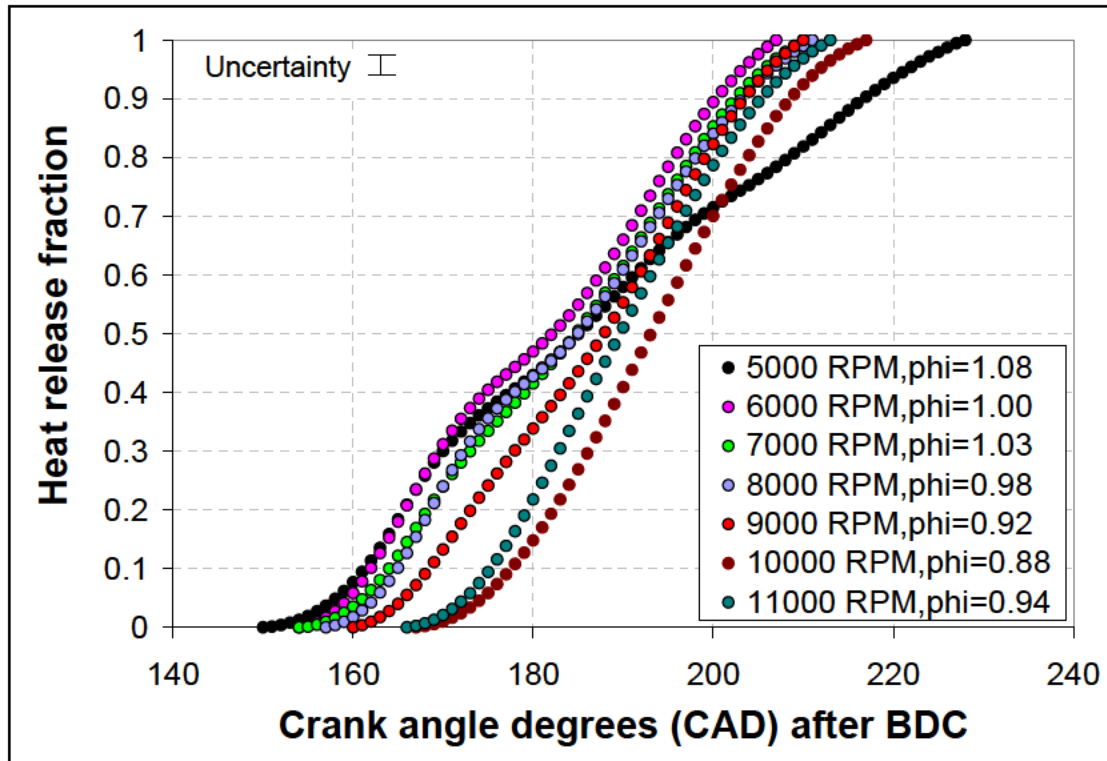


Figure 5–35: Heat release fraction averaged over 50 engine cycles plotted as a function of crank angle for the OS 25 FX engine operating at different speeds and an equivalence ratio of ~ 0.95 .

5.4.8 Scaling Analysis

A scaling analysis of engine performance on the basis of cylinder pressure measurements acquired from the three OS engines is undertaken to understand the effect of engine size on various parameters investigated in the earlier sections. These include peak cylinder pressure, location of peak cylinder pressure, ignition timing and burn duration, heat release rate etc. During the course of this analysis, comparisons are made while keeping the engine speed and operating equivalence ratio constant across the different cases. This allows engine size to be the sole variable influencing change in engine performance.

Figure 5–36 compares cylinder pressure traces in each of the three engines at four operating speeds and equivalence ratios. Engine size decreases from the OS 46 FX engine to the OS 25 FX engine. In most (but not all) cases, peak cylinder pressures are highest in the OS25FX and lowest in the OS 40FX which is consistent with the fact that the OS25FX has the highest geometric compression ratio and the OS40FX has the lowest geometric compression ratio (see Table 5–2). Port timing does not vary significantly between the three engines resulting in a consistent behavior outside of the combustion phase of the cycle.

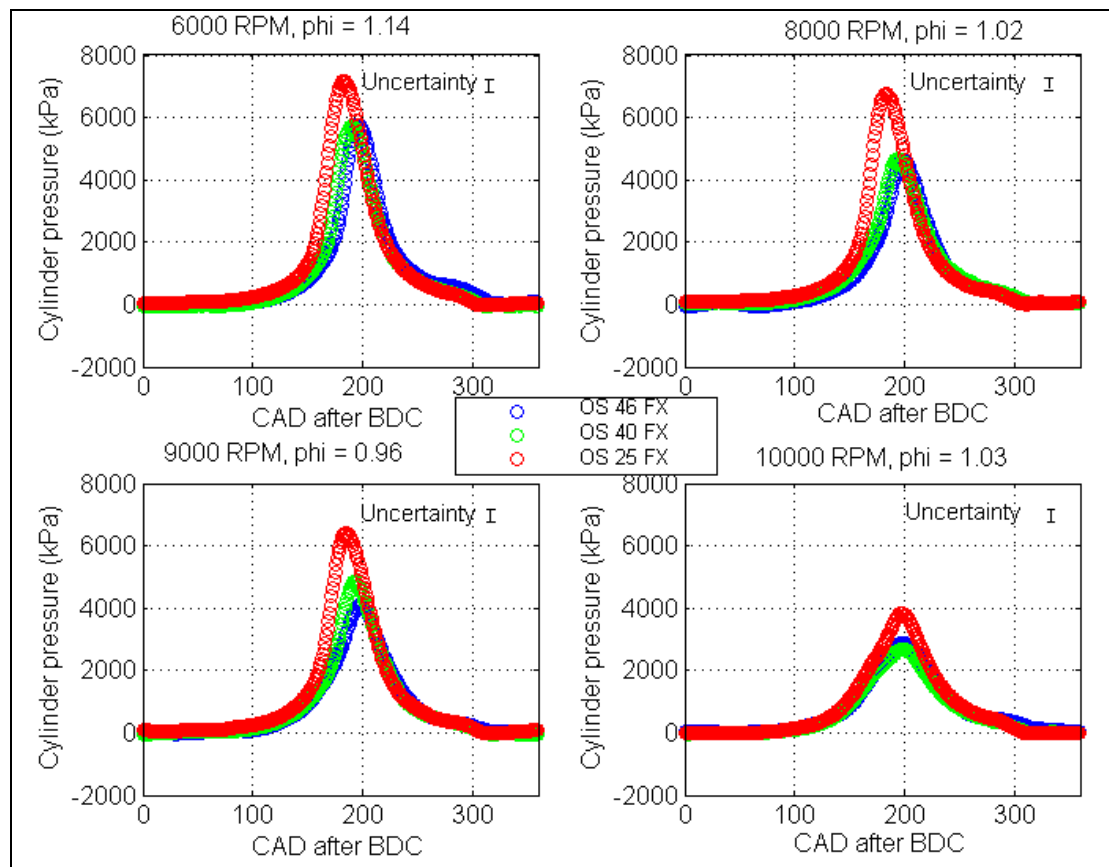


Figure 5–36: Cylinder pressure traces for the three different engines tested in this work at constant engine speed and equivalence ratio.

Figure 5–37 shows various quantities estimated using cylinder pressure measurements as a function of engine displacement at three speed/equivalence ratio

combinations. Peak cylinder pressure increases as engine size is reduced. The location of the peak cylinder pressure appears to move earlier in the cycle as engine size is reduced. The coefficient of variation in peak cylinder pressure decreases with decreasing engine size. Combustion also appears to start earlier in the cycle as engine size is reduced. The burn duration results are more scattered but seem to suggest that burn duration increases with decrease in engine size. The difference between indicated and measured brake power decreases with decreasing engine size.

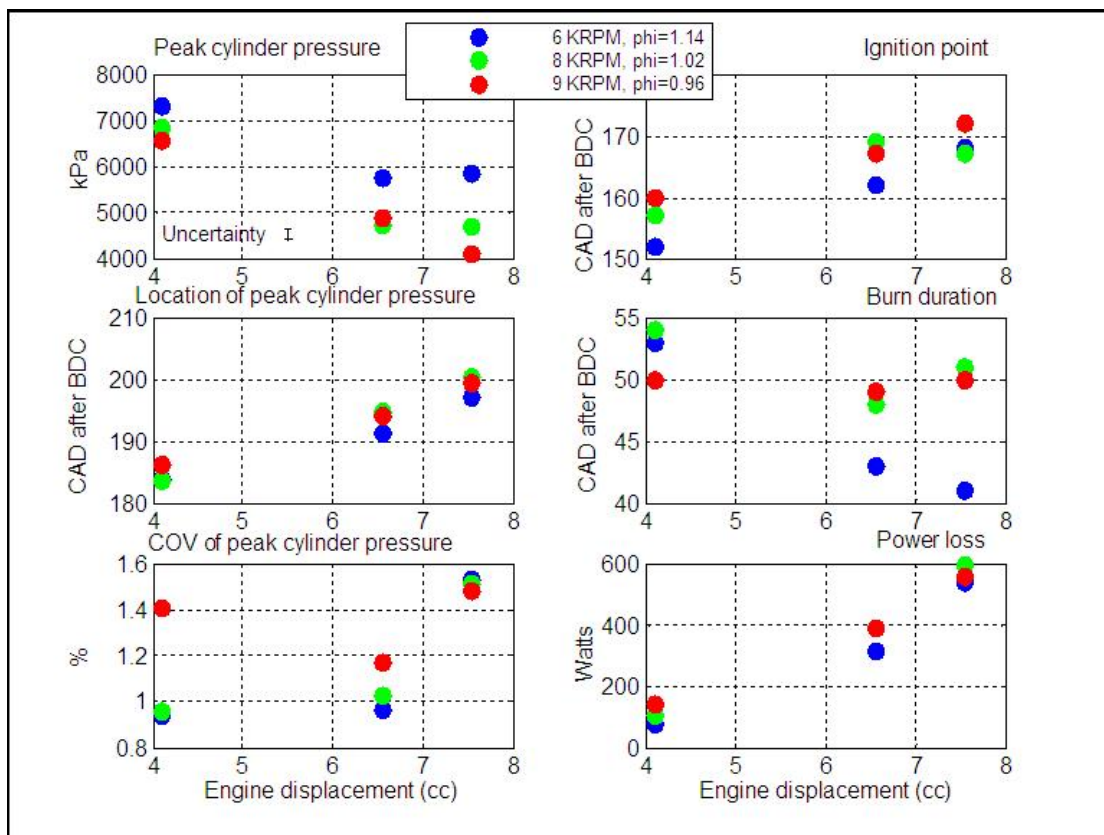


Figure 5–37: Various estimated quantities for the three different engines tested in this work at 3 engine speed/equivalence ratio combinations as a function of engine displacement.

Figure 5–38 shows estimated mass fraction burned profiles for the three engines at four different speed/equivalence ratio combinations. For engine speeds of 6000–9000 rpm, mass fraction burned rate is appears to become stretched for the

smallest engine resulting in an increasing burn duration. The nature of the mass fraction burned curve for the engines seem to suggest that the probability of secondary burning discussed earlier increases as engine size decreases. At higher engine speeds of 10000 rpm, the mass fraction burned curves for all three engines are seen to follow each other closely.

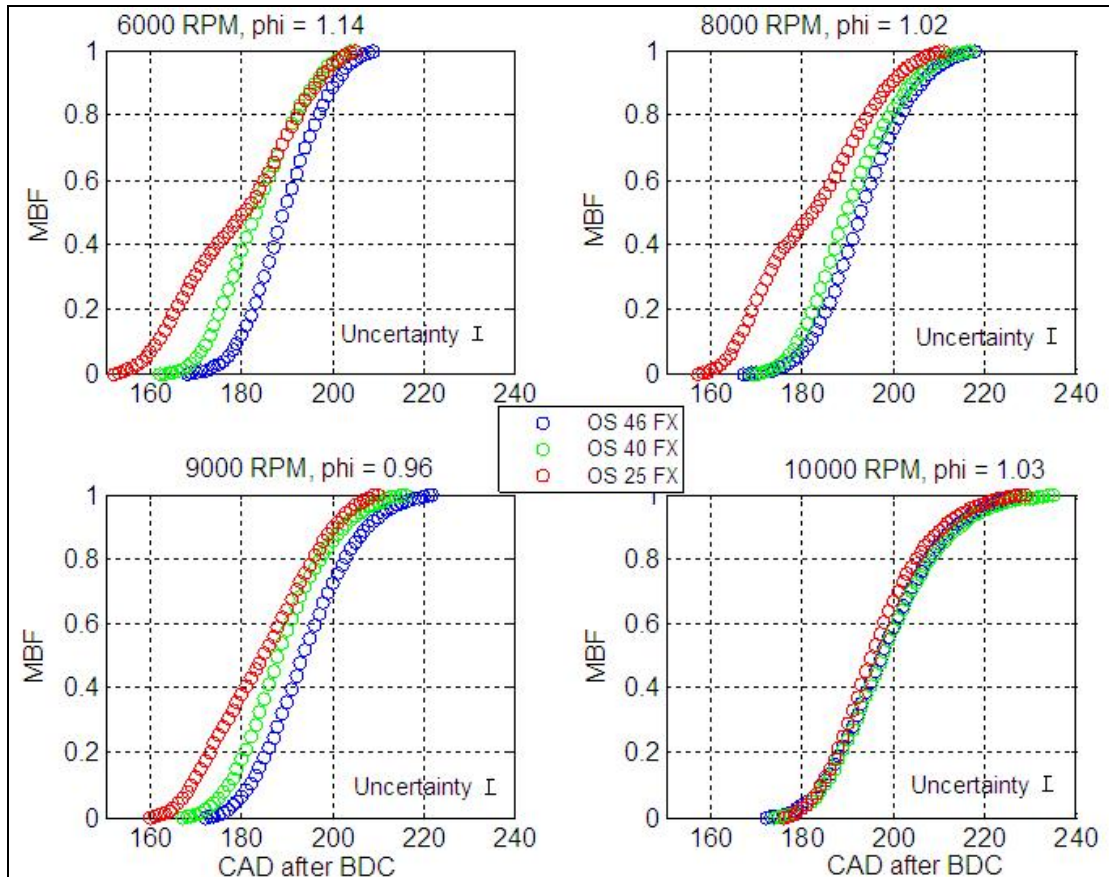


Figure 5–38: Mass burned fraction profiles for the three different engines tested in this work at four speed/equivalence ratio combinations.

Figure 5–39 shows net heat release as a function of crank angle after BDC in the three engines at four different speed–equivalence ratio combinations. The figure shows that the heat release rate is highest in the OS 46 engine and decreases with engine size. However, this difference decreases with increasing engine speed. The

double peaks in net heat release rate only appear at low speeds in the smallest engine. It is suppressed at higher engine speeds.

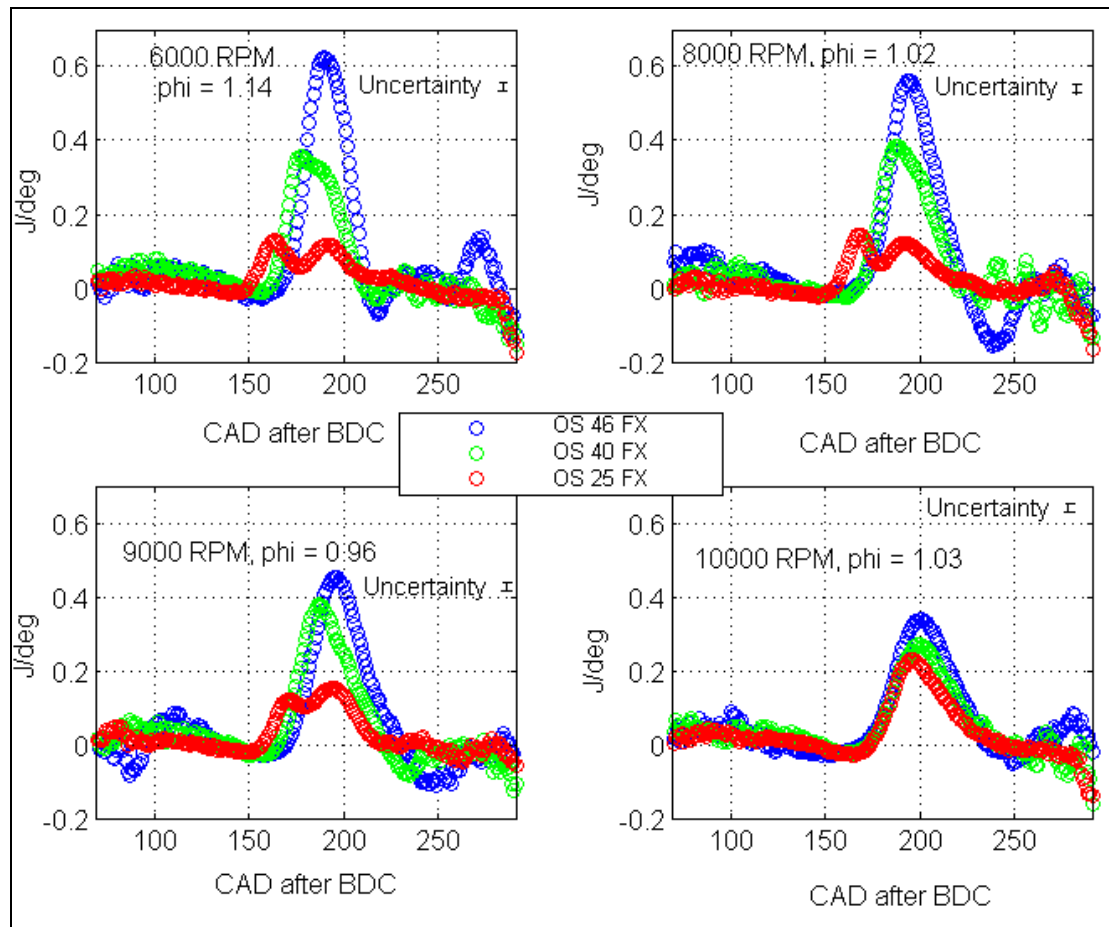


Figure 5–39: Net heat release rates for the three different engines tested in this work at conditions of different constant engine speeds and equivalence ratios plotted as a function of crank angle degrees.

Chapter 6 : Combustion Visualization and Analysis

6.1 Combustion Analysis in Miniature IC Engines

The overall energy balance applied to the engine in Chapter 4 provided indirect evidence that losses due to incomplete combustion are the largest contributors to total energy loss. Therefore, understanding flame initiation, propagation, and flame structure appears to be very important to understanding how small engine performance scales with size. The first attempt to understand the combustion process was through the cylinder pressure measurements reported in Chapter 5. One of the more intriguing findings was evidence of a two-stage combustion process. However, inferring heat release rate and mass fraction burned from pressure measurements is challenging and requires the use of models. The objective of this chapter is to use in-situ visualization of the combustion chamber to provide more direct indications of heat release rate in order to corroborate the findings of the pressure measurement analysis and to gain further insight into the combustion process occurring in these engines, how it differs from that occurring in conventional-scale engines, and why. The results will be summarized in the final portion of the chapter by placing glow fuel combustion in miniature engines on a regime diagram generated for conventional-scale engines.²¹⁹

There has been very little work investigating combustion in small, glow-fueled engines. The results of Chapter 5 suggest that the combustion process is considerably different in character from traditional spark ignition gasoline or direct injection diesel engines. The most detailed information is reported by Manente²²⁰ who reported ‘dual mode combustion’ in miniature glow engines where the charge

sometimes ignited and burned homogeneously and sometimes burned in a premixed flame mode. However, the modifications required to achieve optical access – like relocating the glow plug to near the bottom of the engine cylinder – were so severe that it is unclear how closely the combustion process observed in this engine is related to combustion in the unmodified engine. Therefore, a key goal of this work was to provide optical access with as few changes as possible to the physical structure of the engine. In this regard, the author would like to acknowledge the diligent efforts of Dylan Rebois who designed the aluminum support disks and the quartz bowl that formed the key components of the combustion visualization setup.

6.2 Setup for In-Cylinder Optical Visualization

6.2.1 Experimental Setup

Optical access is achieved by replacing the stock cylinder head (Fig. 6–1) with a quartz disc with a hole at its center (Fig. 6–2) to admit the glow plug (OS#8 glow plug with $\frac{1}{4}$ –32 threads) and that has been machined around the hole to duplicate the ‘bowl’ around the glow plug. The quartz disc is clamped to the cylinder liner using an aluminum ring in exactly the same way as the stock head is clamped to the liner. Optical access is provided through the edges of the disc as illustrated in Fig. 6–2 and through the top of the quartz element via an array of holes bored through the aluminum ring.

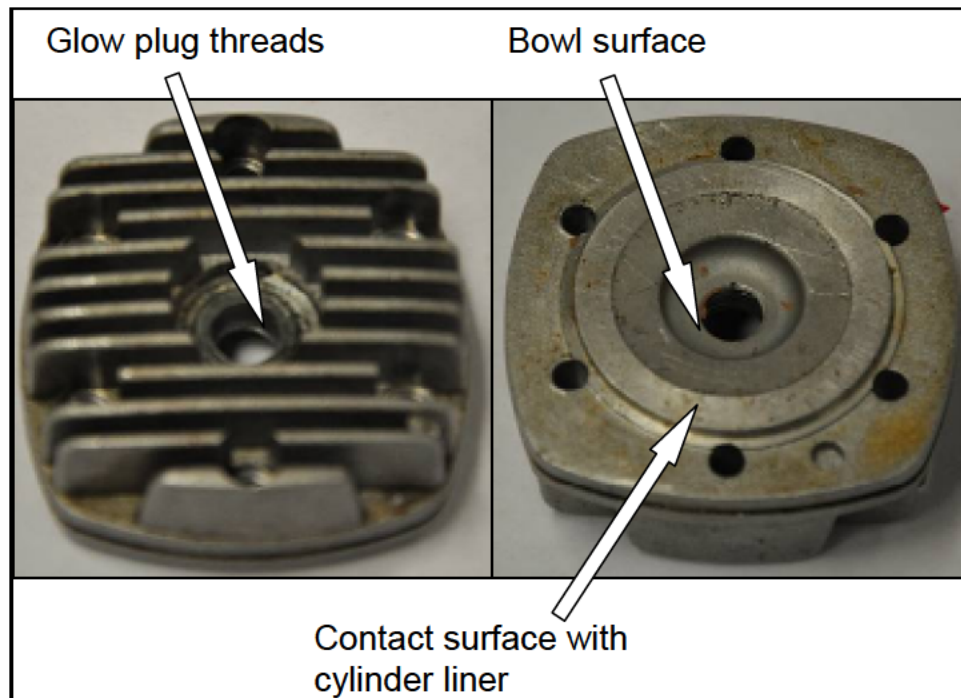


Figure 6–1: Photographs showing the top and bottom of a stock cylinder head for the OS 46 FX engine.

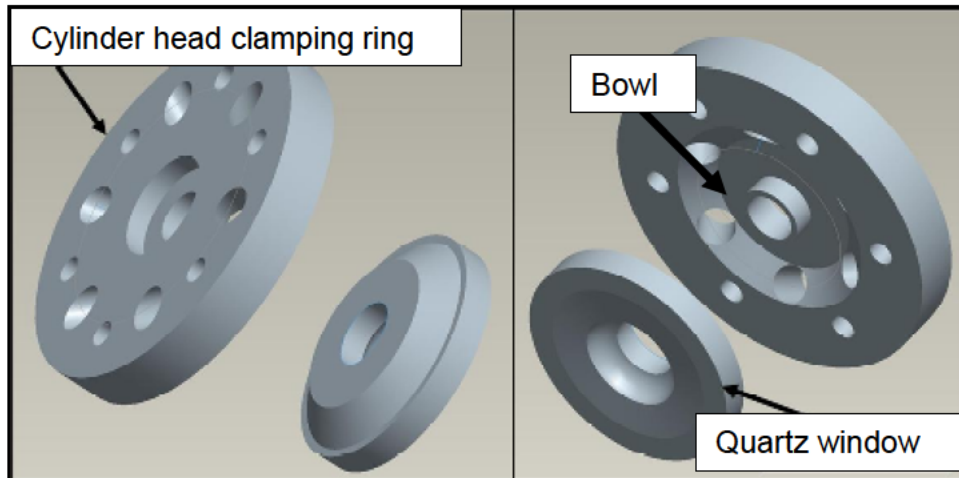


Figure 6–2: Two views of the CAD design in PRO/e for the clamping ring and the quartz bowl to replace the stock cylinder head for the OS 46 FX engine.

Figure 6–3 shows photographs of the front and back sides of the aluminum clamping disk with glow plug installed. Figure 6–4 shows photographs of the front and back sides of the quartz cylinder head with bowl. The original cylinder head bolts are used to sandwich the quartz bowl between the clamping ring and the cylinder liner. The quartz bowl fits directly into the matching recess machined into the bottom surface of the aluminum disk. Gas sealing is achieved on the sides of the aluminum boss that supports the glow plug and aligns with a matching hole in the quartz bowl. Gas sealing is also provided by the flat face of the aluminum disk above the quartz bowl.

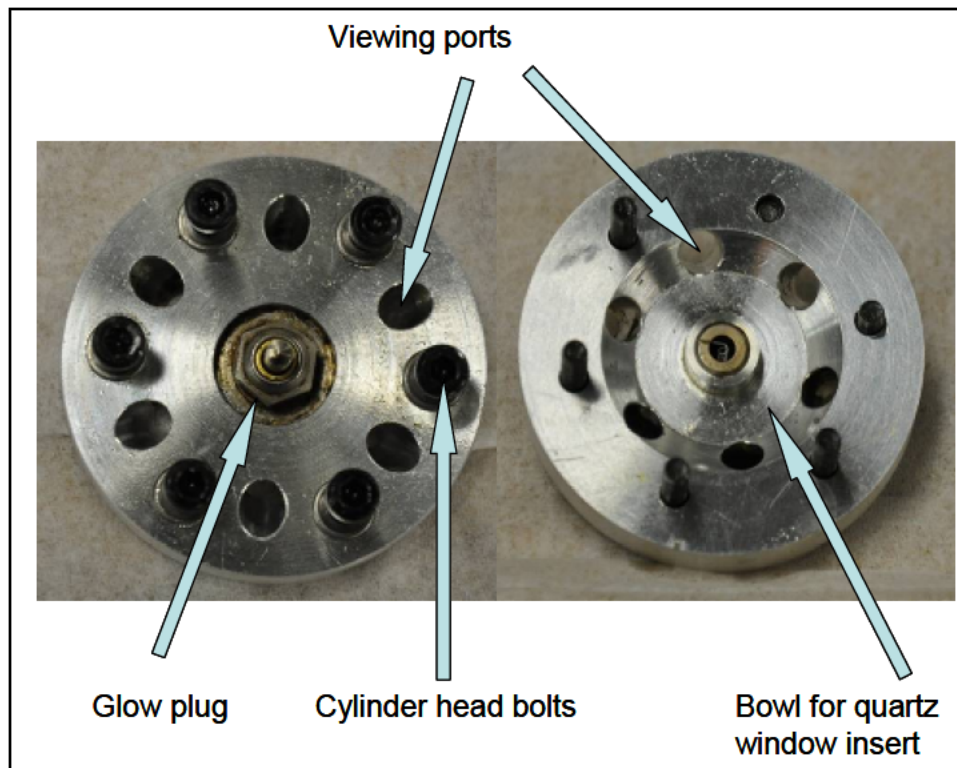


Figure 6-3: Photographs showing the top and bottom sides of the aluminum clamping ring with glow plug attached.

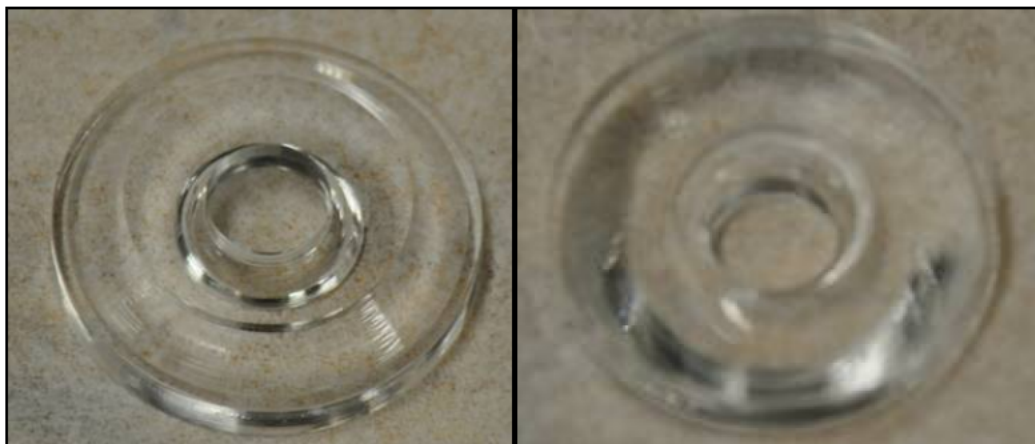


Figure 6-4: Photographs showing the top and bottom sides of the quartz bowl.

Figure 6-5 shows a photograph of the quartz window assembly mounted and secured with cylinder head bolts on the OS 46 FX engine. The quartz bowl was machined by Precision Glass Incorporated. The construction of the window required fire polishing of the internal surfaces due to the miniature dimensions. The windows,

while providing a clear visualization of the in-cylinder processes, posed difficulties during extended use within the engine. The two major issues faced were degradation of optical access due to soot buildup on the window surface and mechanical failure (cracking).

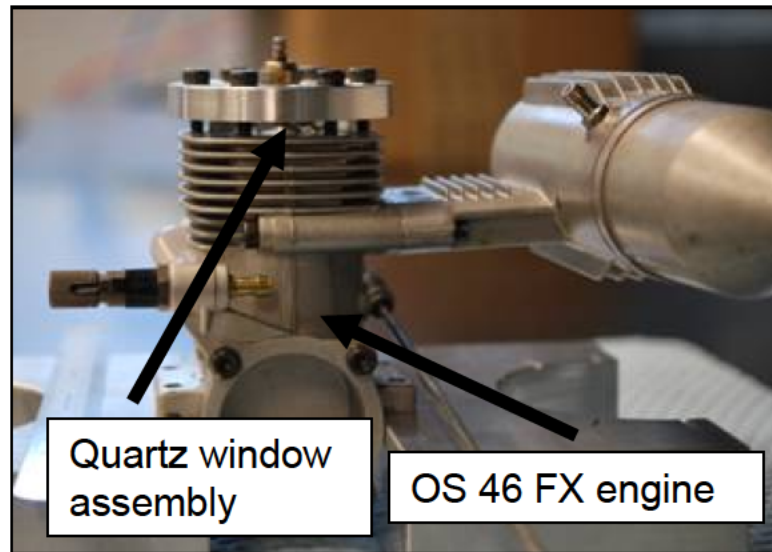


Figure 6–5: Photograph of the OS 46 FX engine with the quartz window assembly.

Figure 6–6 is a photograph of a window after use for a total run time of about an hour at engine speeds ranging from 7000 to 8000 rpm and various fuel–air mixture ratios. The accumulation of soot is clearly visible on the internal surface of the bowl and optical access was considerably degraded. The solution to this problem was to reduce the experiment run time to about 15 minutes. The window was then removed and cleaned using ordinary soap solution and a fine brush.

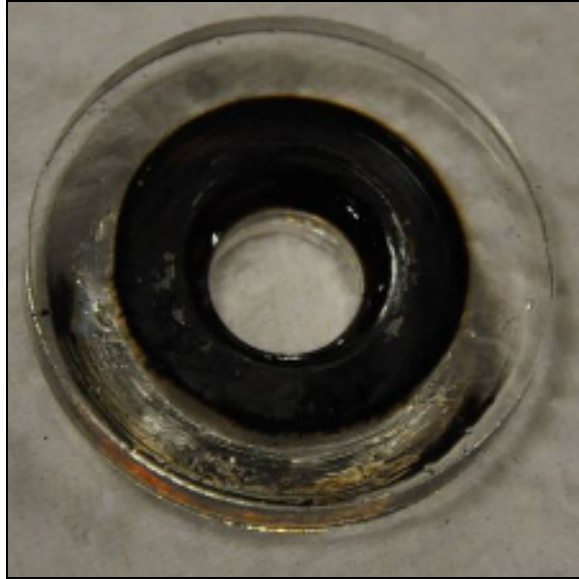


Figure 6–6: Photograph of the quartz bowl showing accumulation of soot particles after extended use.

A secondary problem was the form of miniature cracks on the top surface of the window bordering the support disk. While these cracks were very small, they made it difficult to achieve a gas-tight seal after reinstallation. Figure 6–7 shows a photograph of the window with cracks after use on the engine. This problem was solved by using a high temperature, high pressure sealant called Copaltite²²¹ which was applied in trace quantities in the cracked areas on the window. This provided sufficient sealing for engine tests to be carried out as before.

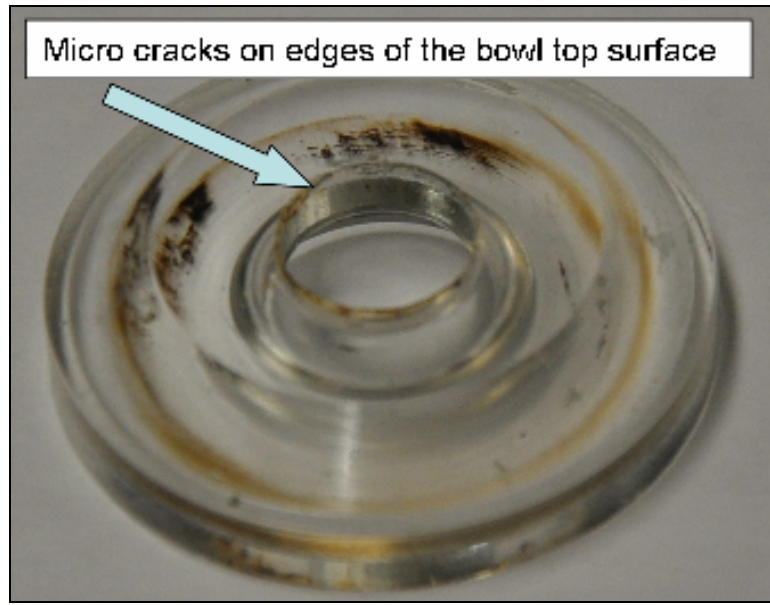


Figure 6–7: Photograph of the quartz window showing miniature cracks after use on the OS 46 FX engine.

Figure 6–8 shows the high speed camera used in this work. The v12.1 Phantom camera is made by Vision Research Inc. and its specifications and the values of the settings used in this work are listed in Table 6–1. The camera is controlled using a software package called Phantom camera control software v675.2 developed by Vision Research. Image resolution and frame rate were selected by trial and error so as to capture sufficient light from the combustion process while maximizing the number of images acquired in each cycle. The exposure time is calculated automatically for the selected frame rate. The number of images acquired for all engine settings post trigger was 3600. Once the images were acquired and stored on the camera, the movie file containing 3600 images where each image has a file size of 1 MB to give a total size of 3.6 GB was found to take 3 minutes to transfer to the PC over the Ethernet cable. The issues with soot degradation and cracking of quartz windows reduced experiment run time to about 15 minutes. The choice of the number

of images selected post trigger was influenced by this factor. This was selected based on the time required to transfer the movie file to a PC. A movie file of 3600 images where each image has a file size of 1 MB has a total size of 3.6 GB and takes 3 minutes to transfer from the camera to the PC over the Ethernet cable. The ‘sync’ setting on the camera was set to internal as it was triggered using the camera software.



Figure 6–8: High speed Phantom camera (model v12.1) made by Vision Research Inc. used to acquire combustion images through the quartz window.

Parameter	Limiting value	Selected value
Image resolution	1280 x 800 (max)	800 x 600
Number of pixels	1024000 (max)	1024000
Frame rate	680000 (max)	5000
Exposure time	1 micro second (min)	200 micro seconds

Table 6–1: Limiting values for the various operating settings on the high speed Phantom camera and the values selected in this particular research.

Figure 6–9 shows the experimental setup for in–cylinder visualization. The engine is held to the test stand using aluminum support blocks and retaining bolts.^{vi} A nose cone is connected to the propeller to facilitate engine start up. The propeller serves multiple purposes. First, it provides a load on the engine enabling it to operate stably over a range of speeds. Second, it provides cooling air to the engine. Third, it provided a time reference for the high speed photographs as the blade cut across the field of view of the camera. This is captured in post–processing and used to associate crank angles with each in–cylinder image. The location of the propeller with respect to TDC was measured before and after every engine run and was found to be unaffected by the engine run. While simple and convenient, this method for determining a time has a relatively large uncertainty ranging from 20–40 CAD. This uncertainty is due to the fact that the propeller blade has a finite width and it is not possible to estimate the exact part of the blade that crosses the field of view of the camera in each engine revolution. This results in an uncertainty which is lower for higher engine speeds when a thinner blade is used. The uncertainty is higher for lower engine speeds when a thicker blade is required.

^{vi} The green hose seen in the Fig. 6–9 is for exhaust gas pressure which is transmitted to the fuel tank. The air intake tube connected to the carburetor is not in contact with the engine during normal operation.

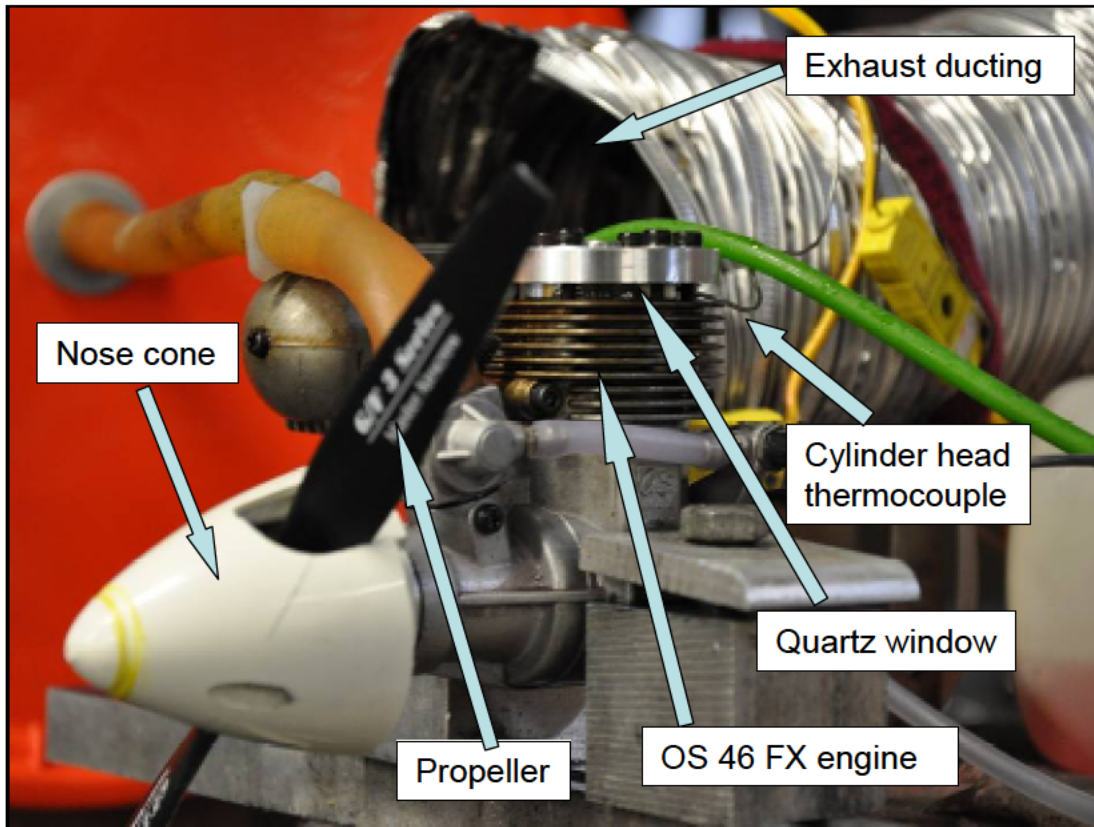


Figure 6–9: Photograph of the engine test setup on a stand with nose cone and propeller for engine loading.

The key objectives of this experiment are to determine the mode of flame initiation and propagation. Additional analysis is performed to determine the cycle-to-cycle variation in combustion intensity and to correlate it with engine speed and fuel–air mixture ratio. The uncertainty in the location of the photographs with respect to TDC does not affect either of these analyses.

Fuel and air flow rates are measured as described in Chapter 2. These measurements are used to estimate engine fuel–air mixture ratio. Engine speed is measured using a Monarch optical speed sensor. Cylinder head and exhaust gas temperatures are monitored using K–type thermocouples.

6.2.2 Experimental Procedure

The camera is positioned in the right location to capture images through the quartz window as well as to view the blade of the propeller cutting across the field of view. The camera lens is kept covered by the lens cap and a current session reference is obtained for the camera using the control software.²²² The camera is focused on the cylinder head bolts closest to the quartz window and the zoom is set to provide the desired field of view. The best combustion images were obtained when the background light in the room was minimized. The engine is started in the usual way using a starter motor pressed to the nose cone. For a particular propeller installed on the engine, a range of operating speeds is possible at different throttle and mixture valve settings. Associated with the propeller is also a maximum possible engine speed. If the engine speed to be investigated is smaller than the maximum speed possible with a certain propeller, a smaller propeller is required to be installed.

For an installed propeller, the throttle valve is kept wide open post engine startup to achieve required engine speed at a particular mixture setting (usually rich of stoichiometric). Leaning the mixture ratio results in higher engine/propeller speed. Engine speed is adjusted back to the required constant value by closing the throttle valve. Thus, simultaneous manipulation of throttle and mixture valves allows a constant engine speed to be maintained with the same propeller. At any setting, the camera is triggered using the control software and a movie is recorded. Simultaneously, measurements are obtained from the flow, speed and temperature sensors using the LABVIEWTM data acquisition setup. Once the images are acquired, the movie file is transferred to the PC over the Ethernet cable. This takes about 3

minutes and the throttle is adjusted to keep the engine running at a low idle speed to reduce mechanical degradation of the quartz window. Once the movie file is transferred, the mixture valve is adjusted to a new setting and the throttle valve is adjusted to obtain the required engine speed. Data is obtained for mixture settings ranging from rich to lean at a constant speed. At the end of the run, the engine is shut off using the throttle valve. The camera is used to acquire a background image which is used during post-processing. The cylinder head is then disassembled and the quartz window is cleaned before being reassembled using the high temperature bonding agent as mentioned previously. The location of the propeller with respect to TDC is measured to obtain the time reference. Table 6–2 lists the propellers used with the engine, the corresponding engine speeds and the fuel–air mixture ratios for which imaging data was obtained in this work.

	Engine speeds (rpm)				
	7000	8000	9000	10000	14000
Propeller size	11x7.5	12x4	10x6	10x6	8x6
Fuel–air mixture ratios explored	0.26,0.37,0.38,0.39,0.42	0.29,0.29,0.33,0.37,0.41,0.42	0.18,0.27,0.34,0.37	0.14,0.19,0.21,0.28	0.20,0.24,0.25,0.26
Time between successive images (CAD)	8.5	9	11	12	16

Table 6–2: Propeller sizes used with the OS 46 FX engine along with the corresponding engine speeds and fuel–air mixtures explored in this study.

6.2.3 Effect of Mixture Ratio

Figures 6–10 and 6–11 are false color images of natural luminescence occurring from the combustion chamber for two consecutive cycles of the OS–46FX engine operating at a speed of 8000 rpm and a fuel–air mixture ratio of 0.21 or an equivalence ratio of about 1. The corresponding crank angles at approximately 10 CAD intervals are shown in the upper left hand corner of each image and the white lines show the approximate edges of the combustion chamber bowl. The sides of the bowls are curved and the white lines are mere approximations. The exhaust port is located to the left of the bowl center. The bright spot in the center of the images that remains illuminated throughout the engine cycle is the glow plug.

The images from the two cycles show an increase in background luminescence that spreads throughout the chamber beginning at about 100 and ending at about 180 CAD suggests that the combustion event occurs within this interval. The variation in overall luminescence intensity between these cycles is small indicating a low amount of cycle to cycle variation. Average light intensity and coefficient of variation (COV) which characterizes cycle–to–cycle variation are defined and presented in later sections. Cycle to cycle variation is seen to be a strong function of fuel–air mixture ratio and engine speed. The images of both cycles suggest that the mixture to the left of the glow plug ignites first and a flame front propagates outwards. (See 93.4 – 112.8 CAD in Fig. 6–10 and 83.6–193.1 CAD in Fig. 6–11).

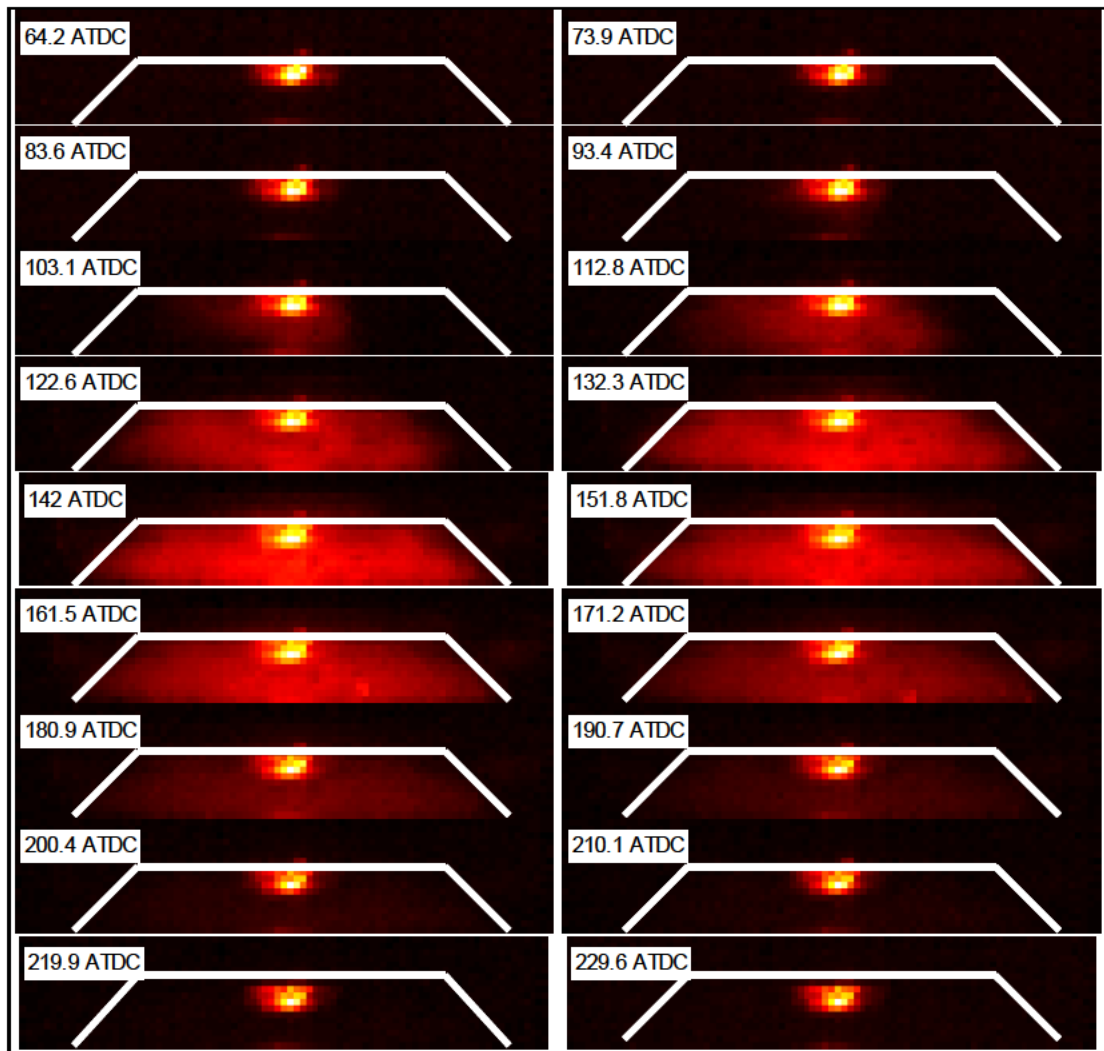


Figure 6–10: High speed false color images of a single engine cycle during the combustion phase in the OS 46 FX engine at 8000 rpm and a fuel air mixture ratio of 0.21. Uncertainty in crank angle location is about 40 degrees CAD.

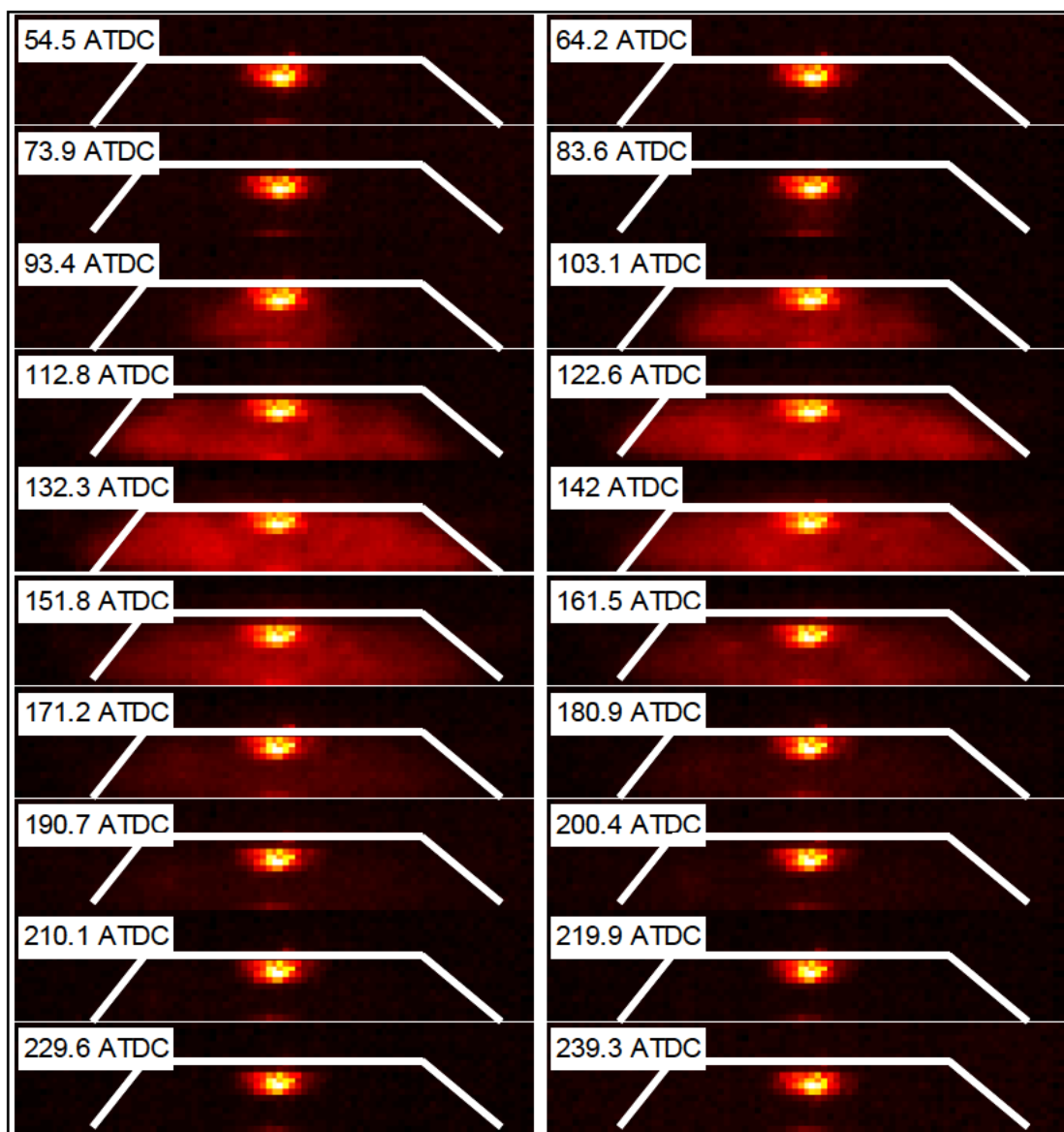


Figure 6–11: High speed false color images of the cycle immediately following the cycle shown in Fig. 6–9. The OS 46 FX engine is operating at 8000 rpm and a fuel air mixture ratio of 0.21. Uncertainty in crank angle location is about 40 degrees CAD.

Since the images are purely of the light emitted from by radiation from the soot particles, there is no way to infer the location of the flame from the images. This makes it difficult to infer whether the combustion is characteristic of a premixed turbulent flame or of an HCCI type event. However, the gradual spread of combustion from the exhaust port throughout the bowl indicates a propagation type of

phenomenon (possibly initiated by hot products near the exhaust port that are left over from the previous cycle) which is more typical of a premixed flame than that of HCCI combustion. Figure 6–12 shows images of combustion luminosity for an HCCI type combustion event occurring in a gasoline–fueled single cylinder research engine at the University of Michigan.²²³ As seen in Fig. 6–12 and observed in several other studies²²⁴ a hallmark of HCCI combustion is the development and growth of multiple ignition sites. The generally accepted explanation for this is that the high compression ratios used in HCCI engines raise the premixed charge of fuel and air to the temperature and pressure conditions required for auto–ignition.²²⁵

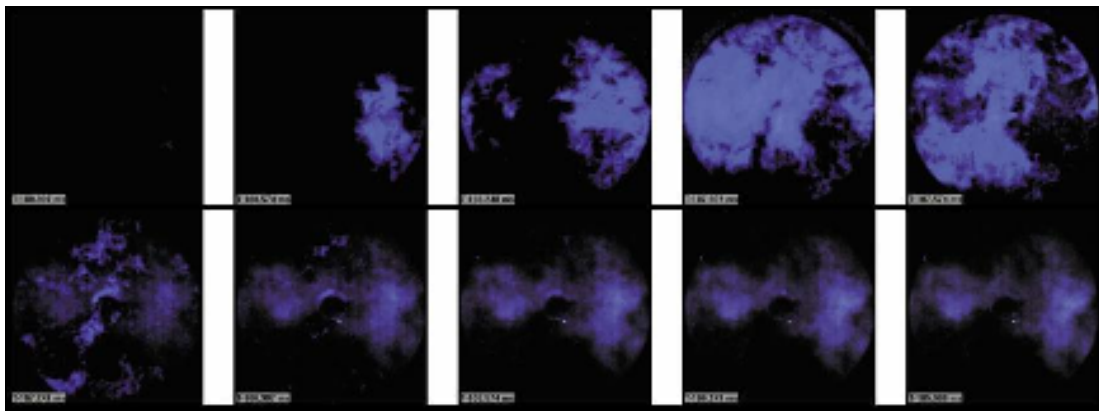


Figure 6–12: High speed images of the combustion process in an optically accessible single cylinder research engine operating at a speed of 700 rpm and an equivalence ratio of 0.52 in a purely HCCI combustion mode on gasoline fuel at the University of Michigan[223]. The images are taken 1.4 crank angle degrees apart.

As a comparison, Figure 6–13 shows high speed images of combustion in a spark ignition engine equipped with a quartz piston. In the images by Rashidi²²⁶ in Fig. 6–13, the spark plug is located at the top of the figure and flame propagation begins at the spark plug and continues outwards. Fig. 6–14 shows images acquired by Sauter et al.²²⁷ who used a PhotoMultiplierTube–Camera to acquire ultraviolet

radiation and visible light from the combustion process in an engine cylinder operated in a spark-ignition and HCCI mode. The images from spark ignition combustion clearly show the propagation of a wrinkled flame from the left to the right. HCCI combustion on the other hand shows formation of multiple ignition points similar to Fig. 6-12.

The images acquired from glow engines in this work do not show any evidence of multiple ignition sites. The spread of combustion is observed to be uneven but is found to originate from the glow plug at all conditions and propagate outwards. This behavior is typical of a premixed turbulent flame structure and is similar to that observed in Fig. 6-13 and that corresponding to spark-ignition combustion in Fig. 6-14.

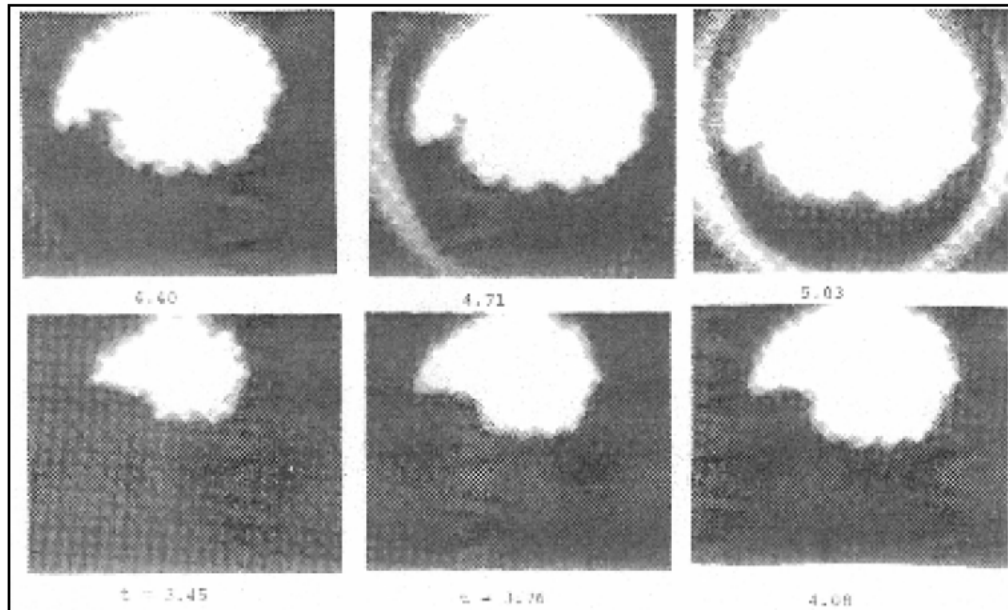


Figure 6-13: Consecutive images of flame propagation in a spark ignition engine where t represents the time after the spark in milliseconds [226].

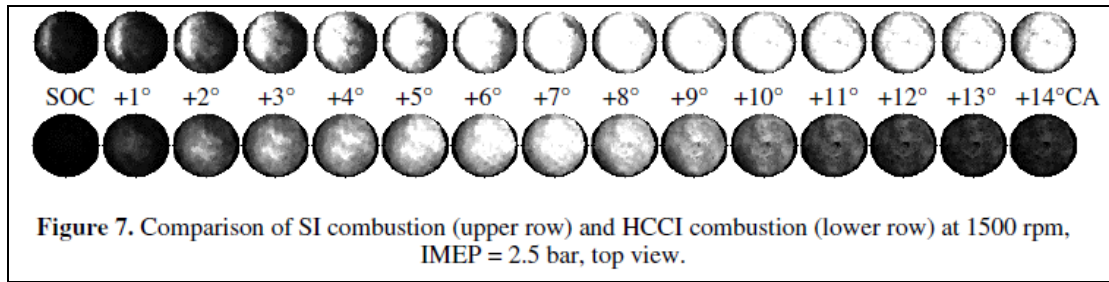


Figure 6–14: High–speed images showing combustion processes in an engine operated in a spark ignition mode as well as in HCCCI mode [227].

Figure 6–15 shows the high speed images of the combustion events during another cycle of the OS 46 FX engine operating at 8000 rpm and a fuel–air mixture ratio of 0.21. The figure illustrates several types of irregularities observed in the combustion process in some engine cycles. A soot particle or combustion of a fuel droplet is visible to the left of the glow plug from 122.6 ATDC to 151.8 ATDC and appears to travel some distance across the face of the bowl to the left. Other isolated areas of luminosity at different locations in the cylinder volume suggest that combustion does not always occur via a propagating flame front. For example, a re–ignition event seems to begin in the lower left of the image at 151.8 ATDC and this could possibly be evidence for the secondary combustion events observed in the pressure measurements reported in Chapter 5.

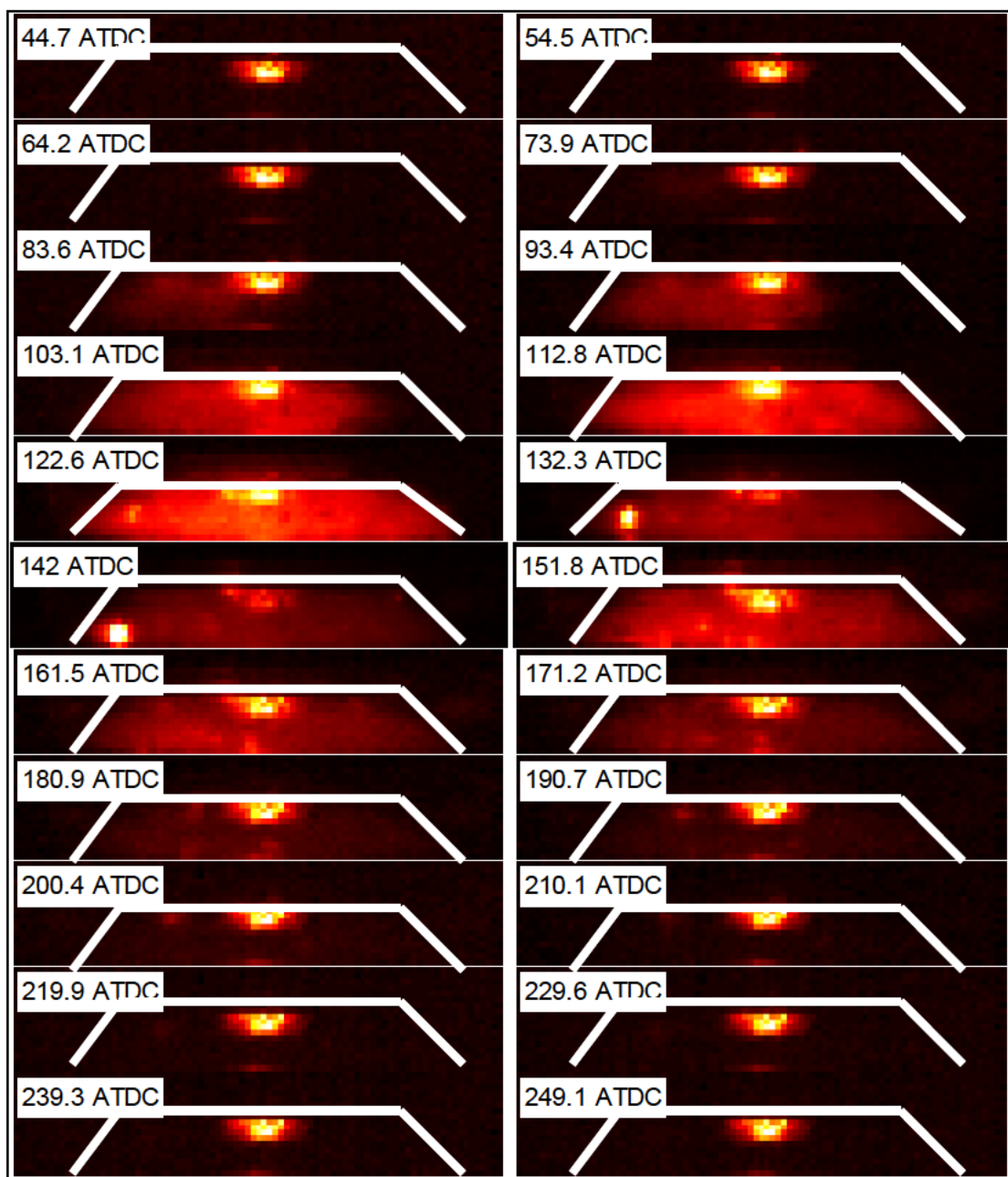


Figure 6–15: High speed false color images of a single engine cycle during the combustion phase in the OS 46 FX engine at 8000 rpm and a fuel air mixture ratio of 0.21 showing the formation of soot as well as evidence of a thin films of fuel burning on the walls of the quartz window. Uncertainty in crank angle location is about 40 degrees CAD.

Figure 6–16 shows image intensity computed from the high speed images in the OS 46FX engine as a function of crankshaft revolutions. Seven engine cycles are

shown; the engine is operating at a speed of 8000 rpm and a fuel–air mixture ratio of 0.21. The images are first cropped so as to retain the area roughly that around the edges of the bowl.

Intensity for each processed image is obtained by first importing the image into MATLABTM as a matrix that assigns a value between 0 to 1 for each pixel. Total image intensity is computed by summing the values of all pixels in the image. Figure 6–16 shows that the image intensity remains close to a constant value corresponding to the intensity of the light emitted by the glow plug in regions where there is no combustion activity. Combustion events are marked by a large increase and decrease in intensity. Image intensity drops sharply twice per cycle (red dots on Fig. 6–16) when the propeller crosses the field of view of the camera. The figure shows that the luminescence varies significantly from one cycle to another. As in the pressure measurements, the coefficient of variation (see Equations 5–1, 5–2, and 5–3) is also used to describe this variability. It is a normalized measure of the dispersion of the distribution in overall image intensity. Another measure of cycle–to–cycle variability is the ‘normalized maximum cycle intensity’ which is the maximum intensity of each cycle divided by the average maximum intensity over all cycles considered. Both measures are reported in Fig. 6–17.

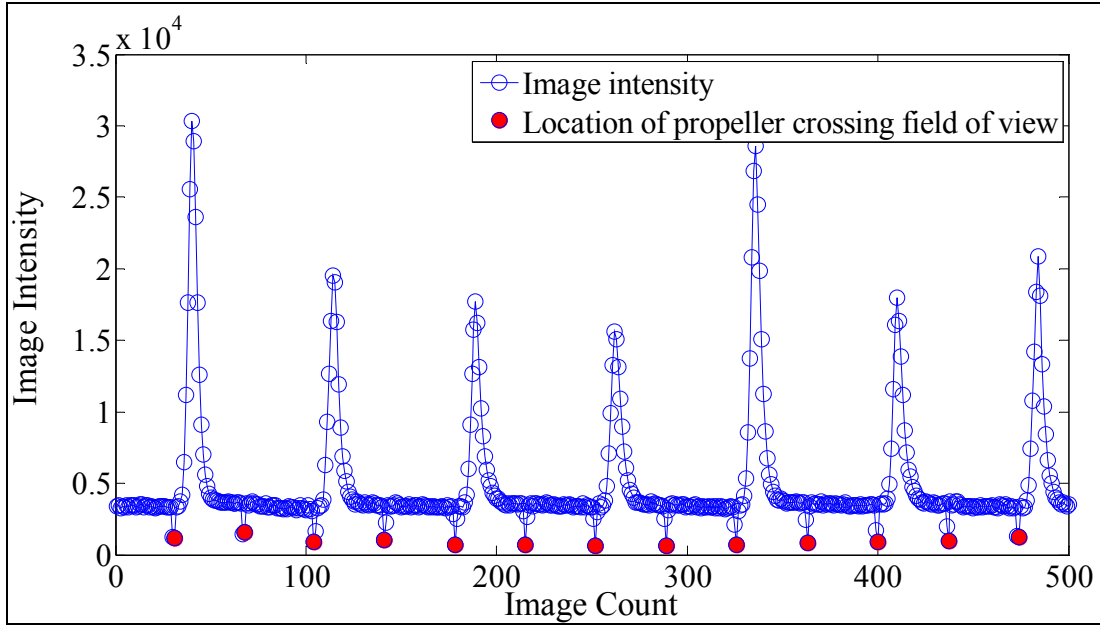


Figure 6–16: Plot showing total image intensity for images taken during the course of the engine cycle for an OS 46 FX engine at a speed of 8000 rpm and a fuel–air mixture ratio of 0.21. The red circles denote points where the propeller crosses the field of view of the camera and which provide a positive time reference for the images.

Figure 6–17 shows that cycle to cycle variation increases as the fuel–air mixture ratio increases from 0.21 to 0.43. This can be seen by the increased scatter in normalized maximum cycle intensity as well as the increase in COV from 20.73% at the leanest setting to 57.34% at the richest setting. Similar increases in combustion variability have also been observed by Rashidi.²²⁸

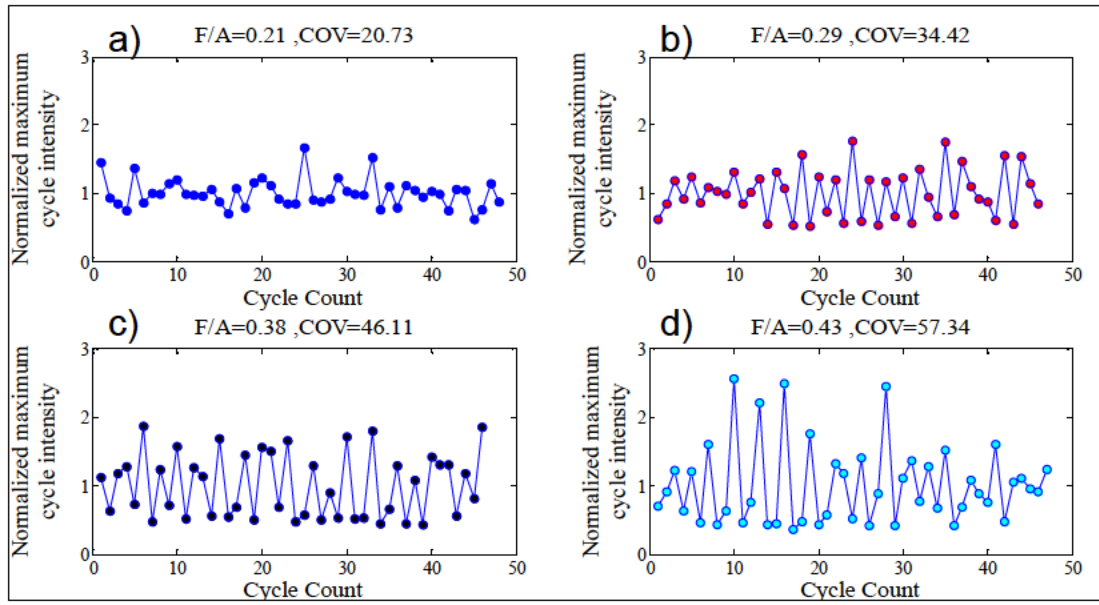


Figure 6–17: Normalized maximum cycle intensity plotted for all the engine cycles captured by the high speed camera for different operating conditions of fuel–air mixture ratio at a constant engine speed of 8000 rpm for the OS 46 FX engine. The stoichiometric value for fuel–air mixture ratio based on fuel chemistry is about 0.227.

Rashidi and others attribute the cycle–to–cycle variations in combustion intensity to variations in turbulence intensities in the vicinity of the spark plug. Cycle–to–cycle variations in miniature engines investigated here could be attributed to similar phenomena in the vicinity of the glow plug as well as temperature and species inhomogeneity within the cylinder volume resulting from unsteady gas dynamics and variation in the effectiveness of the scavenging process from one cycle to another.

6.2.4 Effect of Engine Speed

Figures 6–18 and 6–19 show images of combustion chamber luminiscence in the OS 46 FX engine over two consecutive cycles. The engine is operating at a speed of 14000 rpm and a fuel–air mixture ratio of 0.25. Since the operating speed of the

engine is higher, images are obtained at about 16 crank angle degrees apart for the same exposure time of the camera (200 microseconds). Obtaining a high speed of 14000 rpm from this engine required the use of a small propeller as listed in Table 6–2. This required the camera to be oriented at an angle where one of the cylinder head bolts was present in the field of view – hence the dark area visible to the left of the glow plug in all figures. However, this does not affect any of the analysis or observations made using the acquired images.

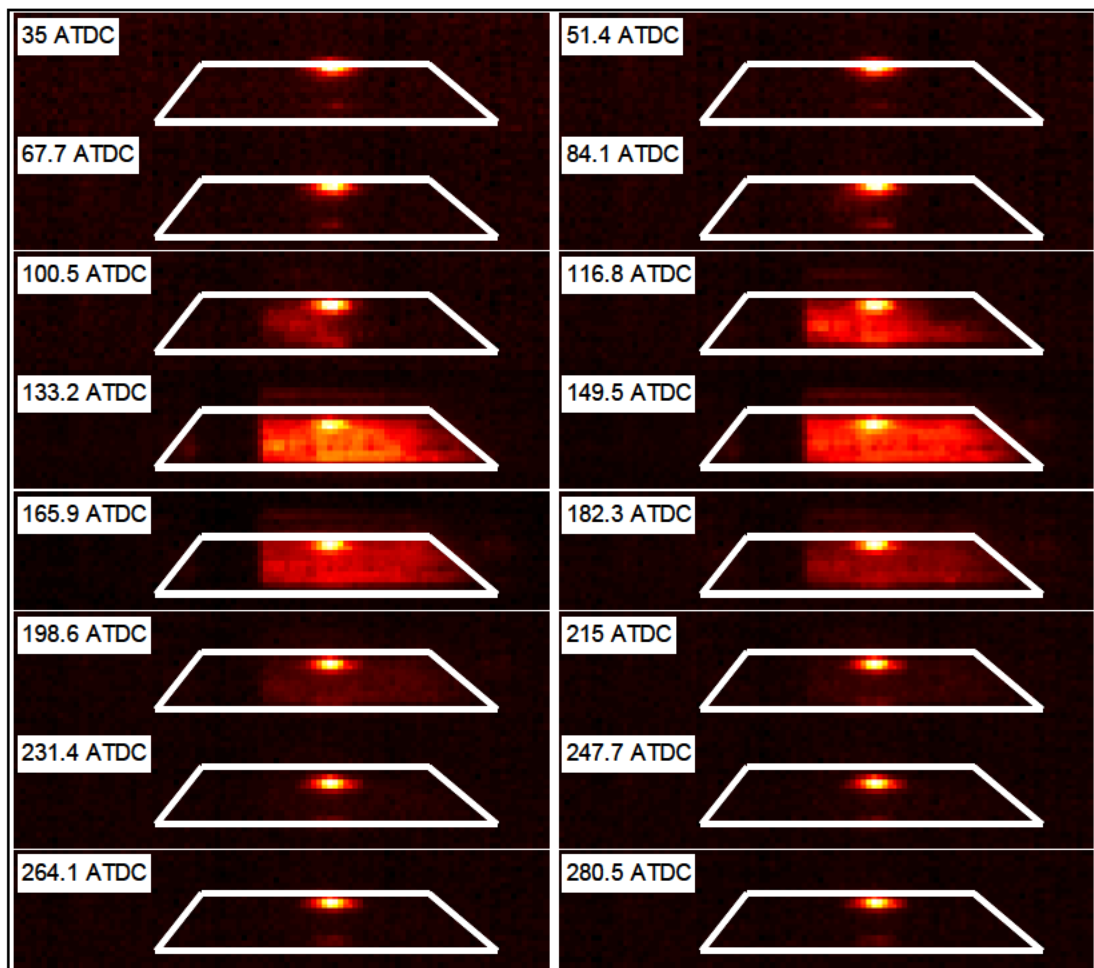


Figure 6–18: High speed false color images acquired during the combustion phase of a single cycle of the OS 46 FX engine operating at a speed of 14000 rpm and a fuel–air mixture ratio of 0.25. Uncertainty in crank angle location is about 20 degrees CAD.

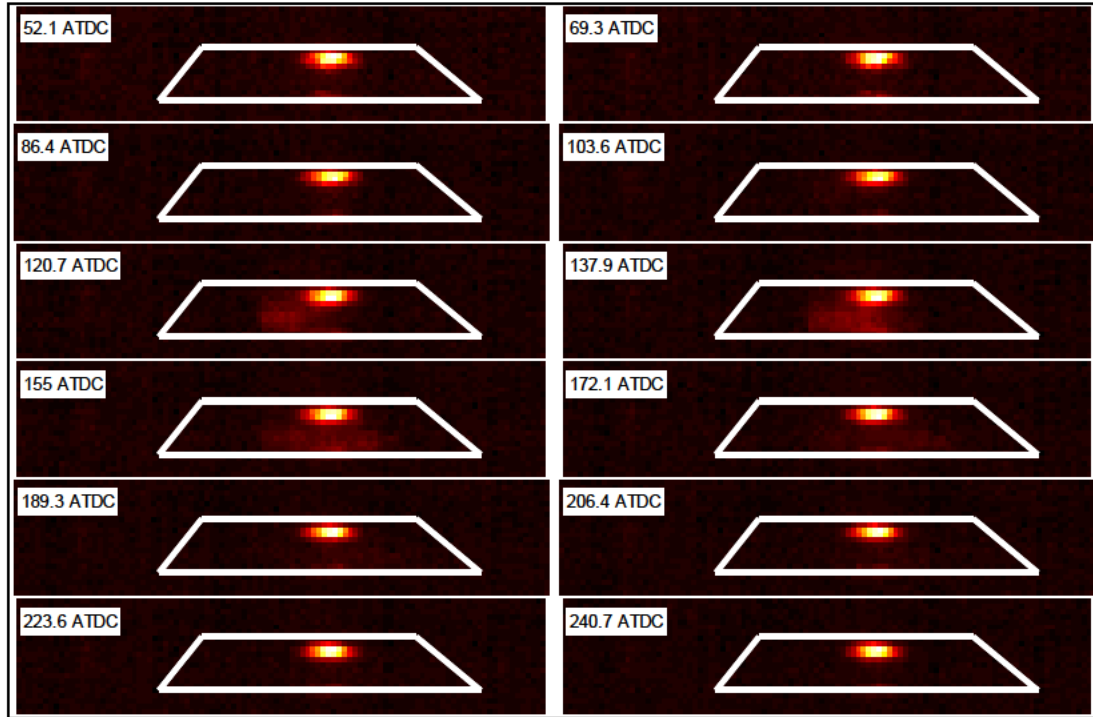


Figure 6–19: High speed false color images acquired during the combustion phase of a consecutive cycle of the OS 46 FX engine operating at a speed of 14000 rpm and a fuel–air mixture ratio of 0.25. Uncertainty in crank angle location is about 20 degrees CAD.

Figure 6–18 shows that combustion events initiate preferentially on the left side of the glow plug. However Fig. 6–19 shows similar behavior but is much weaker suggesting that cycle–to–cycle variations at this engine speed and F/A ratio are large. This is confirmed in Fig. 6–20 which shows that cycle to cycle variations are considerably larger at 14000 rpm than 8000 rpm when operating at approximately the same equivalence ratio (see Fig. 6–17 for comparison). Therefore, engine speed also appears to have a significant influence on cycle to cycle variation in combustion intensity.

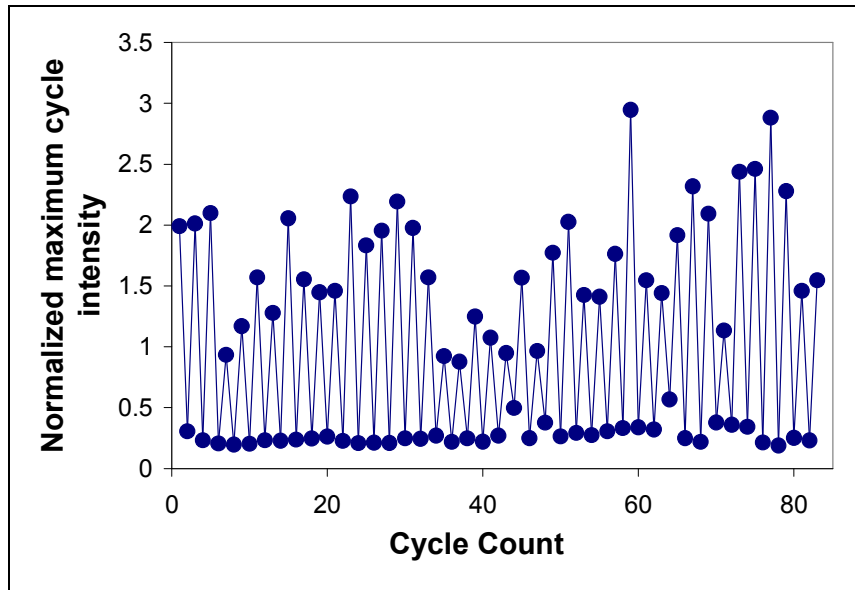


Figure 6–20: Normalized maximum cycle intensity for the OS 46 FX engine operating at a speed of 14000 rpm and a fuel–air mixture ratio of 0.25.

Figure 6–21 summarizes the COVs of combustion chamber luminescence observed in the OS 46FX engine at various fuel/air ratios and engine speeds. It shows that cycle-to-cycle variability generally increases with increasing engine speed and mixture ratio. The data at 10000 rpm also suggest that cycle-to-cycle variability is minimum at a particular rpm when the mixture is stoichiometric. Finally, the data show that cycle-to-cycle variability is a stronger function of F/A at higher engine speeds providing further evidence of the importance of both parameters.

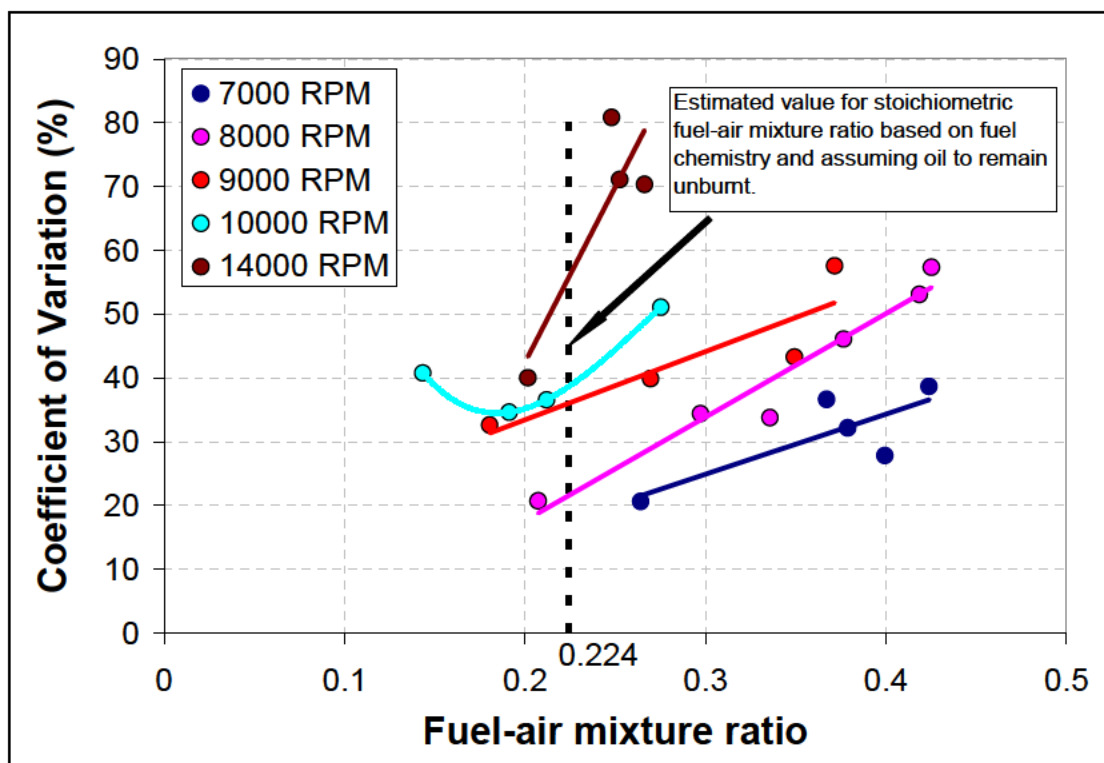


Figure 6-21: Coefficient of variation of maximum image intensity as a function of fuel-air mixture ratio for the OS 46 FX engine operating at speeds of 7000, 8000, 9000, 10000 and 14000 rpm.

6.3 Combustion Regimes in Miniature Engines

The influence of turbulence on premixed flames depends to a great extent on the length scale of the turbulence compared to the thickness of the reaction zone. For example, if the flame is thin compared to the turbulence length scale, then turbulence's primary mode of influence is to wrinkle the flame. On the other hand, if the flame is thick compared to the turbulence length scale, the reaction zone is referred to as 'distributed' and the primary effect of turbulence is on the rate of mixing occurring within it. Turbulent flames are classified or assigned to 'regimes' based upon the relationship between these two length scales.²²⁹ Identifying the regime

is important because it enables one to determine what types of turbulent combustion models are most appropriate.

- Abraham and Williams²³⁰ showed that combustion in conventional-scale gasoline and diesel engines generally occurs in a wrinkled laminar flame regime and this has driven the development of IC engine combustion models.^{231 232} The combustion regime associated with miniature engines is not known but is probably different than that occurring in conventional-scale engines for the following reasons: Engine operating speeds are considerably higher and engine dimensions are almost an order of magnitude smaller than conventional-scale engines.
- The crankcase scavenged two-stroke operation potentially results in much greater charge dilution by combustion products.
- The engines tend to operate considerably rich of stoichiometric as seen from the measurements presented in Chapter 3.

Therefore, the objective of this section is to identify the combustion regime associated with miniature engine operation as a first step toward developing a fundamental understanding of combustion in miniature engines and toward developing appropriate modeling strategies.

The images obtained in this study are solely from the light emitted from soot radiation. They do not provide information about the structure of the propagating flame front. Confirming the existence of different regimes of combustion experimentally requires the use of chemiluminescence or Schlieren imaging to

capture the structure and location of the flame front. Schlieren imaging was initially attempted. However, the various curved surfaces of the quartz bowl mean that a new and highly specialized optical system would need to be developed. Chemiluminescence imaging of OH/CH radicals present in the flame zone is possible with the existing optical setup and an intensified CCD camera. Unfortunately, however, the frame rates of these cameras are too slow to capture multiple images in a single cycle. The usual solution to this problem is to do phase-locked acquisition where images obtained in different cycles are pieced together to create a composite picture of one cycle. In this case, however, large cycle to cycle variations make this virtually impossible.

6.3.1 Turbulence Length Scales and Combustion Regimes

The two turbulence length scales used in the classification of turbulent premixed flames are the Kolmogorov microscale and the integral length scale. The Kolmogorov microscale (denoted by l_k) gives the dimension of the smallest eddies in the flow while the integral length scale (denoted by l_0) gives the dimension of the largest eddies in the flow.

Three different regimes of turbulent combustion are defined depending on the size of the turbulence length scale relative to the laminar flame thickness δ_L .²³³ Wrinkled laminar flames occur when the thickness of the laminar flame is smaller than the Kolmogorov microscale.

$$\delta_L \leq l_k \quad (6-1)$$

In this case, the effect of turbulence is to wrinkle the laminar flame surface. A flamelet in an eddy is produced when the thickness of the laminar flame is greater than the Kolmogorov microscale but less than the integral length scale.

$$l_0 > \delta_L > l_k \quad (6-2)$$

In this case, the effect of turbulence is to break up the flame sheet into burning eddies. Distributed reactions result when the thickness of the laminar flame is larger than the integral length scale.

$$\delta_L > l_0 \quad (6-3)$$

In this case, transport within the flame – and hence the reaction rate – is strongly influenced by the turbulence.

6.3.2 Damköhler Number and Reynolds Number

Two non-dimensional numbers, the Damköhler number and the turbulent Reynolds number are usually used to characterize turbulent combustion processes. The Damköhler number is defined as the ratio of a characteristic time required for mixing to a characteristic time required for combustion,

$$Da = \frac{\text{characteristic flow time}}{\text{characteristic reaction time}} = \frac{\tau_{flow}}{\tau_{reaction}} \quad (6-4)$$

In premixed flames, the characteristic time for mixing is defined to be the lifetime of large eddies in the flow while the characteristic chemical time is based on the properties of a laminar flame. The characteristic time for mixing is given by,

$$\tau_{flow} = \frac{l_0}{v'_{rms}} \quad (6-5)$$

where v'_{rms} is the turbulence intensity, and the characteristic time for combustion is given by,

$$\tau_{reaction} = \frac{\delta_L}{S_L} \quad (6-6)$$

where S_L is the laminar flame speed.

Combining equations 6-4, 6-5 and 6-6 gives the following expression for the Damköhler number,

$$Da = \frac{\left(\frac{l_0}{v'_{rms}} \right)}{\left(\frac{\delta_L}{S_L} \right)} = \left(\frac{l_0}{v'_{rms}} \right) \left(\frac{S_L}{\delta_L} \right) \quad (6-7)$$

The Damköhler number is important because it provides an indication of the relative importance of chemical kinetics vs. turbulence in controlling reaction rate. For example, when the Damköhler number is large ($Da \gg 1$), the chemical reaction time is small relative to the mixing time and so mixing sets the reaction rate. This is often referred to as a ‘fast chemistry’ regime. In contrast, when the Damköhler number is small ($Da \ll 1$), the reaction time is large compared to the mixing time and the reaction rate is set by the chemical kinetics. This is often referred to as a ‘slow chemistry’ regime.

The turbulence Reynolds number represents the ratio of inertial forces to viscous forces in the flow under the effect of turbulence. It is defined using the integral length scale and turbulence intensity as follows,

$$Re_T = \frac{v'_{rms} l_0}{\nu} \quad (6-8)$$

where ν is the kinematic viscosity. When the turbulence Reynolds number is high, inertial forces dominate transport whereas when the turbulence Reynolds number is low, viscous forces dominate transport. The turbulence Reynolds number is important in turbulent combustion because it sets the length and time scales of the turbulence.

6.3.3 Regime Diagrams

A regime diagram is a non-dimensional representation of how the ratios of various flow length scales – including the ratio of turbulence length scale to reaction zone thickness – depend on two fundamental dimensionless parameters: the Turbulence Reynolds number and the Damköhler number. Figure 6–22 is an example that was regenerated based on the work of Abraham et. al. The horizontal and vertical axes are the turbulence Reynolds number and Damköhler number respectively.

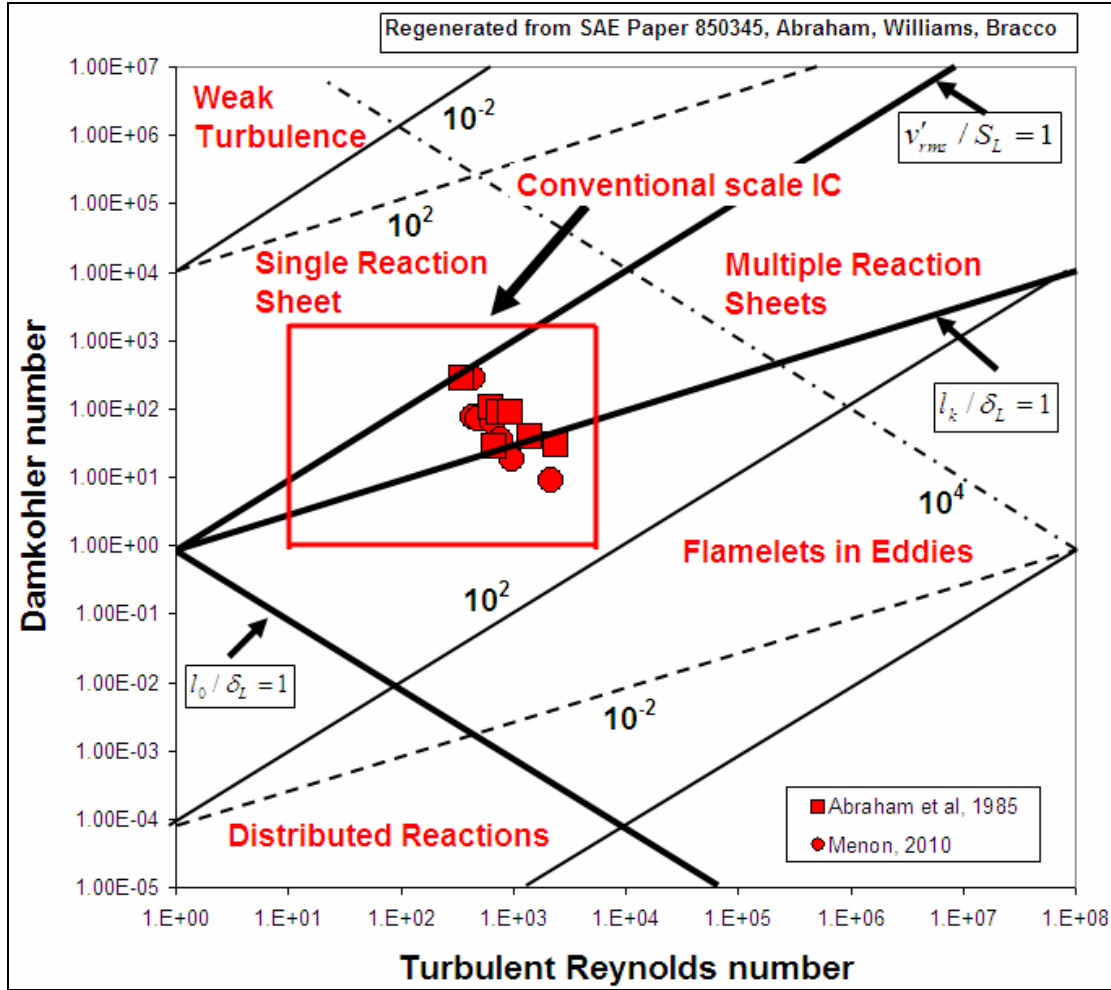


Figure 6–22: Operating points for internal combustion engines listed in Table 6–3 on the combustion regime diagram.

The horizontal lines are contours of constant $\frac{v'_{rms}}{S_L}$, $\frac{l_k}{\delta_L}$ and $\frac{l_0}{\delta_L}$. These ratios show how turbulence rates and turbulence length scales relate to flame speed and flame thickness. Contours corresponding to values of 1 for these ratios form the boundaries between different combustion regimes. Above the line $\frac{v'_{rms}}{S_L} = 1$, combustion is faster than the turbulence and combustion is expected to occur within a single reaction sheet that is wrinkled by the effect of turbulence. Above the

line $\frac{l_k}{\delta_L} = 1$, the reaction zone is thinner than the smallest turbulence length scale and combustion is expected to occur in multiple sheets that are also wrinkled under the effects of turbulence. Below the line $\frac{l_0}{\delta_L} = 1$, the reaction zone is thicker than the largest scale of the turbulence and combustion is expected to occur in a distributed manner. In the intermediate region between the lines $\frac{l_k}{\delta_L} = 1$ and $\frac{l_0}{\delta_L} = 1$ where the reaction zone is thicker than the smallest turbulence length scale but thinner than the largest turbulence length scale. Combustion is expected to occur in the flamelet in eddy regime where the turbulence wrinkles and breaks the laminar flame apart and combustion continues in small turbulent eddies. The square symbols on Fig. 6–22 correspond to Abraham et. al's predictions for where various gasoline and diesel IC engines are located in the space while the box shows Abraham et al.'s prediction for where most IC engine combustion processes would lie. Note that while the box spans the flamelet and flame sheet regimes, most of it lies in the flame sheet regime.

6.3.4 Procedure for Placing Engines on the Regime Diagram

Placing engines on the regime diagram is not a trivial exercise as it requires estimating the Damköhler and Reynolds number at a variety of operating conditions. This, in turn, requires carefully quantifying the range of conditions possible in the engine and determining the laminar flame speed and thickness at each condition. The procedure used here to estimate the Damköhler number and turbulence Reynolds number in different engines is as follows:

- Obtain the geometric properties of the engine. These include
 - Bore (L)
 - Stroke (B)
 - Radius of crankshaft (usually \sim Stroke/2) (r_c)
 - Ratio of connecting rod length to crank radius (~ 4 for miniature IC engines) (R)
 - Length of connecting rod (S)
 - Clearance height (h)
 - Geometric compression ratio (CR)
 - Engine displacement (V_{disp})
- Establish the engine operating conditions of interest. These include:
 - Engine speed (rpm) (N)
 - Spark timing (CAD) (θ) – In the case of miniature glow ignited engines, there is no established spark timing and ignition timing is treated as a variable to be explored in the study.
 - Stoichiometric fuel–air ratio for assumed fuel $-(F / A)_{\text{stoich}}$
 - Equivalence ratio (ϕ) on mass basis.
 - Temperature and pressure of intake air (T_0, P_0).
 - Dilution level of mixture in engine cylinder in terms of the mass fraction of diluents (Y_{dil}). The diluents are usually combustion products from the previous cycle.

- Compute the fuel–air ratio of the mixture using the equivalence ratio and the stoichiometric fuel–air ratio.

$$F / A = \phi \cdot (F / A)_{stoich} \quad (6-9)$$

- Compute the mass fractions of all species in the unburned fuel–air mixture.
- Estimate the reference laminar flame speed for the fuel–air mixture. This is accomplished using a flame speed correlation for established fuels,

$$S_{L,ref} = B_M + B_2 (\phi - \phi_M)^2 \quad (6-10)$$

where B_M , B_2 and ϕ_M are constants for a specific fuel.²³⁴ Similar correlations are not available for the glow fuels used in the small two–stroke engines considered here so a flame speed calculation is performed using CANTERA²³⁵, a chemical kinetics software package. The reaction mechanism is the same as used in Section 4.5.3 for calculation of fuel–air mixture transport properties.

- Estimate the clearance volume using engine displacement and the compression ratio,

$$V_c = \frac{V_{disp}}{(CR - 1)} \quad (6-11)$$

- Estimate the volume of the cylinder at the time of ignition using,²³⁶

$$V = V_c \left(1 + 0.5(CR - 1) \left[R + 1 - \cos(\theta) - (R^2 - \sin^2(\theta))^{0.5} \right] \right) \quad (6-12)$$

- Estimate the pressure and temperature in the cylinder at the point of ignition using isentropic relations,

$$P = P_0 \left(\frac{V_{disp} + V_c}{V} \right)^\gamma \quad (6-13)$$

$$T = T_0 \left(\frac{V_{disp} + V_c}{V} \right)^{(\gamma-1)} \quad (6-14)$$

- Correct the laminar flame speed obtained previously to the pressure and temperature at the time of ignition using,²³⁷

$$S_L = S_{L,ref} \left(\frac{T}{T_o} \right)^\lambda \left(\frac{P}{P_o} \right)^\beta (1 - 2.1Y_{dil}) \quad (6-15)$$

where the exponents λ and β are given by,

$$\lambda = 2.18 - 0.8(\phi - 1) \text{ and } \beta = -0.16 + 0.22(\phi - 1)$$

- Use CANTERA to estimate transport properties of the fuel–air mixture in the engine cylinder at the assumed ignition pressure and temperature. These properties include:
 - Density (ρ)
 - Thermal conductivity (k)
 - Kinematic viscosity (μ)
 - Specific heat at constant pressure (C_p)

- Compute the mean piston speed using,

$$\bar{S}_p = \frac{2LN}{60} \quad (6-16)$$

- Compute turbulence intensity using,

$$v'_{rms} = \bar{S}_p / 2 \quad (6-17)$$

This is the correlation used by Abraham²³⁸ based on previous work by Bracco²³⁹ based on LDV measurements made in internal combustion engines.

- Compute the integral turbulence length scale using,

$$l_o = 0.21h \quad (6-18)$$

This is also used by Abraham in previous work.

- Compute the turbulence Reynolds number,

$$\text{Re}_T = \frac{\rho v'_{rms} l_o}{\mu} \quad (6-19)$$

- Compute the thermal diffusivity of the fuel–air mixture at conditions corresponding to ignition,

$$\alpha = \frac{k}{\rho C_p} \quad (6-20)$$

- Compute the flame thickness using,²⁴⁰

$$\delta_L = \frac{2\alpha}{S_L} \quad (6-21)$$

- Compute the Damköhler number using,

$$Da = \frac{l_o / v'_{rms}}{\delta_L / S_L} = \left(\frac{l_o}{\delta_L} \right) \left(\frac{S_L}{v'_{rms}} \right) \quad (6-22)$$

This procedure is ‘checked’ by applying it to the same engines investigated by Abraham et. al.²⁴¹. The properties and operating conditions of these engines are summarized in Table 6–3. The Damköhler and Reynolds numbers calculated for these engines using the methodology described above are shown by the round symbols in Fig. 6–22. The fact that they coincide with Abraham’s results indicates that applying the procedure outlined above to conventional–scale engines gives results that are

consistent with those of other researchers. Now that we have a validated tool, the next step is to apply it to the small glow-fueled engines of interest in this thesis.

	Displacement	Compression Ratio	Speed	Spark Advance	Equivalence Ratio	Charge Dilution
1	847	8.7	1500	40	0.6	0.1
2	847	8.7	1500	35	1	0.1
3	805	8.6	1500	27	0.87	0.12
4	612	4.8	1380	55	1.15	0.2
5	375	5.5	600	13	1	0.2
6	727	7.9	1220	30	1.13	0.2
7	823	8.5	5000	25	1	0.2
	cc		rpm	Deg BTDC		

Table 6–3: Operating conditions for different engines investigated in the work of Abraham et al.

Engines 1–5 were operated on propane and 6–7 were operated on octane.

6.3.5 Combustion Regimes in Miniature IC Engines

Five different parameters are chosen as variables and the effect of each on the location of the engines in the combustion regime diagram is analyzed using the procedure outlined in 6.3.4. Table 6–4 gives the ranges over which each parameter was varied. The ‘baseline value’ of a parameter is the constant value assigned to it while one of the other parameters is varied. The ranges are assigned based on the range of small engine operating conditions observed in Chapters 1 through 5. The fuel is assumed to be methanol in all cases.

Variable parameter	Range explored	Baseline value	Units
Displacement	0.16–7.54	N/A	cc
Equivalence ratio	0.6–1.6	1	
Speed	5000–15000	10000	rpm
Ignition timing	10 BTDC–5 ATDC	5 BTDC	CAD
Charge dilution	0–45	45	%

Table 6–4: Variable parameters explored in the analysis of combustion regimes for methanol fueled two–stroke miniature IC engines.

6.3.5.1 Effect of Engine Size And Equivalence Ratio

The symbols in Fig. 6–23 show the effect of engine size and equivalence ratio on the location of engines in the combustion regime diagram. The baseline combustion mode at stoichiometric conditions lies below the box outlined by Abraham et al. but still well within the flamelet in eddies regime. Decreasing engine size moves the operating point to the left and down in the regime diagram but not out of the flamelet in eddies regime. This combined shift occurs because decreasing the integral length scale decreases both the Damköhler number and the turbulent Reynolds number. The effect of operating off stoichiometric on the rich or lean side moves shifts the engine down in the regime diagram and can be dramatic for very rich or lean mixtures as it can drive the engine well into the distributed reaction zone regime.

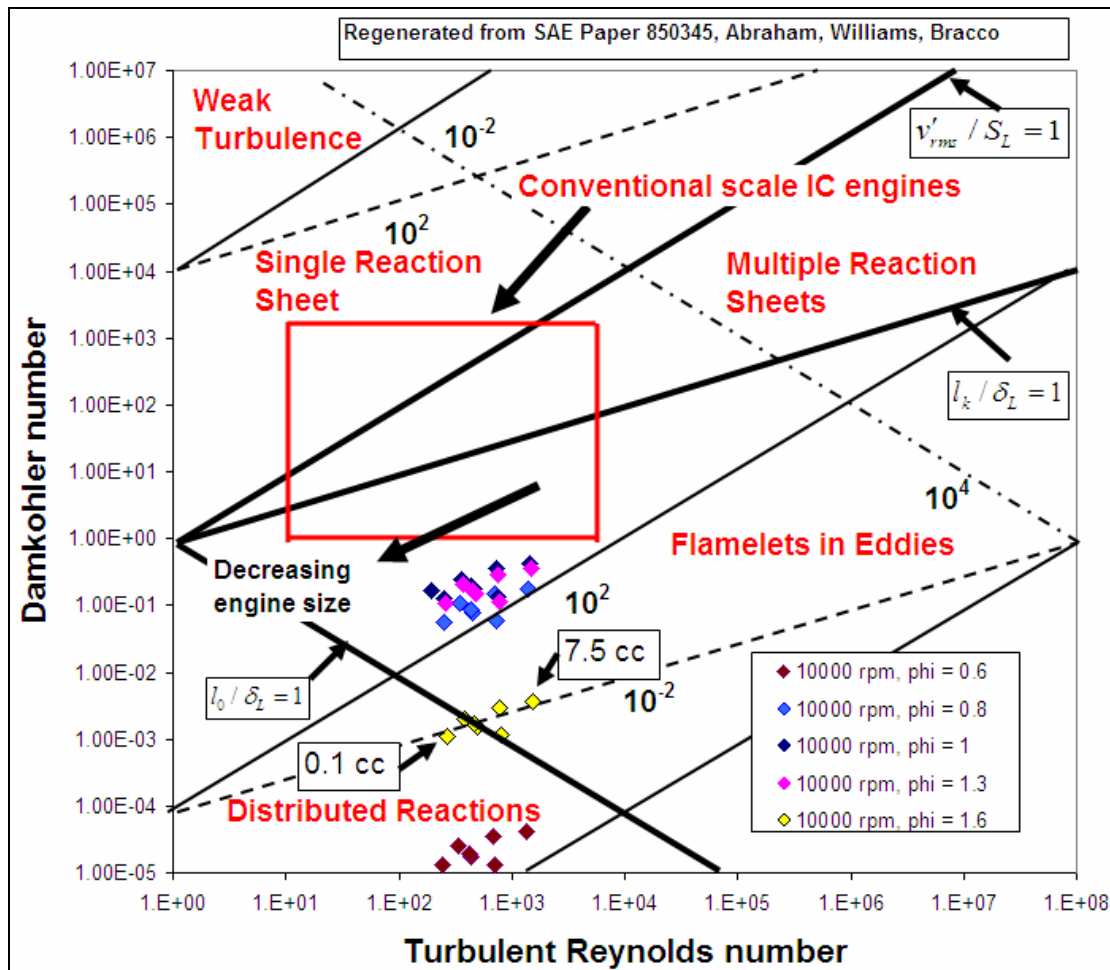


Figure 6–23: Operating points for methanol fueled two–stroke miniature internal combustion engines showing the effect of variation in engine size and equivalence ratio.

6.3.5.2 Effect of Engine Size and Engine Speed

Figure 6–24 shows the effect of engine size and operating speed on the location of the engines in the combustion regime diagram. The principal effect of increasing engine speed is to increase the mean piston thereby increasing the turbulence intensity. This, in turn, increases the turbulent Reynolds number and decreases the Damköhler number. The net effect of increasing speed is to shift the location of the engines in the regime diagram lower and to the right in the figure. However, the effect of speed is not as strong as that of equivalence ratio. While the

combustion regime lies outside the range associated with conventional-scale engines, realistic changes in speed will not drive it out of the flamelet in eddies regime.

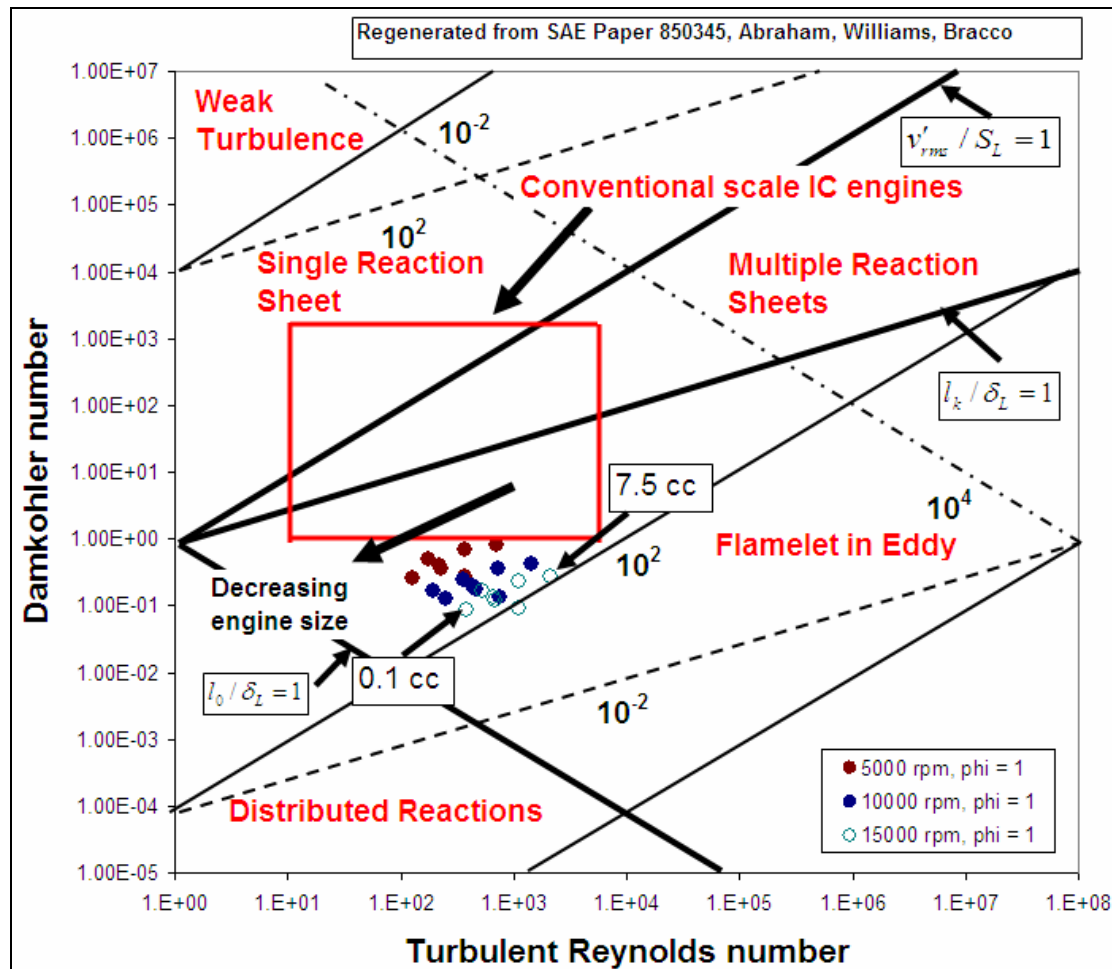


Figure 6–24: Operating points for methanol fueled two–stroke miniature internal combustion engines showing the effect of variation in engine size and engine speed.

6.3.5.3 Effect of Engine Size and Ignition Timing

Figure 6–25 shows the effect of variation of engine size and ignition timing on the location of the engines in the combustion regime diagram. Retarding ignition timing from the baseline value of 5 degrees BTDC increases the pressure and temperature at the point of ignition. This increases the flame speed resulting in an increase in Damköhler number without any change in the turbulent Reynolds number.

Thus, the location of the engines in the regime diagram shifts upward by a small amount and the combustion mode remains in the flamelet in eddies regime.

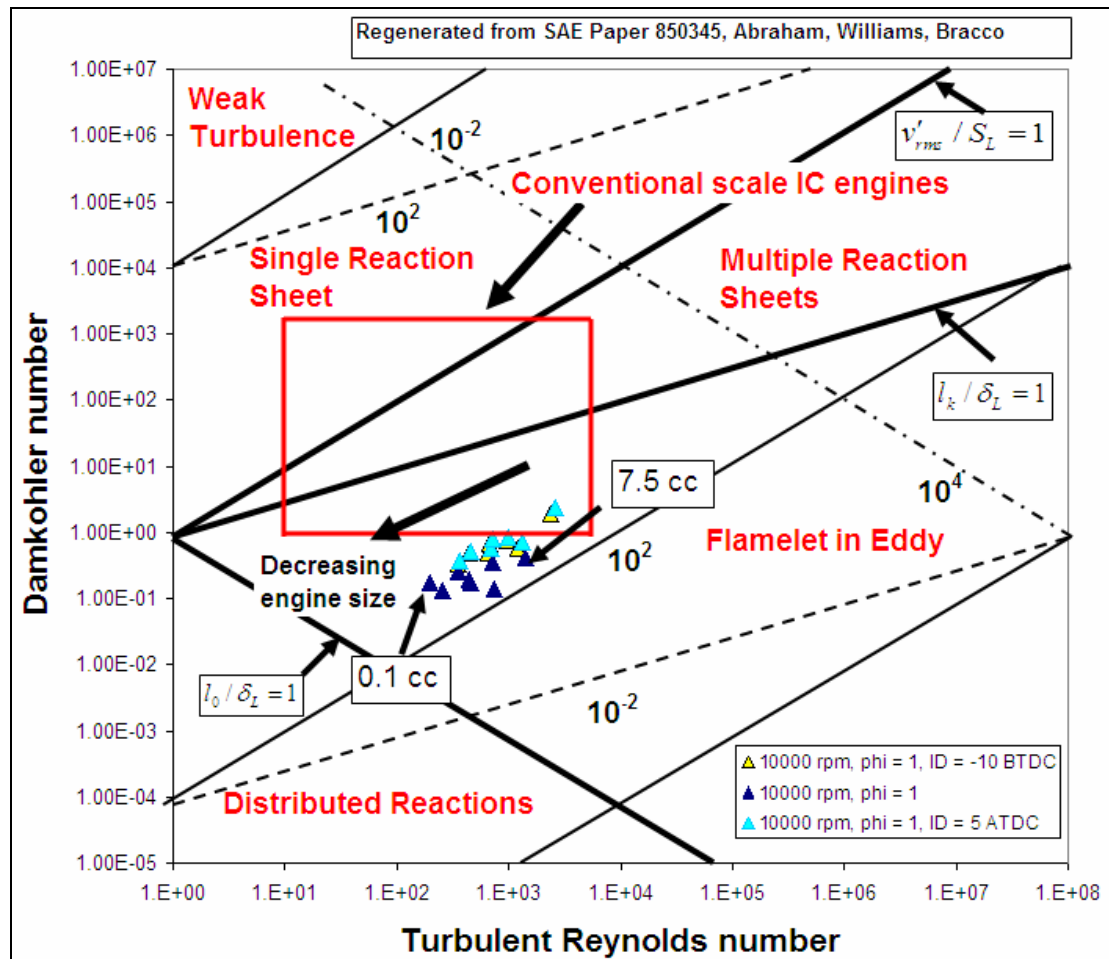


Figure 6–25: Operating points for methanol fueled two–stroke miniature internal combustion engines showing the effect of variations in engine size and ignition timing.

6.3.5.4 Effect of Engine Size and Charge Dilution

Figure 6–26 shows the effect of charge dilution and engine size on the location of the engine in the combustion regime diagram. The primary effect of increasing charge dilution is to reduce the laminar flame speed as can be seen in Eqn. 6–18. For a charge dilution value of greater than 45%, the flame speed is negative. The decrease in flame speed contributes to a decrease in Damköhler number with no

change in the turbulent Reynolds number. The net effect is shift the location of the engines on the regime diagram downward while still occupying the flamelet in eddies regime but tending towards the distributed reaction regime. Changing the in charge dilution seems to have the strongest effect on the location of the engines in the regime diagram after the effect of change in equivalence ratio. Finally, it should be noted that while the baseline charge dilution of 45% puts the baseline engine well outside the regime associated with conventional-scale engines, reducing the dilution to 0% as in a conventional 4-stroke engine puts small engines in the same general combustion regime as conventional-scale engines.

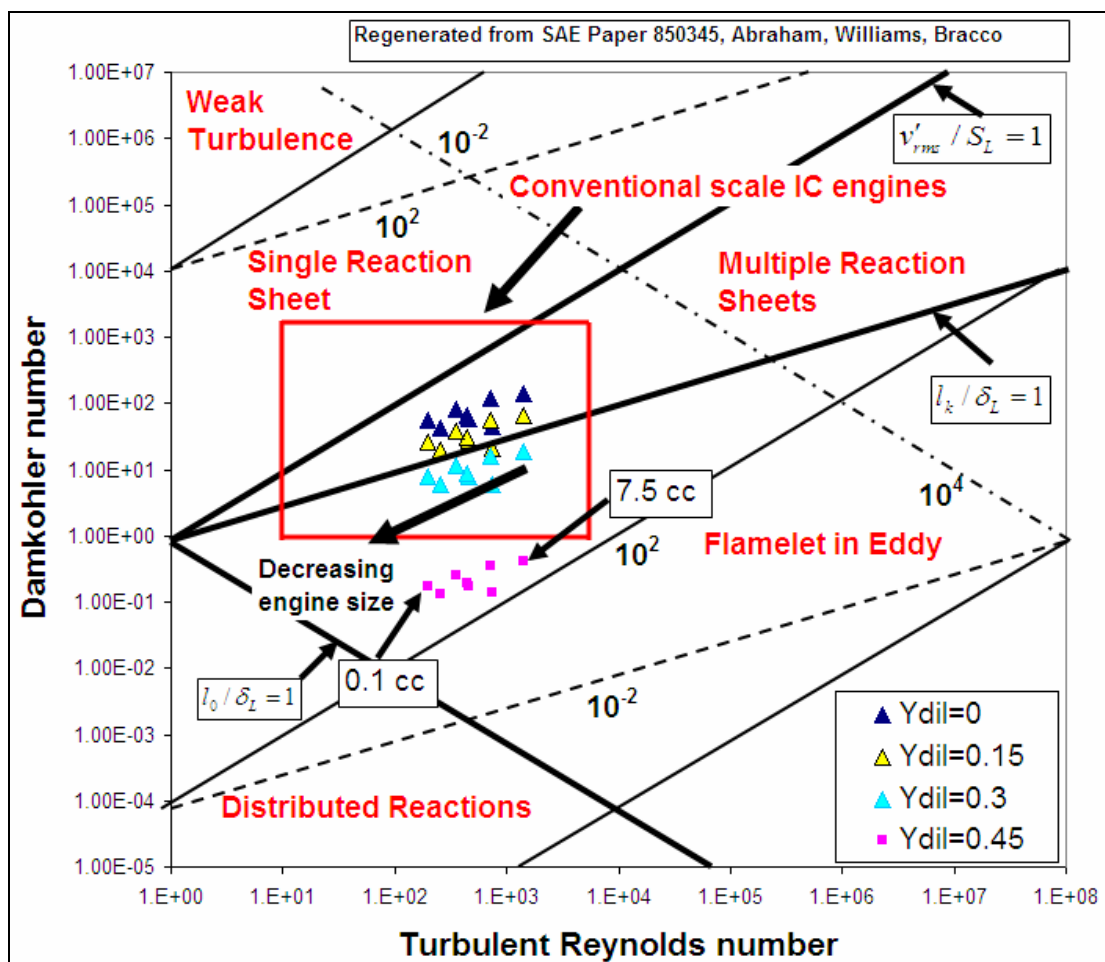


Figure 6–26: Operating points for methanol fueled two–stroke miniature internal combustion engines showing the effect of variation in engine size and charge dilution.

Chapter 7 : Investigation of Engine–Generator Setup

7.1 Generators

As mentioned in Chapter 1, several miniature portable applications require electrical power to drive sensors and other electronic instrumentation. Miniature generators designed for use with model airplane engines are available commercially from at least one manufacturer.²⁴² The objective of this chapter is to evaluate the performance of one particular engine–generator system to develop an understanding of what type of performance is available today.

The basic function of a generator is to convert input mechanical power from the prime mover (in this case a small IC engine) into electrical power. This is accomplished by passing an electrical conductor through a perpendicular magnetic field. The potential difference between the ends of the wire (or electromotive force (e.m.f) generated) is proportional to the magnetic flux density, the velocity of the conductor, and the length of the conductor. The EMF can be generated by rotating a set of electrical conductors (windings) in a magnetic field or by rotating a magnetic circuit around a stationary set of windings.²⁴³ The windings where electrical power is produced are known as the ‘armature’. The field can be constructed using permanent magnets or electromagnets. In the case of electromagnets, a field excitation current is also required. Since the field lines form closed loops, the current produced in the armature is naturally AC. Adding additional current–carrying circuits enables one to generate two or three–phase AC output. A mechanical device called a commutator can be used to produce DC output from a single phase machine.

Figures 7–1 and 7–2 show front and rear photographs of the Sullivan Products S675–300 AC generator evaluated in this research work. The manufacturer’s specifications are listed in Table 7–2. The armature is stationary and the field rotates. The field is produced by a set of 10 rare earth magnets. The magnets are made of an alloy of Neodymium, iron and boron and are one of the strongest known types of permanent magnets. The armature windings are insulated using polyamide–imide which is a thermoplastic with very good electrical insulation and mechanical strength properties.

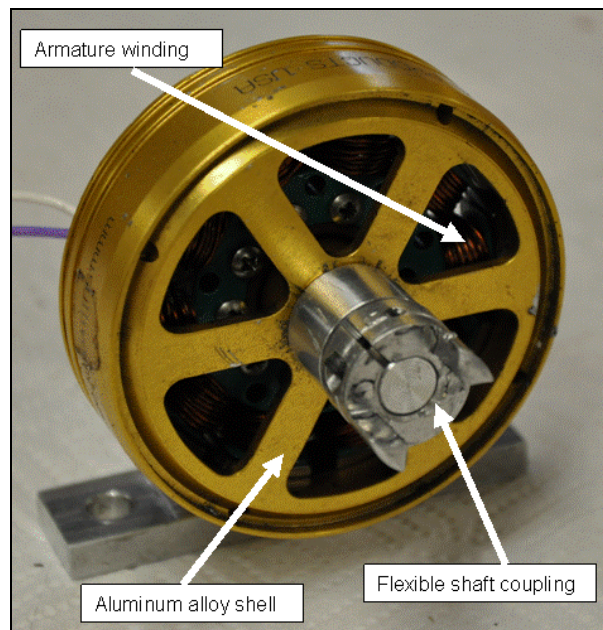


Figure 7–1: Front side photograph of the Sullivan Products S675–300 AC generator evaluated in this study.

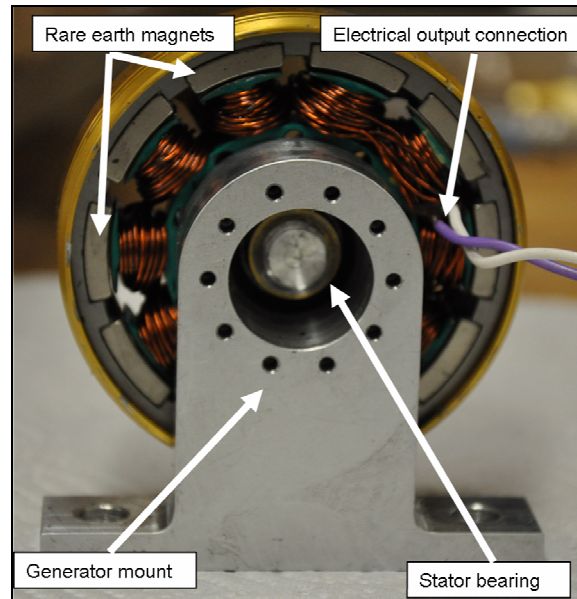


Figure 7-2: Rear side photograph of the S675-300.

Manufacturer	Sullivan products	
Model	S675-300	
Diameter	76	mm
Thickness	24	mm
Weight	341	gm
Suitable with engines of displacement	<19cc (1.2 cu.in.)	
Maximum power output	500	W
Standard armature winding type	Single phase	

Table 7-1: Manufacturer's specifications for the AC generator tested here.

7.2 Apparatus

The Sullivan generator tested in this work is compatible with engines having displacement between 5 to 25 cc (0.3 to 1.5 cu.in.). The OS 46 and OS 40 engines (engine A and B in Fig. 2-3) were possible candidates for use in the engine-generator system. Measurements are reported here for the operation of the OS 46 FX engine with the Sullivan generator. A flexible coupling/pulley assembly was used to connect the engine to the generator. The coupling compensated for minor misalignment between the engine and generator while the pulley provided a means to start the

engine. Figure 7–3 shows the engine coupled to the generator and Fig. 7–4 shows the engine–generator installed in the dynamometer.

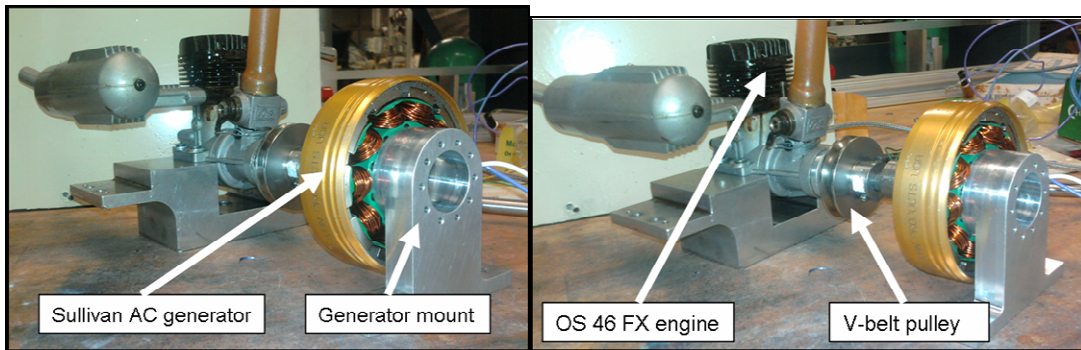


Figure 7–3: Photograph of the OS 46 FX engine in combination with the Sullivan generator.

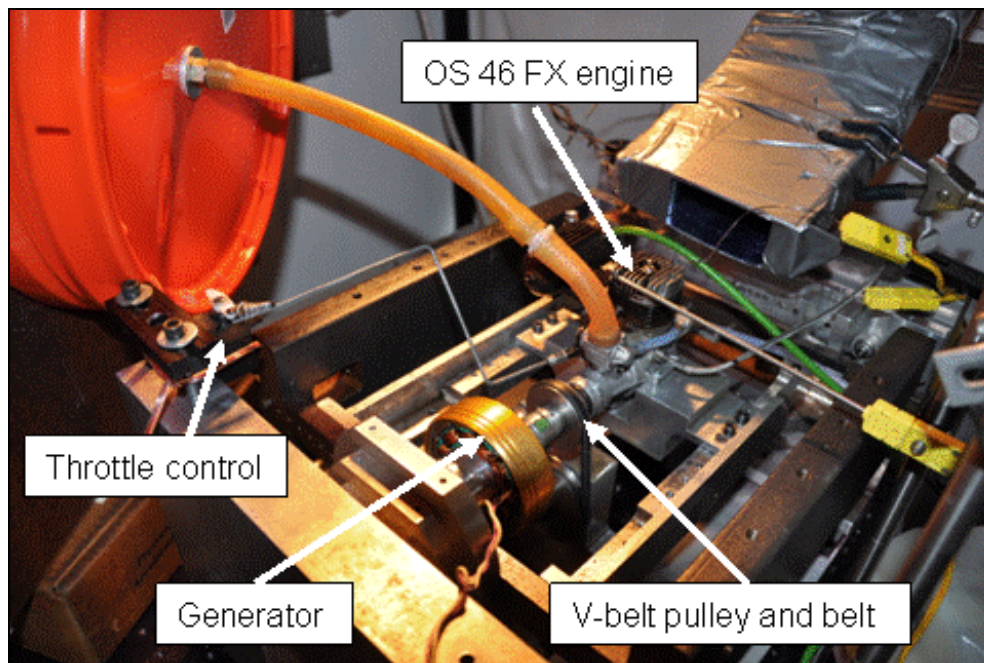


Figure 7–4: Photograph of the engine–generator setup on the dynamometer.

Figure 7–5 is a schematic diagram and 7–6 is a photograph of the resistor load bank used to apply electrical load on the engine. Twenty 10 ohm, 25 W resistors are connected in groups of four resistors each. Each group has a resistance of 2.5 ohms. The four switches on the load bank allow four different electrical loads to be applied to the engine by connecting the load banks progressively in parallel. Table 7–2

summarizes the positions of the switches, the corresponding resistances connected in parallel and the resulting net resistance of the circuit. The resistors are mounted on aluminum supports and the assembly is convectively cooled by an air blower.

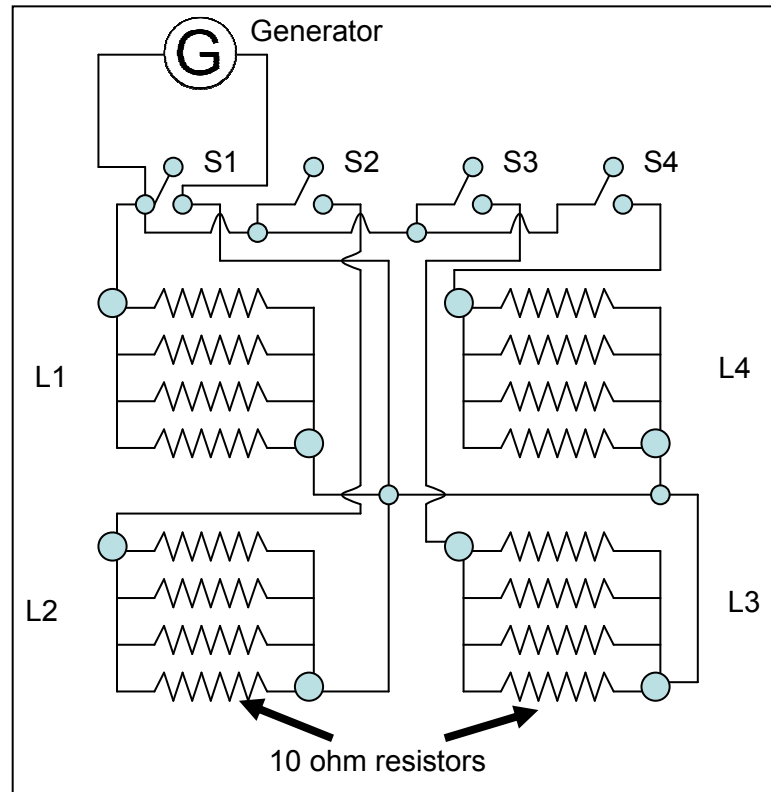


Figure 7–5: Schematic layout of the load bank setup for engine–generator tests.

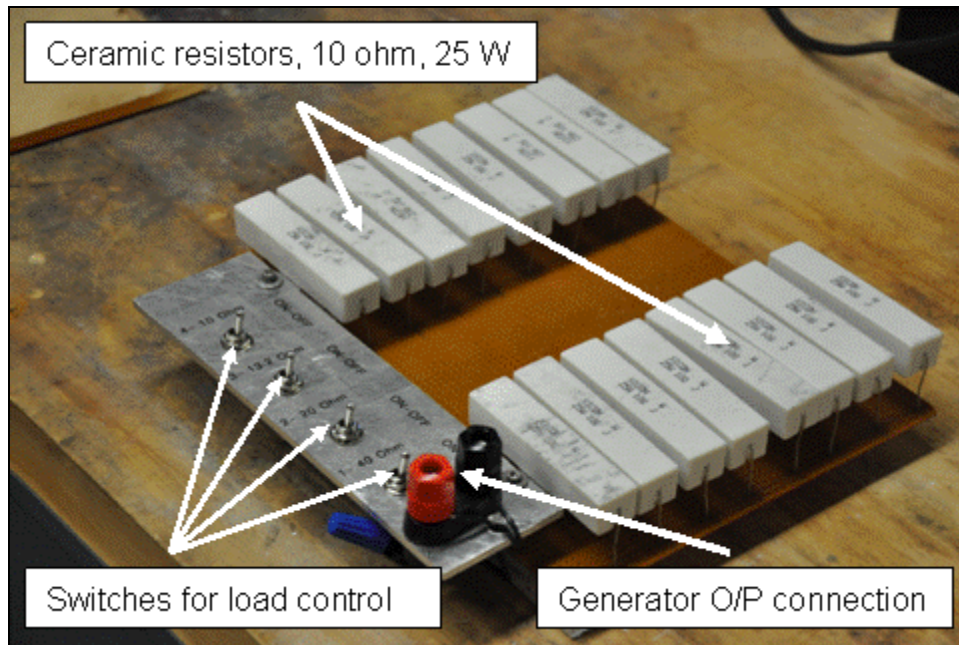


Figure 7–6: Photograph of the resistor load bank used to apply electrical load to the engine–generator setup.

Switches in the ‘ON’ position	Resistances in parallel	Net resistance
S1	L1	2.5
S1,S2	L1,L2	1.25
S1,S2,S3	L1,L2,L3	0.833
S1,S2,S3,S4	L1,L2,L3,L4	0.625
		ohm

Table 7–2: Positions of switches, corresponding resistors connected and net resistance for the different settings on the load bank.

A Tektronix TDS3000B oscilloscope is used to measure the amplitude and frequency of the generator’s AC output. It was necessary to measure current independently since the resistors’ resistance changes with temperature over the course of an experiment. These measurements were made using a model 82372 Craftsman digital clamp–on ammeter.

7.3 Procedure

Engine performance is measured in the same manner described in Chapter 2 (Section 2.12). The engine is started using a starter motor. No electrical load is applied. The engine power output is controlled using the throttle and mixture valves. Once the engine is set to the required operating conditions, the switches on the load bank are used to set different levels of electrical load on the engine. Measurements of engine performance (torque, speed, fuel flow rate, EGT, etc.) and generator electrical output (V, I) are made for each setting of the load bank. These measurements are repeated for different engine operating conditions.

7.4 Data Processing

Electrical power is calculated using the measured RMS values for AC voltage and current,

$$P_{generator,electrical} = V_{RMS} * I_{RMS} \quad (7-1)$$

Engine mechanical power output and efficiency are obtained from the torque, speed and fuel flow rate measurement as mentioned in Section 2.10 of Chapter 2 as described previously. Generator efficiency is obtained using the following expression,

$$\eta_{generator} = \frac{P_{generator,electrical}}{P_{engine,mechanical}} \quad (7-2)$$

where $P_{generator,electrical}$ is the electrical power output from the generator and $P_{engine,mechanical}$ is the mechanical power output from the engine.

7.5 Results

Results are presented here for four different operating conditions which are summarized in Table 7–3 below.

Throttle setting	Setting	F/A ratio	Equivalence ratio
Fully open	Rich	0.29	1.28
Fully open	Lean	0.17	0.75
Half open	Rich	0.29	1.28
Half open	Lean	0.22	0.97

Table 7–3: Throttle setting, fuel/air mixture ratio and equivalence ratio for the engine operating conditions reported in this section.

Figure 7–7 shows the applied electrical load and associated operating speed for each engine operating condition. The generator winding has a fixed resistance and is measured to be 0.4 ohms. As the switches are progressively turned on, net resistance of the load bank decreases. For a constant voltage output, current drawn by the circuit increases and power increases as square of the current. Decreasing the electrical load thus increases the total power dissipation and the mechanical load on the engine resulting in a small decrease in engine speed.

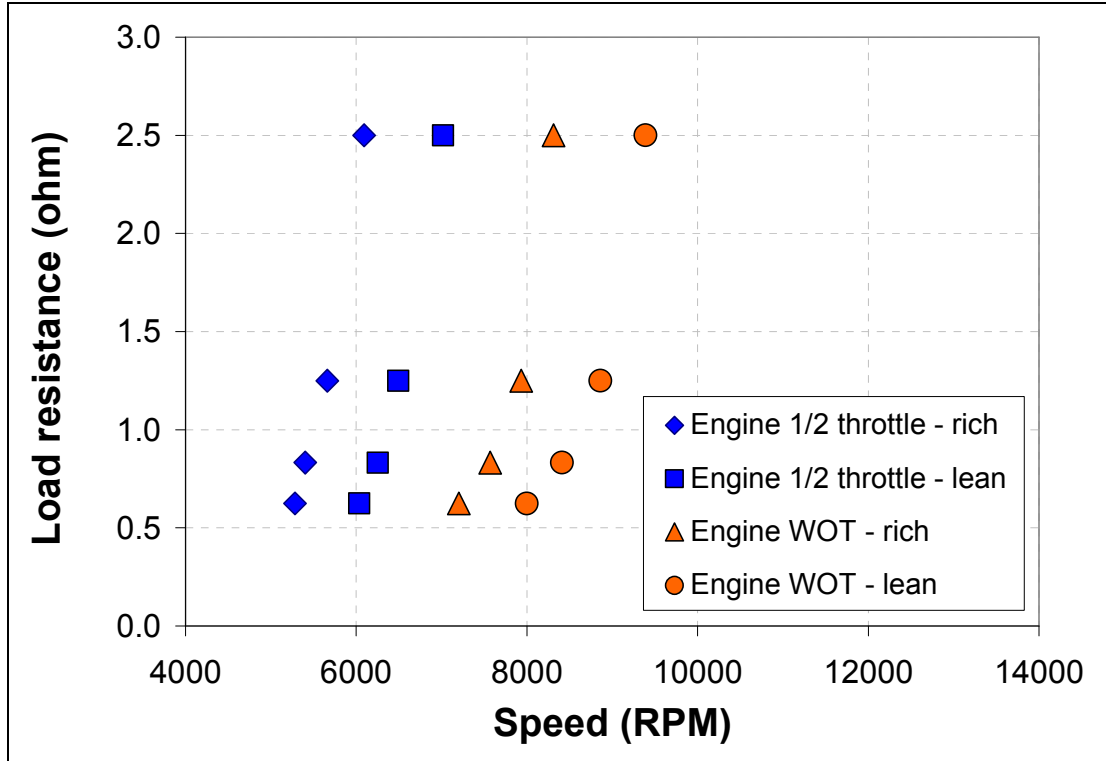


Figure 7-7: Applied load and associated engine/generator speed for different engine operating conditions.

Figure 7-8 is a plot of RMS AC current and Fig. 7-9 is a plot of RMS AC voltage for the associated engine-generator speed at each engine operating condition. It shows that voltage is a linear function of engine speed and is independent of the engine operating conditions and applied electrical load. This is consistent with the standard expression for a generator's output voltage:²⁴⁴

$$V_{O/P} = Blv \quad (7-3)$$

where B is the magnetic flux density in Tesla, l is the length of the electrical conductor in meters and v is the rotational speed of the conductor in meter/s.

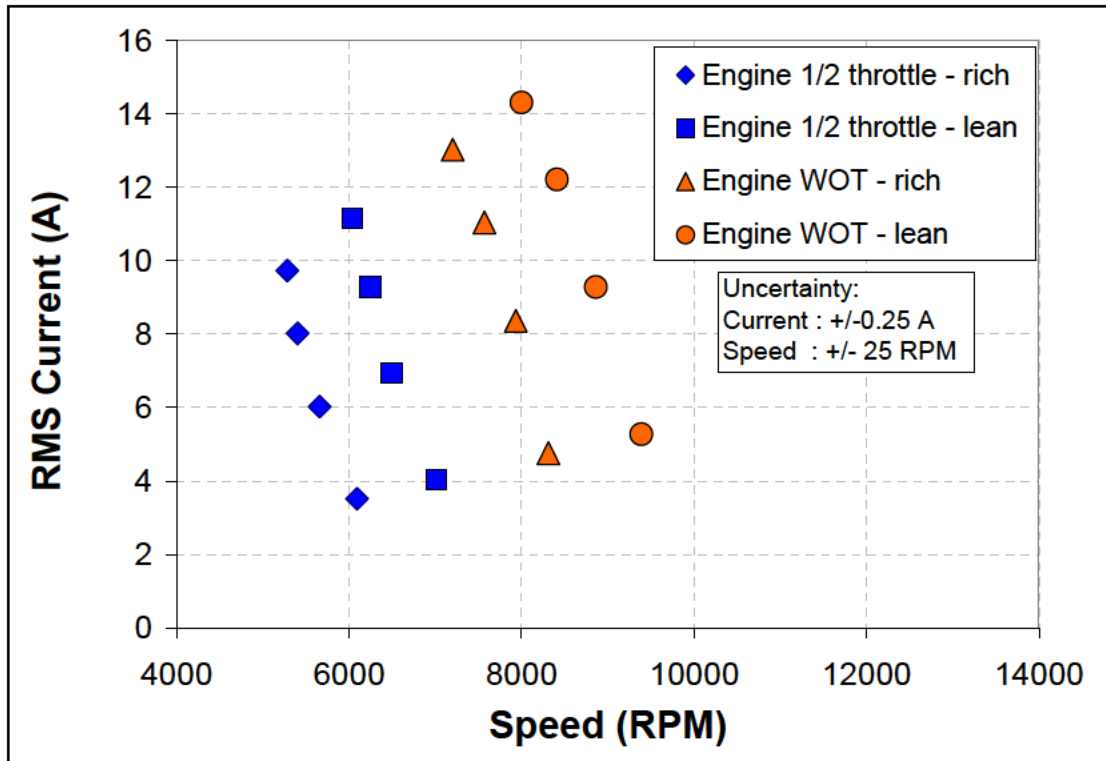


Figure 7–8: Generator current and speed at different engine operating conditions.

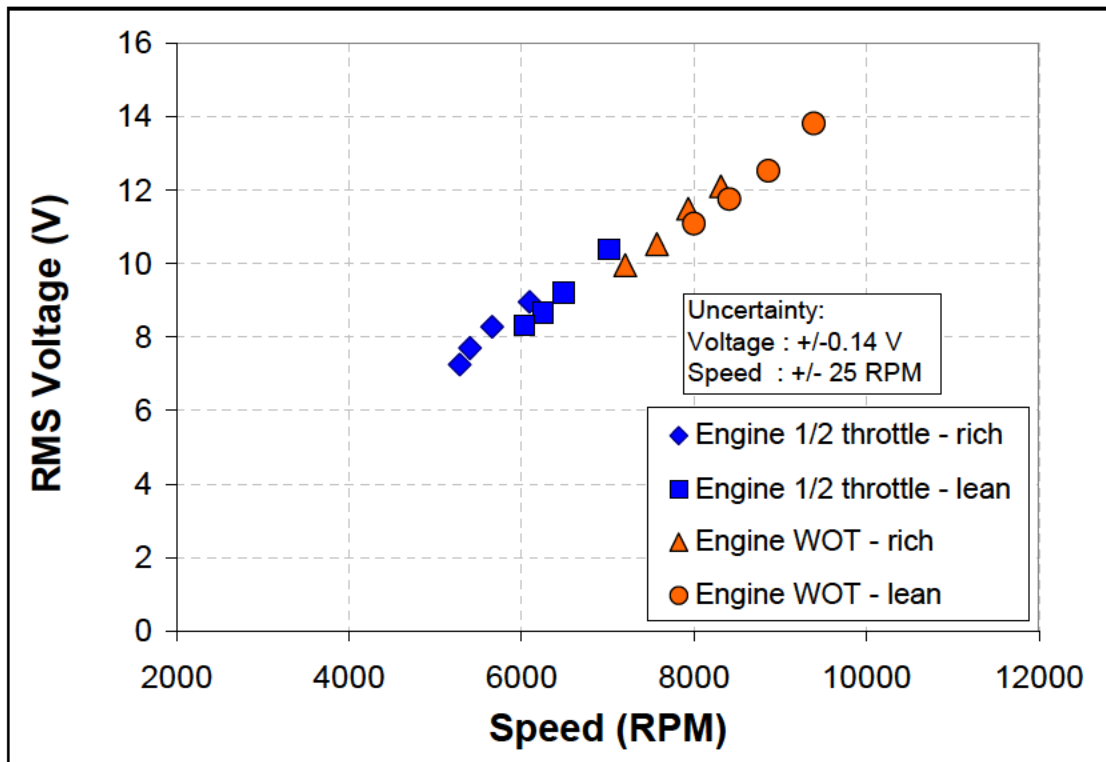


Figure 7–9: Measured RMS values for AC voltage and speed for different engine operating conditions.

Figure 7–10 shows generator output voltage plotted as a function of rotational speed. Voltage output correlates linearly to rotational speed and the slope of the line gives the value for the product Bl from Eqn. 7–3. This relationship can now be used to estimate generator voltage output at any rotational speed. Knowing the required output current, generator power output can be further estimated.

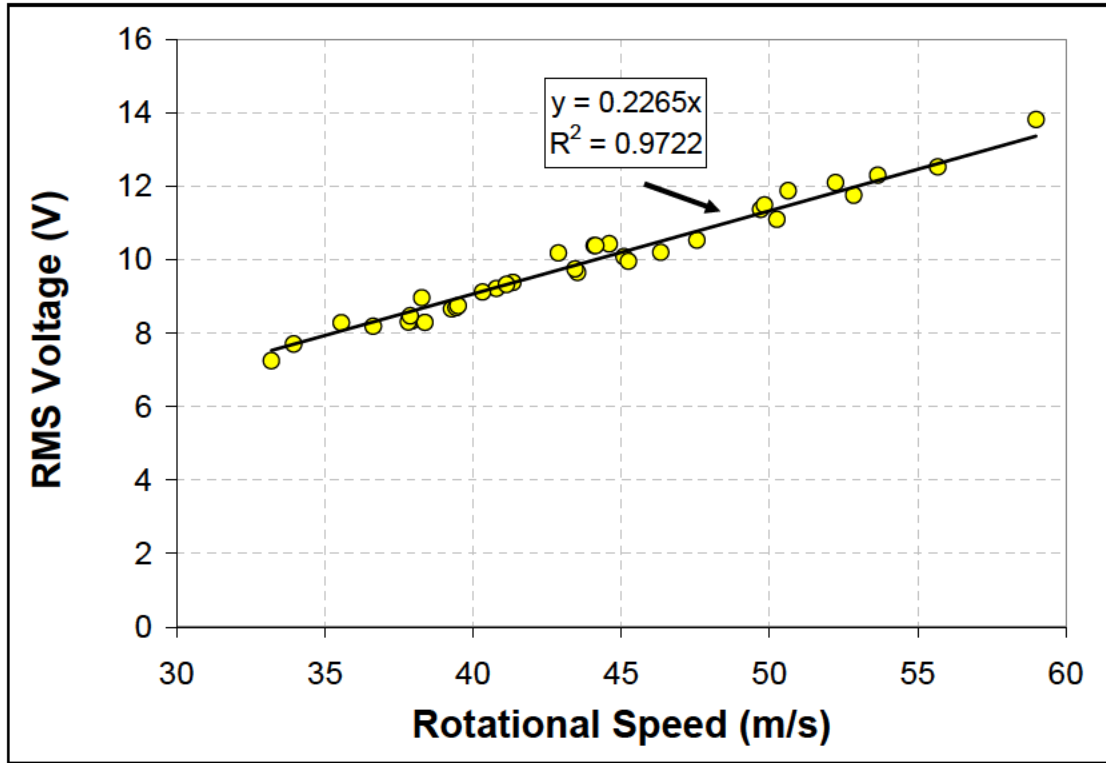


Figure 7–10: Measured RMS values for AC voltage and speed for different engine operating conditions.

Figure 7–11 shows engine torque and speed corresponding to two throttle positions and two mixture settings at each throttle position. Table 7–3 earlier lists the throttle positions and the fuel/air and equivalence ratios of the mixture for each engine operating condition reported here. For a fixed throttle setting, engine torque increases with decreasing engine speed and approaches its peak value with increasing electrical load.

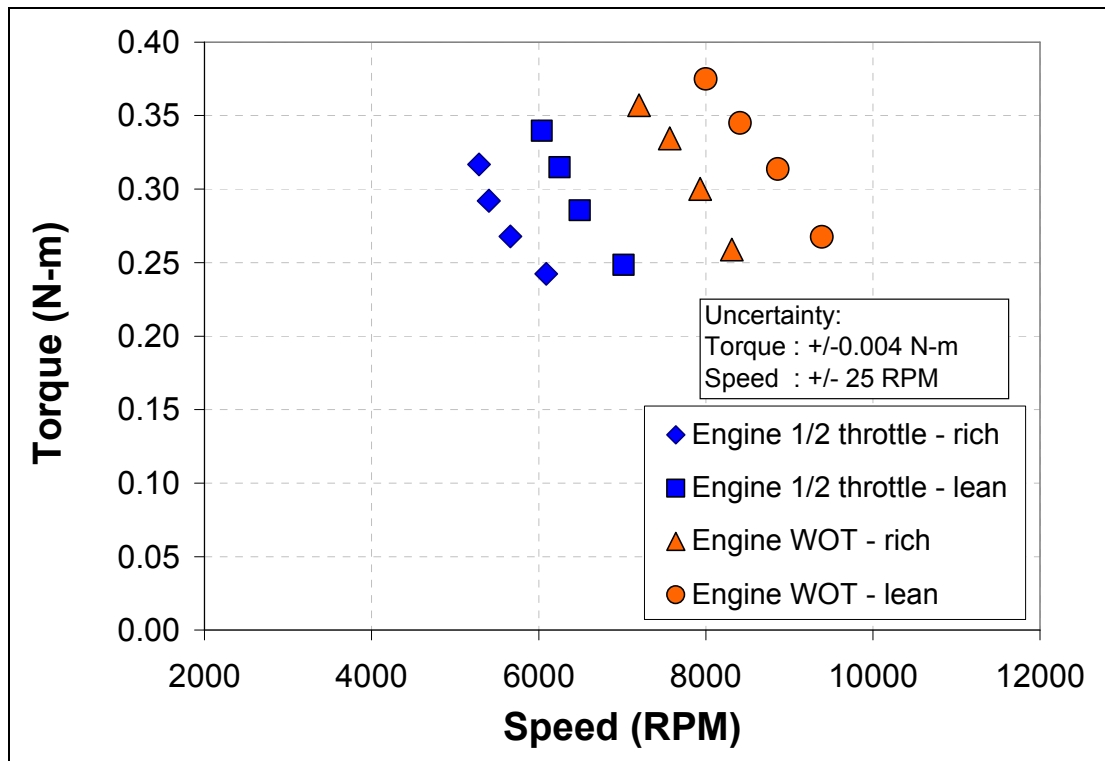


Figure 7-11: Engine torque and speed at different engine operating conditions.

Figure 7-12 shows the power produced by the engine and power produced by the generator for the four different operating conditions. It also shows the difference between engine mechanical power output and generator electrical power output which represents losses in the generator. As seen in the figure, generator losses are directly proportional to engine speed and can be represented by a linear fit whose equation is presented in the figure. This correlation can be used to estimate generator losses at any engine speed. Estimation of generator output power as described previously combined with generator losses allows the calculation of required engine power output to produce a given electrical power output. Figure 7-13 shows this calculation for the generator tested here.

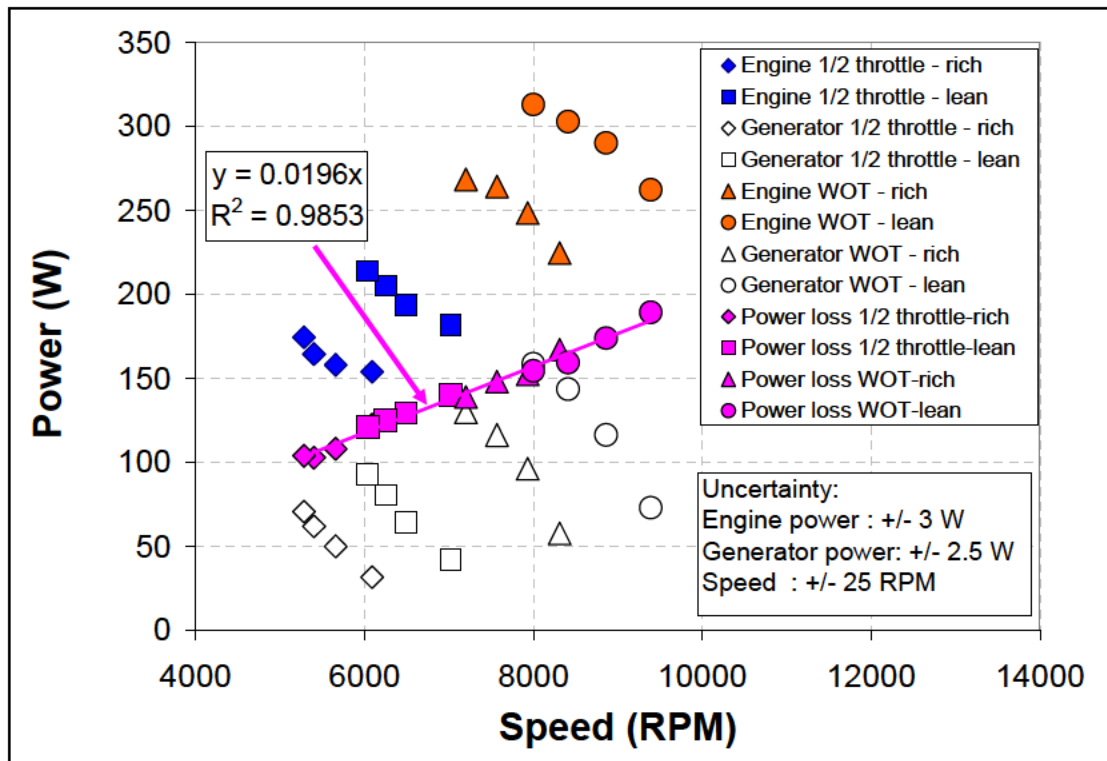


Figure 7–12: Measured engine and generator power output and operating speeds at different engine operating conditions. Also presented are estimates for generator power loss.

The filled symbols in Fig. 7–13 represent generator electrical power output corresponding to an operating speed and output load current. Generator voltage is set by the operating speed. The open symbols represent the engine power output which needs to be input to the generator to produce the corresponding electrical power output. The difference between generator input and generator output at any particular speed and load setting represents generator loss.

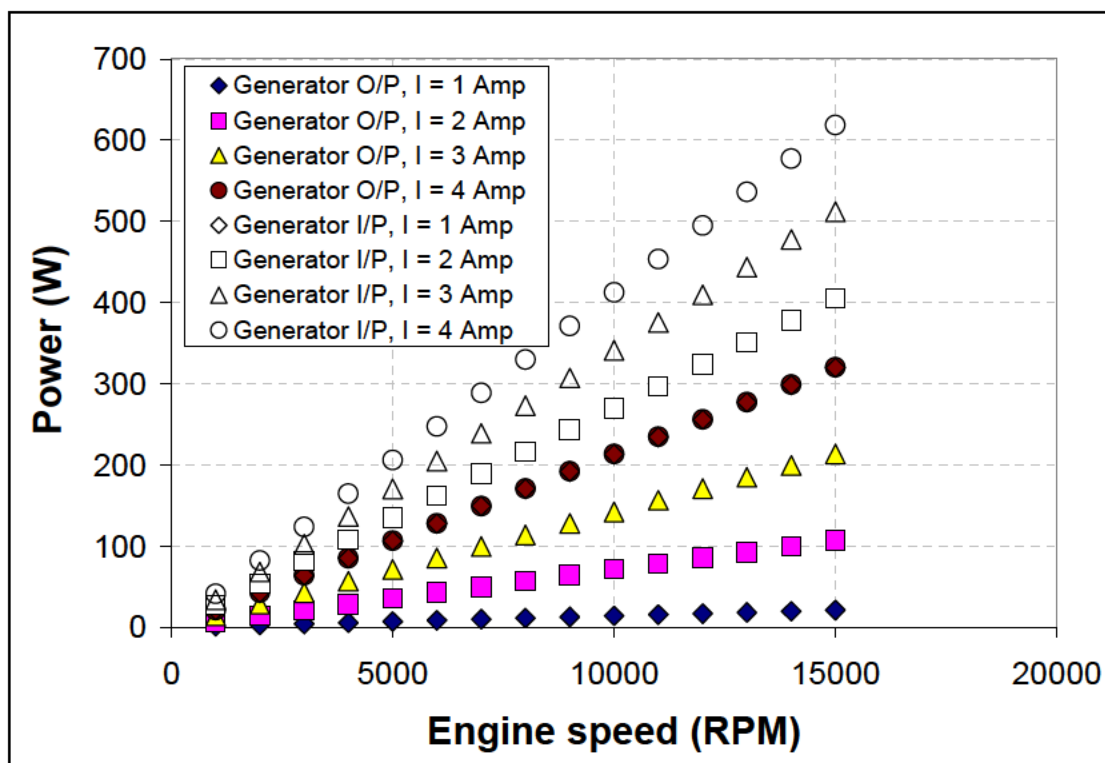


Figure 7-13: Generator power output and required mechanical power input for different load currents and speeds.

Engine power output at a constant speed and throttle position depends on the fuel-air mixture setting. As seen in the performance characteristics for the OS 46 FX engine presented in Chapter 3, engine power output peaks at different values of equivalence ratios depending on engine speed. Figure 7-14 shows the mechanical power input required by the generator to produce different output currents at different operating speeds. Superimposed on the plot are measurements of power output for the OS 46 FX engine obtained from engine tests alone. Considering the case for the engine and generator operating at 11000 rpm, it is possible to operate the engine at a fuel-air mixture ratio that gives the maximum power output of the engine at this speed of 410 W. If the generator is required to produce a load current of 4 Amps at 11000 rpm, it would result in stalling the engine since the power input required by the

generator to satisfy the load is about 450 W. This figure shows a basic power mapping scheme that helps determine what levels of electrical power output are possible at different engine/generator speeds. However, the key parameter to be optimized while determining the operating points of the engine and generator is overall system efficiency.

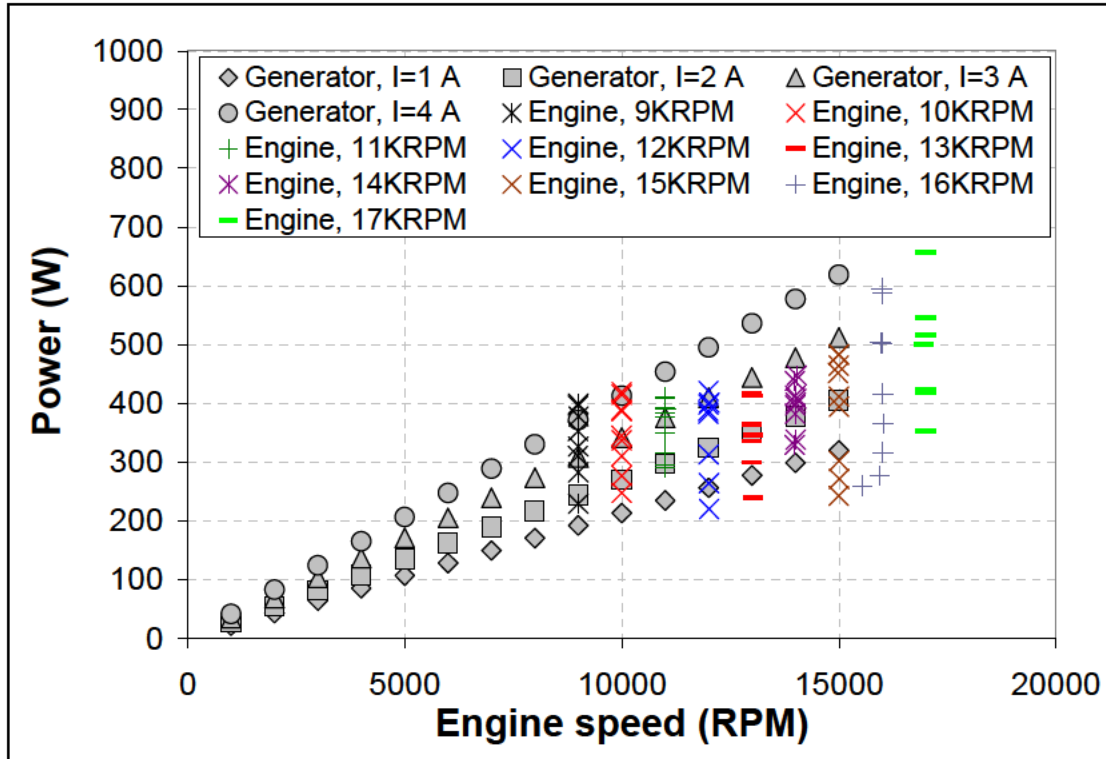


Figure 7–14: Power required by generator to produce different load currents at different operating speeds. Power output from the OS 46 FX engine at different constant engine speeds and fuel–air mixture settings are also presented.

Figure 7–15 presents overall efficiency of the engine and that of the generator as measured using Eqn. 7–2. System efficiency which is the product of engine and generator efficiency is also presented for the different operating conditions. The maximum measured value of the generator is seen to be about 50% at a speed of

about 8000 rpm. The corresponding overall efficiency of the engine at this operating point is about 10.5% resulting in a system efficiency of about 5.3%.

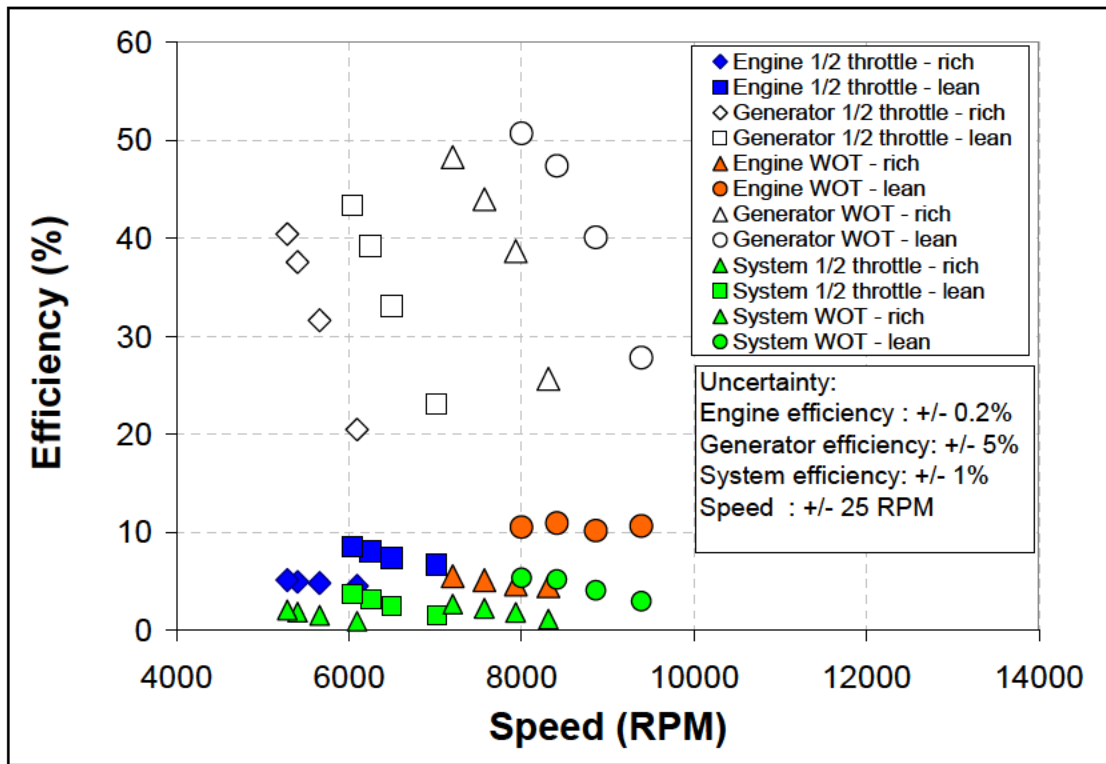


Figure 7–15: Engine, generator and system efficiencies and speed at different engine operating conditions.

Generator efficiency can be further plotted as a function of output current. This is presented in Fig. 7–16. For a fixed current output, generator power output and generator losses are linearly proportional to speed. This causes generator efficiency to be independent of speed as seen in Fig. 7–16.

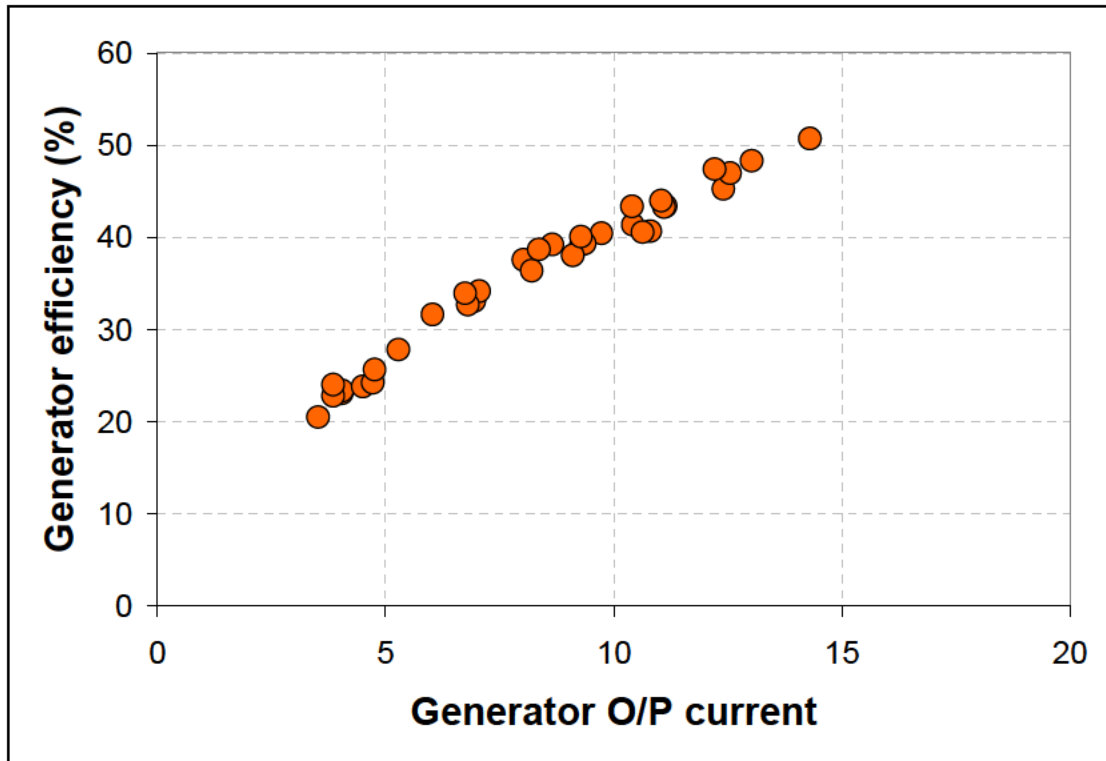


Figure 7-16: Generator efficiency as a function of output current.

System efficiencies reported in Fig. 7-15 do not represent those at optimized operating conditions of the engine and the generator. As can be seen in Fig. 7-14, the power required by the generator can be supplied by the engine operating at different speeds and equivalence ratios. An optimal system would be obtained with maximum system efficiency if the engine were operated at the most efficient setting for the required generator power input. A power matching scheme to arrive at the highest system efficiency given the required electrical power output from the generator is presented in Fig. 7-17.

Figure 7-17 shows five subplots:

A. Generator efficiency as a function of load current

- B. Contours of constant power output in Watts as a function of generator voltage output in Volts and load current in Amps. The secondary y-axis on the right side shows corresponding generator speed in krpm.
- C. Input mechanical power needed by the generator (Watts) to produce the required electrical output as a function of generator speed in krpm.
- D. Power output from the OS 46 FX engine (Watts) as a function of fuel air mixture ratio for different constant engine speeds in krpm.
- E. Overall efficiency for the OS 46 FX engine (%) as a function of fuel air mixture ratio for different constant engine speeds in krpm.

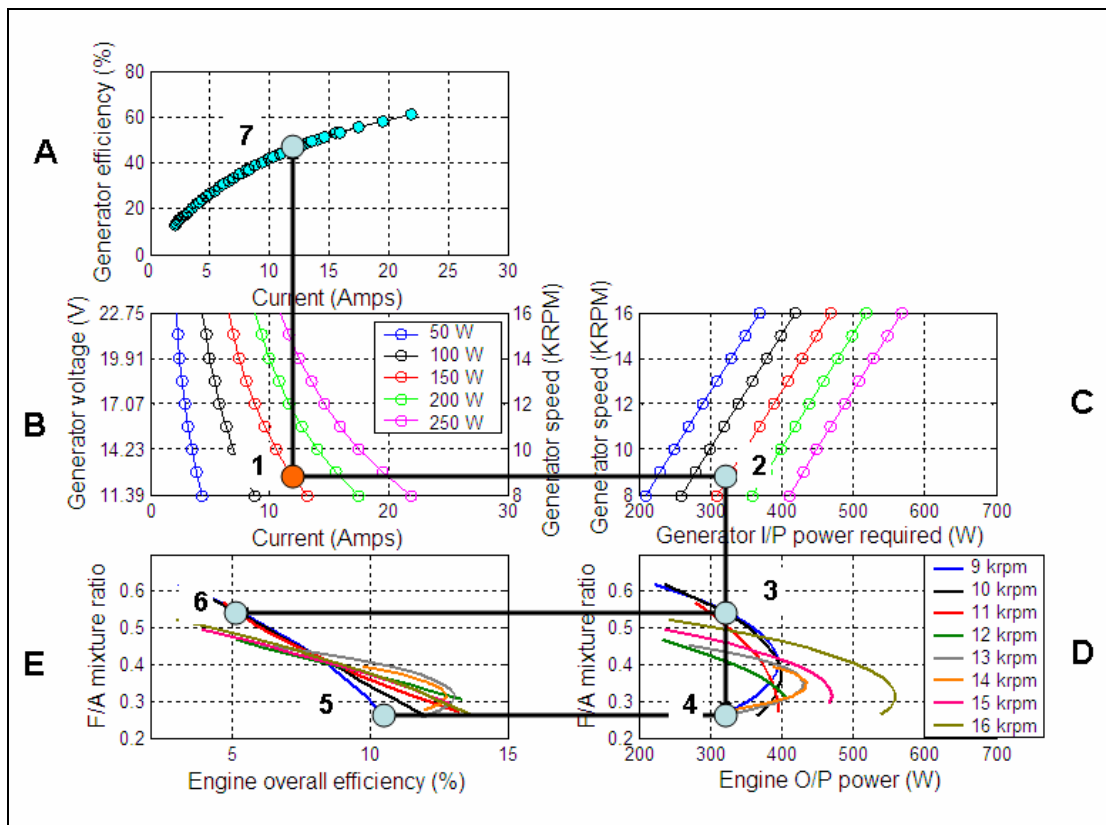


Figure 7-17: Schematic of the optimization procedure to determine best operating point for an engine/generator combination for maximum system efficiency.

The legends for figures A and C are the same as that shown in figure B. The legend for figure E is the same as the one for figure D. Let us now consider the case for a device that requires a power output of 150 W at an operating voltage of about 12.8 V. The generator speed that delivers this voltage is 9000 rpm and the corresponding current output is 11.71 Amps. This corresponds to point 1 marked on plot B of Fig. 7–17. Moving along the horizontal line marked in the plot to plot C and finding the corresponding data point (point 2) gives the required power input from the engine to produce this amount of electrical power as 329 Watts. Moving downwards from point 2 to plot D gives two data points (point 3 and point 4) on the engine speed curve of 9000 rpm that can provide this input power to the generator. It is assumed here that the engine and generator are directly coupled and operate at the same speed. Moving horizontally from points 3 and 4 to the left gives the corresponding efficiency at points 6 and 5 respectively. As seen in Fig. 7–17, the engine efficiency is higher at point 5 (10.5 %) as compared to that at point 6 (5 %). The efficiency of the generator for this operating point can be obtained by moving vertically upwards from point 1 in plot B to find point 7 in plot A. This gives a generator efficiency of 50% corresponding to a load current of 11.71 Amps. System efficiency while operating the engine at point 5 is 5.25% while that at point 6 is 2.5%. This type of analysis helps estimate the optimal operating condition for the engine and generator to maximize system efficiency. Further modifications to Fig. 7–17 are possible by allowing the engine and generator to operate at different speeds with a transmission between the two as well as by operating the engine at different throttle settings. Plots D and E in this case are generated for wide open throttle.

Figure 7–18 shows that the AC frequency is a linear function of engine speed. This is also consistent with the standard expression for operating frequency,²⁴⁵

$$f = \frac{P * n_s}{120} \quad (7-4)$$

where P is the number of magnetic poles, n_s is the synchronous speed in rpm and f is the frequency of the generated AC voltage. Equation 7–4 shows that AC frequency is independent of engine operating conditions and applied electrical load. As would be expected, most payloads or devices driven by an engine–generator of the type shown here would require voltage to be supplied at a fixed frequency. This would necessitate the use of a frequency control system to provide constant frequency output. This would additionally introduce losses into the system which would have to be accounted for in the scheme shown in Fig. 7–17.

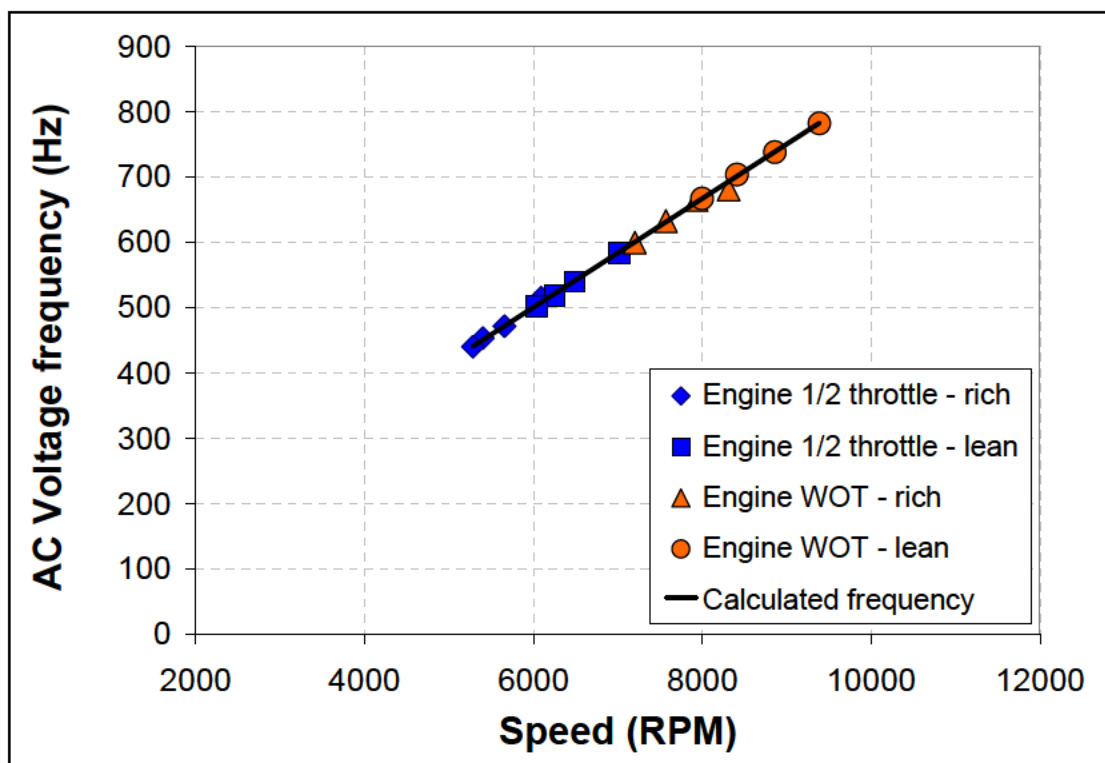


Figure 7-18: AC and mechanical frequencies at different engine operating conditions.

7.6 Power and Energy Density

The power and energy density of a device capable of producing electrical power using the engine-generator combination tested here can be determined given the results presented in Section 7.5. Table 7-4 below summarizes the performance of the system while operating at conditions corresponding to peak power output (8000 rpm, WOT, fuel-air mixture = 0.17) as measured in this work. Power density of the system weighing about 1.83 kg, at this operating condition for an endurance of 2.14 hours, is seen to be about 82 W/kg and energy density is seen to be about 176 W-hr/kg.

Engine weight	488	g
Generator weight	341	g
Peak power output	150	W
System efficiency @ peak power	5.3	%
Fuel flow rate	0.00013	kg/s
Fuel weight	1	kg
System weight	1.83	kg
Fuel heating value	21.84	MJ/kg
Endurance	2.14	hr
System power density	82.1	W/kg
System energy density	175.8	W-hr/kg

Table 7–4: Performance of the engine–generator system consisting of the OS 46 engine with the Sullivan S675–300 generator at operating conditions corresponding to peak power output.

The data is also utilized to generate a performance curve for the system plotted in a power density – energy density space as shown in Fig. 7–19. Figure 7–19 also shows data for the performance of the OS 46 engine at peak power output. The performance of the combined system is seen to be below that of the engine alone due to energy loss in the generator. System performance is seen to be better than some of the other devices surveyed here and is observed to be capable of achieving the target objective with further improvements in engine and generator efficiency. At 1.83 kg, the total system weight with fuel is higher than that of the other systems. This means that a reduction in size by utilizing lighter materials without sacrificing efficiency is required to make this system viable for small portable power applications.

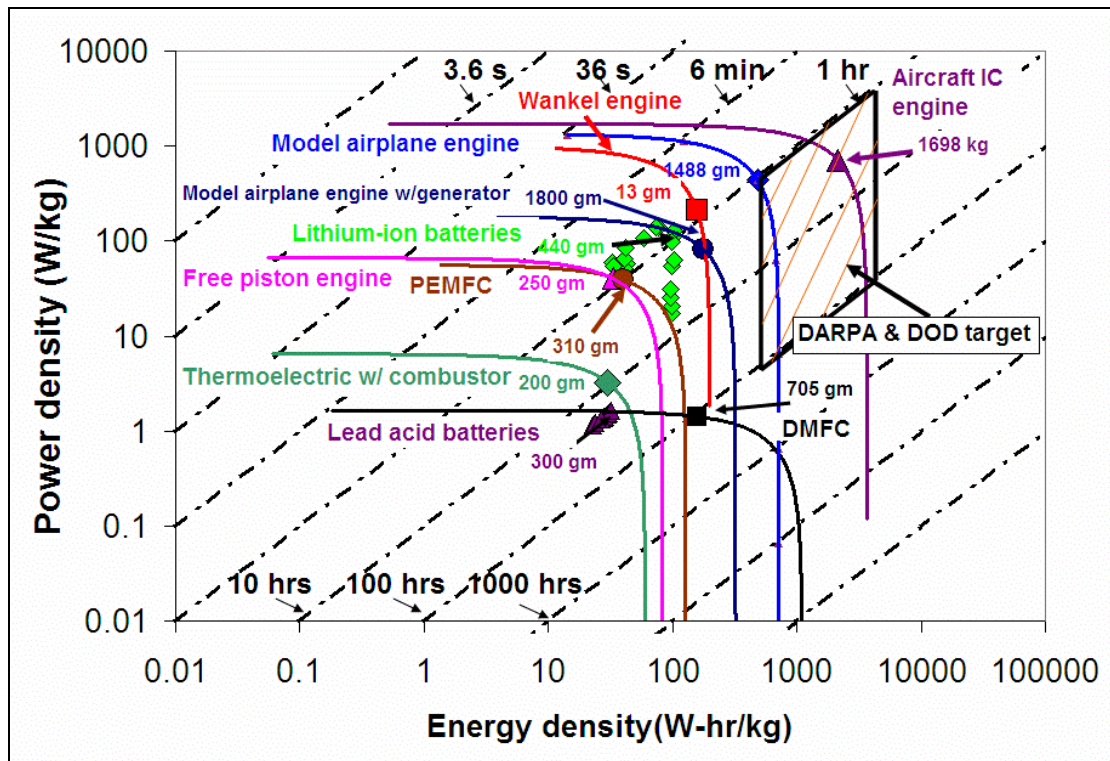


Figure 7–19: Power density and energy density of different systems along with a data set corresponding to the OS 46 engine alone and in an engine–generator system consisting of the OS 46 engine with the Sullivan S675–300 model generator operating at conditions of peak power output.

Chapter 8 : Conclusions and Future Work

8.1 Summary and Conclusions

This dissertation has reported the results of a comprehensive investigation of the scaling of small piston engine performance. It has investigated the scaling of overall engine performance and losses, and has conducted a more detailed investigation of the combustion process occurring inside the smallest commercially available piston engines. Six separate aspects of the problem were investigated. These are:

- Performance characterization of miniature glow fuel IC engines
- Scaling analysis of engine performance with engine size
- Estimation of energy losses in miniature glow fuel IC engines
- Scaling of energy losses with engine size
- In-Cylinder pressure measurements and combustion imaging studies to understand ignition and combustion processes
- Investigation of a coupled engine-generator system capable of being incorporated in a portable power application

The introduction identifies the need for miniature heat engines, shows that the energy density of existing battery technologies is insufficient to meet these needs, and shows that these needs can only be met by power and energy systems that consume fuels with energy densities that are approximately 100 times greater – like liquid hydrocarbons. The current state of the art in miniature engines and miniature engine research is summarized. The key finding is that small internal combustion engines

could meet DARPA and DOD targets for power and energy density in sub-kilogram packages if their efficiency could be improved to levels even half those of automobile engines. The problem is that no reliable performance data for miniature engines exist nor do we understand why today's engines are so inefficient. Therefore, the objectives of this thesis are to provide these data and answer this question.

Chapter 2 describes the development of a dynamometer system capable of making reliable and repeatable measurements of engine performance in a very challenging test environment. It is demonstrated that the system can determine power to within 5% and efficiency to within 8%. The critical aspects of the measurements are controlling vibration, controlling engine speed automatically while varying the equivalence ratio, damping oscillations in air flow measurements, making accurate fuel flow measurements at flow rates (as low as 0.005 gs^{-1}) that are not spanned by traditional instrumentation, and discovering which combinations of instrumentation and dynamometer hardware work reliably with each engine. The latter is extremely important. The flexibility of the system is also demonstrated as the same basic components are used to measure engine performance, thermal losses, frictional losses, cylinder pressure, and engine-generator performance.

Chapter 3 presents comprehensive performance measurements for nine single cylinder, two-stroke, glow ignition IC engines ranging in displacement from 0.16 cc to 7.5 cc (0.010 cu.in to 0.46 cu.in.). These data are combined with similar data for conventional-scale engines found in the literature to identify how key engine performance parameters with engine size. While both engine power output and efficiency follow power law scaling that decrease with decreasing engine size,

efficiency deviates from the ‘conventional–scale’ power law at engine sizes of about 15 to 20 cc (0.9 cu.in. to 1.2 cu.in.) displacement and begins to approach zero much more quickly. Extrapolating this trend to find the length scale associated with zero efficiency (or thermodynamic break–even) indicates that the minimum length scale of a two–stroke heat engine is about 3 mm. This result is in the same range as similar estimates made by other researchers using very different methods. It should be noted, however, that 3mm does not represent an absolute physical barrier but rather the limit associated with *currently existing technology*. It is possible that improvements in engine design, high temperature materials, fuel–air mixing, and combustion technology could lead to smaller engines with useful levels of efficiency.

Chapter 4 describes the results of a comprehensive analysis of engine loss mechanisms so as to understand the physical processes responsible for the dramatic reduction in efficiency with scale measured in Chapter 3. An energy balance conducted on a control volume analysis of the engine shows that the major energy loss processes are: incomplete combustion, heat transfer, sensible enthalpy in the exhaust, and mechanical and fluid friction. Dynamometer measurements are used to quantify each loss excepting incomplete combustion which is inferred from the other terms by enforcing an overall energy balance. Comparisons are made at two conditions – constant speed and fuel–air mixture ratio, and constant mean piston speed – and are used to identify the effect of engine size on different energy loss mechanisms. The key finding is that incomplete combustion is by far the most important loss mechanism relative to the total power of the engine. Losses in order of decreasing importance are combustion, heat transfer, exhaust enthalpy, and

mechanical and fluid friction. This is almost the opposite of the arrangement of losses in conventional-scale engines which is: exhaust enthalpy, heat transfer, friction and combustion. Therefore, the most important challenge in realizing the performance benefits of small internal combustion engines is improving combustion efficiency.

Chapter 5 describes cylinder pressure measurements made in three different size miniature engines that are used to understand the combustion process generally and how it is affected by scale. The effects of engine speed, fuel–air mixture ratio and engine size on parameters such as the location and magnitude of the peak cylinder pressure, mass burned fraction, heat release rate, ignition point, burn duration and cycle–to–cycle variation are reported. The key finding is that equivalence ratio and engine speed are the most important parameters governing peak cylinder pressure and peak engine performance. Peak cylinder pressure and heat release rate decreases as speed increases and equivalence ratio deviates from 1. Ignition delay and coefficient of variation increase as speed increases and the equivalence ratio deviates from 1. In smaller engines and at low speed, there is evidence suggesting that a two–stage combustion process occurs. It begins with localized ignition in the region around the glow plug and is followed by a delayed secondary ignition. Evidence of this behavior disappears in all engines as speed increases or fuel to air ratio deviates from stoichiometric suggesting that this is less influenced by scale than the local Damköhler number. One possible explanation of this apparent re–ignition is that radiation from a turbulent combustion process initiated at the glow plug ignites residual fuel near the walls after a delay. Another possible explanation is that this is an artifact of the combustion kinetics in which rising pressure suppresses chain

branching reactions which re-start once the pressure starts to decrease after the piston passes TDC. In either case, this suggests that a major source of inefficiency could be the loss of un-reacted fuel.

Chapter 6 attempts to gain more insight into the combustion process by using a high speed camera to image natural luminescence from the combustion chamber and placing small IC engines on a turbulent combustion regime diagram to see where they lie relative to conventional-scale engines. The key finding of the imaging experiments is that the COV (coefficient of variation) of the natural flame luminescence increases with increasing speed and as fuel to air ratio deviates from the stoichiometric value. This is consistent with the findings of the cylinder pressure measurements although the COV's associated with flame luminosity are much higher than those associated with pressure. This could be caused by soot sticking and then becoming dislodged from the quartz windows. The key finding of the regime diagram analysis is that miniature piston engines operate entirely in the 'flamelet in eddy' regime whereas conventional-scale piston engines span the 'wrinkled laminar flamesheet' and 'flamelet in eddy' regimes but lie mostly in the flame sheet regime. Reducing engine scale drives the combustion regime even closer to distributed reaction. Therefore, it is clear that the approaches used to model combustion in conventional-scale engines are not appropriate for use in miniature engines and different approaches will need to be developed.

Finally, Chapter 7 describes the performance of a hybrid engine-generator system intended as a kilogram-scale battery replacement. The peak system efficiency corresponding to a un-optimized operational setting is found to be 5.3%. A procedure

for improving system efficiency by identifying the optimum engine–generator operating conditions is developed and demonstrated.

8.2 Key Findings and Contributions

1. Developed a dynamometer system and experimental methodologies capable of providing reliable, repeatable measurements of power, overall thermodynamic efficiency, volumetric efficiency, thermal efficiency, mechanical efficiency, fuel pressure, and cylinder pressure in miniature engines producing between 1–750 W (0.001–1 hp) of power with engine displacement ranging from 0.1 to 7.5 cc. This is a unique facility whose measurement breadth and accuracy far exceeds those of any other.
2. Incomplete combustion accounts for 60-70% of total energy loss in sub 500g engines. Combustion efficiency drops from 18% for 450g engine to just 3% for a 15 g engine. This is in contrast to conventional-scale engines where combustion efficiencies are > 95%. The remaining losses in order of decreasing importance are heat transfer, sensible enthalpy in the exhaust, and friction. This ordering is almost opposite to the ordering in a conventional-scale engine.
3. The minimum cylinder bore diameter of a two stroke glow ignition engine *based on current technology* is about 3 mm.
4. Measured peak engine power output is often significantly lower than manufacturers' claims – when such claims are made.
5. Overall engine efficiency at peak power ranges from 4–16% (smallest engine to the largest engine). No efficiency data is available from manufacturers.

6. Scaling laws were developed for peak engine torque, peak power output, overall efficiency at peak power and peak normalized power as a function of engine displacement. Scaling of power output showed two distinct correlations – one for two stroke and another for four stroke engines. Scaling of overall efficiency also showed two correlations – the difference being the presence or absence of an exhaust muffler.
7. Intake losses are mainly governed by engine operating speed and flow path configuration (presence/absence of an exhaust muffler).
8. Measured mean gas temperature for this class of engines running on glow fuel as a function of fuel–air mixture ratio. Friction losses are a linear function of engine speed. Surface contact due to breakdown of the lubrication film is the major contributor to frictional loss in miniature glow ignited IC engines.
9. The sensible enthalpy loss in the exhaust is independent of mixture ratio at constant speed providing further evidence that small IC engines are combustion limited.
10. Cylinder pressure measurements suggest a two-stage combustion process may occur at low speeds and near-stoichiometric conditions. Combustion appears to originate at or near the glow plug.
11. Small IC engines operate in a ‘wrinkled laminar’, a ‘flamelet in eddy’, or even ‘distributed reaction’ regimes depending on operating conditions and engine size. This suggests that combustion modeling techniques developed for conventional-scale engines which operate in the ‘wrinkled laminar flame’

regime are inappropriate and new techniques must be developed for use in small-scale engines.

12. Measured the performance of an engine-generator system constructed entirely of off-the-shelf components. A system weighing 1.83 kg is capable of delivering a power density of 82 W/kg for 2.14 hours with an energy density of 176 W-hr/kg.
13. Developed a procedure for identifying optimum engine-generator system operating conditions.

8.3 Future Work

This dissertation has advanced the understanding of performance and scaling issues in miniature glow ignited IC engines. A preliminary understanding of the ignition and combustion processes and its dependence on engine operating conditions has been developed. Future work envisioned in this area of research is summarized below.

1. Performance characterization of more engines (of different displacements, of same displacement with different designs, of different configurations such as 4 stroke, compression ignition and spark ignition) is required to establish a more detailed scaling analysis for miniature IC engines.
2. Further investigation of the effect of the presence or absence of a muffler. This could be done by operating the larger engines without a muffler and by developing numerical models (1D wave equations) of the flow passage dynamics.

3. Alternative methods of engine loss characterization can be pursued to validate the results presented in this study. This could include cylinder pressure measurements in motored engines to estimate frictional and pumping losses and a different kind of thermal loss estimate based on measurements of coolant flow and temperatures on the outer surface of the engine. Incomplete combustion losses could be validated by measuring the chemical composition of the exhaust using a gas analyzer. It could also be computed using a gross heat release analysis using cylinder pressure measurements, estimated gas temperature, associated heat transfer as well as blowby losses.
4. Engine cycle simulations based on a 1-dimensional approach could be utilized to study the gas and energy exchange processes occurring during the engine cycle. Features such as double peaks in engine delivery ratio and variations in location of peak engine power output/efficiency with respect to engine speed, size and fuel-air mixture ratio could be investigated. Such a model could utilize mass burned fraction/heat release rate developed from cylinder pressure measurements to model the combustion process. Alternately, engine combustion could be modeled using a full chemical kinetic simulation coupled with a 1-dimensional gas flow model to investigate phenomena such as secondary burning and double peaks in net heat release rates observed in this work.
5. Chemiluminescence imaging of OH and CH could be used to track flame location and propagation. This would greatly improve our understanding of

the flame propagation mechanism as well as the combustion regime in miniature glow ignited IC engines.

6. A case study could be performed to investigate the effect of replacing batteries with an engine-generator system for various mission profiles. This would be based on generator performance characteristics developed in this study and the technique identified here that allows one to find the optimal operating conditions for the engine-generator assembly to maximize system efficiency. Different engines could be considered by incorporating their respective operating maps and the effect of adjustable transmission systems enabling a certain level of decoupling of engine and generator speeds can also be explored.
7. One of the reasons many of these small engines run rich is that they are fuel cooled. Operating at the lean equivalence ratios necessary for acceptable thermodynamic efficiency may dramatically decrease engine lifetime. Therefore, improved high temperature materials are required.
8. These engines use very simple carburetors so it is possible that poor fuel-air mixing is a major contributor to the poor overall combustion efficiency. Therefore, the fuel-air mixing process in these engines must be investigated and new technologies for improving the mixing process may need to be developed.
9. Additional investigation of the two-stage combustion process observed in some cylinder pressure measurements. The investigation would include imaging of the in-cylinder combustion process with simultaneous pressure

measurements and a chemical kinetic investigation of the combustion process to see if the phenomenon can be explained by the pressure-dependence of the chain branching reactions.

Appendix A

A.1 Energy Balance With Control Volume Around Each Engine Component

A single engine cycle is considered for a two-stroke crankcase-scavenged internal combustion engine. A flow path is established for the fuel-air mixture through the engine components and loss mechanisms at each location are identified. Figure A-1 illustrates the details of this technique.

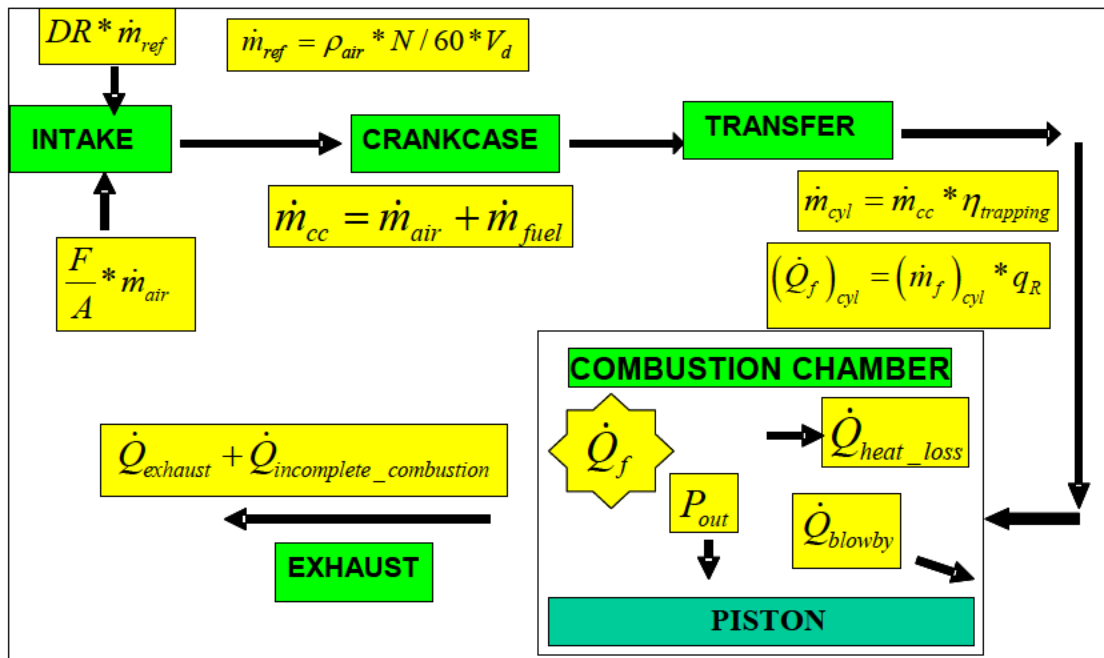


Figure A-1: Energy balance in a two stroke engine with control volumes drawn around individual engine components.

The engine is separated into five major components for analysis. These are the engine intake, the crankcase, the transfer ports, the combustion chamber and the exhaust system. The intake system includes the intake channel, the throttle valve and the carburetor. The piston is included within the combustion chamber. The major energy release and energy loss mechanisms occurring in each of the components during the course of a single engine cycle are identified. Mechanical friction which

occurs due to the rubbing of contact surfaces in the bearings and piston–cylinder interface as well as fluid friction which occurs in the engine channels is modeled separately as it occurs at different locations in the engine. The processes occurring in each of these components as part of the engine cycle can now be defined.

Air enters into the intake system through the intake channel and mixes with the fuel entering through the carburetor. The throttle valve is assumed to be fully open and there are no throttling losses associated with the engine intake. The amount of air entering the engine is less than the ideal amount of air that can be ingested by the engine operating at a specific speed. The difference between the ideal and actual amount of air ingested by the engine is given by the delivery ratio of the engine. Delivery ratio is defined as,

$$DR = \frac{\text{mass of air delivered to the engine}}{\text{reference mass of air}} \quad (\text{A-1})$$

The reference mass of air is defined as the product of the volumetric displacement of the engine, density of atmospheric air and the engine operating speed.

$$\text{reference mass of air} = V_d * N / 60 * \rho_{air} \quad (\text{A-2})$$

The actual amount of air entering the engine crankcase through the intake can be expressed using equations A-1 and A-2 as,

$$(\dot{m}_a)_{CC} = DR * V_d * N / 60 * \rho_{air} \quad (\text{A-3})$$

Since the engine utilizes a carburetor for fuel–air mixing, the amount of fuel entering into the engine is proportional to the amount of ingested air. The mass of fuel entering the engine crankcase can be described using the fuel–air mixture ratio.

$$(\dot{m}_f)_{CC} = (\dot{m}_a)_{CC} * \left(\frac{F}{A} \right) \quad (A-4)$$

The net mass of fuel and air entering the engine crankcase can be expressed as,

$$(\dot{m}_{total})_{CC} = (\dot{m}_a)_{CC} + (\dot{m}_f)_{CC} = (\dot{m}_a)_{CC} * \left(1 + \left(\frac{F}{A} \right) \right) \quad (A-5)$$

During the downward motion of the piston, the mass in the crankcase is compressed and as the transfer ports are uncovered, fresh fuel–air mixture is inducted into the engine cylinder as part of the scavenging process. However, during this process some amount of fresh charge is lost to the exhaust via short–circuiting, while the remaining charge pushes out and replaces the burnt gas from the previous cycle. The amount of fresh charge inducted into the combustion chamber by the scavenging process can be described by the trapping efficiency.

$$(\dot{m}_{total})_{CYL} = (\dot{m}_{total})_{CC} * \eta_{trapping} \quad (A-6)$$

Using equations A–5 and A–6, the total mass of fresh charge in the cylinder after the scavenging process can be expressed as,

$$(\dot{m}_{total})_{CYL} = (\dot{m}_a)_{CC} * \left(1 + \left(\frac{F}{A} \right) \right) * \eta_{trapping} \quad (A-7)$$

Using equations A–3 and A–7,

$$(\dot{m}_{total})_{CYL} = DR * V_d * N / 60 * \rho_{air} * \left(1 + \left(\frac{F}{A} \right) \right) * \eta_{trapping} \quad (A-8)$$

The mass of unburnt fuel in the cylinder can be obtained using the total mass of the fresh mixture and the air–fuel mixture ratio. The total mass in the cylinder can be expressed as,

$$(\dot{m}_{total})_{CYL} = (\dot{m}_f)_{CYL} * \left(1 + \left(\frac{A}{F}\right)\right) \quad (A-9)$$

Hence we have,

$$(\dot{m}_f)_{CYL} = \frac{(\dot{m}_{total})_{CYL}}{\left(1 + \left(\frac{A}{F}\right)\right)} \quad (A-10)$$

Using equations A-8 and A-10,

$$(\dot{m}_f)_{CYL} = \frac{DR * V_d * N / 60 * \rho_{air} * \left(1 + \left(\frac{F}{A}\right)\right) * \eta_{trapping}}{\left(1 + \left(\frac{A}{F}\right)\right)} \quad (A-11)$$

$$(\dot{m}_f)_{CYL} = DR * V_d * N / 60 * \rho_{air} * \frac{F}{A} * \eta_{trapping} \quad (A-12)$$

The energy carried by the fresh fuel–air mixture into the combustion chamber can be described using the mass of fuel in the mixture and the energy content of the fuel.

$$(\dot{Q}_f)_{CYL} = (\dot{m}_f)_{CYL} * Q_R \quad (A-13)$$

The fuel–air mixture undergoes ignition and combustion processes in the combustion chamber. A part of the energy released by the combustion process is converted into useful work done on the piston. Some of the fresh charge is lost due to blowby through the piston–cylinder interface into the crankcase volume. This lost charge represents an enthalpy loss due to unburnt fuel. Another part of the energy released by the combustion process is transferred by convective heat transfer to the cylinder walls from where it is further transferred to the atmosphere via conductive heat transfer through the walls and convective cooling on the engine outer wall. The

energy balance within the combustion chamber with the intake, exhaust and transfer ports closed can be expressed as,

$$\left(\dot{Q}_f\right)_{CYL, released} = P_{out} + \dot{Q}_{heat_loss} + \dot{Q}_{blowby} \quad (A-14)$$

During the final process of the engine cycle, exhaust gases are transferred from the combustion chamber to the exhaust system and released into the atmosphere. The exhaust gases carry a sensible portion of energy released during the combustion process. In addition the exhaust gases comprise of unburnt fuel–air mixture which is the result of incomplete combustion within the combustion chamber. These two energy loss terms comprise the total energy transferred out of the engine through the exhaust system and can be expressed as,

$$\left(\dot{Q}\right)_{exhaust} = \dot{Q}_{exhaust_enthalpy} + \dot{Q}_{incomplete_combustion} \quad (A-15)$$

Fluid friction losses or pumping losses occur in each of the engine components due to contact between the gas mixture and the engine walls. Mechanical frictional losses occur at the different contact surfaces within the engine. These include the crankshaft bearings, the crankshaft pin–connecting rod interface and the piston–cylinder liner interface. Fluid friction and mechanical friction terms are coupled into a single frictional energy loss term defined for the engine cycle.

$$\left(\dot{Q}\right)_{friction} = \dot{Q}_{mechanical_friction} + \dot{Q}_{fluid_friction} \quad (A-16)$$

This completes the energy balance for the two stroke cycle engine. The major energy loss mechanisms contributing to the performance of the engine and identified by the preceding analysis are:

- Air intake losses

- Scavenging losses
- Energy loss by heat transfer
- Energy loss by mass blowby
- Sensible energy loss in the exhaust
- Energy loss due to incomplete combustion
- Energy loss due to fluid and mechanical friction

The physical processes occurring within the engine are highly complicated and involve interplay of several energy interactions at the same time. Two of the assumptions made during the energy balance performed in the preceding analysis are:

- Energy available from unburnt fuel–air mixture left over from the previous cycle in the combustion chamber is neglected.
- Energy transfer internally from the walls to the fuel–air mixture as it passes through the various engine components is assumed to be negligible.

Appendix B

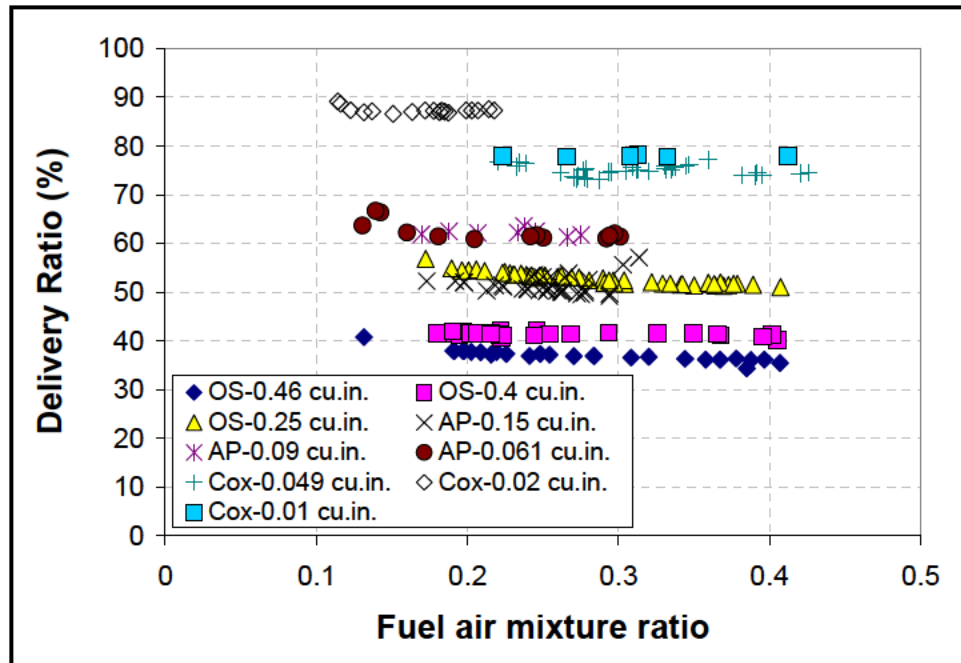


Figure B-1: Delivery ratio at different fuel air mixture ratios and a constant engine speed of 12000 rpm for all engines.

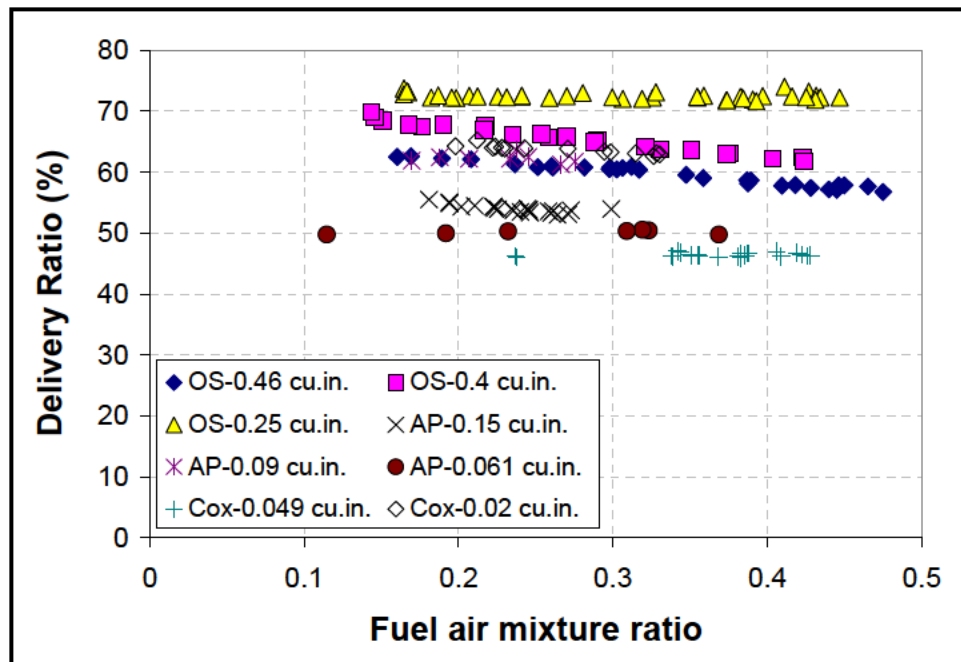


Figure B-2: Delivery ratio at different fuel air mixture ratios and a constant mean piston speed of 4.77 ms^{-1} for all engines.

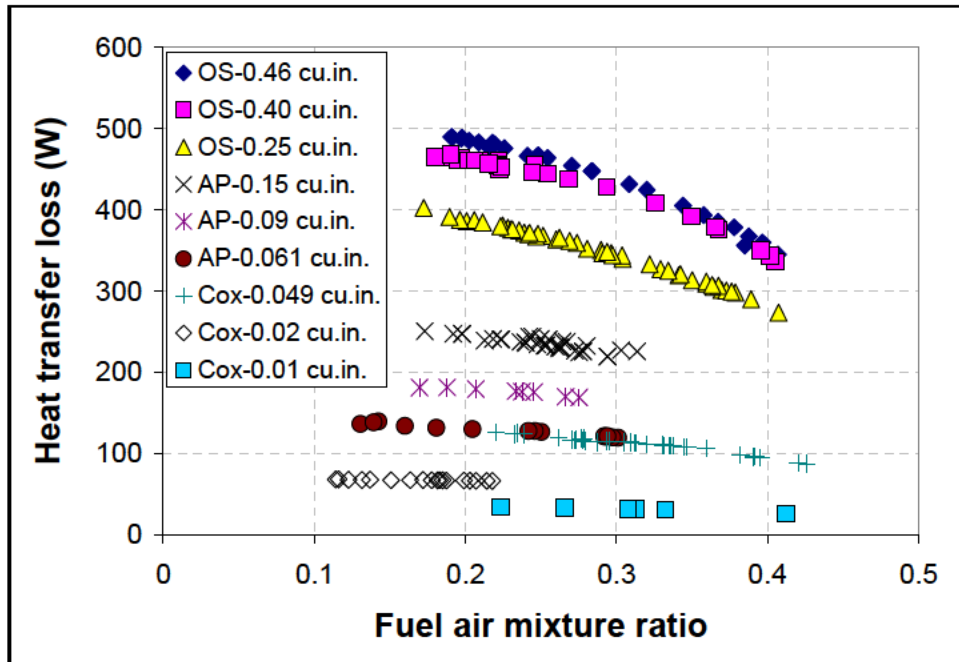


Figure B-3: Heat transfer loss at different fuel air mixture ratios and a constant engine speed of 12000 rpm for all engines.

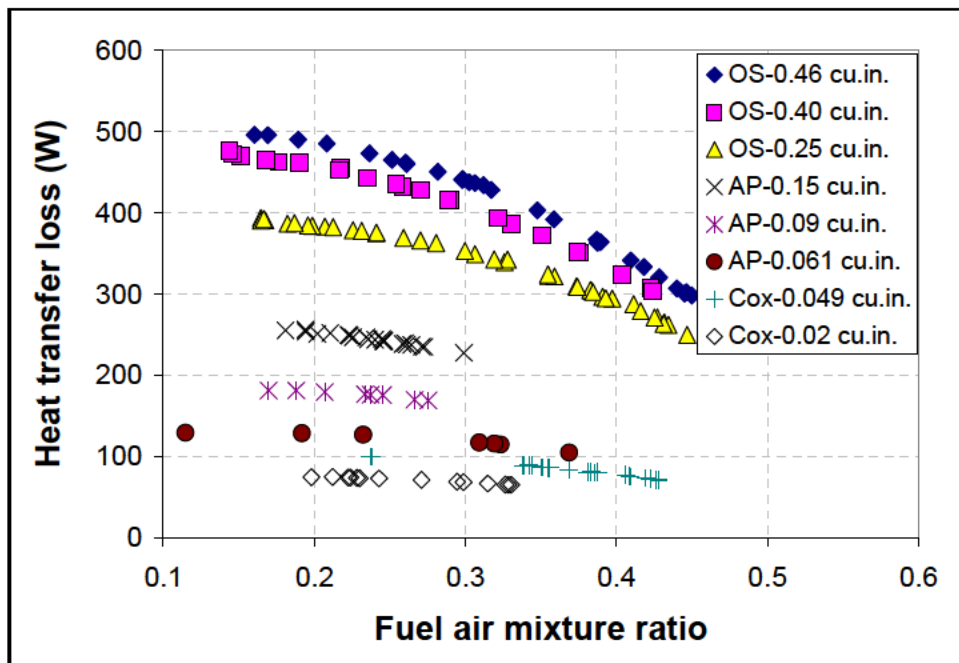


Figure B-4: Heat transfer loss at different fuel air mixture ratios and a constant mean piston speed of 4.77 ms^{-1} for all engines.

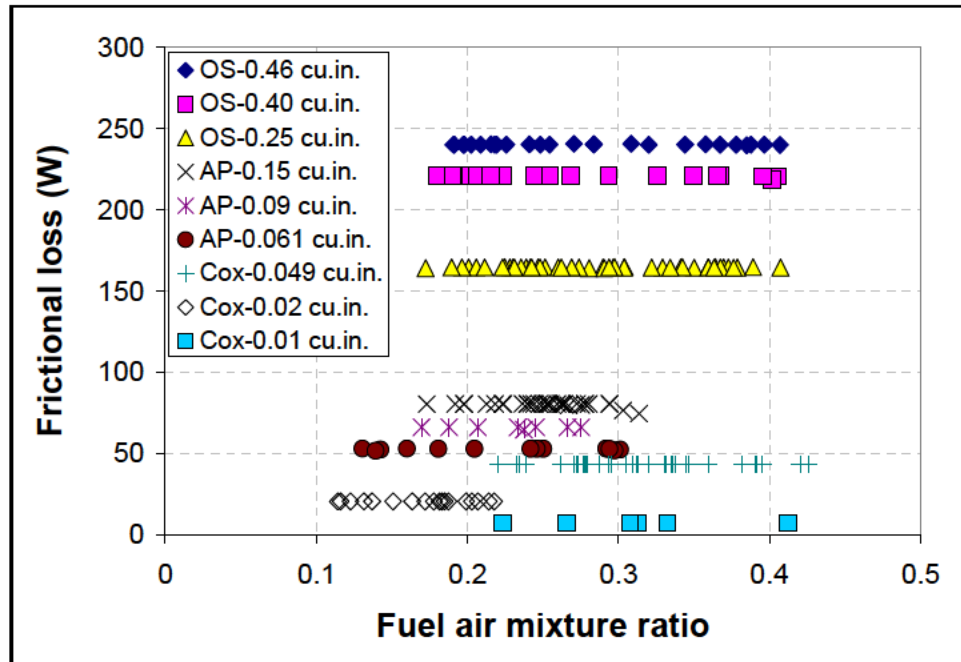


Figure B-5: Frictional loss at different fuel air mixture ratios and a constant engine speed of 12000 rpm for all engines.

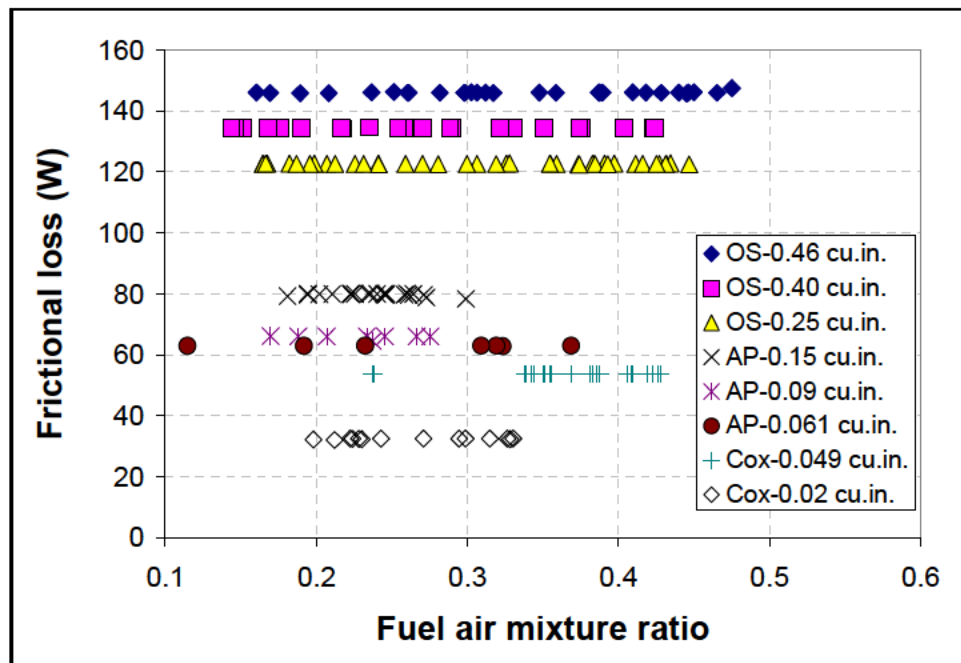


Figure B-6: Frictional loss at different fuel air mixture ratios and a constant mean piston speed of 4.77 ms^{-1} for all engines.

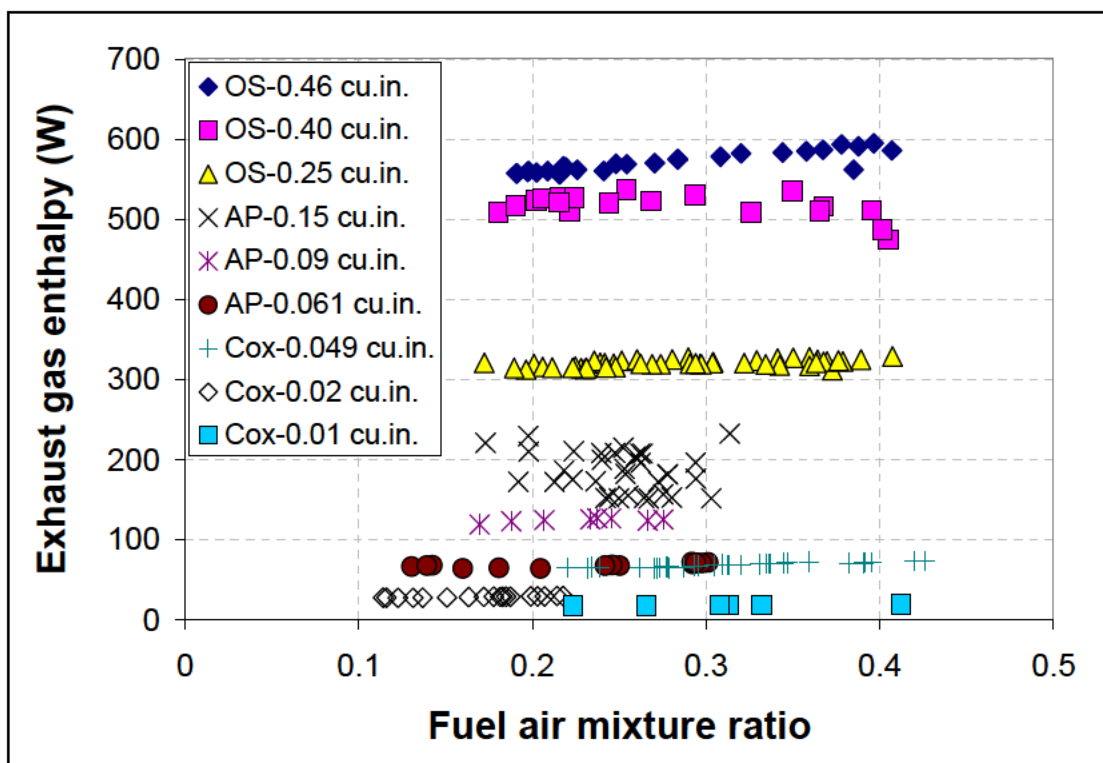


Figure B-7: Enthalpy released in exhaust at different fuel air mixture ratios and a constant engine speed of 12000 rpm for all engines.

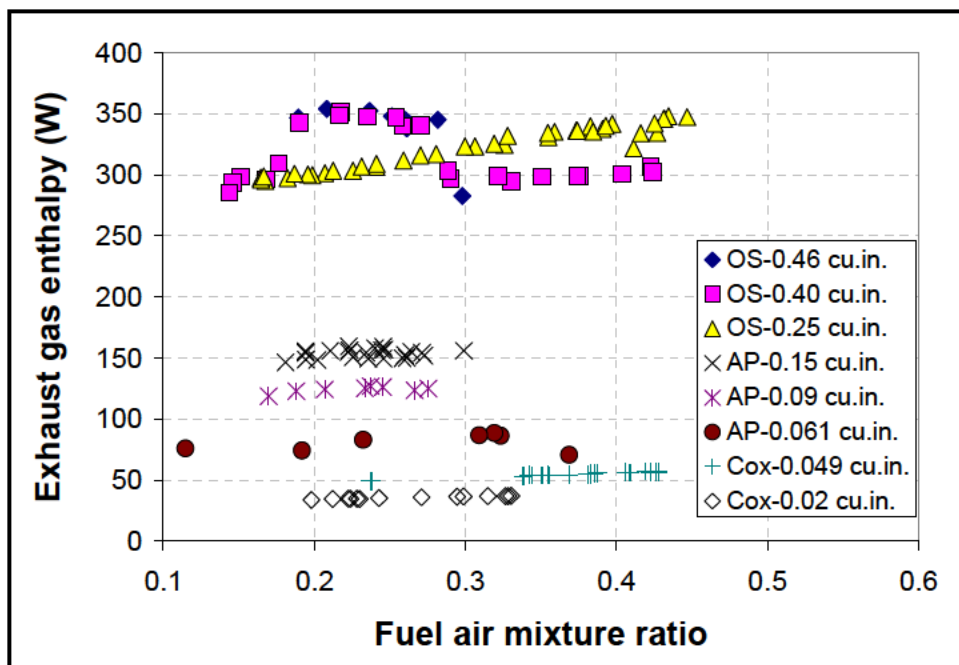


Figure B-8: Enthalpy released in the exhaust at different fuel air mixture ratios and a constant mean piston speed of 4.77 ms^{-1} for all engines.

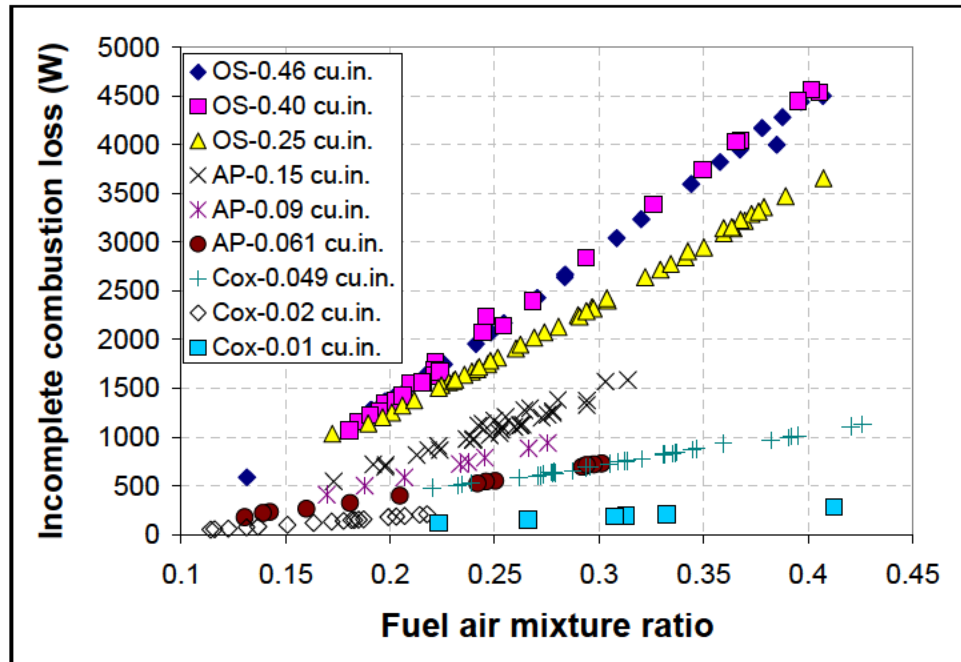


Figure B-9: Incomplete combustion losses at different fuel air mixture ratios and a constant engine speed of 12000 rpm for all engines.

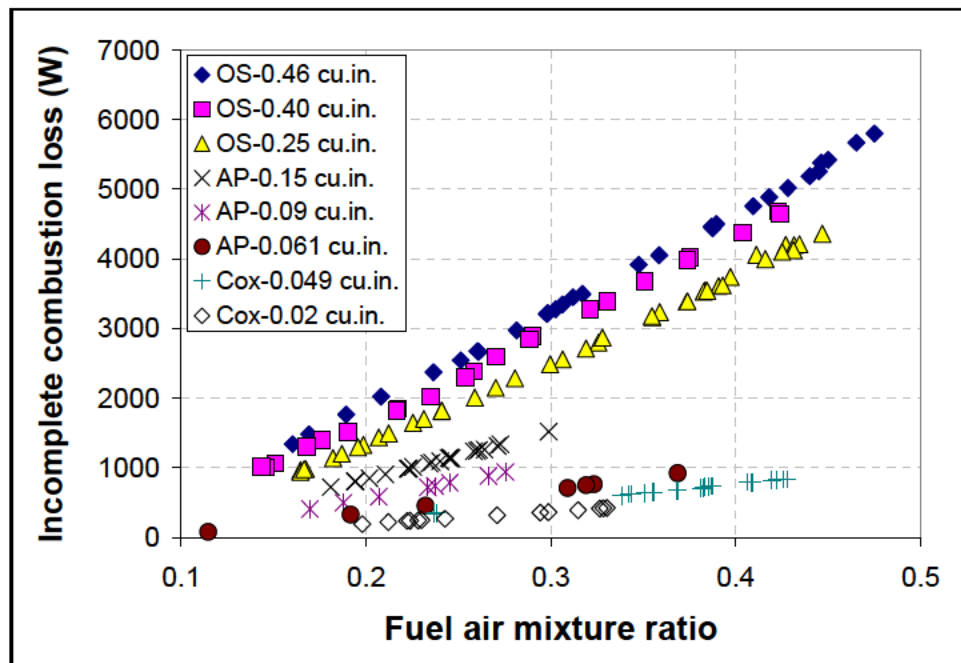


Figure B-10: Incomplete combustion losses at different fuel air mixture ratios and a constant mean piston speed of 4.77 ms⁻¹ for all engines.

Appendix C

C.1 Elements Considered in Reaction Mechanism for Hydrocarbon And

Nitrogen

H
O
C
N
AR

C.2 Species Considered in Reaction Mechanism for Hydrocarbon And Nitrogen

H
H₂
O
O₂
O₃
OH
H₂O
HO₂
H₂O₂
CH
CH₂
CH₂(S)
CH₃
CH₄
CO
CO₂
HCO
CH₂O
CH₂OH
CH₂OOH
CH₃O
CH₃OH
CH₃CO
CH₃HCO
CH₃CH₂O
CH₃O₂
CH₃OOH
CH₃NO
CH₃NO₂
CH₃ONO
CH₃ONO₂

H2CNO2
HCN
C2H2
C2H3
C2H4
C2H5
C2H6
HCCO
HCCOH
CH2CO
N
N2
NO
NO2
NO3
HNO
HONO
HONO2
N2O
AR
C
C2
C2H
C2O
CH2HCO
CH2OH
C2H2OH
OCHCHO
C2H5CHO
C2H5CO
NH
NH2
NH3
NNH
N2H2
H2NO
CN
C2N2
NCN
CH3CN
CH2CN
H2CN
NCO
HOCN
HNCO
HCNO

Appendix D

D.1 Transport Properties File for the Nitromethane/Methanol Reaction

Mechanism

AR	0	136.500	3.330	0.000	0.000	0.000
C	0	71.400	3.298	0.000	0.000	0.000 ! *
C2	1	97.530	3.621	0.000	1.760	4.000
C2O	1	232.400	3.828	0.000	0.000	1.000 ! *
CN2	1	232.400	3.828	0.000	0.000	1.000 ! OIS
C2H	1	209.000	4.100	0.000	0.000	2.500
C2H2	1	209.000	4.100	0.000	0.000	2.500
C2H2OH	2	224.700	4.162	0.000	0.000	1.000 ! *
C2H3	2	209.000	4.100	0.000	0.000	1.000 ! *
C2H4	2	280.800	3.971	0.000	0.000	1.500
C2H5	2	252.300	4.302	0.000	0.000	1.500
C2H6	2	252.300	4.302	0.000	0.000	1.500
C2N	1	232.400	3.828	0.000	0.000	1.000 ! OIS
C2N2	1	349.000	4.361	0.000	0.000	1.000 ! OIS
C3H2	2	209.000	4.100	0.000	0.000	1.000 ! *
C3H4	1	252.000	4.760	0.000	0.000	1.000
C3H6	2	266.800	4.982	0.000	0.000	1.000
C3H7	2	266.800	4.982	0.000	0.000	1.000
C4H6	2	357.000	5.180	0.000	0.000	1.000
I*C3H7	2	266.800	4.982	0.000	0.000	1.000
N*C3H7	2	266.800	4.982	0.000	0.000	1.000
C3H8	2	266.800	4.982	0.000	0.000	1.000
C4H	1	357.000	5.180	0.000	0.000	1.000
C4H2	1	357.000	5.180	0.000	0.000	1.000
C4H2OH	2	224.700	4.162	0.000	0.000	1.000 ! *
C4H8	2	357.000	5.176	0.000	0.000	1.000
C4H9	2	357.000	5.176	0.000	0.000	1.000
I*C4H9	2	357.000	5.176	0.000	0.000	1.000
C5H2	1	357.000	5.180	0.000	0.000	1.000
C5H3	1	357.000	5.180	0.000	0.000	1.000
C6H2	1	357.000	5.180	0.000	0.000	1.000
C6H5	2	412.300	5.349	0.000	0.000	1.000 ! JAM
C6H5O	2	450.000	5.500	0.000	0.000	1.000 ! JAM
C5H5OH	2	450.000	5.500	0.000	0.000	1.000 ! JAM
C6H6	2	412.300	5.349	0.000	0.000	1.000 ! SVE
C6H7	2	412.300	5.349	0.000	0.000	1.000 ! JAM
CH	1	80.000	2.750	0.000	0.000	0.000
CH2	1	144.000	3.800	0.000	0.000	0.000
CH2(S)	1	144.000	3.800	0.000	0.000	0.000

CH2*	1	144.000	3.800	0.000	0.000	0.000
CH2CHCCH	2	357.000	5.180	0.000	0.000	1.000 ! JAM
CH2CHCCH2	2	357.000	5.180	0.000	0.000	1.000 ! JAM
CH2CHCH2	2	260.000	4.850	0.000	0.000	1.000 ! JAM
CH2CHCHCH	2	357.000	5.180	0.000	0.000	1.000 ! JAM
CH2CHCHCH2	2	357.000	5.180	0.000	0.000	1.000 ! JAM
CH2CO	2	436.000	3.970	0.000	0.000	2.000
CH2O	2	498.000	3.590	0.000	0.000	2.000
CH2OH	2	417.000	3.690	1.700	0.000	2.000
CH3	1	144.000	3.800	0.000	0.000	0.000
CH3CC	2	252.000	4.760	0.000	0.000	1.000 ! JAM
CH3CCCH2	2	357.000	5.180	0.000	0.000	1.000 ! JAM
CH3CCCH3	2	357.000	5.180	0.000	0.000	1.000 ! JAM
CH3CCH2	2	260.000	4.850	0.000	0.000	1.000 ! JAM
CH3CHCH	2	260.000	4.850	0.000	0.000	1.000 ! JAM
CH3CH2CCH	2	357.000	5.180	0.000	0.000	1.000 ! JAM
CH3CHO	2	436.000	3.970	0.000	0.000	2.000
CH3CH2O	2	362.6	4.53	0.000	0.000	1.000
CH2CHO	2	436.000	3.970	0.000	0.000	2.000
CH3CO	2	436.000	3.970	0.000	0.000	2.000
CH3O	2	417.000	3.690	1.700	0.000	2.000
CH3OH	2	481.800	3.626	0.000	0.000	1.000 ! SVE
CH4	2	141.400	3.746	0.000	2.600	13.000
CH4O	2	417.000	3.690	1.700	0.000	2.000
CN	1	75.000	3.856	0.000	0.000	1.000 ! OIS
CNC	1	232.400	3.828	0.000	0.000	1.000 ! OIS
CNN	1	232.400	3.828	0.000	0.000	1.000 ! OIS
CO	1	98.100	3.650	0.000	1.950	1.800
CO2	1	244.000	3.763	0.000	2.650	2.100
H	0	145.000	2.050	0.000	0.000	0.000
H2C4O	2	357.000	5.180	0.000	0.000	1.000 ! JAM
H2	1	38.000	2.920	0.000	0.790	280.000
H2CCCCCH	2	357.000	5.180	0.000	0.000	1.000 ! JAM
H2CCCCCH2	2	357.000	5.180	0.000	0.000	1.000 ! JAM
H2CCCH	2	252.000	4.760	0.000	0.000	1.000 ! JAM
H2CN	1	569.000	3.630	0.000	0.000	1.000 ! os/jm
H2NO	2	116.700	3.492	0.000	0.000	1.000 ! JAM
H2O	2	572.400	2.605	1.844	0.000	4.000
H2O2	2	107.400	3.458	0.000	0.000	3.800
HC2N2	1	349.000	4.361	0.000	0.000	1.000 ! OIS
HCCHCCH	2	357.000	5.180	0.000	0.000	1.000 ! JAM
HCCO	2	150.000	2.500	0.000	0.000	1.000 ! *
HCNN	2	150.000	2.500	0.000	0.000	1.000 ! *
HCCOH	2	436.000	3.970	0.000	0.000	2.000
HCN	1	569.000	3.630	0.000	0.000	1.000 ! OIS
HCO	2	498.000	3.590	0.000	0.000	0.000

HE	0	10.200	2.576	0.000	0.000	0.000 ! *
HCNO	2	232.400	3.828	0.000	0.000	1.000 ! JAM
HOCN	2	232.400	3.828	0.000	0.000	1.000 ! JAM
HNCO	2	232.400	3.828	0.000	0.000	1.000 ! OIS
HNNO	2	232.400	3.828	0.000	0.000	1.000 ! *
HNO	2	116.700	3.492	0.000	0.000	1.000 ! *
HNOH	2	116.700	3.492	0.000	0.000	1.000 ! JAM
HO2	2	107.400	3.458	0.000	0.000	1.000 ! *
N	0	71.400	3.298	0.000	0.000	0.000 ! *
N2	1	97.530	3.621	0.000	1.760	4.000
N2H2	2	71.400	3.798	0.000	0.000	1.000 ! *
N2H3	2	200.000	3.900	0.000	0.000	1.000 ! *
N2H4	2	205.000	4.230	0.000	4.260	1.500
N2O	1	232.400	3.828	0.000	0.000	1.000 ! *
NCN	1	232.400	3.828	0.000	0.000	1.000 ! OIS
NCO	1	232.400	3.828	0.000	0.000	1.000 ! OIS
NH	1	80.000	2.650	0.000	0.000	4.000
NH2	2	80.000	2.650	0.000	2.260	4.000
NH3	2	481.000	2.920	1.470	0.000	10.000
NNH	2	71.400	3.798	0.000	0.000	1.000 ! *
NO	1	97.530	3.621	0.000	1.760	4.000
NCNO	2	232.400	3.828	0.000	0.000	1.000 ! OIS
NO2	2	200.000	3.500	0.000	0.000	1.000 ! *
O	0	80.000	2.750	0.000	0.000	0.000
O2	1	107.400	3.458	0.000	1.600	3.800
O3	2	180.000	4.100	0.000	0.000	2.000
OH	1	80.000	2.750	0.000	0.000	0.000
C2H5CO	2	424.600	4.820	0.000	0.000	1.000 ! NMM
C2H5CHO	2	435.2	4.662	2.7	0.0	1.0 ! WJP, PROPANAL
CH2OH	2	417.000	3.690	1.700	0.000	2.000
CH2HCO	2	436.000	3.970	0.000	0.000	2.000
CH3O2	2	481.800	3.626	0.000	0.000	1.000 ! WJP
CH3CH2CCH	2	357.100	4.720	0.000	0.000	1.000 ! NMM
CH3HCO	2	436.000	3.970	0.000	0.000	2.000
CH3NO	2	436.000	5.180	0.000	0.000	2.000
CH3NO2	2	436.000	5.180	0.000	0.000	2.000
CH3ONO	2	436.000	5.180	0.000	0.000	2.000
HNO2	2	436.000	5.180	0.000	0.000	2.000
HONO	2	572.400	3.600	1.844	0.000	3.000
HNC	2	116.700	3.492	0.000	0.000	1.000
CNO	1	232.400	3.828	0.000	0.000	1.000
HNO3	2	436.000	5.180	0.000	0.000	2.000
NO3	2	436.000	5.180	0.000	0.000	2.000
H2CNH	2	436.000	5.180	0.000	0.000	2.000
H2CNO	2	436.000	5.180	0.000	0.000	2.000
H2CNO2	2	486.076	4.271	3.46	0.000	2.000

CH3OOH	2	481.800	3.626	0.000	0.000	1.000 ! CH3OOH
OCHCHO	1	440.200	4.010	0.000	0.000	2.000 ! NMM

Appendix E

E.1 Cylinder Pressure Measurements For The OS 40 FX Engine

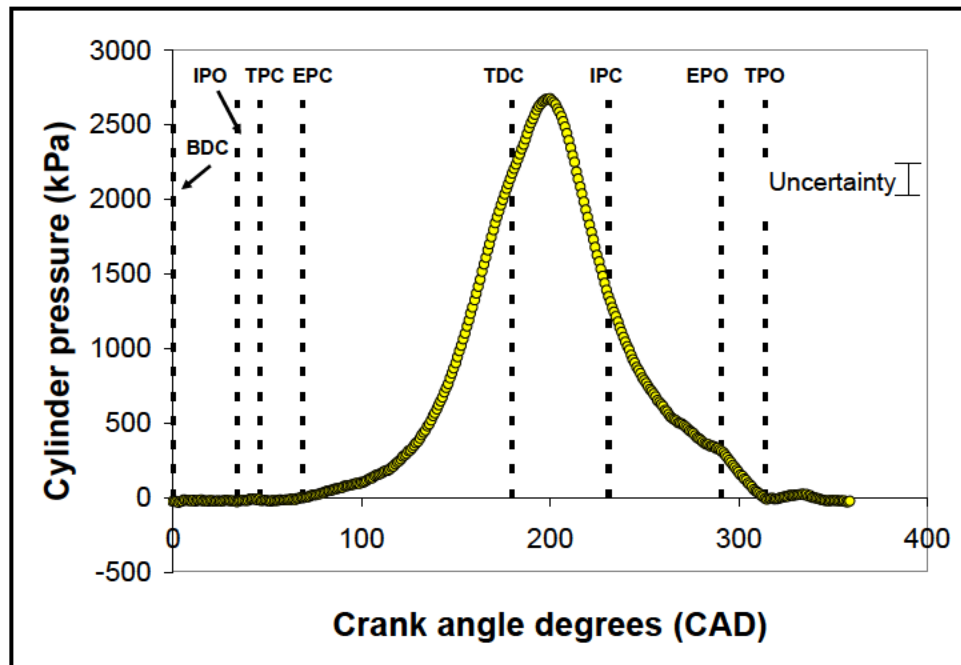


Figure E-1: Cylinder pressure plotted as a function of crank angle for a fired engine cycle for the OS 40 FX engine operating at a speed of 10000 rpm and an equivalence ratio of 0.95.

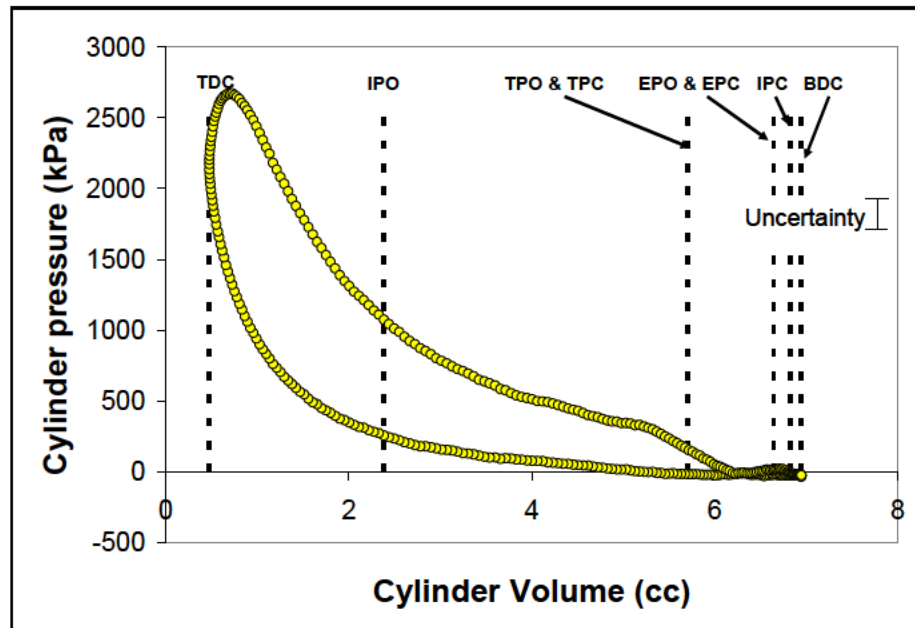


Figure E-2: Cylinder pressure plotted as a function of cylinder volume for a fired engine cycle for the OS 40 FX engine operating at a speed of 10000 rpm and an equivalence ratio of 0.95.

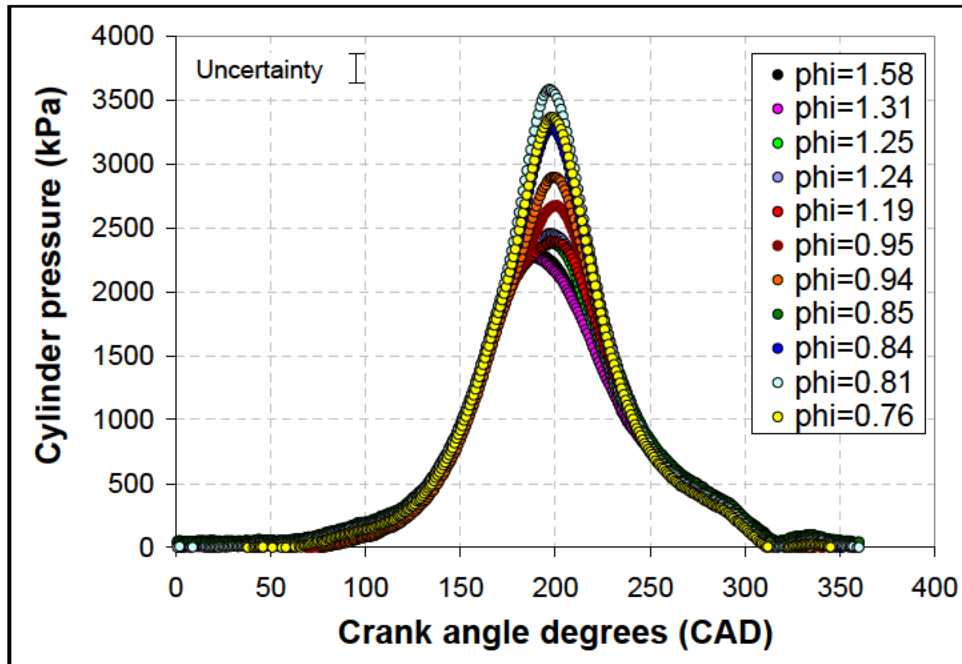


Figure E-3: Cylinder pressure averaged over 50 cycles plotted as a function of crank angle for the OS 40 FX engine operating at a speed of 10000 rpm and different equivalence ratios.

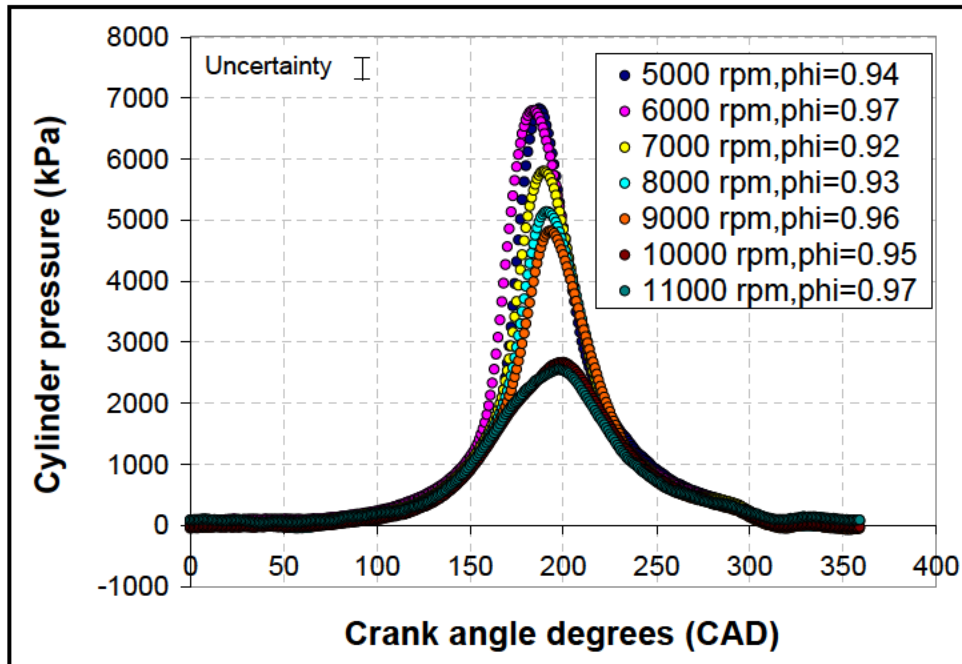


Figure E-4: Cylinder pressure averaged over 50 cycles plotted as a function of crank angle for the OS 40 FX engine operating at an equivalence ratio of ~ 0.95 and different engine speeds.

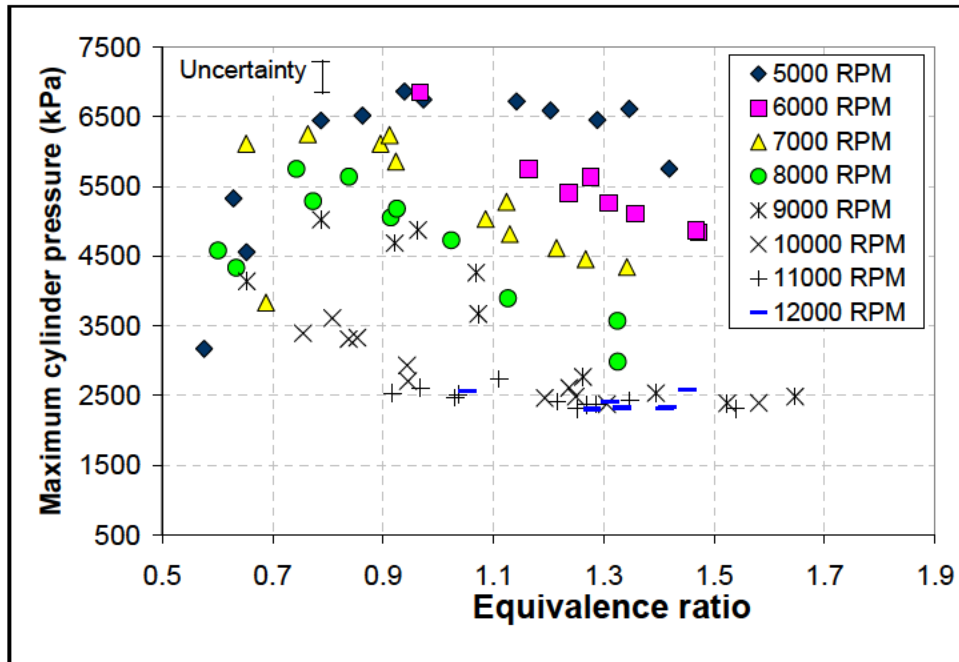


Figure E-5: Peak cylinder pressure averaged over 50 cycles plotted as a function of equivalence ratio for the OS 40 FX engine operating at different engine speeds.

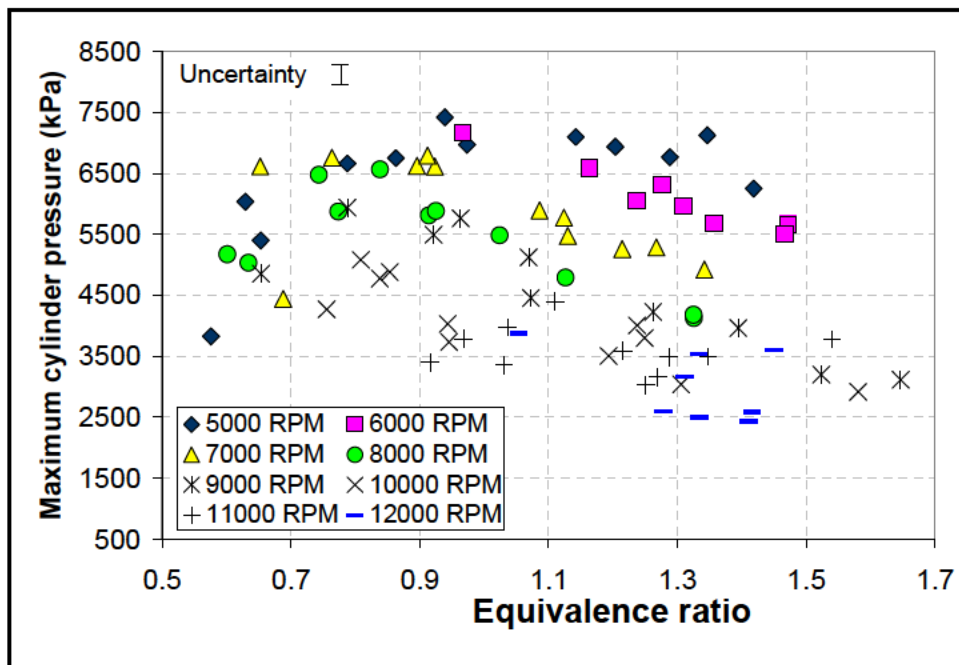


Figure E-6: Peak cylinder pressure over 50 cycles plotted as a function of equivalence ratio for the OS 40 FX engine operating at different engine speeds.

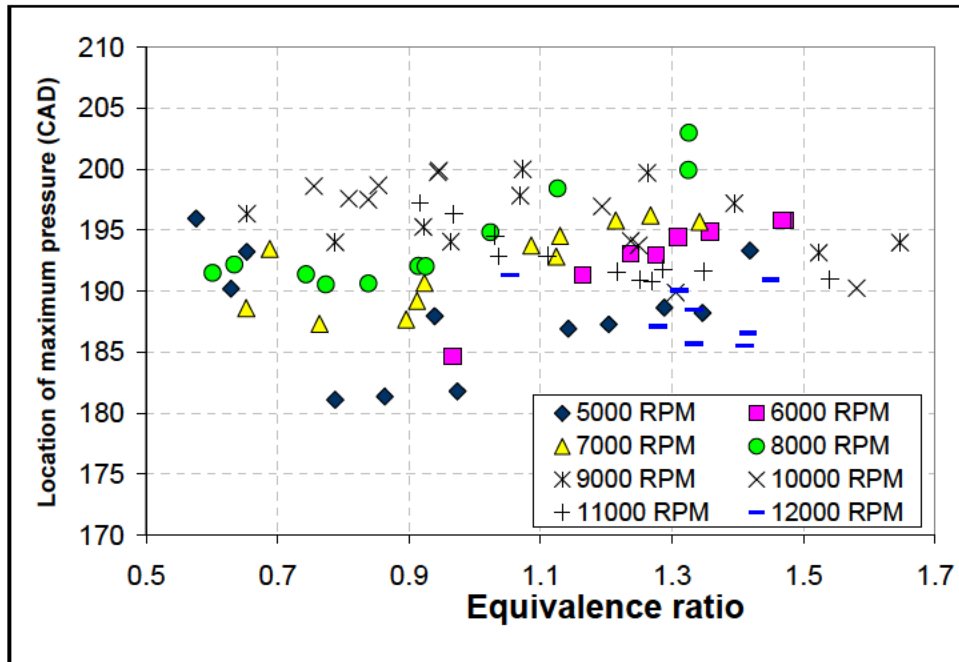


Figure E-7: Location of peak cylinder pressure averaged over 50 cycles plotted as a function of equivalence ratio for the OS 40 FX engine operating at different engine speeds.

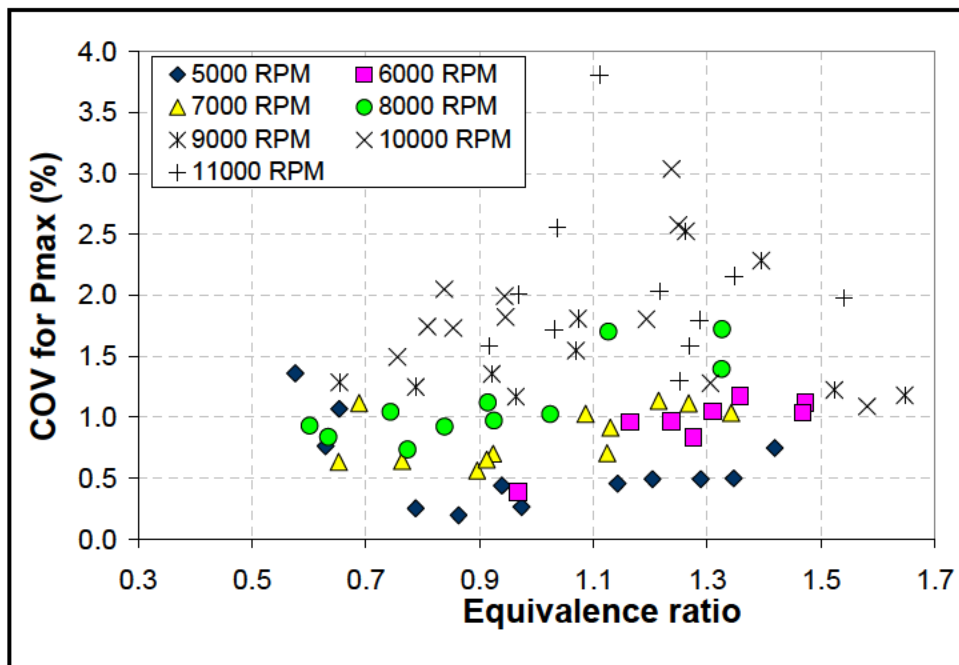


Figure E-8: Coefficient of variation for peak cylinder pressure plotted as a function of equivalence ratio for the OS 40 FX engine operating at different engine speeds.

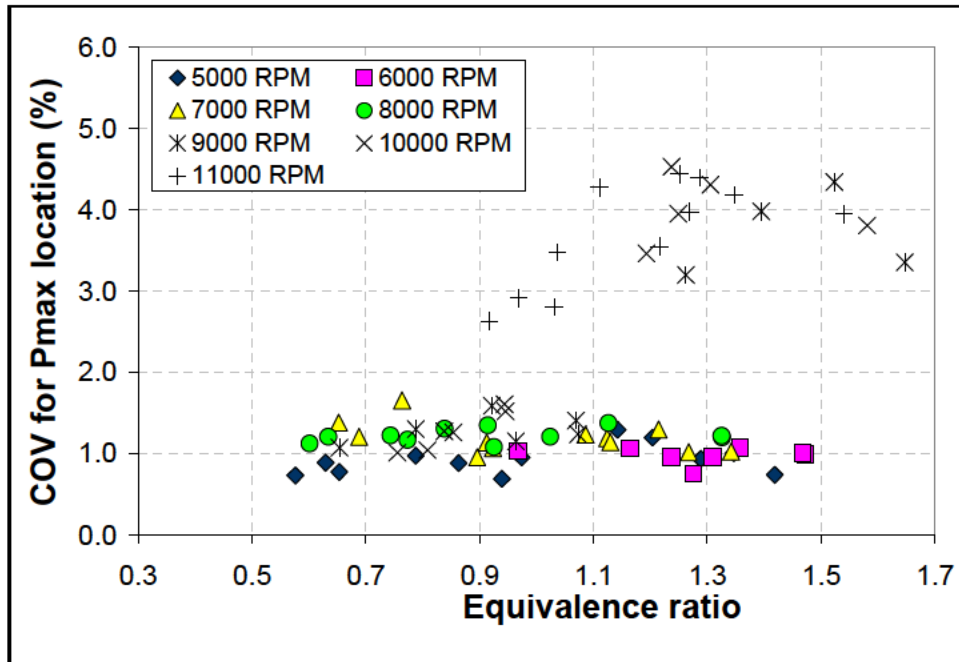


Figure E-9: Coefficient of variation for location of peak cylinder pressure plotted as a function of equivalence ratio for the OS 40 FX engine operating at different engine speeds.

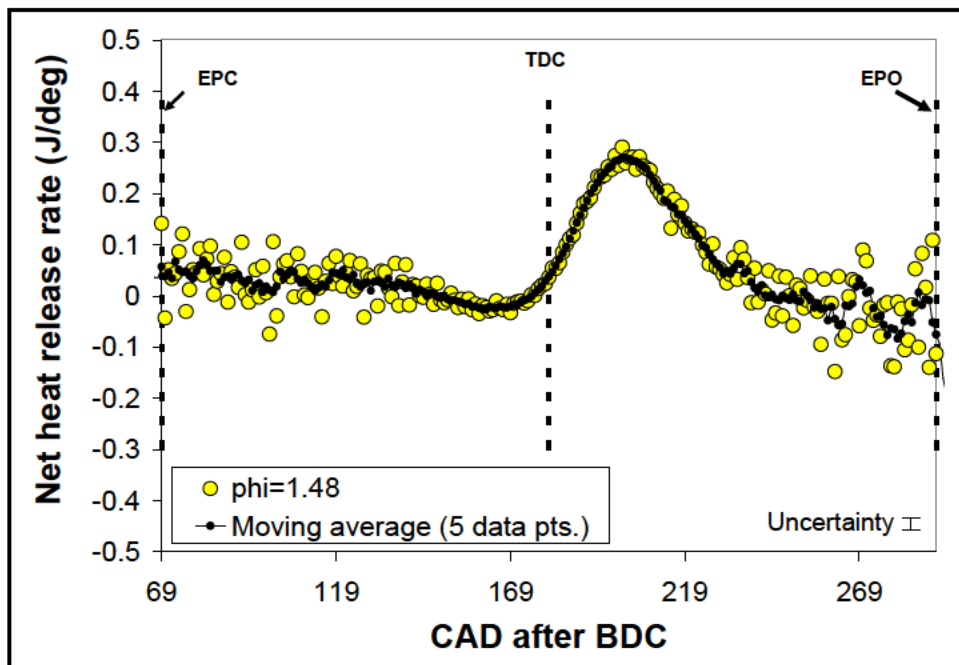


Figure E-10: Net heat release rate and a moving average estimated for the same over 5 data points plotted a function of crank angle for the OS 40 FX engine operating 10000 rpm and an equivalence ratio of 1.48.

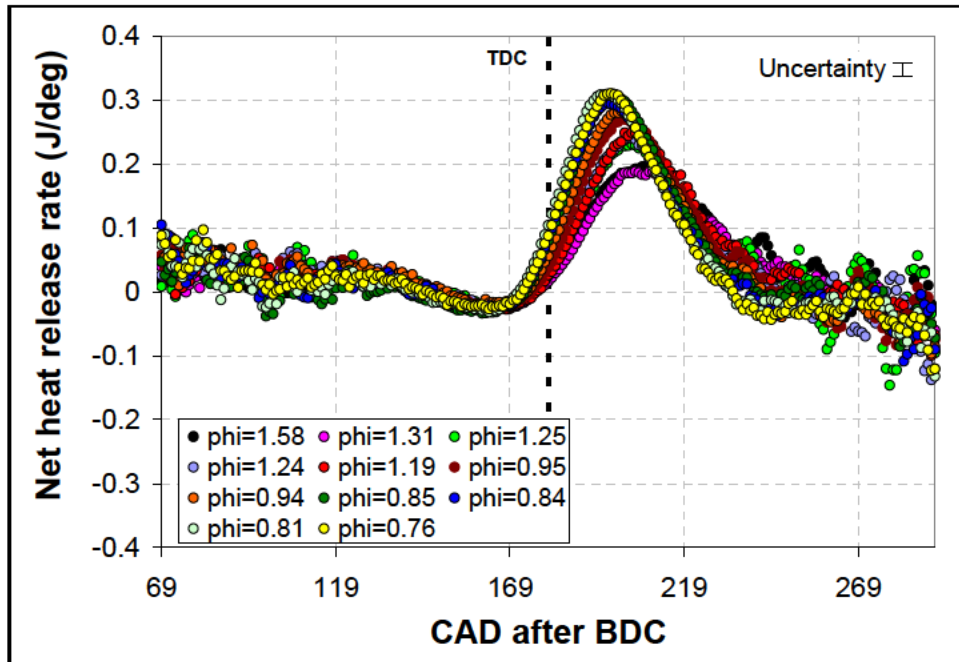


Figure E-11: Five point moving point average of the net heat release rate estimated for the OS 40 FX engine plotted as a function of crank angle for the engine operating at 10000 rpm and different equivalence ratios.

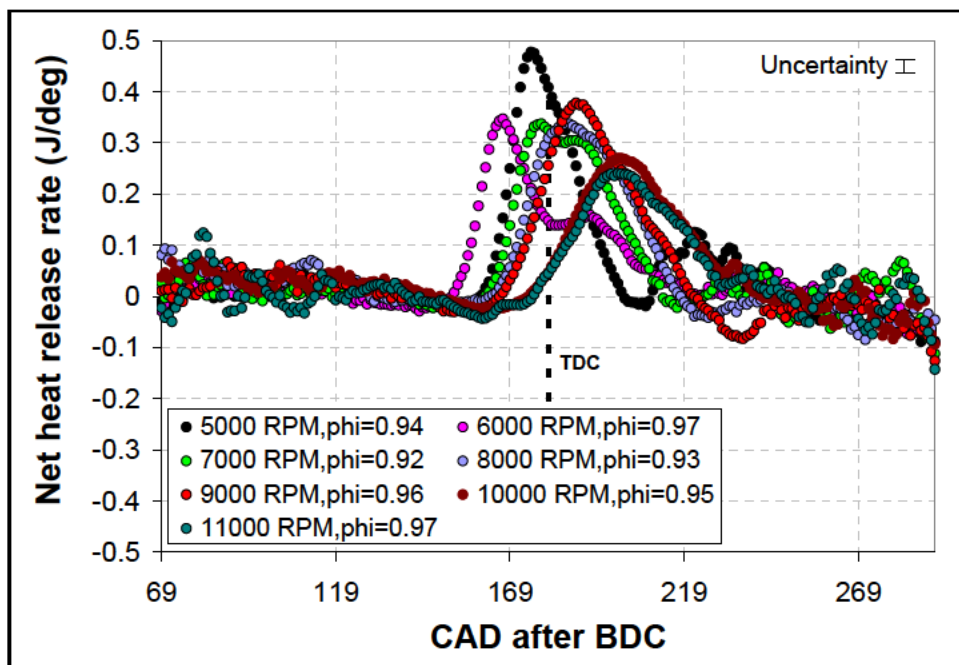


Figure E-12: Five point moving point average of the net heat release rate estimated for the OS 40 FX engine plotted as a function of crank angle for the engine operating at different speeds and an equivalence ratio of ~ 0.95 .

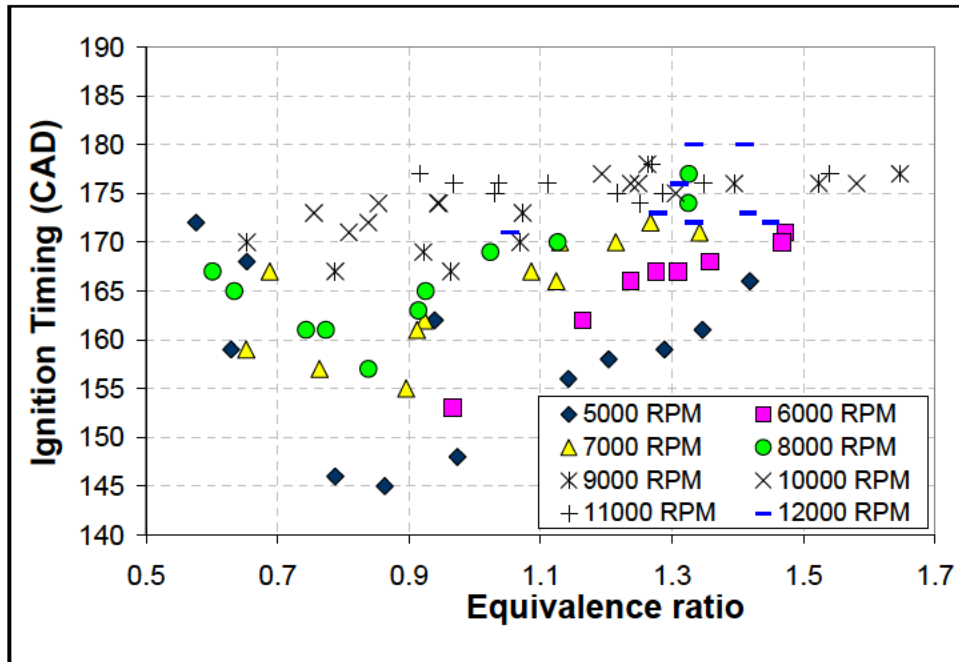


Figure E-13: Ignition timing location averaged over 50 cycles plotted as a function of equivalence ratio for the OS 40 FX engine operating at different engine speeds.

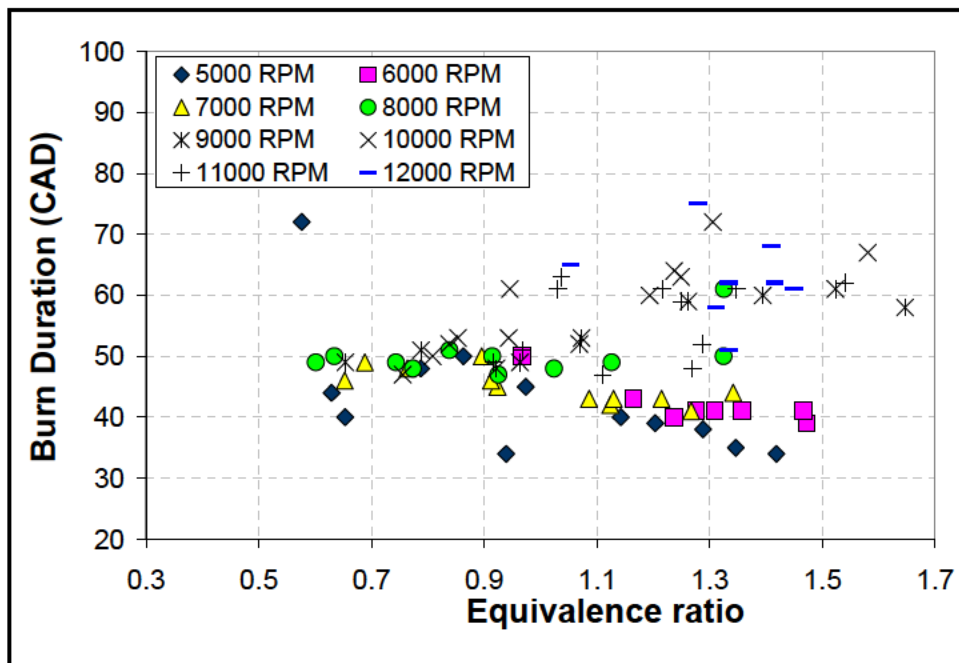


Figure E-14: Burn duration in crank angle degrees averaged over 50 cycles and plotted as a function of equivalence ratio for the OS 40 FX engine operating at different engine speeds.

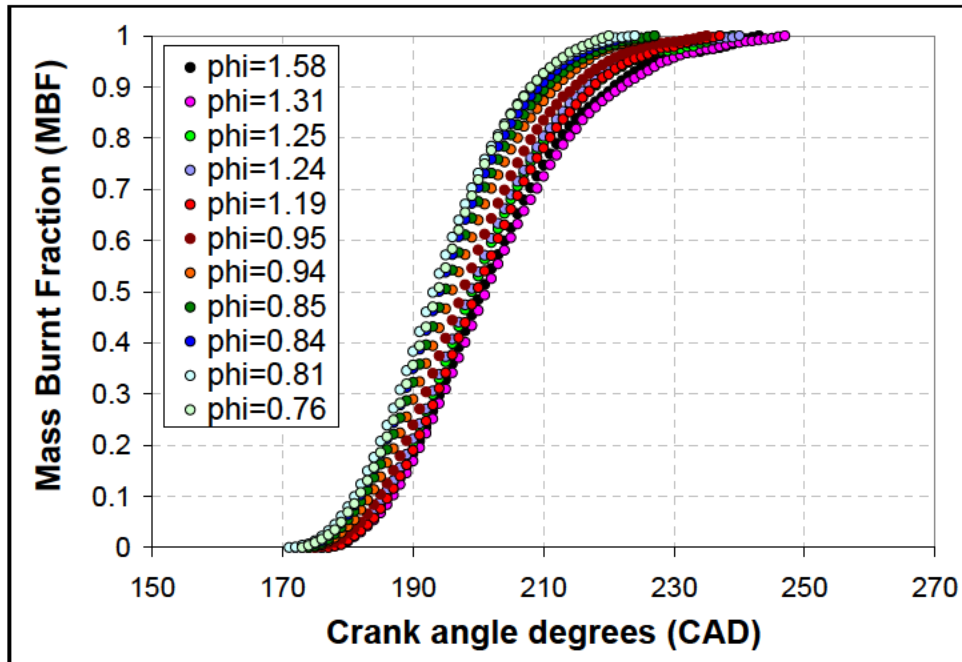


Figure E-15: Mass burnt fraction profiles averaged over 50 engine cycles plotted as a function of crank angle for the OS 40 FX engine operating at 10000 rpm and different equivalence ratios.

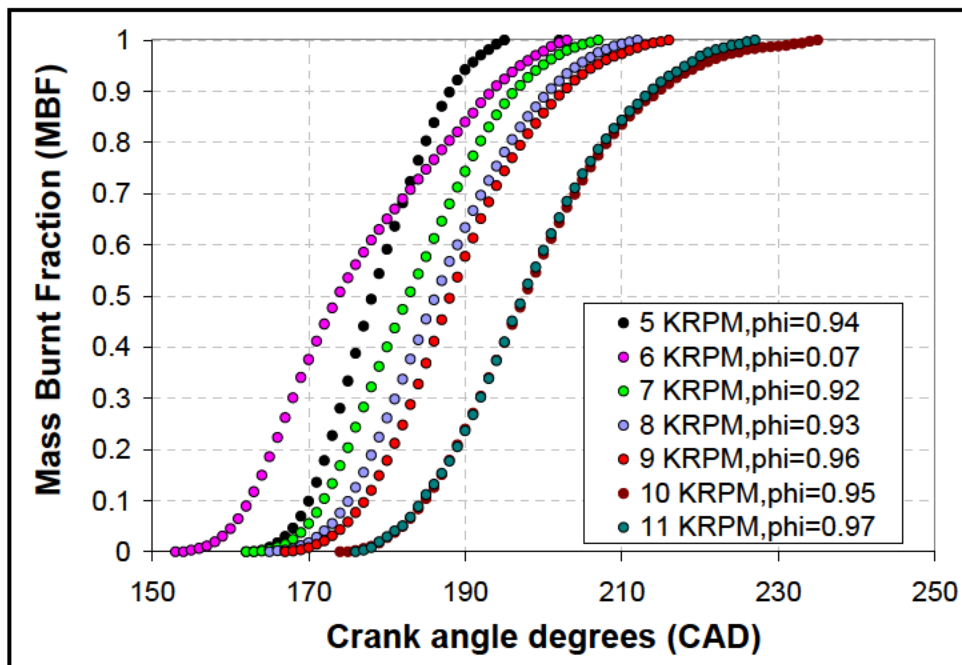


Figure E-16: Mass burnt fraction profiles averaged over 50 engine cycles plotted as a function of crank angle for the OS 40 FX engine operating at different speeds and an equivalence ratio of ~ 0.95 .

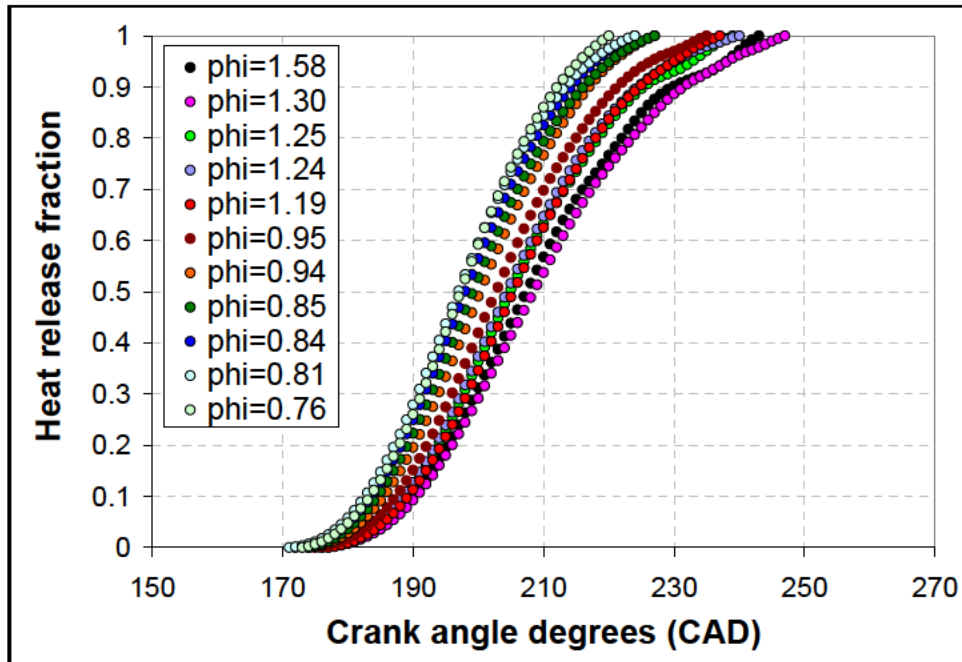


Figure E-17: Heat release fraction averaged over 50 engine cycles plotted as a function of crank angle for the OS 40 FX engine operating at 10000 rpm and different equivalence ratios.

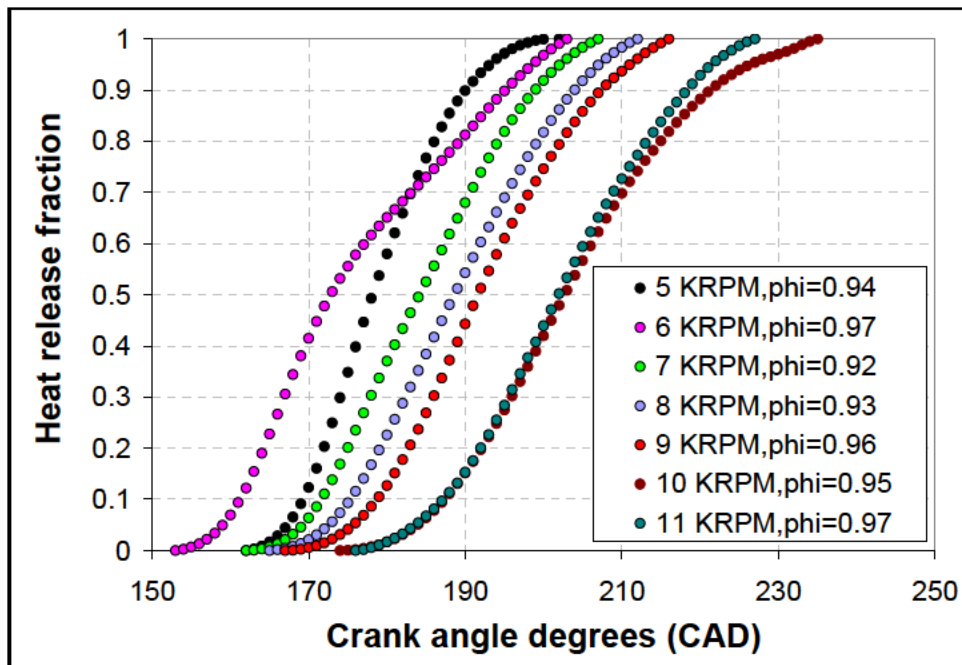


Figure E-18: Heat release fraction averaged over 50 engine cycles plotted as a function of crank angle for the OS 40 FX engine operating at different speeds and an equivalence ratio of ~ 0.95 .

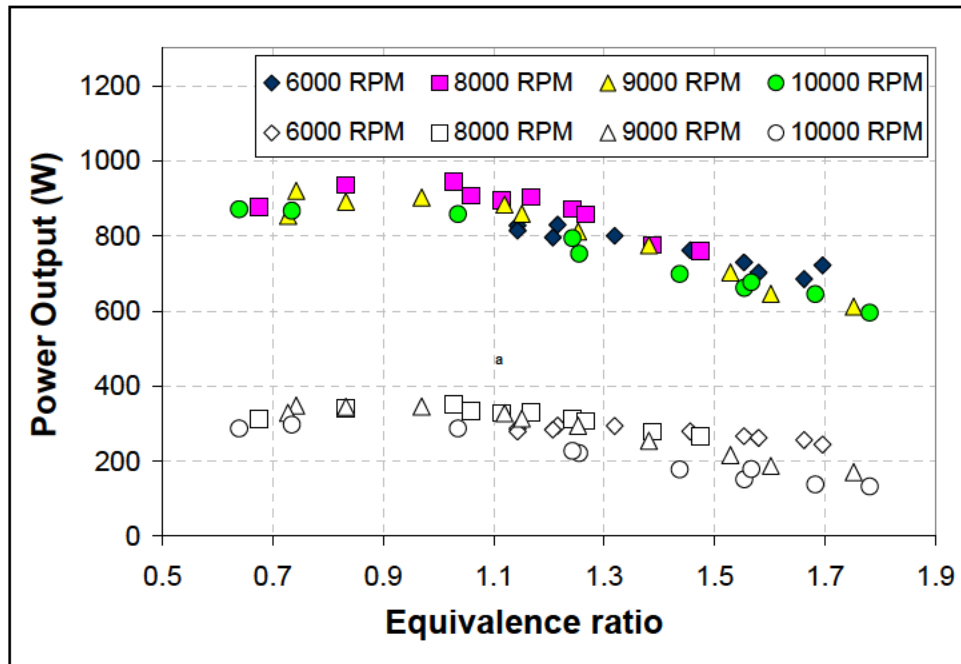


Figure E-19: Indicated and brake power output plotted as a function of equivalence ratio for the OS 40 FX engine operating at different speeds.

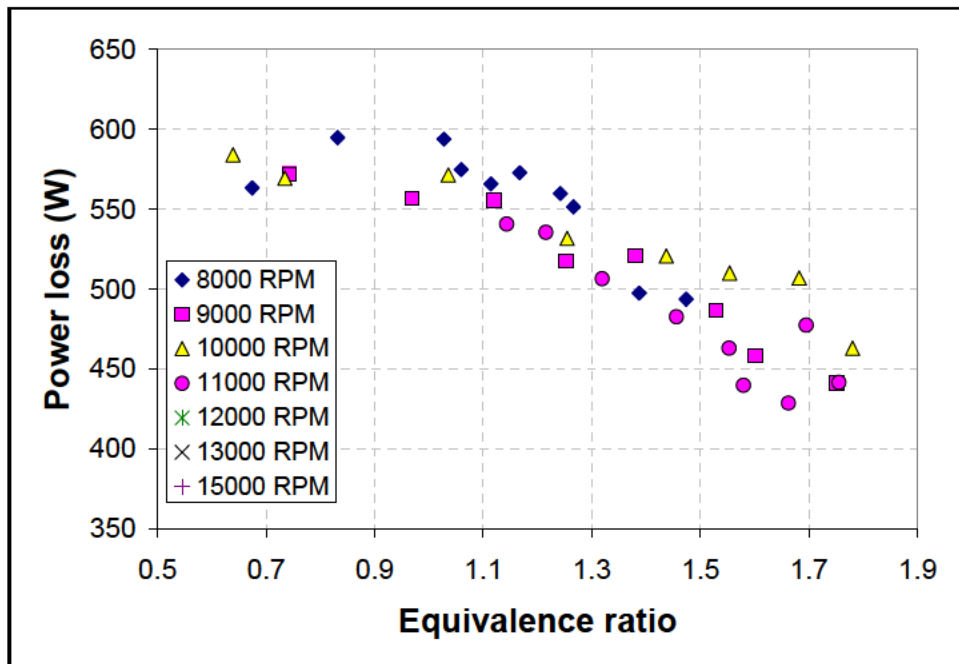


Figure E-20: Power loss plotted as a function of equivalence ratio for the OS 40 FX engine operating at different speeds.

E.2 Cylinder pressure measurements for the OS 46 FX Engine

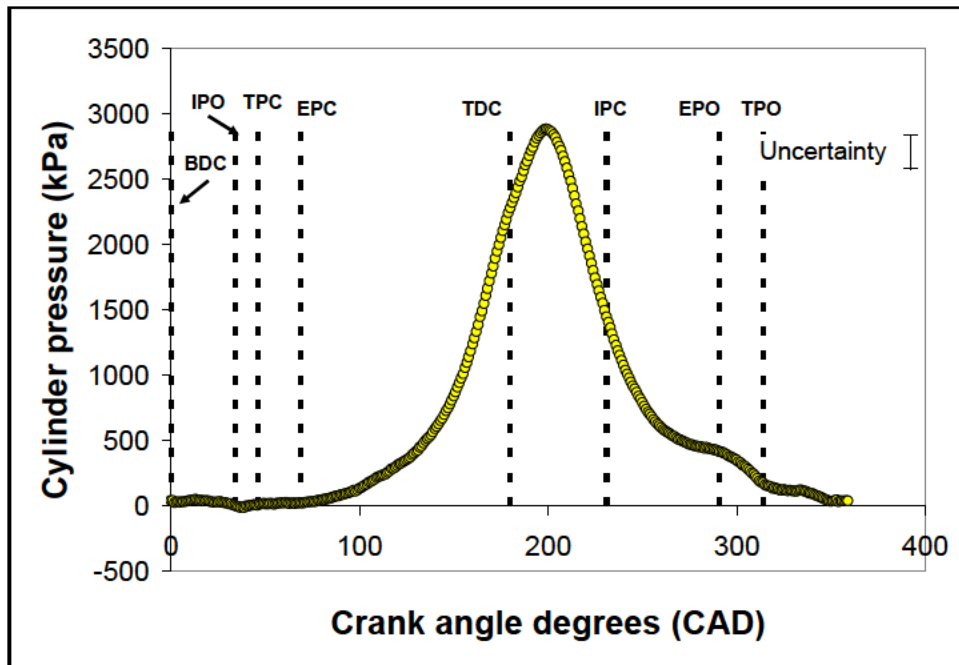


Figure E-21: Cylinder pressure plotted as a function of crank angle for a fired engine cycle for the OS 46 FX engine operating at a speed of 10000 rpm and an equivalence ratio of 1.03.

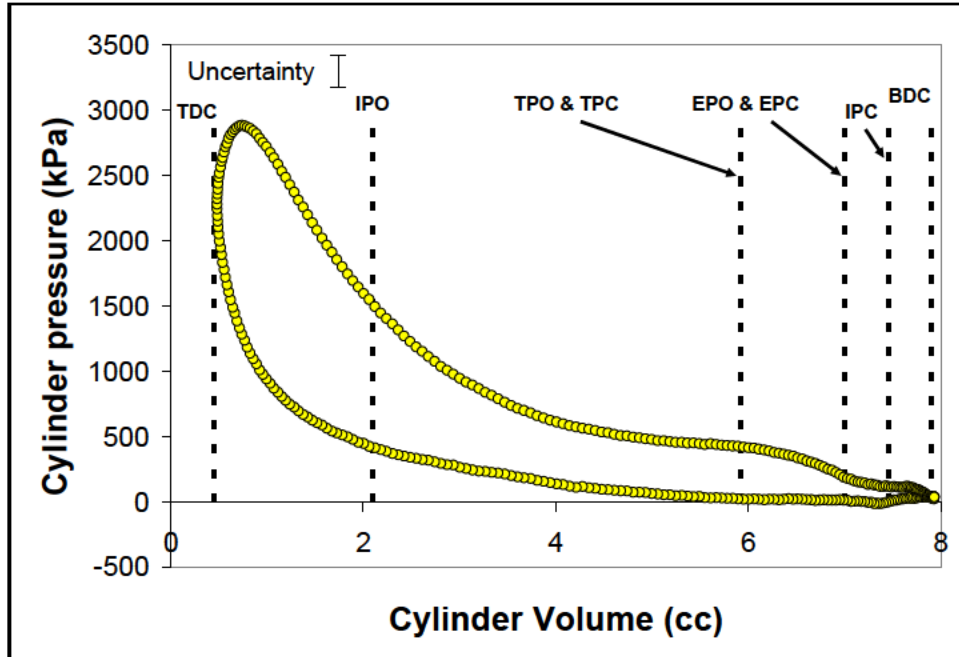


Figure E-22: Cylinder pressure plotted as a function of cylinder volume for a fired engine cycle for the OS 46 FX engine operating at a speed of 10000 rpm and an equivalence ratio of 1.03.

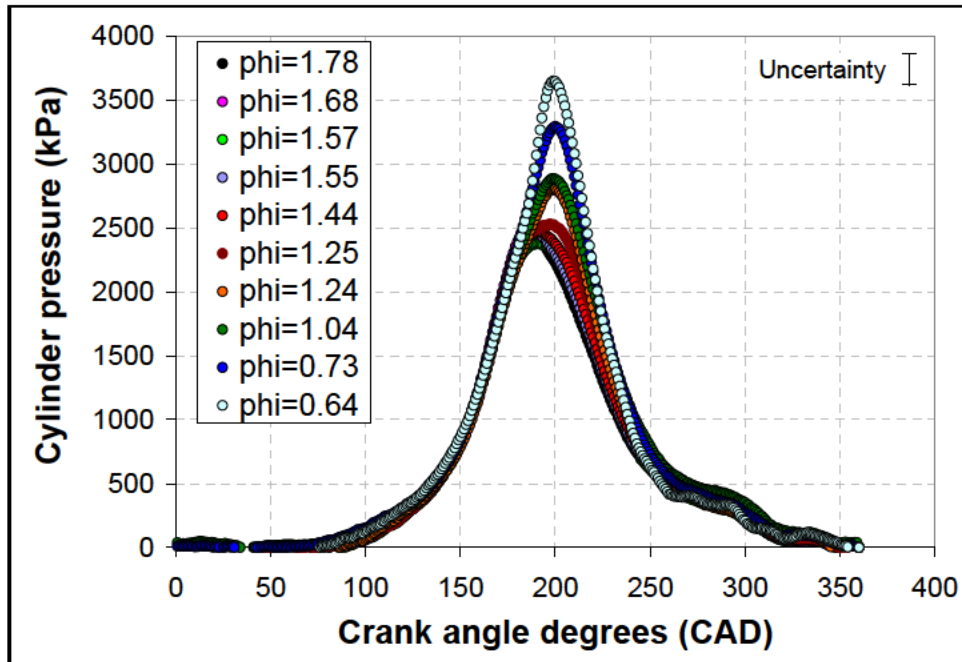


Figure E-23: Cylinder pressure averaged over 50 cycles plotted as a function of crank angle for the OS 46 FX engine operating at a speed of 10000 rpm and different equivalence ratios.

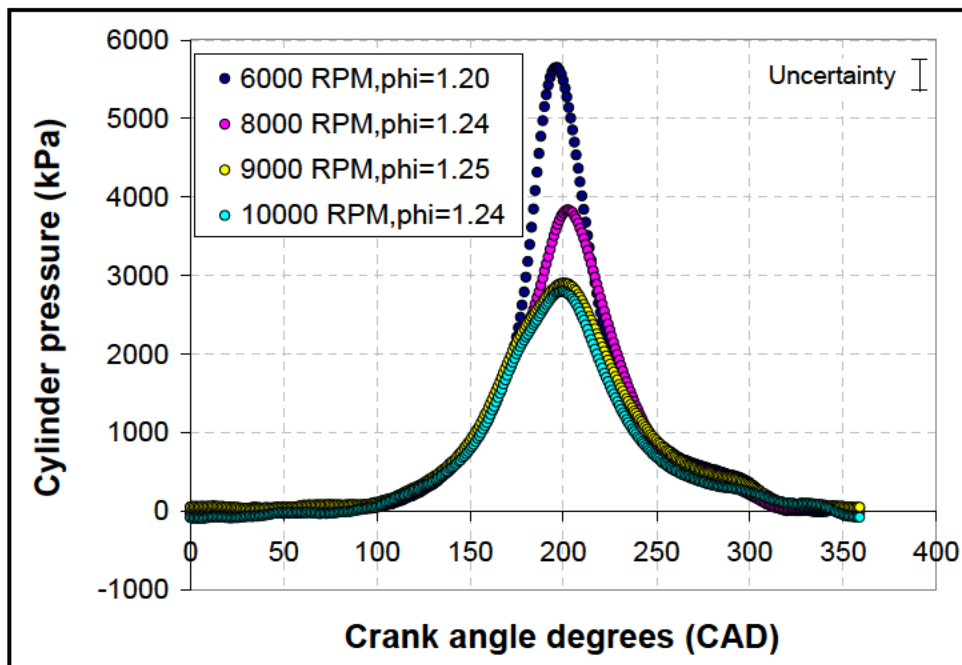


Figure E-24: Cylinder pressure averaged over 50 cycles plotted as a function of crank angle for the OS 46 FX engine operating at an equivalence ratio of ~ 1.2 and different engine speeds.

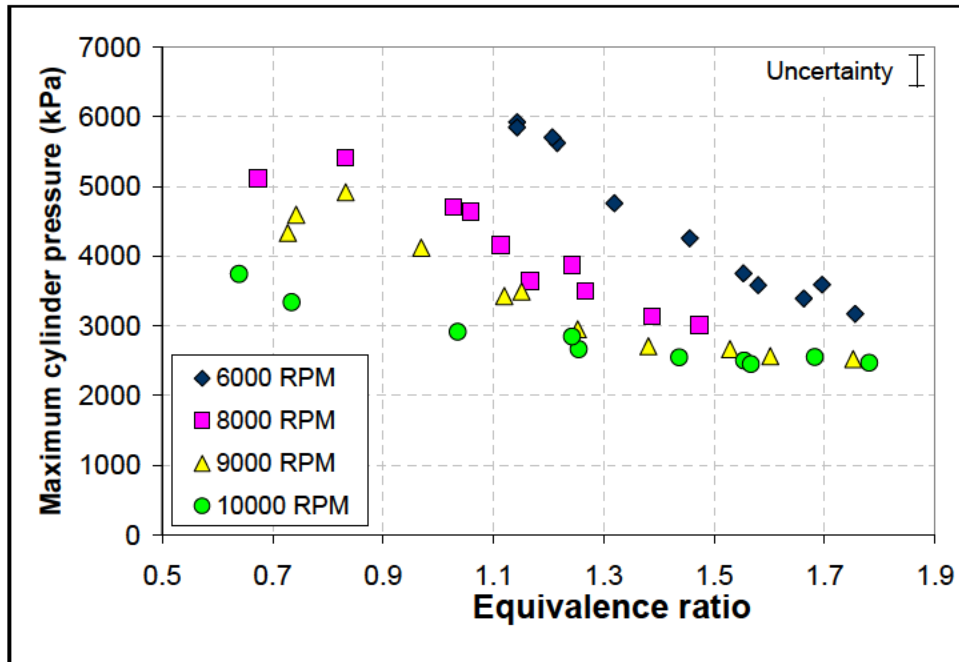


Figure E-25: Peak cylinder pressure averaged over 50 cycles plotted as a function of equivalence ratio for the OS 46 FX engine operating at different engine speeds.

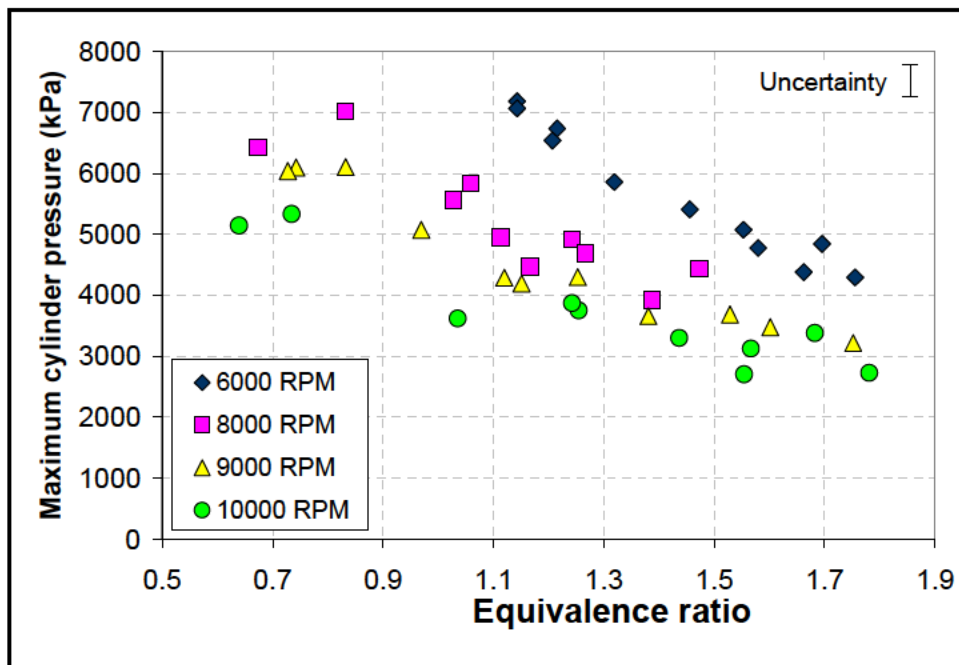


Figure E-26: Peak cylinder pressure over 50 cycles plotted as a function of equivalence ratio for the OS 46 FX engine operating at different engine speeds.

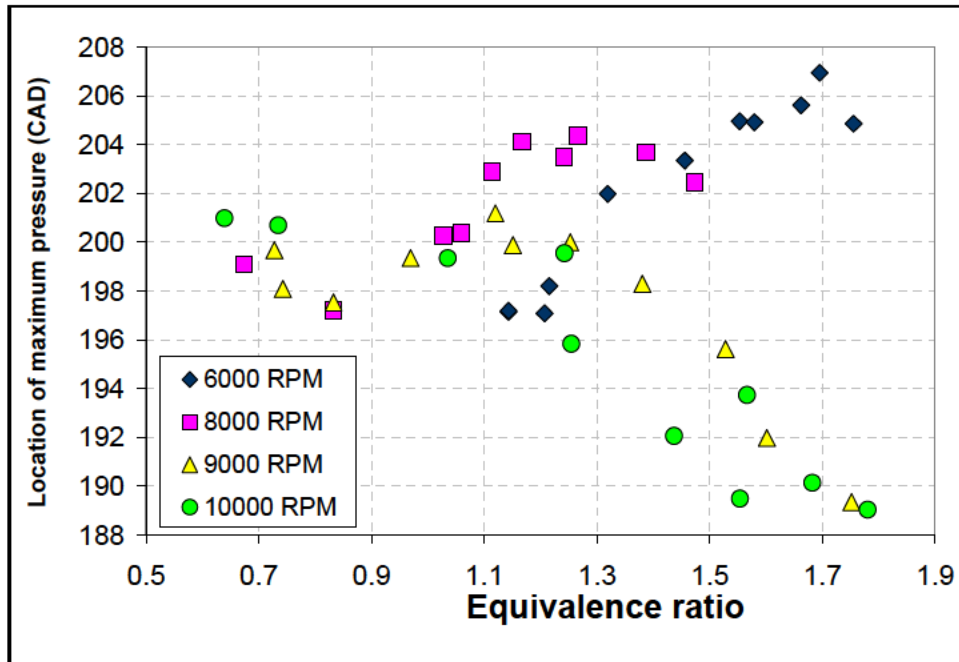


Figure E-27: Location of peak cylinder pressure averaged over 50 cycles plotted as a function of equivalence ratio for the OS 46 FX engine operating at different engine speeds.

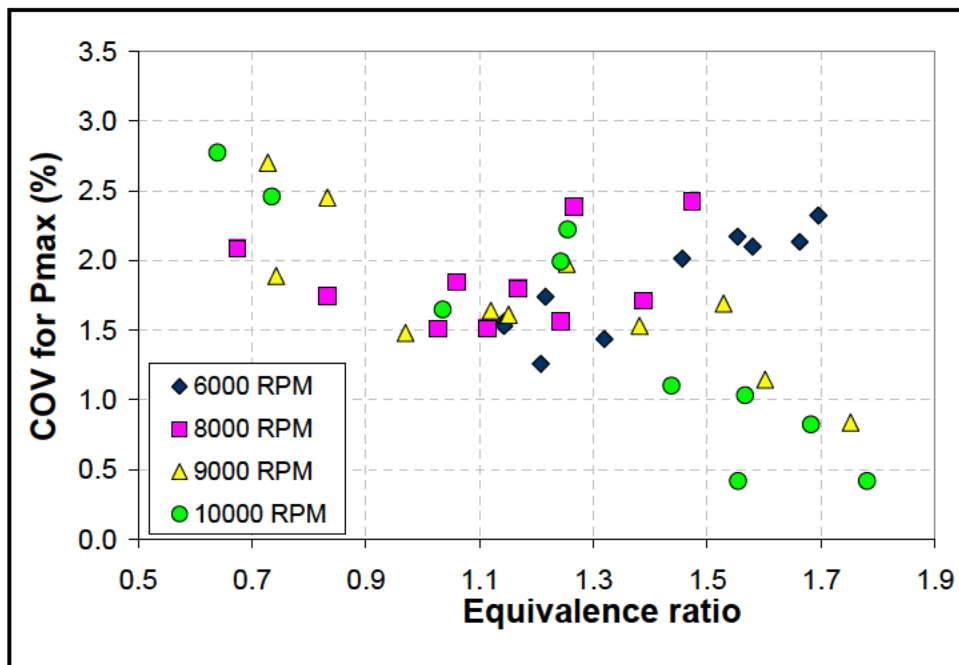


Figure E-28: Coefficient of variation of peak cylinder pressure plotted as a function of equivalence ratio for the OS 46 FX engine operating at different engine speeds.

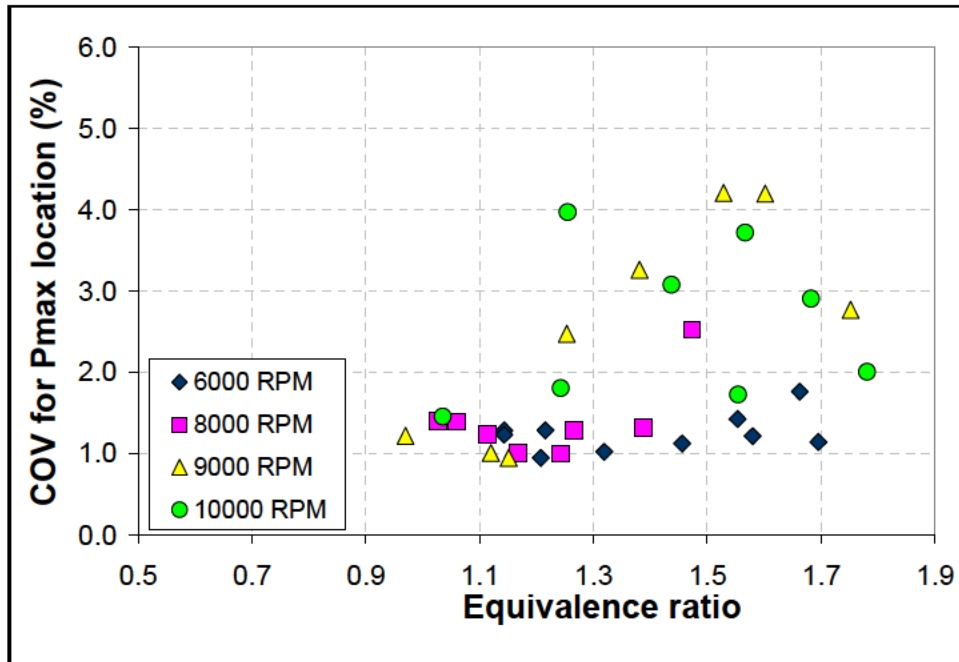


Figure E-29: Coefficient of variation of location of peak cylinder pressure plotted as a function of equivalence ratio for the OS 46 FX engine operating at different engine speeds.

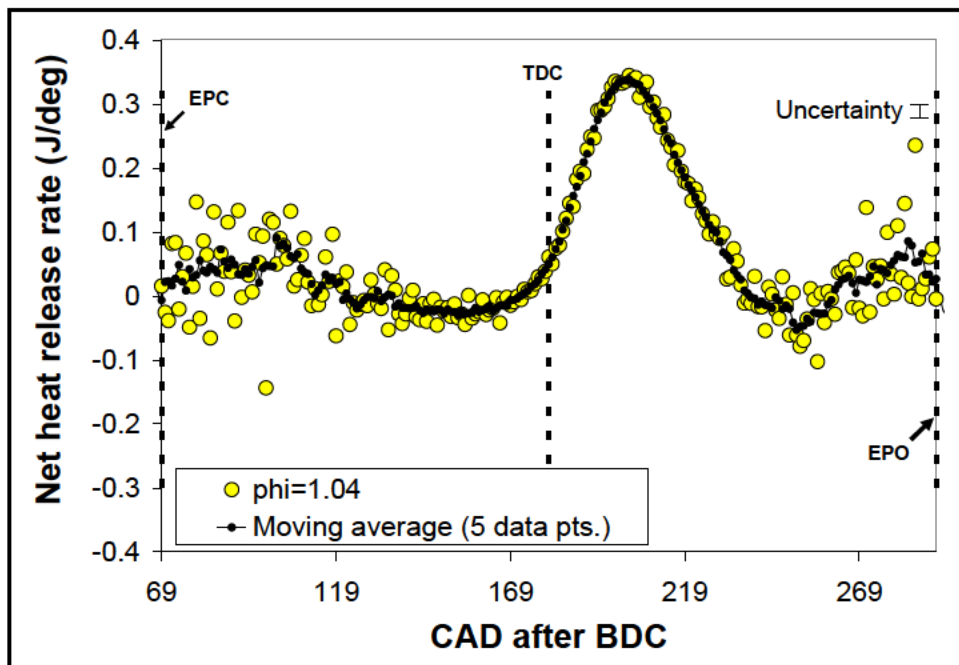


Figure E-30: Net heat release rate and a moving average estimated for the same over 5 data points plotted a function of crank angle for the OS 46 FX engine operating 10000 rpm and an equivalence ratio of 1.04.

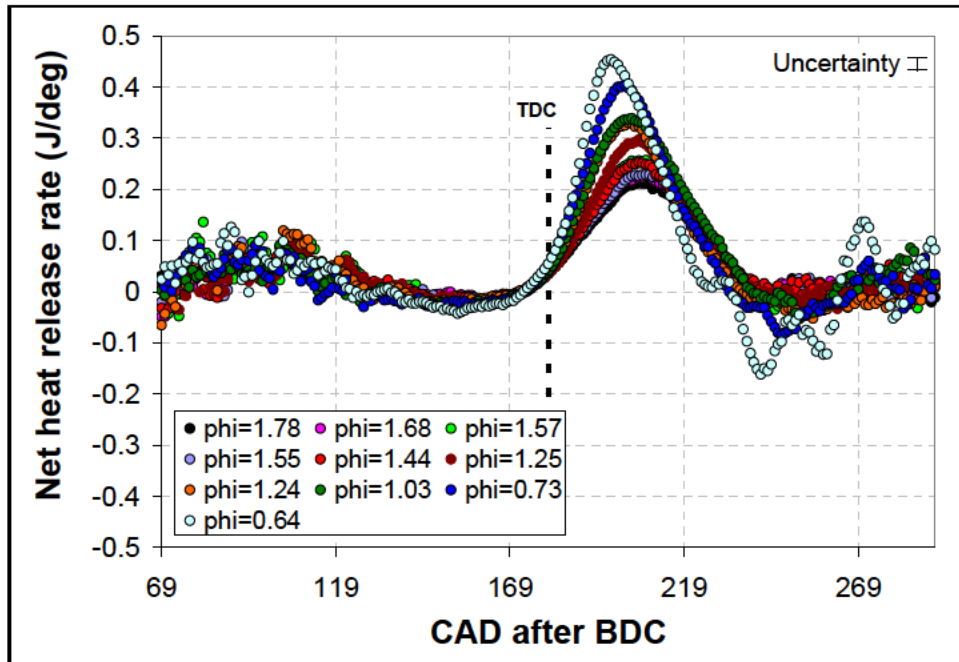


Figure E-31: Five point moving point average of the net heat release rate estimated for the OS 46 FX engine plotted as a function of crank angle for the engine operating at 10000 rpm and different equivalence ratios.

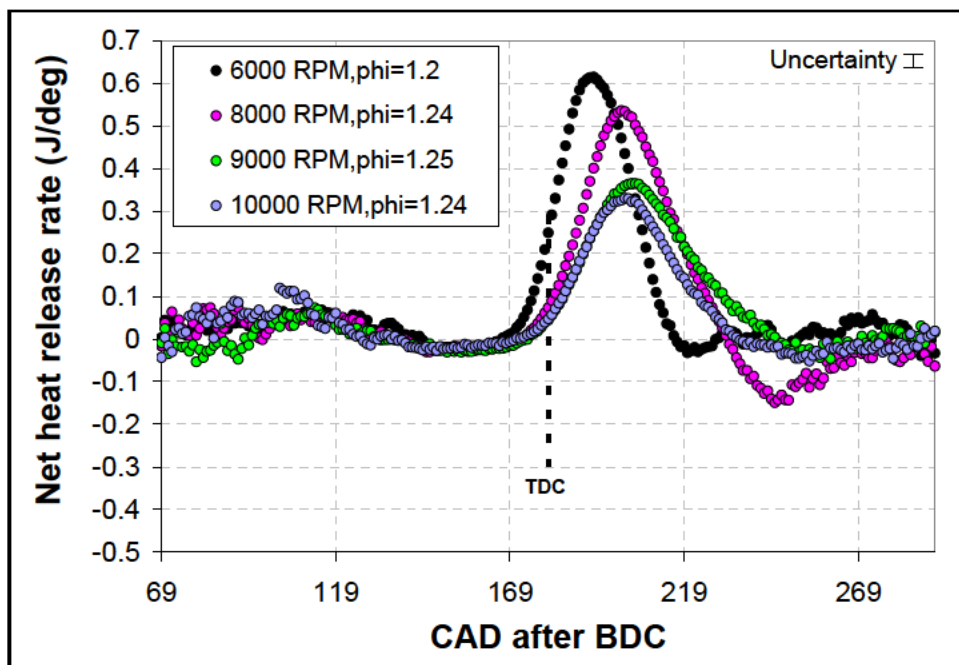


Figure E-32: Five point moving point average of the net heat release rate estimated for the OS 46 FX engine plotted as a function of crank angle for the engine operating at different speeds and an equivalence ratio of ~ 1.2 .

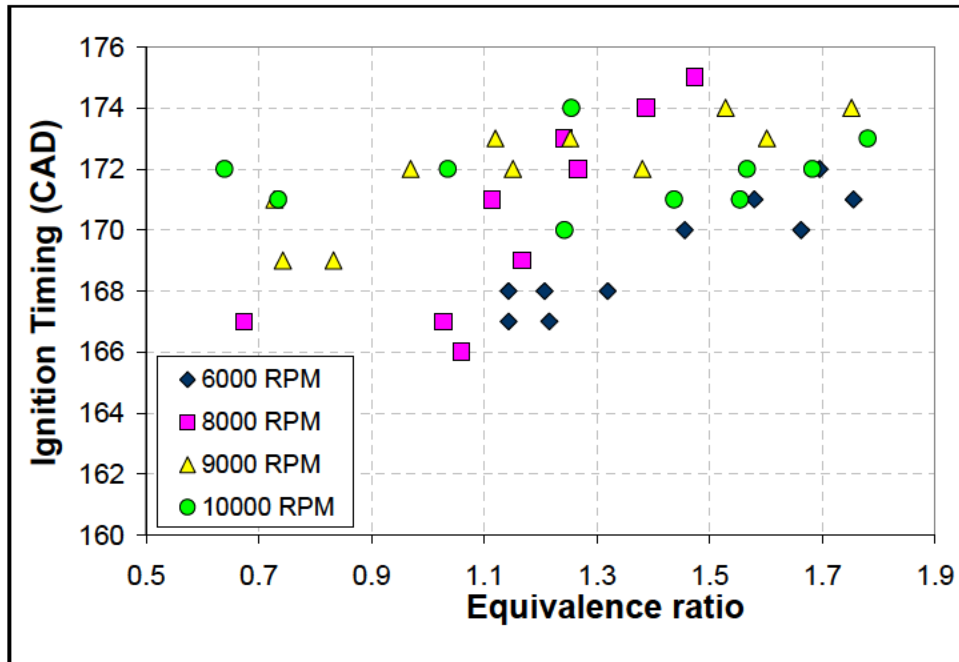


Figure E-33: Ignition timing location averaged over 50 cycles plotted as a function of equivalence ratio for the OS 46 FX engine operating at different engine speeds.

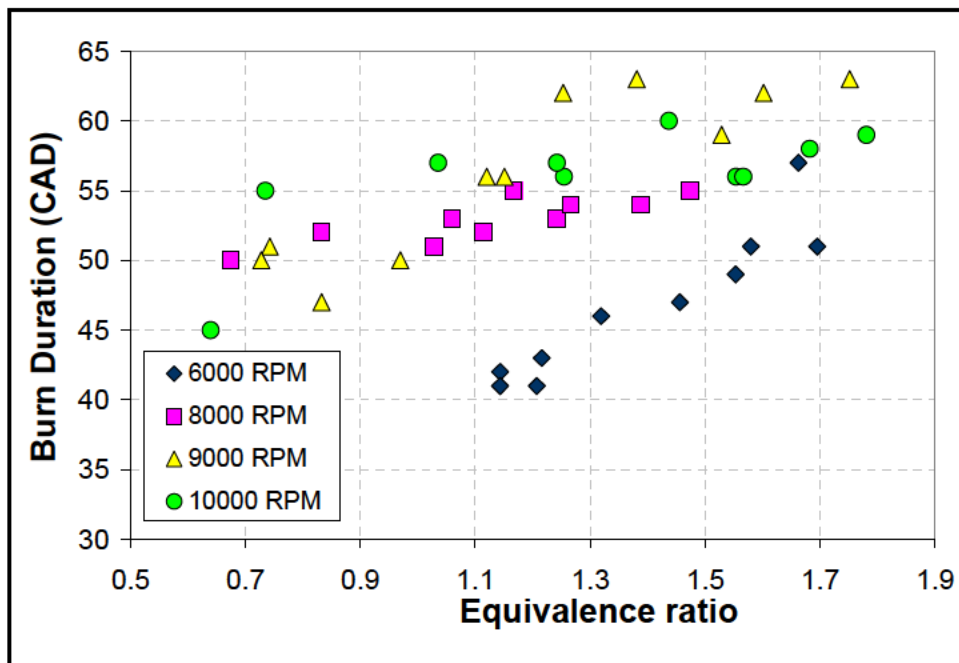


Figure E-34: Burn duration in crank angle degrees averaged over 50 cycles and plotted as a function of equivalence ratio for the OS 46 FX engine operating at different engine speeds.

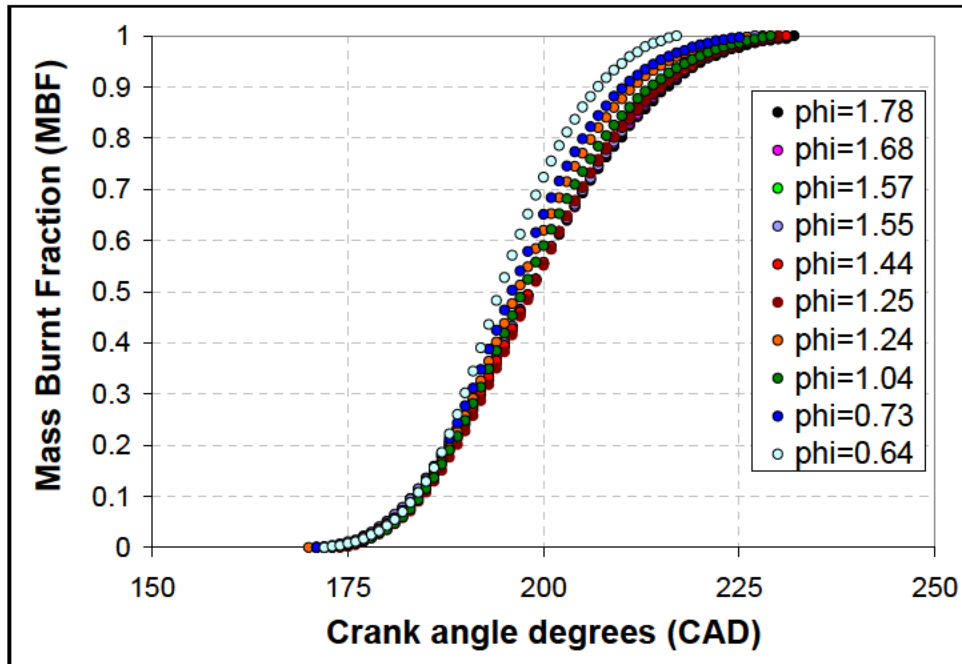


Figure E-35: Mass burnt fraction profiles averaged over 50 engine cycles plotted as a function of crank angle for the OS 46 FX engine operating at 10000 rpm and different equivalence ratios.

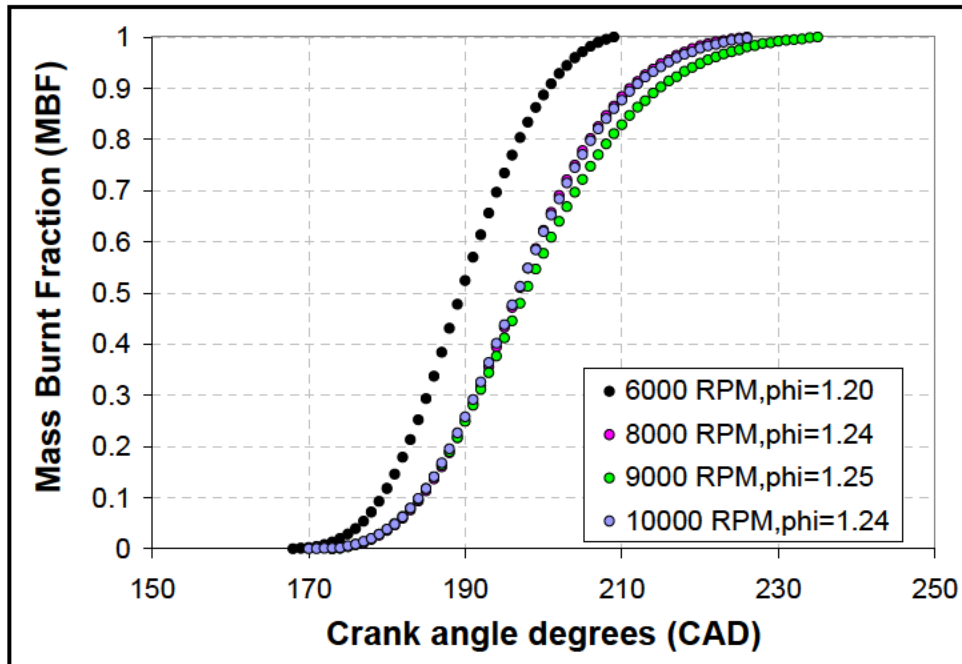


Figure E-36: Mass burnt fraction profiles averaged over 50 engine cycles plotted as a function of crank angle for the OS 46 FX engine operating at different speeds and an equivalence ratio of ~ 1.2.

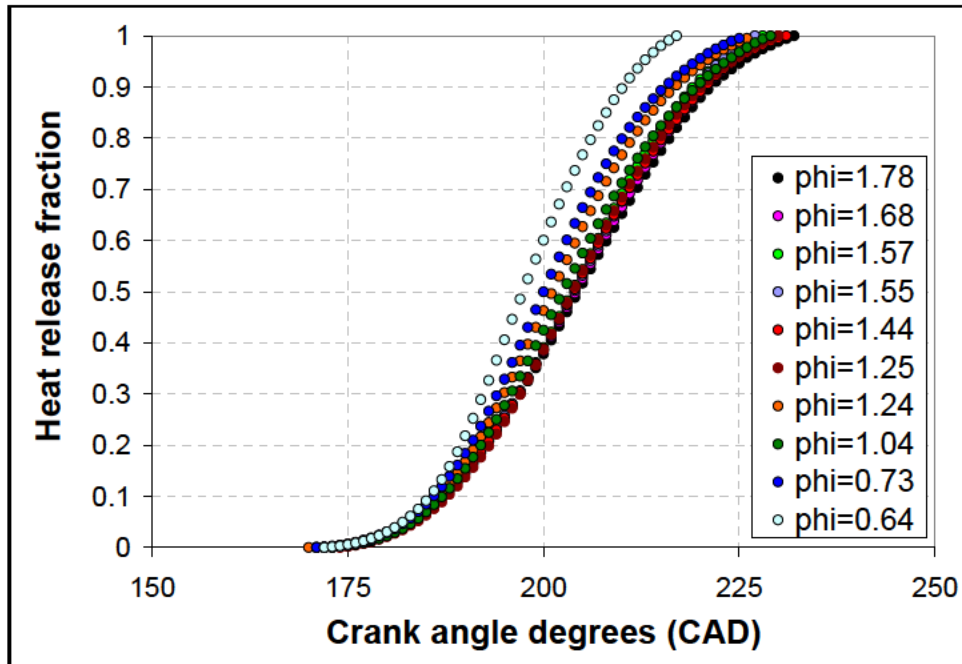


Figure E-37: Heat release fraction averaged over 50 engine cycles plotted as a function of crank angle for the OS 46 FX engine operating at 10000 rpm and different equivalence ratios.

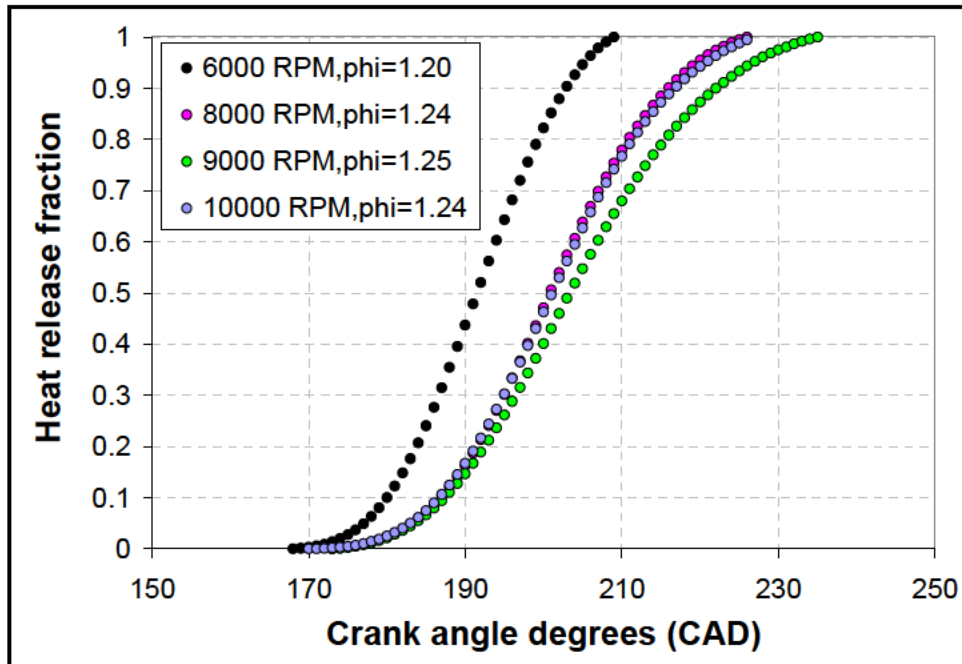


Figure E-38: Heat release fraction averaged over 50 engine cycles plotted as a function of crank angle for the OS 46 FX engine operating at different speeds and an equivalence ratio of ~ 1.2 .

Appendix F

F.1 Estimation of mass burning fraction from gross heat release rate

For a premixed charge in an engine, the mass of fuel trapped in the cylinder volume prior to ignition can be estimated as,

$$m_f = m(1 - x_r) / [(A/F) + 1] \quad (\text{F-1})$$

where x_r is the mass fraction of residual gases and A/F is the air/fuel ratio. It is assumed that the A/F ratio of the trapped and delivered unburnt mixture is the same.

We now have,

$$\frac{\delta Q_{ch}}{dt} = Q_{HV} \frac{dm_{f,b}}{dt} = Q_{HV} \frac{m_f}{m} \frac{dm_b}{dt} \quad (\text{F-2})$$

where Q_{HV} is the heating value of the fuel, $m_{f,b}$ is the mass fraction of fuel burnt at the end of time interval dt and m_b mass fraction of fuel burnt at the end of the combustion process. The mass burnt fraction can now be estimated using equations F-1 and F-2 as,

$$\frac{dx_b}{dt} = \frac{1}{m} \frac{dm_b}{dt} = \frac{[(A/F) + 1]}{m(1 - x_r) Q_{HV}} \frac{\delta Q_{ch}}{dt} \quad (\text{F-3})$$

This method further assumes that there is negligible amount of dissociation in the burnt gases. The same technique cannot be applied to net heat release rate as it has heat transfer and mass transfer losses folded into the expression.

Estimation of conversion efficiency using mass burnt fraction

When Eqn. F-3 is utilized with the gross heat release rate as described in Section 5.2.8.5 of Chapter 5, it is possible to estimate the conversion efficiency of the

fuel which is defined as the amount of fuel actually burnt compared to that present in the fuel–air mixture.²⁴⁶ Using the heating value of the fuel and the definition of mass burnt fraction we have,

$$x_b = \frac{m_b}{m_{f,b}} = \frac{m_b Q_{HV}}{m_{f,b} Q_{HV}} = \frac{q_b}{q_{f,b}} = q_f \quad (\text{F-4})$$

Using equations F-3 and F-4 we have,

$$q_f = \frac{q_b}{q_{f,b}} = 1 - \exp \left\{ -a \left[\frac{(\theta - \theta_{ign})}{\Delta \theta_b} \right]^{m+1} \right\} \quad (\text{F-5})$$

The conversion efficiency can be defined at the end of the combustion process and can be obtained by integrating Eqn. F-5 over the combustion duration. This gives the combustion efficiency as,

$$\eta_{conv} = \frac{q_b}{q_{f,b}} = 1 - \exp(-a) \quad (\text{F-6})$$

The parameter a can be expressed as,

$$a = -\ln(1 - \eta_{conv}) \quad (\text{F-7})$$

Appendix G

G.1 Measurement Error

The difference between the ‘true’ value and the measured value is defined as measurement error. It is composed of two components: systematic error and random error.

G.1.1 Random Error

Random error is defined as the component of the measurement that changes in magnitude every time a constant attribute or quantity is measured. In the test setup here, vibration in the cradle and electrical noise in signals from different sensors form the major contributors to random error. Random error can be reduced by averaging and are estimated based on statistical variations in the measurement data set. The standard deviation ($S_{\bar{x}}$) is a measure of the scatter about the true mean (\bar{x}) caused by random error. The standard deviation of a data sample, S_x is given by:

$$S_{\bar{x}} = \frac{1}{\sqrt{M}} \sqrt{\sum_{k=1}^M \frac{(x_k - \bar{x})^2}{M-1}} \quad (G-1)$$

where M is the number of measurements made and \bar{x} is the mean of the individual measurements x_k given by:

$$\bar{X} = \frac{1}{M} \sum_{k=1}^M X_k \quad (G-2)$$

G.1.2 Systematic Error

Systematic uncertainty is defined as the component of measurement error which stays constant during repeated measurements of an attribute or quantity. The linearity and repeatability limits of different sensors used in the test setup and the

offset in signal output by the data acquisition system form the major contributors to systematic error. The systematic uncertainty in a measurement can be calculated by taking the root-mean-square sum of the contributions $b_1, b_2, \dots b_m$ from various aspects of the measurement:

$$B = \sqrt{(b_1)^2 + (b_2)^2 + \dots + (b_M)^2} \quad (\text{G-3})$$

G.1.3 Total Uncertainty

The total uncertainty is the sum of the uncertainties due to systematic and random errors. The true value of the measurement (X_t) is defined to lie in an interval with a certain level of confidence. This interval is given by:

$$X_t = \bar{X} \pm U \quad (\text{G-4})$$

where \bar{X} is the mean and U is the deviation from the mean..

For 95% confidence, U is given by

$$U = 2\sqrt{\left(\frac{B}{2}\right)^2 + (S_{\bar{x}})^2} \quad (\text{G-5})$$

where B represents the total systematic uncertainty in the measurement and S_x represents the contribution to the uncertainty from random processes. The latter can be minimized by averaging a large number of measurements. In this work, $M=1200$.

G.2 Uncertainty of a computed result

So far, we have only discussed how to determine uncertainty in the fundamental measurements made on the dynamometer (voltage, temperature, speed, etc.) But the things we are really after (eg. Torque, power, efficiency and even load cell force and speed) are computed from one or more of the fundamental

measurements. Therefore, uncertainties in each measured quantity as well as the proportionality constants used to infer force, speed etc. all interact to influence the overall uncertainty in the fundamental measurements. The general method for propagating uncertainties through calculations is as follows:

For a generalized result $R = f(\bar{p}_1, \bar{p}_2, \dots, \bar{p}_j)$, the total uncertainty in R is given by:

$$U_r = \sqrt{(\Theta_1 * u_1)^2 + (\Theta_2 * u_2)^2 + \dots + (\Theta_j * u_j)^2} \quad (G-6)$$

$$\Theta_j = \frac{\partial R}{\partial \bar{p}_j} \quad (G-7)$$

where u_j is the uncertainty in the quantity \bar{p}_j and Θ_j is the sensitivity coefficient of R with respect to \bar{p}_j .

Equations G-6 and G-7 are used to determine the uncertainties in all computed such as force, torque, speed, fuel flow rate, fuel pressure, temperature, engine power and efficiency while equations G-1 through G-5 are used to determine the uncertainties u_j in all of the fundamental measured quantities.

G.3 Uncertainty analysis for a least squares fit

A least squares fit is used when calibrating the load cell and determining the fuel flow rate. In the case of the load cell, the slope and intercept obtained from the fit are used to convert the force on the load cell from Volts to mass units. In the case of the fuel flow rate, the weighted least-squares linear fit of fuel weight vs time yields the fuel flow rate. In each case, the individual data points upon which the fit is based contain systematic and random errors. And, these errors are different from data point

to data point. Equations G-8 and G-9²⁴⁷ give the best fit values for the slope and intercept assuming that the uncertainty of the independent variable (x) is negligible compared to the uncertainty in the dependent variable (y). The term e_i in the equations refers to the error in y-variable. Equations G-10 and G-11 give the corresponding uncertainties. While expressions do exist for computing the uncertainty in slope and intercept when both variables are uncertain, they are much more complex and are not really necessary here: In the case of the fuel flow measurement, the signal sent by the scale over the serial port are time stamped at the computer. This happens at a very high speed (1200 bits per second) and the uncertainty in time information is negligible. In the case of the load cell calibration, the independent variables are the calibration masses which are known to within 0.01%.

$$a = SLOPE = \frac{\left(\sum \frac{x_i}{e_i^2}\right)\left(\sum \frac{y_i}{e_i^2}\right) - \left(\sum \frac{x_i y_i}{e_i^2}\right)\left(\sum \frac{1}{e_i^2}\right)}{\left(\sum \frac{x_i}{e_i^2}\right)^2 - \left(\sum \frac{x_i^2}{e_i^2}\right)\left(\sum \frac{1}{e_i^2}\right)} \quad (G-8)$$

$$b = INTERCEPT = \frac{\left(\sum \frac{x_i y_i}{e_i^2}\right) - a\left(\sum \frac{x_i^2}{e_i^2}\right)}{\left(\sum \frac{x_i}{e_i^2}\right)} \quad (G-9)$$

$$a_{error} = Error\ in\ slope = \sqrt{\frac{\left(\sum \frac{1}{e_i^2}\right)}{\left(\sum \frac{x_i^2}{e_i^2}\right)\left(\sum \frac{1}{e_i^2}\right) - \left(\sum \frac{x_i}{e_i^2}\right)^2}} \quad (G-10)$$

$$b_{error} = \text{Error in intercept} = \sqrt{\frac{\left(\sum \frac{x_i^2}{e_i^2}\right)}{\left(\sum \frac{x_i^2}{e_i^2}\right)\left(\sum \frac{1}{e_i^2}\right) - \left(\sum \frac{x_i}{e_i}\right)^2}} \quad (\text{G-11})$$

Appendix H

H.1 Estimation of Pressure Drop in Engine Intake Tubing

Air flow rate into the engine is measured using an air flow meter described in Section 2.8.3. The sensor is connected to the engine using plastic tubing. A plenum is also incorporated into the flow path between the air flow meter and the engine carburetor as described in Section 2.8.3. The purpose of the plenum is to damp out fluctuations in engine air flow so that the flow meter sees a unidirectional flow of air into the meter. The introduction of components upstream of the engine intake causes an additional pressure drop. The true intake pressure seen by the engine is less than the atmospheric pressure by the amount equal to the pressure drop in the flow components including the air flow meter, the plenum and the tubing. This pressure drop has been quantified and utilized to correct measured engine power output to standard temperature and pressure conditions. The corrections themselves are presented in Section 2.14. The methods of estimation of pressure drop and the estimated values for one case of the OS 46 engine operating at maximum power are presented here.

Pressure drop in the air mass flow meter is estimated using information supplied in the manual for the instrument. The pressure drop for both air flow meters used in this work – Model 40211 and Model 41211 is provided as a function of flow rate. Pressure drop in the tubing and plenum is estimated using the Darcy friction factor estimated for the corresponding flow rate using the following relation,²⁴⁸

$$\Delta P_L = f \frac{L}{D} \frac{\rho V_{avg}^2}{2} \quad (H-1)$$

where ΔP_L is the pressure drop in the pipe, f is the Darcy friction factor for the pipe which is selected to be 0.002 for plastic tubing, L is the length of the pipe, D is the diameter, ρ is the density of air and V_{avg} is the average velocity of air in the pipe.

Table H-1 below shows the calculation of pressure drop for the operating point corresponding to maximum power output for the OS 46 engine.

Component	Length	Diameter	Inlet pressure	Pressure drop	Exit pressure
Air mass flow meter (Model 40211)	N/A	N/A	1.0054	0.0029	1.00246
Plastic tube 1	25	19.3	1.00246	3.9e-7	1.00246
Plastic tube 2	160	13.75	1.00246	9.8e-11	1.00246
Plenum	350	264	1.00246	8.2e-11	1.00246
Plastic tube 3	235	14	1.00246	2.2e-11	1.00246
	mm	mm	bar	bar	bar

Table H-1: Pressure drop calculation in engine air flow setup for the OS 46 engine operating at a speed of 17000 rpm. Engine air flow rate at this operating point is 0.75 gs^{-1} (36.7 lpm). Total pressure drop equals 0.003 bar.

Bibliography

-
- ¹ Wilson, J.R., "Uavs: A Worldwide Roundup", Aerospace America, Vol.5, May 2007, pp. 30-35.
- ² Davis, W.R., Kosicki, B., Boroson, M., and Kosticshack, D., "Micro Air Vehicles for Optical Surveillance", The Lincoln Laboratory Journal, Vol. 9, No. 2, 1996.
- ³ Dunn-Rankin, D., Leal, E.M., and Walther, D., "Personal Power Systems", Progress in Energy and Combustion Science, Vol. 31, Issues 5-6, 2005, pp. 422-465.
- ⁴ http://www.applelinks.com/index.php/more/ifixit_iphone_3g_s_teardown last downloaded 08/01/2010.
- ⁵ <http://www.anandtech.com/show/2802/4> last downloaded 08/01/2010.
- ⁶ Lewis, N.S., "Portable Energy for the Dismounted Soldier", Jason Program Office, MITRE Corp., McLean, VA. June 2003.
- ⁷ <http://www.absak.com/library/power-consumption-table> last downloaded 08/01/2010.
- ⁸ http://www.rinitech.com/docs/1007_PersonalCooling.pdf last downloaded 08/01/2010.
- ⁹ <http://bestminirefrigerator.com/portable-mini-refrigerator/> last downloaded 08/01/2010.
- ¹⁰ http://www.grainger.com/Grainger/DEWALT-Cordless-DrillDriver-Kit-4HVVH5?cm_mmc=Google%20Base-_-Power%20Tools-_-Cordless%20Tools-_-4HVVH5 last downloaded 08/01/2010.
- ¹¹ Patil, A.S., et al, "Portable Fuel Cell Systems for America's Army: Technology Transition to the Field", Journal of Power Sources, Vol. 136, Issue 2, October 2004, pp. 220-225.
- ¹² <http://www.ior.com.au/ecflist.html> last downloaded 08/01/2010.
- ¹³ <http://hypertextbook.com/facts/2003/EvelynGofman.shtml> last downloaded 08/01/2010.
- ¹⁴ <http://hypertextbook.com/facts/2003/JuliyaFisher.shtml> last downloaded 08/01/2010.
- ¹⁵ <http://www.allaboutbatteries.com/Battery-Energy.html> last downloaded 08/01/2010.
- ¹⁶ <http://www.designation-systems.net/dusrm/m-151.html> last downloaded 06/04/2010.
- ¹⁷ Menon, S., Moulton, N. and Cadou, C. P., "Development of a Dynamometer for Measuring Small Internal-Combustion Engine Performance", *AIAA Journal of Propulsion and Power*, Vol.23, No.1, Jan-Feb 2007.
- ¹⁸ http://www.rcuniverse.com/product_guide/engineprofile.cfm?engine_id=4 last downloaded 02/23/2010.
- ¹⁹ <http://www.eiffelaender.com/enginepics.htm> last downloaded 02/23/2010.
- ²⁰ http://www.davisdieseldevelopment.com/diesel_products.php last downloaded 02/23/2010.
- ²¹ "Meeting the Energy Needs of Future Warriors", Committee of Soldier Power/Energy Systems, National Research Council, 2004.

-
- ²²Wilkinson, P., "Aircraft Engines of the World", 1948.
- ²³Shah, K., and Besser, R.S., "Key Issues in the Microchemical Systems-Based Methanol Fuel Processor: Energy Density, Thermal Integration, and Heat Loss Mechanisms", Journal of Power Sources Volume 166, Issue 1, 30 March 2007, pp. 177-193.
- ²⁴Nowak, R., and Lyons, K., "Dod End User Perspective and DARPA Palm Power Program", Presentation at the DOE Fuel Cell Portable Power Workshop, January 15-17, 2002, Phoenix, Arizona.
- ²⁵<http://www.powerstream.com/BB.htm> last downloaded 02/23/2010.
- ²⁶<http://www.powerstream.com/LL.htm> last downloaded 02/23/2010.
- ²⁷<http://www.fuelcellstore.com/en/pc/viewPrd.asp?idcategory=52&idproduct=1103> last downloaded 02/23/2010.
- ²⁸<http://www.sfc.com/en/man-portable-jenny.html> last downloaded 02/23/2010.
- ²⁹Norton, D.G., Vlachos, D.G et al, "Portable Power Generation via Integrated Catalytic Microcombustion-Thermoelectric Devices", Proceedings of the 24th Army Science Conference, 2004.
- ³⁰Tian, L., Kittelson, D.B., and Durfee, W.K., "Miniature HCCI Free Piston Engine Compressor for Orthosis Application", Small engine technology conference, Nov 3-5, 2009, Penang, Malaysia.
- ³¹Fu, K., Knobloch, A.J., et al, "Design and Experimental Results of Small-Scale Rotary Engines", Proceedings of 2001 ASME International mechanical engineering and congress and exposition, November 11-16, 2001, New York, NY.
- ³²Spearing, M.S., "Design of High Power Density MEMS Materials and Testing Requirements", CAMTEC Nanotesting Workshop, 11 April 2006.
- ³³Menon, S., Moulton, N. and Cadou, C. P., "Development of a Dynamometer for Measuring Small Internal-Combustion Engine Performance", AIAA Journal of Propulsion and Power, Vol.23, No.1, Jan-Feb 2007.
- ³⁴<http://www.sullivanuav.com/home.html> last downloaded 02/23/2010.
- ³⁵<http://www.sullivanuav.com/home.html> last downloaded 02/23/2010.
- ³⁶Wilkinson, P., "Aircraft engines of the world", 1948.
- ³⁷Finol, C.A., and Robinson, K., "Thermal Modeling Of Modern Engines: A Review of Empirical Correlations to Estimate the In-Cylinder Heat Transfer Coefficient", Proceedings of the Institution of Mechanical Engineers, Part D: Journal of Automobile Engineering, Vol. 220, No. 12, 2006, pp. 1765-178.
- ³⁸Heywood, J.B., "Internal Combustion Engine Fundamentals", McGraw-Hill, 1988, pp 671.
- ³⁹Fernandez-Pello, C.A., "Micro-Power Generation Using Combustion: Issues and Approaches", Proceedings of the Combustion Institute, Vol.29, 2002, pp. 883-899.
- ⁴⁰Mills, A.F., "Heat Transfer", Taylor & Francis US, 1992.

-
- ⁴¹Lee, D.H., and Kwon, S., "Heat Transfer and Quenching Analysis of Combustion in a Micro Combustion Vessel", *Journal of micromechanics and micro-engineering*, Vol. 12, 2002, pp. 670–676.
- ⁴²Epstein, A., "Millimeter-Scale, Micro-Electro-Mechanical Systems Gas Turbine Engines", *Journal of Engineering for Gas Turbines and Power*, Vol. 126, No. 2, April 2004, pp. 205–226.
- ⁴³Leach, T., and Cadou, C., "The Role of Structural Heat Exchange and Heat Loss in the Design of Efficient Silicon Micro-Combustors", *Proceedings of the Combustion Institute* Vol. 30, Issue 2, January 2005, pp. 2437-2444.
- ⁴⁴ Taylor, C.F., "The Internal Combustion Engine in Theory and Practice, Volume 1: Thermodynamics, Fluid Flow, Performance", MIT press, Second edition, 1985, pp. 429.
- ⁴⁵ Skjoedt, M., Butts, R., Assanis, D.N., and Bohac, S.V., "Effects of Oil Properties on Spark-Ignition Gasoline Engine Friction", *Tribology International* Vol. 41, Issue 6, June 2008, pp. 556-563.
- ⁴⁶ Sher, E., Heywood, J.B., "The Two Stroke Cycle Engine", Taylor and Francis, 1989, pp. 367.
- ⁴⁷ Sher A, Levinzon-Sher B, and Sher B, "Miniaturization Limitations of HCCI Internal Combustion Engines", *Applied Thermal Engineering*, Vol. 29, 2009, pp. 400–411.
- ⁴⁸ Heywood, J.B., "Internal Combustion Engine Fundamentals", McGraw-Hill, 1988, pp. 599.
- ⁴⁹ Sher A, Levinzon-Sher B, and Sher B, "Miniaturization Limitations of HCCI Internal Combustion Engines", *Applied Thermal Engineering*, Vol.29, 2009, pp. 400–411.
- ⁵⁰"Numerical Simulation of The Combustion of Hydrogen–Air Mixture in Micro-Scaled Chambers. Part I: Fundamental Study", *Chemical Engineering Science* Vol. 60, Issue 13, July 2005, pp. 3497-3506.
- ⁵¹Li, J., Chou, S.K., Yang, W.M., and Li, Z.W., "A Numerical Study on Premixed Micro-Combustion of CH₄–Air Mixture: Effects of Combustor Size, Geometry and Boundary Conditions on Flame Temperature", *Chemical Engineering Journal* Vol. 150, Issue 1, July 2009, pp. 213-222.
- ⁵²Von Elbe, G., and Lewis, B., "Burning Velocities, Quenching, and Stability Data on Non-Turbulent Flames of Methane and Propane with Oxygen and Nitrogen: Application of Theory of Ignition, Quenching, and Stabilization to Flames of Propane and Air", *Symposium on Combustion and Flame, and Explosion Phenomena*, Vol. 3, Issue 1, 1949, pp. 80-89.
- ⁵³Miesse, C.M, Masel, R.I., Jensen, C.D., Shannon, M.A., and Short, M., "Submillimeter-Scale Combustion", *AIChE Journal*, Vol.50, 2004, pp. 3206–3214.
- ⁵⁴Ronney P.D. et al, "Combustion in Microscale Heat-Recirculating Burners", *The third asia-pacific conference on combustion*, June 24-27, 2001, Seoul, Korea.
- ⁵⁵Manente, V., "Characterization of Glow Plug and HCCI Combustion Processes in a Small Volume at High Engine Speed", Phd thesis, Lund University, Sweden, 2007.
- ⁵⁶Papac, J.E., "Combustion in a Miniature Combustion Engine", MS thesis, 2004.
- ⁵⁷Sher, E., and Heywood, J.B., "The Two Stroke Cycle Engine", Taylor and Francis, 1989, pp. 157.
- ⁵⁸Annen, K.D., Stickler, D.B., and Woodroffe, J., "Linearly-Oscillating Miniature Internal Combustion Engine (Mice) for Portable Electric Power", 41st Aerospace Sciences Meeting and Exhibit 6-9 January 2003, Reno, Nevada.

-
- ⁵⁹ Sher, E., and Levinzon, D., "Scaling-Down of Miniature Internal Combustion Engines: Limitations and Challenges", *Heat Transfer Engineering*, Vol. 26, Issue 8, October 2005, pp. 1-4.
- ⁶⁰ Taylor, C.F., "The Internal Combustion Engine in Theory and Practice, Volume 1: Thermodynamics, Fluid Flow, Performance", MIT press, Second edition, 1985, pp. 217.
- ⁶¹ Bauer, T., "Emissions Characterization of a Direct Injection Retro-Fit Kit for Small Two-Stroke Cycle Engines", EnviroFit International, Ltd.
- ⁶² Ma, F., Ding, S., Wang, Y., Wang, Y., Wang, J., and Zhao, S., "Study on Combustion Behaviors and Cycle-By-Cycle Variations in a Turbocharged Lean Burn Natural Gas S.I. Engine with Hydrogen Enrichment", *International Journal of Hydrogen Energy*, Vol. 33, Issue 23, December 2008, pp. 7245-7255.
- ⁶³ Chinn, P. G. F., "Import Review", *Model Airplane News*, Morris, pp. 28, 1957.
- ⁶⁴ Gierke, D., "We Test 10 .60 Engines: Which Is Right For You?", *Model Airplane News*, Morris, Vol.131, Iss.5; pp.28.
- ⁶⁵ Gierke, D., "Part I Dynamometer and Engine Performance Analysis", *Flying Models*, June, 1973, pp. 21-25.
- ⁶⁶ Gierke, D., "Part II Dynamometer and Engine Performance Analysis", *Flying Models*, July, 1973, pp. 43-51.
- ⁶⁷ Gierke, D., "Part III Dynamometer and Engine Performance Analysis", *Flying Models*, July, 1973, pp. 38-47.
- ⁶⁸ Gierke, D., "Two-Stroke Glow Engines for R/C Aircraft", *Air Age Inc.*, 1994, pp. 48.
- ⁶⁹ Raine, R. Moyle, K., and Otte, G., "A Cost Effective Teaching and Research Dynamometer for Small Engines", *Int. Journal of engineering education*, Vol.18, No.1, 2002, pp 50-57.
- ⁷⁰ Roberts, C.P., Salter, R.G., Smith, M.I., and Tang, K.Y., "Study of Miniature Engine-Generator Sets", *Ohio state university research foundation*, Columbus, May 1953.
- ⁷¹ Younggy, S., Sung-Ho, C., Chang, and Sam-Ok, K., "Performance Test and Simulation of a Reciprocating Engine for Long Endurance Miniature Unmanned Aerial Vehicles", *Proceedings of the Institution of Mechanical Engineers, Part D: Journal of Automobile Engineering*, Vol. 219, No. 4, 2005, pp. 573-581.
- ⁷² Sookdeo, T., "Performance Measurement, Simulation, and Analysis of the Cox Tee Dee 0.010, The World's Smallest Production Internal Combustion Engine", *Masters thesis*, University of Maryland at College Park, 2006.
- ⁷³ Chon, D.M., and Heywood, J.B., "Performance Scaling of Spark-Ignition Engines: Correlation and Historical Analysis of Production Engine Data", *SAE paper no. 2000-01-0565*, 2000 SAE World Congress & Exposition, Cobo Center, Detroit, MI, March 6-9, 2000.
- ⁷⁴ Peterson, R. B., "Size Limits for Regenerative Heat Engines", *Microscale Thermophysical Engineering*, Vol. 2, 1998, pp. 121-131.
- ⁷⁵ Sher, E., and Levinzon, D., "Scaling-Down of Miniature Internal Combustion Engines: Limitations and Challenges", *Heat Transfer Engineering*, Vol. 26, Issue 8, October 2005, pp. 1 – 4.

-
- ⁷⁶ Sher, A., Levinzon-Sher, D., and Sher, E., "Miniaturization Limitations of HCCI Internal Combustion Engines", *Applied Thermal Engineering* Vol. 29, 2009, pp. 400–411.
- ⁷⁷ Papac, J. and Dunn-Rankin, D. "Combustion in a Centimeter Scale Four Stroke Engine", Western States Section/The Combustion Institute Spring Meetingpaper 04S-12, UC Davis, March 29–30, 2004.
- ⁷⁸ Ball, J.K., Raine, R.R., and Stone, C.R., "Combustion Analysis and Cycle-By-Cycle Variations in Spark Ignition Engine Combustion Part 1: An Evaluation of Combustion Analysis Routines by Reference to Model Data", *Proceedings of the Institution of Mechanical Engineers, Part D: Journal of Automobile Engineering*, Vol. 212, No. 5, 1998, pp. 381-399.
- ⁷⁹ Manente, V., "Characterization of Glow Plug and HCCI Combustion Processes in a Small Volume at High Engine Speed", Phd thesis, Lund University, Sweden, 2007.
- ⁸⁰ Onishi S., Jo S. H., Shoda K., Jo P. D., and Kato S., "Active Thermo-Atmosphere Combustion, ATAC, A New Combustion Process For Internal Combustion Engine", SAE 790501.
- ⁸¹ Papac, J. and Dunn-Rankin, D., "Characteristics of Combustion in a Miniature Four-Stroke Engine", *Journal of aeronautics, astronautics and aviation Series A*, Vol. 38, 2006, pp. 77-88.
- ⁸² Roberts, C.P., Salter, R.G., Smith, M.I., and Tang, K.Y., "Study of Miniature Engine-Generator Sets", Ohio state university research foundation, Columbus, May 1953.
- ⁸³ Heywood, J.B., Sher, E., "The Two-Stroke Cycle Engine", 1999, pp. 9.
- ⁸⁴ Heywood, J.B., Sher, E., "The Two-Stroke Cycle Engine", 1999, pp. 4.
- ⁸⁵ "OS Engines: MAX-50SX RING & 40,46,61,91 'FX SERIES', Owners Instruction Manual", O.S.Engines Mfg.Co.Ltd.
- ⁸⁶ Gierke, D., "O.S. MAX .46AX", *Model airplane news*, October 2004.
- ⁸⁷ Fu, K., Knobloch, A. et al. "Design and Experimental Results of Small Scale Rotary Engines", *Proceedings of 2001 ASME International Mechanical engineering congress and exposition*, November 11-16, 2001, New York, NY.
- ⁸⁸ ASME Standard, Standard test method for heat of combustion of liquid hydrocarbon fuels by bomb calorimeter, D240, 2002.
- ⁸⁹ Papac, J., Figueroa, I., and Dunn-Rankin, D., "Performance Assessment of a Centimeter-Scale Four-Stroke Engine," Paper 03F-91, Fall Technical Meeting, Western States Section, Combustion Institute, October 2003, UCLA.
- ⁹⁰ Makovsky, A., and Lenji, L., "Nitromethane - Physical Properties, Thermodynamics, Kinetics of Decomposition, And Utilization as Fuel", *Chemical Reviews*, Vol. 58, Issue 4, 1958, pp. 627-644.
- ⁹¹ Menon, S., "Performance Measurement and Scaling in Small Internal Combustion Engines", Master's Thesis, 2005.
- ⁹² Moulton, N., "Performance Measurement and Simulation of A Small Internal Combustion Engine", Masters Thesis, 2007.
- ⁹³ Moulton, N., "Performance Measurement and Simulation of A Small Internal Combustion Engine", Masters Thesis, 2007.

-
- ⁹⁴ “Hysteresis Brakes and Clutches”, 2nd Edition, November 2003, Magtrol Inc., USA.
- ⁹⁵ Menon, S., Moulton, N. and Cadou, C. P., “Development of A Dynamometer for Measuring Small Internal-Combustion Engine Performance”, *AIAA Journal of Propulsion and Power*, Vol.23, No.1, Jan-Feb 2007.
- ⁹⁶ http://www.electro-sensors.com/product_info.php/cPath/19/products_id/41, last downloaded 10/22/2010.
- ⁹⁷ Winterborne, D., and Pearson, R., “Design Technologies for Engine Manifolds - Wave Action Methods for IC Engine”.
- ⁹⁸ Heywood, J. B., “Internal Combustion Engine Fundamentals”, McGraw-Hill Book Company, 1988, pp. 51.
- ⁹⁹ Taylor, C.F., “The Internal Combustion Engine in Theory and Practice, Volume 1: Thermodynamics, Fluid Flow, Performance”, MIT press, Second edition, 1985, pp. 27.
- ¹⁰⁰ Chon, D.M., and Heywood, J.B., "Performance Scaling of Spark-Ignition Engines: Correlation and Historical Analysis of Production Engine Data," SAE paper no. 2000-01-0565, 2000 SAE World Congress & Exposition, Cobo Center, Detroit, MI, March 6-9, 2000.
- ¹⁰¹ Gierke, David, “Break-In: The Secret to Longevity and Reliability”, Model Airplane News, Nov 2001.
- ¹⁰² ASME-PTC 19.1, ASME Test Standard, 1998.
- ¹⁰³ Menon, S., Moulton, N. and Cadou, C. P., “Development of a Dynamometer for Measuring Small Internal-Combustion Engine Performance”, *AIAA Journal of Propulsion and Power*, Vol.23, No.1, Jan-Feb 2007.
- ¹⁰⁴ “Engine Power Test Code-Spark Ignition and Compression Ignition- Gross Power Rating”, SAE J1995 Standard, June 1995.
- ¹⁰⁵ Menon, S., Moulton, N. and Cadou, C. P., “Development of a Dynamometer for Measuring Small Internal-Combustion Engine Performance”, *AIAA Journal of Propulsion and Power*, Vol.23, No.1, Jan-Feb 2007.
- ¹⁰⁶ Heywood, J. B., “Internal Combustion Engine Fundamentals”, McGraw-Hill Book Company, 1988, pp. 830.
- ¹⁰⁷ Heywood, J. B., “Internal Combustion Engine Fundamentals”, McGraw-Hill Book Company, 1988, pp. 831.
- ¹⁰⁸ Komotori, K., and Watanabe, E., “A Study of the Delivery Ratio Characteristics of Crankcase-Scavenged Two-Stroke Cycle Engines”, *SAE Transactions*, Vol.78, 1969, pp.608-636.
- ¹⁰⁹ Motoyama, Y., and Gotoh, T., “The Effect of Higher Compression Ratio in Two-Stroke Engines”, SAE paper 931512, 1993.
- ¹¹⁰ McMahon, T., and Bonner, J., “On Size and Life”, *Scientific American Library* 1983, pp. 61-62.

-
- ¹¹¹ Troy, S., Leach, T., Moulton, N., and Cadou, C., “ Performance Scaling and Measurement for Hydrocarbon Fueled Engines with Mass Less Than 1 Kg”, AIAA’s 1st technical conference and workshop on unmanned aerospace vehicles, May 20-23, 2002, Portsmouth, VA.
- ¹¹² Wilkinson, P., ”Aircraft Engines of the World”, 1948.
- ¹¹³ <http://www.carfolio.com/>, downloaded 01/01/2010.
- ¹¹⁴ <http://www.kohlerengines.com/onlinecatalog/serieslanding.htm?series=Aegis>, downloaded 01/05/2010.
- ¹¹⁵ http://www.briggsandstratton.com/engine_power/engine_series.aspx, downloaded 01/05/2010.
- ¹¹⁶ <http://www.honda-engines.com/pro.htm>, downloaded 01/05/2010.
- ¹¹⁷ <http://www.honda-engines.com/pro.htm>, downloaded 01/05/2010.
- ¹¹⁸ Papac, J. and Dunn-Rankin, D., “Characteristics of Combustion in a Miniature Four-Stroke Engine”, Journal of aeronautics, astronautics and aviation Series A, Vol. 38, 2006, pp. 77-88.
- ¹¹⁹ Roberts, C.P., Salter, R.G., Smith, M.I., and Tang, K.Y., “Study of Miniature Engine-Generator Sets”, Ohio state university research foundation, Columbus, May 1953.
- ¹²⁰ Taylor, C.F., “The Internal Combustion Engine in Theory and Practice: Volume 1 – Thermodynamics, Fluid Flow, Performance”, MIT press, second edition, revised 1985, pp. 444.
- ¹²¹ Brinkman, N.D., “Ethanol Fuel- A Single Cylinder Engine Study of Efficiency and Exhaust Emissions”, SAE paper 810345, 1981.
- ¹²² Chon, D.M., and Heywood, J.B., "Performance Scaling of Spark-Ignition Engines: Correlation and Historical Analysis of Production Engine Data," SAE paper no. 2000-01-0565, 2000 SAE World Congress & Exposition, Cobo Center, Detroit, MI, March 6-9, 2000.
- ¹²³ BP Products handbook, last downloaded 10/18/2010.
- ¹²⁴ Chon, D.M., and Heywood, J.B., "Performance Scaling of Spark-Ignition Engines: Correlation and Historical Analysis of Production Engine Data," SAE paper no. 2000-01-0565, 2000 SAE World Congress & Exposition, Cobo Center, Detroit, MI, March 6-9, 2000.
- ¹²⁵ Taylor, C.F., “The Internal Combustion Engine in Theory and Practice: Volume 1 – Thermodynamics, Fluid Flow, Performance”, MIT press, second edition, revised 1985, pp 404.
- ¹²⁶ Heywood, J. B., “Internal Combustion Engine Fundamentals”, McGraw-Hill Book Company, 1988, pp. 50.
- ¹²⁷ Leach, T., and Cadou, C. P., "The Role of Structural Heat Exchange and Heat Loss in the Design Of Efficient Silicon Micro-Combustors", 30th International Symposium on Combustion, Chicago, July26-30, 2004.
- ¹²⁸ Peterson, R. B., “Size Limits For Regenerative Heat Engines”, Microscale Thermophysical Engineering, Vol. 2, 1998, pp. 121-131.
- ¹²⁹ Leach, T., and Cadou, C. P., “The Role of Structural Heat Exchange and Heat Loss in the Design of Efficient Silicon Micro-Combustors”, 30th International Symposium on Combustion, Chicago, July26-30, 2004.

-
- ¹³⁰ Sher, A., Levinzon-Sher D., and Sher B., “Miniaturization Limitations of HCCI Internal Combustion Engines”, *Applied Thermal Engineering*, Vol. 29, 2009, pp. 400–411.
- ¹³¹ Sher, E., and Levinzon, D., “Scaling-Down of Miniature Internal Combustion Engines: Limitations and Challenges”, *Heat Transfer Engineering*, Vol. 26, Issue 8, October 2005, pp. 1-4.
- ¹³² Heywood, J. B., “Internal Combustion Engine Fundamentals”, McGraw-Hill Book Company, 1988, pp. 762.
- ¹³³ Watts, P.A., and Heywood, J.B., “Simulation Studies of the Effects of Turbocharging and Reduced Heat Transfer on Spark-ignition Engine Operation”, SAE paper 800289, 1980.
- ¹³⁴ Lavoie, G.A., and Blumberg, P.N., “A Fundamental Model for Predicting Fuel Consumption, NO_x and HC Emissions of the Conventional Spark-ignited Engine”, *Combustion science and technology*, Vol.21, pp.225-258, 1980.
- ¹³⁵ Rakopoulos, C.D., and Giakoumis, E.G., “Second-law Analyses Applied to Internal Combustion Engines Operation”, *Progress in Energy and Combustion Science*, Vol. 32, Issue 1, 2006, pp. 2-47.
- ¹³⁶ Rakopoulos, C.D., “Evaluation of a Spark Ignition Engine Cycle Using First and Second Law Analysis Techniques”, *Energy Conversion and Management*, Vol. 34, Issue 12, December 1993, pp. 1299-1314.
- ¹³⁷ Rakopoulos, C.D., and Kyritsis, D.C., “Comparative Second-law Analysis of Internal Combustion Engine Operation for Methane, Methanol, and Dodecane fuels “, *Energy*, Vol. 26, Issue 7, July 2001, pp. 705-722.
- ¹³⁸ Spanogle and Buckley, “The NACA Combustion Chamber Gas-Sampling Valve and Some Preliminary Test Results”. NACA TN 454 1933.
- ¹³⁹ Schweitzer and DeLuca, “The Tracer Gas Method of Determining the Charging Efficiency of Two Stroke Cycle Diesel Engines”, NACA TN 838 1942.
- ¹⁴⁰ Heywood, J. B., “Internal Combustion Engine Fundamentals”, McGraw-Hill Book Company, 1988, pp. 239.
- ¹⁴¹ Wentworth, J.T., “Piston and Ring Variables Affect Exhaust Hydrocarbon Emissions”, SAE paper 680109, SAE Transactions Vol.77, 1968.
- ¹⁴² Cheng, K.Y, Shayler, P.J., and Murphy, M., “The Influence of Blow-by on Indicated Work Output from a Diesel Engine under Cold Start Conditions”, *Proceedings of the Institute of Mechanical Engineers, Part D, Journal of automobile engineering*, Vol.218, pp. 333-340.
- ¹⁴³ “Scaling-Down of Miniature Internal Combustion Engines: Limitations and Challenges”, Eran Sher, Diana Levinzon, *Heat Transfer Engineering*, Vol. 26, Issue 8, October 2005 , pp. 1-4.
- ¹⁴⁴ Taylor, C.F., *The Internal Combustion Engine in Theory and Practice: Volume 1 – Thermodynamics, Fluid flow, Performance*”, MIT press, second edition, revised 1985, pp 179.
- ¹⁴⁵ Winterborne, D., and Pearson, R., “Design Technologies for Engine Manifolds - Wave Action Methods for IC Engine”.
- ¹⁴⁶ Abraham, J., Williams, F.A., and Bracco, F.V., “A Discussion of Turbulent Flame Structures in Premixed Charges”, SAE paper 850345, *Engine combustion analysis: New approaches*, 1985, pp. 156.

-
- ¹⁴⁷ Liou, T-M., and Santavicca, D.A., "Cycle Resolved LDV Measurements in a Motored IC Engine", ASME Transactions, Journal of Fluids Engineering, Vol.107, 1985, pp.232-240.
- ¹⁴⁸ Heywood, J. B., "Internal Combustion Engine Fundamentals", McGraw-Hill Book Company, 1988, pp. 340.
- ¹⁴⁹ Heywood, J. B., "Internal Combustion Engine Fundamentals", McGraw-Hill Book Company, 1988, pp. 217.
- ¹⁵⁰ Taylor, C.F., The Internal Combustion Engine in Theory and Practice: Volume 1 – Thermodynamics, Fluid flow, Performance", MIT press, second edition, revised 1985, pp 179.
- ¹⁵¹ Winterborne, D., and Pearson, R., "Design Technologies for Engine Manifolds - Wave Action Methods for IC Engine".
- ¹⁵² Heywood, J. B., "Internal Combustion Engine Fundamentals", McGraw-Hill Book Company, 1988, pp. 672.
- ¹⁵³ Heywood, J. B., "Internal Combustion Engine Fundamentals", McGraw-Hill Book Company, 1988, pp. 677.
- ¹⁵⁴ Heywood, J. B., "Internal Combustion Engine Fundamentals", McGraw-Hill Book Company, 1988, pp. 672
- ¹⁵⁵ Heywood, J. B., "Internal Combustion Engine Fundamentals", McGraw-Hill Book Company, 1988, pp. 685-686
- ¹⁵⁶ Finol, C.A., and Robinson, K., "Thermal modeling of Modern Engines: A Review of Empirical Correlations to Estimate the In-cylinder Heat Transfer Coefficient", Proceedings of the Institution of Mechanical Engineers, Part D: Journal of Automobile Engineering, Volume 220, Number 12 / 2006, pp. 1765-1781.
- ¹⁵⁷ Taylor C.F., and Toong, T.Y., "Heat Transfer in Internal Combustion Engines", ASME paper 57-HT-17, 1957.
- ¹⁵⁸ Annand, W.J.D., "Heat Transfer in the Cylinders of Reciprocating Internal Combustion Engines", Proceedings of the Institution of Mechanical engineer, Vol.177, No.36, 1963, pp. 973-990.
- ¹⁵⁹ LeFeuvre, T., Myers, P.S., and Uyehara, O.A., "Experimental Instantaneous Heat Fluxes in a Diesel Engine and their Correlation", SAE paper 690464, SAE Transactions, Vol.78, 1969.
- ¹⁶⁰ Taylor, C.F., The Internal Combustion Engine in Theory and Practice: Volume 1 – Thermodynamics, Fluid flow, Performance", MIT press, second edition, revised 1985, pp 274.
- ¹⁶¹ Pinkel, B., "Heat-transfer Processes in Air-cooled Engine Cylinders", NACA-TR-612, 1938.
- ¹⁶² LeFeuvre, T., Myers, P.S., Uyehara, O.A., "Experimental Instantaneous Heat Fluxes in a Diesel Engine and their Correlation", SAE paper 690464, SAE transactions, Vol.78, 1969.
- ¹⁶³ Pinkel, B., "Heat-Transfer Processes in Air-Cooled Engine Cylinders", NACA-TR-612, 1938.
- ¹⁶⁴ Annand, W.J.D., and Ma, T.H., "Instantaneous Heat Transfer Rates to the Cylinder Head Surface of a Small Compression-Ignition Engine", Proceedings of the institution of mechanical engineers, Vol.185, No.71, 1970, pp. 976-987.

-
- ¹⁶⁵ Borman, G., and Nishiwaki, K., “A Review of Internal Combustion Engine Heat Transfer”, Progress in energy combustion science, Vol.13, 1987, pp. 1-46.
- ¹⁶⁶ Heywood, J. B., “Internal Combustion Engine Fundamentals”, McGraw-Hill Book Company, 1988, pp. 676.
- ¹⁶⁷ Taylor C.F., and Toong, T.Y., “Heat Transfer in Internal Combustion Engines”, ASME paper 57-HT-17, 1957.
- ¹⁶⁸ Taylor C.F., and Toong, T.Y., “Heat Transfer in Internal Combustion Engines”, ASME paper 57-HT-17, 1957.
- ¹⁶⁹ Pinkel, B., “Heat-Transfer Processes in Air-Cooled Engine Cylinders”, NACA-TR-612, 1938.
- ¹⁷⁰ Pinkel, B., and Ellerbrock, H. H., “Correlation of Cooling Data from an Air-Cooled Cylinder and Several Multicylinder Engines”, NACA-TR-683, 1940.
- ¹⁷¹ Schey, O.W., Pinkel, B., and Ellerbrock, H.H., “Correction of Temperatures of Air-Cooled Engine Cylinders for Variation in Engine and Cooling Conditions”, NACA-TR-612, 1938.
- ¹⁷² Taylor C.F., and Toong, T.Y., “Heat Transfer in Internal Combustion Engines”, ASME paper 57-HT-17, 1957.
- ¹⁷³ Bendtsen, A.B., Glarborg P., and Dam-Johansen K., “Low Temperature Oxidation of Methane: The Influence of Nitrogen Oxides”, Combustion science and technology, Vol.151, Issue 1, 2000, pp. 31-71.
- ¹⁷⁴ D. Goodwin, “Cantera: Object-Oriented Software for Reacting Flows”, California Institute of Technology, available at <http://code.google.com/p/cantera/> (2010).
- ¹⁷⁵ Boyer, E., “Combustion Characteristics and Flame Structure of Nitromethane Liquid Monopropellant”, PhD Thesis, Pennsylvania State university, 2005.
- ¹⁷⁶ Gregory P. Smith, David M. Golden, Michael Frenklach, Nigel W. Moriarty, Boris Eiteneer, Mikhail Goldenberg, C. Thomas Bowman, Ronald K. Hanson, Soonho Song, William C. Gardiner, Jr., Vitali V. Lissianski, and Zhiwei Qin, *GRI-Mech 3.0*, available at http://www.me.berkeley.edu/gri_mech/
- ¹⁷⁷ Heywood, J. B., “Internal Combustion Engine Fundamentals”, McGraw-Hill Book Company, 1988, pp. 674.
- ¹⁷⁸ Taylor, C.F., “The Internal Combustion Engine in Theory and Practice: Volume 1 – Thermodynamics, Fluid Flow, Performance”, MIT press, second edition, revised 1985, pp 328.
- ¹⁷⁹ Heywood, J.B., and Sher, E., “The Two-Stroke Cycle Engine: Its Development, Operation And Design”, Taylor and Francis, 1999, pp. 367.
- ¹⁸⁰ Heywood, J.B., and Sher, E., “The Two-Stroke Cycle Engine: Its Development, Operation And Design”, Taylor and Francis, 1999, pp. 367.
- ¹⁸¹ Heywood, J. B., “Internal Combustion Engine Fundamentals”, McGraw-Hill Book Company, 1988, pp. 674.

-
- ¹⁸² Heywood, J. B., "Internal Combustion Engine Fundamentals", McGraw-Hill Book Company, 1988, pp. 674.
- ¹⁸³ Rousseau, S., Lemoult, B., and Tazerout, M., "Combustion Characterization of Natural Gas in a Lean Burn Spark-Ignition Engine", Proceedings of the Institution of Mechanical Engineers, Part D: Journal of Automobile Engineering, Vol. 213, No. 5, 1999, pp. 481-489.
- ¹⁸⁴ Brunt, M., Pond, C., and Biundo, J., "Gasoline Engine Knock Analysis Using Cylinder Pressure Data", SAE Paper Number: 980896, 1998.
- ¹⁸⁵ Zervas, E., "Correlations between Cycle-To-Cycle Variations and Combustion Parameters of a Spark Ignition Engine", Applied Thermal Engineering, Vol. 24, Issues 14-15, October 2004, pp. 2073-2081.
- ¹⁸⁶ Mendera, K.Z., Spyra, A., and Smereka, M., "Mass Fraction Burned Algorithm based on the pv Product", Journal of KONES Internal Combustion Engines, 2002, No.3-4, ISSN 1231-4005.
- ¹⁸⁷ Heywood, J. B., "Internal Combustion Engine Fundamentals", McGraw-Hill Book Company, 1988, pp. 508.
- ¹⁸⁸ Wlodarczyk, M., "Long-Life Fiber-Optic Pressure Sensors for Reciprocating Machinery Monitoring", 9th Trade Fair and Conference Sensor, May 1999, Nuremberg, Germany.
- ¹⁸⁹ Wlodarczyk, M., "Embedded Fiber-Optic Combustion Pressure Sensor for Automotive Engine Controls", 1998 FISITA World Automotive Congress, September 27- October 1 1998, Paris, France.
- ¹⁹⁰ <http://www.optrand.com/>, last downloaded 10/04/2010.
- ¹⁹¹ <http://www.encoder.com/model121.html>, last downloaded 10/13/2010.
- ¹⁹² <http://www.encoder.com/model260.html>, last downloaded 10/13/2010.
- ¹⁹³ http://mechatronics.mech.northwestern.edu/design_ref/sensors/encoders.html, last downloaded 10/04/2010.
- ¹⁹⁴ Zervas, E., "Correlations Between Cycle-To-Cycle Variations and Combustion Parameters of a Spark Ignition Engine", Applied Thermal Engineering, Volume 24, Issues 14-15, October 2004, Pages 2073-2081.
- ¹⁹⁵ Mendera, K.Z., Spyra, A., and Smereka, M., "Mass Fraction Burned Algorithm based on the pv Product", Journal of KONES Internal Combustion Engines, 2002, No.3-4, ISSN 1231-4005.
- ¹⁹⁶ Rassweiler, G.M. and Withrow, L., "Motion Pictures of Engine Flames Correlated With Pressure Cards", SAE Transactions, Vol.83, pp 185-204, 1938.
- ¹⁹⁷ Heywood, J. B., "Internal Combustion Engine Fundamentals", McGraw-Hill Book Company, 1988, pp. 385.
- ¹⁹⁸ Heywood, J.B., and Sher, E., "The Two-Stroke Cycle Engine: Its Development, Operation and Design", Taylor and Francis 1999, pp. 218.
- ¹⁹⁹ McCuiston, Jr. F.D., Lavoie, G.A. and Kauffman, C.W., "Validation of a Turbulent Flame Propagation Model for a Spark Ignition Engine", SAE Paper No. 770045, 1977.

-
- ²⁰⁰ Heywood, J. B., "Internal Combustion Engine Fundamentals", McGraw-Hill Book Company, 1988, pp. 390.
- ²⁰¹ Stiesch, G., "Modeling Engine Spray and Combustion Processes", Birkhäuser, 2003, pp. 16.
- ²⁰² Krieger, R. B., and Borman G. L., "The Computation of Apparent Heat Release for Internal Combustion Engines", ASME Paper 66-WA-DGP-4, 1966.
- ²⁰³ Heywood, J. B., "Internal Combustion Engine Fundamentals", McGraw-Hill Book Company, 1988, pp. 386.
- ²⁰⁴ Rohrer, R., and Chehroudi, B., "Preliminary Heat Release Analysis in a Single-Cylinder Two-Stroke Production Engine", SAE Paper Number: 930431.
- ²⁰⁵ Rohrer, R., and Chehroudi, B., "Preliminary Heat Release Analysis in a Single-Cylinder Two-Stroke Production Engine", SAE Paper Number: 930431.
- ²⁰⁶ Heywood, J. B., "Internal Combustion Engine Fundamentals", McGraw-Hill Book Company, 1988, pp. 546.
- ²⁰⁷ Mendera, K.Z., Spyra, A., and Smereka, M., "Mass Fraction Burned Algorithm based on the p_v Product", Journal of KONES Internal Combustion Engines, 2002, No.3-4, ISSN 1231-4005.
- ²⁰⁸ Brown, B.R., "Combustion Data Acquisition and Analysis", Final year project, Loughborough university.
- ²⁰⁹ Menon, S., "Performance Measurement and Scaling in Small Internal Combustion Engines", Master's Thesis, 2006.
- ²¹⁰ Eriksson, L., and Andersson, I., "An Analytic Model for Cylinder Pressure in a Four Stroke SI Engine", SAE Paper 2002-01-0371.
- ²¹¹ Alasfour, F.N., "Butanol – A Single Cylinder Engine Study: Engine Performance", International journal of engine research, Vol.21, 21-30, 1997.
- ²¹² Heywood, J. B., "Internal Combustion Engine Fundamentals", McGraw-Hill Book Company, 1988, pp. 831.
- ²¹³ Bade Shrestha, S.O., and Narayanan, G., "Landfill Gas with Hydrogen Addition – A Fuel for SI Engines", Fuel, Vol.87, 2008, pp. 3616-3626.
- ²¹⁴ Lakshminarayanan, P.A., Aghav, Y.V., Dani, A.D. and Mehta P.S., "Accurate Prediction of the Rate of Heat Release in a Modern Direct Injection Diesel Engine", Proceedings of the institution of mechanical engineers, part D: Journal of automobile engineering, Vol.216, No.8, 2002, pp. 663-675.
- ²¹⁵ Jindal, S., Nandwana, B.P., and Rathore, N.S., "Comparative Evaluation of Combustion, Performance, and Emissions of Jatropa Methyl Ester and Karanj Methyl Ester in a Direct Injection Diesel Engine". Energy Fuels, 2010, Vol. 24, No. 3, pp. 1565–1572.
- ²¹⁶ Asad, U., and Zheng, M., "Fast Heat Release Characterization of a Diesel Engine", International journal of thermal sciences, Vol.47, 2008, pp. 1688-1700.
- ²¹⁷ Heywood, J. B., "Internal Combustion Engine Fundamentals", McGraw-Hill Book Company, 1988, pp. 394.

-
- ²¹⁸ Rassweiler, G.M. and Withrow, L., "Motion Pictures of Engine Flames Correlated with Pressure Cards", SAE Transactions, Vol.83, pp. 185-204, 1938.
- ²¹⁹ Abraham, J., Williams, F.A., Braccor, F.V., "A Discussion of Turbulent Flame Structures in Premixed Charges", SAE paper 850345, Engine combustion analysis: New approaches, 1985, pp. 156.
- ²²⁰ Manente, V., "Characterization of Glow Plug and HCCI Combustion Processes in a Small Volume at High Engine Speed", Phd thesis, Lund University, Sweden, 2007.
- ²²¹ <http://www.escopro.com/copaltite-sealants.html> , last downloaded 09/27/2010.
- ²²² <http://www.visionresearch.com/Service--Support/FAQs/> last downloaded 10/28/2010.
- ²²³ Zigler, B.T., Walton, S.M., Assanis, D., et al., "An Imaging Study Of Compression Ignition Phenomena of Iso-Octane, Indolene And Gasoline Fuels in a Single-Cylinder Research Engine", Journal of engineering for gas turbines and power, September 2008, Vol.130.
- ²²⁴ Nygren et al, "Three-Dimensional Laser Induced Fluorescence of Fuel Distributions in an Hcci Engine", Proceedings of the combustion institute, Vol.29, 2002, pp 679-685.
- ²²⁵ Olsson, J.O., Tunestal, P., Johansson, B., Fiveland, S., Agama, R., Willi, M., and Assanis, D., 2002, "Compression Ratio Influence on Maximum Load of a Natural Gas Fueled HCCI Engine", SAE paper 2002-01-0111.
- ²²⁶ Rashidi, M., "The Nature of Cycle-By-Cycle Variation in the S.I. Engine from High Speed Photographs", Combustion and Flame, Vol. 42, 1981, pp. 111-122.
- ²²⁷ Sauter, W., Nauwerck, A., Han, K-M., Pfeil, J., Velji, A., Spicher, U., "High Speed Visualization of Combustion in Modern Gasoline Engines", Journal of Physics, Conference Series, Vol. 45, 2006, pp. 120-132.
- ²²⁸ Rashidi, M., "The Nature of Cycle-By-Cycle Variation in the S.I. Engine from High Speed Photographs", Combustion and Flame, Vol. 42, 1981, pp. 111-122.
- ²²⁹ Turns, S., "An Introduction to Combustion – Concepts and Applications", McGraw-Hill, International edition, 2000, pp. 457-458.
- ²³⁰ Abraham, J., Williams, F.A., and Bracco, F.V., "A Discussion of Turbulent Flame Structures in Premixed Charges", SAE paper 850345, 1985.
- ²³¹ Cheng, W.K., and Diringer, J.A., "Numerical Modeling of SI Engine Combustion with a Flame Sheet Model", SAE, Paper No. 910268, 1991.
- ²³² Verhelst, S., and Shepperd, C.G.W., "Multi-Zone Thermodynamic Modelling of Spark-Ignition Engine Combustion – An Overview", Energy Conversion and Management, Vol.50, Iss.5, May 2009, pp. 1326-1335.
- ²³³ Turns, S., "An Introduction to Combustion – Concepts and Applications", McGraw-Hill, International edition, 2000, pp. 458.
- ²³⁴ "Burning Velocities of Mixtures of Air with Methanol, Isooctane and Indolene at High Pressures and Temperatures", Combustion and Flame, Vol.48, 1982, pp. 191-210.
- ²³⁵ Goodwin, D.G., "CANtera: An Open-Source, Object-Oriented Software Suite for Combustion".

-
- ²³⁶ Heywood, J. B., “Internal Combustion Engine Fundamentals”, McGraw-Hill Book Company, 1988, pp. 44.
- ²³⁷ Metghalchi, M., and Keck, J.C., “Burning Velocities of Mixtures of Air with Methanol, Isooctane and Indolene at High Pressures and Temperatures”, *Combustion and Flame*, Vol.48, 1982, pp. 191-210.
- ²³⁸ Abraham, J., Williams, F.A., and Bracco, F.V., “A Discussion of Turbulent Flame Structures in Premixed Charges”, SAE paper 850345.
- ²³⁹ Liou, T.M., Hall, M., Santavicca D.A. and Bracco F.V., “Laser Doppler Velocimetry Measurements in Valved and Ported Engines”, SAE paper 840375, 1985.
- ²⁴⁰ Turns, S.R., “An Introduction to Combustion: Concepts and Applications”, McGraw-Hill, 2nd edition, 2000, pp. 215.
- ²⁴¹ Abraham, J., Williams, F.A., and Bracco, F.V., “A Discussion of Turbulent Flame Structures in Premixed Charges”, SAE paper 850345, 1985.
- ²⁴² <http://www.sullivanuav.com/products/alternators.html> , last downloaded 07/15/10.
- ²⁴³ Valkenburgh, V., Nooger and Neville Inc., “Basic Electricity”, John F Rider Publisher Inc., 1954.
- ²⁴⁴ Whitaker, J.C., “The Electronics Handbook”, Taylor and Francis, 2005, pp. 269.
- ²⁴⁵ Sahay, K., and Pathak, S., “Basic Concepts of Electrical Engineering”, New age international, 2006.
- ²⁴⁶ Stiesch, G., “Modeling Engine Spray and Combustion Processes”, Birkhäuser, 2003.
- ²⁴⁷ Shine, A., “Fitting Experimental Data to Straight Lines”, www.che.udel.edu/pdf/FittingData.pdf, last downloaded 10/04/2010.
- ²⁴⁸ Cengel, A.Y., and Cimbala, J.M., “Fluid Mechanics – Fundamentals and Applications”, McGraw-Hill, 2006, pp. 329.